Doctoral theses at NTNU, 2023:178

Ali Payami Golhin

# Functional and Optical Properties of Structured Surfaces in Additive Manufacturing

## Technologies for appearance evaluation in the quality assurance of 3D-printed polymers

Doctoral thesis

NTNU
Norwegian University of Science and Technology
Thesis for the Degree of Philosophiae Doctor
Faculty of Engineering
Department of Manufacturing and Civil Engineering

NTNU
Norwegian University of Science and Technology

Ali Payami Golhin

# Functional and Optical Properties of Structured Surfaces in Additive Manufacturing

## Technologies for appearance evaluation in the quality assurance of 3D-printed polymers

Thesis for the Degree of Philosophiae Doctor

Trondheim, June 2023

Norwegian University of Science and Technology
Faculty of Engineering
Department of Manufacturing and Civil Engineering

NTNU
Norwegian University of
Science and Technology

**NTNU**
Norwegian University of Science and Technology

Thesis for the Degree of Philosophiae Doctor

Faculty of Engineering
Department of Manufacturing and Civil Engineering



ISBN 978-82-326-7060-4 (printed ver.)
ISBN 978-82-326-7059-8 (electronic ver.)
ISSN 1503-8181 (printed ver.)
ISSN 2703-8084 (online ver.)

Doctoral theses at NTNU, 2023:178

Printed by NTNU Grafisk senter

# Preface

The doctoral thesis presented here was written as part of the requirements for a Doctor of Philosophy (Ph.D.) degree to be conferred by the Norwegian University of Science and Technology (NTNU) in March 2023. The author has performed all the work in the presented work, and all external sources or other intellectual property holders are cited following ethical standards in scientific research. The doctoral study was started on 17 October 2019 and is part of a larger research project called ApPEARS program (2019-2023), funded by The European Union's Horizon 2020 research and innovation program under the Marie Skłodowska-Curie grant agreement No. 814158. Most of the work has been completed at NTNU in the Department of Manufacturing and Civil Engineering and at The Norwegian Color and Visual Computing Laboratory in the Department of Computer Science. In the context of ApPEARS, part of the time was spent at the Technical University of Denmark - DTU, as well as the Fogra research institute for media technologies in Germany. However, the project has also involved a wide range of academic, industrial, and private institutions:

**Beneficiaries:**

Norges Teknisk-Naturvitenskapelige Universitet (NTNU), Norway
Danmarks Tekniske Universitet (DTU), Denmark
Fogra Forschungsinstitut für Medientechnologien e.V., Germany
University of Leeds (LEEDS), UK
University of the West of England, Bristol (UWE), UK
Linköpings Universitet (LIU), Sweden
Fraunhofer-Gesellschaft zur Förderung der angewandten Forschung e.V (FHG), Germany
Conservatoire national des arts et métiers (CNAM), France

**Partner Organizations:**

Canon Production Printing (CPP), Netherlands
L'Oréal (LOREAL), France
Technische Universität Darmstadt (TUDA), Germany
Physikalisch-Technische Bundesanstalt (PTB), Germany
Stratasys LTD (STRATASYS), Israel
Merck KGaA (MERCK), Germany
3D Life Print (3DLP), UK
Barbieri electronic OHG des Barbieri Siegfried & C. (BAEL), Italy

This work was supervised primarily by Professor Are Strandlie of the Department of Manufacturing and Civil Engineering at NTNU. Co-supervision of the project was provided by Professor Kristian Martinsen (NTNU), Professor Sotirios Grammatikos (NTNU), Associate Professor Aditya Suneel Sole (NTNU), Dr. David Bue Pedersen (DTU). Nine peer-reviewed research papers have either been submitted for publication or have already been published as part of this study, presenting a detailed analysis of laboratory experiments, numerical modeling, and statistical analysis.

Ali Payami Golhin

Gjøvik, Norway
March 2023

ApPEARS
APPEARANCE PRINTING
European Advanced Research School

Funded by the Horizon 2020 programme
of the European Union. Grant # 814158

## Acknowledgments

This thesis has been written as part of the Appearance Printing - European Advanced Research School (ApPEARS) program as an Early Stage Researcher (ESR) 14. ApPEARS is funded by The European Union's Horizon 2020 research and innovation program under Marie Skłodowska-Curie (grant agreement No. 814158). This Ph.D. program aimed to define a method for measuring the optical properties of structured surfaces, focusing on the appearance of 3D-printed objects. ApPEARS is a collaboration among 16 academic and industrial partners as part of a European consortium. The Ph.D. project was conducted at the Advanced and Sustainable Engineering Materials Laboratory (ASEM-lab) and the Norwegian Color and Visual Computing Laboratory at the Norwegian University of science and technology (NTNU) in Gjøvik. Particular collaborations have been conducted as ApPEARS secondments with the Department of applied mathematics and computer science (DTU Compute) and Department of Mechanical Engineering (DTU Mechanical Engineering) at the Technical University of Denmark (DTU), along with the Fogra Forschungsinstitut für Medientechnologien e.V. in Germany.

My first and foremost thanks go to my dissertation supervisor, Professor Are Strandlie, for his patience, guidance, and support throughout my doctoral journey. I would like to thank my co-supervisors Professor Sotirios Grammatikos, Associate Professor Aditya Suneel Sole, Dr. David Bue Pedersen (DTU), and Professor Kristian Martinsen (NTNU) for their valuable suggestions and support. I would like to thank the members of my dissertation committee, Professor Stergios Goutianos, Associate Professor Kaida Xiao, and Associate Professor Doriana Marilena D'Addona, for their valuable input and feedback.

I am grateful to all ApPEARS members, especially Professor Jon Yngve Hardeberg, Anne Hilde Ruen Nymoen, Anneli T. Østlien, Dr. Jeppe Revall Frisvad, Professor Philip John Green, Dr. Andreas Kraushaar, Majid Ansari-Asl, Riccardo Tonello, Tanzima Habib, Donatela Saric, and Abigail Trujillo. I would like to thank my colleagues at the Department of Manufacturing and Civil Engineering, Pål Erik Endrerud, Kenneth Kalvåg, and Tor Erik Nicolaisen, for their time and assistance at the Additive Manufacturing laboratory "AddLab". I am also grateful to Torbjørn Skogsrud and Iver Eugen Jensen for their exceptional leadership. Thanks to Jens Fossan Tingstad, Tanjir Alam, and Markus Sebastian Bakken Storeide for their friendly approach and interesting discussions.

Finally, I would like to extend my appreciation to my family and friends for their love and support. Especially tremendous thanks to my beloved Elin Radinia for her patience and enormous support throughout this journey.

## Abstract

Quality assurance of additively manufactured parts requires assessment of appearance and surface finish quality. Appearance investigation is a primary step to ensure that the manufactured parts meet the required structural, functional, and dimensional specifications, as well as possess the desired aesthetic qualities. Among the attributes considered when assessing an appearance are color, gloss, haze, translucency, texture, and surface finish. In advanced manufacturing, this process is particularly critical in industries where consumer perception and brand image are crucial, such as biomedical, automotive, aerospace, and consumer-oriented applications.

This thesis explores studies concerning structured surfaces in the additive manufacturing of polymers. During this project, the primary components of the manufacturing process were examined and considered, including materials, design, production, quality control, and optimization. Experimental and statistical analyzes were conducted to determine the optical and functional properties of the additively manufactured layers and how primary processing parameters affect additive manufacturing. A number of additive manufacturing (AM) machines were investigated, including Fused Filament Fabrication (FFF), Material Jetting (MJT), Stereolithography (SLA), and Selective Laser Sintering (SLS). PolyJet as an MJT technology was considered the specialization. Several conclusions were drawn from the investigations and findings are reported for further development of PolyJet technology.

An optimization and enhancement method has been developed to improve the properties of the material and the appearance of the final parts over a more extended period. Several properties were considered, such as optical properties, mechanical properties, life cycle response, and implementation of digital materials used for prototyping, medical purposes, and harsh environmental applications. A long-term descriptive study examined the color appearance, tensile behavior, and glass transition temperature of MJT objects in weathering chambers. Specific challenges were identified, and solutions were proposed according to Taguchi analysis to meet the quality goal of advanced manufacturing.

An extensive literature review was conducted to examine the surface characteristics of 3D-printed objects with a particular focus on surface roughness. A comparative study has been conducted to determine the manufacturing factors influencing the lifetime, surface quality, and dimensional accuracy. Further investigations addressed these challenges, resulting in a comprehensive overview of the available AM techniques and identifying the most critical parameters influencing surface roughness.

We have addressed the complexity of appearance assessment and the need for interpreting data and correlating them using multivariate statistical analysis. It has been discussed how printing parameters should be incorporated into advanced appearance modeling, taking into consideration that MJT objects possess complex appearances, are semi-translucent, and require a comprehensive study of their appearance. For instance, the build orientation and wedge angle determine whether we use cost-effective reflectance models, such as bidirectional reflectance distribution function (BRDF), or more sophisticated, accurate, and expensive models, such as bidirectional surface scattering distribution functions (BSSRDF), depending on the application requirements. In addition, it has been demonstrated that MJT is a promising technique that provides realistic objects that have very low appearance deficiencies, which is necessary for expanding the application of additive manufacturing.

Many other aspects of appearance in additive manufacturing were examined in conceptual investigations, including gloss, haze, translucency, texture, and reflectance modeling. This led to a deeper understanding of total control over appearance during prototyping and design. An industry 4.0 manufacturing environment will rely heavily on the latter. Compared to the other studies examining optical properties, these investigations focused primarily on appearance behavior rather than general applications in optics or for mechanical purposes. The differences and challenges of these results are more relevant to human perception of appearance than laser-based applications in photonics.

**Keywords:**

Additive Manufacturing, Material Jetting, Dynamic Mechanical Analysis, Tensile test, Appearance, Surface modification

# Sammendrag

Kvalitetssikring av additivt produserte deler krever vurdering av utseende og overflatekvalitet. Utseendeundersøkelse er et essensielt skritt for å sikre at de produserte delene oppfyller de nødvendige strukturelle, funksjonelle og dimensjonale spesifikasjonene, samt at delene har de ønskede estetiske kvalitetene. De vurderte egenskapene er farge, glans, uklarhet, gjennomskinnelighet, tekstur og overflatefinish. I avansert produksjon er denne prosessen spesielt kritisk i bransjer der forbrukeroppfatning og merkevareimage er avgjørende, for eksempel innenfor biomedisinske anvendelser, bilindustri, romfart og forbrukerorienterte applikasjoner.

Denne avhandlingen dreier seg om å studere strukturerte overflater i additiv produksjon av polymerer. I løpet av dette prosjektet ble de primære komponentene i produksjonsprosessen undersøkt og vurdert, inkludert materialer, design, produksjon, kvalitetskontroll og optimalisering. Eksperimentelle og statistiske analyser ble utført for å bestemme de optiske og funksjonelle egenskapene til de additivt produserte lagene og hvordan primære prosessparametere påvirker additiv produksjon. En rekke additive manufacturing (AM)-maskiner ble undersøkt, eksempelvis Fused Filament Fabrication (FFF), Material Jetting (MJT), Stereolithography (SLA) og Selective Laser Sintering (SLS). PolyJet som en MJT-teknologi har blitt spesielt fokusert på. Flere konklusjoner og funn som kan bidra til videreutvikling av PolyJet-teknologien har blitt rapportert.

En optimaliserings- og forbedringsmetode er utviklet for å forbedre egenskapene til materialet og utseendet til de endelige delene over en lengre periode. Flere egenskaper ble vurdert, for eksempel optiske egenskaper, mekaniske egenskaper, livssyklusrespons og implementering av digitale materialer brukt til prototyping, medisinske formål og oppførsel i krevende fysiske miljø. En beskrivende studie som gikk over lengre tid undersøkte fargeutseendet, strekkoppførselen og glassovergangstemperaturen til MJT-objekter i forvitringskamre. Spesifikke utfordringer ble identifisert, og løsninger ble foreslått i henhold til Taguchi-analyse for å møte kvalitetsmål relevant for fremstilling av avanserte produkter.

En omfattende litteraturgjennomgang ble utført for å undersøke overflateegenskapene til 3D-printede objekter med spesielt fokus på overflateruhet. En sammenlignende studie er utført for å bestemme produksjonsfaktorene som påvirker levetiden, overflatekvaliteten og dimensjonsnøyaktigheten. Ytterligere undersøkelser tok for seg disse utfordringene, noe som resulterte i en omfattende oversikt over tilgjengelige AM-teknikker og identifisering av de mest kritiske parametrene som påvirker overflateruheten.

Vi har tatt opp kompleksiteten i en vurdering av utseendet og behovet for å tolke data og korrelere dem ved hjelp av multivariat statistisk analyse. Det har blitt diskutert hvordan utskriftsparametere bør inkorporeres i avansert utseendemodellering, tatt i betraktning at MJT-objekter har komplekst utseende og er halvgjennomsiktige.. For eksempel avgjør orienteringen av de additivt tilvirkede lagene og kilevinkelen om vi bruker kostnadseffektive reflektansmodeller, for eksempel toveis reflektansfordelingsfunksjon (BRDF), eller mer sofistikerte, nøyaktige og kostbare modeller, for eksempel toveis flatespredningsfordelingsfunksjoner (BSSRDF), avhengig av den aktuelle anvendelsen. I tillegg har det blitt demonstrert at MJT er en lovende teknikk som gir realistiske objekter som har svært få mangler med tanke på utseendet, noe som er nødvendig for å utvide bruken av additiv produksjon.

Mange andre aspekter ved utseende i additiv produksjon ble undersøkt i konseptuelle undersøkelser, inkludert glans, uklarhet, translucens, tekstur og refleksjonsmodellering. Dette førte til en dypere forståelse av total kontroll over utseende under prototyping og design. Et industri 4.0 produksjonsmiljø vil avhenge sterkt av sistnevnte. Sammenlignet med de andre studiene som undersøkte optiske egenskaper, fokuserte disse undersøkelsene først og fremst på utseendeatferd i stedet for generelle anvendelser innen optikk eller for mekaniske formål. Forskjellene og utfordringene til disse resultatene er mer relevante for menneskelig oppfatning av utseende enn laserbaserte applikasjoner innen fotonikk.

## List of Abbreviations and Nomenclature

3DP: 3D Printing
3DS: 3D Scanning
3SPTM: Scan, Spin, and Selectively Photocure
ABS: Acrylonitrile Butadiene Styrene
AM: Additive Manufacturing
ANN: Artificial Neural Networks
ANOM: Analysis of Means
ANOVA: Analysis of Variance
APF: Arburg Plastic Freeforming
AR: Anisotropic Reflectance
ASA: Acrylonitrile Styrene Acrylate
BJ: Binder Jetting
BO: Build Orientation
BRDF: Bidirectional Reflectance Distribution Function
BSDF: Bidirectional Scattering Distribution Function
BSSRDF: Bidirectional Scattering-Surface Reflectance Distribution Function
BTDF: Bidirectional Transmittance Distribution Function
CAx: Computer-Aided technology
CB: Carbon Black
CCT: Correlated Color Temperature
CDLP: Continuous Direct Light Processing
CIE: The International Commission on Illumination
CLIP: Continuous Liquid Interface Production
CLSM: Confocal Laser Scanning Microscope
CMM: Coordinate Measuring Machines
CMYK-W: Cyan, Magenta, Yellow, Black, and White
CNC: Computer Numerical Control
CQA: Critical Quality Attribute
DED: Directed Energy Deposition
DfAM: Design for Additive Manufacturing
DIW: Direct-Ink-Writing
DLF: Directional Light Production
DLP: Digital (Direct) Light Processing
DM: Digital material
DMA: Dynamic Mechanical Analysis
DMD: Direct Metal Deposition
DoD: Drop on Demand
DoE: Design of experiment
DPP: Daylight Polymer Printing
DTAM: Digital Thread in Additive Manufacturing
E-Modulus: Elastic Modulus
ED: Energy Density
FDM: Fused Deposition Modeling
FEP: Fluorinated Ethylene Propylene
FFF: Fused Filament Fabrication
FPT: Fringe Projection Technique
FV: Focus Variation
GLM: Generalized Linear Model
GRF: General Reflectance Function
GU: Gloss Unit
HDPE: High-Density Polyethylene
HL: Hot Lithography
HSS: High-Speed Sintering
HVS: Human Visual System
LC: 3D Laser Coating
LCD: Light Crystal Display
LENS: Laser Engineered Net Shaping
LOC: Lab-on-chip
LOM: Laminated Object Manufacturing
LPBF: Laser Powder Bed Fusion
MEMS: Microelectromechanical System
MEX: Material Extrusion Additive Manufacturing
MJF: Multi Jet Fusion
MJP: MultiJet Printing
MJT: Material Jetting
MPVP: Mask-Projection Vat Photopolymerization
NPJ: NanoParticle Jetting

O3DP: Optical 3D Printing
PA: Polyamides
PAEK: Polyaryletherketone
PBF: Powder Bed Fusion
PBS: Polybutylene Succinate
PC: Polycarbonate
PCA: Principal Component Analysis
PCL: Polycaprolactone
PDMS: Polydimethylsiloxane
PE: Polyethylene
PEEK: Polyetheretherketone
PEI: Polyetherimide
PEKK: Polyetherketoneketone
PET: Polyethylene Terephthalate
PLA: Polylactic Acid
PMMA: Polymethyl Methacrylate
PP: Polypropylene
PPP: Primary Processing Parameters
PPFT: Post-Production Finishing Techniques
PPSF: Polyphenylsulfone
PS: Polystyrene
PSO: Particle Swarm Optimization
PTFE: Polytetrafluoroethylene
PVA: PolyVinyl Alcohol
PVC: Polyvinyl Chloride
RRP: Roughness Reduction Percentage
RSM: Response Surface Methodology
SDL: Selective Deposition Lamination
SEM: Scanning Electron Microscope
SGC: Solid Ground Curing
SHS: Selective Heat Sintering
SLA: Stereolithography
SLS: Selective Laser Sintering
SOS: Symbiotic Organism Search
SRQ: Sub-Research Questions
SPD: Spectral Power Distribution
SVBRDF: Spatially Varying Bidirectional Reflectance Distribution Function
TCS: Test Color Samples
$T_g$: Glass Transition Temperature
TPP: Two-photon Photopolymerization
TPU: Thermoplastic Polyurethane
TSR: Tele-Spectroradiometer
UAV: Unmanned Aerial Vehicle
UV: Ultraviolet
VPP: Vat Photopolymerization
XMT: X-ray Micro-computed Tomography

# Contents

# List of Figures

# List of Tables

## Appended publications and contribution

This thesis is supported by the following publications, which are provided as appendices.

**Journals**

I. A. P. Golhin, A. Strandlie, and P. J. Green, The influence of wedge angle, feedstock color, and infill density on the color difference of FDM objects, Journal of Imaging Science and Technology, 65(5): 1-15 (2021). https://doi.org/10.2352/J.ImagingSci.Technol.2021.65.5.050408

II. A. P. Golhin, A. S. Sole, A. Strandlie, Color appearance in rotational material jetting, The International Journal of Advanced Manufacturing Technology, 124, 1183–1198 (2023). https://doi.org/10.1007/s00170-022-10536-1

III. A. P. Golhin, R. Tonello, J. R. Frisvad, S. Grammatikos, A. Strandlie, Surface roughness of as-printed polymers: A comprehensive review. The International Journal of Advanced Manufacturing Technology, (2023), Accepted.

IV. A. P. Golhin, C. Srivastava, A. Strandlie, A. S. Sole, S. Grammatikos, Effects of accelerated aging on the appearance and mechanical performance of materials jetting products. Materials and Design, 228, 111863 (2023). https://doi.org/10.1016/j.matdes.2023.111863

V. A. P. Golhin, A. Strandlie, Appearance evaluation of digital materials in material jetting, Optics and Lasers in Engineering, 168, (2023) 107632. https://doi.org/10.1016/j.optlaseng.2023.107632

VI. A. P. Golhin, A. Strandlie, Optical properties of tilted surfaces in material jetting, Optics and Laser Technology, (2023), Submitted.

VII. A. P. Golhin, A. S. Sole, A. Strandlie, BRDF representation in response to the build orientation in 3D-printed digital materials, Journal of Manufacturing Processes, (2023), Submitted.

**Conferences**

VIII. A. P. Golhin, C. Srivastava, J. F. Tingstad, A. S. Sole, A. Strandlie, S. Grammatikos, Additive manufacturing of multilayered polymer composites: Durability assessment, the 20th European Conference on Composite Materials (ECCM20), École Polytechnique Fédérale de Lausanne (EFPL), Switzerland, 26-30 June 2022. https://doi.org/10.5075/epfl-298799_978-2-9701614-0-0

IX. A. P. Golhin, A. Strandlie, A. S. Sole, Evaluation of surface texture in material jetting, euspen's 23rd International Conference & Exhibition (ICE 2023), Technical University of Denmark (DTU), Copenhagen, Denmark, 12-16 June 2023, Accepted.

Other relevant contributions (not formally part of the submitted dissertation)

- P. Golhin, Generation of micro- and nano-textured surfaces. European Commission. 2021.
- P. Golhin, 3D-printing og brobygging (NTNU). Forskningstorget i Gjøvik [Kunstnerisk og museal presentasjon]. NORGES FORSKNINGSRÅD, NTNU, Medarrangører: Gjøvik kommune og Vitensenteret Innlandet; Gjøvik. 2021-09-22 - 2021-10-03.
- P. Golhin, Surface roughness of 3D-Printed models as a function of the manufacturing process. The Colorlab workshop on Measuring, Understanding, and Reproducing Material Appearance. The Norwegian Color and Visual Computing Laboratory; Gjøvik. 2021-10-26 - 2021-10-26.

## Declaration of authorship

**Publication I**
A. P. Golhin designed and conducted experiments and the analysis and wrote the article. A. Strandlie and P. J. Green contributed to the paper by editing the manuscript, engaging in productive discussions, and giving valuable feedback, comments, and suggestions.

**Publication II**
A. P. Golhin designed and performed experiments and the analysis and wrote the article. A. S. Sole and A. Strandlie contributed to the paper by reviewing the manuscript, engaging in productive discussions, and giving valuable feedback, comments, and suggestions.

**Publication III**
A. P. Golhin designed the structure of the review paper, analyzed the results, and wrote the article. R. Tonello contributed to the writing of the article and participated in manufacturing the samples. A. Strandlie, J. R. Frisvad, and S. Grammatikos contributed to the paper by reviewing the manuscript, engaging in productive discussions, and giving valuable feedback, comments, and suggestions.

**Publication IV**
A. P. Golhin designed and conducted the laboratory experiments, analyzed the data, and wrote the article. C. Srivastava took part in the design, performing, and writing portion of the mechanical testing. A. Strandlie, A. S. Sole, and S. Grammatikos contributed to the paper by reviewing the manuscript, engaging in productive discussions, and giving valuable feedback, comments, and suggestions.

**Publication V**
A. P. Golhin designed and performed experiments and the analysis and wrote the article. A. Strandlie contributed to the paper by reviewing the manuscript, engaging in productive discussions, and giving valuable feedback, comments, and suggestions.

**Publication VI**
A. P. Golhin designed and performed experiments and the analysis and wrote the article. A. Strandlie contributed to the paper by reviewing the manuscript, engaging in productive discussions, and giving valuable feedback, comments, and suggestions.

**Publication VII**
A. P. Golhin designed and performed experiments and the analysis and wrote the article. A. S. Sole and A. Strandlie contributed to the paper by reviewing the manuscript, engaging in productive discussions, and giving valuable feedback, comments, and suggestions.

**Publication VIII**
A. P. Golhin designed and conducted the laboratory experiments, analyzed the data, and wrote the article. C. Srivastava and J. F. Tingstad took part in the design, performing, and writing portion of the mechanical testing. A. S. Sole, A. Strandlie, and S. Grammatikos contributed to the paper by reviewing the manuscript, engaging in productive discussions, and giving valuable feedback, comments, and suggestions.

**Publication IX**
A. P. Golhin designed and performed experiments and the analysis and wrote the article. A. Strandlie and A. S. Sole contributed to the paper by reviewing the manuscript, engaging in productive discussions, and giving valuable feedback, comments, and suggestions

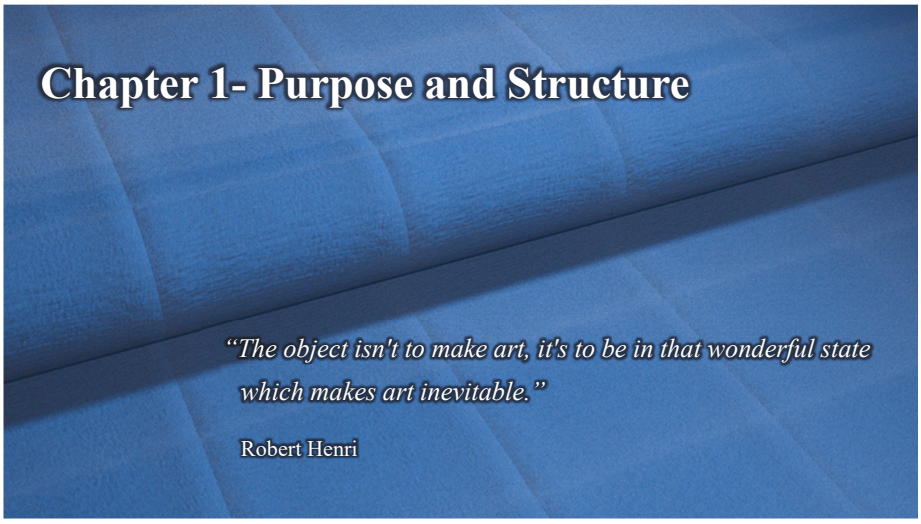


An introduction to the purpose and structure of this dissertation is presented in this chapter. We begin by describing the role of this project in the ApPEARS program. It is followed by a discussion of the project approach and objectives, including the problem statement, motivation, research questions, and goals and scopes. The project contents are further discussed by describing the research design and thesis structure.

# 1. Introduction

The International Commission on Illumination (CIE[1]) describes the term *appearance* as an “aspect of visual perception through which an object is perceived to have attributes such as size, shape, color, texture, gloss, transparency, and opacity” [1]. In the field of perception research, the mechanisms that enable humans to perceive surface features are scientifically referred to as appearance, which is described as "the aspect of visual perception that refers to the recognizing of objects" [2]. According to Pointer [3], appearance consists of physical, physiological, and psychological aspects. A physical property of light is the spectral and spatial distribution of the light emanating from the surface of an object, determined by its optical properties. It is physiological, i.e., the stimulation of the Human Visual System (HVS) by the light, and the sensory response, which enables us to perceive light and interpret our surroundings through interaction with objects within our field of vision, deducing information about a scene [4]. As a final consideration, the psychological aspect of appearance involves the capability to interpret the sensed stimuli resulting from long-term training.

While advances have been made in acquiring [5] and modeling [6] optical properties of materials, the surface quality of 3D-printed objects is mainly unknown to be related to the objective physical properties of a scene. It explains the increasing interest in appearance research in additive manufacturing. This dissertation examines several aspects associated with the appearance of additive manufacturing objects, which are discussed in detail in this introductory chapter.

## 1.1. ApPEARS project

This Ph.D. work is part of ApPEARS project. ApPEARS-ITN is an EU-funded project that aims to address fundamental problems in appearance 3DP by developing user-centered tools and methods that improve our understanding of visual appearance for both computer-generated and printed objects. The program was focused on four main objectives: measuring and evaluating material properties (WP2), reproducing complex surface appearances (WP3), and prediction model and reducing errors in reproduction (WP4), as shown in Figure 1. To utilize this complete reproduction workflow in influential application domains, end-user applications must be developed, along with specialized training (WP5). Accordingly, this Ph.D. project was part of WP5. Ensuring the specification and accurate reproduction of desired visual appearances of 2.5D/3D manufactured objects will substantially improve the workflows for emerging advanced manufacturing technologies.

[1] Commission Internationale de l'Éclairage

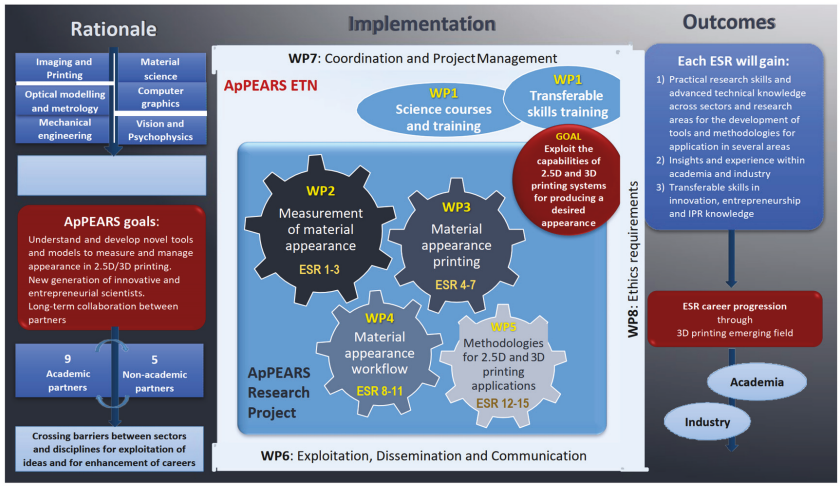


Figure 1. An overview of defined projects, goals, and work packages (WP) in the ApPEARS program [7].

## 1.2. Project approach and objectives

### 1.2.1. Problem statement

Over the past few years, additive manufacturing (AM, often referred to as"3D printing") has received substantial attention from academia and industry for its application to various materials, including metals, ceramics, and polymers. Its primary limitation is its inability to produce objects with a surface quality equivalent to conventional manufacturing processes. Based on 1504 surveys conducted in 2021 [8], 29% stated that poor quality of parts discouraged users from using 3D printing (3DP) more frequently, which was the second major obstacle to AM growth after the cost factor. There is a lack of literature regarding surface modification in the AM process before post-processing, which is very crucial in enhancing the performance of 3D-printed structures. In addition to academic demands, the appearance of AM objects has a significant impact on commercial products and the future of additive manufacturing. According to Hubs' report [9] on the state of 3DP in 2022, 29 % of users had used 3DP for aesthetic or end-use parts, showing a significant growth compared to 21 % in 2021. 3DP is currently used mainly as a tool for prototyping, but aesthetic or functional parts are not far behind.

### 1.2.2. Motivation

The surface of a manufactured object plays a significant role in determining its quality. Surface quality can have a substantial impact on the success or failure of a product, depending on its requirements and application. A high-quality surface must be as smooth as expected, free from defects, and have excellent conformance to the design in both functional and appearance properties. There are often difficulties in meeting the requirements for surface quality. The ability of humans to assess the appearance of objects has been highly developed over evolution. We can distinguish between materials based on their relative

qualities, such as their softness or hardness, flexibility or rigidity, smoothness or roughness, or whether they are fresh or rotten. Humans still perform this task better than most machines because it requires more complex skills such as vision, pattern recognition, and decision-making. However, this task should be automated to realize Industry 4.0 and 5.0 concepts.

Furthermore, humans lack any special inherent abilities for evaluating objects accurately [10], and a complex technical process is required to meet quality requirements for most products. Therefore, it is necessary to find additional clues about the nature of appearance perception itself. It is possible to reduce errors and biases in evaluating the quality of surfaces by using metrics to assess their appearance and functional properties, which was the focus of this research project.

### 1.2.3. Research questions

As a result of integrating material science, mechanical engineering, and color science knowledge in a novel approach to advanced manufacturing, how can the optical properties of structured surfaces manufactured by 3D printers be enhanced in terms of their appearance and functionality?

Four sub-research questions (SRQ) supported the primary research objective, as follows:

- SRQ1: Using additive manufacturing technologies to prepare structured surfaces
- SRQ2: Analyzing the optical and functional properties of the surfaces
- SRQ3: Describing the possible correlation between the basic parameters of material texturing and the functional and optical properties of the surface
- SRQ4: Discussing the possible application of the correlations for the generation of surface texturing with enhanced optical and functional properties

### 1.2.4. Aim and scopes

The principal focus of this thesis is the appearance, primarily color and texture, and functional properties, including elastic modulus (E-modulus), glass transition temperature ($T_g$), and dimension accuracy of polymeric surfaces manufactured by 3D printers. Polymers have been chosen among the various materials manufactured by 2.5D and 3D printers due to their extensive capabilities to reproduce multiple appearances. For this purpose, the primary processing parameters for the most used additive manufacturing techniques, including FFF, SLA, SLA, and MJT, have been studied. In this dissertation, AM is frequently referred to as 3D printing due to the focus on 3D-printed objects. The correlation between manufacturing parameters in FFF and MJT and the surface evaluation results has been explored experimentally, and suggestions have been made for improving the surface quality. According to the UN's recommendations for production and manufacturing (Goal 12) [11], “sustainable consumption and production is about doing more and better with less” and “increasing resource efficiency”. Through additive manufacturing, it is possible to produce better structures with fewer materials in the desired and needed voxels. This will contribute to the UN's sustainability goal 12 by improving the quality of AM products with higher durability. Accordingly, a short-term and long-term study of MJT and evaluating as-printed parts has been conducted. Methodologies and technologies describing the effects of each parameter and their application to enhancing structured surfaces in advanced manufacturing are examined, considering issues arising from uncertainties regarding AM objects. This study focused on the primary process parameters, including pre-processing and processing, to improve the as-printed surface structure of printed parts.

## 1.3. Project contents

### 1.3.1. Research design

As Rowley [12] suggested, the research design refers to an action plan that outlines a path from questions to conclusions and ensures that the research will achieve the desired outcome.

Figure 2 illustrates the scientific approach and the research methodology used in this study. It represents how this dissertation was designed using a four-step iterative approach to achieving this goal. The initial step in this methodology was to identify the research problem by reviewing the current state of the art. As part of determining a state of the art, a review of existing studies on AM technologies, appearance attributes, and application of 3DP technologies for material appearance was conducted, supported by a literature review regarding the texture and roughness of AM polymers. It specified the basis for recognizing the motivation and defining the research objectives. The method was employed for each SRQ to address the primary research question.

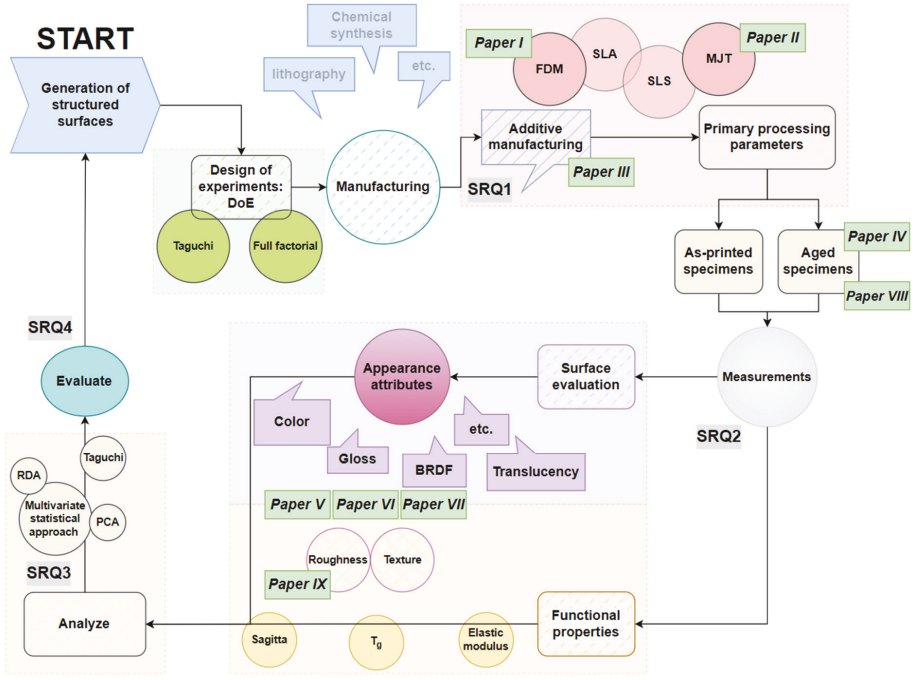


Figure 2. The iterative surface enhancement workflow under four sub-research questions (SRQ) scopes.

According to Figure 2, the research design method comprised the probability of an entirely new iteration based on better identification of the problem based on the research findings. For SRQ1, prototypes were designed and developed based on the possibility of reproducing structured surfaces that were enhanced both in appearance and functionality. To study the as-printed parts (SRQ1-2), the selected AM methods have been used to manufacture several specimens with consideration of their primary processing parameters (PPP), followed by the study of the lifecycle properties of the parts in an accelerated weathering chamber for a short period (SRQ2-3), and by the optimization of the printing process for long-term functionality (SRQ4). As part of the exploratory research, further surveys were conducted through documentation reviews for all significant AM techniques for polymers (SRQ1). At the same time, both SRQ1 and SRQ2 were also studied through experimental evaluations with prototypes at different iterations. The diagram in Figure 3 illustrates the contribution of the thesis papers to the functional and optical aspects of the assessment of the structured surfaces in the thesis.

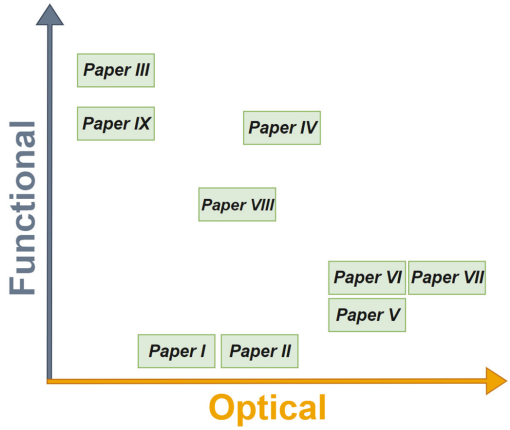


Figure 3. The contribution of the papers in the thesis.

### 1.3.2. Thesis structure

Appended articles have been placed in an extended context to address the research questions. A total of six chapters is included in the thesis. The first chapter describes the state of the art, the research motivation, and the questions. The second chapter describes the theoretical background behind additive manufacturing for appearance 3DP to provide context for the study. Chapter three discusses the surface quality and appearance in 3DP methods. Chapter four considers the scientific approach to surface optical and functional properties and the measurement methods employed during the research. Chapter five concludes with the findings from the appended articles summarized and discussed for each sub-research question. Chapter six concludes the evaluation process and describes the future perspectives.

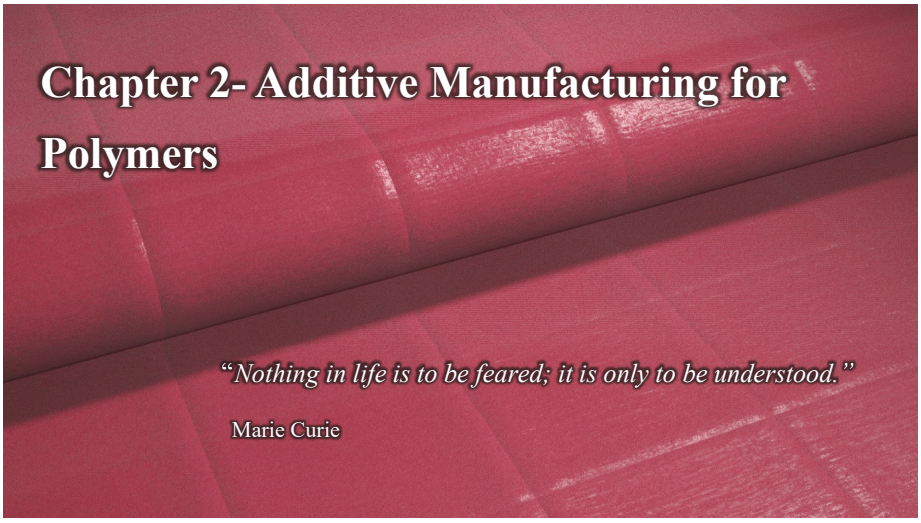


An overview of the theory behind AM for appearance 3DP is presented in this chapter to provide context for the research that focuses primarily on the surface quality of polymers. A description of the surface characteristics and improvements in AM parts is presented at the end of this chapter, along with recent developments, ideas, and state of the art technologies. The structure of this chapter is a concise version of the review paper (Appendix-*Paper III*).

# 2. Additive Manufacturing

## 2.1. Background

The term additive manufacturing refers to the fabrication of 3D objects by joining materials, frequently layer by layer, in accordance with a 3D model. This approach contrasts with subtractive manufacturing methods. AM techniques are also known as additive techniques, additive fabrication, rapid prototyping, additive processes, freeform fabrication, layer manufacturing, and additive layer manufacturing [13]. Compared to conventional 2D printing, 3DP offers greater degrees of appearance creativity in terms of color, gloss, transparency, texture, and goniochromatic effects. In addition to combining materials of different opacities, thicknesses, and finishes, microfacets can also be added to the object surface to control the direction of reflection. The advent of AM revealed many new possibilities. It is a complementary option to the subtractive methods, which have dominated the fabrication and production sector since the first industrial revolution [14, 15]. AM offers enhanced functional device integration possibilities through a broad range of 3D geometries from nanometers to centimeters (the mesoscale). 3DP technologies promise to build parts out of various materials and shapes [16].

Certain AM technologies make printing very accurate, adjustable, and cost-effective compared to conventional prototyping processes for polymeric materials. There are three stages at which it is possible to enhance the microstructure and material appearance of the printed objects: pre-processing, processing, and post-processing (see ) [17]. According to Wohlers [14], the post-processing of samples should be restricted to first-level processes when examining PPPs. Our study focused on pre-processing and processing, as-printed process zone in Figure 4, to study the manufacturing parameters.

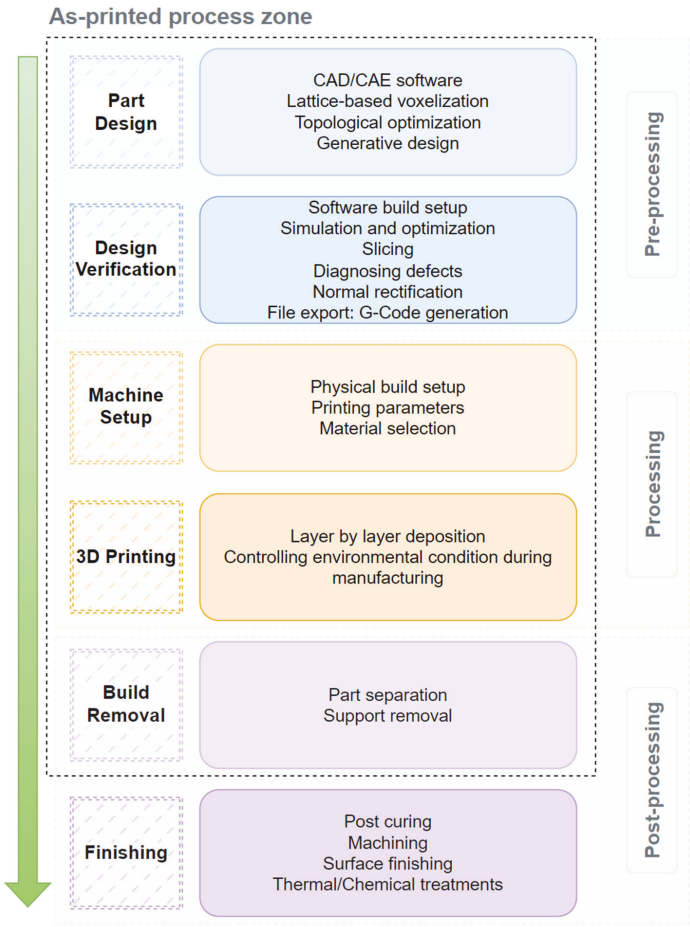


Figure 4. Workflow of additive manufacturing.

Manufacturing new-generation functional devices inspired by the digitalization of the physical world required a new outlook on various materials and manufacturing technologies with the desired surface condition. To date, many approaches have been followed by the industry to provide novel materials and structures, like casting and laser and computer-aided mechanical cutting. However, these techniques are still struggling to cope with the upscaling and complex production of novel systems and devices such as metamaterials [18-21], integrated micro-optics [22], and lab-on-chips (LOCs) [23].

3DP has been classified into seven categories by the ISO/ASTM 52900 Standard in 2021 [24]. Following this standard, Table 1 lists related AM technologies for 3DP polymeric materials with their standard terminologies.

Table 1. A detailed description of polymer AM categories and their characteristics [25-32].

| Process category | Standard abbreviation | Key process | Basic AM principle | Applications |
|---|---|---|---|---|
| Material Extrusion | MEX | FDM / FFF, DIW | The AM process of selectively dispensing material through an orifice or nozzle | Electrical housings/enclosures, prototypes, jigs and fixtures, investment casting patterns, solid monolithic parts, scaffolds, biologically compatible tissue implants, tailored composite materials |
| Material Jetting | MJT | PolyJet, MJP | An AM process that involves selectively depositing droplets of reactive feedstock material to curing with energy, e.g., photopolymer resin and wax | Full-color product prototypes, injection mold-like prototypes, low-run injection molds, medical models |
| Vat Photopolymerization | VPP | SLA, DLP, CLIP | An AM vat process in which liquid photopolymer is selectively cured by light-activated polymerization within a vat | Injection mold-like, polymer prototypes, jewelry (investment casting), dental applications, hearing aids |
| Powder bed fusion | PBF | SLS MJF | The AM process of selectively fusing regions of a powder bed using thermal energy | Functional polymer parts, complex ducting (hollow designs), low-run part production |
| Binder Jetting | BJT | BJ | The AM process involves selectively depositing a liquid bonding agent to fuse powders together | Full-color models, sacrificial models for sand casting |
| Directed Energy Deposition | DED | LENS, DLF, DMD, LC | An AM technique in which thermal energy is focused on melting materials during the process of depositing them | Near-net-shape parts, feature additions, and repair of existing components |
| Sheet Lamination | SHL | UAM, LOM | An AM method in which sheets of material are bonded together to form a part | Composite parts |

This chapter highlights the basics, an overview of the major categories, technical realization, characteristics, advantages, drawbacks, perspectives, and some applications of AM. Attention is given to discussing the differences among types and an ongoing research trend related to appearance 3DP. Four commonly used key processes in appearance printing using polymers are discussed, including FFF, PolyJet, SLA, and SLS, which were used to print several parts of this project. Thermoplastics are the primary polymers in FFF and SLS, whereas thermoset resins are the predominant polymers in MJT and SLA/DLP [29]. In particular, this thesis focuses on using FFF and PolyJet techniques, as outlined in the papers in the appendices.

### 2.1.1. Material Extrusion – FFF Process

Fused filament fabrication (FFF), or fused deposition modeling (FDM), has a significant share of the AM market due to its sizeable economic potential in many industries. This process is commonly used to manufacture polymeric parts from filament feedstock. In FFF, molten polymer is deposited layer by layer through an extrusion nozzle to construct a three-dimensional (3D) object [33]. It would be possible to print objects with various colors and appearances if the nozzle could support multi-material extrusion. Another method uses filament with a predefined appearance [34, 35].

Several advantages make FFF 3DP a popular choice for both consumers and businesses. A few of the main benefits of FF 3DP include: being comparatively inexpensive compared to other 3DP technologies and being easy to use and set up, making them ideal for home users and small businesses. This process is compatible with various materials, including plastics, metals, and composites, which can add color to 3DP [36]. Moreover, FFF parts are highly accurate and repeatable and can be post-processed to achieve a wide range of finishes, including painting and sanding [33]. However, this technology has some disadvantages, including rougher surface finishes, slower printing speed than other 3DP technologies, such as SLA and SLS, and the potential for warping and other dimensional errors [17, 37].

In FFF, the pre-processing parameters include the slice thickness, the infill, the support material, and the type of material. Processing parameters include layer height (thickness), print speed, the size and shape of the nozzle, the speed of extrusion, and infill percentage. The specific parameters will vary based on the printer and software being used. Depending on the material, the correct temperature for the build plate typically ranges between 60 and 80 °C. Usually, the first layer height should be between 0.2 and 0.3 millimeters, the extrusion temperature will vary between 190-220 °C, and the nozzle size is typically 0.4 to 0.6 mm [17, 37, 38]. The review paper (*Paper III*) in the appendices provides more details on the PPPs in the FFF technique.

Many parameters influence the static mechanical properties of the FFF objects, such as filament material, printhead parameters, build platform, and printing environmental conditions. Many materials can be used in the FFF technology, including thermoplastics, metals, ceramics, and composites. Each material has a unique set of properties, which can be exploited to produce a particular part. In FFF, thermoplastics are most used due to their low cost and ease of processing. ABS and PLA are two of the most popular thermoplastics for FFF, and both have high mechanical strength and heat resistance. To choose the suitable material for the 3DP project, it is essential to understand the differences between the two materials. ABS is a thermoplastic that is derived from petroleum [39]. This material is strong, durable, and heat-resistant. The PLA plastic is derived from cornstarch and is a bioplastic. This material is biodegradable, but it is not as strong as ABS. PETG is another thermoplastic derived from petroleum.

Despite its strength, durability, and heat resistance, the material is more expensive [40, 41]. Among other polymers, the significant polymeric feedstock materials include HiPS, PVA, Nylon (PA), PC, PC-ABS, TPU, and PEEK [41]. Polymeric composites are also used in FFF to create parts with specific mechanical and thermal characteristics. A carbon fiber composite, e.g., can be used to construct light and mechanically robust components [41].

### 2.1.2. Material Jetting – PolyJet Process

Material Jetting (MJT), as reported in the ISO/ASTM 52900:2021, fabricates objects by jetting materials onto a build platform in either a Drop on Demand (DoD) or a continuous manner. The jetting process is similar to that of a standard inkjet printer. PolyJet, Multijet printing (MJP), Objet, and XJet's NanoParticle Jetting (NPJ) are the main processes in MJT. Due to the availability of high-resolution MJT printers, it is now feasible to create single parts with a variety of optical properties, such as color, gloss, and even gonio-chromatic effects. A variety of appearance levels can be achieved by printing varnish halftones, arranging printing materials in halftone patterns to create a variety of color shades, or printing microfacets on top of the surface to produce anisotropic reflectance (AR) [42].

With the PolyJet 3DP technology, layers of a liquid photopolymer are jetted onto a build platform in layers as thin as 16 µm. Inkjet heads provide precision by jetting the material in a controlled manner, which results in exceptionally accurate and repeatable results. It is similar to stereolithography but uses ultraviolet (UV) LEDs instead of a single laser beam to cure the photopolymer resin. The UV lamps immediately cure each layer after it is jetted, allowing it to be bonded to the layer below. The printhead is designed to switch between various materials; however, it must be purged of one material before it can be jetted with another. Materials are processed by PolyJet 3D printers in two ways: by material jetting and by photopolymerization. A photopolymerization process uses light to cure photopolymer materials, typically a UV light source. Using a piezoelectric effect, droplets are jetted from the print head across the build platform, depositing material layer by layer [43].

The main advantages of PolyJet printing include printing in various colors and color gradients since it uses a different material for each color. Furthermore, it has the ability to create prints with high levels of detail and the possibility to print large objects. A significant benefit of PolyJet is that there is no heat involved in the 3D printing; hence warping, distortions, and shrinkage are highly unlikely to occur. Because material jetting is not limited by the size of the nozzle, it is also possible to produce parts with highly detailed features and complex geometries. However, it required using support materials [44-46].

The disadvantages are the cost of PolyJet 3D printers and materials, specialized training, and the time needed to print objects using PolyJet 3D printers. Due to the need to jet each layer separately, the build time can be extensive. Furthermore, even tiny particles can cause defects in the printed parts if the build platform is not maintained clean and free of debris. Again, the limited material options and inability to produce large quantities are other disadvantages of MJT [47, 48].

The primary adjustable parameters in the PolyJet technology are resolution, material, layer thickness, printing speed, and material feed rate. The layer thickness is typically the most critical parameter, as it directly impacts the resolution of the print. The material feed rate and build speed factors can significantly impact print time and accuracy. As a result, the print head's functionality and the build platform are essential [49-51].

The drop size, velocity, and curing energy are essential factors corresponding to the photo resin droplets. Drop size refers to the width of individual droplets ejected from the print head. The drop velocity determines how quickly the droplets travel from the print head to the build platform. The curing energy determines how much energy is required to cure a droplet [50].

The PolyJet 3D printer can print a wide variety of photopolymers, from rigid to flexible, opaque to transparent, standard to biocompatible, and has varying degrees of hardness [52, 53]. Photopolymers, and thermoplastics, such as epoxy resins, polyester resins, UV-curable resins, elastomers, and waxes, are among the materials used with PolyJet technology. The most common support materials are water-soluble PVA and breakaway supports. Vero and Tango photopolymers are specific brands of these materials [15, 54].

As a result, prototypes and end-use parts with a wide range of physical and mechanical properties can be produced [55, 56]. For instance, functional polymers such as scaffolds for tissue engineering, multi-material structures, and memory shape polymers are considered for 4D printing [57-59]. While elastomers and thermoplastics are utilized more commonly than photopolymers, photopolymers can aesthetically, physically, and thermally replicate these materials. [60].

### 2.1.3. Vat Photopolymerization – SLA Process

Stereolithography (SLA) photopolymerization involves using a laser to cure a polymer resin exposed to the light source to enable rapid prototyping and small-scale production. With laser beam tracing, a chemical reaction occurs on the surface of a vat of photopolymer resin, ideally resulting in the desired 3D shape. The one-photon energy should stimulate a polymerization reaction within the photosensitive monomer mixture, like acrylate and epoxy-based resins [61, 62]. The required power for polymerization is usually provided by near-UV radiation, but visible light is also possible [63]. 2D layers are created by selectively exposing the material to light and stacking these layers on top of each other, fabricating the 3D structure. This process is followed by a washing operation with a solvent (e.g., isopropyl alcohol) to remove the unexposed material before being post-curing using UV light [16].

In SLA, the surface finish of the objects can be very smooth, precise, and controlled. In addition, it can create very complex shapes that would be difficult or impossible to achieve with alternative technologies. There are also a few disadvantages to this technology, including its relatively low printing speed compared to other 3DP technologies and the fragile and delicate nature of the objects produced. Generally, SLA requires toxic chemicals, which may pose a risk to health and safety [64, 65].

The main parameters affecting the stereolithography process are resin type, wavelength, power, scanning speed, the UV laser's focus, as well as the vat's size and shape [66, 67]. The photopolymer resin type determines the properties of the final print. The viscosity of the resin affects the flow and curing of resins; more viscous resins will flow more slowly and cure more slowly. Depending on the UV laser's wavelength, the photopolymer's absorption coefficient is determined. The absorption coefficient measures how much UV light is absorbed by the photopolymer [68, 69]. In general, the higher the absorption coefficient, the more UV light is absorbed and the faster the photopolymer will cure. The speed at which a photopolymer is cured depends on the power of the UV laser, with higher power indicating a quicker cure time. The thickness of the cured layer is determined by the scanning speed of the UV laser, and slower scanning speeds result in thicker cured layers and lower print

accuracy. UV laser focus determines the width of the cured line, and a narrower focus produces a thinner line [68, 70, 71]. The type of photopolymer used determines the mechanical properties of the cured object, including its toughness, strength, and stiffness [72, 73]. The vat's size and shape determine the cured object's size and shape. Similar to FFF, the build platform temperature during the printing process impacts the flow of resin and the curing process [72, 74, 75].

The most used photopolymers for SLA are epoxy resins, acrylate resins, and polyurethane resins. Some available SLA resins include PC-Like Advanced High Temp, PC-Like Translucent/Clear, ABS-Like Translucent/Clear, ABS-Like Black/White, and PP-Like Translucent White [76]. Photopolymer resins are more expensive than other materials and are hazardous [77].

### 2.1.4. Powder Bed Fusion – SLS Process

Selective laser sintering (SLS) is an exact 3DP technology that employs a laser beam to sinter/fuse/melt fine powder particles together (particle size ∼10–150 μm [78]) selectively to form thin (∼20 μm [79]) layers. A layer-by-layer process is repeated until the model has been completed [80]. Due to high precision, the powder bed fusion (PBF) process has recently received considerable attention from academia and industry. It shapes accuracy in producing complex objects with functional attributes, especially for small-sized parts [81]. Polymer SLS systems build in the liters per hour range, orders of magnitude faster than FFF or SLA equipment. Despite this, the pre- and post-heating procedures are time-consuming. Further post-processing steps might follow, subject to the peculiarities of the particular technological and material variants.

In SLS, traditional manufacturing methods can create complex shapes that would otherwise be difficult or impossible to produce. The principle of using advanced laser sources allows light intensity to melt almost any substance [79]. Thus, polymers [78], metals [82], ceramics [83], and polymers-ceramics composite materials [84] can be fused separately or together using a laser to produce a solid object. However, sintering materials together is not yet fully developed. Some materials are easier to sinter selectively than others to overcome shortcomings like brittleness, porosity, and structural shrinkage [85].

Compared with other 3DP technologies, SLS can create complex lattice-based shape shapes as it does not necessitate support. It makes SLS ideal for fabricating parts with intricate geometries. SLS has some disadvantages, including the need for post-processing to remove un-sintered powder and the possibility of warping due to uneven cooling. Furthermore, printing single prototypes can be both expensive and time-consuming. In some cases, the finished parts may not be as strong or durable as those produced using other manufacturing techniques. Further, SLS is not suitable for large-scale production [86-88].

The main parameters that can be adjusted in selective laser sintering (SLS) include the type of powder material and the laser power, the scanning speed, layer thickness, and the hatching spacing [89, 90]. Several other factors influence the surface quality of SLS components, including the powder quality, the build parameters, and the post-processing [29, 91, 92]. SLS is a versatile technology that can create objects from various materials. In terms of polymers, nylon, and polycarbonate are the most employed powders [15].

## 2.2. Surface characteristics and improvement in AM parts

### 2.2.1. Surface quality in FFF parts

FFF parts suffer from chordal errors or defects due to tessellating the CAD model, causing dimensional variation in FFF parts. The staircase effect causes roughness on the outer surface. Start-stop errors (seams), support structure burrs, and low-dimensional accuracy are other defects that may arise [17, 93]. Accordingly, their surface finish (Figure 5) is not as smooth as that of parts made using other AM methodologies, such as stereolithography (SLA) or selective laser sintering (SLS).

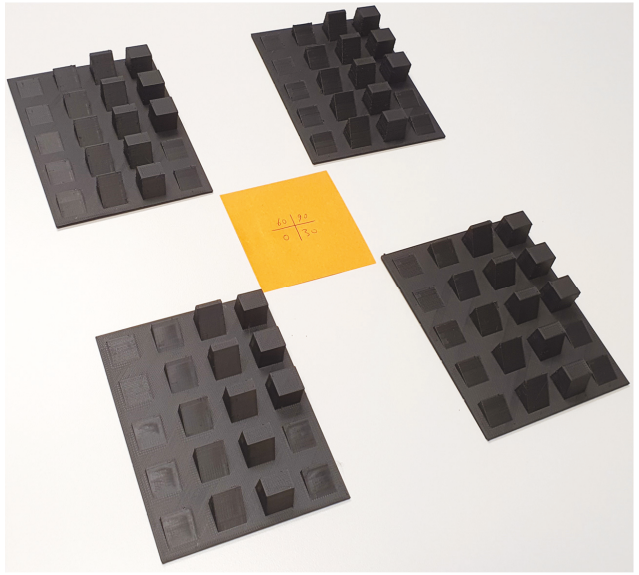

Figure 5. The rough surfaces of FFF-printed samples. Specimens manufactured using black PLA filament, adaptive slicing option on the wedge angles ([0°-90°], 5° step), and different infill densities (0, 30, 60, and 90 % as shown in the center)

The surface modification of FFF-manufactured parts is usually complex and expensive compared to the initial printing cost. In particular, the processes of deliberately modifying the surfaces of polymeric materials through an understanding of slicing and tool-pathing workflow are challenging topics [94, 95]. Researchers are more interested in rapid casting and rapid tooling using FFF [96-98], but the inferior dimensional accuracy and surface quality prevent these applications from taking off. There is a strong correlation between dimensional accuracy and surface finish for replicas. Low dimensional accuracy and inadequate surface finish may prevent manufacturing on a commercial scale of tailored rapid tooling components [41].

However, there are some methods for enhancing the surface finish in FFF objects. The surface finish of an FFF part generally deteriorates with increasing layer thickness, which is the main PPP parameter that

can be controlled. A thinner layer thickness can enhance the surface finish of an FFF part. As a result, manufacturing time and costs may increase [41]. In addition, using a polymer with a higher melting point, e.g., PETG, can improve the surface finish. Thus, the polymer will become more viscous, reducing sagging and warping [99].

The type of support material used also impacts the surface finish of an FFF part. FFF involves building a piece on a platform surrounded by a support structure. In addition to holding the part in place, the support structure prevents warping or sagging. Hence, the type of support material used can affect the surface finish of the component. If the bed is not level, prints will not adhere properly and will likely warp or curl. Poor adhesion to the build plate is another common cause of surface quality problems, caused by an unclean build plate, an incorrect build plate temperature, or an incorrect first layer height. Also, incorrect extrusion temperatures or nozzle sizes can result in surface quality issues [99-101]. For instance, Reddy et al. [102] reported that 80 °C to 100 °C is an optimal model temperature for the studied ABS polymer. In their study, the low adhesion of part material with a build platform under 80 °C and the lower dimensional accuracy above 100 °C were problematic in the FFF process. This project does not include post-processing, such as sanding, polishing, and painting, which can also affect the surface finish of an FFF model.

### 2.2.2. Surface quality in PolyJet parts

The PolyJet 3DP process provides high levels of detail and resolution; however, it cannot generally manufacture lattice-based geometries due to its solidity in infill density set to 100%. The PolyJet models represent smooth and glossy surfaces with consistent colors as materials are mixed in the same layer but with different color cartridges. Furthermore, the parts can also be printed with a variety of different textures, including wood grain and leather grain. A PolyJet 3DP process can produce fine features and a consistent surface finish with little to no visible layer lines [103, 104].

As each droplet of material contains its own mini-pool of ink, the printer can mix and match colors as it lays down each layer. Thus, designers have a great deal of flexibility in the appearance of their parts. As a result, the MJT is an ideal method for applications in which appearance is an essential factor, such as in consumer products or jewelry [105, 106]. It is possible to improve the surface quality of PolyJet parts by using a finer resolution setting during printing. As reported in *Paper II*, the selection glossy finish and a specific color, e.g., black photo resins, can also help to have a more consistent and smoother surface on the as-printed parts. In addition, whenever possible, avoid using a support material on prime surfaces. In most cases, a smoothing agent is used during the post-processing stage to improve surface quality [107].

### 2.2.3. Surface quality in SLA parts

SLA can produce excellent surface quality, depending on the method and materials used. Generally, SLA parts have a smooth surface finish with high accuracy and detailed resolution. SLA is ideal for creating jewelry, medical models, dental implants, and other small objects [108]. However, there can be some issues with warping or curling, particularly with larger parts [109]. Furthermore, SLA printing involves layer-by-layer printing, which limits the surface quality compared to traditional subtractive manufacturing, which provides a machined and polished finish.

SLA 3D printers are widely used in consumer electronics, aerospace, and medical industries, as final products [73, 110]. Therefore, the durability of SLA 3DP is of utmost importance [111]. The long-term performance of SLA 3D-printed parts depends on their UV exposure performance, which refers to the appearance or color change that occurs after UV irradiation, and the change cannot be reversed. The first stage of UV exposure during SLA 3DP is known as the "yellowing stage", followed by the second stage, known as the "stabilization stage" [112, 113]. As a result of the UV exposure of SLA 3DP, especially for 30 minutes, it has been observed that the UV exposure accelerates rapidly at the beginning of the exposure and then slows down.

The following methods can be used to improve the surface quality of SLA [108, 114-117]:

- The SLA machine should be set to a higher resolution. A finer layer thickness will end up in smaller pixels, creating a smoother surface.
- A lower layer thickness will result in thinner layers that will be less visible on the finished product.
- A finer mesh will result in a smoother surface, since the triangle meshes will be smaller.
- Using a shorter cure time. This will prevent the formation of voids and bubbles in the cured resin, which can result in a rougher surface finish.
- The resin will be cured more entirely if the light intensity is increased, resulting in a smoother surface.
- By using a resin with finer particle size. The smaller particles will fill in the gaps between the larger ones, resulting in a smoother surface finish.
- The resin should have a low viscosity. It will prevent the formation of voids and bubbles in the cured resin, which may result in a rougher surface finish.
- It is recommended to use a resin with a higher shore hardness. Over time, this will result in a more rigid surface less likely to show signs of wear.
- Considering a different SLA machine. Due to the quality of their optics and/or build platforms, some machines produce a better surface finish than others.

### 2.2.4. Surface quality in SLS parts

An SLS part generally has a rougher surface than a part produced by another 3DP technology, owing to how the powder is deposited and melted during the building process. It is often necessary to perform post-processing to achieve the highest possible surface quality. However, there are several methods to enhance the surface quality in adjusting PPPs, including using a higher laser power, a smaller laser spot size, a faster scan speed, thinner layers, and finer powders [86, 118, 119].

SLS 3DP polymers are highly sensitive to UV light, and exposure to UV light will cause the polymers to degrade over time. As a result of the degradation of the polymers, the physical and mechanical properties of the 3D-printed parts can be affected, and the parts may also become brittle and break. UV radiation can also cause the polymers to change color, making the parts yellow or brown over time. 3D-printed parts should be protected from UV radiation and stored in a dark, cool environment [120]. To improve the surface quality, the powder material type, the powder particles' size and shape, the laser power and wavelength, the laser scanning speed, and the layer thickness can be adjusted. Besides, the environment inside the SLS machine, the build platform temperature, and the post-processing methods should be altered [121, 122].

## 2.3. Post-processing

The use of process parameter optimization to achieve the desired surface finish is not the ultimate approach in the AM. Following the completion of the AM build, specific post-processing steps should usually be performed to achieve samples that can be studied. Post-production finishing techniques (PPFTs) are broadly classified into mechanical and chemical finishing processes. Support removal, surface treatment and coating, and heat treatment are the most notable examples of these steps [123].

Post-processing can have a significant effect on the surface structure. According to Kinstlinger et al. [124], sintered PCL surfaces in SLS parts were smooth and shiny after 3-5 minutes of exposure to DCM vapor. They could lower the $R_a$ value from 115.6 ± 28.0 μm for an obviously rough surface of sintered PCL pieces to 3.9 ± 2.4 μm using vapor-smoothing. In fact, the roughness of smoothed PCL may be overestimated due to slight curvature at the edges of the SEM images, demonstrating that the average roughness was in the range of sub-micrometer. For personal use, this roughness range is in line with the expectations, especially for those who use acetone vapor to smooth ABS or DCM to smooth PLA components. Lalehpour et al. used an acetone vapor bath to enhance roughness for different designs and the smoothing of ABS parts. They reported a maximum 95% roughness decrease from 60 μm to 2 μm.

Moreover, total exposure time as a post-processing parameter had more influence on the smoothing process than other input parameters, while the dimensional changes were negligible after post-processing [33]. Y. Luo et al. [125] proposed a surface modification model for PLA/Halloysite composite scaffolds that would allow the fabrication of a surface that is both hydrophilic and antibacterial while also retaining osteogenic properties. The surface roughness of SLS products is caused by partly melted powder particles on the surface layer, as opposed to other production methods such as injection molding. As a result, the actual surface roughness must be determined concerning the application [123]. In MJT printing, the remaining support structures can be removed either with a water jet or in combination with alkaline solutions such as sodium hydroxide (NaOH) or potassium hydroxide (KOH) [126].

Fine sanding is typically required to remove the residual support structure at the attachment locations, either by hand or with a powered tool. Cosmetic finishing and UV protection can be achieved by hand sanding, delicate abrasive sprays, coating, or painting the component. The paint can be designed to absorb incident UV radiation when used, thus mitigating the risk of long-term embrittlement for some photopolymers. Automated systems for post-processing are increasingly becoming available, offering solutions to support removal, surface finishing, and waste stream treatment. However, the equipment for surface finishing, consisting of rotational agitation, ultrasonics, and chemical treatment, is not yet developed for emerging personal printers and AM for the small-scale markets.

Having described in this chapter the characteristics and fabrication of structured surfaces using AM technologies for polymers, the next chapter discusses the *appearance 3D printing* techniques and their multi-material capabilities in detail.

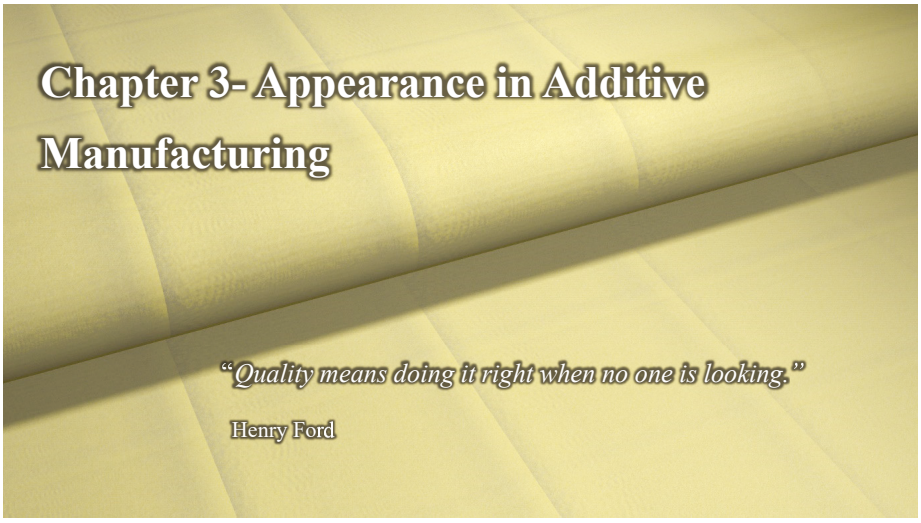


This chapter provides a brief overview of the theory behind the *appearance 3D printing*. This establishes a context for the research primarily focused on multicolored 3D objects. In addition to describing recent developments, ideas, and state of the art technologies, this chapter discusses methods that can improve the surface appearance of AM products for aesthetic purposes.

# 3. Appearance 3D printing

## 3.1. 3D printing process

Object appearance printing involves the control of multiple 3D printing parameters for high-fidelity reproduction of both the shape and the appearance of a 3D object [36]. Most appearance 3DP involves printing 3D objects in full color using multi-material additive manufacturing, where several materials are used to create enhanced 3D models. In addition to their different colors, the materials can have various properties, such as toughness or flexibility. As a result of this technology, models with other appearances or functional parts with different properties are usually created.

Several AM technologies can be classified as color 3DP with the full-color spectrum, including Color FFF and PolyJet by Stratasys Inc., MultiJet Fusion from Hewett Packard Inc., ColorJet Printing (CJP) by 3D System Inc, SDL processing from Mcor Inc, 3DP developed by Z Corp Inc and 3D System Inc, and multi-material powder bed fusion. As discussed earlier, color FFF and PolyJet are the two most well-known methods that employ colored feedstocks to generate full-color objects [127].

According to J. Yuan [36], the main categories of color reproduction are colorimetric difference assessment, computer-assisted colorization, optical parametric modeling, and voxel droplet jetting. As shown in Figure 6, the most frequent color 3DP processes for these color reproduction methods are MJT, BJT, SHL, MEX, and VPP, consecutively. Plastic-based types are first explored in terms of the distribution of printing materials, followed by powder- and paper-based types. To achieve full-color 3DP, MJT, BJT, and MEX apply various color reproduction methods and very complex surface color characteristics, while SHL and VPP use fewer types.

### 3.1.1. Appearance in the FFF process

FFF 3DP produces prints that are relatively accurate and detailed for regular workshop purposes since the material can be deposited in thin layers, typically around 20 μm in thickness. Using a wide range of colorful filaments, an FFF 3D printer can produce parts in various colors, including black and white, and a full spectrum of colors. A few manufacturers offer 3D printers that can produce over 16 million colors by combining FFF and Inkjet technologies [128]. There are, however, some limitations to FFF 3DP concerning color reproduction, as also discussed in *Paper I* [127]. This technique is not well suited to printing complex color gradients or patterns and is generally limited to producing single colors.

Color mixing using multi-material hot-end nozzles has not yet been fully developed [129, 130]. However, mixing colors while producing the filament and printing 3D objects in predefined colors is possible using a single nozzle [131]. Yet, FFF 3DP is not as capable of producing vibrant colors as other AM techniques, such as material jetting. Color selection for 3D-printed parts requires a few considerations. The first thing to consider is why the parts are being printed. When printing prototypes or parts for functional testing, the color of the components is less important than the material, they are constructed from. For easy identification, it is advisable to choose a neutral color, such as white or gray [132, 133].

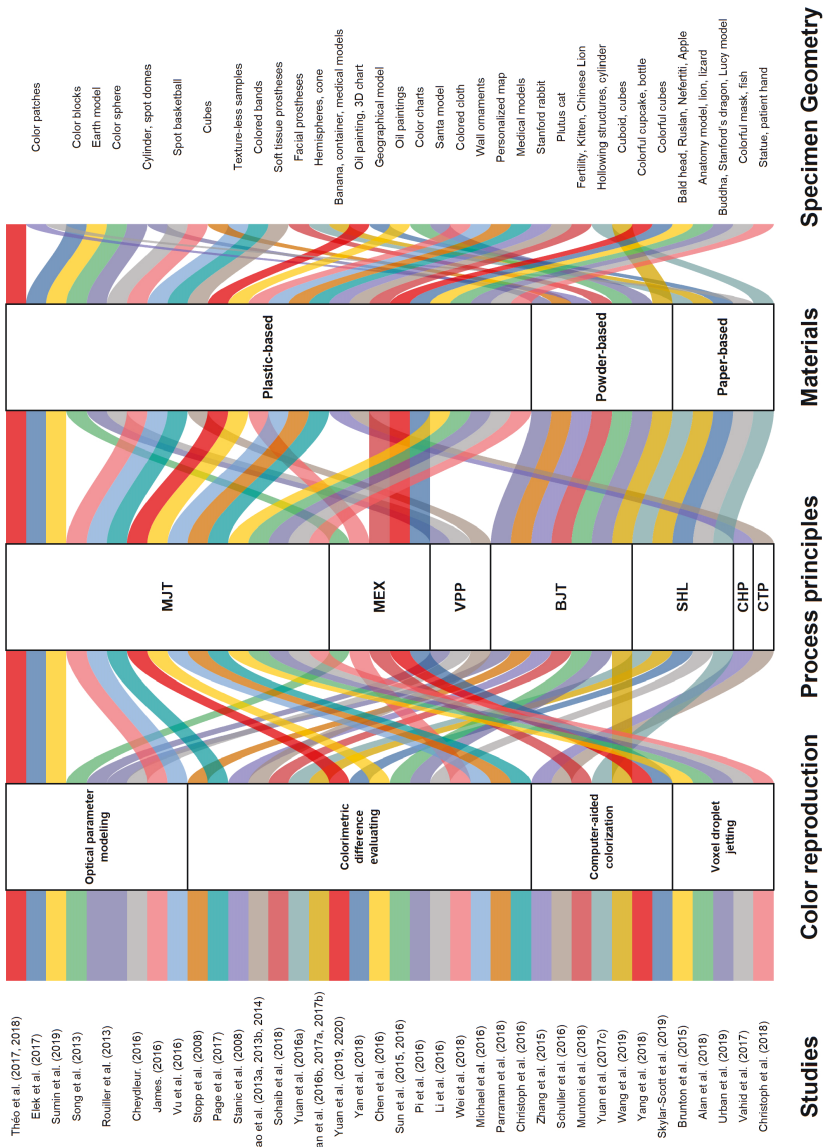


Figure 6. An overview of the significant color features reproduction methods (data from [36])

Choosing colors for aesthetic purposes or marketing purposes is much more critical. In these situations, it is crucial to consider the overall appearance and feel of the finished product. For instance, a brightly lit store will require choosing colors that will stand out and attract attention. Alternatively, if the product will be used in a more subdued environment, then subtle colors will be appropriate. The color of 3D-printed parts can also influence their cost. As a general rule, the more colors used, the more expensive the parts will be.

Finally, FFF 3D-printed parts are not as durable as traditional manufacturing methods but are more durable than other forms of 3DP. Many materials, including polymers, are known to be damaged by UV exposure [134]. As a result of prolonged exposure to UV light, FFF 3D-printed parts can become brittle and break. These parts are, therefore, unlikely to survive in harsh environments for an extended period [135]. In contrast to SLS, FFF allows for an attractive appearance in 3D printing. However, FFF is limited for aesthetic purposes due to its rough surface and vulnerability in mixing materials of different colors simultaneously compared to the PolyJet technology, except for using limited multi-color filament (Figure 7).

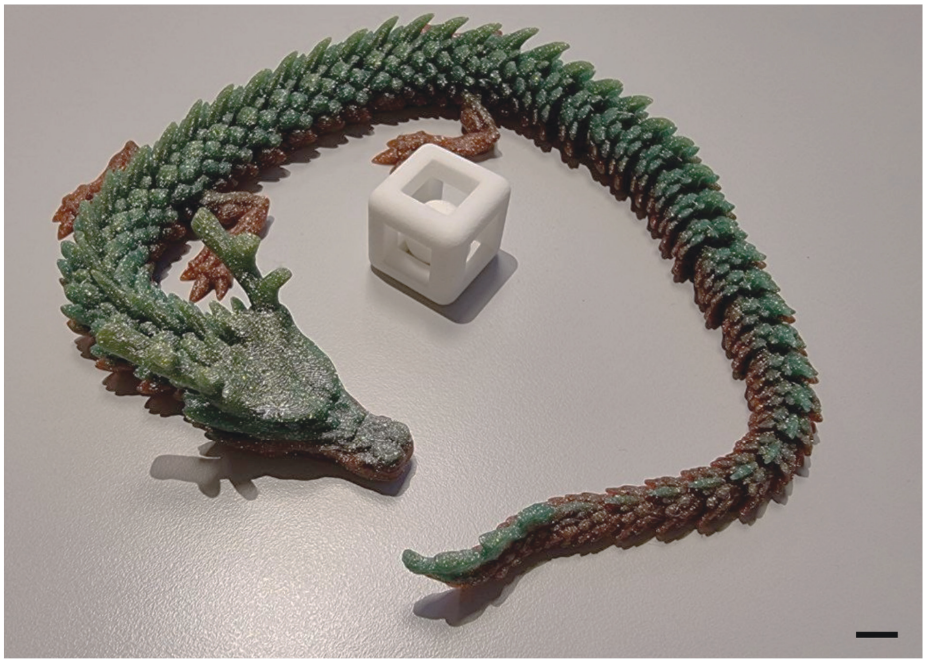

Figure 7. Appearance 3DP in FFF using multicolor PETG filament (the dragon) versus the mono-color-limited SLS printing (the white NTNU 3D logo in the middle); printed at Addlab, the Department of Manufacturing and Civil Engineering – NTNU (Scale bar represents 10 mm).

### 3.1.2. Appearance in the PolyJet process

PolyJet allows the creation of 3D prototypes, models, and other objects requiring accurate representation of the appearance of a full-color 3D model. Ideally, an appearance 3D printer using PolyJet technology deposits tiny droplets of material with different appearances into the voxels needed according to the design. UV light completely cures the droplets, allowing layers to be built up quickly [106].

PolyJet-based manufacturing is gaining a lot of attention in full-color 3DP, which is the advantage of this technology over other AM techniques. This method deposes resins in CMYKW (cyan, magenta, yellow, black, and white) and can simultaneously print different materials [136]. Due to the high-resolution MJT machines available today, it is feasible to print materials with vastly different properties, such as a rigid, glassy polymer and a soft, rubbery material with elastic moduli that differ by nearly three orders of magnitude at room temperature [137]. It is also possible with PolyJet 3DP technology to reproduce color gradients and variations that are not possible with other 3DP technologies [42].

As shown in Figure 8, MJT objects are generally semi-translucent, complicated in appearance, and represent a mixture of textures by applying ink in layers [42, 138]. Therefore, the appearance attributes of detailed properties on the surface are difficult to measure by conventional methods. Still, it is possible to achieve satisfying results by decreasing the influence of errors in the measurement process and following a reproducible workflow.


Figure 8. The appearance of objects printed in different conditions using the MJT 3DP technique; Specimens printed at the middle swath and different build orientation ([0º-90º], 15º step) a) on the rotary build platform, b) the appearance and visibility of structured surfaces, c) the translucency in the colored layers, and d) surface appearance under a standard D50 illumination in a light booth.

### 3.1.3. Appearance in the SLA process

SLA can produce parts with a wide range of colors and vibrancy. Similar to MJT technologies, stereolithography also utilizes a light-sensitive resin that can be cured with different wavelengths of light. Since the photopolymer resin is transparent and the laser can be tuned to different wavelengths, other colors can be created. Afterward, the colors are combined to form the final object with a different appearance, ranging from subtle shades to vibrant hues. Furthermore, stereolithography is known for its high accuracy, resolution, and color capabilities, making it a proper candidate for high-detail applications [76, 139]. As a result, it is possible to print realistic 3D objects with a few post-processing requirements. For instance, a study published in 2013 by Kaida Xiao et al. employed an SLA 3D printer to print soft prostheses. It took spectrophotometer measurements on the surface color points of the prosthesis. Nevertheless, the application of SLA and other VPP processes for appearance 3DP is limited compared to MEX and MJT AM processes [36].

### 3.1.4. Appearance in the SLS process

While SLS is a high-speed technology, its color palette is limited to black and white. The SLS process is well suited to producing prototypes and small batches. Medical implants and automotive components are also increasingly being built using this technology [140]. The growth of these emerging applications can be accelerated through multi-material powder bed fusion techniques. Currently, mono-color and single-powder techniques are the only commercial techniques available for polymers. Thus, SLS 3DP is still in its infancy as a process for producing appearance 3D objects.

In the case of materials or powders with different properties, such as colors, it may be more challenging to predict the sintering characteristics when they are combined. One of the most notable breakthroughs was achieved by Aerosint [141], which developed a commercialized SLS machine that was able to process multiple materials simultaneously. However, this technology is limited to metals and ceramics and requires fundamental research on the material properties and process parameters of multi-material SLS. An in situ identification of material parameters with a short particle-based code appears to be the best approach to modeling multi-material PBF processes with the recent development of particle methods and computing hardware [142]. Thus, there is a growing expectation that the appearance of 3DP can be achieved using SLS processes. Figure 9 represents the shape and appearance of samples manufactured using FFF, SLA, and SLS technologies. It illustrates that dimensional accuracy and print quality highly depend on the selected design, materials, and methods. For instance, doping SLA resin with silver particles can cause more defects for some designs more than others. The doping of 3D models can, however, provide them with new properties and functionality.

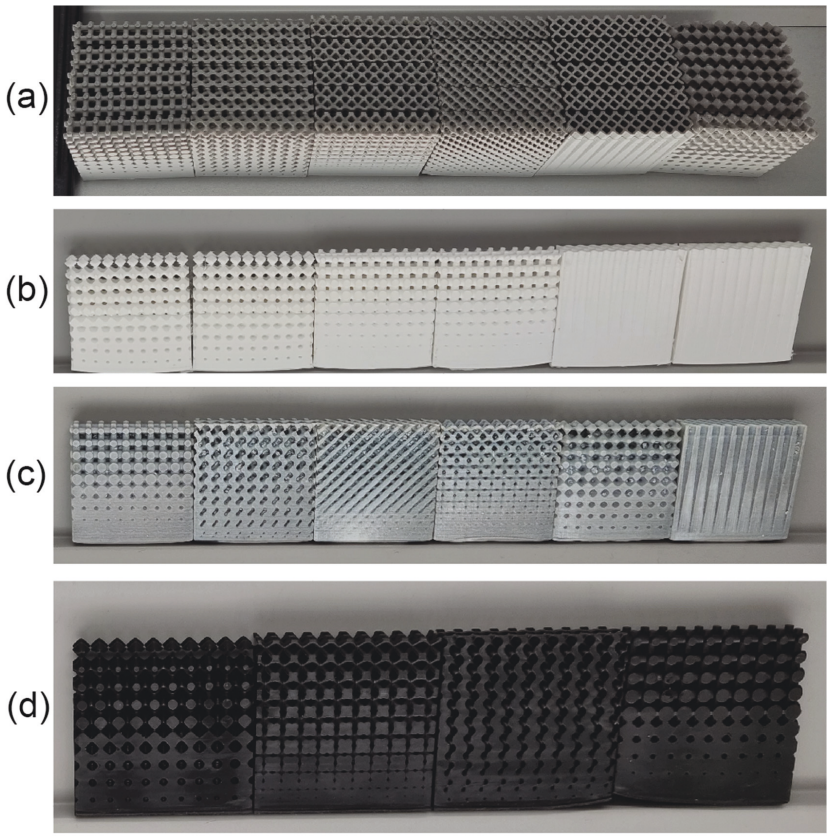


Figure 9. The gradient lattice-based structures. The as-printed objects were 3D-printed using: a) FFF with PLA filament, b) SLS using PA12 (2200) powder, c) SLA using a PrimaCreator Value resin doped by silver particles, and d) SLA using black resin (Loctite 3D Onyx rigid PRO410).

### 3.2. Surface quality in multi-material 3DP

Full-color and appearance-oriented 3DP technologies are versatile, with various applications requiring high surface quality. A full-color 3D printer can be used to create models of existing products or parts, which may prove helpful when redesigning or improving outcomes. This technology is often used to build prototypes, models, and marketing materials. In marketing materials, full-color 3DP is often used to create models of products or parts for use at trade shows or other marketing events [143, 144]. Additionally, full-color 3DP can be used in packaging or labels during the design process. It has been demonstrated that the surface microstructure of AM objects can be rougher (ranging between 3 to 4 μm) than that of typical cast pieces (2 to 3 μm). It may be of clinical relevance for implant structures but not for other applications in dentistry [145].

In appearance 3DP, the surface texture of an object is important because it can affect how light reflects off it (see Figure 8c and d). Smooth surfaces reflect light evenly, while rough surfaces scatter light in different directions. Depending on the texture of the surface, this can result in an object appearing glossy or matte [146]. As this technology is still in its infancy, only a few studies are available. In 3DP, the following factors are most critical for controlling the appearance [147, 148]:

- Machine: A few brands and models of 3D printers on the market claim to offer full-color printing capabilities. However, not all of them are designed for realistic 3DP. A 3D printer designed specifically for printing in full color is essential for the most accurate results.
- Material: 3D printers require particular feedstocks to produce full-color multicolored prints.
- Software: Another resource is software capable of generating full-color 3D models. While a few software programs on the market offer this capability, such as Cuttlefish, there is a lack of integration between the software and the 3D printer for appearance manufacturing.

Throughout this chapter, we discussed the *appearance 3D printing* using FFF, PolyJet, SLA, and SLS. A summary of the additive manufacturing factors affecting surface quality is given in Figure 10. The next chapter discusses the appearance attributes and their corresponding metrics that are necessary for evaluating the optical properties of an AM-structured surface.

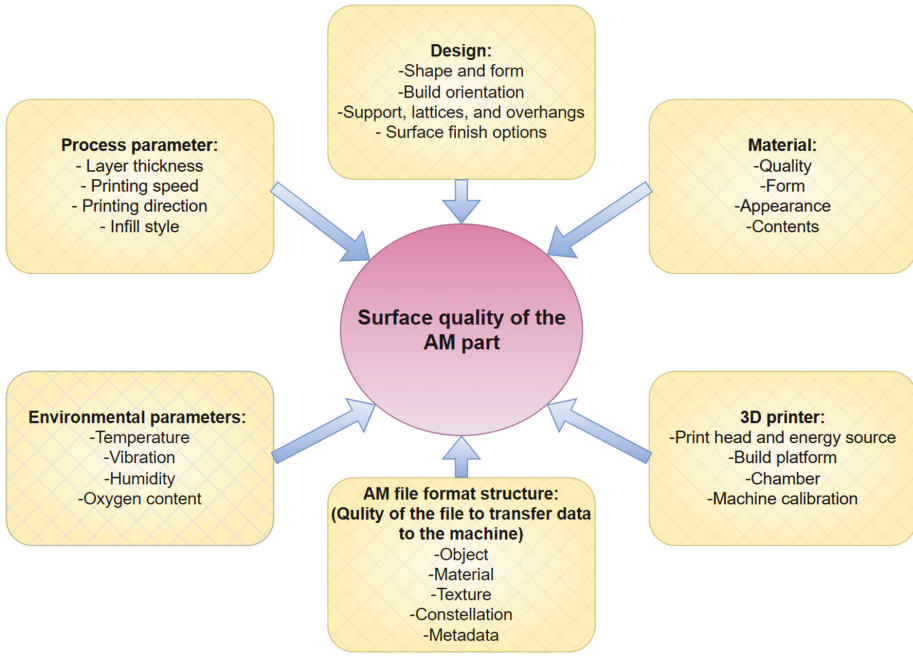


Figure 10. Additive manufacturing factors affect surface quality [41, 149].

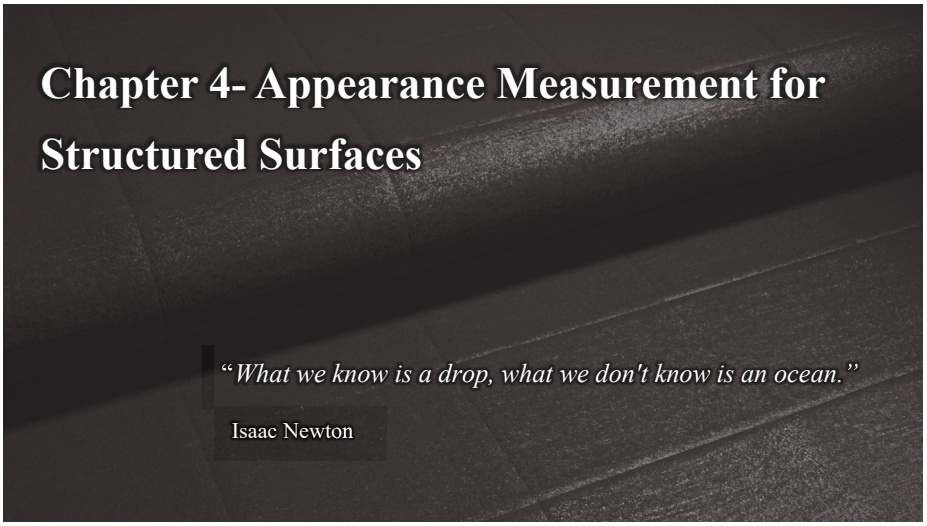

# Chapter 4- Appearance Measurement for Structured Surfaces

"*What we know is a drop, what we don't know is an ocean.*"

Isaac Newton

This chapter discusses appearance evaluation and its implementation in additive manufacturing. An overview of the scientific approach to the surface optical properties of AM polymers is provided. Later, the metric methods used for measuring appearance attributes are discussed. This thesis studied mainly the four primary appearance attributes of structured surfaces, including color, gloss, translucency, and texture. For most polymer-based AM technologies, translucency coexists with other appearance attributes, forming a part of the overall visual characteristics. As the work progressed and more information was obtained, we narrowed our focus to the role of AM process parameters on color appearance and part functionality.

# 4. Appearance attributes and measurements

## 4.1. Appearance attributes

The appearance of objects is a complex psycho-visual phenomenon that involves various visual aspects, including color, gloss, transparency, texture, translucency, sparkle, haze, etc. [150]. Visible light is the region of electromagnetic energy with wavelengths of approximately 380-780 nm. All industries are concerned with the appearance of their products since the appearance of an object determines its visual quality. Moreover, customers anticipate that any group of the same product will appear uniform. It is common for consumers to associate low quality with the differences they observe between similar products [151]. Pointer [3] defines the total appearance as "a description of the shape, size, texture, gloss and any other apparent quality". Figure 11 illustrates the most prominent appearance attributes when recognizing objects. The following section provides a more detailed explanation of the main appearance attributes.

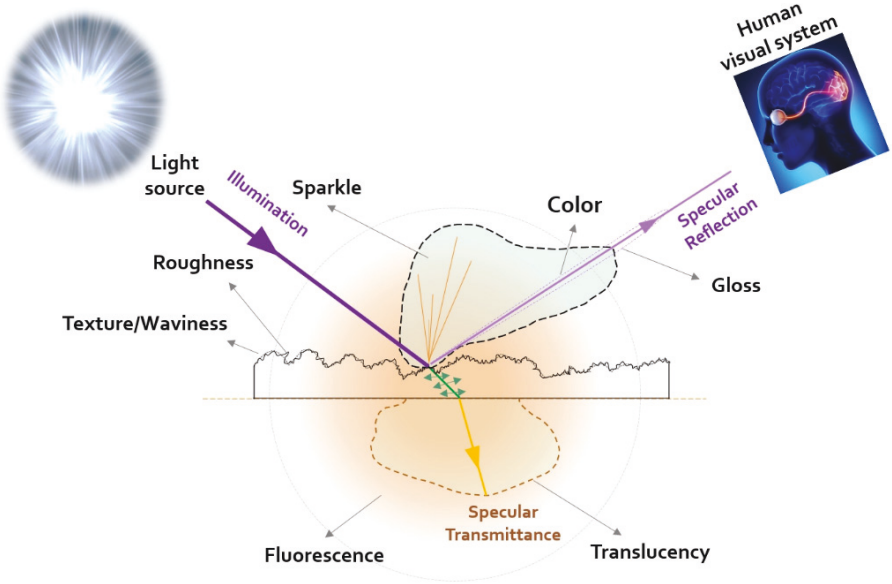


Figure 11. Object appearance recognition process and appearance attributes.

### 4.1.1. Color

In terms of appearance, color is undeniably the most prominent characteristic. There is a long history of color perception, and the color perception mechanisms are generally well understood. Still, color science for 3D objects remains complex, and there is still much to learn regarding how colors are perceived and measured. As a result of the growth of color science, appearance research can be considered an extension of this discipline [152].

Color science aims to understand how color is perceived by humans and to apply that knowledge to improve the appearance of products and displays. The use of color science can be found in several fields, including product design, graphic design, and video production [151].

Numerous factors influence the color appearance of objects, including the geometry of the illumination, the shape of the objects, and the reflectance properties of their materials. The geometric characteristics determine the color of an object, including diffuse reflectance and transmittance [151]. Moreover, many viewing parameters assess the appearance of color, including the illuminant, luminance, media (surround), and background. Table 2 lists various attributes associated with the color appearance [150, 151].

Table 2. Color attributes [153].

| Attribute | Description | Relevant equation |
|---|---|---|
| Brightness (Q) | It defines how much light an area reflects | |
| Lightness (J) | It defines how much light a colored area reflects in comparison to a reference white | $J = \frac{\mathrm{Q}}{Q_w}$ |
| Colorfulness (M) | This attribute refers to an area that exhibits more or less chromatic characteristics, depending on the degree of hue apparent | |
| Chroma (C) | A measure for colorfulness with the brightness of a reference white. It can also be defined based on a* (red-green) and b* (blue-yellow) according to CIELAB color space | $C = \frac{\mathrm{M}}{Q_w} = \sqrt{a^{*2} + b^{*2}}$ |
| Saturation (s) | Color intensity as a function of brightness | $s = \frac{\mathrm{C}}{\mathrm{J}} = \frac{\mathrm{M}}{\mathrm{Q}}$ |
| Hue (H and h) | Hue is described in the following elements:<br>- Hue composition (H): color appearance (e.g., 10GY)<br>- Hue angle (h): color difference (e.g., 0° to 360°)<br>A specific area appears to be similar to one of the four unitary hues: red (R), yellow (Y), green (G), blue (B), or a combination of two of these hues. | $h = \arctan\frac{b^*}{a^*}$ |

Illuminants are classified as standardized light sources by CIE and standard observer response functions that specify colors numerically by three numbers, called tristimulus values. Based on these values, two chromaticity coordinates are plotted in 2D in a diagram known as chromaticity, which encompasses all real objects and spectral colors within an area similar to a horseshoe. Following the acquisition of a subset of colors visible to the human eye, color spaces are established based on uniform color scales [151].

A CIE color space defines color in terms of three characteristics: lightness, chroma, and hue, usually represented by the CIE L*C*h color space [153]. The most common CIE color space is XYZ, which is based on the tristimulus values of a given color. The CIE XYZ color space is the basis for other CIE color spaces. CIE1976 (L* a* b*), also known as CIELAB, is another widely used color space. Colors in the CIELAB are perceived as more uniform than colors in the XYZ color space. Color management

and color matching are often performed using CIELAB. CIE L* C* h is a cylindrical representation of CIELAB, and it helps represent colors more accurately in terms of human perception. CIE1976 u', v' or CIELUV color space is another proper color space for color management. It is a 3D, roughly uniform color space generated by plotting in rectangular coordinates. This theory is based on the opponent color theory of human vision, which states that there are three primary colors: red, green, and blue, orthogonal to each other [153].

There have also been several device-specific color scales developed for televisions and monitors (RGB, sRGB, etc.) based on additive color mixing, as well as for printers (CMYK), considering subtractive color mixing. Without a perfect color space, further development is necessary [151]. Various fields, including photography, printing, and computer graphics, use the CIE color spaces [150, 151]. In most material jetting 3D printers, CMYK is the primary colorant in the material cartridges.

In appearance assessments for AM objects, color fidelity can be considered as the extent to which the color of the object being assessed matches the actual color of the reference object. A fidelity metric is a methodology that simulates the illumination of 3D-printed models with a test illuminant and a reference illuminant with a comparable correlated color temperature (CCT) to determine an index that indicates the difference degree between the two sources by several metrics (CIE-Ra, CQS-Qf, CRI-CAM02UCS, CRI2012, IES-Rf, CIE-Rf). A general workflow for calculating fidelity indices is illustrated in Figure 12. A spectral power distribution (SPD) is used as the input. CIE recommends a wavelength range of 380-780 nm and a maximum interval of 5 nm [153].

Before calculating the SPD of the reference illuminant (daylight illuminant or Planckian radiator) at the identical CCT, the CCT of the test source should be determined. After correction for chromatic adaptation, color coordinates and tristimulus values in a particular color space are calculated for a set of test color samples (TCSs) according to the test source and the reference illuminant. Each TCS is calculated based on the color difference of the illuminants. Through rescaling, color differences are translated into general and special color rendering/fidelity indices [154]. Thorough information regarding the application of color spaces and the calculation of color difference can be found in the appendix articles.

In structured surfaces, the color appearance attribute refers to the overall appearance and perception of the color. Surface type, lighting, and the viewer's preferences can all affect the viewer's perception. Surface texture can have a significant impact on color. Smooth, glossy surfaces reflect more light and appear brighter, whereas rough, matte surfaces absorb more light and appear darker [150, 151]. To determine the color appearance attribute in AM polymers, the surface finishes and other appearance attributes such as gloss, texture, and translucency of the object should be considered, as human perception of the color [150].

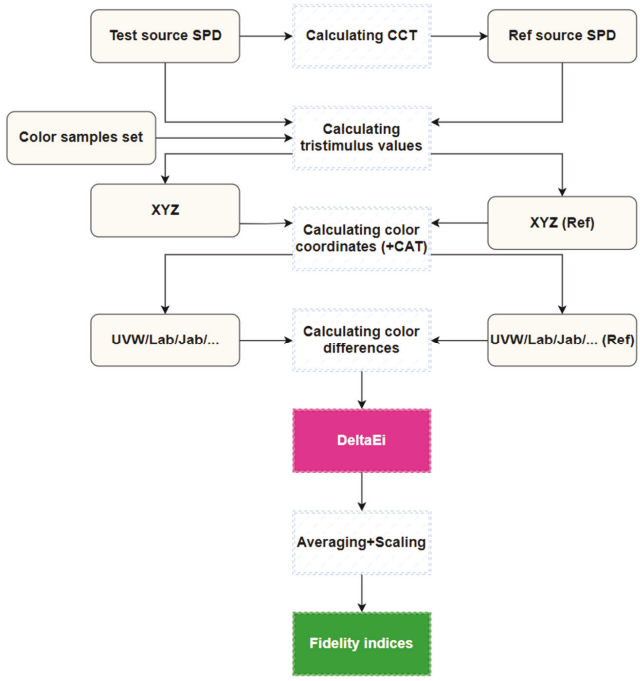


Figure 12. The general workflow for calculating fidelity indices (reproduced with permission from [154]).

### 4.1.2. Gloss

An attribute describing a material's gloss appearance or perception measures its reflective or shiny appearance. Specifically, it depends on how light is reflected from the surface at and near the specular, mirror angle, and direction. As defined by Hunter and Judd [155], specular gloss is the ratio between the light reflected from a surface at a specific light incident angle and light reflected from the opposite side of the surface normal on the same object. Hunter and Harold [156] recognized, however, that gloss perception involves more than just specular reflections. Typically, gloss is perceived independently of color. However, it may be influenced by or contribute to the perceived color of the target. Generally, gloss is perceived as separate from color as part of the total visual experience [157].

Gloss Unit (GU) is usually measured on a scale of 1 to 100, with 100 representing the highest gloss level. Light is reflected strongly by surfaces that have a high gloss. Many fabricated objects are considered in the semi-gloss category. However, some matte products have a very low gloss, while others, e.g., metallic surfaces, have a high gloss [151]. Following ASTM Method 2008, measurement angles can be designated as 20, 60, and 85 degrees, subject to the corresponding gloss of the surface [158]. There are, however, specific industries that use different angles. For instance, ceramics and film industries use the 45° gloss meter, while paper and vinyl manufacturers use the 75° gloss meter [151].

Figure 13 shows the positions of the light source and the detector for measuring the gloss of low, medium, and high gloss surfaces (making angles of 85°, 60°, and 20°, respectively). Accordingly, the main three classes of gloss are as follows [151, 159]:

- Low gloss: The measurement of low gloss surfaces is improved by using grazing angles of 85°, which is recommended when GU is less than 10 at 60°. This angle offers a wider measurement region to average gloss differences on rough or slightly uneven surfaces such as matte AM polymers.

- Medium or Semi-gloss: The reference angle of 60 degrees is the standard measurement angle for all products, with a gloss of 10-70 GU being the most satisfactory. The complementary angles (85° and 20°) are often used for extreme gloss levels when measuring gloss levels below or above the stated range.

- High gloss: High gloss surfaces can be measured with improved resolution at an acute angle of 20°. This geometry is commonly used to measure surfaces measuring 70 GU and above at an angle of 60°. There is a greater sensitivity to haze effects when observing a surface at a 20° angle. In the 20° readings, the different glosses of these two samples are obviously discernible. As a result, measuring gloss for high gloss AM polymers is challenging and subject to many errors due to the structured surfaces.

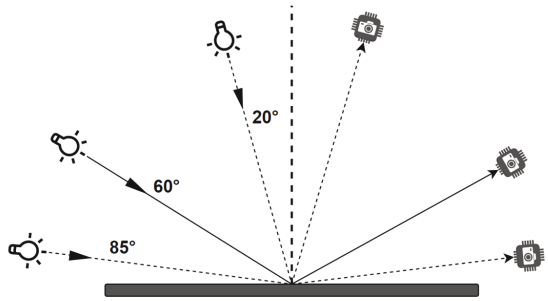


Figure 13. Positions of the light source (left side) and detector (right side) for gloss measurement.

The gloss attribute is critical in AM because it affects the aesthetics of a 3D-printed object. It is common to use the gloss appearance attribute and its distribution pattern to assess the finished product quality in AM technology. A high gloss finish can give an object a more polished appearance with a very high degree of smoothness, while a low gloss finish can give a more matte appearance [160, 161]. The texture of the surface can affect the glossiness, making the surface appear rough or smooth. In general, a rougher surface will appear less glossy [151]. Son and Lee [162] studied a disc (diameter of 100 mm) manufactured by an SLA system using an ABS-like resin. They reported polishing decreased surface roughness; however, glossiness and transparency decreased due to micro-roughness formation on the surface. Chemical treatments help achieve a high gloss and shiny finish [162], but controlling PPPs can help control surface texture more effectively (Figure 14).

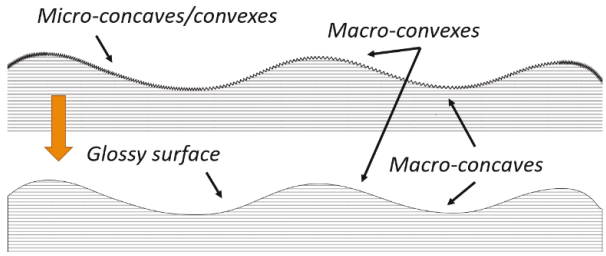


Figure 14. A schematic of high-gloss surfaces (the smooth surface below) that is achieved by applying surface treatments on micro-concaves/convexes.

### 4.1.3. Transparency and translucency

CIE (2006) [163] emphasizes that "translucency is a subjective term that relates to a scale of values going from total opacity to total transparency". Transparency is the property of a material that allows light to pass through it without being scattered. In contrast, translucency refers to a material that transmits light but simultaneously scatters 10% of the transmitted light [164]. A translucent material lies between the extremes of complete transparency and turbidity. In turbid substances, approximately half of the light transmitted is scattered. Full opacity happens when no light is transmitted [151]. Transparent objects appear clear, whereas translucent objects appear frosted or milky due to diffusing light. Many polymers are translucent, e.g., acrylics, PMMAs, polypropylene, and polycarbonate [165-167].

In AM objects, the level of transparency is expressed as a percent in the range of 0 to 100 %, where the object is considered partially transparent. An object with a transparency value of 0% is completely opaque with a solid appearance, while an object with a transparency value of 100% is completely transparent with a see-through effect. Adding this technique to additive manufacturing can result in translucent surfaces appearing to glow. For instance, SLA produces translucent parts (50-60% transparency) when parts are manufactured in clear material [168]. By lacquering them, they can be made more transparent (up to 90% transparency) by applying an epoxy-like resin as a coating. Different levels of transparency can be achieved through other AM techniques, such as MJT and FFF, using clear feedstocks. Transparency can be used to create a variety of interesting visual effects [169]. A possible application of translucent additive manufacturing is making customized eyeglasses, sunglasses, and custom-fitted contact lenses.

There is a significant effect of surface texture on transparency. The rougher the surface, the more light will be scattered, thus making the object appear less translucent and vice versa. Gerardin et al. [170] proposed a classification system for transparency and translucency in computer graphics (Figure 15). Increasing subsurface absorption gradually turns transparent materials opaque but not translucent; increasing subsurface scattering turns transparent materials translucent and eventually wholly opaque. Increasing surface roughness makes transparent materials appear translucent but not fully opaque.

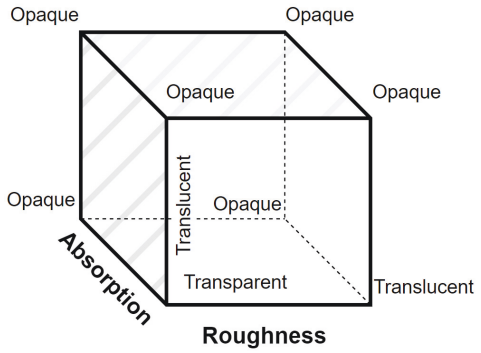


Figure 15. Cuboid classification system for translucency/transparency in computer graphics.

### 4.1.4. Texture

A geometric attribute refers to a 3D characteristic of an object. Since AM constructs objects layer by layer, the geometric attributes of the object are determined by the order in which the layers are deposited. The three primary geometric attributes are form, feature, and dimension. *Form* refers to the overall shape of an object, while the *feature* refers to a specific, identifiable part of an object. *Dimension* refers to the size and location of a feature [151, 171]. Although the texture is intuitively apparent, it is challenging to distinguish since there are different definitions of topographic features on surfaces. As per ASTM E2380-05 [172], the texture is "The visible surface structure depending on the size and organization of small constituent parts of a material; typically, the surface of a woven fabric". Therefore, a texture appearance attribute describes how the surface of an object appears visually.

Evidently, this definition is incomplete and, perhaps, is spoiled by the example, which is not entirely accurate. The surface texture definition must distinguish between a texture linked with topological, physical, and structural surface irregularities (e.g., metallic surfaces and woven fabrics) and subsurface texture. Nonuniformity in colorants causes spatial variations in appearance, e.g., metallic automobile finish. Additionally, it may be necessary to distinguish between 2D and 3D surface variations. A printed picture of a ceramic piece would be an example of the first type. On the other hand, the surface of a genuine ceramic piece would be the second type. There is also a distinction between surface pattern and texture. An argument could be made that the pattern of a surface is inherent. In contrast, surface texture refers to how the pattern is perceived, which is influenced by other variables, such as the viewing distance and the illumination direction [150].

Based on ISO 25178-2 [171], surface texture refers to “geometrical irregularities contained in a scale-limited surface” that remain following a sequence of processes performed on the extracted primary surface. After removing the *form* (if necessary) from the primary surface with an F-operation, S- and L-filters are applied to remove *small* and *large* lateral components, respectively. The definition of texture has been expanded. For instance, according to the CIRP[2] encyclopedia [173], “Surface texture is the

[2] Collège International pour la Recherche en Productique

geometrical irregularities present at a surface. Surface texture does not include those geometrical irregularities contributing to the form or shape of the surface".

Similarly, as we discussed for other appearance attributes, textured surfaces can influence color, gloss, translucency, and many other characteristics of AM appearance. In terms of color and color difference, the texture's chromaticity can significantly impact the perception of a difference between two samples [150]. Xin et al. [174] confirmed that surface texture influences color difference. Researchers have investigated how color and color difference are affected by the coarseness of metallic automotive coatings [175-177]. Arai and Baba [178] investigated the micro local gloss of textured painted surfaces and reported a color-difference metric may help to incorporate texture as an additional parametric effect. Texture impacts translucency by affecting how light reflects and transmits as it passes through the surface. Rough surfaces will reflect light more than smooth surfaces due to the more reflective surface available on the objects, while smooth surfaces will allow more light to pass through. This also affects the glossiness. Rough surfaces with textured structures may exhibit diffuse light reflection, whereas smooth surfaces with less texture may exhibit specular light reflection [179]. However, light interaction remains a complex phenomenon [180].

As represented in Figure 16, the analysis of texture can be divided into two categories [150]:

- Syntactic (Statistical) - the texture is determined by statistics selected from the total textural region (e.g., using co-occurrence matrices or run lengths)
- Analytical (Structural) - the texture is analyzed as a set of primitives (e.g., autocorrelation and Fourier analysis)

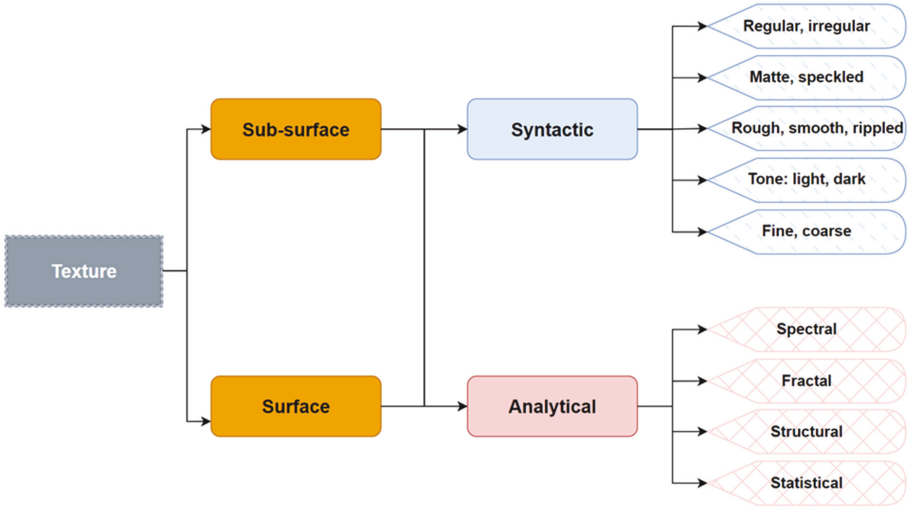


Figure 16. Analytical and syntactic approaches to texture analysis.

Various methods have been developed to capture the inherent texture fineness or coarseness [181-183]. A fractal-based texture classification is an approach for correlating coarseness with fractal dimension, which is considered an analytical method. Identifying the possible correlation between the PPP of 3DP and the surface appearance attributes such as color and texture can result in enhanced structured surfaces. Figure 17 represents how a printing parameter (here, the build orientation-BO) can influence the surface texture. Building a part with AM involves accumulating the orientation of materials as the part is being constructed [184]. A build orientation can significantly impact the quality, cost, and build time of 3D-printed products.

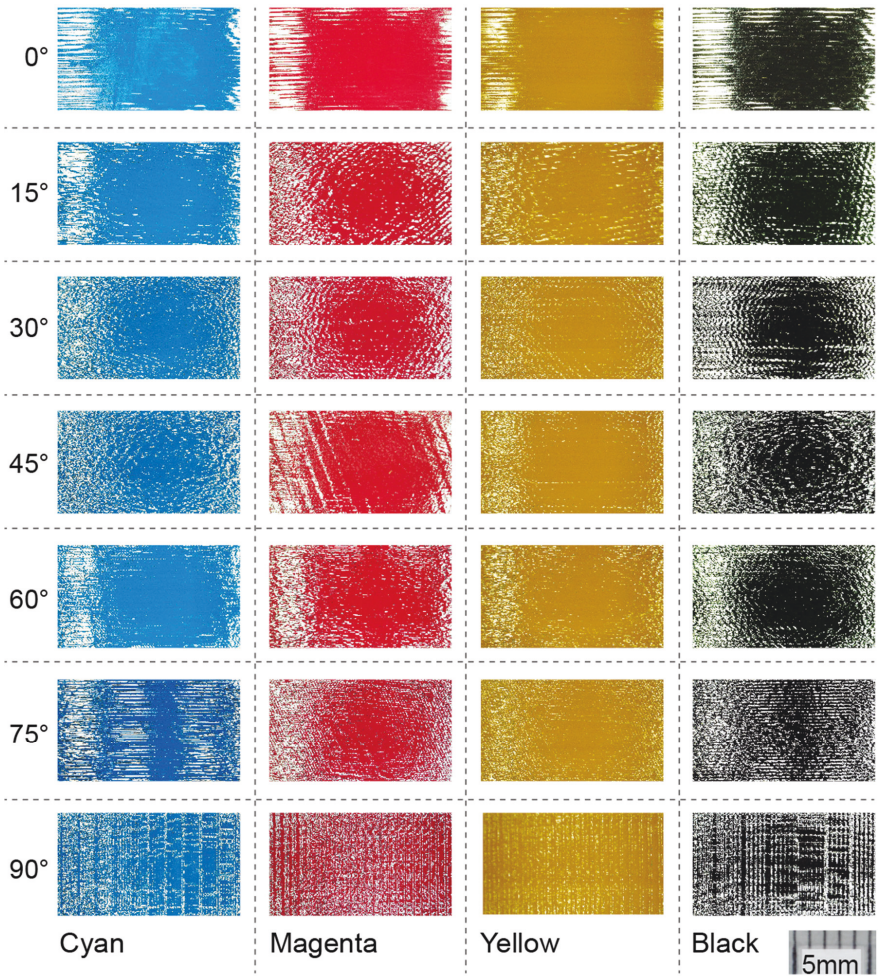


Figure 17. The surface texture as the function of build orientation ([0º-90º], 15º step).

## 4.2. Structured surfaces in translucent AM polymers

Two main categories of parameters determine how light interacts with a material. In the first category, electromagnetic fields are described in detail regarding their interaction with materials. There is also the possibility of describing how radiant energy is redistributed inside a material employing dissipative (absorption) and non-dissipative (scattering) effects [5]. The parameters that determine how light interacts with materials are classified in Figure 18.

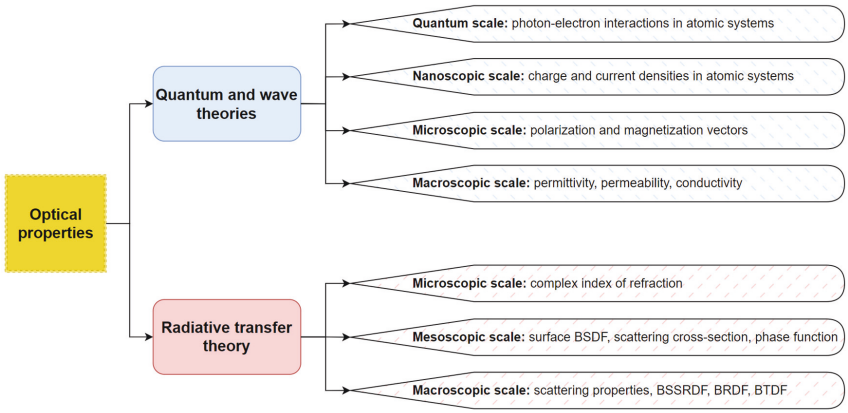


Figure 18. Optical properties theories for translucent materials.

The roughness of a surface is characterized by the distribution of microfacet normals (Figure 19). There are different scales of optical properties. At the nanoscale and microscale, geometric features are similar in size to wavelengths. As a result, field models take multiple scattering and phase properties into account, and the optical specifications are used in Maxwell's equations as physical parameters. The significant determinants at the micro/millimeter scale are size/normal distributions and radiative transfer scattering properties. A collective bidirectional distribution function (e.g., the BRDF, BSDF, and BSSRDF) models the scattering effects of an array of features at the macroscopic scale [5].

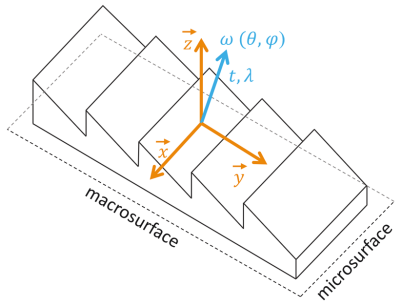


Figure 19. Simplified schematic of the main dimensions in a general reflectance model for a textured AM surface.

Considering the appearance attributes, the reflectance of physical surfaces is a complex phenomenon intricately dependent on the light spectrum, time, and spherical angles of incident and reflected light beams. A general reflectance function (GRF) describing the incident beam with $\lambda_i$ spectral value; consists of 16 dimensions (16D).

$$Y_r^{GRF} = GRF(\lambda_i, x_i, y_i, z_i, t_i, \theta_i, \varphi_i, \lambda_v, x_v, y_v, z_v, t_v, \theta_v, \varphi_v, \theta_t, \varphi_t)$$

where $r = [r_1, \dots, r_{16}]$ represents the multi-index matching partial indices. As shown in Figure 19, $x_i, y_i, z_i$ are illuminating surface locations in time $t_i$ and spherical incidence angles of $\omega_i = [\theta_i, \varphi_i]$. $\theta$ is the elevation and $\varphi$ is the azimuthal angle. It is observed at the time $t_v$ from surface location $x_v, y_v, z_v$ and spherical reflectance angles $\omega_v = [\theta_v, \varphi_v]$ with spectrum $\lambda_v$. Transmittance angles are expressed as $\omega_t = [\theta_t, \varphi_t]$. Figure 20. Represents collective scattering distribution functions for translucent objects. Accordingly, a classification of reflectance models is depicted in Figure 21.

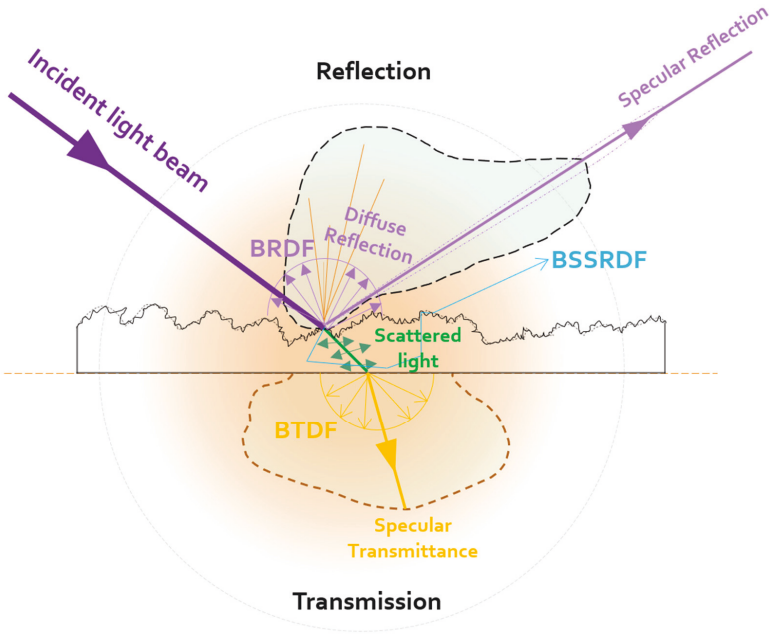


Figure 20. A schematic of collective scattering distribution functions.

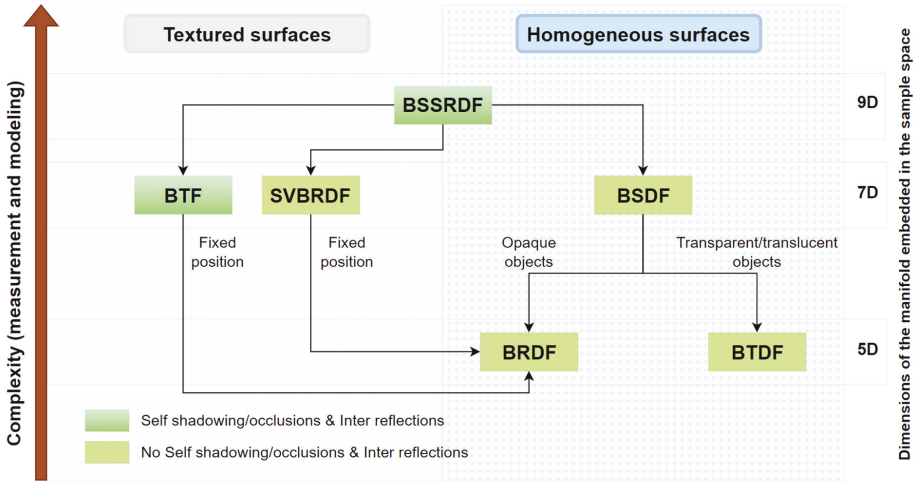


Figure 21. Taxonomy of specified reflectance functions derived as further simplifications of the BSSRDF [185, 186].

As seen in Figure 21, not all collective bidirectional distribution functions are suitable for texture surfaces. The following is a brief explanation of each function:

- BSSRDF - Bidirectional Scattering-Surface Reflectance Distribution Function:
  The BSSRDF includes all surface as well as subsurface scattering. It models incident and emergent light at distinct surface positions. This model accounts for spectrally varying absorptions and scatterings, and phase modulation. It is challenging to measure BSSRDF reliably, and no full models have been published yet. This model is possibly the best GRF approximation we can measure in the near future [186].

- BRDF - Bidirectional Reflectance Distribution Function:
  In BRDF modeling, illumination, and viewing geometry are used to determine the reflectance of a target. A BRDF can be used to determine how much light is reflected from a surface in a particular direction. As a function of wavelength, both the optical and structural properties of the surface influence the BRDF [187]. It consists of an optimal, un-textured representation with many developed models, but is appropriate for opaque materials. Five variables that determine the BRDF are the incidence angle, the exit angle, the polarization of the incident light, the polarization of the reflected light, and the observation time [186]. A BRDF appearance attribute can be used in AM to assess the appearance of an object [5, 148, 188]. It is frequently used to describe the appearance of materials such as metal, glass, or polymers. For BRDF, the surface should be homogenous and un-textured, which heavily depends on the AM techniques.

For instance, BRDF may not be suitable for FFF surfaces with rough and large-scale textures. The spatially varying BRDF (SVBRDF) was developed using texture mapping functions for opaque 3D objects [186].

- BTDF - Bidirectional Transmittance Distribution Function:
  The BTDF is similar to the BRDF, except that it describes the transmittance properties of thin scattering films. Accordingly, the light emerges from the other side of the surface and in the direction of the opposing hemisphere, not significantly separated from the point of incidence [5]. This function is optimal for transparent homogeneous materials as an un-textured representation [186].

- BSDF - Bidirectional Scattering Distribution Function:
  The macroscopic BSDF approximates the BSSRDF, which considers macroscopic local scattering for the incident and emergent lights at the same position on the surface [185, 186]. BSDF is a generalization of BRDF and BTDF [186].

## 4.3. Appearance measurement

Since perception is a psychological phenomenon, manufacturers previously relied heavily on professional observers to make decisions regarding the modification or regulation of a process to achieve the desired outcome. As a result, evaluating appearance has been more of an art than a science up to this point. As human abilities also vary from person to person and with time, attitude, and age, expert opinions can differ and lead to disagreements [150, 189]. In recent years, using quantitative measurements made by instruments has replaced long-term qualitative assessments based on human judgment. To advance appearance technology and appearance research, color and other appearance attributes must be expressed mathematically. Additive manufacturing uses similar methods for measuring the appearance of materials such as textiles, paints, plastics, paper, food, and ceramics [151].

Figure 22 illustrates the CIE recommended 0°|45° and 45°|0° geometries [150], as well as measurement geometry with diffuse (d) illumination in a sphere geometry. A diffuse illumination method employs an Ulbricht sphere in dull white paint to provide homogeneous and diffuse illumination and observe an object virtually from all directions in space.

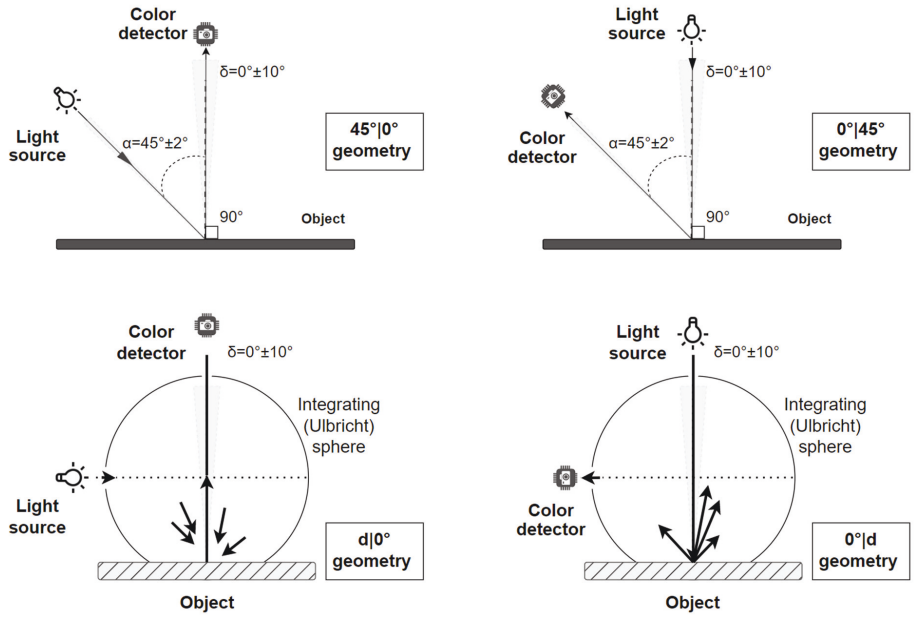


Figure 22. The diagrammatic representation of primary geometries of illumination and measurement

The main color-measuring instruments are tristimulus colorimeters, spectroradiometers, and spectrophotometers [189]. Figure 23 depicts the difference between a tele-spectroradiometer and other color-measuring instruments.

### 4.3.1. Tristimulus colorimeter

Tristimulus colorimeters are the most common spectroradiometers, frequently used as affordable and handheld instruments in R&D labs for color quality control purposes. As long as the illuminant and observer conditions are fixed, e.g., D65/2°, the device can measure color tristimulus values. Generally, the instrument is used to measure surface and self-luminous colors, e.g., computer monitors. It consists of a light source (for non-luminous surfaces), an integrating sphere, and a detector. Several filters are included to provide comparable results to the CIE XYZ color-matching functions. It is, however, challenging to obtain reliable repeatability and instrumental agreement of the tristimulus colorimeter due to the poor reproducibility and aging of the filters in the detectors [189].

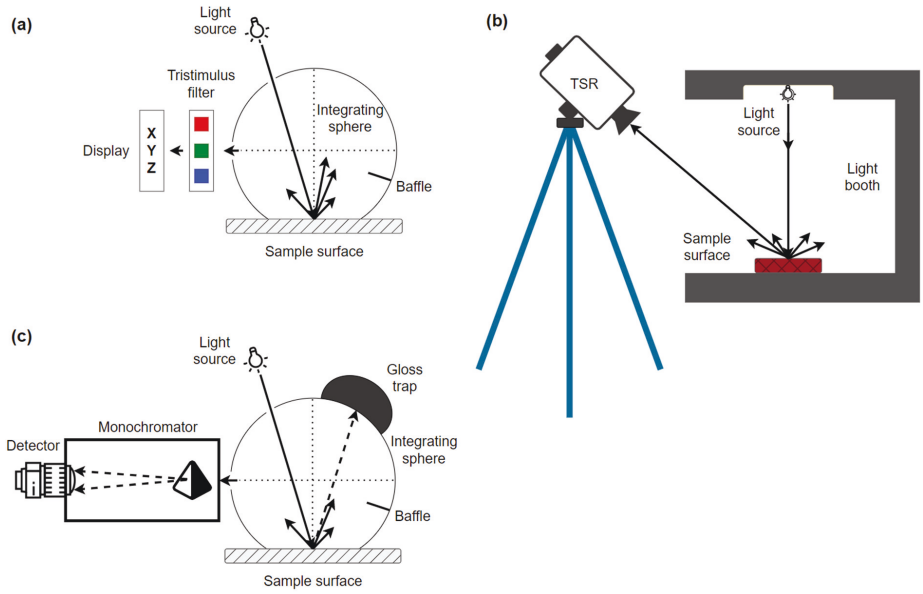


Figure 23. The essential components of each sort of color measuring instrument. a) 0°|d tristimulus colorimeter, b) tele-spectroradiometer (TSR) measuring surface color in a light booth tristimulus at CIE viewing geometries 0°|45°, and c) 0°|d spectrophotometer.

### 4.3.2. Tele-spectroradiometer

One of the most reliable tools for measuring light is a spectroradiometer, which can measure both intensity and wavelength for radiance, chromaticity, and luminance [190]. These instruments have extensive accuracy; however, contactless measurement is more susceptible to calibration, environmental errors, and measurement geometry. The most common type of spectroradiometer is the tele-spectroradiometer (TSR). The TSR is employed to remotely determine the color of an object when it is in its normal observing posture and viewing conditions. In a TSR, the three main components are a monochromator, a detector, and a telescope. Any tele-spectroradiometer can detect both surface colors and self-luminous materials. An external light source is necessary for measuring surface colors but is not essential for self-luminous stimuli. This instrumentation allows measurement results to correlate with actual viewing conditions [189].

In the case of AM, it is beneficial for cross-media color reproduction, such as matching a 3D model on display with the output objects from a 3D machine. Non-contact color measurement systems, including TSRs, are valuable tools for capturing the appearance of non-self-luminous colors of 2.5D and 3D-printed objects due to their feasibility, accuracy, contactless features, affordability, and flexibility in measuring multidimensional geometries and structured surfaces [127]. Thus, they are suitable for industrial applications, especially when the accessible surface is small, textured, or other appearance

measurement instruments cannot be utilized due to their form and geometry. As discussed in the appendices for aged samples, a similar set of challenges applies to curved surfaces (*Papers IV and VIII*).

Regarding non-self-luminous colors, including 2.5D and 3D objects, the samples must be illuminated by a source that provides light that covers the entire spectrum. In addition, the essential measurement of counts is influenced by the detector's sensitivity to each wavelength in most uncalibrated TSR readings. Therefore, the instrument must be calibrated using a reference light source with a determined absolute SPD following the requisite precision. The instrument manufacturer typically includes a calibration plate in the instrument package [150].

By calibrating, spectroradiometers are used to quantify radiometric results such as irradiance (in $W/m^2$) or radiance (in $W/m^2Sr$). An entire spectrum can be captured in one acquisition, differentiating wavelengths based on where the light hits the detector array. Radiometric energy is determined across the visible spectrum (360–830 nm) at 1 nm intervals [191]. However, for practical purposes, the range can be narrowed to 380 to 780 nm at fixed intervals of 5 nm, 10 nm, or 20 nm. For radiance and irradiance units, their colorimetric values are reported as illuminance (in lux) and luminance (in $cd/m^2$) [189].

In the later steps, the data is analyzed using a combination of algorithms and computer software to generate measurements for various parameters, including irradiance, brightness (cd), flux (Lumens or Watts), chromaticity, color temperature, and dominant and peak wavelengths. Some more advanced spectrometer software packages contain capabilities such as 2- and 20-degree observers, baseline overlay comparisons, transmission and reflectance calculations, and distance-dependent candela computations.

### 4.3.3. Spectrophotometer

A spectrophotometer measures the ratio of the incident and reflected lights within the visible spectrum. The measurement is conducted at a fixed interval, e.g., 5 nm, 10 nm, or 20 nm, and reported as the surface reflectance of a color. The system has three optical elements: a light source (illumination), a detector (viewing), and a monochromator. Lighting and viewing should comply with one of CIE recommendations: 0°|45°, 45°|0°, 0°|d, and d|0°. The 45°|0° and 0°|45° geometries are extensively used in computer graphics, and the 0°|d and d|0°geometries are commonly used in surface coloring (textiles, paint, polymers). As a general rule, spectrophotometers are the preferred instrument for surface analysis, quality control, and recipe formulation, where the size and geometry of the object can satisfy the measurement requirements. Metamerism can also be evaluated by this method, i.e., how color differences change with differing illuminations. A spectrophotometer is also reasonably accurate and stable over time compared to an absolute standard; however, more expensive than tristimulus colorimeters. Figure 24 illustrates several instruments used in this study to examine surface appearance attributes.

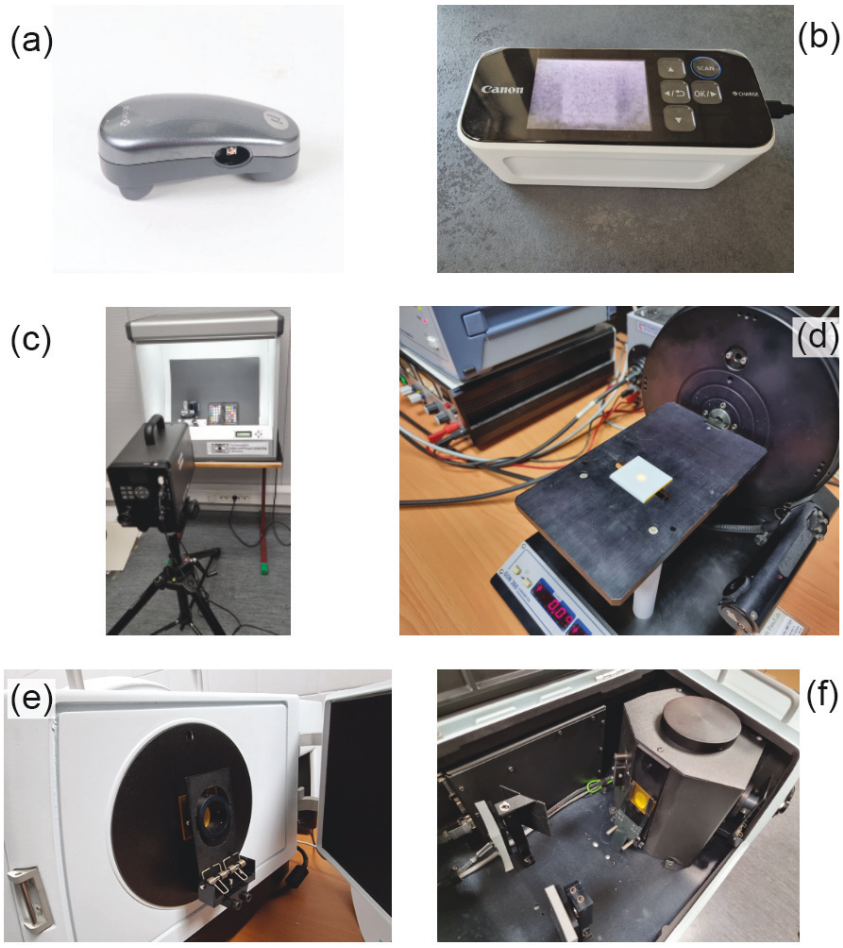


Figure 24. a) X-Rite i1Pro spectrophotometer, b) surface reflectance analyzer by Canon, used for gloss measurement, c) spectroradiometer CS-2000 by Konica Minolta, d) GON 360 goniometer for specular transmission and reflection measurements of translucent surfaces, e) the reflectance and f) transmission/absorption chambers in Perkin Elmer Lambda 1050+ spectrophotometer.

Figure 25 depicts the equipment used to study the surface texture as part of this project. Both tactile and optical instruments were used for 3D surface finish measurements and surface texture analysis. Optical measurements are often preferred over tactile measurements when evaluating texture. There is a thorough comparison of these two categories in the review paper (*Paper III*). To capture the material appearance of 3D-printed objects using a TSR, the reduction of environmental noise and data processing are crucial factors to consider (see Figure 25f).

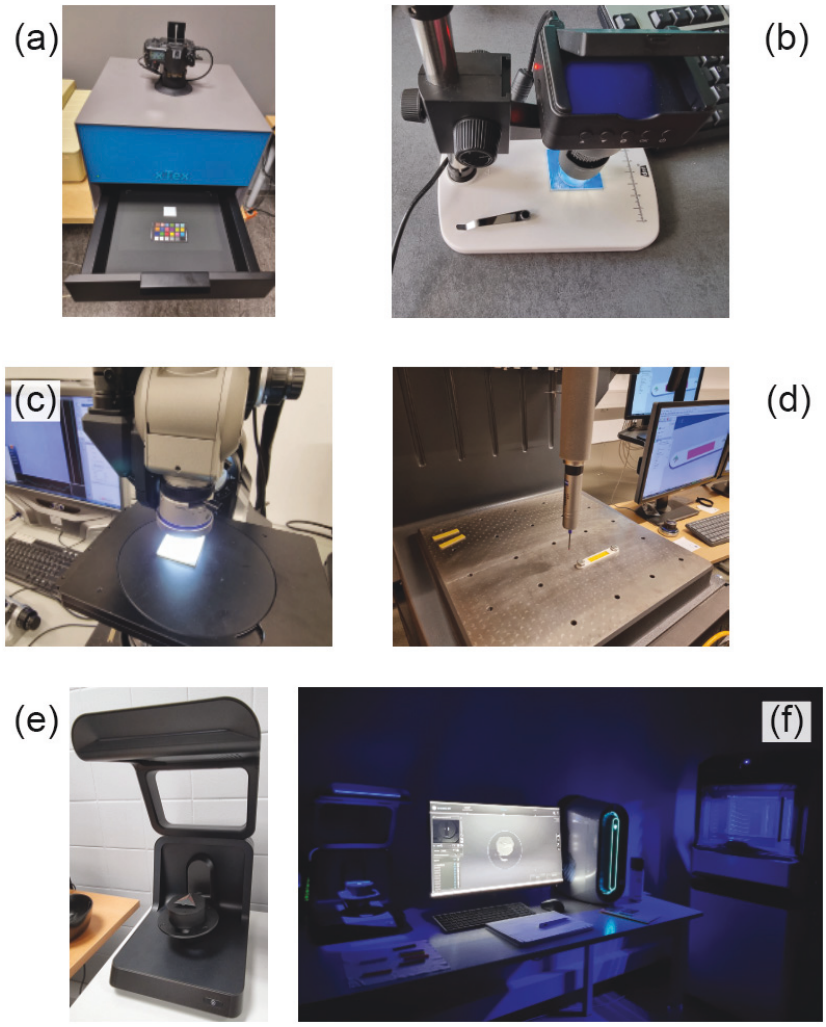


Figure 25. a) xTex scanner by Vizoo, b) digital microscope camera, c) confocal microscope, d) coordinate measuring machines (CMM) for tactile evaluation of the 3D parts, e) Shining 3D scanner, and f) Stray lights due to J55 3D printer and computer sets affecting optical measurements in the 3D scanning process.

### 4.3.4. Errors in appearance measurement in AM objects

To determine the appearance of 3D objects, it is necessary to reduce the noise and errors during capturing optical material properties, communicate appearance attributes, and scan, model, and control 3DP

systems to enhance their appearance. Generally, the three error categories that limit measurement accuracy are systematic, random, and periodic [192]. Systematic errors are deviations from the projected "correct" value mainly caused by the wrong measurement setup, calibration mistakes, human operator, stray light, or the instrument. The electronic and optical components, software, and power supply all play a role in the quality of a spectroradiometer system [193]. In particular, errors can also occur during physical measurements due to spectroradiometer error sources resulting from noise in the measurement environment, non-uniformity of the spectralon, and capturing delay due to the computer hardware and software. Variations in the mean caused by random errors reflect the noise generated by the detector, internal electronics, or the light source. This error can be mitigated by extending the integration time or doing repeated scans. Periodic errors occur due to repeated periodic or pseudo-periodic events such as environmental vibrations, humidity, air movement, and temperature variations [192].

As a result, the output signal is affected by several variables, including the amplitude of the detected flux, its polarization and direction, and wavelength distribution. The inaccuracy of measuring instruments and the standards used to calibrate them leads to a more significant error throughout the measurement process [192, 193]. Furthermore, the geometry and irregularity in the specimens should be considered during the measurement. For instance, missed nuzzles or high absorbance of dust for specific colors in MJT objects are typical issues that can be avoided through TSR measurement. To minimize multidimensionality errors, it is necessary to consider the analyzing approaches for selecting the measurement area on textured surfaces, choosing the correct field of view, focusing, repeating the measurements on other surfaces, and using the reference surface, in addition to minimizing multidimensionality errors.

Stray light and measurement accuracy should be considered when evaluating texture and roughness, particularly for semi-translucent AM polymers (Figure 25f). The term *stray light* refers to the light that travels in a direction other than that intended. Stray light can cause peak distortions and photometric errors in optical measurements [151]. Peak distortion occurs when the stray light intensity exceeds the desired light intensity. It may result in distortion or even concealment of the peaks of the desired light. Consequently, measuring the intensity of the desired light may not be easy. Due to these issues, it is becoming increasingly challenging to develop workflows for achieving the complete appearance of the materials during both the design and manufacturing phases.

Controlling, or ideally eliminating, stray light in optical measurements is a challenging task. During the research conducted to support this thesis, we attempted to reduce the impact of stray light by using filters or carefully designing the optics. When designing translucent 3D models, especially for MJT specimens, stray light transmission inside the material is often an inherent limitation of the system and must be considered. To accomplish this, we considered a bi-layer design with a matte and opaque background and the proper size to fully cover the measurement area. Also, baffles and black and matte curtains were used, the aperture was reduced, measurements were conducted in a room painted with black matte paints, and all necessary lights were eliminated or reduced to minimum levels, e.g., indicator lights.

To conclude this chapter, we reviewed the main appearance attributes and their metric measurements. A focus was placed on color and texture, as well as images of some of the most significant instruments used in this study to assess optical appearances.


This chapter discusses the purpose, results, and relevance of thesis publications according to each sub-research question. For this purpose, a selection of the theoretical and practical contributions from the papers has been discussed. The full articles are available in the appendix.

# 5. Summary of the publications

## 5.1. Paper I

**The influence of wedge angle, feedstock color, and infill density on the color difference of FDM objects (Golhin et al., 2021)**

***Purpose:*** This study aimed to evaluate the influence of the CAD design and slicing parameters in the preprocessing stage on the color difference of FDM objects. Therefore, we described a method for controlling texture generation in the pre-processing step of PLA filaments to alter their color appearance deliberately.

***Findings:*** This study provided insight into the influence of additive manufacturing pre-processing steps on the color difference between structured surfaces. There was evidence that the wedge angle of the elements in the design, the slicing process, and the infill density affect the color appearance of the printed parts in a predictable manner. According to this study, PLA filaments with low infill density and wedge angles provided a high-fidelity color appearance. Due to the increasing CIEDE2000 values at higher wedge angles and infill densities, optimizing the design and selecting the best printing process for the feature FDM printing was possible. According to experimental findings, blue PLA filaments exhibited a more stable color during manufacturing, which means that the filament color can affect the appearance of the same feedstock material. Although the measurements of color difference were unstable due to the layer-by-layer nature of the AM objects, standard spectrophotometers could be used to evaluate the appearance in a comparable manner with TSRs. As a result of the discussed results, it is possible to deliberately alter the color appearance of printed parts in PLA filaments by controlling the generation of surface texture during the pre-processing process.

***Relevant Sub-research question(s):*** FDM additive manufacturing technology was used to prepare structured surfaces in response to SRQ1. Regarding SRQ2, it examined the optical properties of the surfaces produced by FDM. As part of SRQ3, it developed a model that described the possible correlation between the basic parameters of material texturing and the color appearance of the surface. A final explanation of the use of the model for generating surface textures with enhanced color fidelity was provided concerning SRQ4.

## 5.2. Paper II

**Color appearance in rotational material jetting (Golhin et al., 2023)**

***Purpose:*** Using a rotary disc as a build platform, this study examined the correlation between observed color/texture appearance and PolyJet controller parameters.

***Findings:*** Shorter radial printing in MJT using a rotational build platform reduces costs and led to faster printing. Color reproduction did not necessarily become more accurate due to this process. Using a rotary build platform to print on different zones affected the gloss, translucency, and roughness of the printed surface. However, it did not result in samples failing industrial color-matching tests. For instance, a 0.5 mm thickness difference led the CIEDE2000 color difference to rise above 5, culminating in the appearance of an undesired color.

Based on the studied parameters, while changes in the swath or thickness had a negligible effect on the variation of lightness and hue, alterations in surface texture and physical geometry had a significant impact. Thickness had a greater effect on color appearance than swath selection, which was directly influenced by lightness but depended on the ink material. According to the CMM measurement, more low-height asperities were observed in the middle zones of the manufacturing process. A scanned 3D model of the surface confirmed that the height distribution was representative of repeated layers. The effect of lightness on the CIEDE2000 was correlated based on listwise correlation and PCA analysis.

For most specimens, CIEDE2000 could be discerned by an inexperienced observer based on the selected 3DP parameters. The color reproduction in PolyJet printers using rotary discs can, however, meet the criterion of color fidelity in practical situations with different illuminations. MJT objects exhibited all relevant visual characteristics, including color, gloss, translucency, shape, shading, and texture, stimulating visual representation sufficiently to stimulate the intended color. Other appearance attributes should also be addressed to evaluate the total appearance of objects manufactured by rotational MJT.

***Relevant Sub-research question(s):*** In this experimental paper, the four SRQs were considered. In response to SRQ1, MJT additive manufacturing technology was used to prepare structured surfaces. As for SRQ2, it examined the optical properties of the surfaces produced by PolyJet. Within SRQ3, it developed a framework based on the principal component analysis (PCA) that described the possible correlation between the basic parameters of material structuring and the color appearance of the surface. The final explanation of the use of the model for generating surface textures with enhanced color fidelity and texture was provided regarding SRQ4.

## 5.3. Paper III

**Surface roughness of as-printed polymers: A comprehensive review (Golhin et al., 2023)**

***Purpose:*** This review paper was intended to summarize and evaluate the current state of polymer additive manufacturing. It identified significant recent research and described the current trend in the roughness assessment of 3D-printed polymers.

***Findings:*** It has been determined that FFF, SLA, DLP, SLS, and MJT are the principal AM methods for polymers based on scientific publications and market interest. It has been revealed that FFF and MJT provide full-color appearance printing options, which are used in other research papers in this thesis to analyze the appearance of AM objects. Furthermore, the roughness ranges in the review paper contributed to understanding surface morphology and structure, particularly for MJT technology, which was considered in the conference paper IX. According to the publications, PLA, ABS, Nylon (PA), PCL, PE, and PP were the most frequently referred polymers, consecutively. In the reviewed articles, tactile roughness measurement and $R_a$ were often cited as the primary methods and roughness metrics. $R_z$, however, performed better than $R_a$ since it accurately represented both tactile and visual roughness.
This paper proposed a workflow for enhancing the texture appearance of AM polymers based on the roughness parameter. It was discussed how the functional properties of the structured surface in polymer AM can affect their applications. Aside from the surface texture and topography, a suitable surface roughness modification can ensure the desired performance requirements for defined applications. Accordingly, the application and challenges corresponding to the surface roughness were discussed.

***Relevant Sub-research question(s):*** This comprehensive review paper provided a deep understanding relevant to all four SRQs. An in-depth understanding of SRQ1 was provided: Applying additive manufacturing technologies to create structured surfaces. It offered a detailed and comprehensive literature review on analyzing the optical and functional properties of the structured surfaces in AM technology (SRQ2), focusing on their surface roughness and dimensional accuracy. It also discussed analytical methods describing the possible correlation between the basic parameters of material texturing and the surface roughness for as-printed parts (SRQ3). Furthermore, it corresponds to SRQ4: The use of the model for the generation of surface texturing with enhanced optical and functional properties by optimization of surface roughness.

## 5.4. Paper IV

**Effects of accelerated aging on the appearance and mechanical performance of materials jetting products (Golhin et al., 2023)**

***Purpose:*** The purpose of the study was to use a PolyJet 3D printer to manufacture bi-layer polymer structures and study the functional and optical properties of their structured surfaces. We examined the appearance, mechanical, and physicochemical properties of acrylic-simulated parts following 103 days of accelerated aging.

***Findings:*** Studied polymer structures displayed higher elastic modulus (E) and glass transition temperature ($T_g$) values during the aging process. As determined by Taguchi and Redundancy Analysis (RDA), mechanical and physicochemical properties varied the most after 58 days of accelerated aging, with elastic modulus retention ranging from 149.21% to 116.6% and $T_g$ of 116.6%. In general, exposure to ultraviolet light reduced the mechanical and optical fidelity of the parts.
Distinct colors and mechanical properties were observed due to the dynamic responses of the photo resins to weathering agents as shown in Figure 26. For instance, magenta samples showed remarkably similar hue distributions to yellow materials in the CIE1976 u', v' chromaticity diagram after 12 days. Therefore, specimen's behavior is changed accordingly. For both color difference and its RMSE, most of the minimum values were reached between 33 and 58 days after the experiment began. A 58-day accelerated weathering in the QUV chamber resulted in the most significant variation in E and $T_g$. Dynamic Mechanical Analysis (DMA) samples display a curvature along their length due to the aging process, post-UV curing, and the circular layer-by-layer structure observed in MJT pieces.

The Taguchi analysis indicated that color appearance solely correlated with the photo resin factor. Nevertheless, E and $T_g$ were affected by all factors studied, including color, swath, and finishing. The MJT pieces appeared to have less elastic modulus and glass transition temperature variation due to printing on the outer swath or selecting a gloss-on-matte finish. Based on mean CIEDE2000 color differences, black and cyan photo resins showed significantly lower color differences and higher reliability than magenta and yellow photo resins. PolyJet materials are generally complex to test mechanically due to their viscoelastic properties. Despite this, they provided a reasonable level of mechanical durability during this long-term study. However, evaluating 3D-printed objects, particularly multi-layer AM products, is critical for long-term success. By using it, new avenues can be opened in the field of additive manufacturing for improving 3DP algorithms and multi-layer compatibility.

***Relevant Sub-research question(s):*** This experimental study examined the four SRQs. MJT additive manufacturing technology was used to prepare bilayer structures in response to SRQ1. As for SRQ2, it assessed the functional and optical properties of the PolyJet-produced structured surfaces. This work described the correlation between the basic parameters of material structuring and the surface's optical and functional properties, considering SRQ3. For this purpose, the Taguchi and RDA methods were employed to examine the effects of manufacturing parameters, such as color, position on the build platform (swath), and finishing options between layers, on the response variables. An analysis of

desirability was conducted to minimize the color and corresponding RMSE values and maximize the elastic modulus and glass transition temperature. According to SRQ4, the final explanation of how to use the model for generating surface textures with enhanced mechanical and color appearances for long-term applications is provided.

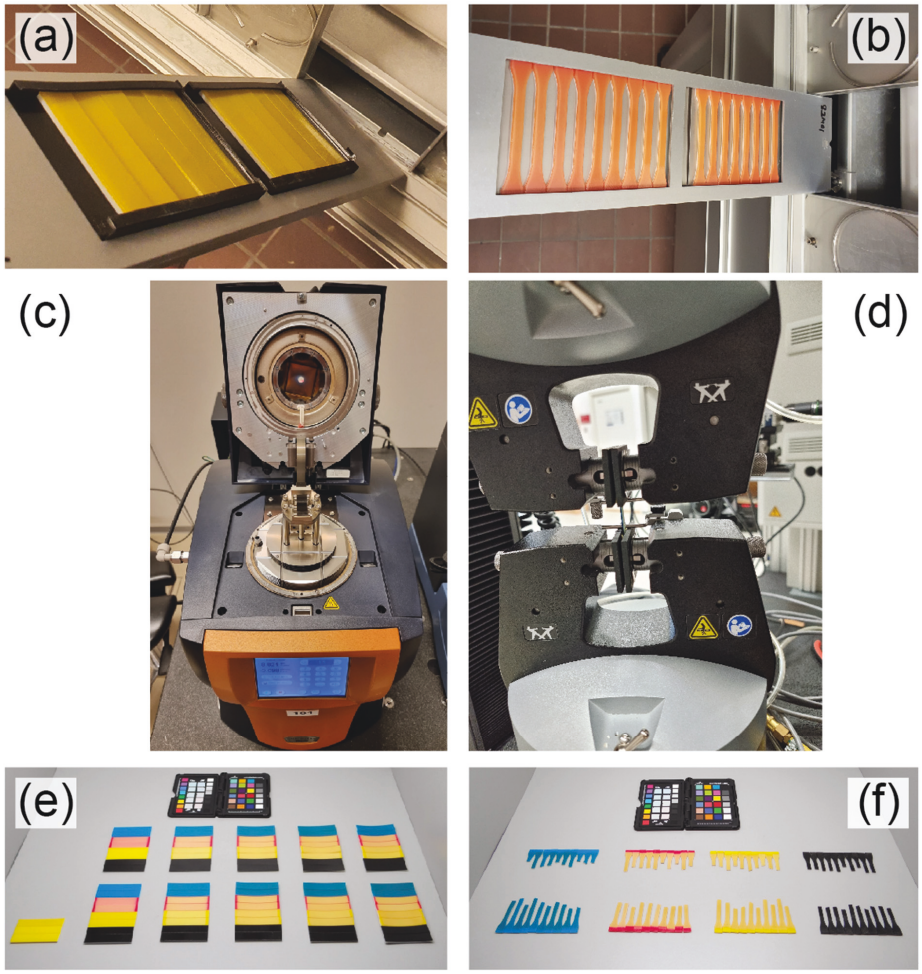


Figure 26. The functional study of 3D-printed coupons: a) DMA and b) Tensile test coupons in the QUV accelerated weathering chamber, c) DMA and d) Tensile universal testing machines, and e) DMA and f) Tensile test coupons after aging and in a light booth under standard D50 illumination.

## 5.5. Paper V

**Appearance evaluation of digital materials in material jetting (Golhin et al., 2023)**

***Purpose:*** This paper attempted to provide insight into how the bilayer structure influences the reproduction of the material jetting appearance. For this purpose, all primary appearance attributes were studied.

***Findings:*** Observations at the microscopic level revealed that MJT objects appear differently under different illuminations and at different microscopic scales. The texture appears less homogeneous due to microscopic inhomogeneities and subsurface turbulence in layers as a consequence of layer-by-layer rotational printing, vibrations of the rotary disc used as the build platform, and translucency of photo resins. According to spectrophotometry, there was an increase in transparency and a decrease in albedo and color fidelity when there was no white background plate. In terms of CIE1976 u', v', and chroma, a monolayer CMYKW resin significantly deviated from the Pantone color matching scheme. Moreover, the increase in absorbance associated with doubling the thickness of monolayer samples was not compensated for by increased reflectance and lower albedo. As in transmittance conditions, gloss perception was also characterized by monolayer/bilayer structures. Bilayer specimens were found to have higher gloss and haze levels than monolayer specimens. White backgrounds had a greater impact on color, translucency, and scattering than gloss and haze results. Because of vertical measurements, gloss, haze, and scattering were elevated, while horizontal measurements were the opposite. Based on renderings of spherical 3D models, cyan, magenta, and yellow photo resins had significantly different appearances in monolayer structures.

***Relevant Sub-research question(s):*** This experimental paper addressed the four SRQs. A structured surface was prepared using additive manufacturing technology in response to SRQ1. As for SRQ2, it examined the optical properties of the surfaces produced by PolyJet. Concerning SRQ3, BRDF models for specular angles related to the gloss measurements were visualized. Furthermore, rendered images based on surface texture models were illustrated and Spearman rank correlation was used to describe a correlation between manufacturing conditions and the appearance of the surface. With SRQ4, the explanation of the use of the model for 3D printing with improved appearance and texture was presented.

## 5.6. Paper VI

**Optical properties of tilted surfaces in material jetting (Golhin et al., 2023)**

***Purpose:*** As a necessary step towards reproducing full-color appearances, this paper examined how the build orientation influences optical properties and appearance attributes of 3D-printed objects.

***Findings:*** Microscopy showed that MJT objects produced at different build orientations (BOs) had different textures and surface characteristics, including layer configurations, gas porosities, droplet separation, and subsurface turbulence in layers. Tilting the manufactured surface caused microscopic inhomogeneities that affected the optical properties of MJT objects due to their translucency. As an explanation, processing forces like gravity and centrifugal force affected texture variation. BO affected the reflectance, transmittance, and absorbance of CMY colors more than black photo resin, according to spectrophotometric analysis. PCA score distribution explained spectral shifts. Although each photo resin responded differently to the principal components, the materials studied showed the same variation in reflectance and transmittance. The Kendall rank correlation coefficient for transmittance measurements showed that BO 75° deviated more. Reflectance shifts were greatest for BOs 60° and 90°. It also revealed the texture and manufactured layer variation affected reflectance more than transmittance. The variation in the microsurface normal direction affected gloss, haze, and scattering results. The CIEDE2000 color difference increased by less than 2 due to using different BOs. Tilting surfaces from 0° to 90° reduced vertical gloss and haze. Regardless of direction, BO increased subsurface scattering results. Furthermore, BO significantly affected the surface texture and layer orientation, affecting all studied attributes and varying surface quality. Results also suggested that the measurement direction significantly affects the gloss results in AM. In response to different BO, the study of the gloss and scattering were more crucial than color appearance in MJT products.

***Relevant Sub-research question(s):*** SRQ1 was addressed by preparing a structured surface using material jetting. Regarding SRQ2, it examined the optical properties of 3D-printed surfaces. Concerning SRQ3, the BRDF models of specular angles were visualized based on gloss measurements. A PCA was used to describe the correlation between build orientation and surface appearance based on rendered images derived from surface texture models. For SRQ4, an explanation of how the model may improve the appearance and texture of 3D-printed objects was extended.

## 5.7. Paper VII

**BRDF representation in response to the build orientation in 3D-printed digital materials (Golhin et al., 2023)**

***Purpose:*** This study evaluated light reflection on the MJT surfaces based on BRDF measurements using a gonio-spectrophotometer for 3D-printed objects using different build orientations.

***Findings:*** BRDF model can explain the surface reflectance at different viewing angles for MJT objects due to their smooth and homogenous surfaces. Incorrect orientation can reduce the accuracy of material jetting. The texture and surface roughness study carried out in this paper noticed higher build orientation wedge angle increased surface roughness, especially for vertical 3D-printed surfaces. Horizontal printing deposited material layers on top of each other, creating a smoother surface texture. When printed vertically, layers were deposited at a non-horizontal angle, creating an irregular surface texture, especially for wedge angles of 90 degrees. The results also exhibited that object orientation affects CMYK hue distribution as viewed at different geometries, particularly for cyan and magenta compared to yellow and black resins. RDA and PCA techniques identified spectral bands that contributed more to BRDF changes and the correlation between variables like build orientation and surface reflectance. Incorporating luminance distribution (Y) and PCA scores of reflectances helped understand 3D-printed surface appearance and texture, which could improve printing process optimization.

***Relevant Sub-research question(s):*** A methodology for addressing SRQ1 and SRQ2 was developed by manufacturing surfaces and analyzing their optical reflectances. Regarding SRQ3, BRDF models based on 328 different measurement geometries were visualized and compared for all the examined BOs. The BRDF model was described using a PCA and the significant measurement geometries were determined to model the surface reflectance using fewer measurement geometries. In response to SRQ4, an explanation of how the model could be used to achieve more efficient measurement was provided.

## 5.8. Paper VIII

**Additive manufacturing of multilayered polymer composites: Durability assessment (Golhin et al., 2022)**

***Purpose:***

This conference paper examined the role of short-term aging in the color appearance, and mechanical and physicochemical properties of acrylic-simulated parts. We conducted experimental studies as part of *Paper IV,* " Effects of accelerated aging on the appearance and mechanical performance of material jetting products ", emphasizing the behavior of the materials over a short period.

***Findings:***

The results of this 2-week study formed a basis for a long-term aging study on the MJT parts. It is confirmed the best factor parameters for each performance characteristic vary according to the design of experiments. In terms of color appearance, after two weeks of aging, black and then cyan samples showed significantly stronger color fidelity than magenta and yellow photoresins. In particular, black-on-white with a glossy-on-matte finish manufactured on the outer swath demonstrated the highest color and mechanical fidelity, with no significant aging effects on the studied properties. There was an increase in elastic modulus and $T_g$ due to the inner swath and GoG finish. During mechanical testing, cyan samples demonstrated higher E and $T_g$ than black, whereas magenta and yellow samples exhibited unstable behavior. In the weathering test, all aged MJT coupons exhibited significantly different optical and functional properties compared to un-aged reference coupons. It indicated that post-curing due to ultraviolet (UV) absorption can explain the observed more rigid materials with altered appearance and mechanical properties.

***Relevant Sub-research question(s):***

To respond to SRQ1, MJT additive manufacturing technology was utilized. A study of the color appearance and functional properties of the 3D-printed structured surfaces is being conducted as part of SRQ2. This study investigated a possible correlation between material structuring parameters and the surface's optical and functional properties over a short period, considering SRQ3. The Taguchi method was also used to investigate the effects of manufacturing parameters, such as color, location on the build platform, and layer finishing options on response variables.

## 5.9. Paper IX

**Evaluation of surface texture in material jetting (Golhin et al., 2023)**

***Purpose:*** This conference paper is intended to study the impact of the additive manufacturing process on the texture of structured surfaces.

***Findings:*** Based on the results of the FFT analysis applied to the height maps, the minimum arithmetic mean (5.7 μm) and maximum FWHM (3.8 μm) were within the middle swath, indicating a significant trend in swath selection. Using the PSD results, the periodicity of the layers was determined, and their widths were calculated. During the transition from the inner area to the outer edge of the build platform, the layer thickness decreased from 305 mm to 303 mm, resulting in closer layers being printed. Centrifugal forces may have increased along the radius of the disc as a result of this effect. This resulted in smoother surfaces on the middle swath of the build platform. This area, however, required more time to print than the inner swath. Using 3DP technology under optimized conditions resulted in parts with improved surface quality in the middle swath. As MJT technology with rotary trays is now capable of creating prototypes for home and office use, these results may help to improve the understanding of the surface texture in these printers and reduce post-processing steps.

***Relevant Sub-research question(s):*** Experimental studies were conducted as part of *Paper II* "Color appearance in rotational material jetting" project, emphasizing tactile and optical scanning of the surface text. In response to SRQ1, MJT additive manufacturing technology was used to prepare additively manufactured structures. For SRQ2, the texture of the structured surfaces was assessed.

# Chapter 6- Conclusions and Future Perspectives

*"Life's greatest adventure is in doing one's level best."*

Arthur Morgan, Red Dead Redemption 2

# 6. Summary

## 6.1. Conclusions

The workflow of AM should ensure that a fundamental aspect of the process is the ability to match the desired appearance of materials, including color, gloss, texture, translucency, etc. The appearance attributes determine whether a product is accepted or rejected most rapidly. It is necessary whether it is the requirements of real life, the requirements of computer-generated designs, reproductions, or manufactured products.

As introduced in Chapter 1, the advent of AM revealed many new possibilities affected by the textured surfaces of AM products. Therefore, the surface modification approach must also meet these high-performance requirements. As part of this thesis, a thorough investigation of surface quality in 3D printing was conducted, both from the viewpoint of appearance and functionality. A discussion of the most prominent AM techniques, their parts surface quality, and appearance and measurement techniques for 3D objects followed.

Chapter 2 presented the background and an introduction to the studied AM methods and 3DP techniques under different categories. Through focusing on polymers, these methods included FFF, PolyJet, SLA, and SLS methods. Then, their relevant surface issues have been briefly provided. It is revealed from the literature review that the workflow of surface modification in the pre-processing step heavily depends on the complexity of the design and the desired quality-time-cost balance. As mentioned for the PolyJet technology, the MJT samples present more challenges than other FFF and SLS due to their semi-translucent and full-color appearance, which can be affected by high gloss and detailed textures.

Chapter 3 discussed how the success of technological advancements in additive manufacturing in the long term is dependent on the surface quality and functional properties of the parts. In particular, we referred to several fields, such as medical models, which must be printed as accurately as possible regarding their color and surface roughness. To discuss how primary processing parameters can be optimized to improve surface quality for functionality and appearance, it is necessary to introduce the methods and the primary printing parameters. This topic followed the appearance context in Chapter 4 by discussing the appearance attributes, including color, gloss, transparency, translucency, and texture. This is completed by discussing the optical investigation of textured surfaces, appearance measurement methods, and possible errors and challenges in the experimental part.

Finally, in Chapter 5, the results from the papers were summarized as a conclusion of identifying printing variables and their effects on the appearance of the objects. An explanation of how structured surfaces are manufactured is provided in the papers, along with the main factors that affect the quality of the AM parts. Among the topics covered were pre-processing and processing factors such as design and build orientation, material type, parameters associated with the printing system, environmental factors, their short-term and long-term effects, and the influence of the initial post-processing itself.

According to the proposed models in the papers, the observed color is caused by light interference at the multilayered surface of printed materials. The texture effect on color, gloss, haze, scattering, translucency, and BRDF was explained in the papers, focusing on the electromagnetic theory of light interference. A set of statistical descriptors is used to describe texture effects on light interference, considering the role of the printing setting, which is then can improve appearance prediction. According

to this research, each application requires different adjustments or changes to its printing parameters, considering the synergy among the appearance attributes, so the optimization process varies from one application to another.

In conclusion, despite remarkable progress in exploring individual aspects of appearance measurement, the field of total appearance measurement and reproduction is still in its infancy. Application of appearance measurement findings to industries such as 3D printing holds significant promise for improving the quality and aesthetics of printed objects, which ultimately benefits various industries that require accurate and realistic representations of appearance.

## 6.2. Future perspective

The technology of 3D printing is becoming increasingly refined and widespread, and its applications in aesthetics and functionality are increasing. It has been observed that the field of appearance measurement has experienced a significant surge in recent years, resulting in numerous new studies and innovative findings. Color, texture, and gloss have been explored in these works primarily as individual aspects of appearance. However, having accurate measurements and reproductions of total appearance is essential for the quality and aesthetics of 3D-printed objects. Researchers and practitioners can develop robust methodologies for capturing and reproducing the total appearance of objects in 3D printing by leveraging the innovative results achieved to date. This holistic approach would facilitate the development of material databases and optimization algorithms specifically tailored for 3D printing, thereby improving the efficiency of the manufacturing process.

3DP has been used to create art, as developed in the approach of 2.5D printing. It allows for creating paintings, artistic replicas, sculptures, and other artworks that would be impractical to create using conventional methods. Furthermore, appearance 3DP can make jewelry, eyeglasses, and many other items that are impossible or difficult to generate using subtractive manufacturing methods. It is expected that industry standardization will increase, including adopting the 3Mf file format, which contains material data, color, texture, geometry, printer configuration information, support structure, and topologically-optimized lattices, as well as reliability and repeatability across 3DP technologies. The use of 3DP for end-use parts and serial production is becoming more viable. It is critical to consider scalable quality control as end-use production applications increase, particularly critical components. It is possible to achieve this by strategically utilizing 3DP process data and simulation software and implementing scalable testing strategies, considering the fidelity to the initial 3D model.

For future work, we expect that by combining the boundary constraint theory with the prediction model for coloring performance, researchers will be able to rethink and develop robust appearance additive manufacturing aimed at modulating computational material assignment precisely to achieve a generic accurate reproduction framework for color matching. The design of test benchmarks, practical instructions, and numerical analysis models for assessing the performance of color reproduction is also vital for fulfilling accurate material-aware full-color additive manufacturing. It is also expected to extend the high color fidelity full-color 3DP to 4D additive manufacturing with an accurate color response. There is also expected to be an increasing focus on other appearance attributes to achieve high-fidelity total appearance in 3D printing. The field of functional material design also encompasses this new research area with high integrity to the appearance 3D printing.

# Bibliography

[1] C.I.d. l'Éclairage, Definition of appearance in CIE's e-ILV, CIE S 017:2020, Commission Internationale de l'Éclairage, 2020.
[2] ASTM, Standard Terminology of Appearance, in: A. E284-17 (Ed.) ASTM International West Conshohocken, PA, 2017, pp. 1-25. https://doi.org/10.1520/E0284-17.
[3] M.R. Pointer, Measuring visual appearance-a framework of the future. Project 2.3 measurement of appearance, (2003).
[4] B.L. Anderson, Visual perception of materials and surfaces, Current biology 21(24) (2011) R978-R983.
[5] J.R. Frisvad, S.A. Jensen, J.S. Madsen, A. Correia, L. Yang, S.K.S. Gregersen, Y. Meuret, P.E. Hansen, Survey of models for acquiring the optical properties of translucent materials, Comput. Graph. Forum, Wiley Online Library, 2020, pp. 729-755. https://doi.org/10.1111/cgf.14023.
[6] J. Dorsey, H. Rushmeier, F. Sillion, Digital modeling of material appearance, Elsevier 2010.
[7] ApPEARS project: Structure concept, 2019. https://www.appears-itn.eu/about/structure/.
[8] T. Roberts, Additive manufacturing trend report 2021: 3D printing market growth in the year of the COVID-19 3D Hubs B.V, 2021.
[9] M.G. Isaac Simon, 3D Printing Trend Report 2022: Market changes and technological shifts in the 3D printing market, 3D Hubs B.V, 2022.
[10] N. Baudet, J.-L. Maire, M. Pillet, The visual inspection of product surfaces, Food Qual. Preference 27(2) (2013) 153-160.
[11] Goal 12: Ensure sustainable consumption and production patterns, 2022. https://www.un.org/sustainabledevelopment/sustainable-consumption-production/.
[12] J. Rowley, Using case studies in research, Management research news (2002).
[13] A.C.F.o.A.M. Technologies, A.C.F.o.A.M.T.S.F.o. Terminology, Standard terminology for additive manufacturing technologies, Astm International 2012.
[14] T. Wohlers, 3D printing and additive manufacturing: Global state of the industry, Wohlers Report 2020, Wohlers Associates, 2020.
[15] S. Yusheng, Y. Chunze, Z. Yan, W. Jiamin, W. Yan, Y. Shengfu, Y. Chen, Materials for Additive Manufacturing, Academic Press, [N.p.], 2021.
[16] L. Jonušauskas, S. Juodkazis, M. Malinauskas, Optical 3D printing: Bridging the gaps in the mesoscale, J. Opt. 20(5) (2018). https://doi.org/10.1088/2040-8986/aab3fe.
[17] J.S. Chohan, R. Singh, Pre and post processing techniques to improve surface characteristics of FDM parts: A state of art review and future applications, Rapid Prototyping J. 23(3) (2017) 495-513. https://doi.org/10.1108/RPJ-05-2015-0059.
[18] X. Zheng, H. Lee, T.H. Weisgraber, M. Shusteff, J. DeOtte, E.B. Duoss, J.D. Kuntz, M.M. Biener, Q. Ge, J.A. Jackson, Ultralight, ultrastiff mechanical metamaterials, Science 344(6190) (2014) 1373-1377. https://doi.org/10.1126/science.1252291.
[19] J.L. Silverberg, A.A. Evans, L. McLeod, R.C. Hayward, T. Hull, C.D. Santangelo, I. Cohen, Using origami design principles to fold reprogrammable mechanical metamaterials, Science 345(6197) (2014) 647-650.
[20] A. Sihvola, Metamaterials in electromagnetics, Metamaterials 1(1) (2007) 2-11.
[21] D.R. Smith, J.B. Pendry, M.C.K. Wiltshire, Metamaterials and negative refractive index, Science 305(5685) (2004) 788-792. https://doi.org/10.1126/science.1096796.
[22] M.C. Wu, L.-Y. Lin, S.-S. Lee, K. Pister, Micromachined free-space integrated micro-optics, Sensors and Actuators A: Physical 50(1-2) (1995) 127-134. https://doi.org/10.1016/0924-4247(96)80096-3.
[23] Á. Ríos, M. Zougagh, M. Avila, Miniaturization through lab-on-a-chip: Utopia or reality for routine laboratories? A review, Anal. Chim. Acta 740 (2012) 1-11. https://doi.org/Miniaturization through lab-on-a-chip: Utopia or reality for routine laboratories? A review.
[24] Additive manufacturing - General principles - Fundamentals and vocabulary, ISO/ASTM 52900:2021, International Organization for Standardization: Geneva, Switzerland, 2021, pp. 1-36.
[25] D. Svetlizky, M. Das, B. Zheng, A.L. Vyatskikh, S. Bose, A. Bandyopadhyay, J.M. Schoenung, E.J. Lavernia, N. Eliaz, Directed energy deposition (DED) additive manufacturing: Physical

characteristics, defects, challenges and applications, Mater. Today 49 (2021) 271-295. https://doi.org/https://doi.org/10.1016/j.mattod.2021.03.020.
[26] S.D. Nath, S. Nilufar, An overview of additive manufacturing of polymers and associated composites, Polymers 12(11) (2020) 2719. https://doi.org/10.3390/polym12112719.
[27] M. Rafiee, R.D. Farahani, D. Therriault, Multi-material 3D and 4D printing: a survey, Adv. Sci. 7(12) (2020) 1902307. https://doi.org/10.1002/advs.201902307.
[28] C.M. González-Henríquez, M.A. Sarabia-Vallejos, J. Rodriguez-Hernandez, Polymers for additive manufacturing and 4D-printing: Materials, methodologies, and biomedical applications, Prog. Polym. Sci. 94 (2019) 57-116. https://doi.org/10.1016/j.progpolymsci.2019.03.001.
[29] S.C. Ligon, R. Liska, J. Stampfl, M. Gurr, R. Mülhaupt, Polymers for 3D Printing and Customized Additive Manufacturing, Chem. Rev. 117(15) (2017) 10212-10290. https://doi.org/10.1021/acs.chemrev.7b00074.
[30] B.L. Alex Xu, Martin Erharter, Vatche Kourkejian, Polymer additive manufacturing market today and in the future, 2021. https://www.rolandberger.com/en/Insights/Publications/Polymer-additive-manufacturing-Market-today-and-in-the-future.html. (Accessed 1 July 2021).
[31] I. Karakurt, L. Lin, 3D printing technologies: techniques, materials, and post-processing, Curr. Opin. Chem. Eng. 28 (2020) 134-143. https://doi.org/10.1016/j.coche.2020.04.001.
[32] S.C. Daminabo, S. Goel, S.A. Grammatikos, H.Y. Nezhad, V.K. Thakur, Fused deposition modeling-based additive manufacturing (3D printing): techniques for polymer material systems, Mater. Today Chem. 16 (2020). https://doi.org/10.1016/j.mtchem.2020.100248.
[33] A. Lalehpour, C. Janeteas, A. Barari, Surface roughness of FDM parts after post-processing with acetone vapor bath smoothing process, Int. J. Adv. Manuf. Technol. 95(1-4) (2018) 1505-1520. https://doi.org/10.1007/s00170-017-1165-5.
[34] J. Yuan, M. Zhu, B. Xu, G. Chen, Review on processes and color quality evaluation of color 3D printing, Rapid Prototyping J. 24(2) (2018) 409-415. https://doi.org/10.1108/RPJ-11-2016-0182.
[35] S. Vyavahare, S. Teraiya, D. Panghal, S. Kumar, Fused deposition modelling: A review, Rapid Prototyping J. 26(1) (2020) 176-201. https://doi.org/10.1108/RPJ-04-2019-0106.
[36] J. Yuan, G. Chen, H. Li, H. Prautzsch, K. Xiao, Accurate and Computational: A review of color reproduction in Full-color 3D printing, Materials and Design 209 (2021) 1-17. https://doi.org/10.1016/j.matdes.2021.109943.
[37] A.D. Mazurchevici, D. Nedelcu, R. Popa, Additive manufacturing of composite materials by FDM technology: A review, Indian J. Eng. Mater. Sci. 27(2) (2020) 179-192.
[38] C. Palanisamy, R. Raman, P. Dhanraj, Additive manufacturing: a review on mechanical properties of polyjet and FDM printed parts, Polymer Bulletin (2021). https://doi.org/10.1007/s00289-021-03899-0.
[39] O.A. Mohamed, S.H. Masood, J.L. Bhowmik, Optimization of fused deposition modeling process parameters for dimensional accuracy using I-optimality criterion, Meas J Int Meas Confed 81 (2016) 174-196. https://doi.org/10.1016/j.measurement.2015.12.011.
[40] I. Farina, N. Singh, F. Colangelo, R. Luciano, G. Bonazzi, F. Fraternali, High-performance Nylon-6 sustainable filaments for additive manufacturing, Materials 12(23) (2019). https://doi.org/10.3390/ma122333955.
[41] H. Wu, W.P. Fahy, S. Kim, H. Kim, N. Zhao, L. Pilato, A. Kafi, S. Bateman, J.H. Koo, Recent developments in polymers/polymer nanocomposites for additive manufacturing, Prog Mater Sci 111 (2020). https://doi.org/10.1016/j.pmatsci.2020.100638.
[42] T.M. Tanksale, P. Urban, Trichromatic reflectance capture using a tunable light source: Setup, characterization and reflectance estimation, IS and T International Symposium on Electronic Imaging Science and Technology, 2016. https://doi.org/10.2352/issn.2470-1173.2016.9.mmrma-355.
[43] D.S. Engstrom, B. Porter, M. Pacios, H. Bhaskaran, Additive nanomanufacturing - A review, J. Mater. Res. 29(17) (2014) 1792-1816. https://doi.org/10.1557/jmr.2014.159.
[44] N. Vidakis, M. Petousis, N. Vaxevanidis, J. Kechagias, Surface roughness investigation of poly-jet 3D printing, Mathematics 8(10) (2020) 1-14. https://doi.org/10.3390/math8101758.
[45] K.E. Aslani, F. Vakouftsi, J.D. Kechagias, N.E. Mastorakis, Surface Roughness Optimization of Poly-Jet 3D Printing Using Grey Taguchi Method, Proceedings - 2019 3rd International Conference on

Control, Artificial Intelligence, Robotics and Optimization, ICCAIRO 2019, 2019, pp. 213-218. https://doi.org/10.1109/ICCAIRO47923.2019.00041.
[46] T. Chen, J. Dilag, S. Bateman, Surface topology modification of organic substrates using material jetting technologies, Materials and Design 196 (2020). https://doi.org/10.1016/j.matdes.2020.109116.
[47] O. Gülcan, K. Günaydın, A. Tamer, The state of the art of material jetting—a critical review, Polymers 13(16) (2021). https://doi.org/10.3390/polym13162829.
[48] P. Szymczyk-Ziółkowska, M.B. Łabowska, J. Detyna, I. Michalak, P. Gruber, A review of fabrication polymer scaffolds for biomedical applications using additive manufacturing techniques, Biocybern. Biomed. Eng. 40(2) (2020) 624-638. https://doi.org/10.1016/j.bbe.2020.01.015.
[49] L. Rebaioli, I. Fassi, A review on benchmark artifacts for evaluating the geometrical performance of additive manufacturing processes, Int. J. Adv. Manuf. Technol. 93(5-8) (2017) 2571-2598. https://doi.org/10.1007/s00170-017-0570-0.
[50] H. Kim, Y. Lin, T.L.B. Tseng, A review on quality control in additive manufacturing, Rapid Prototyping J. 24(3) (2018) 645-669. https://doi.org/10.1108/RPJ-03-2017-0048.
[51] L. Bass, N.A. Meisel, C.B. Williams, Exploring variability of orientation and aging effects in material properties of multi-material jetting parts, Rapid Prototyping J. 22(5) (2016) 826-834. https://doi.org/10.1108/RPJ-11-2015-0169.
[52] F. Alifui-Segbaya, S. Varma, G.J. Lieschke, R. George, Biocompatibility of Photopolymers in 3D Printing, 3D Print. Addit. Manuf. 4(4) (2017) 185-191. https://doi.org/10.1089/3dp.2017.0064.
[53] I. Gibson, D. Rosen, B. Stucker, M. Khorasani, Additive manufacturing technologies, Springer 2014. https://doi.org/10.1007/978-1-4939-2113-3.
[54] M. Revilla-León, M.J. Meyers, A. Zandinejad, M. Özcan, A review on chemical composition, mechanical properties, and manufacturing work flow of additively manufactured current polymers for interim dental restorations, J. Esthetic Restorative Dent. 31(1) (2019) 51-57. https://doi.org/10.1111/jerd.12438.
[55] X. Wei, A. Bhardwaj, L. Zeng, Z. Pei, Experimental investigation of stratasys J750 polyjet printer: Effects of finish type and shore hardness on surface roughness, ASME 2019 14th International Manufacturing Science and Engineering Conference, MSEC 2019, 2019. https://doi.org/10.1115/MSEC2019-2998.
[56] K. Thakare, X. Wei, Z. Pei, Dimensional accuracy in polyjet printing: A literature review, ASME 2019 14th International Manufacturing Science and Engineering Conference, MSEC 2019, 2019. https://doi.org/10.1115/MSEC2019-3018.
[57] W.-Y. Yeong, C.-K. Chua, K.-F. Leong, M. Chandrasekaran, M. Lee, Development of scaffolds for tissue engineering using a 3D inkjet, Virtual Modelling and Rapid Manufacturing: Advanced Research in Virtual and Rapid Prototyping Proc. 2nd Int. Conf. on Advanced Research in Virtual and Rapid Prototyping, 28 Sep-1 Oct 2005, Leiria, Portugal, CRC Press, 2005, p. 115.
[58] M. Sugavaneswaran, G. Arumaikkannu, Analytical and experimental investigation on elastic modulus of reinforced additive manufactured structure, Mater. Des. 66 (2015) 29-36. https://doi.org/10.1016/j.matdes.2014.10.029.
[59] Z.X. Khoo, J.E.M. Teoh, Y. Liu, C.K. Chua, S. Yang, J. An, K.F. Leong, W.Y. Yeong, 3D printing of smart materials: A review on recent progresses in 4D printing, Virtual Phys. Prototyp. 10(3) (2015) 103-122. https://doi.org/10.1080/17452759.2015.1097054.
[60] PolyJet Materials and Uses: Tips and Tricks, 2018. https://grabcad.com/tutorials/polyjet-materials-and-uses-tips-and-tricks. (Accessed 4/5 2022).
[61] C. Esposito Corcione, A. Greco, A. Maffezzoli, Photopolymerization kinetics of an epoxy-based resin for stereolithography, J. Appl. Polym. Sci. 92(6) (2004) 3484-3491. https://doi.org/10.1002/app.20347.
[62] C. Tröger, A.T. Bens, G. Bermes, R. Klemmer, J. Lenz, S. Irsen, Ageing of acrylate-based resins for stereolithography: thermal and humidity ageing behaviour studies, Rapid Prototyping J. (2008). https://doi.org/10.1108/13552540810907983.
[63] Z. Wang, R. Abdulla, B. Parker, R. Samanipour, S. Ghosh, K. Kim, A simple and high-resolution stereolithography-based 3D bioprinting system using visible light crosslinkable bioinks, Biofabrication 7(4) (2015) 045009. https://doi.org/10.1088/1758-5090/7/4/045009.

[64] B. Barraza, F. Olate-Moya, G. Montecinos, J.H. Ortega, A. Rosenkranz, A. Tamburrino, H. Palza, Superhydrophobic SLA 3D printed materials modified with nanoparticles biomimicking the hierarchical structure of a rice leaf, Sci. Technol. Adv. Mater. 23(1) (2022) 300-321. https://doi.org/10.1080/14686996.2022.2063035.
[65] J. Bonilla-Cruz, J.A.C. Sy, T.E. Lara-Ceniceros, J.C. Gaxiola-López, V. García, B.A. Basilia, R.C. Advincula, Superhydrophobic μ-pillars: Via simple and scalable SLA 3D-printing: The stair-case effect and their wetting models, Soft Matter 17(32) (2021) 7524-7531. https://doi.org/10.1039/d1sm00655j.
[66] K. Salonitis, Stereolithography, in: S. Hashmi (Ed.), Comprehensive materials processing, Elsevier Ltd 2014, pp. 19-67. https://doi.org/10.1016/B978-0-08-096532-1.01001-3.
[67] I. Kim, S. Kim, A. Andreu, J.H. Kim, Y.J. Yoon, Influence of dispersant concentration toward enhancing printing precision and surface quality of vat photopolymerization 3D printed ceramics, Addit. Manuf. 52 (2022). https://doi.org/10.1016/j.addma.2022.102659.
[68] A. Medellin, W. Du, G. Miao, J. Zou, Z. Pei, C. Ma, Vat photopolymerization 3D printing of nanocomposites: A literature review, J. Micro Nano-Manuf. 7(3) (2019). https://doi.org/10.1115/1.4044288.
[69] M.M. Ribo, Vat photopolymerization process chain, Technical University of Denmark, Kgs. Lyngby, 2020.
[70] W.L. Wang, C.M. Cheah, J.Y.H. Fuh, L. Lu, Influence of process parameters on stereolithography part shrinkage, Mater. Des. 17(4) (1996) 205-213. https://doi.org/https://doi.org/10.1016/S0261-3069(97)00008-3.
[71] S. Zakeri, M. Vippola, E. Levänen, A comprehensive review of the photopolymerization of ceramic resins used in stereolithography, Addit. Manuf. 35 (2020). https://doi.org/10.1016/j.addma.2020.101177.
[72] S. Corbel, O. Dufaud, T. Roques-Carmes, Materials for stereolithography, in: P.J. Bártolo (Ed.), Stereolithography: Materials, Processes and Applications, Springer US, Boston, MA, 2011, pp. 141-159. https://doi.org/10.1007/978-0-387-92904-0_6.
[73] M. Srinivasan, N. Kalberer, P. Kamnoedboon, M. Mekki, S. Durual, M. Özcan, F. Müller, CAD-CAM complete denture resins: an evaluation of biocompatibility, mechanical properties, and surface characteristics, J. Dent. 114 (2021) 103785. https://doi.org/10.1016/j.jdent.2021.103785.
[74] Q. Yang, Z. Lu, J. Zhou, K. Miao, D. Li, A novel method for improving surface finish of stereolithography apparatus, Int. J. Adv. Manuf. Technol. 93(5-8) (2017) 1537-1544. https://doi.org/10.1007/s00170-017-0529-1.
[75] M. Behzadnasab, A.A. Yousefi, D. Ebrahimibagha, F. Nasiri, Effects of processing conditions on mechanical properties of PLA printed parts, Rapid Prototyping J. (2019). https://doi.org/10.1108/RPJ-02-2019-0048.
[76] Selecting a Material for Stereolithography (SLA) 3D Printing, 2022. https://www.protolabs.com/resources/design-tips/a-guide-to-stereolithography-3d-printing-materials/. 2022).
[77] A. Väisänen, L. Alonen, S. Ylönen, M. Hyttinen, Organic compound and particle emissions of additive manufacturing with photopolymer resins and chemical outgassing of manufactured resin products, J. Toxicol. Environ. Health Part A Curr. Iss. 85(5) (2022) 198-216. https://doi.org/10.1080/15287394.2021.1998814.
[78] S.F.S. Shirazi, S. Gharehkhani, M. Mehrali, H. Yarmand, H.S.C. Metselaar, N. Adib Kadri, N.A.A. Osman, A review on powder-based additive manufacturing for tissue engineering: Selective laser sintering and inkjet 3D printing, Sci. Technol. Adv. Mater. 16(3) (2015). https://doi.org/10.1088/1468-6996/16/3/033502.
[79] C.Y. Yap, C.K. Chua, Z.L. Dong, Z.H. Liu, D.Q. Zhang, L.E. Loh, S.L. Sing, Review of selective laser melting: Materials and applications, Appl. Phys. Rev. 2(4) (2015). https://doi.org/10.1063/1.4935926.
[80] F. Lupone, E. Padovano, F. Casamento, C. Badini, Process phenomena and material properties in selective laser sintering of polymers: A review, Materials 15(1) (2022). https://doi.org/10.3390/ma15010183.

[81] J. Saroia, Y. Wang, Q. Wei, M. Lei, X. Li, Y. Guo, K. Zhang, A review on 3D printed matrix polymer composites: its potential and future challenges, Int. J. Adv. Manuf. Technol. 106(5-6) (2020) 1695-1721. https://doi.org/10.1007/s00170-019-04534-z.
[82] B. Vandenbroucke, J.P. Kruth, Selective laser melting of biocompatible metals for rapid manufacturing of medical parts, Rapid Prototyping J. (2007).
[83] H.-H. Tang, M.-L. Chiu, H.-C. Yen, Slurry-based selective laser sintering of polymer-coated ceramic powders to fabricate high strength alumina parts, J. Eur. Ceram. Soc. 31(8) (2011) 1383-1388.
[84] S. Eosoly, N.E. Vrana, S. Lohfeld, M. Hindie, L. Looney, Interaction of cell culture with composition effects on the mechanical properties of polycaprolactone-hydroxyapatite scaffolds fabricated via selective laser sintering (SLS), Materials Science and Engineering: C 32(8) (2012) 2250-2257.
[85] F.S. Shirazi, M. Mehrali, A.A. Oshkour, H.S.C. Metselaar, N.A. Kadri, N.A. Abu Osman, Characterization and mechanical properties of calcium silicate/citric acid–based polymer composite materials, Int. J. Appl. Ceram. Technol. 12(2) (2015) 371-376.
[86] M. Launhardt, A. Worz, A. Loderer, T. Laumer, D. Drummer, T. Hausotte, M. Schmidt, Detecting surface roughness on SLS parts with various measuring techniques, Polym. Test 53 (2016) 217-226. https://doi.org/10.1016/j.polymertesting.2016.05.022.
[87] V. Manoharan, S.M. Chou, S. Forrester, G.B. Chai, P.W. Kong, Application of additive manufacturing techniques in sports footwear: This paper suggests a five-point scoring technique to evaluate the performance of four AM techniques, namely, stereolithography (SLA), PolyJet (PJ), selective laser sintering (SLS) and three-dimensional printing (3DP), in four important aspects of accuracy, surface finish, range of materials supported and building time for protot, Virtual Phys. Prototyp. 8(4) (2013) 249-252. https://doi.org/10.1080/17452759.2013.862958.
[88] C. Rajpoot, SLA 3D Printing Advantages And Disadvantages - Detailed, 2021. https://themechninja.com/07/sla-3d-printing-advantages-and-disadvantages-detailed/. (Accessed 01 October 2022 2022).
[89] R.-J. Wang, L. Wang, L. Zhao, Z. Liu, Influence of process parameters on part shrinkage in SLS, The International Journal of Advanced Manufacturing Technology 33(5) (2007) 498-504. https://doi.org/10.1007/s00170-006-0490-x.
[90] T. Kozior, The Influence of Selected Selective Laser Sintering Technology Process Parameters on Stress Relaxation, Mass of Models, and Their Surface Texture Quality, 3D Print. Addit. Manuf. 7(3) (2020) 126-138. https://doi.org/10.1089/3dp.2019.0036.
[91] R.D. Goodridge, K.W. Dalgarno, D.J. Wood, Indirect selective laser sintering of an apatite-mullite glass-ceramic for potential use in bone replacement applications, Proc. Inst. Mech. Eng. Part H J. Eng. Med. 220(1) (2006) 57-68. https://doi.org/10.1243/095441105X69051.
[92] P. Minetola, F. Calignano, M. Galati, Comparing geometric tolerance capabilities of additive manufacturing systems for polymers, Addit. Manuf. 32 (2020). https://doi.org/10.1016/j.addma.2020.101103.
[93] F. Bürenhaus, E. Moritzer, A. Hirsch, Adhesive bonding of FDM-manufactured parts made of ULTEM 9085 considering surface treatment, surface structure, and joint design, Weld. World 63(6) (2019) 1819-1832. https://doi.org/10.1007/s40194-019-00810-4.
[94] S. Bose, S.F. Robertson, A. Bandyopadhyay, Surface modification of biomaterials and biomedical devices using additive manufacturing, Acta Biomater. 66 (2018) 6-22. https://doi.org/10.1016/j.actbio.2017.11.003.
[95] A. Maguire, N. Pottackal, M.A.S.R. Saadi, M.M. Rahman, P.M. Ajayan, Additive manufacturing of polymer-based structures by extrusion technologies, Oxford Open Materials Science 1(1) (2020). https://doi.org/10.1093/oxfmat/itaa004.
[96] I. Gibson, L.K. Cheung, S. Chow, W. Cheung, S. Beh, M. Savalani, S. Lee, The use of rapid prototyping to assist medical applications, Rapid Prototyping J. (2006).
[97] S.R. Addanki, M.A. Dharap, J.V.L. Venkatesh, Development of rapid tooling for investment casting using fused deposition modeling process, Advanced Materials Research, 2014, pp. 155-165. https://doi.org/10.4028/www.scientific.net/AMR.970.155.
[98] M. Horáček, O. Charvát, T. Pavelka, J. Sedlák, M. Madaj, J. Nejedlý, J. Dvooáček, Medical implants by using RP and investment casting technologies, The 69th WFC 8 (2011) 107-111.

[99] J.M. Barrios, P.E. Romero, Improvement of surface roughness and hydrophobicity in PETG parts manufactured via fused deposition modeling (FDM): An application in 3D printed self-cleaning parts, Materials 12(15) (2019). https://doi.org/10.3390/ma12152499.
[100] T.C. Yang, C.H. Yeh, Morphology and mechanical properties of 3D printed wood fiber/polylactic acid composite parts using Fused Deposition Modeling (FDM): The effects of printing speed, Polymers 12(6) (2020) 1334. https://doi.org/10.3390/POLYM12061334.
[101] P. Wang, B. Zou, S. Ding, Modeling of surface roughness based on heat transfer considering diffusion among deposition filaments for FDM 3D printing heat-resistant resin, Appl Therm Eng 161 (2019). https://doi.org/10.1016/j.applthermaleng.2019.114064.
[102] B. Reddy, N. Reddy, A. Ghosh, Fused deposition modelling using direct extrusion, Virtual Phys. Prototyp. 2(1) (2007) 51-60.
[103] I.S. Rêgo, T.V.C. Marcos, D.R. Pinto, R.G.S. Vilela, V.A.B. Galvão, A. Pivetta, G.P. Camilo, J.R.T. Silva, B.C. Lima, A.K. Carvalhal, R.L. Cardoso, J.F.A. Martos, A.M. Santos, A.C. Oliveira, P.G.P. Toro, Ground experimentation with 3D printed scramjet inlet models at hypervelocities, Aerosp Sci Technol 55 (2016) 307-313. https://doi.org/10.1016/j.ast.2016.06.009.
[104] B. Msallem, N. Sharma, S. Cao, F.S. Halbeisen, H.F. Zeilhofer, F.M. Thieringer, Evaluation of the dimensional accuracy of 3D-printed anatomical mandibular models using FFF, SLA, SLS, MJ, and BJ printing technology, Journal of Clinical Medicine 9(3) (2020). https://doi.org/10.3390/jcm9030817.
[105] B. Dorweiler, P.E. Baqué, R. Chaban, A. Ghazy, O. Salem, Quality control in 3D printing: Accuracy analysis of 3D-printed models of patient-specific anatomy, Materials 14(4) (2021) 1-13. https://doi.org/10.3390/ma14041021.
[106] X. Wei, N. Zou, L. Zeng, Z. Pei, PolyJet 3D Printing: Predicting Color by Multilayer Perceptron Neural Network, Annals of 3D Printed Medicine 5 (2022) 1-7. https://doi.org/10.1016/j.stlm.2022.100049.
[107] N.N. Kumbhar, A.V. Mulay, Post Processing Methods used to Improve Surface Finish of Products which are Manufactured by Additive Manufacturing Technologies: A Review, J. Inst. Eng. Ser. C 99(4) (2016) 481-487. https://doi.org/10.1007/s40032-016-0340-z.
[108] S. Martínez-Pellitero, M.A. Castro, A.I. Fernández-Abia, S. González, E. Cuesta, Analysis of influence factors on part quality in micro-SLA technology, Procedia Manuf. 13 (2017) 856-863. https://doi.org/10.1016/j.promfg.2017.09.143.
[109] J. Glückstad, D. Palima, Light robotics: Structure-mediated nanobiophotonics, Elsevier 2017.
[110] S. Zips, L. Hiendlmeier, L.J.K. Weiß, H. Url, T.F. Teshima, R. Schmid, M. Eblenkamp, P. Mela, B. Wolfrum, Biocompatible, flexible, and oxygen-permeable silicone-hydrogel material for stereolithographic printing of microfluidic lab-on-a-chip and cell-culture devices, ACS Appl. Polym. Mater. 3(1) (2020) 243-258. https://doi.org/10.1021/acsapm.0c01071.
[111] D. Miedzińska, R. Gieleta, A. Popławski, Experimental study on influence of curing time on strength behavior of sla-printed samples loaded with different strain rates, Materials 13(24) (2020) 5825. https://doi.org/10.3390/ma13245825.
[112] C.C. Wang, J.Y. Chen, J. Wang, The selection of photoinitiators for photopolymerization of biodegradable polymers and its application in digital light processing additive manufacturing, J. Biomed. Mater. Res. Part A 110(1) (2022) 204-216. https://doi.org/10.1002/jbm.a.37277.
[113] M. Rank, A. Sigel, Y. Bauckhage, S. Suresh-Nair, M. Dohmen, C. Eder, C. Berge, A. Heinrich, 3d printing of optics based on conventional printing technologies, Springer Series in Optical Sciences, 2021, pp. 45-167. https://doi.org/10.1007/978-3-030-58960-8_3.
[114] S.O. Onuh, K.K.B. Hon, Optimising build parameters for improved surface finish in stereolithography, Int J Mach Tools Manuf 38(4) (1998) 329-342. https://doi.org/https://doi.org/10.1016/S0890-6955(97)00068-0.
[115] J.M. Park, J. Jeon, J.Y. Koak, S.K. Kim, S.J. Heo, Dimensional accuracy and surface characteristics of 3D-printed dental casts, J. Prosthet. Dent. 126(3) (2021) 427-437. https://doi.org/10.1016/j.prosdent.2020.07.008.
[116] Y. Sano, R. Matsuzaki, M. Ueda, A. Todoroki, Y. Hirano, 3D printing of discontinuous and continuous fibre composites using stereolithography, Addit. Manuf. 24 (2018) 521-527. https://doi.org/https://doi.org/10.1016/j.addma.2018.10.033.

[117] M.K. Alazzawi, B. Beyoglu, R.A. Haber, A study in a tape casting based stereolithography apparatus: Role of layer thickness and casting shear rate, Journal of Manufacturing Processes 64 (2021) 1196-1203. https://doi.org/https://doi.org/10.1016/j.jmapro.2021.02.040.
[118] M. Akilesh, P.R. Elango, A.A. Devanand, R. Soundararajan, P.A. Varthanan, Optimization of selective laser sintering process parameters on surface quality, 3D Printing and Additive Manufacturing Technologies 2018, pp. 141-157. https://doi.org/10.1007/978-981-13-0305-0_13.
[119] Z. Xu, Y. Wang, D. Wu, K.P. Ananth, J. Bai, The process and performance comparison of polyamide 12 manufactured by multi jet fusion and selective laser sintering, Journal of Manufacturing Processes 47 (2019) 419-426. https://doi.org/10.1016/j.jmapro.2019.07.014.
[120] T. Puttonen, M. Salmi, J. Partanen, Mechanical properties and fracture characterization of additive manufacturing polyamide 12 after accelerated weathering, Polym. Test 104 (2021). https://doi.org/10.1016/j.polymertesting.2021.107376.
[121] Y. Xiong, H. Pei, Q. Lv, Y. Chen, A facile fabrication of PA12/CNTs nanocomposites with enhanced three-dimensional segregated conductive networks and electromagnetic interference shielding property through selective laser sintering, ACS Omega 7(5) (2022) 4293-4304. https://doi.org/10.1021/acsomega.1c06021.
[122] M. Pelanconi, G. Bianchi, P. Colombo, A. Ortona, Fabrication of dense SiSiC ceramics by a hybrid additive manufacturing process, J Am Ceram Soc 105(2) (2022) 786-793. https://doi.org/10.1111/jace.18134.
[123] A. Holländer, P. Cosemans, Surface technology for additive manufacturing, Plasma Processes Polym. 17(1) (2020). https://doi.org/10.1002/ppap.201900155.
[124] I.S. Kinstlinger, A. Bastian, S.J. Paulsen, D.H. Hwang, A.H. Ta, D.R. Yalacki, T. Schmidt, J.S. Miller, Open-Source Selective Laser Sintering (OpenSLS) of nylon and biocompatible polycaprolactone, PLoS One 11(2) (2016). https://doi.org/10.1371/journal.pone.0147399.
[125] Y. Luo, A. Humayun, D.K. Mills, Surface modification of 3d printed pla/halloysite composite scaffolds with antibacterial and osteogenic capabilities, Appl. Sci. 10(11) (2020). https://doi.org/10.3390/app10113971.
[126] O. Gülcan, K. Günaydın, A. Çelik, Investigation on surface roughness of polyjet-printed airfoil geometries for small UAV applications, Aerosp. 9(2) (2022). https://doi.org/10.3390/aerospace9020082.
[127] A. Payami Golhin, A. Strandlie, P. John Green, The influence of wedge angle, feedstock color, and infill density on the color difference of FDM objects, J. Imaging Sci. Technol. 65(5) (2021) 1-15. https://doi.org/10.2352/J.ImagingSci.Technol.2021.65.5.050408.
[128] C. V., The Top Full Color 3D Printers on the Market, 2021. https://www.3dnatives.com/en/top-14-color-3d-printers-191120194/. (Accessed October 2, 2022 2022).
[129] D. Baca, R. Ahmad, The impact on the mechanical properties of multi-material polymers fabricated with a single mixing nozzle and multi-nozzle systems via fused deposition modeling, Int. J. Adv. Manuf. Technol. 106(9-10) (2020) 4509-4520. https://doi.org/10.1007/s00170-020-04937-3.
[130] M.H. Ali, N. Mir-Nasiri, W.L. Ko, Multi-nozzle extrusion system for 3D printer and its control mechanism, Int. J. Adv. Manuf. Technol. 86(1-4) (2016) 999-1010. https://doi.org/10.1007/s00170-015-8205-9.
[131] P. Silapasuphakornwong, C. Panichkriangkrai, P. Punpongsanon, M. Suzuki, K. Uehira, An Exploration into Color Reproduction for Inkjet FDM Color 3D Printing, IS and T International Symposium on Electronic Imaging Science and Technology, 2022. https://doi.org/10.2352/EI.2022.34.15.COLOR-180.
[132] R. Spina, Performance analysis of colored PLA products with a fused filament fabrication process, Polymers 11(12) (2019) 1-16. https://doi.org/10.3390/polym11121984.
[133] D. Frunzaverde, V. Cojocaru, C.R. Ciubotariu, C.O. Miclosina, D.D. Ardeljan, E.F. Ignat, G. Marginean, The Influence of the Printing Temperature and the Filament Color on the Dimensional Accuracy, Tensile Strength, and Friction Performance of FFF-Printed PLA Specimens, Polymers 14(10) (2022). https://doi.org/10.3390/polym14101978.
[134] A.W. Signor, M.R. VanLandingham, J.W. Chin, Effects of ultraviolet radiation exposure on vinyl ester resins: characterization of chemical, physical and mechanical damage, Polym Degradation Stab 79(2) (2003) 359-368. https://doi.org/https://doi.org/10.1016/S0141-3910(02)00300-2.

[135] C. Basgul, T. Yu, D.W. MacDonald, R. Siskey, M. Marcolongo, S.M. Kurtz, Does annealing improve the interlayer adhesion and structural integrity of FFF 3D printed PEEK lumbar spinal cages?, J. Mech. Behav. Biomed. Mater. 102 (2020). https://doi.org/10.1016/j.jmbbm.2019.103455.
[136] Y.L. Cheng, K.C. Huang, Preparation and characterization of color photocurable resins for full-color material jetting additive manufacturing, Polymers (Basel) 12(3) (2020) 650. https://doi.org/10.3390/polym12030650.
[137] L. De Noni, L. Zorzetto, F. Briatico-Vangosa, M. Rink, D. Ruffoni, L. Andena, Modelling the interphase of 3D printed photo-cured polymers, Compos. B. Eng. 234 (2022). https://doi.org/10.1016/j.compositesb.2022.109737.
[138] R.P. Singh Tomar, F.I. Ulu, A. Kelkar, R.V. Mohan, Investigation of process induced variations in polyjet printing with digital polypropylene via homogeneous 3D tensile test coupon, American Society of Mechanical Engineers (ASME), 2019. https://doi.org/10.1115/IMECE2019-11639.
[139] L. Griffiths, Formlabs adds colour to SLA 3D printing with Color Kit, 2017. https://www.tctmagazine.com/additive-manufacturing-3d-printing-news/formlabs-adds-colour-sla-3d-printing-color-kit/. (Accessed 1 October 2022 2022).
[140] S. Madheswaran, K. Sivakumar, E. Prakash, S. Kalaivanan, N. Someswaran, J. Vishnudeepan, Applications of Additive Manufacturing—A Review, Springer Proceedings in Materials, 2021, pp. 21-27. https://doi.org/10.1007/978-981-15-8319-3_3.
[141] K. Eckes, How multi-powder deposition will transform industrial 3D printing, 2018. https://aerosint.com/powder-deposition-multimaterial-printing/. (Accessed 1 September 2022 2022).
[142] M. Mehrpouya, D. Tuma, T. Vaneker, M. Afrasiabi, M. Bambach, I. Gibson, Multimaterial powder bed fusion techniques, Rapid Prototyping J. (2022).
[143] L. Ren, Z. Song, H. Liu, Q. Han, C. Zhao, B. Derby, Q. Liu, L. Ren, 3D printing of materials with spatially non-linearly varying properties, Materials and Design 156 (2018) 470-479. https://doi.org/10.1016/j.matdes.2018.07.012.
[144] Y.L. Cheng, C.H. Chang, C. Kuo, Experimental study on leveling mechanism for material-jetting-type color 3D printing, Rapid Prototyping J. 26(1) (2020) 11-20. https://doi.org/10.1108/RPJ-09-2018-0227.
[145] H. Hesse, M. Özcan, A review on current additive manufacturing technologies and materials used for fabrication of metal-ceramic fixed dental prosthesis, J. Adhes. Sci. Technol. (2021). https://doi.org/10.1080/01694243.2021.1899699.
[146] O. Elek, D. Sumin, R. Zhang, T. Weyrich, K. Myszkowski, B. Bickel, A. Wilkie, J. Krivanek, Scattering-aware Texture Reproduction for 3D Printing, ACM Trans. Graph. 36(6) (2017) 15. https://doi.org/10.1145/3130800.3130890.
[147] P. Urban, Graphical 3D Printing: Challenges, Solutions and Applications, London Imaging Meeting, Society for Imaging Science and Technology, 2020, pp. 87-90.
[148] D. Sumin, T. Rittig, V. Babaei, T. Nindel, A. Wilkie, P. Didyk, B. Bickel, J. Kriváne k, K. Myszkowski, T. Weyrich, Geometry-aware scattering compensation for 3D printing, ACM Trans. Graph. 38(4) (2019). https://doi.org/10.1145/3306346.3322992.
[149] G.D. Goh, Y.L. Yap, H.K.J. Tan, S.L. Sing, G.L. Goh, W.Y. Yeong, Process–Structure–Properties in Polymer Additive Manufacturing via Material Extrusion: A Review, Crit Rev Solid Statae Mater Sci 45(2) (2020) 113-133. https://doi.org/10.1080/10408436.2018.1549977.
[150] R.W.G. Hunt, M.R. Pointer, Measuring colour, John Wiley & Sons 2011.
[151] A.K.R. Choudhury, Principles of colour and appearance measurement: Object appearance, colour perception and instrumental measurement, Elsevier 2014.
[152] A. Sole, D. Gigilashvili, H. Midtfjord, D. Guarnera, G.C. Guarnera, J.B. Thomas, J.Y. Hardeberg, On the acquisition and reproduction of material appearance, Lecture Notes in Computer Science (including subseries Lecture Notes in Artificial Intelligence and Lecture Notes in Bioinformatics), 2019, pp. 26-38. https://doi.org/10.1007/978-3-030-13940-7_3.
[153] C.I.d. l'Éclairage, Colorimetry CIE 015:2004, Commission Internationale de l'Éclairage, 2004, pp. 1-82.
[154] S. Jost, C. Cauwerts, P. Avouac, CIE 2017 color fidelity index Rf: a better index to predict perceived color difference?, J. Opt. Soc. Am. A 35(4) (2018) B202-B213. https://doi.org/10.1364/JOSAA.35.00B202.

[155] R.S. Hunter, D.B. Judd, Development of a method of classifying paints according to gloss, ASTM Bulletin (97) (1939) 11-18.
[156] R. Hunter, R. Harold, The measurement of appearance, 2nd Ed ed., Wiley New York 1987.
[157] F. Willmouth, Quantitative assessment of transparency, Plastics and Rubber: Materials and Applications 1 (1976) 101-108.
[158] Standard Test Method for Specular Gloss 2008, in: A. D523-89 (Ed.) ASTM International West Conshohocken, PA, 2008, pp. 1-5.
[159] Standard Test Method for Specular Gloss 2018, in: A. D523-14 (Ed.) ASTM International West Conshohocken, PA, 2018, pp. 1-5.
[160] W. Elkhuizen, T. Essers, Y. Song, J. Geraedts, C. Weijkamp, J. Dik, S. Pont, Gloss, color, and topography scanning for reproducing a Painting's appearance using 3D printing, J. Comput. Cult. Heritage 12(4) (2019). https://doi.org/10.1145/3317949.
[161] W.S. Elkhuizen, B.A.J. Lenseigne, T. Baar, W. Verhofstad, E. Tempelman, J.M.P. Geraedts, J. Dik, Reproducing oil paint gloss in print for the purpose of creating reproductions of old masters, Proceedings of SPIE - The International Society for Optical Engineering, 2015. https://doi.org/10.1117/12.2082918.
[162] J. Son, H. Lee, Preliminary study on polishing SLA 3D-printed ABS-like resins for surface roughness and glossiness reduction, Micromachines 11(9) (2020). https://doi.org/10.3390/MI11090843.
[163] C.I.d. l'Éclairage, A framework for the measurement of visual appearance, CIE 175:2006, Commission Internationale de l'Éclairage, 2006.
[164] a.M.R.L. J. B. Hutchings, Translucency, its perception and measurement, AIC Congress - Color '05, 10th Congress of the International Colour Association, Grenada, Spain, 2005, pp. 835-838.
[165] R. Udroiu, New Methodology for Evaluating Surface Quality of Experimental Aerodynamic Models Manufactured by Polymer Jetting Additive Manufacturing, Polymers 14(3) (2022). https://doi.org/10.3390/polym14030371.
[166] D.J. Luning Prak, N.J. Adams, J.L. VanBriesen, J.S. Cowart, J.S. Schubbe, B.W. Baker, Swelling behavior and tensile strength of additively manufactured and commercial O-rings in the presence of linear, branched, cyclic, and aromatic compounds and alcohols, J Elastomers Plast (2022). https://doi.org/10.1177/00952443221104105.
[167] P. Gruber, G. Ziółkowski, M. Olejarczyk, E. Grochowska, V. Hoppe, P. Szymczyk-Ziółkowska, T. Kurzynowski, Influence of bioactive metal fillers on microstructural homogeneity of PA12 composites produced by polymer Laser Sintering, Arch. Civ. Mech. Eng. 22(3) (2022). https://doi.org/10.1007/s43452-022-00442-4.
[168] G. Khanolka, Can you 3d print transparent parts?, 2018. https://blogs.truventor.ai/blogs/transparent-3d-printing/. (Accessed 7 September 2022 2022).
[169] L. Langnau, Make it clear: choices for 3D printing transparent parts, 2015. https://www.designworldonline.com/make-it-clear-choices-for-3d-printing-transparent-parts/. (Accessed 7 Septembe 2022.
[170] M. Gerardin, L. Simonot, J.-P. Farrugia, J.-C. Iehl, T. Fournel, M. Hébert, A translucency classification for computer graphics, Electronic Imaging 2019(6) (2019) 203-1-203-7.
[171] Geometrical product specifications (GPS) — Surface texture: Areal — Part 2: Terms, definitions and surface texture parameters, ISO 25178-2:2021, International Organization for Standardization: Geneva, Switzerland, 2021, pp. 1-64.
[172] A.S. E, Standard test method for measuring pavement texture drainage using an outflow meter 2009, ASTM E2380-05, American Society for Testing and Materials (ASTM) International West …, 2009, pp. 1-4.
[173] S. Chatti, L. Laperrière, G. Reinhart, T. Tolio, CIRP encyclopedia of production engineering, Springer 2019.
[174] J.H. Xin, H.L. Shen, C. Chuen Lam, Investigation of texture effect on visual colour difference evaluation, Color Research & Application: Endorsed by Inter-Society Color Council, The Colour Group (Great Britain), Canadian Society for Color, Color Science Association of Japan, Dutch Society for the Study of Color, The Swedish Colour Centre Foundation, Colour Society of Australia, Centre Français de la Couleur 30(5) (2005) 341-347.

[175] W. Ji, M. Luo, E. Kirchner, Assessing colour appearance and colour differences for automobile coatings—methods for assessing coarseness, Proceedings of the tenth Congress of the International Colour Association. Granada: AIC, 2005, pp. 631-634.
[176] S. Kitaguchi, S. Westland, M. Luo, Suitability of texture analysis methods for perceptual texture, Proceedings, 10th Congress of the International Colour Association, 2005, pp. 923-926.
[177] B. Han, G. Cui, M. Luo, Texture effect on evaluation of colour difference, Bangkok, Thailand. AIC03–8th Congress of the International Colour Association, 2003, pp. 176-180.
[178] H. Arai, G. Baba, Micro-brilliance of anisotropic paint surfaces, Proceedings oj" A IC C% ur 2005, the 10th Congress of the International Colour Association, 2005, pp. 813-816.
[179] A. Obregon, R.J. Goodkind, W.B. Schwabacher, Effects of opaque and porcelain surface texture on the color of ceramometal restorations, The Journal of prosthetic dentistry 46(3) (1981) 330-340.
[180] H.-K. Kim, S.-H. Kim, J.-B. Lee, S.-R. Ha, Effects of surface treatments on the translucency, opalescence, and surface texture of dental monolithic zirconia ceramics, The Journal of Prosthetic Dentistry 115(6) (2016) 773-779. https://doi.org/https://doi.org/10.1016/j.prosdent.2015.11.020.
[181] R.M. Haralick, Statistical and structural approaches to texture, Proc. IEEE 67(5) (1979) 786-804.
[182] M. Sharma, S. Singh, Evaluation of texture methods for image analysis, The Seventh Australian and New Zealand Intelligent Information Systems Conference, 2001, IEEE, 2001, pp. 117-121.
[183] M. Singh, S. Singh, Spatial texture analysis: a comparative study, 2002 International Conference on Pattern Recognition, IEEE, 2002, pp. 676-679.
[184] M. Taufik, P.K. Jain, Role of build orientation in layered manufacturing: A review, Int. J. Manuf. Technol. Manage. 27(1-3) (2013) 47-73. https://doi.org/10.1504/IJMTM.2013.058637.
[185] D. Guarnera, G.C. Guarnera, A. Ghosh, C. Denk, M. Glencross, BRDF representation and acquisition, Comput. Graph. Forum, Wiley Online Library, 2016, pp. 625-650. https://doi.org/10.1111/cgf.12867.
[186] M. Haindl, J. Filip, Representation, Visual Texture, Springer 2013, pp. 9-22.
[187] F.E. Nicodemus, Directional reflectance and emissivity of an opaque surface, Appl. Optics 4(7) (1965) 767-775.
[188] I. Tastl, M.A. Lopez-Alvarez, A. Ju, M. Schramm, J. Roca, M. Shepherd, A soft-proofing workflow for color 3D printing - Addressing needs for the future, IS and T International Symposium on Electronic Imaging Science and Technology, 2019. https://doi.org/10.2352/ISSN.2470-1173.2019.6.MAAP-479.
[189] S.J. Sangwine, R.E. Horne, The Colour Image Processing Handbook, Springer Science & Business Media 1998.
[190] X. Li, X. Han, J. Liu, X. Li, M. Cui, G. Wu, Luminance prediction of paper model surface based on non-contact measurement, Tehnicki Vjesnik 28(4) (2021) 1331-1337. https://doi.org/10.17559/TV-20200131145934.
[191] A.K.R. Choudhury, Principles of colour and appearance measurement: Visual measurement of colour, colour comparison and management, Woodhead Publishing 2014.
[192] W.E. Schneider, R. Young, Spectroradiometry methods, Handbook of Applied Photometry, ed. Casimer De Cusatis (1997) 252.
[193] H. Kostkowski, Reliable Spectroradiometry, Spectroradiometry Consulting, La Plata, Maryland, USA (1997).

# Appendix

## Paper I:

A. P. Golhin, A. Strandlie, and P. J. Green, The influence of wedge angle, feedstock color, and infill density on the color difference of FDM objects, Journal of Imaging Science and Technology, 65(5): 1-15 (2021). https://doi.org/10.2352/J.ImagingSci.Technol.2021.65.5.050408

*Journal of Imaging Science and Technology*® 65(5): 050408-1–050408-15, 2021.


# The Influence of Wedge Angle, Feedstock Color, and Infill Density on the Color Difference of FDM Objects

**Ali Payami Golhin and Are Strandlie**
*Department of Manufacturing and Civil Engineering, Norwegian University of Science and Technology, 2815 Gjøvik, Norway*
*E-mail: payami.ag@gmail.com*

**Philip John Green**▲
*Department of Computer Science, Norwegian University of Science and Technology, 2815 Gjøvik, Norway*

**Abstract.** *The surface appearance in additive manufacturing (AM) has attracted attention in recent years due to its importance in evaluating the quality of 3D printed structures. Fused Deposition Modeling (FDM), also known as Fused Filament Fabrication (FFF), holds an important share of the AM market because of its large economic potential in many industries. Nevertheless, the quality assurance procedure for FDM manufactured parts is usually complicated and expensive. The enhancement of the appearance at different illumination and viewing angles can be exploited in various applications, such as civil engineering, aeronautics, medical fields, and art. There are two steps in improving the microstructure and material appearance of printed objects, including pre-processing and post-processing. This study aims to elucidate the role of the pre-processing phase in the development of FDM parts through the assessment of color differences. For this purpose, a set of polymeric samples with different wedge (slope) angles were 3D printed using an FDM printer. The color difference between the elements is discussed and correlated with the pre-processing parameters. It is revealed that the wedge angle of the elements in the design, slicing process, and infill density could alter the color appearance of the printed parts in a predictable trend. This research suggests that low infill density and wedge angles in polylactide filaments can result in a more stable color appearance.* © *2021 Society for Imaging Science and Technology.*
[DOI: 10.2352/J.ImagingSci.Technol.2021.65.5.050408]

## 1. INTRODUCTION

The introduction of additive manufacturing (AM) has given rise to many new possibilities. It is a complementary option to the subtractive methods that have dominated the manufacturing and production sector since the first industrial revolution. AM offers improved functional device integration capabilities, thanks to a wide range of 3D geometry, ranging from micrometers to centimeters [1]. The fast-paced AM marketplace has also shifted from industrial applications to customized manufacturing. The variation in color property can deeply influence the customized product to some extent, which is also known as the subdivision of color 3D printing [1]. Full-color 3D printing and accurate color reproduction are highly desired when 3D objects were manufactured by AM techniques. On this basis, color fidelity and color preference have significant influence on the overall quality of the product [2].

Color 3D printing is gaining increasing popularity in recent years, as it enables customized production in various industrial applications based on different substrates, including plastic [3–7], powder [8, 9], paper [10–14], metal [15, 16], glass [17], food [18], and organism [19]. While the seven categories of applications for color 3D printing techniques range from processes to coloring materials in 3D printing, they follow the same subtractive color theory standardized by the CIE (Commission Internationale de L'Eclairage) and the ICC (International Color Consortium) for 2D printing. The quality of surface colors of AM objects can be evaluated based on color stability and color reproduction methods. Nevertheless, the procedures for evaluating 3D objects are less than traditional 2D objects, demanding a detailed guideline for managing the color process of 3D printed objects [1].

The instrumental measurement geometry is one of the critical factors when it comes to color measurement. Since there is no CIE standard for the measurement of 3D prints, appearance measurement for AM technology requires careful considerations due to the variation in color and illumination geometries [20]. However, several attempts have been made to develop appearance assessments for 3D color printing processing [7, 19, 21–23]. Accordingly, a framework of color image reproduction for 3D color printing has been introduced by Xiao et al. [2]. They proposed that the performance of color reproduction can be significantly improved by applying the framework.

There are several AM technologies that can be classified as color 3D printing with the full-color spectrum, including Color FDM and PolyJet introduced by Stratasys Inc., MultiJet Fusion from Hewett Packard Inc.p, SDL processing from Mcor Inc. and 3DP developed by Z Corp Inc. and 3D system Inc. MultiJet Fusion 3DP, and SDL processing are based on the 3D printing of CMY(K) ink on printing materials with a single color, while Color FDM and PolyJet require colored feedstocks in order to generate a full color by melting materials together. This is a complex project which makes color 3D printing generally more sophisticated than conventional color printing technologies [2].

According to ISO/ASTM standard 52,900:2015, fused deposition modeling (FDM) is classified as a material

▲ IS&T Member.

Received June 4, 2021; accepted for publication Sept. 22, 2021; published online Oct. 14, 2021. Associate Editor: Masaru Tsuchida.
1062-3701/2021/65(5)/050408/15/$25.00

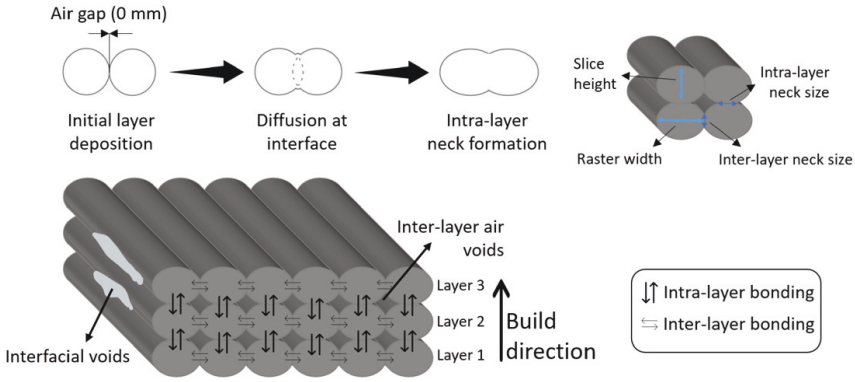


Figure 1. Bonding and stages of bond formation in the FDM process.

extrusion-based AM technique [24]. FDM is the most economical technique among other AM methods due to its advantages such as the high strength of its materials, cost-effectiveness, ease of printing, multicolor and glossiness appearance, and environmentally friendly nature [25, 26]. In this regard, FDM is an excellent candidate for biomedical, marine, and aerospace applications such as mechanical housings, antennas, satellites, thermal management components, and unmanned aerial vehicles (UAV) [4–6].

While the developments of FDM 3D printing and the mechanical properties of printed polymers have been remarkable thus far [27–29], manufactured objects tend to suffer from the inferior surface quality, including undesirable color variation, pronounced striations, high roughness, and voids [30]. In other words, the smoothness, precision, and topography of FDM parts are not comparable with some other AM techniques such as PolyJet and Multi-Jet [29]. FDM objects are printed in a layer-upon-layer routine after the successive completion of each cross-section based on the computer-aided design (CAD) data [25, 31]. Thus far, this is not the sole reason that explains the drawbacks of this technique. This is primarily caused by the filamentary nature of the FDM technique. For instance, high-temperature variation during layer by layer part fabrication procedure and inappropriate infill density can affect the print quality [30]. Morphology is poor due to various limiting factors such as phase transformations, rapid cooling, and exhaustive energy. Moreover, the FDM printed parts deviate from the initial geometry, as well as volumetric errors and hardware settings [32–35].

On top of all these limitations, FDM is a dominant AM technique in the market due to its various advantages, including cost, printing time, bio-degradable materials, and simplicity [25].

The FDM parts require significant post-production finishing techniques (PPFTs) to meet its large market [25]. For a variety of applications, manufacturers use coating and painting methods to obtain the desired surface finish. However, these techniques pose several challenges that need to be overcome to form the printing process. For example, there is an accumulation problem along the edge of the object and then inside the part at the beginning of the FDM process. This problem cannot be solved by coating or painting since it requires a specific number of outlines to package the part according to the required response [25, 36].

In general, two types of bonding exist in the FDM process, including inter-layer and intra-layer bonding. The high thermal expansion of pure polymers creates a loose bond between the layers during printing, leading to the formation of the staircase (Figure 1). As an inherent issue, the formation of staircases has a significant negative influence on the surface appearance of FDM parts [9–13].

The infill density defines the level of incorporating material inside the fabricated object. It may vary from 0 to 100%, depending on the required balance between material consumption and mechanical properties [10]. Generally, a higher infill density leads to a heavier and stronger part, which increases the cost and the material used for the printing process. The density and pattern of infill are important process parameters that can influence the surface quality as well. As such, they should be selected appropriately considering the design and strength requirements, as well as the build time of the printed part [2]. For instance, surface artifacts such as gaps and porosity have been observed even at 100% infill density under a scanning electron microscope (SEM) [11].

There is a wide range of filaments in the market with different colors, however, 3D printing contains unreal tristimulus values based on standard color charts compared to the designed CAD file. In order to calculate the color difference between two objects, the CIE recommended two alternates for RGB, including CIELCH ($L^*C^*h$) and uniform color scales: CIE 1976 ($L^*a^*b^*$) or CIELAB. The CIE76 ($\Delta E_{ab}$) formula was the first color-difference formula based on CIELAB values. It has been succeeded by the CMC (Color Measurement Committee) in 1984 and followed by improvement in CIE94 and CIEDE2000 formulas [37, 38],

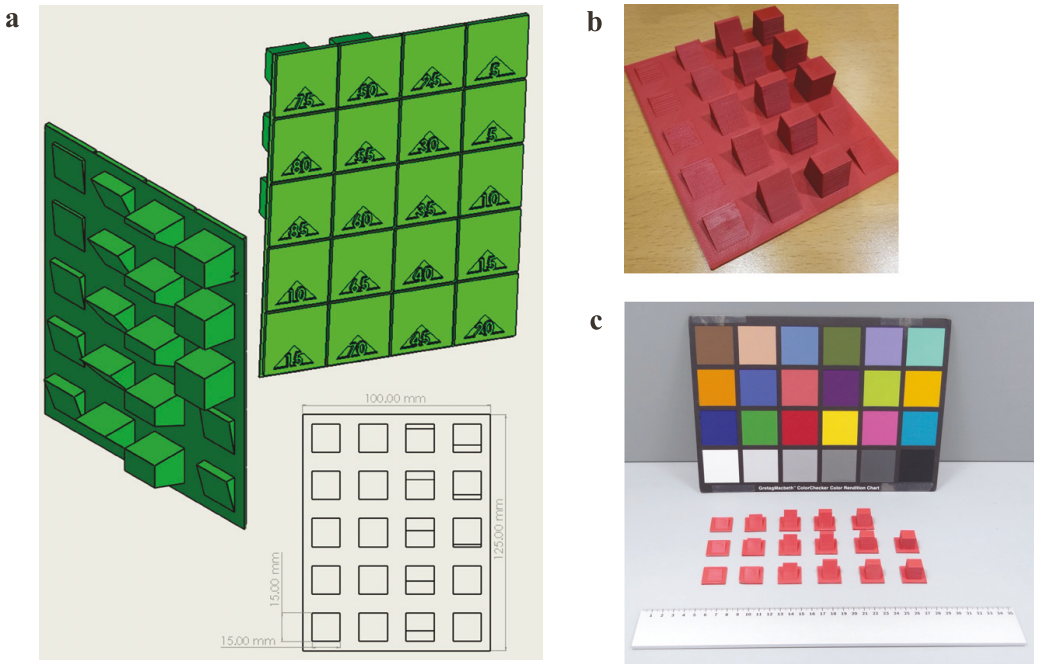


Figure 2. (a) The design, (b) as-3D printed model, and (c) separated specimens with different wedge angles placed in a light box under D50 light source. The sample was printed using a red PLA filament with an infill density of 0%.

whereby

$$\Delta E^*_{ab} = \sqrt{(\Delta L^*)^2 + (\Delta a^*)^2 + (\Delta b^*)^2} \tag{1}$$

$$\Delta E^*_{\mathrm{CMC}} = \sqrt{\left(\frac{\Delta L^*}{lS_L}\right)^2 + \left(\frac{\Delta C^*}{CS_C}\right)^2 + \left(\frac{\Delta h^*}{S_h}\right)^2} \tag{2}$$

$$\Delta E^*_{94} = \sqrt{\left(\frac{\Delta L^*}{k_L S_L}\right)^2 + \left(\frac{\Delta C^*}{k_C S_C}\right)^2 + \left(\frac{\Delta h^*}{k_h S_h}\right)^2} \tag{3}$$

$$\Delta E^*_{2000} = \sqrt{\left(\frac{\Delta L^*}{k_L S_L}\right)^2 + \left(\frac{\Delta C^*}{k_C S_C}\right)^2 + \left(\frac{\Delta h^*}{k_h S_h}\right)^2 + R_T f(\Delta C^* \Delta h^*)}, \tag{4}$$

where $LCh$ is Lightness (the same one as in $L^*a^*b^*$), chroma (the distance out from the neutral axis – saturation) and hue, the constant values of $k_L$ (lightness), $k_C$ (chroma), and $k_h$ (hue) in computer graphic arts are usually unity [39]. Other parameters refer to the hue rotation term ($R_T$), and the compensation for lightness ($S_L$), chroma ($S_C$), and hue ($S_h$). CIEDE2000, as the most recent formula, has become the recommended industry standard for all calculations except textiles, which still use CMC [40].

Knowledge of color science is crucial for the success of 3D printed parts. While color stability and the appearance of 3D surfaces have been reported [15], studies of color differences based on the printing processes are lacking. Therefore, this study aimed to evaluate the influence of the CAD design and the slicing parameters in the pre-processing stage on the color difference of FDM objects. Accordingly, we emphasize a method to deliberately alter the color appearance of 3D printed surfaces by controlling the generation of texture in the pre-processing stage for polylactice (PLA) filaments.

## 2. DESIGNS AND METHODS

Due to feasibility and a broad application of SolidWorks in additive manufacturing, the structured surface models were created in SolidWorks CAD 2020 (Dassault Systems, Velizy, France) in the native format (*.sldprt) and subsequently imported to the Prusa Slicer for the slicing process. Both software are well known CAD systems of the manufacturing community due to their ease of use and extended functionality unavailable in open source software [15].

The design and appearance of the 3D-printed model, together with separated wedge specimens, are displayed in Figure 2. All separated wedges were stored in the as-printed state without post-processing after 3D printing. To focus on the role of design features and the color attribute, "blue" and "red" matte filaments have been used to print physical models. In order to decrease the influence of the printing layout of samples with different wedge angles (distribution at a work platform) on the surface properties, a high density of parts with reduced size in the base area (15 × 15 mm) is chosen as the main design criterion.

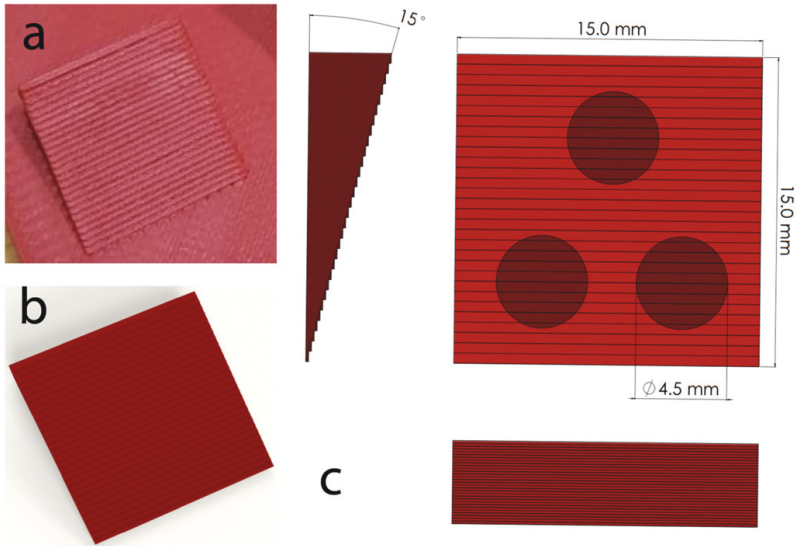


Figure 3. (a) The 15° wedge angle feature on the dull red sample 15, (b) the twin digital model, and (c) measurement positionings of the 4.5 mm aperture on the surface.

This means that these features are positioned as closely together as possible, while they could be split easily. Additional attention was paid to wedge angles 5°, 10°, and 15°. These tilted surfaces were duplicated in the design at different locations on the build platform, and recognizing staircase problems were more critical for low-wedge angles.

The CAD model was exported using the fine STL from SolidWorks (tolerance 0.12 mm) to be read and interpreted by the print setup software. G-codes were obtained using PrusaSlicer 2.2.0 software in the slicing step. 3D printing was performed using a Prusa i3 MK2.5 3D printer with a 0.4 mm nozzle, layer heights from 0.15 mm at the bottom and 0.07 mm at the studied wedge features, step size in $X/Y$ axis −0.01 mm, maximum speed 200 mm/s, and the working area of $250 \times 210 \times 210$ mm$^3$. PLA filaments were sourced from add:north, Sweden. The X-PLA filament had a diameter of 1.75 mm (diameter tolerance 0.025 mm) in two matte colors of red and blue. Although these colors were stated by the manufacturer, the printed blue color was more of a cyan color, and red was reproduced in dull red. Thus, they would be so-called cyan and dull red from in this paper. Wedge angles from 0 to 90 at 5 degrees intervals were printed using these two colors feedstocks and for each different infill density. The adjustable maximum and minimum infill densities were limited to 0 and 90%, and it was not possible to apply more than 90% for this design. The values of 30 and 60% were also applied to track the role of this pre-processing parameter on the surface color.

The spectral diagrams on the surface of the printed FDM part were measured by a spectrophotometer (X-Rite i1 Pro, Switzerland) under a D50 light source. A 45:0 degree viewing geometry under the standard CIE Publication 15.2 was used to study the surface of the 3D-printed wedges. The optical resolution and physical sampling interval within the 380–730 nm spectral range were 10 and 3.5 nm, respectively. Calibration was performed with the standard white ceramic patch of the device before each series of measurements. To avoid errors due to other sources of light, all measurements were done in a dark room. The rear side of the instrument was kept rested on a planar surface, and the aperture was placed perpendicular on three different areas of sample surfaces (hatched circles in Figure 3c) to ensure the correct optical angles. The trend in the spectral results has been controlled using a tele-spectroradiometer (TSR) model CS-2000 from Konica Minolta assessing samples at the same 45:0 geometry, placed in a D50 light box. The TSR lens was perpendicularly positioned by a 1° field of view at a distance of 50 cm from the target specimens.

The results were averagely extracted from at least three times of measurements for each wedge. The minimum thickness per raster/layer on the surface (print resolution) was 0.07 mm. It is estimated that a minimum of eight layers was investigated for each measurement. Finally, the color difference ($\Delta E^*_{ab}$) values were calculated using a color engineering toolbox in MatLab [15].

All data files were recorded in $L^*a^*b^*$, $LCh$, and $XYZ$ using ColorPort 2.0 software in order to overcome the limitations of chromaticity diagrams like RGB in this study. Therefore, all spectral diagrams were extracted from the measurement directly. Finally, the color difference values were calculated using the Eq. (4) of CIEDE2000, where the parametric factors for $K_L$, $K_C$, and $K_H$ were set to 1 [41].

## 3. RESULTS AND DISCUSSION

The i1Pro spectrophotometer used in this study was inspected and tested to examine the intrinsic error caused by the measuring device. Figure 4 provides the spectral results and color different specifications based on 25 measurements of the standard ceramic tile (white reference) under D50 illumination.

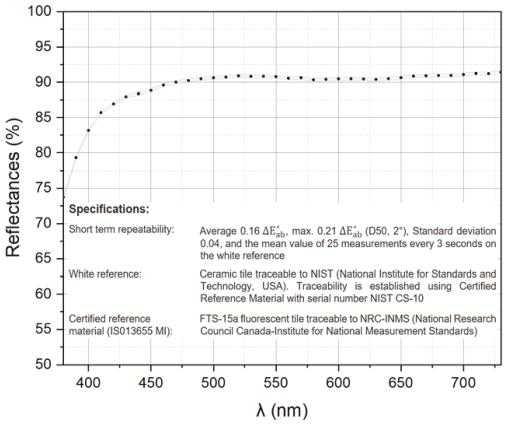


Figure 4. The average spectral and corresponding standard deviation area of the spectrophotometer. The attached specifications represent the reproducibility of the measurements and measurement uncertainty.

Spectral results of the cyan FDM samples at different infill densities are shown in Figure 5. The distributed reflectance spectra were recorded from the wavelength of 380 to 730 nm at intervals of 10 nm. As can be seen, the reflectance behavior is almost the same at different wedge angles and infill density and limited to values between approximately 5 and 55%. However, the graphs shifted to a lower level by increasing the wedge angle. It means that the 0° and 90° had the maximum and minimum reflectance values, respectively and eventually confirmed by the higher lightness value (L) in $L^*a^*b^*$ values.

In this work, the procedures attempted to follow ISO/TS 23031:2020 (E) [16]. Thus, the evaluation of the spectral differences between the reference and test spectra, and the corresponding color difference, could be performed with the root-mean-square error (RMSE) and mean color differences from the mean (MCDM), respectively [17, 18]. The definitions are as follows.

$$\mathrm{RMSE} = \sqrt{\frac{1}{N}\sum_{i=1}^{N}(r_{r,i} - r_{t,i})^2} \tag{5}$$

$$\mathrm{MCDM} = \frac{1}{N}\sum_{i=1}^{n}\Delta E(C_i, C_m)^2, \tag{6}$$

where $N$ is the number of reflectance readings, $r_r$ and $r_t$ are the references and test spectrum. $C_i$ and $C_m$ are the CIELAB color coordinates of the $i$th readings and the average reflectance of all readings, respectively.

Figure 6 represents the chromaticity coordinates of each sample on different wedges. As illustrated in Figure 7, when the infill density was fixed, the distribution of $x$–$y$ values for angle 0° was almost in the same range in the case of different infill densities. However, the distribution for the rest angles barely followed a certain pattern.

The color characteristics results in Figures 8–10 give the same interpretation as the chromaticity diagram results. In Fig. 9, infill densities of 0% and 90% represent a larger color gamut compared to other cyan samples. The size and

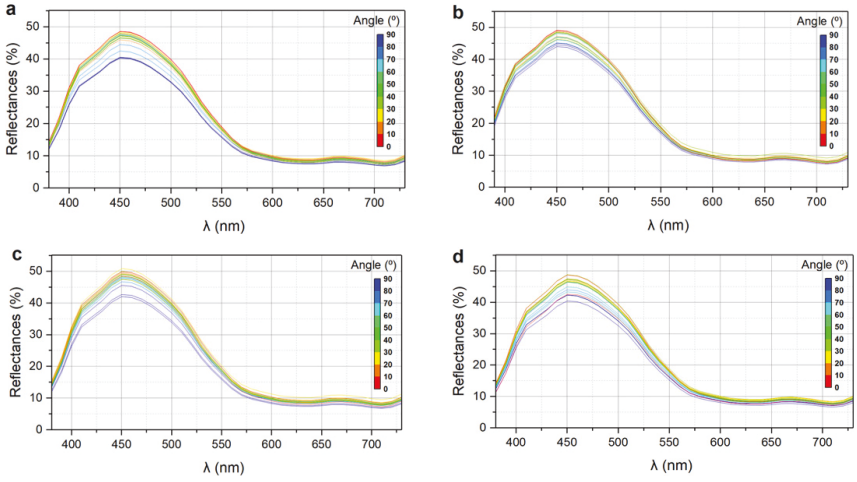


Figure 5. Reflectance spectra of cyan FDM specimens at different infill densities: (a) 0, (b) 30, (c) 60, and (d) 90%.

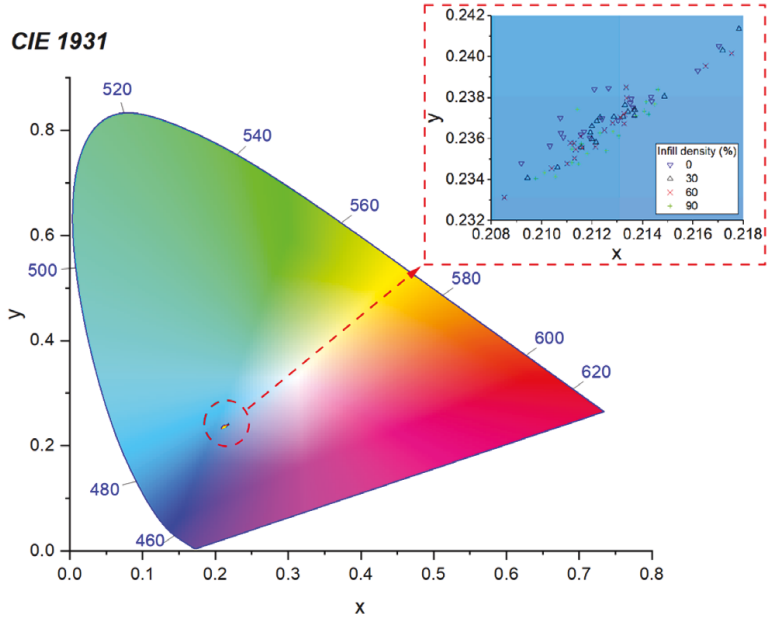


Figure 6. The enlarged and the chromaticity coordinates of the cyan samples at different wedges according to the CIE 1931 $x$–$y$ chromaticity diagram (D50).

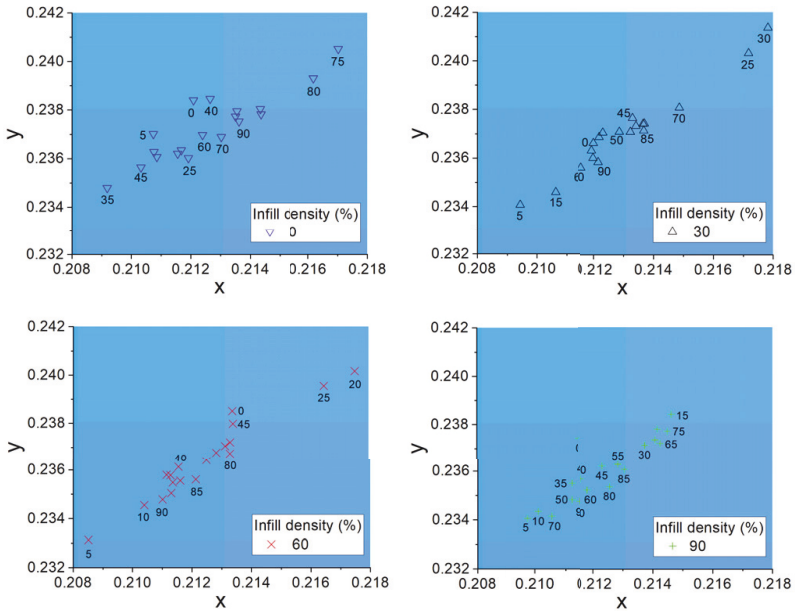


Figure 7. The chromaticity coordinates of the cyan samples at different infill densities according to the CIE 1931 $x$–$y$ chromaticity diagram (D50).

direction of color change in selected wedge angles in Fig. 10 reveal the CIEDE2000 color difference and the $a^*$ and $b^*$ direction according to the reference sample at 0° angle. Generally, it can be seen that the color change in $a^*b^*$-plane for higher wedge angles was more significant than the lower angles at different infill densities (Fig. 10).

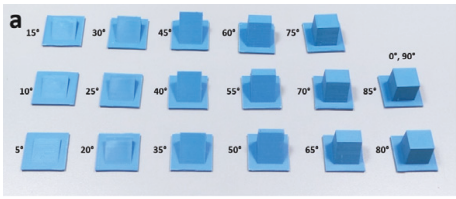


| | Wedge angle | | | | | |
|---|---|---|---|---|---|---|
| | 0° | 20° | 40° | 60° | 80° | 90° |
| L* | 51.3 | 51.2 | 50.3 | 50.6 | 47.6 | 47.0 |
| a* | -15.4 | -14.2 | -14.9 | -14.5 | -13.0 | -13.4 |
| b* | -37.8 | -37.7 | -37.2 | -37.8 | -35.1 | -35.5 |
| C | 40.8 | 40.2 | 40.1 | 40.5 | 37.4 | 38.0 |
| h° | 247.9 | 249.4 | 248.1 | 249.0 | 249.7 | 249.3 |

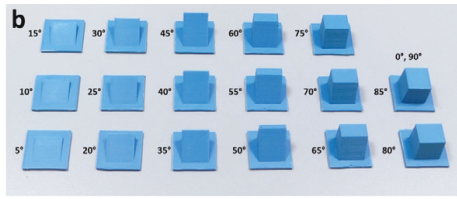


| | Wedge angle | | | | | |
|---|---|---|---|---|---|---|
| | 0° | 20° | 40° | 60° | 80° | 90° |
| L* | 51.3 | 50.2 | 51.1 | 50.1 | 49.3 | 48.7 |
| a* | -14.8 | -14.5 | -14.7 | -14.3 | -13.9 | -13.8 |
| b* | -38.4 | -37.8 | -38.1 | -38.1 | -36.9 | -37.1 |
| C | 41.1 | 40.5 | 40.8 | 40.7 | 39.4 | 39.6 |
| h° | 248.9 | 249.1 | 248.9 | 249.4 | 249.3 | 249.6 |

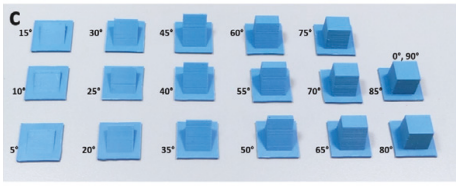


| | Wedge angle | | | | | |
|---|---|---|---|---|---|---|
| | 0° | 20° | 40° | 60° | 80° | 90° |
| L* | 52.0 | 52.8 | 51.1 | 50.2 | 49.6 | 47.5 |
| a* | -15.0 | -13.8 | -14.8 | -14.3 | -13.8 | -13.7 |
| b* | -38.0 | -37.5 | -38.4 | -38.3 | -37.3 | -36.8 |
| C | 40.8 | 40.0 | 41.2 | 40.9 | 39.8 | 39.3 |
| h° | 248.5 | 249.9 | 249.0 | 249.6 | 249.6 | 249.6 |

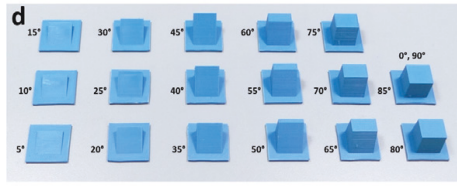


| | Wedge angle | | | | | |
|---|---|---|---|---|---|---|
| | 0° | 20° | 40° | 60° | 80° | 90° |
| L* | 48.1 | 50.2 | 49.9 | 49.0 | 47.6 | 46.6 |
| a* | -14.6 | -13.8 | -14.3 | -13.9 | -13.3 | -13.3 |
| b* | -36.4 | -37.4 | -37.9 | -37.5 | -36.5 | -36.3 |
| C | 39.2 | 39.9 | 40.5 | 40.0 | 38.8 | 38.7 |
| h° | 248.2 | 249.7 | 249.3 | 249.7 | 250.0 | 249.8 |

Figure 8. Photograph and color characteristics of cyan surfaces under a D50 illumination at different infill densities: (a) 0, (b) 30, (c) 60, and (d) 90%.

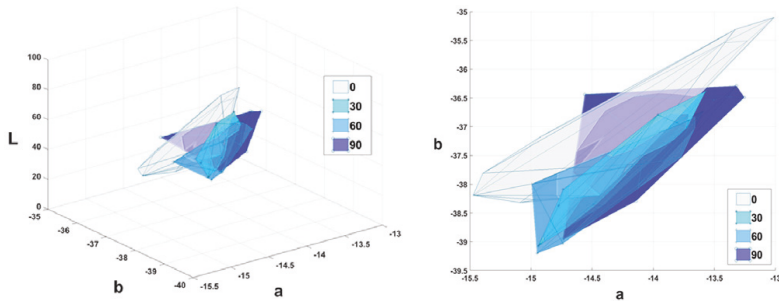


Figure 9. The color gamut of the cyan samples at different infill densities (%).

The average $L^*a^*b^*$ values for each wedge were used to calculate the CIEDE2000 color difference to identify the color difference between each sample group. The average measured reflectance of the wedge of 0° (the flat horizontal zone) is called the reference value for each sample. According to the opponent-colors theory of color vision expressed in CIELAB, $L$ defines lightness, and $a^*$ denotes the red/green value, and $b^*$ the yellow/blue value. Figure 11 shows

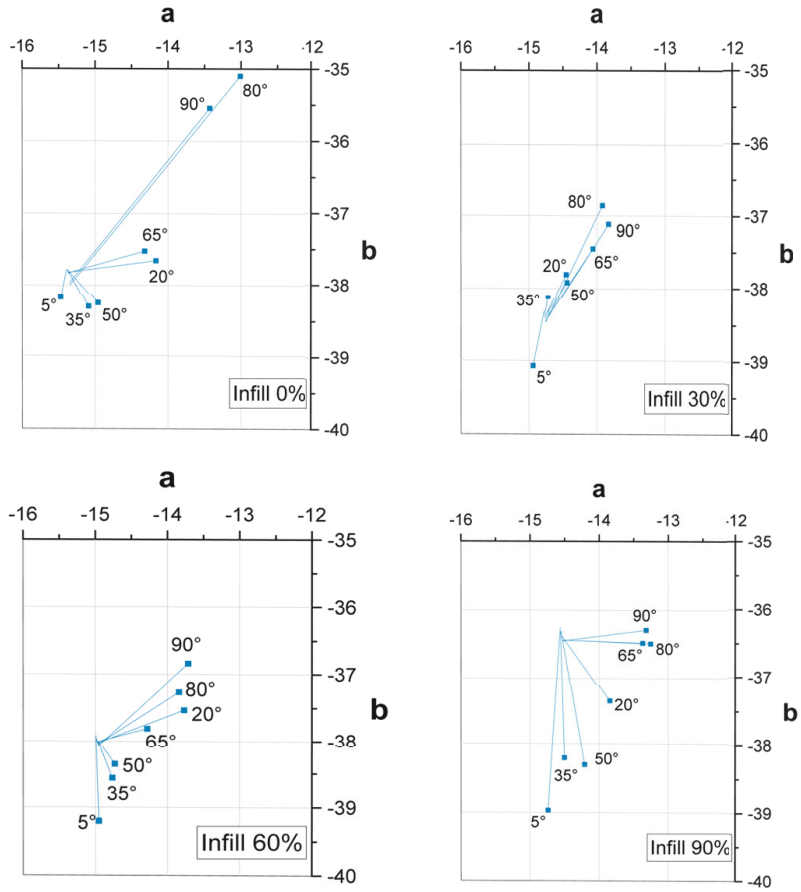


Figure 10. $L^*a^*b^*$ values of selected wedge angles of the cyan samples at different infill densities. The attached lines represent the CIEDE2000 value and direction, corresponding to the reference angle of 0°.

CIEDE2000 results from cyan samples assessed under the same appearance measurement condition. In general, the trend in CIEDE2000 values reveals that the higher infill density gives the most significant color difference at a wedge angle $< 60°$. At higher angles, however, the trend is reversed, that is, the zero-infill density displayed the highest color variation, except at 90°, where the 60% infill had a slightly higher value. In total, 30% infill appeared to represent more stable results concerning the color attribute of cyan samples, particularly at low wedge angles. Furthermore, the slope ranges from 40° to 65° meant a small threshold of color difference.

Measurements for the dull red samples resulted in a similar trend in the spectral (lightness shift in Figure 12), and the chromaticity coordinates based on the 1931 CIE (distribution of results in Figure 13). Again, the diagram shifted to the lower reflectance values for higher wedge angles at different infill levels. The range of spectral values was roughly the same between 5 and 60%.

The zero-infill samples indicated a loose convergence of the $x$ and $y$ results in terms of the distribution of chromaticity values (Figures 13 and 14). Similar to the cyan samples, the distribution of the $x$–$y$ values for sloping surfaces did not follow a certain pattern. It may suggest that although the stability of the color is noticeable on a flat FDM surface, reproducing the color is difficult for the inclined surface. It is not only because of the presence of layers and physical irregularities on the extrusion-based AM surfaces, but also it can be because of the color inconsistency in the filaments as the general feedstock for FDM printers.

Color characteristics and color gamut in Figures 15–17 indicate that the color change in the $a^*b^*$-plane for higher wedge angles is generally more extensive than the lower angles at different infill densities. The variation in the lightness ($L^*$) played the main role in the color difference on wedges for both samples.

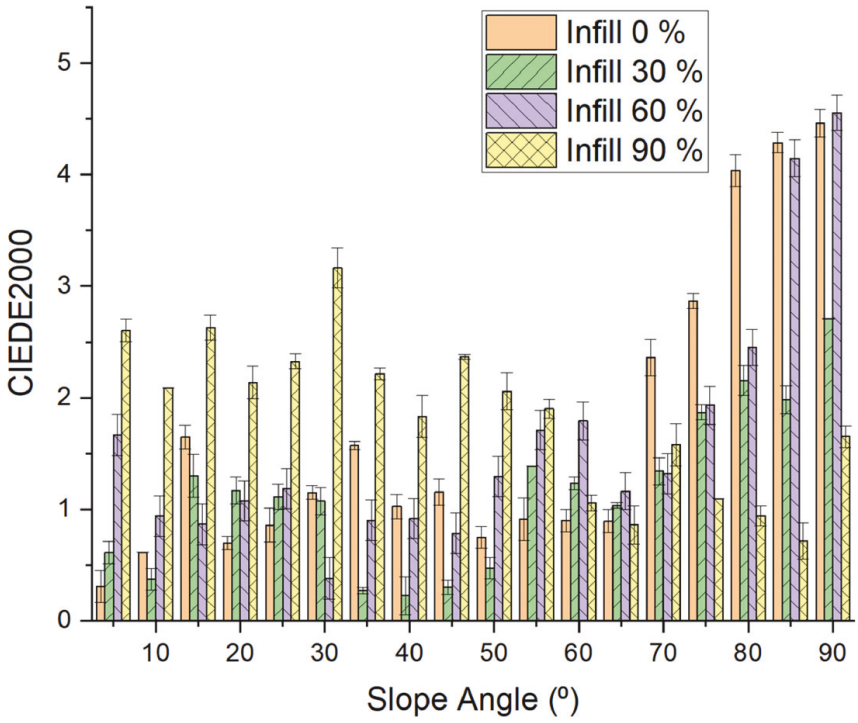


Figure 11. Average MCDM values of CIEDE2000 color difference and the corresponding RMSE for cyan samples at different infill densities.

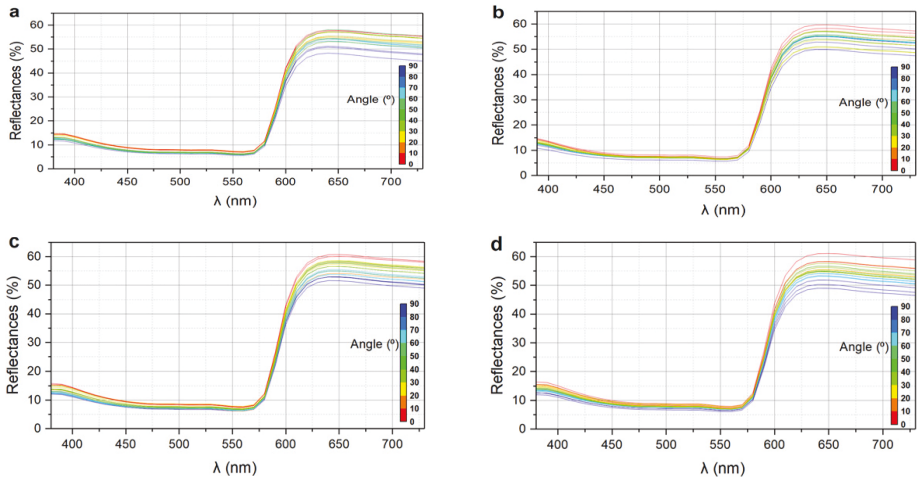


Figure 12. Reflectance spectra of dull red FDM specimens at different infill densities: (a) 0, (b) 30, (c) 60, and (d) 90%.

The CIEDE2000 results from the dull red samples in Figure 18 suggested an incremental trend in the color difference in the upper wedge angles. However, the average value of color differences indicated that the unfilled samples had more color differences (Figure 19). Generally, it can be seen from the average CIDE2000 for different infill values that the higher density inside the FDM parts is associated with higher color differences. However, the correlation

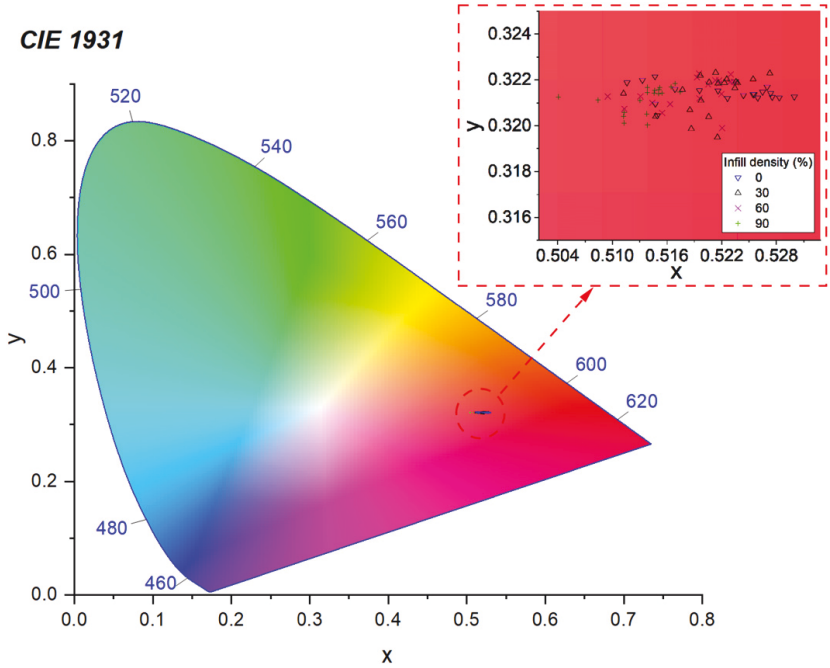


Figure 13. The enlarged and the chromaticity coordinates of the dull red samples at different wedges according to the CIE 1931 *x–y* chromaticity diagram (D50).

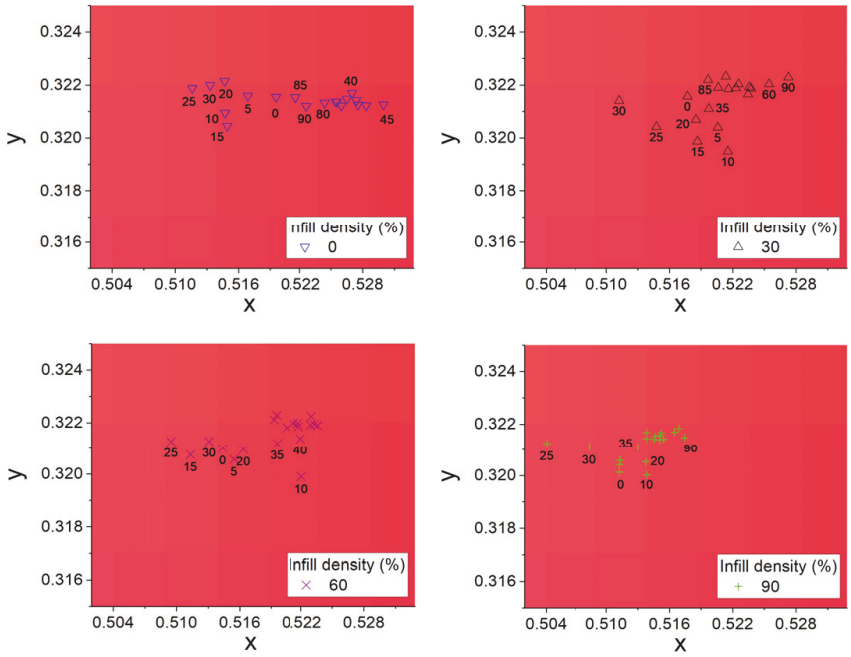


Figure 14. The chromaticity coordinates of the dull red samples at different infill densities according to the CIE 1931 *x–y* chromaticity diagram (D50).

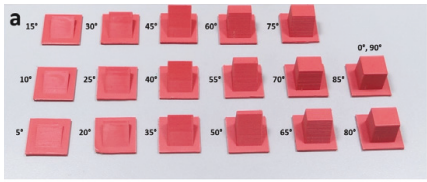


| | Wedge angle | | | | | |
|---|---|---|---|---|---|---|
| | 0° | 20° | 40° | 60° | 80° | 90° |
| L* | 49.6 | 49.0 | 46.9 | 47.4 | 46.4 | 45.4 |
| a* | 51.8 | 50.0 | 51.2 | 51.8 | 50.4 | 49.2 |
| b* | 24.1 | 23.1 | 24.5 | 24.7 | 23.8 | 23.0 |
| C | 57.1 | 55.1 | 56.8 | 57.3 | 55.7 | 54.3 |
| h° | 25.0 | 24.8 | 25.6 | 25.5 | 25.2 | 25.1 |

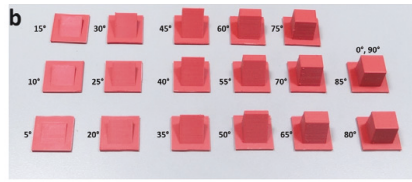


| | Wedge angle | | | | | |
|---|---|---|---|---|---|---|
| | 0° | 20° | 40° | 60° | 80° | 90° |
| L* | 50.1 | 47.7 | 47.6 | 47.8 | 47.1 | 45.5 |
| a* | 51.7 | 50.3 | 51.0 | 51.5 | 49.9 | 49.9 |
| b* | 23.9 | 23.0 | 24.1 | 24.6 | 23.6 | 24.1 |
| C | 57.0 | 55.3 | 56.4 | 57.1 | 55.3 | 55.5 |
| h° | 24.8 | 24.6 | 25.3 | 25.6 | 25.3 | 25.8 |

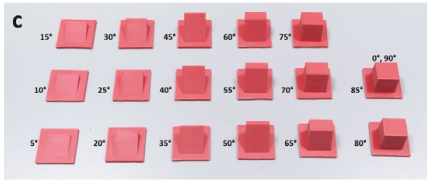


| | Wedge angle | | | | | |
|---|---|---|---|---|---|---|
| | 0° | 20° | 40° | 60° | 80° | 90° |
| L* | 50.7 | 49.2 | 49.1 | 47.3 | 47.3 | 46.6 |
| a* | 51.6 | 51.0 | 52.0 | 50.6 | 49.7 | 49.8 |
| b* | 23.4 | 23.2 | 24.3 | 24.0 | 23.3 | 23.4 |
| C | 56.7 | 56.0 | 57.4 | 56.0 | 54.9 | 55.0 |
| h° | 24.3 | 24.5 | 25.1 | 25.3 | 25.1 | 25.2 |

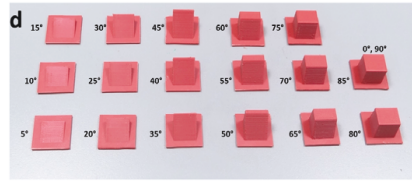


| | Wedge angle | | | | | |
|---|---|---|---|---|---|---|
| | 0° | 20° | 40° | 60° | 80° | 90° |
| L* | 51.1 | 48.7 | 48.6 | 48.2 | 47.2 | 45.9 |
| a* | 51.4 | 50.1 | 50.0 | 49.9 | 49.2 | 48.4 |
| b* | 22.8 | 22.5 | 22.9 | 23.0 | 22.8 | 22.3 |
| C | 56.2 | 54.9 | 55.0 | 55.0 | 54.2 | 53.3 |
| h° | 24.0 | 24.1 | 24.6 | 24.7 | 24.8 | 24.7 |

Figure 15. Photograph and color characteristics of dull red surfaces under a D50 illumination at different infill densities: (a) 0, (b) 30, (c) 60, and (d) 90%.

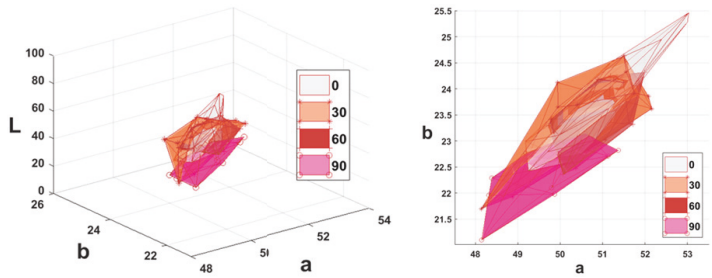


Figure 16. The color gamut of the dull red samples at different infill densities (%).

between the mean color difference and wedge angle in both cyan and dull red samples is not linear. The number of layers, the staircase effect, and the random errors due to variation in printing conditions can affect the layered microstructures significantly [42].

In particular, the formation of stairs is an inherent issue with the FDM method and affects surface quality significantly in comparison with traditional manufacturing techniques such as injection molding [31, 42]. For instance, while there was only a base layer at the flat surface, it reached 18, 37, 57, 78, 99, 123, 150, and 179 layers for wedge angles from 5° to 40°, consecutively. Then it is limited to the maximum 214 layers for 45° to 90° samples. In this case, the horizontal width of stairs was 0.83, 0.41, 0.26, 0.19, 0.15, 0.12,

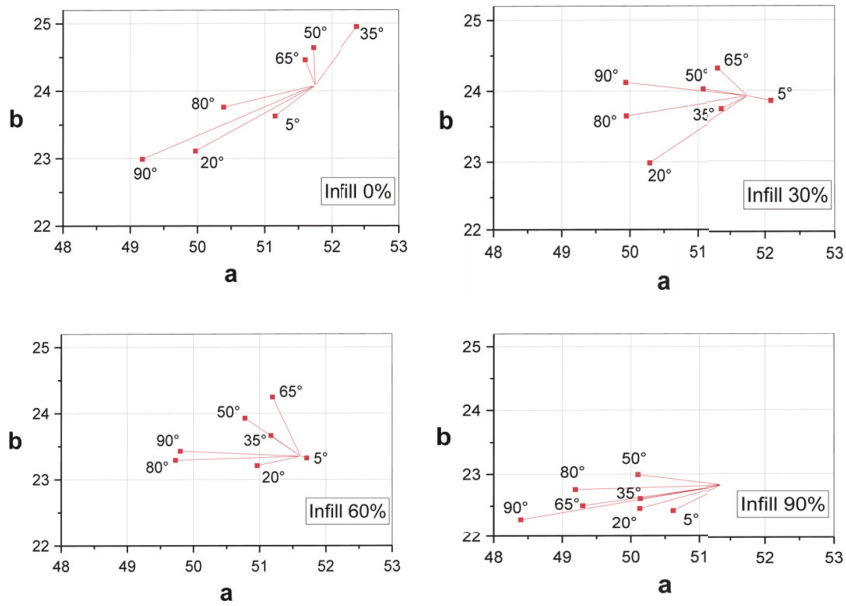


Figure 17. *L*a*b** values of selected wedge angles of the red samples at different infill densities. The attached lines represent the CIEDE2000 value and direction, corresponding to the reference angle of 0°.

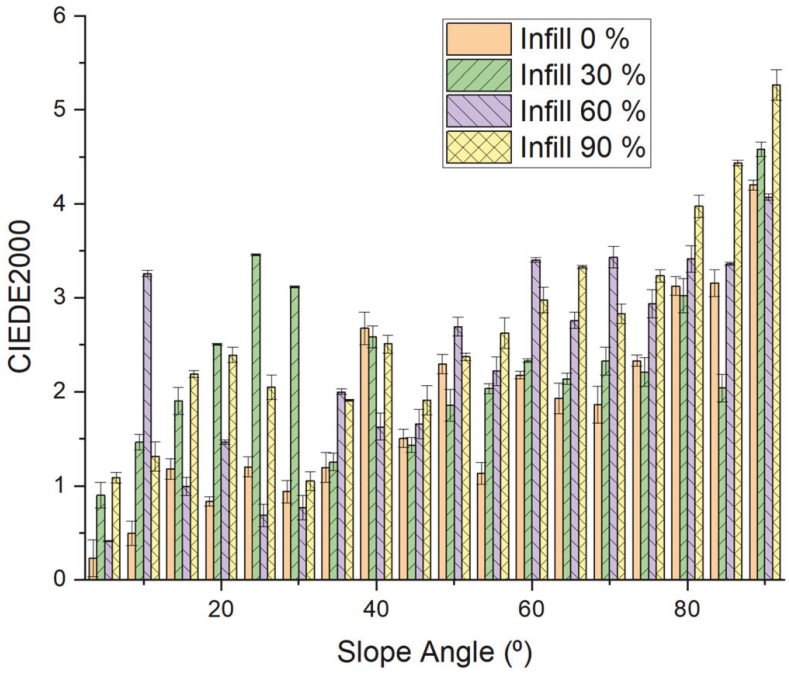


Figure 18. The MCDM value of CIEDE2000 color difference and the corresponding RMSE for dull red samples at different infill densities.

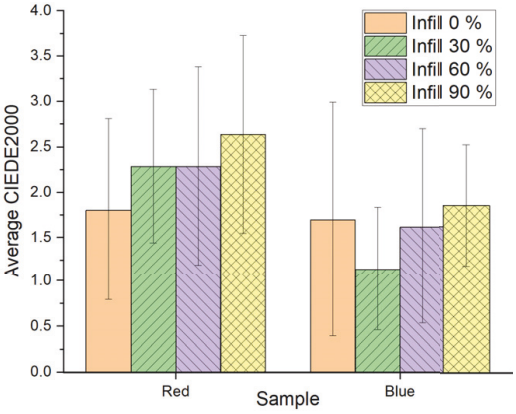


Figure 19. The MCDM CIEDE2000 color difference for each set of measurements. Each column bar represents an average value for color difference in wedge angles between 0° to 90° at intervals of 5°.

0.10, 0.08 mm for wedge angles from 5° to 45°, consecutively. It reached a value less than the layer thickness (0.07 mm) at 50°, where the horizontal width of stairs started to decrease to 0.06, 0.05, 0.04, 0.03 mm for 55° to 70°, consecutively. For the rest angles, it was less than 0.03 mm.

Although there was a meaningful association between the variations in staircase effect and the wedge angles as expected, the correlation between slope angles and color differences was non-linear due to many influential printing factors. In particular, environmental factors can impose irregularities on the surface, resulting in a rougher surface, which consequently can affect the spectral results. It includes variation in temperature, humidity, platform vibration, airflow, dust particles, etc. [25, 43].

Regarding the infill 0%, a small bump was observed at lower wedge angles in some cyan samples, resulting from incubating hot air in the surface elements during the printing process at temperature of 215°C. These bumps could affect the color difference results and explain the irregularity in the color of the unfilled samples of the cyan parts.

The notable RMSE errors in the color difference resulted from the uncertainty raised by the layer-upon-layer nature of FDM 3D printing. Considering the role of wedge angles in the design step, the polynomial fitting results with 95% confidence in Figure 20 suggest that the color difference increases exponentially at higher wedge angles. In particular, the wedge angles of 80° to 90° for the two filaments showed a significant color difference. According to the CIEDE2000 formula [11, 12], the color difference of 1 is generally considered unnoticed and barely perceptible by the average human observer. An experienced observer can only notice $\Delta E$ between 1 and 2. In the case of $2 < \Delta E^*_{ab} < 3.5$, the difference is also noticed by an inexperienced observer. The difference is noticeable in the range of 3.5 to 5, and $\Delta E^*_{ab} < 6$ is typically considered an acceptable match in commercial reproduction in printing presses. Regarding human vision, it is more sensitive to color differences if two colors actually touch each other [40, 44]. According to the calculated color difference in Fig. 20, $\Delta E^*_{ab}$ ranges were less than 5 for all samples. It means the maximum color difference is possible to be noticed by an inexperienced observer for high wedge angles. However, it is not easy to recognize the appearance difference due to the color in the case of lower wedge angles. Considering the intrinsic errors due to the measuring device in Fig. 4 (mean $\Delta E^*_{ab} = 0.16$), the error was less than the measured minimum color difference ($\Delta E^*_{ab} = 0.22$) for both samples in dull red (infill 0% and wedge angle 5°) and cyan (infill 30% and wedge angle 40°) colors. In other words, the spectrophotometer was sufficiently accurate to record the minor color differences for microtextured samples 3D-printed by the FDM method.

The above results suggest a pathway based on the studied parameters for the simulation and design of 3D-printed objects. For instance, defining boundary conditions and constraints in a 3D design for topology optimization (TO) is a potential application as a mathematical method for increasing the performance of the machine to print optimized surfaces.

## 4. CONCLUSIONS

This study represented an insight into the influence of additive manufacturing pre-processing steps on the color difference of structured surfaces. For this purpose, two filament spools with different colors from the same material and manufacturer were used to print samples with different wedge angles and infill densities. The increasing CIEDE2000 values at higher wedge angles and infill densities uncovered an idea to optimize the design and select the best printing process for the feature FDM printing. As indicated in this study, while the measurements of the color difference were unstable because of the layer-by-layer nature of the AM objects, it is possible to evaluate the appearance using standard spectrophotometers. The color attribute has been examined among other appearance properties, by measuring tristimulus values of a color stimulus. According to the results, the change in the lightness ($L^*$) played the main role in the color variation on the wedges. The variation in staircase effect corresponding to the wedge angles had a significant correlation. It was revealed that the lower reflectance at the higher wedge angle was mainly due to the smaller horizontal width of stairs. Experimental work revealed the color cyan PLA filaments can offer a more stable color during manufacturing, which means that the filament color can affect the appearance of the same feedstock material. However, the dominant factor for the color difference was the layers formation and the staircase effect. Overall, the discussed results are instrumental in altering the color appearance of printed parts deliberately by means of controlling the generation of surface texture in the pre-processing stage in the case of PLA filaments. It suggests a possibility to generate micro-textures at lower

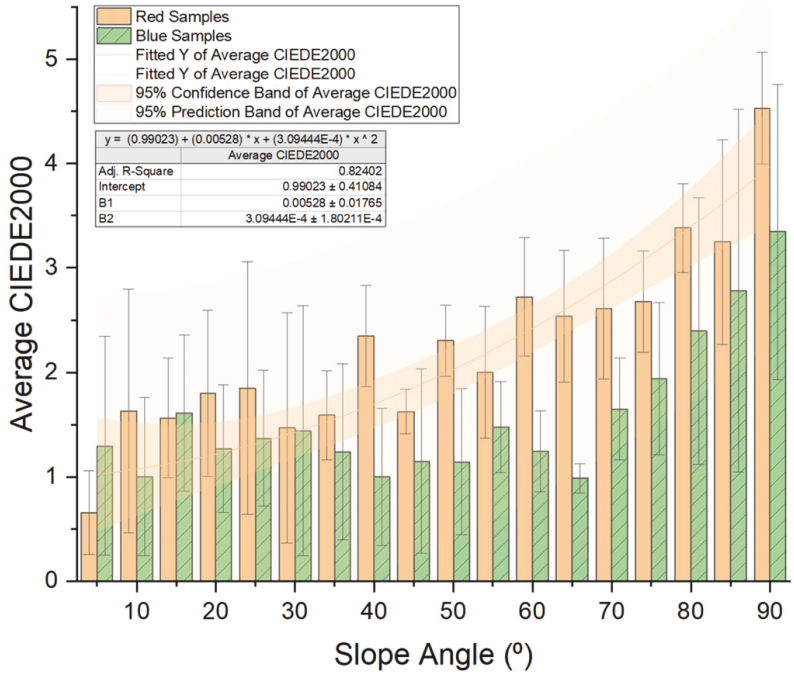


Figure 20. 95th percentile polynomial fitting results for cyan and dull red PLA samples at different wedge angles.

wedge angles and fewer infill densities for PLA filaments through topological optimization and generative designs.

## ACKNOWLEDGMENT

The authors gratefully acknowledge the support from the ApPEARS-ITN Program at the Norwegian University of Science and Technology. This work has received funding from the European Union's Horizon 2020 research and innovation program under the Marie Skłodowska-Curie grant agreement No. 814158. We wish to thank European Research Council (ERC) and Prof. Peter Nussbaum for their support.

## REFERENCES

[1] J. Yuan, M. Zhu, B. Xu, and G. Chen, "Review on processes and color quality evaluation of color 3D printing," Rapid Prototyping J. **24**, 409–415 (2018).

[2] K. Xiao, A. Sohiab, P. Sun, J. M. Yates, C. Li, and S. Wuerger, "A colour image reproduction framework for 3D colour printing," Proc. SPIE **10153**, 1015318 (2016).

[3] S. R. Mogali, W. Y. Yeong, H. K. J. Tan, G. J. S. Tan, P. H. Abrahams, N. Zary, N. Low-Beer, and M. A. Ferenczi, "Evaluation by medical students of the educational value of multi-material and multi-colored three-dimensional printed models of the upper limb for anatomical education," Anat. Sci. Educ. **11**, 54–64 (2018).

[4] M. Inoue, T. Freel, A. V. Avermaete, and W. M. Leevy, "Color enhancement strategies for 3D Printing of X-ray computed tomography bone data for advanced anatomy teaching models," Appl. Sci. **10**, 1571 (2020).

[5] L. Ding, W. Lu, J. Zhang, C. Yang, and G. Wu, "Preparation and performance evaluation of duotone 3D-printed polyetheretherketone as oral prosthetic materials: A proof-of-concept study," Polymers **13**, 1949 (2021).

[6] J. Weiler and S. Kuznetsov, "Crafting colorful objects: A DIY method for adding surface detail to 3D prints," *Proc. Conf. on Human Factors in Computing Systems* (ACM, New York, NY, 2017), pp. 2217–2223.

[7] J. Yuan, J. Tian, C. Chen, and G. Chen, "Experimental investigation of color reproduction quality of color 3D printing based on colored layer features," Molecules **25**, 2909 (2020).

[8] G. Chen, X. Wang, H. Chen, and C. Chen, "Realization of rapid large-size 3D printing based on full-color powder-based 3DP technique," Molecules **25**, 2037 (2020).

[9] X. Wang, G. Chen, J. Yuan, and L. Cai, "Research on cutting-bonding process of powder based 3D printing model," *Lecture Notes in Electrical Engineering* (Springer, Berlin, Heidelberg, 2019), pp. 495–500.

[10] J. Tian, J. Yuan, H. Li, D. Yao, and G. Chen, "Advanced surface color quality assessment in paper-based full-color 3D printing," Materials **14**, 1–13 (2021).

[11] X. Yan, J. Yuan, and G. Chen, "Applications analysis of paper-based color 3D printing in the map industry," *Lecture Notes in Electrical Engineering* (Springer, Berlin, Heidelberg, 2018), pp. 377–383.

[12] M. Cui, X. Li, G. Wu, and Q. Cao, "Measurement and evaluation of the surface color of 3D paper product," *Lecture Notes in Electrical Engineering* (Springer, Berlin, Heidelberg, 2019), pp. 108–113.

[13] J. Yuan, J. Tian, D. Yao, and G. Chen, "Color assessment of paper-based color 3D prints using layer-specific color 3D test charts," *Lecture Notes in Electrical Engineering* (Springer, Berlin, Heidelberg, 2021), pp. 123–131.

[14] J. Yuan, L. Cai, X. Wang, and G. Chen, "Visualization of biomedical products based on paper-based color 3D printing," *Proc. IS&T Printing for Fabrication 2019* (IS&T, Springfield, VA, 2019), pp. 128–131.

[15] D. Buchbinder, H. Schleifenbaum, S. Heidrich, W. Meiners, and J. Bültmann, "High power selective laser melting (HP SLM) of aluminum parts," Phys. Procedia **12**, 271–278 (2011).
[16] J. Gu, B. Liu, H. Yang, and X. Li, "A fast and CMP-free TSV process based on wafer-level liquid-metal injection for MEMS packaging," *2016 IEEE 29th Int'l. Conf. on Micro Electro Mechanical Systems (MEMS)* (IEEE, Piscataway, NJ, 2016), pp. 569–572.
[17] H. M. Wang, G. X. Chen, and W. B. Zhang, "3D printing of topographic map based on UV ink-jet printer," *Applied Mechanics and Materials* (Trans Tech Publ, Baech, Switzerland, 2014), Vol. 469, pp. 309–312.
[18] J. Yang, L. W. Wu, and J. Liu, "Rapid prototyping and fabrication method for 3-D food objects," US Patent 6,280,785 (2001).
[19] K. Xiao, F. Zardawi, R. van Noort, and J. M. Yates, "Color reproduction for advanced manufacture of soft tissue prostheses," J. Dent. **41**, e15–e23 (2013).
[20] A. Sohaib, K. Amano, K. D. Xiao, J. M. Yates, C. Whitford, and S. Wuerger, "Colour quality of facial prostheses in additive manufacturing," Int. J. Adv. Manuf. Technol. **96**, 881–894 (2018).
[21] P. L. Sun and Y. P. Sie, "Color uniformity improvement for an inkjet color 3D printing system," *IS&T Electronic Imaging: Color Imaging XXI: Displaying, Processing, Hardcopy, and Applications* (IS&T, Springfiled, VA, 2016), pp. COLOR-342.1–COLOR-342.6.
[22] C. Li, L. Zheng, and Y. Xiao, "Study on the influencing factors of color reproduction in color 3D printing," *Lecture Notes in Electrical Engineering* (Springer, Berlin, Heidelberg, 2020), pp. 156–163.
[23] K. Xiao, F. Zardawi, R. V. Noort, and J. M. Yates, "Developing a 3D colour image reproduction system for additive manufacturing of facial prostheses," Int. J. Adv. Manuf. Technol. **70**, 2043–2049 (2014).
[24] H. Li, T. Wang, J. Sun, and Z. Yu, "The effect of process parameters in fused deposition modelling on bonding degree and mechanical properties," Rapid Prototyping J. **24**, 80–92 (2018).
[25] S. Vyavahare, S. Teraiya, D. Panghal, and S. Kumar, "Fused deposition modelling: a review," Rapid Prototyping J. **26**, 176–201 (2020).
[26] E. H. Baran and H. Y. Erbil, "Surface modification of 3D printed PLA objects by fused deposition modeling: a review," Colloid Interfac. **3**, 25 (2019).
[27] A. Yahamed, P. Ikonomov, P. D. Fleming, A. Pekarovicova, P. Gustafson, A. Q. Alden, and S. Alrafeek, "Mechanical properties of 3D printed polymers," J. Print Media Technol. Res. **5**, 273–289 (2016).
[28] A. Yahamed, P. Ikonomov, P. D. Fleming, A. Pekarovicova, and P. Gustafson, Designed structures for bone replacement, "Designed structures for bone replacement," J. Print Media Technol. Res. **5**, 291–307 (2016).
[29] A. Yahamed, M. Joyce, P. D. Fleming, A. Pekarovicova, and P. Ikonomov, "Polymers for 3D printed structures, precision, topography and roughness," Int. J. Multidisciplinary Res. Studies **1**, 43–59 (2018).
[30] D. J. Roach, C. Roberts, J. Wong, X. Kuang, J. Kovitz, Q. Zhang, T. G. Spence, and H. J. Qi, "Surface modification of fused filament fabrication (FFF) 3D printed substrates by inkjet printing polyimide for printed electronics," Addit. Manuf. **36**, 101544 (2020).
[31] M. Taufik and P. K. Jain, "Part surface quality improvement studies in fused deposition modelling process: a review," Aust. J. Mech. Eng. **13**, 1–25 (2020).
[32] A. K. Sood, R. Ohdar, and S. S. Mahapatra, "Improving dimensional accuracy of fused deposition modelling processed part using grey Taguchi method," Mater. Des. **30**, 4243–4252 (2009).
[33] S. Masood, W. Rattanawong, and P. Iovenitti, "A generic algorithm for a best part orientation system for complex parts in rapid prototyping," J. Mater. Process. Technol. **139**, 110–116 (2003).
[34] Y.-S. Liao and Y.-Y. Chiu, "A new slicing procedure for rapid prototyping systems," Int. J. Adv. Manuf. Technol. **18**, 579–585 (2001).
[35] M. Livesu, S. Ellero, J. Martínez, S. Lefebvre, and M. Attene, "From 3D models to 3D prints: an overview of the processing pipeline," *Comput. Graph. Forum* (Wiley Online Library, Hoboken, NJ, 2017), pp. 537–564.
[36] B. N. Turner and S. A. Gold, "A review of melt extrusion additive manufacturing processes: II. Materials, dimensional accuracy, and surface roughness," Rapid Prototyping J. **21**, 250–261 (2015).
[37] M. Dattner and D. Bohn, "European energy efficiency improvement by means of visualisation and benchmarking tailored to the print and media industry," International Circular of Graphic Education and Research **3**, 42–54 (2010).
[38] M. R. Luo, G. Cui, and B. Rigg, "The development of the CIE 2000 colour-difference formula: CIEDE2000, Color Research & Application: Endorsed by Inter-Society Color Council, The Colour Group (Great Britain), Canadian Society for Color, Color Science Association of Japan, Dutch Society for the Study of Color, The Swedish Colour Centre Foundation, Colour Society of Australia," Centre Français de la Couleur **26**, 340–350 (2001).
[39] G. A. Klein and T. Meyrath, *Industrial Color Physics* (Springer, Berlin, Heidelberg, 2010).
[40] W. Mokrzycki and M. Tatol, "Colour difference $\Delta E$ – A survey," Machine Graphics and Vision **20**, 383–411 (2011).
[41] P. Green, *A Colour Engineering Toolbox* (John Wiley & Sons, Hoboken, NJ, 2003).
[42] A. D. Valino, J. R. C. Dizon, A. H. Espera Jr., Q. Chen, J. Messman, and R. C. Advincula, "Advances in 3D printing of thermoplastic polymer composites and nanocomposites," Prog. Polym. Sci. **98**, 101162 (2019).
[43] S. D. Nath and S. Nilufar, "An overview of additive manufacturing of polymers and associated composites," Polymers **12**, 2719 (2020).
[44] J. Schanda, *Colorimetry: Understanding the CIE System* (John Wiley & Sons, Hoboken, NJ, 2007).

## Paper II:

A. P. Golhin, A. S. Sole, A. Strandlie, Color appearance in rotational material jetting, The International Journal of Advanced Manufacturing Technology, 124, 1183–1198 (2023). https://doi.org/10.1007/s00170-022-10536-1

The International Journal of Advanced Manufacturing Technology (2023) 124:1183–1198
https://doi.org/10.1007/s00170-022-10536-1

ORIGINAL ARTICLE

# Color appearance in rotational material jetting

**Ali Payami Golhin**[1] · **Aditya Suneel Sole**[2] · **Are Strandlie**[1]

Received: 16 June 2022 / Accepted: 11 November 2022 / Published online: 29 November 2022


**Abstract**
Material jetting (MJT) is a recognized additive manufacturing (AM) method to combine various materials and create a wide range of designed appearances. However, the measured color of MJT objects is frequently different from the color provided in the printer software. As a result, estimating the color quality and the measured color attributes of an object before printing is vital for accurate color reproduction. This study investigates the color variation based on the texture in an object 3D-printed using the MJT method on a rotary tray. The novel radial shape of the rotary tray build platform and variation in the layers structure were targeted as the main factors that can increase the uncertainty in accurate color reproduction. The influence of the PolyJet printer setup has been examined by thickness variation of the colored layers, location on the tray (swath selection), ink color, and finish type between layers. Color quality was assessed by comparing the produced object color by calculating spectral and colorimetric differences. Spearman rank correlation coefficient and principal component analysis (PCA) methods were used to analyze the direct or indirect influence of independent categorical factors on the measured color variables. Based on the studied parameters, switching swathes did not fail printer objects for industrial color matching. In contrast, a thickness variation as small as 0.5 mm could cause CIEDE2000 above 5 for most models, resulting in unnatural color reproduction. Color differences in most objects might be discernible to inexperienced observers, depending on the 3D printing parameters.

**Keywords** 3D printing · Material jetting · PolyJet · Color accuracy · Surface texture · Appearance

## 1 Introduction

The rapid development of office 3D printers offers a broader range of innovative designs that were previously impossible to produce using traditional manufacturing methods. Vat photopolymerization (VPP) [1] and material jetting (MJT) [2] are two examples of current AM methods that have been adapted to the personal 3D printing market. It opens new avenues for the economy and society due to its rapid development in recent years. While material jetting has made significant advances in the enhancement of surface roughness [3], the technology has yet to catch up with the development of fused filament fabrication (FFF) in terms of personal applications [4, 5].

✉ Ali Payami Golhin
payami.ag@gmail.com; ali.p.golhin@ntnu.no

[1] Department of Manufacturing and Civil Engineering, Norwegian University of Science and Technology, 2815 Gjøvik, Norway

[2] Department of Computer Science, Norwegian University of Science and Technology, 2815 Gjøvik, Norway

Prototyping is the primary purpose of personal 3D printers. Data from over 10,000 3D printers shows that they are mostly used for prototypes, hobbies, gadgets, art/fashion, and scale models [6]. This means that rather than mechanical or thermal capabilities, the quality of 3D-printed items is judged primarily based on their tactile and appearance perception. Instrumental color measurement is an indirect practical method of analyzing a product based on its appearance to evaluate the processing performance and quality of manufactured products. However, visual color assessments and color perception are qualitative, subjective, and controversial. It has become an industry concept of quality control to determine, among other things, color strength, color difference, match prediction, shade sorting, and whiteness measuring [7]. A spectroradiometer is a valuable tool for measuring light over complex shapes and designs, as it measures both wavelength and intensity for radiance, luminance, and chromaticity remotely.

The reproduction of appearance is one of the most significant aspects of 3D printing using MJT technology [8]. Since 2014, several companies, including 3D systems, MCOR-technology, HP Multi Jet Fusion (MJF), and Stratasys,

have introduced multicolor 3D printers based on powder, paper, or plastic [9]. Currently, color reproduction systems use halftoning techniques, which combine different inks spatially at the surface of an object to create colors. As a result, the object exhibits a variety of artifacts, particularly when viewed from a closer distance [8]. Y. Cheng et al. [10] prepared photocurable resins for MJT and colored the resin with CMYKW colors to achieve full-color printing using a homemade MJT printer. They developed mechanical mechanisms, automatic print head alignment algorithms, leveling mechanisms, and color dithering methods to improve color consistency. Using a custom MJT printer for 3D printing, V. Babaei et al. proposed a method for reproducing color using a 3D printing process. They create colors by combining inks with different thicknesses inside the volume of the object by 3D color contouring, which was inspired by the inherent ability of 3D printers to layer different materials over one another. Most of these studies, however, focused on the conventional movement of the build platform in MJT 3D printers.

Rotational 3D printing is currently being introduced to help reduce the size and complexity of 3D printers without using large robot arms. PolyJet® 3D printing, developed by Stratasys, is a promising MJT method that utilizes a rotary tray to create realistic-looking colored parts, such as physical replicas of biological structures, prototype samples, educational models, and artistic designs [11]. Office 3D printers have recently repurposed MJT for the personal 3D printing market. The PolyJet system builds three-dimensional objects by jetting fine droplets of photopolymer in CMYKW (cyan, magenta, yellow, black, and white), solidifying when exposed to ultraviolet light [11]. Thermoplastics and elastomers are used more frequently than photopolymers in some production environments, yet they can simulate these materials mechanically, thermally, and visually [12]. As a result of the high-resolution 3D printers available in MJT, it is now possible to print single objects with numerous colors and various surface properties, including a variety of color shades, anisotropic reflectance (AR), gloss, halftone patterns, and goniochromatic effects [11].

While the dimension accuracy and surface finishing in the manufactured objects represent high manufacturing quality, printed objects have a measured color that often differs from the selected color in the printer software. Currently, limited studies have been conducted on accurate color reproduction methods for various color 3D printing materials. Compared to color studies on AM processes with color reproduction capability, such as FDM [13–15] as the dominant AM technique, materials jetting allows for greater control over the color reproduction of 3D-printed items. For instance, X. Wei et al. [16] studied the significant-finish effects type on measured color, as well as the interaction effects of finish type and specified color. L. Zheng et al. [17] characterized the achievable range of color by comparing the gamut of PolyJet color 3D printing and ink-jet printing on a paper surface. Effects of the number of printing layers, hue, brightness, saturation, and chromatic aberration have been studied by C. Li et al. [18]. The colorimetric characterization of 3D printers using highly translucent printing materials was addressed by c. A. Arikan et al. [19]. In another study, O. Elek et al. [20] developed a self-contained, end-to-end system for the translucent resin to produce high-frequency color texture. A. Brunton et al. developed techniques [21, 22] for precise and efficient material placement control in multi-jet 3D printers for halftoning, vital in accurate color reproduction. X. Wei et al. [11, 23] demonstrated that the response surface methodology (RSM) and multilayer perceptron (MLP) neural network model perform well in predicting the measured color. These studies, however, were carried out on standard XYZ build platforms, with industrial Stratasys J750 PolyJet or HP Multi Jet Fusion (MJF) printers as the primary printers.

Studies [24, 25] have shown the significant influence of build orientation, i.e., planar, vertical, and inclined surfaces, on the surface quality and roughness of MJT parts. G. Kim and Y. Oh [26] reported that the surface quality of MJT printing is superior to SLA printing on all inclined surfaces except for the vertical surface, which has an inclination of 90°. Build orientation can also affect the surface appearance of 3D-printed parts. Manufactured objects can also be designed so that they appear differently from various viewpoints or by using the reflection properties of colors to achieve viewpoint-dependent appearances [27]. A few studies have mentioned the rotary build platform model of MJT technology [27, 28] and the liquid jetting at a rotary disk [29]. However, the effect of centrifugal force caused by the rotating build platform on shaping the layers and color quality has yet to be investigated.

Using rotational 3D printing, 3D printers may become smaller and easier for office applications. Different patterns are created on the surface because the tray rotates about a vertical axis, presenting new challenges. Therefore, it will be necessary to examine the surface texture and the quality of 3D-printed objects to develop rotational 3D printing methods. Accordingly, this work presents a texture study to statistically analyze connections between observed color and four PolyJet control parameters, including the specified color, design thickness ($\Delta t$), swath (manufacturing track) location on the build platform, and finish type. In order to clarify the contribution of the rotary tray to the color appearance of the samples, we studied the texture and layers of the samples manufactured at different places on the build platform. At the end of this work, we examined the possible conditions of color reproduction using a PolyJet 3D printer by evaluating multivariate analysis over the studied parameters and response variables.

## 2 Materials and methods

### 2.1 Experimental design

The role of printing location on the build platform (swath), the thickness of layers, color, and finish type is studied using a full factorial design of experiments as three control factors connected to the measured color. The Stratasys J55 3D printer was used to prepare the samples. A J55 placement zone consists of three areas of the same width: inner, mid, and outer (Fig. 1). The innermost location of the parts should be utilized first for optimal placement and reduced build time. The finish types between the colored layer and white bottom substrate were selected glossy on glossy (GoG) and glossy on matte (GoM) for studying as-printed samples. The specimen dimensions were $10 \times 10 \times 3.5$ $mm^3$ for color study (Fig. 2) and $60 \times 13 \times 3.5$ $mm^3$ for texture evaluation and trial color evaluation, respectively. The thresholds for each parameter were chosen to eliminate the influence of post-processing, as well as the limitations imposed by processing software and the 3D printer. For instance, the matte surface finish was avoided due to surface alteration during the support removal process. Furthermore, parts were designed with the minimum size required for measurement to counteract the effect of extended radial layers.


**Fig. 2** As-printed MJT samples for color evaluations as observed under D50 daylight illumination

The primary specimens were 3 mm thick with 1.5-mm support material at the bottom, 1-mm white background, and 1-mm colored material on top (Fig. 2). This design method is based on Stratasys best practices for PolyJet and according

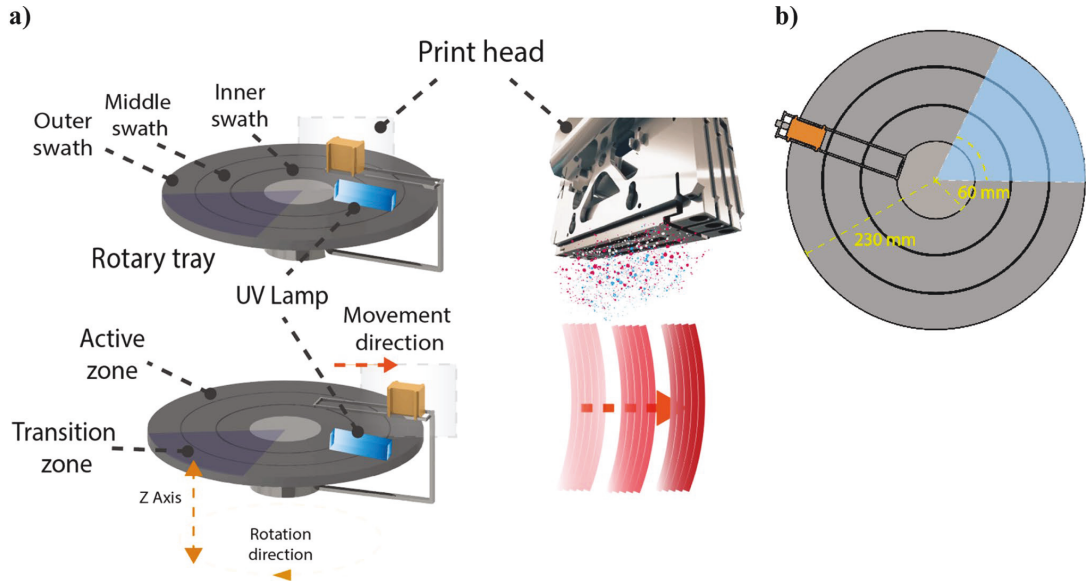


**Fig. 1** **a** Illustration of swathes and main zones of the rotary tray. **b** Top view of the swathes with the same width (60 mm) in a J55 PolyJet 3D printer. Samples were printed in a swath from the inner zone toward the outer area of the tray

to Pantone validated color matching system. It states that printed parts should have a wall thickness of at least 1-mm white background for optimal color reproduction. Since the defects and errors in observed CIEL*a*b* values for replicated samples were minimal in the trial experiments, one piece is studied under each experimental condition for the main investigation. In order to investigate the influence of each printing process parameter on the color quality, two sets of experiments have been conducted to reach the optimum condition using the minimum required samples. Levels for each of the experiments are shown in Table 1. In experiment 1, samples with a thickness of 1 mm in the colored layer were manufactured in different swaths. As part of experiment 2, samples with different thicknesses were 3D-printed in the middle swath of the rotating disk of the 3D printer. In both experiments, two different surface finishing options were selected between the white background and CMYK-colored layers. A total of 48 color samples were subjected to in-depth spectral analysis.

## 2.2 Measurements

A Konica Minolta CS-2000 tele-spectroradiometer (TSR) was used to determine the spectral radiance at the 3D-printed object surface in the 380–780 nm spectral range (Fig. 3). The physical sampling interval was 10 nm, whereas the optical resolution was 1 nm. Using 45:0° viewing geometry, the surface of the 3D-printed item was evaluated according to CIE Publication 15.2 [30]. Each series of measurements was calibrated with the white Spectralon patch (Barium sulfate coating). The obtained radiances have been averaged from measurements in the field of view of 0.2° on three-centric regions of the surfaces to overcome edge loss in measuring reflectance on semi-translucent materials. At least ten horizontally distrusted 3D-printed layers were present at each targeted location on the studied surface. Any site having odd coloration, external particles, or support materials was avoided.

Measurements were taken in a dark room to avoid errors caused by other light sources such as ambient lighting. Radiance spectra have been recorded considering noise reduction due to the possible stray lights in the darkroom of the measurement.

Calculations were performed using the computational color science toolbox in MATLAB 2021 [31]. For this purpose, CIEXYZ tristimulus values were calculated according to the CIE 2° color-matching functions, using the sample reflectance and under the D50 illuminant. CIEL*a*b*

**Table 1** Experiments and their levels

| Color | Finishing | Experiment 1 | | Experiment 2 | |
|---|---|---|---|---|---|
| | | Swath | Thickness (mm) | Swath | Thickness (mm) |
| Cyan | GoG and GoM[a] | Inn, mid, and out[b] | 1 | Mid | 0.2, 0.5, 1, and 2 |
| Magenta | GoG and GoM | Inn, mid, and out | 1 | Mid | 0.2, 0.5, 1, and 2 |
| Yellow | GoG and GoM | Inn, mid, and out | 1 | Mid | 0.2, 0.5, 1, and 2 |
| Black | GoG and GoM | Inn, mid, and out | 1 | Mid | 0.2, 0.5, 1, and 2 |

[a]GoG, glossy on glossy finish; GoM, glossy on matte finish

[b]Inn, inner (r-tray < 120 mm); Mid, middle (120 mm < r-tray < 180 mm); O, outer (180 mm < r-tray < 230 mm) swath

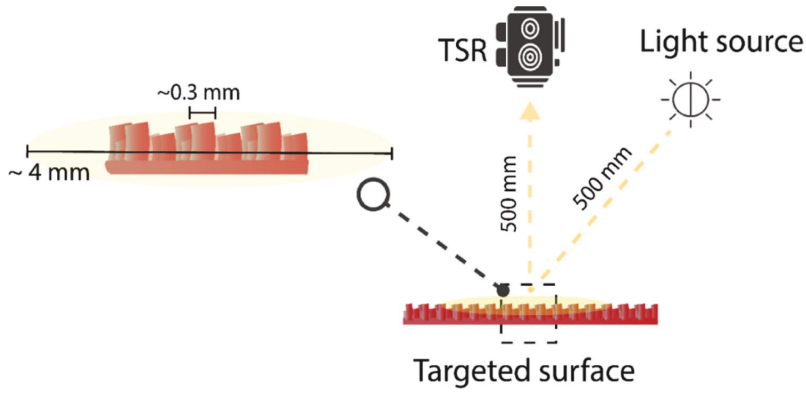


**Fig. 3** Schematic diagram of the measurement setup using a tele-spectroradiometer. The enlarged area represents the comparable size of the measurement area and the average width of the uppermost layers

coordinates were further calculated according to CIE1976 [30] and using the CIEXYZ tristimulus values in Eqs. 1–3.

$$L^* = 116\left(Y/Y_n\right)^{1/3} - 16 \tag{1}$$

$$a^* = 500\left[\left(X/X_n\right)^{1/3} - \left(Y/Y_n\right)^{1/3}\right] \tag{2}$$

$$b^* = 200\left[\left(Y/Y_n\right)^{1/3} - \left(Z/Z_n\right)^{1/3}\right] \tag{3}$$

where $X_n$, $Y_n$, and $Z_n$ are the tristimulus values of a specified white achromatic stimulus (Spectralon).

CIEDE2000 [32] colorimetric differences as given in Eq. 4 was calculated between the object printed on the three swaths. CIEL*a*b* values obtained from the objects with 1-mm thickness printed in the middle swath were used as reference measurements when calculating the CIEDE2000 difference.

$$\text{CIEDE2000} = \sqrt{\left(\frac{\Delta L^*}{k_L S_L}\right)^2 + \left(\frac{\Delta C^*}{k_C S_C}\right)^2 + \left(\frac{\Delta h^*}{k_h S_h}\right)^2 + R_T f(\Delta C^* \Delta h^*)} \tag{4}$$

In Eq. 4, L*, C*, and h* refer to lightness, chroma (the distance out from the neutral axis—saturation), and hue as defined in CIE15.2 [30]. The constant values of $k_L$ (lightness), $k_C$ (chroma), and $k_h$ (hue) are usually unity [33]. Other parameters refer to the hue rotation term ($R_T$) and the compensation for lightness ($S_L$), chroma ($S_C$), and hue ($S_h$).

A total of nine printer objects, including three pieces printed on each swath, have been scanned vertically and horizontally using a coordinate measuring machine (CMM) model Zeiss DuraMax. The step width was set at 10 µm, a probe radius of 1.5 mm was chosen, and the machine was accurate to 2.4 µm. A desktop 3D scanner (Autoscan Inspec, Shining 3D) was utilized in dark conditions. An 8-times rotation was made with the specimens mounted on a turntable every 45° until a 360° view was achieved. An object was scanned with an accuracy of ≤ 10 µm under a blue-light projector emitting structured-light patterns. The distorted dimensions are measured using two 5.0MP CCD cameras on the scanner. The registered point cloud is collected from multiple scans at various object orientations. All digitization was merged using UltraScan 2022 software, and a raw texture-based model in STL (stereolithography) format was created in MeshLab (v2022.02). The 3D coordinates of the object were compared with the CMM results. Following the CMM acquisition, the raw data was processed in Gwyddion (v2.59) to determine layer thickness and heights as well as the topography.

Holmberg et al. [34] examined the surface microstructure changes during machining processes based on the full width at half maximum (FWHM) analysis and optical microscopy study. We utilized the FWHM values to analyze the height distribution. Texture evaluation allows reconstructing of the profile of additive manufacturing and realizing data registration and appearance evaluation.

Surface features in AM technology are the presence of microscale repetitive layers in the surface texture of 3D-printed objects [35]. There are two approaches to the analysis of texture: structural (analytical), where primitives are analyzed, and syntactical (statistical), where statistics are used to determine the texture of the entire textural region [36]. Autocorrelation and Fourier analysis are the most common structural methods for the analysis of texture, while for statistical analysis, co-occurrence matrices or run-lengths are common methods. To evaluate the surface texture analytically, we used Fourier analysis.

The FFT (fast Fourier transform) method removes all high-frequency noise, revealing the actual signal [37]. Several authors have demonstrated that the power spectral density (PSD) of a contact area determines the morphology of its surface [38–40]. Accordingly, we developed an algorithm for evaluating the 3-D geometry of additive manufacturing surfaces. Our method transforms 3D texture into a 2D coarseness profile using 1D Gaussian filtering and FFT filter smoothing. The asymmetric profiles associated with shape have been subtracted from the repeated texture profiles using polynomial fitting tools in OriginPro v9.5 to remove the effects of the form on the texture results.

According to ISO 16610–31, the robust regression Gaussian filter calculates weights individually for a primary profile and a waviness profile using iterative algorithms. Using this filter, the mean line is strongly associated with the general trend of the surface profile with spike discontinuities such as deep valleys and high peaks and is unaffected by outliers. The FFT algorithm was implemented to remove high-frequency noises and reduce the waveforms to the absolute magnitude and phase data in a frequency domain. The power output versus frequency spectrum of the surface profiles was examined by FFT spectra of signals, where power is normalized as the space (time in standard notations)-integral squared amplitude (TISA) using the following equations:

$$P_{xx}\left(e^{j\omega}\right) = \sum_{m=-\infty}^{\infty} r_{xx}(m)e^{-j\omega m} \tag{5}$$

$$\text{TISA(Power)} = \frac{\Delta t\left(R_e{}^2 + I_m{}^2\right)}{n} \tag{6}$$

where $P_{xx}\left(e^{j\omega}\right)$ is the power density or spectrum (PSD), $r_{xx}(m)$ is the auto-correlation function of the input signal, $\Delta t$ is the sampling interval, $R_e$ and $I_m$ are the real and imaginary parts of the transform data, and n is the length of the input sequence. In order to mitigate leakage, the single rectangle window function is applied as follows:

$$N/\sum_{n=0}^{N-1} w(n)^2 \tag{7}$$

where $w(n) = 1$ for $0 \le n \le N-1$, and zero otherwise.

The statistical procedures were based on ISO/TS 23,031:2020 (E). Accordingly, it is possible to evaluate the color difference between reference and test spectra and the root-mean-square error between them using the root-mean-square error (RMSE) and the mean color difference from the mean (MCDM) [41]. The following are the definitions:

$$RMSE = \sqrt{\frac{1}{N}\sum_{i=1}^{N}(r_{r,i} - r_{t,i})^2} \tag{8}$$

$$MCDM = \frac{1}{N}\sum_{i=1}^{N}\Delta E(C_i, C_m) \tag{9}$$

where $r_r$ and $r_t$ are the references and test spectrum, N is the number of reflectance readings, and $C_i$ and $C_m$ are the coordinate colors of the ith measurements and the average reflectance of all measurements, respectively. The RMSE of each quantitative variable is obtained to perform the spectral analysis, comparing the spectra of the target surfaces.

Multivariate analysis of the studied parameters and the response variables were run using principal component analysis (PCA) and the listwise Spearman rank correlation coefficient (Spearman rho, also signified by rs) due to small sample sizes [42]. PCA is a robust way of reducing the dimensionality of data. The raw data is linearly transformed into a set of principal components, which show the most significant variations in the raw sensor data. The PCA method of estimating correlations is a multivariate extension of linear regression to matrices containing independent and dependent variables [43, 44]. Two sets of variables can be viewed as asymmetrical, as one batch is considered an independent variable such as printing parameters, and the other as a dependent variable. In this work, the matrix of appearance variables included measurements of color attributes including dL, dC, and dh.

Furthermore, Spearman rho was utilized to measure the relationship between the frequency of print variables and color attributes. It is a non-parametric measure for categorical data, which evaluates monotonic relationships of data that are not normally distributed regardless of linearity. Spearman rho of + 1 or − 1 refers to the case where each variable is a mathematically ideal monotone function of the other [42]. Statistical analyses were carried out using OriginPro v9.5.

## 3 Results and discussions

### 3.1 Texture evaluation

An optical image of a studied specimen and the corresponding STL model generated by the 3D scanner is shown in Fig. 4; a semicircle pattern can be observed in the corresponding surface texture image for the 3D-printed layers (Fig. 4c).

Using CMM data, Fig. 5 illustrates a closer look at additively manufactured layers and the results of an FFT examination applied to height maps (Z height). The strong peaks for averaged results in Fig. 5c confirm the periodic nature of the layers and the associated surface texture in the specimens studied. Arithmetic means of the periodic distance between layers can be obtained by calculating the average frequency of distances for the PSD peaks.

According to Fig. 5b, the obtained MJT surfaces were relatively smooth with a Z height of less than 15 µm. In addition, height distributions followed a normal distribution. There is a lack of understanding as to the mechanism by which texture affects color appearance on smooth surfaces in semi-translucent MJT materials. It has been suggested

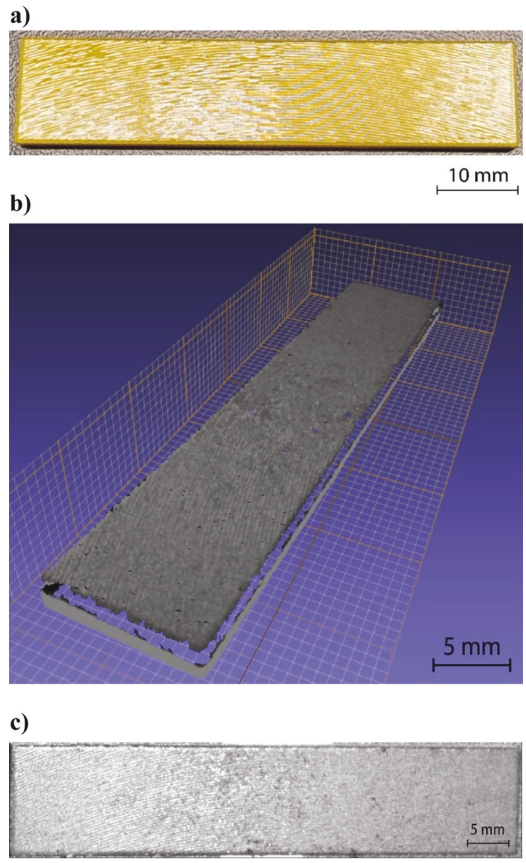


**Fig. 4** **a** 3D-printed samples for texture evaluation, **b** STL model generated from 3D scanning, **c** 2D texture-based model created from the point cloud

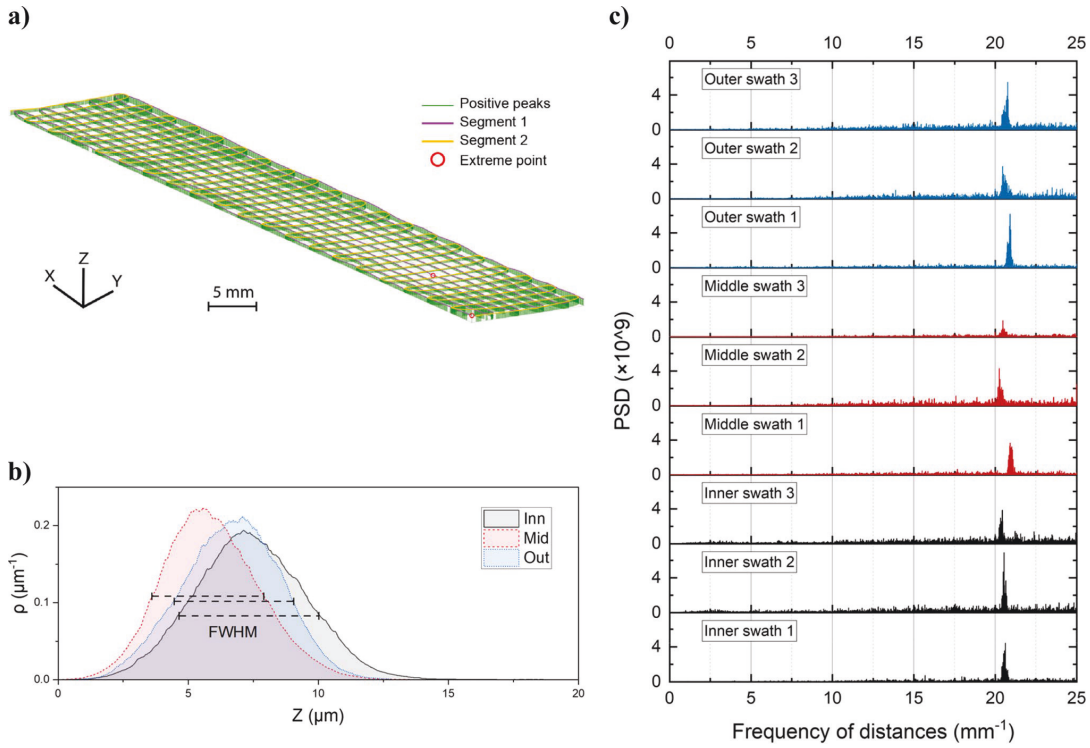


**Fig. 5** **a** Contour plot showing the scanning strategy (exaggerated *Z* profile), **b** Profile of *Z* height distribution, and **c** power spectral density (PSD) results along with the scanning profile

that the texture of the surface influences how light is scattered and how the color is measured as a result [45]. J. H. Bae et al. [46] reported as the visual texture rank increased, inkjet-printed samples were perceived as darker. Nevertheless, this effect was not consistent across colors. Accordingly, the texture of a surface can affect chromatic induction, which is essential for color constancy under full-field viewing conditions.

Table 2 lists the arithmetic mean height of asperities over vertical and horizontal scanning directions according to Fig. 5. CMM measurements show that the mean layer height and FWHM for separate locations on the build platform exhibit a meaningful correlation, where the minimum arithmetic means of layer height (5.69 μm) and FWHM (3.84 μm) belong to the middle swath. Table 2 also suggests that layers become increasingly thinner from 305 to 303 μm as the selected tray radius increases. The difference can be explained by the higher centrifugal force on the build platform in the outer area of the disk. By moving from the inner swath to the outer edge of the tray, the print head of a 3D printer may create a closer layer compared to previous layers.

### 3.2 Color measurement

The chromaticity diagrams in Fig. 6 represent the map of color space for the average of u′ and v′ values corresponding

**Table 2** Mean height of asperities over vertical scanning direction

| Swath | Mean layer distances (μm) | RMSE (μm) | Mean layer heights (μm) | RMSE (μm) | Mean FWHM (μm) | RMSE (μm) |
|---|---|---|---|---|---|---|
| Inner | 305.96 | 1.12 | 7.45 | 0.56 | 4.79 | 0.16 |
| Middle | 305.78 | 4.14 | 5.69 | 0.86 | 3.84 | 0.33 |
| Outer | 303.33 | 2.75 | 7.14 | 0.36 | 4.48 | 0.01 |

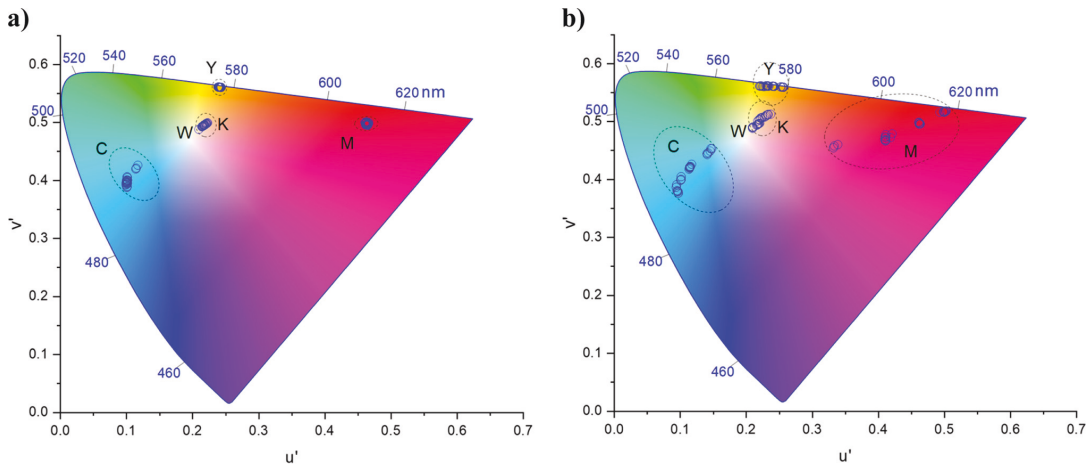


**Fig. 6** Hue stimuli in the CIE1976 $u'$, $v'$ chromaticity diagram for specimens manufactured at different **a** swathes and **b** thicknesses. The wavelengths between 420 and 680 nm are indicated in blue on the graph. C, cyan; M, magenta; Y, yellow; K, black; W, D50 white reference

to each specimen. CMYK points were closer on surfaces printed with different swathes than on objects with various thicknesses. It basically implies a higher color difference because of the thickness variation compared to swathes.

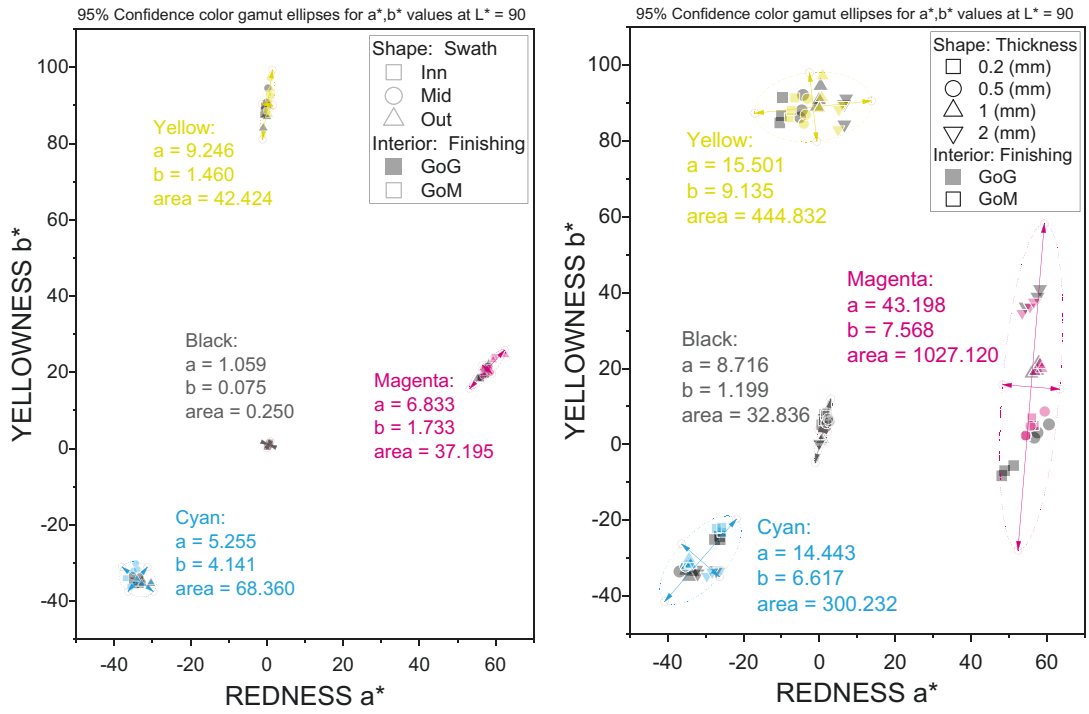


**Fig. 7** 95% confidence color gamut ellipses and yellowness versus redness for specimens related to **a** swath and **b** thickness experiments

The values of redness (a*) and yellowness (b*) at the same lightness (L*) also confirmed the same trend in the CIEL*a*b* color space. In Fig. 7, the 95% confidence color gamut ellipses suggest that magenta was significantly more sensitive to thickness than swath selection. Furthermore, thicker yellow and magenta objects resulted in greater b* and a* values, while the opposite held true for black and cyan objects. The color was more stable in the same lightness among the black samples despite varying printing conditions. For these samples, finishing played no significant role.

The spectral properties of surfaces and illumination also play an essential role in determining color. As a result, when evaluating color quality, it is necessary to consider both colorimetric and spectral measurements [47]. Figure 8 depicts how cyan and yellow colors shifted to lower spectral values for outer swathes than inner areas. In contrast, magenta exhibited the opposite behavior, and black samples were almost immune to spectral shift. On the other hand, lower thicknesses of the CMYK layers (Fig. 9) resulted in higher spectral reflectance for all samples, which indicated that the increased thickness accounted for the lightness reduction and lower spectral reflectance regardless of surface color.

In general, more significant MCDM color differences were observed for the thickness experiment compared to the swath study (Fig. 10), as observed from chromaticity diagrams in Fig. 6. All colors studied, except black, showed the lowest CIEDE2000 values when the middle swath was selected compared to the inner area. CIEDE2000 between central and outer,

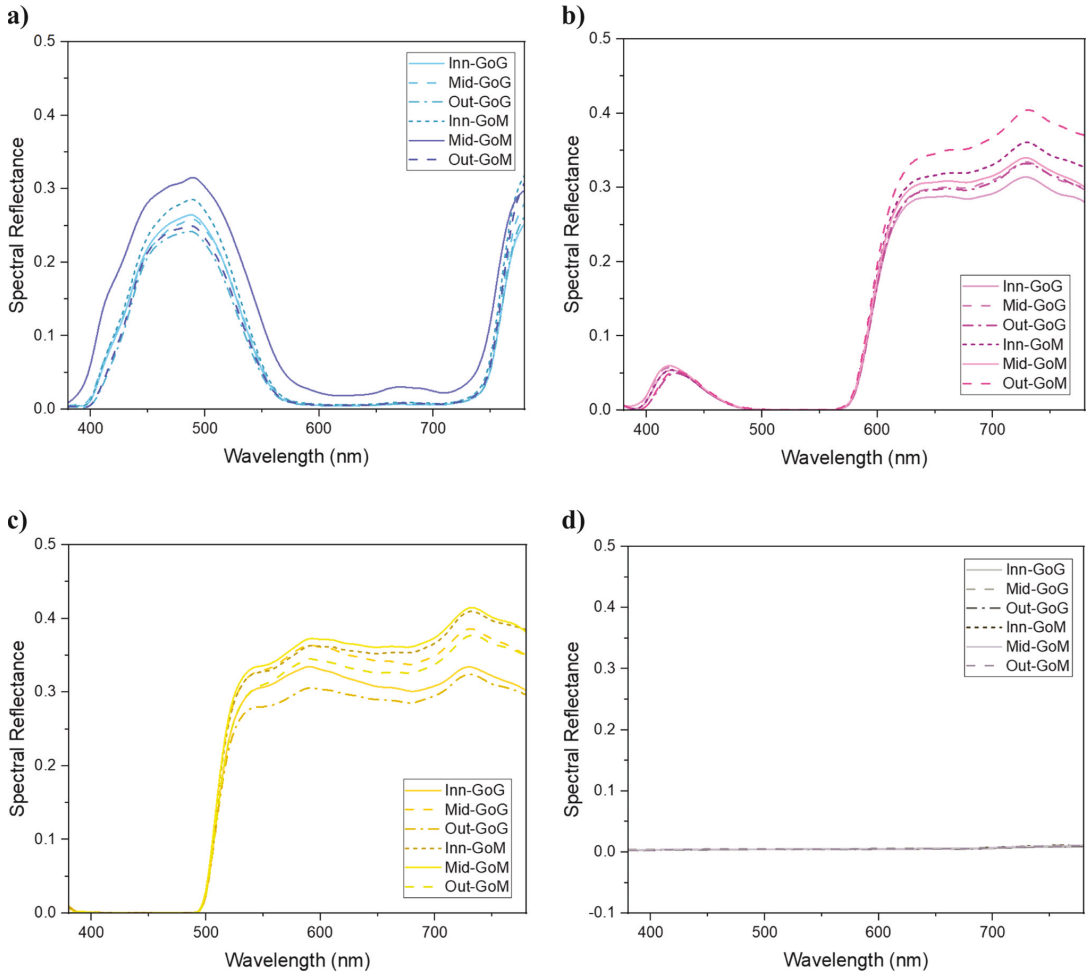


**Fig. 8** Reflectance of **a** cyan, **b** magenta, **c** yellow, and **d** black specimens 3D-printed at different swathes on the build platform

however, produced a different response. Higher layer heights may be compromised by the closer layer distances in the external zones of the tray. According to Table 2, this result aligns with the texture measurements and higher lightness variation due to higher layer heights. It allows parameterization of the swath selection to produce the lowest color differences in the middle swath compared to the other areas of the build platform (Fig. 10a). The transfer distance for light over the 3D-printed structures might be decreased due to a more evenly distributed texture with lower layer heights for this swath.

According to CIEDE2000 for color matching in paper-based printing [48, 49], a color difference of 1 is barely perceptible to the average human. An experienced observer notices CIDE2000 between 1 and 2. Color difference from 2 to 3.5 is also noticeable to an inexperienced observer. However, 5 < CIDE2000 is not an acceptable match for commercial printing presses. The calculated color differences in Fig. 10a and b indicate that CIDE2000 ranges were less than 5. Yellow samples and surfaces with the GoM finish of cyan parts had the most significant color difference visible to inexperienced observers. The appearance difference between black and magenta colors was challenging to distinguish due to their color. Considering commercial purposes, all results were acceptable when switching between segments on the tray. Since human vision is more sensitive to color differences when two colors touch [50], mixing CMYK colors may result in noticeable color differences.

As for the variations in the thickness of colored layers, on the other hand, rather than yellow at the lower thickness and black at the higher thickness, the rest were in assorted

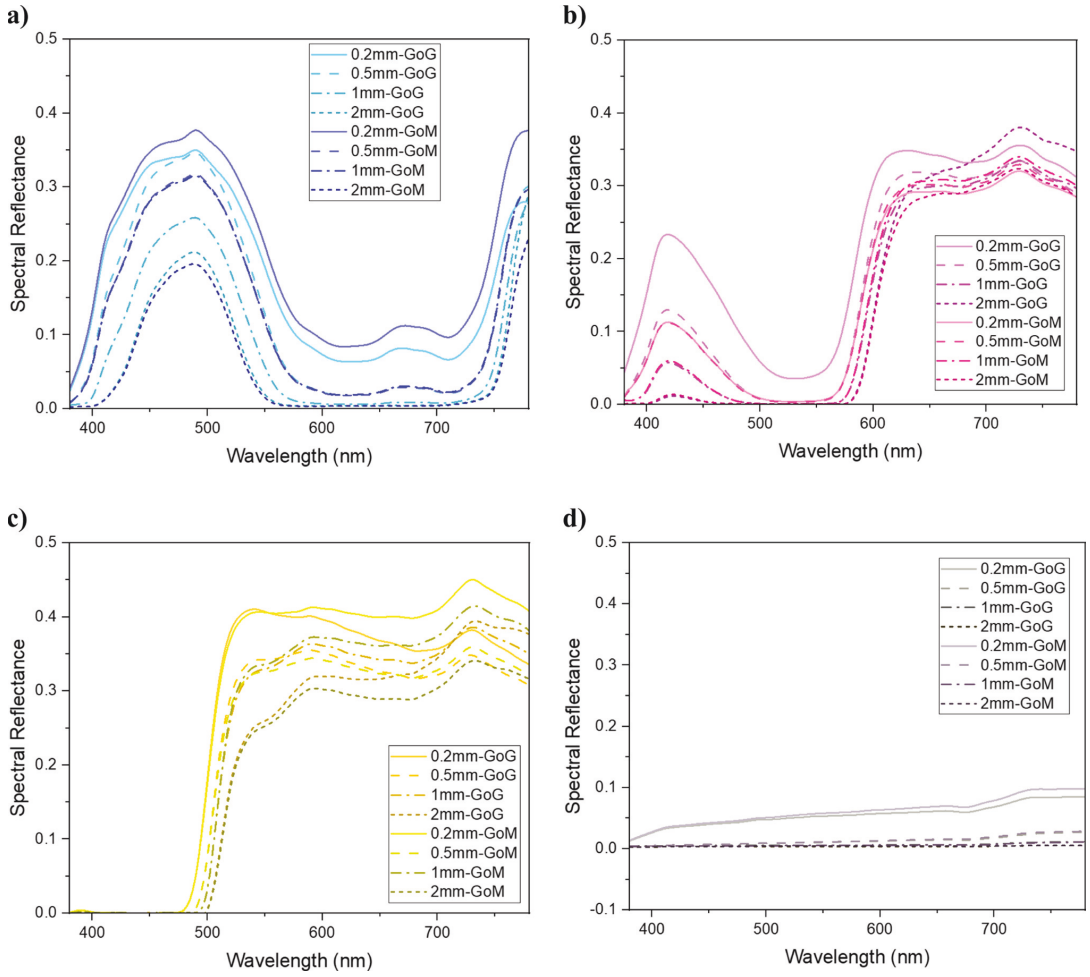


**Fig. 9** Reflectance spectra of **a** cyan, **b** magenta, **c** yellow, and **d** black specimens 3D-printed at different thicknesses

colors and were not acceptable for commercial color reproduction. Compared to 1-mm thick colors, 0.5-mm thickness resulted in a more negligible color difference than 2- and 0.2-mm thickness (Fig. 10c). Similar to the swath study, the CIEDE2000 values were lower for black-colored surfaces. Choosing the GoM finish for cyan, magenta, and yellow colors increased the color difference in the swath experiment (Fig. 10b). However, it did not contribute considerably to thickness evaluation (Fig. 10d).

Figure 11 signifies the relationship between the two main color attributes affected by swath selection. The Euclidean distances revealed that as the radius of the layers on the substrates increased, the variation in lightness and hue values was not linear. Because the absolute difference in lightness and hue between the inner and outer areas of the build platform was minimal when the difference between the mid and inn and out swaths was considered. Further analysis from Table 2 revealed that texture results were able to differentiate the color attributes affected by layers. Consequently, since the layer height of the middle swath differs the most from other swathes, lightness and chroma are more variable, with a more substantial influence on lightness.

Figure 12 displays the MCDM color difference versus RMSE values. In the swath experiment, black was the color with the slightest variation and produced the most consistent results. Cyan had a more pronounced color difference than red and yellow, but a lower RMSE made it less unpredictable to swath changes. Considering thickness changes, both cyan and black color reproduction had

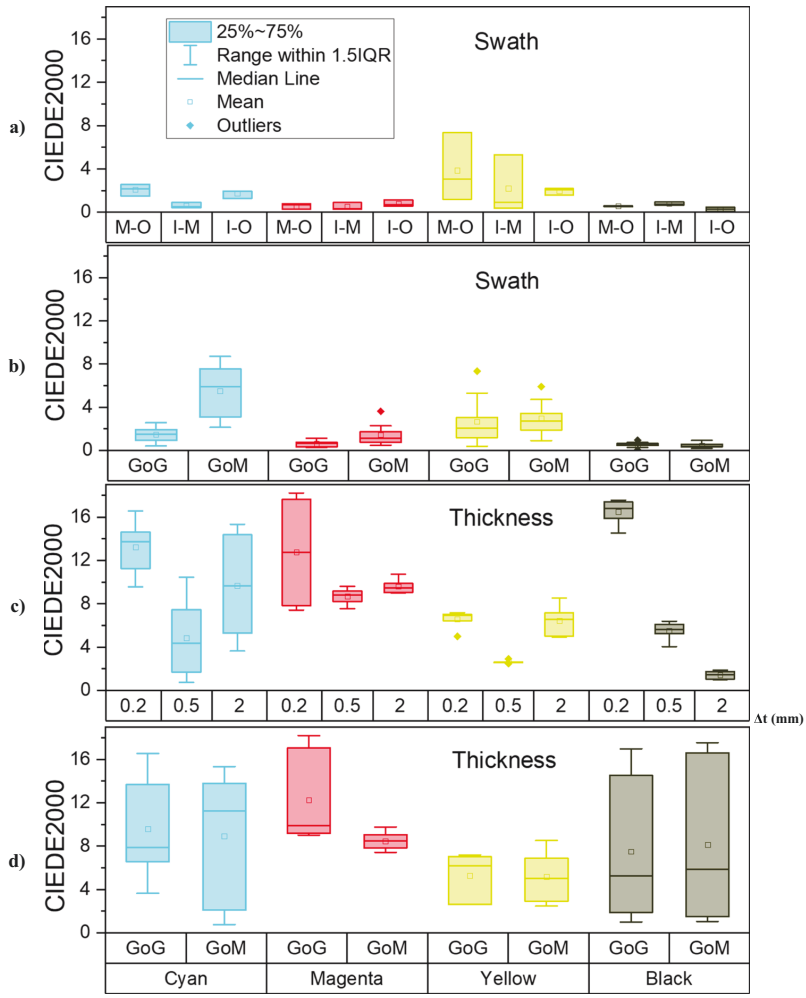


**Fig. 10** CIEDE2000 color difference due to manufacturing parameters for swath and thickness experiments. The influence of **a** choosing different swathes using GoG finish, **b** finishing condition for different swathes, **c** F*t*, and **d** finishing condition for different thicknesses on CIEDE2000. Δ*t*, color layer thickness compared to 1 mm recommended by the manufacturer of the 3D printer; IQR, interquartile; I-M, inner swath versus middle swath; I-O, inner swath versus outer swath; M–O, middle swath versus outer swath

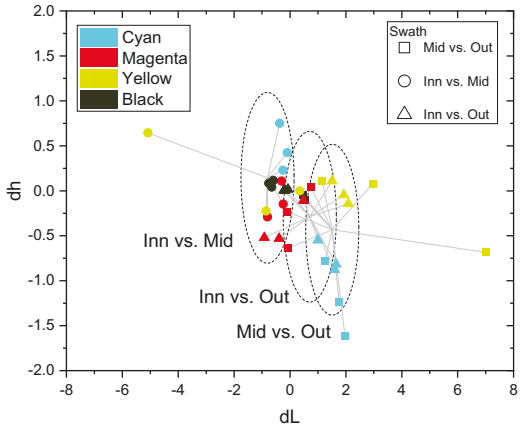


**Fig. 11** The Euclidean distances with 0.95 confidence area for the swath experiment

significantly higher MCDM and RMSE. The reproducibility of yellow appeared to be more sensitive to swath selection than thickness variation. However, color differences for all CMYK colors were nearly double due to colored layer thickness differences.

### 3.3 Multivariate statistical analysis

The PCA correlation type results were presented as ranking diagrams, which used figurative symbols. The direction of maximum change is indicated by arrows on print variables and color attributes. A high correlation is observed between the variables when placed in close or the same direction, and low correlations when placed in the opposite direction. The two lines at a 90°-angle indicate no correlation between the variables. Table 3 implies that the cumulative inertia for the first and the second principal components (PC1 and PC2) reached 91.03% for swath and 83.13% for thickness experiments. Moreover, PC1 and PC2 represented eigenvalues greater than 1. Therefore, based on the Kaiser criterion, two PCs would be appropriate enough to explain the correlation among data in PCA.

The loading plots (Fig. 13) demonstrate lightness had a robust positive effect on PC1 and almost neutral on PC2 for swath evaluation. In contrast, hue had a meaningful negative impact on PC1 and a considerable positive impact on PC2. In contrast, both lightness and hue acted reversely for PC1 and PC2 concerning the variation in thickness. Chroma

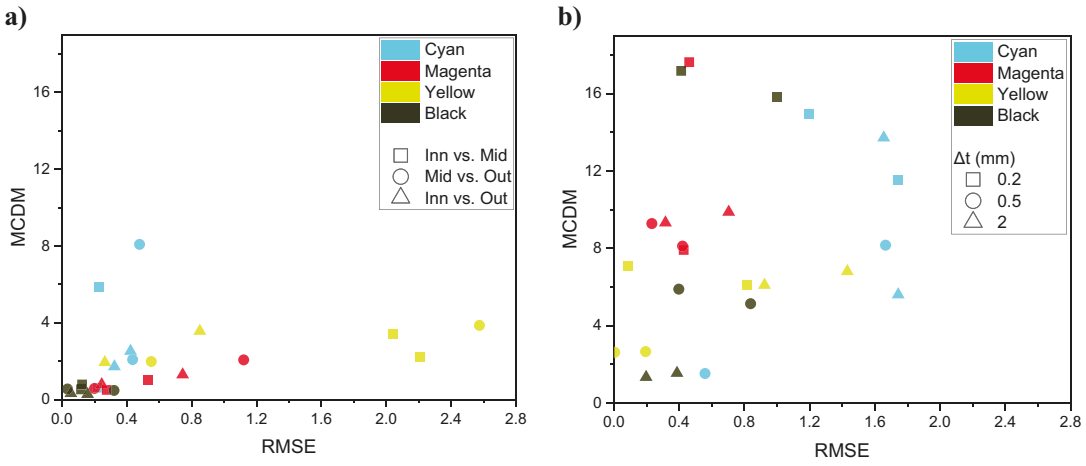


**Fig. 12** RMSE versus MCDM for **a** swath and **b** thickness experiments

**Table 3** Principal components ranking according to their cumulative roles in PCA

| PC ranking | Experiment 1: swath | | | Experiment 2: thickness | | |
|---|---|---|---|---|---|---|
| | Eigenvalue | Percentage of variance (%) | Cumulative (%) | Eigenvalue | Percentage of variance (%) | Cumulative (%) |
| 1 | 1.67 | 55.82 | 55.82 | 1.36 | 45.41 | 45.41 |
| 2 | 1.05 | 35.21 | 91.03 | 1.13 | 37.72 | 83.13 |
| 3 | 0.26 | 8.96 | 100 | 0.50 | 16.86 | 100 |

positively influenced both PC1 and PC2 in both experiments. Accordingly, variations in the printing parameters have affected variations in tristimulus color attributes.

Spearman correlation coefficient was used to establish the significance of each manufacturing condition (Fig. 14). A correlation coefficient greater than 0.50 and 0.70 is considered moderate and robust correlations, respectively if P values are less than 0.05. P values less than 0.01 and Spearman rho higher than 0.60 are generally valid co-occurrences [43]. Accordingly, the correlation coefficient with rs = 0.87 between thickness alteration and dL is strong (P < 0.001). Based on the rank correlation, swath and thickness selection had a more considerable effect on lightness and chroma than color, and the influence of finishing between colored and white layers was negligible. While dL had the greatest impact on color appearance, the effect varied depending on the ink materials specified. Following texture evaluation, results indicate that the variation in swath and thickness, influencing the surface texture and geometries, significantly alters the appearance of color due to the lightness alteration.

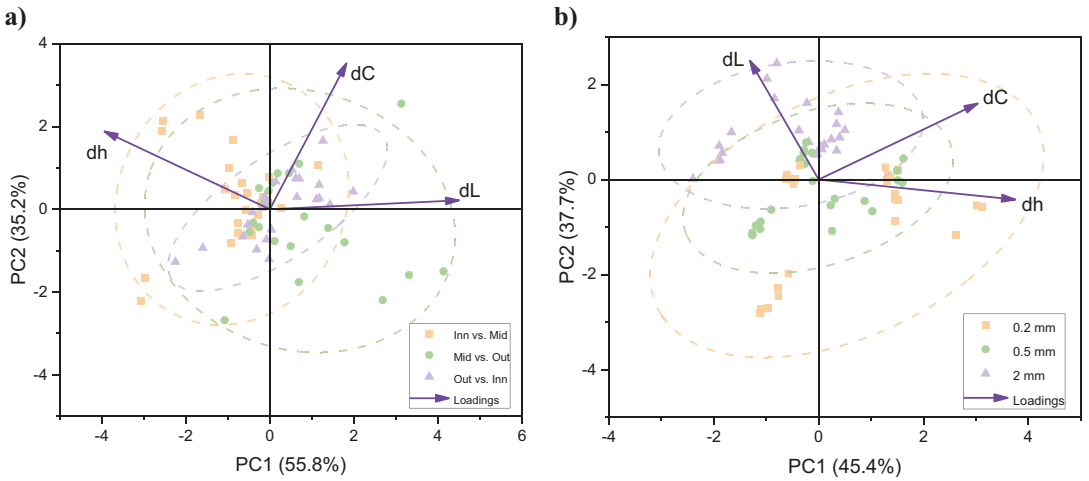


**Fig. 13** Principal components analysis (PCA) ordination diagram (biplot) for **a** swath and **b** thickness experiments. Denoted points show sample scores, 95% confidence ellipses show for the same-colored points, and loading vectors represent explanatory variables (3D printing parameters) and response variables (color attributes), respectively. Horizontal and vertical axes denote the first and second principal components (PC1 and PC2). Correlations between variables are represented by angles between vectors, where the smaller the angle, the greater the correlation. Vectors pointing in the same direction represent positively correlated variables, and vice versa

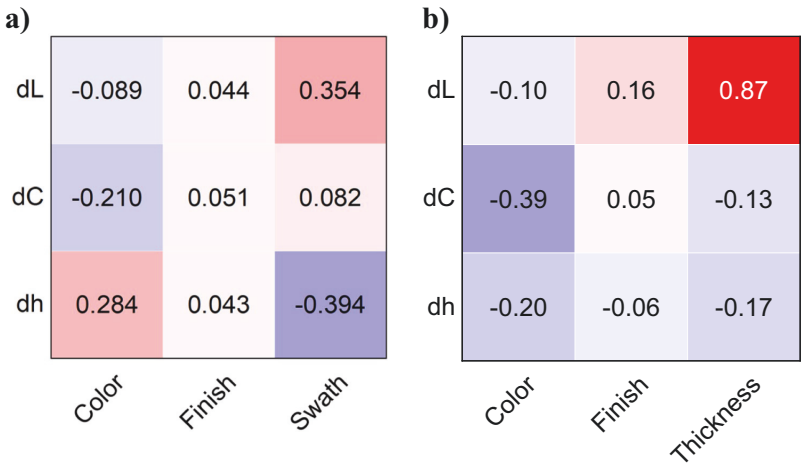


**Fig. 14** The Spearman correlation coefficient results for **a** swath and **b** thickness experiments

## 4 Conclusions

This study investigated relationships between observed color and four PolyJet control parameters: specified color, design thickness, swath location on the build platform, and finish type between colored and substrate layers. We studied the texture and surface layers of samples 3D-printed at separate places on the build platform to determine the effect of the rotary tray on color. Triplets of chromaticity coordinates or standard color values are used to indicate the color of a particular object. The following conclusions were drawn from this study:

The CMM measurement showed that manufacturing in the middle zones resulted in more low-height asperities. Based on the obtained power spectral density (PSD) versus the frequency of distances, the surface asperities could be assumed to be periodic. Therefore, the height distribution was representative of the heights of repeated layers. These results were observed by scanned 3D models of the surface. As a result, the surface layers in the middle of the rotary build platform were thinner.

PCA and listwise correlation analysis correlated the influence of lightness on the higher color difference for thickness experiments. We used multivariate analysis to determine the optimal conditions for color reproduction using a PolyJet 3D printer. While the influence of finishing between colored and white layers was negligible, alteration of swath or thickness, which influenced surface texture and physical geometry, greatly influenced variation in lightness and hue. The color appearance was more sensitive to thickness than swath selection in this regard, which was directly affected by lightness. This, however, was contingent on the ink materials specified. In the swath experiment, the yellow color and glossy colored layer printed on matte white substrate finishing led to a greater color difference. Nevertheless, it was less sensitive to thickness variation than cyan, magenta, and black materials.

Both experiments indicate the importance of adjusting the location on the build platform and thickness during pre-processing. Shorter radial printing generally yields less expensive and faster 3D printing. However, it does not necessarily result in more accurate color reproduction. Printing on different zones of a rotary build platform may also affect the surface roughness, gloss, and translucency. The switching of swathes did not fail samples for industrial color matching. Still, a thickness variation of as small as 0.5 mm could cause most specimens to go above 5 on the CIEDE2000 scale, which resulted in an unnatural appearance due to variation in color reproduction.

Based on the selected 3D printing parameters, color differences could be discernible by an inexperienced observer for the majority of samples. However, color reproduction utilizing rotary disks in PolyJet printers can meet the criterion of color quality in everyday contexts with various illuminations. Combined with our findings, results indicated that the MJT objects had all the relevant visual characteristics, including color, gloss, translucency, shape, shading, and texture, that stimulate the visual representation sufficiently to induce a color difference. As a result, other appearance attributes also should be considered when evaluating the total appearance of parts manufactured by rotational material jetting.

**Author contribution** All authors contributed to the study's conception and design. Material preparation, data collection, and analysis were performed by Ali Payami Golhin. The first draft of the manuscript was written by Ali Payami Golhin, and all authors commented on previous versions of the manuscript. All authors read and approved the final manuscript.

**Funding** Open access funding provided by NTNU Norwegian University of Science and Technology (incl St. Olavs Hospital - Trondheim University Hospital) The funding received on this project was from the ApPEARS-ITN project funded by the European Union's H2020 research and innovation program under the Marie Skłodowska-Curie grant agreement No. 814158.

**Data availability** Data are available at Payami Golhin, Ali, Suneel Sole, Aditya, and Strandlie, Are (2022). Datasets for the submitted paper "Color appearance in rotational material jetting" (version 1) [data set]. Zenodo. https://doi.org/10.5281/zenodo.6640295

**Code availability** Color toolbox is available at MATLAB Central File Exchange, visit https://se.mathworks.com/matlabcentral/fileexchange/40640-computational-color-science-using-matlab-2e. Other codes are custom-made, and they cannot be shared as they are proprietary.

## Declarations

**Ethics approval** Not applicable.

**Consent to participate** Not applicable.

**Consent for publication** Consent to publication has been received from all co-authors before the work is submitted.

**Conflict of interest** The authors declare no competing interests.

## References


1. Vidakis N, Petousis M, Michailidis N et al (2022) High-performance medical-grade resin radically reinforced with cellulose nanofibers for 3D printing. J Mech Behav Biomed Mater 134:105408. https://doi.org/10.1016/j.jmbbm.2022.105408
2. Aslani KE, Korlos A, Kechagias JD et al (2020) Impact of process parameters on dimensional accuracy of PolyJet 3D printed parts using grey Taguchi method. MATEC Web of Conferences. EDP Sci. https://doi.org/10.1051/matecconf/202031801015
3. Aslani KE, Vakouftsi F, Kechagias JD et al (2019) Surface roughness optimization of poly-jet 3d printing using grey Taguchi method. International Conference on Control, Artificial Intelligence, Robotics & Optimization (ICCAIRO). https://doi.org/10.1109/ICCAIRO47923.2019.00041
4. Li Y, Linke BS, Voet H et al (2017) Cost, sustainability and surface roughness quality—a comprehensive analysis of products made with personal 3D printers. CIRP J Manuf Sci Technol 16:1–11. https://doi.org/10.1016/j.cirpj.2016.10.001
5. Fountas NA, Kitsakis K, Aslani K-E et al (2021) An experimental investigation of surface roughness in 3D-printed PLA items using design of experiments. Proc Inst Mech Eng J J Eng Tribol 236:1979–1984. https://doi.org/10.1177/13506501211059306
6. Zhou Q, Jacobson A (2016) Thingi10k: a dataset of 10,000 3d-printing models, arXiv preprint arXiv:1605.04797. 1–8. https://doi.org/10.48550/arXiv.1605.04797
7. Emery KJ, Parthasarathy MK, Joyce DS et al (2021) Color perception and compensation in color deficiencies assessed with hue scaling. Vis Res 183:1–15. https://doi.org/10.1016/j.visres.2021.01.006
8. Babaei V, Vidimče K, Foshey M et al (2017) Color contoning for 3D printing. ACM Trans Graph 36:1–15. https://doi.org/10.1145/3072959.3073605
9. Yuan J, Chen G, Li H et al (2021) Accurate and computational: a review of color reproduction in full-color 3D printing. 209:1–17. https://doi.org/10.1016/j.matdes.2021.109943
10. Cheng YL, Huang KC (2020) Preparation and characterization of color photocurable resins for full-color material jetting additive manufacturing. Polymers (Basel) 12:650. https://doi.org/10.3390/polym12030650
11. Wei X, Zou N, Zeng L et al (2022) PolyJet 3D printing: predicting color by multilayer perceptron neural network. Ann 3D Print Med 5:1–7. https://doi.org/10.1016/j.stlm.2022.100049
12. Stratasys (2018) PolyJet materials and uses: tips and tricks. https://grabcad.com/tutorials/polyjet-materials-and-uses-tips-and-tricks. Accessed 04 May 2022
13. Payami Golhin A, Strandlie A, John Green P (2021) The influence of wedge angle, feedstock color, and infill density on the color difference of FDM objects. J Imaging Sci Technol 65:1–15. https://doi.org/10.2352/J.ImagingSci.Technol.2021.65.5.050408
14. Spina R (2019) Performance analysis of colored PLA products with a fused filament fabrication process. Polymers (Basel) 11:1–16. https://doi.org/10.3390/polym11121984
15. Boulaala M, Elmessaoudi D, Buj-Corral I et al (2020) Towards design of mechanical part and electronic control of multi-material/multicolor fused deposition modeling 3D printing. Int J Adv Manuf Technol 110:45–55. https://doi.org/10.1007/s00170-020-05847-0
16. Wei X, Zeng L, Pei Z (2019) Experimental investigation of PolyJet 3D printing process: effects of finish type and material color on color appearance. ASME International Mechanical Engineering Congress and Exposition, Proceedings (IMECE). https://doi.org/10.1115/IMECE2019-11917
17. Zheng L, Li C, Yang S (2020) Analysis of color gamut in color 3D printing. In: Zhao P, Ye Z et al (eds) Lecture notes in electrical engineering. Springer, Singapore, pp 148–155. https://doi.org/10.1007/978-981-15-1864-5_21
18. Li C, Zheng L, Xiao Y (2020) Study on the influencing factors of color reproduction in color 3D printing. In: Zhao P, Ye Z et al (eds) Lecture notes in electrical engineering. Springer, Singapore, pp 156–163. https://doi.org/10.1007/978-981-15-1864-5_22
19. Arikan CA, Brunton A, Tanksale TM et al (2015) Color-managed 3D printing with highly translucent printing materials. Meas Model Reprod Mater Appear SPIE 2015. https://doi.org/10.1117/12.2083844
20. Elek O, Sumin D, Zhang R et al (2017) Scattering-aware texture reproduction for 3D printing. ACM Trans Graph 36:15. https://doi.org/10.1145/3130800.3130890
21. Brunton A, Arikan CA, Urban P (2015) Pushing the limits of 3D color printing: error diffusion with translucent materials. ACM Trans Graph 35:1–13. https://doi.org/10.1145/2832905
22. Brunton A, Arikan CA, Tanksale TM et al (2018) 3D printing spatially varying color and translucency. ACM Trans Graph 37:1–13. https://doi.org/10.1145/3197517.3201349
23. Wei X, Bhardwaj A, Zeng L et al (2021) Prediction and compensation of color deviation by response surface methodology for PolyJet 3d printing. J Manuf Mater Process 5(4):131. https://doi.org/10.3390/jmmp5040131
24. Kumar K, Kumar GS (2015) An experimental and theoretical investigation of surface roughness of poly-jet printed parts: this paper explains how local surface orientation affects surface roughness in a Poly-Jet process. Virtual Phys Prototyp 10:23–34. https://doi.org/10.1080/17452759.2014.999218
25. Gülcan O, Günaydın K, Çelik A (2022) Investigation on surface roughness of PolyJet-printed airfoil geometries for small UAV applications. Aerospace 9(2):82. https://doi.org/10.3390/aerospace9020082
26. Kim GD, Oh YT (2008) A benchmark study on rapid prototyping processes and machines: quantitative comparisons of mechanical properties, accuracy, roughness, speed, and material cost. Proc Inst Mech Eng B J Eng Manuf 222:201–215. https://doi.org/10.1243/09544054jem724
27. Zeng J, Deng H, Zhu Y et al (2021) Lenticular objects: 3D printed objects with lenticular lens surfaces that can change their appearance depending on the viewpoint. UIST 2021 - Proceedings of the 34th Annual ACM Symposium on User Interface Software and Technology. https://doi.org/10.1145/3472749.3474815
28. Elber G, Kim MS (2021) Synthesis of 3D jigsaw puzzles over freeform 2-manifolds. Comput Graph 102:339–348. https://doi.org/10.1016/j.cag.2021.10.014
29. Wang T, Si Y, Li N et al (2019) Bioinspired tip-guidance liquid jetting and droplet emission at a rotary disk via a surface energy gradient. ACS Nano 13:13100–13108. https://doi.org/10.1021/acsnano.9b05860
30. L'éclairage CID (2004) Colorimetry in CIE 015:2004. Commission Internationale de l'Éclairage. Vienna, Austria
31. Westland S, Ripamonti C, Cheung V (2012) Computational colour science using MATLAB. Wiley, West Sussex
32. Sharma G, Wu W, Dalal EN (2005) The CIEDE2000 color-difference formula: implementation notes, supplementary test data, and mathematical observations. Color Res Appl 30:21–30. https://doi.org/10.1002/col.20070
33. Klein GA, Meyrath T (2010) Industrial color physics. Springer, New York
34. Holmberg J, Berglund J, Wretland A et al (2019) Evaluation of surface integrity after high energy machining with EDM, laser beam machining and abrasive water jet machining of alloy 718. Int J Adv Manuf Technol 100:1575–1591. https://doi.org/10.1007/s00170-018-2697-z
35. Payami Golhin A (2021) Generation of micro-and nano-textured surfaces. European Commission. https://hdl.handle.net/11250/

2983515. Accessed 3 November 2022 https://doi.org/10.5281/zenodo.7293168
36. Hunt RWG, Pointer MR (2011) Measuring colour. Wiley, Chennai
37. Qiu T, Guo Y (2018) 10. Correlation estimation and power spectral density (PSD) estimation of random signals. In: Signal processing and data analysis. De Gruyter, pp 325–376. https://doi.org/10.1515/9783110465082-010
38. Barber J (2003) Bounds on the electrical resistance between contacting elastic rough bodies. Proc R Soc Lond A 459:53–66. https://doi.org/10.1098/rspa.2002.1038
39. Paggi M, Barber J (2011) Contact conductance of rough surfaces composed of modified RMD patches. Int J Heat Mass Transf 54:4664–4672. https://doi.org/10.1016/j.ijheatmasstransfer.2011.06.011
40. Yastrebov VA, Anciaux G, Molinari J-F (2015) From infinitesimal to full contact between rough surfaces: evolution of the contact area. Int J Solids Struct 52:83–102. https://doi.org/10.1016/j.ijsolstr.2014.09.019
41. ISO/TS 23031:2020(E) (2020) Graphic technology — assessment and validation of the performance of spectrocolorimeters and spectrodensitometers. International organization for standardization. Geneva, Switzerland. https://www.iso.org/standard/74361.html
42. Spearman C (1904) The proof and measurement of association between two things, In: Jenkins JJ, Paterson DG (eds) Studies in individual differences: the search for intelligence, Appleton-Century-Crofts, pp 45–58. https://doi.org/10.2307/1412159
43. Xia Y (2020) Chapter Eleven - Correlation and association analyses in microbiome study integrating multiomics in health and disease. In: Sun J (ed) Progress in molecular biology and translational science. Academic Press, pp 309–491. https://doi.org/10.1016/bs.pmbts.2020.04.003
44. Zuur AF, Ieno EN, Smith GM (2007) Principal component analysis and redundancy analysis. In: Analysing ecological data, 1st edn. Springer, New York, pp 193–224. https://doi.org/10.1007/978-0-387-45972-1_12
45. Olkkonen M, Hansen T, Gegenfurtner KR (2008) Color appearance of familiar objects: effects of object shape, texture, and illumination changes. J Vis 8:13–13. https://doi.org/10.1167/8.5.13
46. Bae JH, Hong KH, Lamar TM (2015) Effect of texture on color variation in inkjet-printed woven textiles. Color Res Appl 40:297–303
47. Sohaib A, Amano K, Xiao K et al (2018) Colour quality of facial prostheses in additive manufacturing. Int J Adv Manuf Technol 96:881–894. https://doi.org/10.1007/s00170-017-1480-x
48. Yan X, Yuan J, Chen G (2018) Applications analysis of paper-based color 3D printing in the map industry, In: Zhao P, Ye Z et al (eds) Lecture Notes in Electrical Engineering. Springer, Singapore, pp 377–383. https://doi.org/10.1007/978-981-10-7629-9_46
49. Cui M, Li X, Wu G et al (2019) Measurement and evaluation of the surface color of 3D paper product, In: Zhao P, Ye Z et al (eds) Lecture notes in electrical engineering. Springer, Singapore, pp 108–113. https://doi.org/10.1007/978-981-13-3663-8_16
50. Choudhury AKR (2014) Principles of colour and appearance measurement: object appearance, colour perception and instrumental measurement. Elsevier

## Paper III:

A. P. Golhin, R. Tonello, J. R. Frisvad, S. Grammatikos, A. Strandlie, Surface roughness of as-printed polymers: A comprehensive review. The International Journal of Advanced Manufacturing Technology, (2023), Accepted

# Surface roughness of as-printed polymers: A comprehensive review

Ali Payami Golhin [a,*] (0000-0002-7938-8604) ali.p.golhin@ntnu.no
Riccardo Tonello [b] (0000-0001-8098-3235) rict@dtu.dk
Jeppe Revall Frisvad [b] (0000-0002-0603-3669) jerf@dtu.dk
Sotirios Grammatikos [a] (0000-0003-1430-6089) sotirios.grammatikos@ntnu.no
Are Strandlie [a] (0000-0002-1431-8365) are.strandlie@ntnu.no

[a] ASEMlab - Laboratory of Advanced and Sustainable Engineering Materials, Department of Manufacturing and Civil Engineering, NTNU - Norwegian University of Science and Technology, Gjøvik, Norway
[b] Department of Applied Mathematics and Computer Science, DTU - Technical University of Denmark, Kgs. Lyngby, Denmark
[*] Corresponding author

**Abstract**

Surface roughness is gaining increasing recognition in the processing design methods of additive manufacturing (AM) due to its role in many critical applications. This impact extends not only to various AM product manufacturing but also to indirect applications, such as molding and casting. This review article discusses the role of processing on the surface roughness of AM-printed polymers with limited post-processing by summarizing recent advances. This review offers a benchmark for surface quality improvement of AM processes, considering the surface roughness of polymeric parts. For this purpose, it lists and analyzes the key processes and various printing parameters used to monitor and adjust surface roughness under given constraints. Four AM techniques for manufacturing polymeric parts are compared: fused filament fabrication (FFF), selective laser sintering (SLS), vat photopolymerization (VPP), and material jetting (MJT). A review and discussion of recent studies are presented, along with the most critical process parameters that affect surface roughness for the selected AM techniques. To assist in selecting the most appropriate method of 3D printing, comparable research summaries are presented. The outcome is a detailed survey of current techniques, process parameters, roughness ranges, and their applicability in achieving surface quality improvement in as-printed polymers.

**Keywords:** Additive manufacturing; 3D printing parameters; Polymer; Surface roughness; Surface quality

**List of Abbreviations**

3DP: 3D Printing
ABS: Acrylonitrile Butadiene Styrene
AM: Additive Manufacturing
ANN: Artificial Neural Networks
ANOM: Analysis of Means
ANOVA: Analysis of Variance
ASA: Acrylonitrile Styrene Acrylate
BJT: Binder Jetting
CAD: Computer-Aided Design
CAM: Computer-Aided Modeling
CB: Carbon Black
CLIP: Continuous Liquid Interface Production
CLSM: Confocal Laser Scanning Microscope
CMYK-W: Cyan, Magenta, Yellow, Black, and White
DfAM: Design for Additive Manufacturing
DIW: Direct-Ink-Writing
DLP: Digital (Direct) Light Processing
DM: Digital material
DMD: Digital Micromirror Device
DoE: Design of Experiment
DTAM: Digital Thread in Additive Manufacturing
ED: Energy Density
FDM: Fused Deposition Modeling
FEP: Fluorinated Ethylene Propylene
FFF: Fused Filament Fabrication
FPT: Fringe Projection Technique
FR: Flame Retardant
FV: Focus Variation
GF: Glass Fiber
GLM: Generalized Linear Model
HDDA: Hexanediol Diacrylate
HDPE: High-Density Polyethylene
HL: Hot Lithography
LCD: Light Crystal Display
LOM: Laminated Object Manufacturing
LW: Laser Writing
MCDM: Multi-Criteria Decision Making
MEX: Material Extrusion Additive Manufacturing
MJF: Multi Jet Fusion
MJP: MultiJet Printing
MJT: Material Jetting
MW: Mask-based Writing
PA: Polyamides
PAEK: Polyaryletherketone
PBF: Powder Bed Fusion
PBS: Polybutylene Succinate
PC: Polycarbonate
PCL: Polycaprolactone
PDMS: Polydimethylsiloxane
PE: Polyethylene
PEEK: Polyetheretherketone
PEI: Polyetherimide
PEKK: Polyetherketoneketone
PET: Polyethylene Terephthalate
PLA: Polylactic Acid
PMMA: Polymethyl Methacrylate
PP: Polypropylene
PPFT: Post-Production Finishing Techniques
PPP: Primary Processing Parameters
PPSF: Polyphenylsulfone
PRISMA-ScR: Preferred Reporting Items for Systematic Reviews and Meta-Analyses Extension for Scoping Reviews
PS: Polystyrene
PSO: Particle Swarm Optimization
PTFE: Polytetrafluoroethylene
PVC: Polyvinyl Chloride
QAs: Quality Attributes
RRP: Roughness Reduction Percentage
RSM: Response Surface Methodology
SEM: Scanning Electron Microscope
SHL: Sheet Lamination
SHS: Selective Heat Sintering
SLA: Stereolithography
SLS: Selective Laser Sintering
SOS: Symbiotic Organism Search
TPP: Two-photon Photopolymerization
TPU: Thermoplastic Polyurethane
UAV: Unmanned Aerial Vehicle
VPP: Vat Photopolymerization
XMT: X-ray Micro-computed Tomography

## 1. Introduction

Additive manufacturing (AM), often known as 3D printing, combines materials to fabricate products from 3D model data, typically in a layer-upon-layer process [1]. AM has continued its exponential growth in many applications because of its attributes, such as mass customization, waste minimization, and on-demand design revisions [2]. However, AM parts cannot precisely replicate 3D CAD models due to the inherent surface roughness and accuracy limitations of the AM process. In-process enhancing the quality of the surface in AM technology is presently one of the most significant challenges of advanced manufacturing. It is a critical element for compatibility with surface coatings, the fatigue resistance of the products, liquid trapping, and the presence of moving particles [3].

Recently, the influence of the primary processing parameters (PPP) on the quality assessment of 3D-printed (3DP) objects has received considerable attention from academia and industry. Mainly because optimizing these PPPs provides more fabrication competence based on mass customization, on-demand design revisions, and waste minimization. Enhancing the 3D model, material and process selection, and surface modification can satisfy the performance constraints of the 3DP parts, such as tooling [4], jewelry [5], sensors [6], performance improvement, production, personalization and customization, spare parts, maintenance, repair, art, design, and architecture [7]. Considering the growing applications of personal 3D printers (shortened form as “printer”) and the small-scale market for AM technologies, it is increasingly essential to thoroughly understand the surface morphology created by various 3DP methods. Not surprisingly, most post-processing machines are currently either unavailable or high-priced to most AM users.

Polymers have been the center of attention in fabricating 3D parts because of their cost, availability, ease of production, and appearance options, particularly in the case of entry-level 3DP machines [8, 9]. The Wohlers Report 2021 [10] reported 7.5% growth in AM industry. It shows almost half of AM service providers offer polymer 3D printing, and 29% provide polymers besides other materials, such as metals and ceramics. As a result, over 80% of the AM market is involved with polymeric materials. In addition, polymer powder consumption is mentioned as rising by 43.3% in 2021, overtaking photopolymers as the most commonly used additive manufacturing material. In total, the polymer 3DP market is expected to increase to $24 billion in 2024 and $55 billion in 2030 [11]. Since 2012, 14150 out of 54275 (26.1%) publications in the field of additive manufacturing applied to polymer-based techniques (data from Web of Science, 2023). As almost 80% of the AM market is dedicated to polymer-containing materials, this is still growing, and there is significant potential for future research and development of polymeric AM objects. The polymeric AM parts suffer from poor surface finish and geometric deviation. Among textural appearance attributes, surface roughness is a critical indicator for assessing the quality of a product and the manufacturing process. For many direct and indirect applications, the surface of the printed object must meet specific criteria and properties such as mechanical [12], physical [13], tribological [12], and other quality attributes (QAs) [14].

Surface roughness is a metric relating to the QAs of AM parts because of its impact on the aesthetic appearance and the integrity of the piece in terms of its ability to interface with other components. It influences not only the appearance but also the functional properties of a part [15].

In most circumstances, the finishing process is rarely used to modify the part dimensions except for reducing the surface roughness via sandblasting and polishing or for structural applications [16]. In some cases, various painting and coating methods are used to achieve the required surface finish. These practices are insufficient to form the printing process and must overcome several challenges. For instance, material accumulation in fused filament fabrication (FFF), as a material extrusion (MEX) AM process, occurs along the edges and inside the products, which cannot be resolved by painting or coating [17, 18]. To choose a process based on the specifications of a part, Gordon et al. [19] provided a decision tree as a framework. They suggested the appropriate design modifications considering the desired surface to account for the selected techniques.

Various kinds of polymers are primarily supplied for AM in the shape of filaments, pellets, resin, or powder [20]. Furthermore, composite polymers reinforced by fibers and particles offer a favorable combination for almost all the existing AM methods [20]. While there are many choices of available AM processes to 3D print polymers, the mechanisms of the different AM methods distinctly differ from one another. Polymers are sensitive to printing parameters, mainly changes in temperature. Hence, the printing process and material should be carefully considered according to the end-user applications [11]. Several review papers have previously discussed roughness in AM processes, including material extrusion [18, 21], vat photopolymerization [22, 23], material jetting [24, 25], and selective laser sintering [26, 27] techniques. However, the reviews have not yet observed a thorough study of methods and quality evaluation trends in AM polymer products.

The AM process for polymers presents different challenges in surface quality than conventional manufacturing. A uniform standard for evaluating the roughness and dimensional accuracy of 3D-printed objects does not exist at present. Studying the surface roughness issues and the various PPP techniques for improving surface quality is also lacking in the literature. The roughness of AM technologies differs considerably, as was reported in this study and in the studies that compared 3DP methods [3, 16, 28].

This study focuses on recent advances in investigating the roughness of 3D-printed surfaces. It describes the primary AM processes for polymers and the corresponding PPP in the pre-processing and printing steps. The next section provides an overview of the AM processes for polymers and the research methodology. This is followed by an explanation of roughness measurements and metrics in the next section. For each of the AM methods studied, including FFF, selective laser sintering (SLS), vat photopolymerization (VPP), and material jetting (MJT), the main process parameters as well as surface roughness studies have been presented in separate sections. Furthermore, a discussion on the issues surrounding the setting up of polymer key AM processes. In another section, studies on several AM methodologies and their results were

compared. This review study concludes with a summary, as well as a discussion of future trends and capabilities in the later sections.

## 2. Overview

### 2.1. AM processes for polymers

This work defines AM techniques by ISO 52900 – 2021 [29] and their generally accepted terms. A wide range of advanced manufacturing techniques is available, from the nanoscale to the macroscale. Part size is primarily determined by the working volume afforded by the system of motion of the machine. This literature review is focused on manufacturing at the meso- and micro-scales, where surface roughness can significantly affect the visible quality of parts [30]. Table 1 lists relative characteristics overview of AM techniques for polymers and their most relevant AM applications, including prototypes, medical devices, and precision mechanisms.

In many applications, AM is still in its infancy and requires post-production finishing techniques (PPFTs), which include post-processing and surface finishing [17]. The process can either be used as the primary manufacturing process or as part of a chain of manufacturing processes. Fig. 1 classifies finishing as a critical step and quality assurance information flow in a digital thread in additive manufacturing (DTAM). A series of pre- and/or post-processing is available to alter the surface and significantly enhance the appearance of AM parts. However, some of these methods are limited in changing the surface morphology of complex shapes inexpensively and reliably over time [31]. The following sections will provide a detailed description of AM key processes.

**Table 1** Characteristics overview of polymer AM categories. Data extracted from references [9, 32].

| Process category* | Key process | Basic AM principle | Material feedstock and key materials | Remarks | Applications |
|---|---|---|---|---|---|
| Material Extrusion | FDM / FFF, DIW | Extrusion of melted or liquid material through a nozzle | Thermoplastic filament (PLA, ABS, PEI, TPU, PETG, PC, ASA, HiPS), Ink | Low build speed<br>Low build cost<br>High surface roughness<br>Poor surface finish<br>Full-color and multi-material available<br>Relatively high mechanical properties<br>Can build fully functional parts<br>Feasible and accessible<br>Vertical anisotropy<br>Generally low resolution<br>Typical part size constraint: ~0.01-10 m<br>Smallest feature size: ~0.2-10 mm (~2×path width)<br>*XY* resolution: ~100 µm (FFF) and ~1-100 µm (DIW)<br>Part tolerance: ±0.5 mm | Electrical housings/enclosures, prototypes, jigs and fixtures, investment casting patterns, solid monolithic parts, scaffolds, biologically compatible tissue implants, tailored composite materials |
| Material Jetting | MJ PolyJet, MJP | Reactive curing/fused agent with energy | Photopolymer and thermoset resins (acrylates, PMMA) | Relatively high build speed<br>Medium build cost<br>Low surface roughness<br>Good surface finish<br>Full-color and multi-material available<br>Developed for visual appearance<br>Medium mechanical properties<br>Low waste<br>Limited to certain resins<br>High dimensional accuracy<br>Typical part size constraints: ~0.01-1 m<br>Smallest feature size: ~100-500 µm (*XY*) and 10 µm (*Z*)<br>High resolution: ~10-25 µm<br>Minimum part tolerance: ±0.1 mm (depending on part size) | Full-color product prototypes, injection mold-like prototypes, low-run injection molds, medical models |

| | | | | | |
|---|---|---|---|---|---|
| Powder bed fusion | SLS<br>MJF | Selective fusion of material in a powder bed | Thermoplastic powder bed (PA6, PA11, PA12, PEEK) | Relatively low build speed<br>Large build volume<br>High build cost and energy consumption<br>Rough surface roughness with grainy surface texture<br>High mechanical and chemical properties<br>Complex geometries<br>Self-supporting 3D Printing<br>Less anisotropy<br>Typical part size constraint: ~0.005-1 m<br>Smallest feature size: ~0.5-1 mm<br>*XY* resolution: ~100 nm -100 µm<br>Minimum part tolerance: ±0.2 mm (depending on part size) | Functional polymer parts, complex ducting (hollow designs), low-run part production |
| Binder Jetting | BJT | Reactive curing with a binding agent | Liquid binding agent Powder bed (metals, sand, ceramics, and polymer) | Relatively high build speed<br>Large build volume<br>Relatively high build cost<br>Rough and grainy surface roughness<br>Relatively low mechanical properties<br>Shaping process at room temperature and atmosphere<br>Self-supporting 3D Printing<br>Multi-step process: PPFTs are necessary<br>High surface roughness and low dimensional accuracy<br>Typical part size constraints: ~5-50 mm<br>Smallest feature size: ~50-120 µm<br>Typical resolution: ~100 µm<br>Mainly dedicated to ceramics and metals, but recently developed for printing thermoplastic polymers and polyamides | Full-color models, sacrificial models for sand casting |
| Vat Photopolymerization | SLA, DLP, CLIP | Light reactive photopolymer curing | Photopolymer resin (acrylates and epoxides; standard, castable, transparent, high temperature) | Moderate build speed<br>Relatively high build cost<br>Low surface roughness<br>Good surface finish and accurate dimensions<br>Developed for aesthetic purposes and biocompatible parts<br>Relatively low mechanical properties and shelf life<br>Large parts<br>Limited to photopolymers<br>Post-processing and post-curing are necessary<br>Typical part size constraints: ~0.01-1 mm (Ultra-precision systems), ~5-300 mm (Inverted systems), up to ~1000 mm (Upright systems)<br>Smallest feature size: ~0.03-0.75 mm<br>High resolution: ~0.1-100 µm<br>Part tolerance: ±0.1 mm and less | Injection mold-like, polymer prototypes, jewelry (investment casting), dental applications, hearing aids |
| Sheet Lamination | UAM, LOM | Fusion of stacked sheets | PVC sheet | Relatively high build speed<br>Medium build cost<br>High surface roughness<br>Full-color and multi-material available<br>Relatively high mechanical properties<br>Typical minimum part size constraints: ~ 500 mm<br>Smallest feature size: ~ 0.07-0.2 mm<br>Typical resolution: ~200-300 µm | Composite parts |

* According to ISO/ASTM 52900 standard

Thermoplastics and their composites are the primary polymer materials used for AM [33], which can be divided into crystalline and amorphous states. Table 2 lists some of the main polymers and their specifications used in the AM process. The publication share of main AM polymers is shown in Fig. 2. Most of these polymers are mixed and enhanced by manufacturers under various commercial market trademarks, especially resin-based feedstocks. Besides, many other polymeric compounds are used in specific AM processes, such as polydimethylsiloxane, ethylene vinyl acetate (EVA) [34], and commercial digital materials from 3DP machine manufacturers.

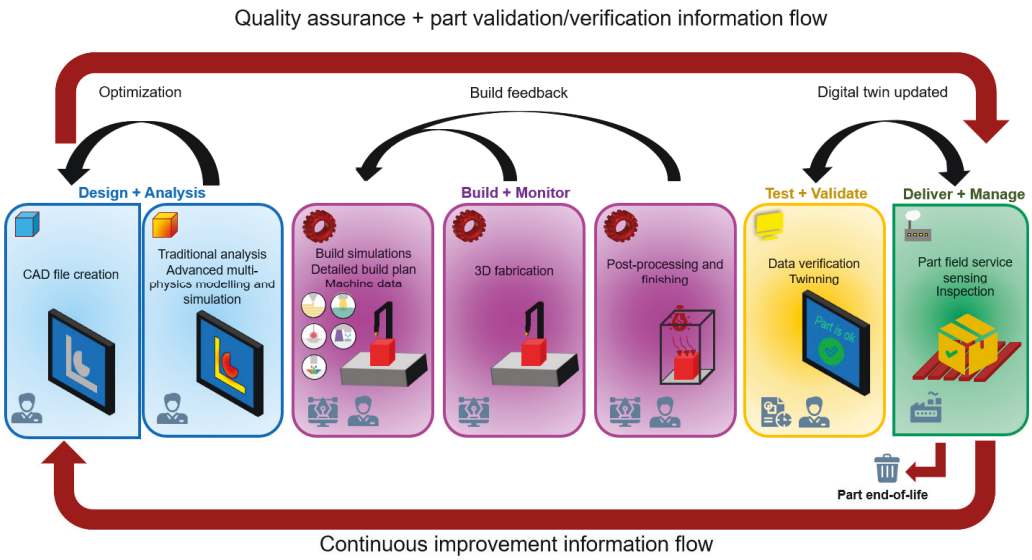


**Fig. 1** Stepping through the digital thread in additive manufacturing (DTAM).

**Table 2** Characteristic overview of different unfilled AM polymers for general purposes.

| | | Materials Properties | | | | | |
|---|---|---|---|---|---|---|---|
| Materials | AM technology* | Tensile strength (MPa) | Tensile modulus (MPa) | Elongation at Yield (%) | Flexural strength (MPa) | Heat deflection temperature (°C) | Ref. |
| ABS | FFF, SLA, BJT, MJT | 15-68 | 1500-4000 | 1.6-6 | 48-110 | 51-99 | [35-37] |
| ASA | FFF, BJT | 29-52 | 1510-2340 | 2-9 | 48 | 91-98 | [35, 36] |
| PA (Nylon) 6, 11, 12 | FFF, SLS, BJT, MJT, SHS | 45-76 | 944-1350 | 4-8 | 37-85 | 55-182 | [35, 36] |
| PBS | FFF | 16-27 | 46-50 | 22-27 | 3.3-5.6 | 50-65 | [36, 38] |
| PC | FFF, SLA, SLS, BJT, MJT | 61-72 | 2200-2500 | 3.5-7 | 92-160 | 48-55 | [35-37] |
| PCL | FFF, SLS, BJT | 5-42 | 343-441 | 3.5-8 | 23-117 | 41-50 | [39, 40] |
| PE (HDPE) | FFF, MJT, SLS | 25-31 | 1070-1550 | 6-15 | 22-28 | 34-42 | [32, 41] |
| PEEK | FFF, SLS | 80-110 | 2843-3950 | 4-6 | 165-185 | 51-107 | [32, 42] |
| PEKK | FFF, SLS | 88-112 | 2900-3790 | 3-8 | 128-168 | 60-98 | [42] |
| PETG (PET, PETT) | FFF | 55-86 | 2800-3710 | 3.8 | 80-116 | 65-80 | [37, 43] |
| PLA | FFF, SLS, BJT | 15-72 | 2020-3600 | 3.5 | 48-115 | 49-52 | [35, 36, 44] |
| PMMA transparent | FFF, SLA, BJT, MJT | 38-72 | 1940-2250 | 2-10 | 73-76 | 41-48 | [43, 45] |
| PP | FFF, SLA, SLS, MJT | 19-58 | 1600-1950 | 6-25 | 55-58 | 46-122 | [37, 46] |
| PPSF/PPSU | FFF | 36-52 | 2068-2100 | 1-3 | 110 | 100-135 | [35, 36] |
| PS | FFF, SLS, MJT | 14-53 | 1900-3500 | 1-4 | 62-100 | 62-80 | [37, 47] |
| PVC | FFF | 37-55 | 2450 - 4700 | 2-6 | 67-96 | 30-75 | [48, 49] |
| TPU (Flexible Polyurethane) | FFF, SLA, SLS, MJT | 21-44 | 8-36 | N/A | 6-10 | 85-110 | [50, 51] |

* Data are compiled from various sources, including material datasheets and publications.

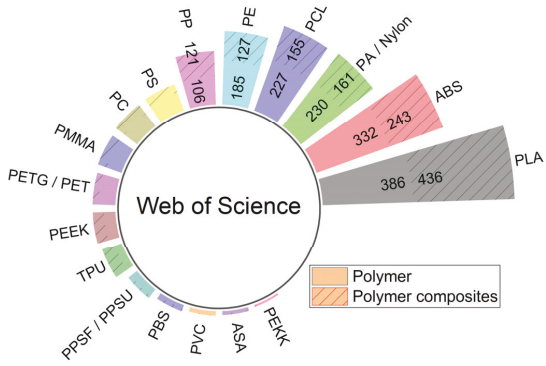


**Fig. 2** Total number of publications corresponding to polymers and their composites in Additive Manufacturing since 2012 (data from Web of Science, 2023).

### 2.2. Research method

This literature review focused on the current state of academic investigation with the broadest possible analysis of all recently published articles on surface roughness and 3D printing parameters. The review process was based on the content analysis of 55 articles. This review paper benefited from the preferred reporting items for systematic reviews and meta-analyses extension for scoping reviews method (PRISMA-ScR) for reporting scoping reviews as a general guide [52].

By utilizing the PRISMA-ScR method, a systematic and comprehensive scoping review approach is provided. A clear reporting framework facilitates transparency and replication of the review process, and a reduction of bias in the selection and interpretation of findings is achieved. It should be noted, however, that the method used had a few limitations. The scoping review methodology used may not provide a comprehensive review of all literature on surface roughness for polymer AM, particularly considering the broadness of the topic. A review process may have been limited by the quality of the selected articles and their generalizability for some methods. Thus, the content analysis of the articles may have been influenced by subjective judgments [52, 53]. For instance, available MJT papers in the studied field were considerably fewer than those for FFF (Fig. 3), resulting in more challenges for generalizations of the results. Besides, there were a variety of hand-made and tweaked 3D printers studied in the literature that may affect the review procedure.

The publications were explored on Web of Science and Scopus to be as comprehensive as possible, as these scientific databases have high coverage of reputed high-impact publications.

Fig. 3 shows the most common terminology and methods for polymers mentioned in the literature. Based on the number of publications in each AM category, 5 key processes are determined to be studied further. Accordingly, the authors selected the FFF process for MEX, SLA and DLP processes for VPP, the SLS process for powder bed fusion (PBF), and the MJT category, including the PolyJet process. Other AM

methods which generally use polymers in the fabrication of different materials and composites have been excluded, such as binder jetting (BJT) and sheet lamination (SHL). The market report on polymer 3DP machine sales [33] also confirms the same trend and technological share for selected key processes. Other techniques which were not mainly dedicated to polymers or rarely used for research are not included in our study. As AM growth is dynamic on a daily basis, their capabilities are sporadically mentioned.

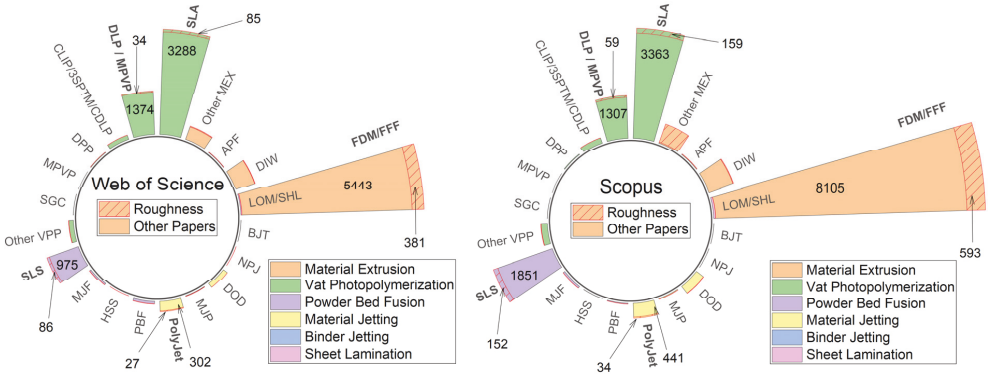


**Fig. 3** The most widely used polymer AM technologies and the total number of publications since 2012 (data from Scopus and Web of Science, 2022).

Various generic keywords, such as "3D*print", "additive manufacturing", and "additive tech*", were employed as criteria in the search section of the title, abstract, and keywords. Following is a formulation of research key strings for AM processes:
*(("3d*print*" OR "advanced manuf*" OR "additive manuf*" OR "additive fabric*" OR "additive proces*" OR "additive tech*" OR "additive method*" OR "additive layer* manuf*"))*

To examine the role of PPP on roughness, the post-processing of samples should be restricted to 1st level processes, as suggested by the Wohlers report [54]. It secures a minimal impact of post-processing on the roughness of the as-printed samples compared to the slightly post-processed replicas. It is usually less than a 20% deviation, depending on the specific needs of the project or application. Most studies reviewed here limited the PPFTs to a minimum number of steps to minimize the dimensional variations.
This work considered journal articles and conference proceedings to obtain a broader understanding of the topic. Upon eliminating duplicates, the titles and abstracts, availability of full text, and English language were screened before the full-text review. Following this, papers were controlled by their relevance to the present review paper, their originality in providing roughness evaluation for polymers, and their comprehensiveness and uniqueness in terms of the studied parameters and reported roughness metrics. Thus, papers that were out of these criteria were excluded from the study, which resulted in 55 articles separately being exported to Endnote and OriginPro 9.9.5 for in-depth analysis. Fig. 4 summarizes the

selection procedure used in the current study. The authors have 3D-printed several specimens for each AM category to visualize the surface roughness and texture conditions discussed.

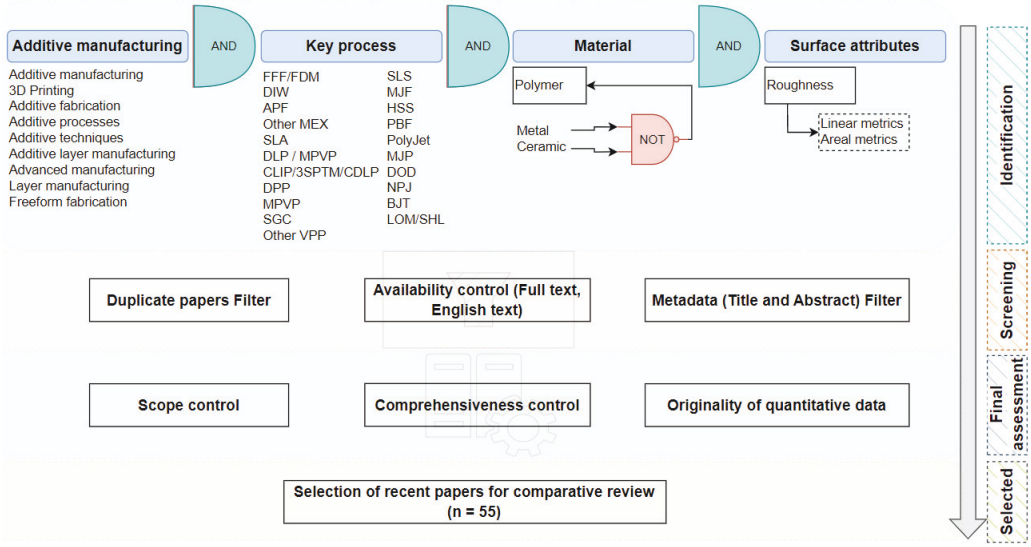


**Fig. 4** An overview of the screening procedure employed in this study.

## 3. Roughness measurements and metrics

Additively manufactured surfaces are composed of various spatial frequency components, including profile, form, waviness, and roughness (Fig. 5). Each of these components has different origins and influences the appearance and functional performance of products differently. The waviness may reveal machine vibration, the form is usually produced by the poor performance of the manufacturing system, and the profile can be ascribed to layer-by-layer manufacturing. Roughness, however, is generated by surface irregularities due to printing and material removal errors. The waviness appears as a signal noise because of the planarity of the motion system and any deformations caused by weight or residual stress [55]. As a result of the specific printing process and materials used, there may be other sources of waviness, including defects in the printing process, thermal distortion, poor adhesion between layers, inadequate support structures, mechanical deformation during post-processing, etc. [56, 57].

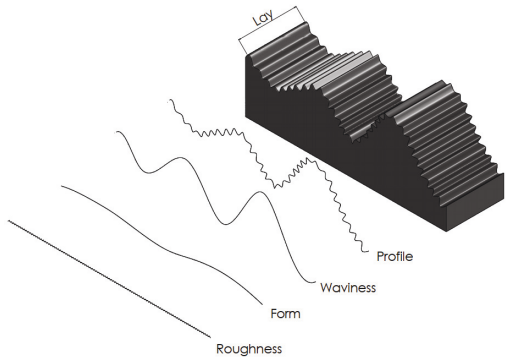


**Fig. 5** General spatial frequency components of additively manufactured surfaces.

Specifically, surface roughness is a critical texture component for assessing the quality of manufactured items by investigating the distribution of topographical features on the surface. Different metrics describe surface roughness because different industry sectors refer to various measures. Due to uncertainty in the surface quality of 3D-printed products, using several metrics would also be efficient [58]. For instance, Trianraphyllou et al. [59] concluded that average area roughness ($S_a$) and area root mean squared height ($S_q$) are appropriate metrics for measuring area surface roughness, as they were not sensitive to measurement parameters such as sampling length and evaluation length. In contrast, area height distribution skewness ($S_{sk}$) was found to sufficiently characterize the upside and downside surfaces from SLM parts.
Surface topography measurements based on data obtained from the 3D scanned images of a sample surface are either reported from a linear measurement, referred to by *R*, or from an aerial surface measurement indicated by *S*. The *R* and S metrics are defined and parameterized in ISO 21920-2 [60] and ISO 25178 [61], respectively. Area Ratio, or the overall real surface area over the theoretical area of a smooth surface, can reveal how rough a surface is. Generally, the standard height-based metrics employed to describe surface roughness based on a linear profile can be derived from Equations (1)-(10) in Table 3. On the other hand, area roughness parameters are sometimes used to describe the roughness variation on a surface (Table 4).

**Table 3** Surface roughness metrics based on linear measurement [60, 62].

| Parameter | Description | Equation* | |
|---|---|---|---|
| $R_a$ (Roughness Average) | The arithmetic average of the absolute values of the roughness profile ordinates | $R_a = \frac{1}{l_e}\int_0^{l_e} \lvert z(x)\rvert dx$ | Equation 1 |
| $R_q$ | Root Mean Squared of measured microscopic peaks and valleys | $R_{\mathrm{q}} = \sqrt{\frac{1}{l_{\mathrm{e}}}\int_0^{l_{\mathrm{e}}} z^2(x)\mathrm{d}x}$ | Equation 2 |
| $R_t$ (Total Height of Profile) | The vertical distance between the maximum profile peak height and the maximum profile valley depth along the evaluation length | $R_{\mathrm{t}} = \underset{x\in X}{max}(z(x)) - \underset{x\in X}{min}(z(x))$ | Equation 3 |
| $R_{sk}$ (Skewness) | Positive skewness indicates that the surface is made up of peaks and asperities, whereas negative $R_{sk}$ refers to dominant valleys on the surface | $R_{\mathrm{sk}} = \frac{1}{R_{\mathrm{q}}^3}\frac{1}{l_{\mathrm{e}}}\int_0^{l_{\mathrm{e}}} z^3(x)\mathrm{d}x$ | Equation 4 |
| $R_{ku}$ (Kurtosis) | A measure of the sharpness of profile peaks | $R_{\mathrm{ku}} = \frac{1}{R_{\mathrm{q}}^4}\frac{1}{l_{\mathrm{e}}}\int_0^{l_{\mathrm{e}}} z^4(x)\mathrm{d}x$ | Equation 5 |
| $R_zDIN$ | The average distance of peaks to valleys (German Standard) | $R_{zDIN} = \frac{1}{s}\sum_{i=1}^{s} R_{t_i}$ | Equation 6 |
| $R_zJIS$ | The average distance of peaks to valleys (Japanese Standard) | $R_{zJIS} = \frac{1}{5}\sum_{i=1}^{5} R_{t_i}$ | Equation 7 |
| $\eta$ | Asperity-peak density | $\eta = \frac{\frac{m_4}{m_2}}{6\pi\sqrt{3}}$ | Equation 8 |
| $\rho$ | Asperity-peak radius | $\rho = 0.375\sqrt{\frac{\pi}{m_4}}$ | Equation 9 |
| $\sigma_s$ | The standard deviation of asperity-peak heights | $\sigma_s = \sqrt{1 - \frac{0.8968}{\alpha}}\sqrt{m_0}$ | Equation 10 |

* $X = \{x \in \mathbf{R} \mid 0 \le x \le l_{\mathrm{e}}\}$, $m_0 = AVG(Z^2)$, $m_2 = AVG\left(\left(\frac{dZ}{dx}\right)^2\right)$, $m_4 = AVG\left(\frac{d^2Z}{dx^2}\right)^2$, $\alpha = \frac{m_0 m_4}{m_2^2}$

The roughness parameter $R_a$ is widely used by researchers in AM studies as a straightforward metric to define and measure. Considering height variation as a general concept makes it easier to understand, but $R_a$ is insensitive to wavelength variations [63]. Li et al. [64] revealed that the highest peak-to-valley distance parameter ($R_z$) was superior to $R_q$ and $R_a$ as standard metrics for measuring surface roughness. Li et al. reached a more significant correlation between $R_z$, tactile evaluation outcomes, and visual assessment results. Other appearance factors, however, influence sensory judgments, such as surface texture and color of the build material. Therefore, $R_z$ alone is insufficient to comprehensively characterize the differences in human perception and surface QAs among samples.

**Table 4** Area roughness parameters [28, 65, 66].

| Parameter | Description | Equation | |
|---|---|---|---|
| $S_a$ | Deviations in the height of the surface points concerning the Mean Reference Plane of the measurement area ($A$) | $Sa = \frac{1}{A}\iint_A \lvert z(x,y)\rvert dxdy$ | Equation 11 |
| $S_z$ | Sum of the largest peak height value and the largest pit depth value within the defined area | $Sz = max(z(x,y)) + min(z(x,y))$ | Equation 12 |
| $S_q$ | Root mean square surface height | $S_q = \sqrt{\frac{1}{\mathrm{A}}\iint_A z^2(x,y)\mathrm{dxdy}}$ | Equation 13 |
| $S_{sk}$ | The skewness of the surface | $S_{\mathrm{sk}} = \frac{1}{S_q^3}\frac{1}{\mathrm{A}}\iint_A z^3(x,y)\mathrm{dxdy}$ | Equation 14 |
| $S_{ku}$ | The kurtosis of the surface | $S_{\mathrm{ku}} = \frac{1}{S_q^4}\frac{1}{\mathrm{A}}\iint_A z^4(x,y)\mathrm{dxdy}$ | Equation 15 |
| $RRP$ | The reduction in surface roughness | $RRP = \frac{S_a^i - S_a^f}{S_a^i} \times 100$ | Equation 16 |

Extraction of the roughness profile is not a common reproducible method because it depends highly on the operational instrument, shape, rotation, and displacement speed [3], as reported in several studies [3, 65]. While 2D profile measurements based on the stylus, according to ISO 4287, are still popular, there is a growing interest in X-ray computed tomography (CT) scan and contactless 3D optical profilometry, according to ISO 25178-2, to obtain more information without scratching the surface.

Launhardt et al. [66] evaluated four alternative methods for evaluating the surface roughness of Polyamide 12 components produced by SLS. According to them, stylus-based techniques scratch the surface somewhat without substantially altering its roughness. Despite being unable to measure the valley depth, the tactile method was the most reproducible among other studied techniques.

On the other hand, optical methods do not physically alter the surface but are hypersensitive to light reflection and surface transparency, leading to defect detection [67]. The advantages of this method, such as contactless measurement and a comparable $R_a$ and roughness trend to tactile systems in the focus variation mode, make it a viable technique for smooth polymeric surfaces. The focus variation is a vertical scanning method with a shallow depth of focus. It simultaneously allows the measurement of steep flanks, form, and surface roughness [68]. Optical methods could also detect a three-dimensional topography of the surface and its roughness.

The focus variation method suffers from error because of the translucent polymer. The fringe projection and confocal laser scanning microscope represent higher roughness values and more sensitive measurements prone to outliers and faults [66]. The lower wear resistance of polymers in tactile methods and the possibility of the semi-translucent appearance in optical techniques make them more sensitive to method selection in roughness measurement.

Beitz et al. [69] used a confocal laser scanning microscope (CLSM) and X-ray micro-computed tomography (XMT) to measure surface roughness. They reported that roughness resulting from XMT data diverged substantially from those obtained from CLSM data. Due to the inability to level peaks, smaller measuring lengths result in higher arithmetic roughness values. The method also has a smaller sample size, resulting in lower surface roughness along the measurements section. Thus, assessing the roughness metrics of AM polymeric surfaces requires identifying the roughness evaluation method.

Regarding test artifacts for quality surface evaluation, most studies have used the twisted pillar (truncheon) [24, 65, 70], sloped surfaces [70-72], standard test artifact [65], or faceted sphere [24, 73] to measure roughness (Fig. 6). The design of an AM artifact should consider adaptability to various AM processes and machine sizes, as well as its ability to perform non-contact and contact measurements, editable geometry, and minimal material and energy consumption. The twisted pillar is the preliminary design for this purpose which consists of a sequence of square segments rotated $0^{\circ}$ to $90^{\circ}$ around a central axis with $3^{\circ}$ or $5^{\circ}$ increments. The design is appropriate for measuring the surface roughness of an angled plane in the range of $0^{\circ}$ to $360^{\circ}$ [24]. Yet, it cannot meet all the above requirements of the measurement. Understanding the measurement process is an essential step in interpreting the results.

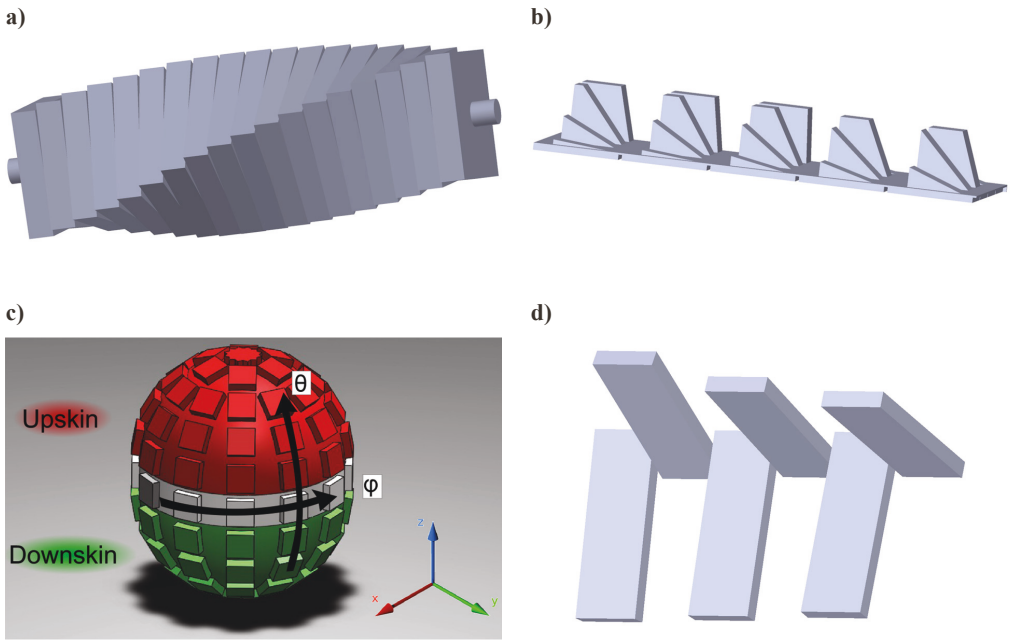


**Fig. 6** 3DP designs for studying build orientation (wedge angles): **a** Twisted tower, **b** Tilted surfaces, **c** Faceted sphere, and **d** Standard Test Artifact (STAR).

## 4. Fused filament fabrication (FFF)

Even though FFF 3DP has made significant advances so far, the fabricated parts tend to have a poor surface finish, including rough surfaces, voids, and prominent striations [2]. The morphology is relatively rough due to various limiting factors such as phase transformations, fast cooling, and exhaustive energy (Fig. 7). Although FFF is attractive for demanding applications, printed parts deviate from their initial designed geometry, volumetric error, and hardware settings in translating a CAD file to a physical object [74, 75]. To control the shape deviation, the corresponding allowances are approximately estimated before printing [76]. However, the FFF parts still required PPFTs to meet the market [17]. For instance, temperature variation during the layer-by-layer part fabrication procedure undesirably affects the printing quality [2].

**Fig. 7** Appearance and accuracy of gradient lattice-based structures in as-printed FFF samples using PLA filament and Prusa i3 mk3s+ (Scale bar represents 1 cm).

Generally, there are two types of bonding in the FFF process: inter-layer and intra-layer (Fig. 8). The high thermal expansion in polymers can play an important role in the weak bonding among the layers during the build process, leading to staircase (stairstep) formation. As an inherent issue, the formation of staircases has a considerable negative impact on the surface quality of FFF components [18, 75].

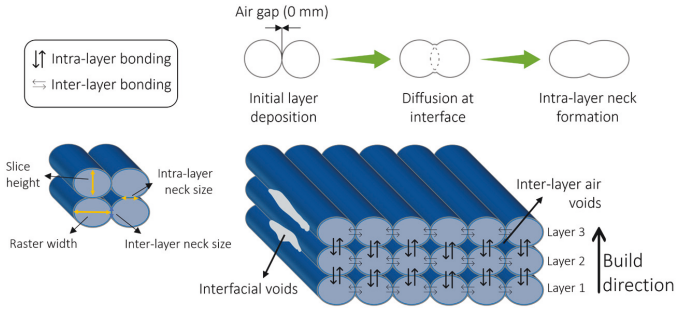


**Fig. 8** Bonding and stages of neck formation in the FFF process.

Among literature reviews on the process parameters of FFF, Turner et al. in 2014 [77] summarized the process design and modeling of FFF. They reviewed the bonding of the raster, the model spread of the

deposited raster, and the motor torque and power. Chohan et al. (2017) [21] have reported a literature review on pre- and PPFTs to improve surface characteristics of FFF parts. In 2018, Singh et al. gathered results from studies on the effect of pre- and post-processing procedures on FFF patterns to develop biomedical implants from the route of AM and investment casting (IC) [78]. Several AM materials and their mechanical performance have been reviewed by Popescu et al. (2018) [79]. In addition, deliberately structuring the polymeric surfaces using FFF 3D printing has become a popular choice for AM processes. Cuan-Urquizo et al. [17] reviewed the literature on the characterization and projection of the mechanical behavior of FFF products using analytical and computational approaches (2019).

### 4.1. Process parameters

In FFF, pre-processing includes instructions generated by a slicer software to gain data, slice the design file into layers of 3D pixels (voxel), model construction, optimization of the toolpath for the printing process, and materials preparation. Parameters directly affecting the process are categorized based on operation, geometry, material, and machine-specific parameters [80]. Generally, the accuracy of the motion system limits the precision of the part. To minimize the issues due to the design and pre-production phase, each voxel must have accurate position information and print-process parameters in tool pathing. In the following, the main process parameters influencing the surface roughness of FFF polymeric surfaces are discussed.

#### 4.1.1. Filament material

The growing interest in using polymers ranging from rubber-like materials to rigid plastics leads to new applications in vehicle parts, shoe soles, and biomedical applications [81]. While high surface quality and desired roughness are advantages for 3DP parts, other material properties and manufacturing features are usually considered in the selection of the AM method. Fig. 9 illustrates a general cumulative performance score based on the comparative scoring of each parameter on a scale between 1 and 9. PLA and ABS are the most well-known feedstock among other materials for FFF. Since PLA filaments can provide better surface quality and biodegradable polymer derived from corn, it is considered more eco-friendly than petroleum-based ABS [82].

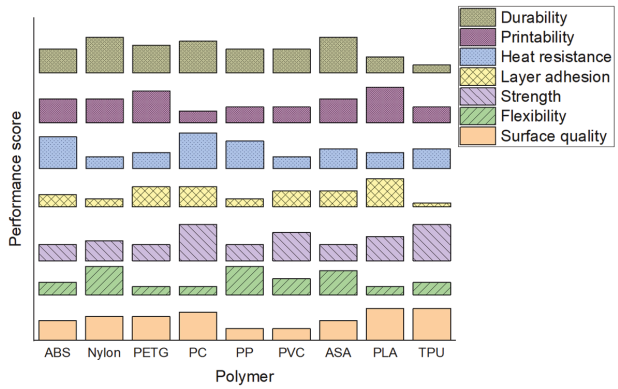


**Fig. 9** Recommended polymers for the FFF process. Data extracted from references [43, 83].

In most cases, materials are already enhanced for optimum performance. Their parameters are challenging to alter later in the production stage but choosing the appropriate material to improve surface roughness is crucial. This may prevent the usage of FFF prototypes in some cases where the surface should be smooth. An overview of the major polymers used in FFF is presented in Table 5.

**Table 5** Typical FFF filaments specifications. Data extracted from references [43, 83].

| Material | Printing Temperature* (°C) | Type | Remarks | Application consideration |
|---|---|---|---|---|
| PLA | 180 - 235 | Standard plastics | Easy to print<br>Low-cost<br>Midcore thermal and mechanical properties<br>Available in various colors and specifications<br>Severely limited by application temperature under 50 °C<br>High surface roughness<br>Biodegradable | Generally non-critical |
| ABS | 200 - 260 | Standard plastics | Difficult to print<br>Low surface roughness<br>Good thermal and mechanical properties | Generally non-critical |
| HiPS | 230 - 250 | Engineering plastics | Midcore mechanical properties<br>Water soluble<br>Biodegradable | Structural purposes |
| PolyVinyl Alcohol (PVA) | 190 - 220 | Engineering plastics | Water soluble<br>Glossy but rough finish<br>Limited mechanical and thermal properties<br>Biodegradable | Structural purposes |
| Nylons (PA) | 235 - 280 | Engineering plastics | Generally difficult to print<br>Good thermal and mechanical properties<br>Low surface quality | Structural purposes |
| PET(G) | 230 - 270 | Engineering plastics | Easy to print<br>Low dimensional accuracy due to shrinkage<br>Good thermal and mechanical properties | Structural purposes |
| Polycarbonate (PC) | 250 - 320 | Engineering plastics | Excellent thermal and good mechanical properties | Structural purposes |
| Polycarbonate ABS (PC-ABS) | 260 - 285 | Advanced plastics | Average printability<br>Good thermal and mechanical properties | Severe conditions |
| TPU | 195 - 230 | Engineering plastics | Generally difficult to print<br>Flexible materials<br>Excellent resistance to abrasion and wear | Structural purposes |
| PEEK | 350-450 | Advanced plastics | Generally difficult to print<br>Excellent thermal and good mechanical properties | Severe conditions |

* Data are compiled from various sources, including material datasheets and publications.

#### 4.1.2. Print temperature

In FFF 3D printing, print temperature and cooling speed play an important role as it affects the quality of the 3D printed object. The model temperature should be high enough to melt the outgoing feedstock before extrusion. However, if the temperature is too high, the filament will melt too rapidly, resulting in a porous and brittle object with poor surface quality [21]. Depending on the type of filament being used, the optimal printing temperature will vary. Typically, PLA is printed at 190-220 °C, while ABS is typically printed at 220-250 °C [35-37]. The ideal printing temperature should be referred to by the filament manufacturer to ensure the best results. A stable temperature at heaters is crucial in the fluidity of material, resulting in a smoother surface finish. Besides, the surface roughness can be decreased by increasing the model temperature because of the solidification delay. However, plastic adhesion with a base plate is problematic in very high or low printing temperatures [21]. As well as affecting the quality of the printed part, the temperature of the nozzle can also affect the speed of the printing process. In general, a higher temperature will lead to faster printing speeds, but it is crucial to find a balance between speed and quality.

#### 4.1.3. Layer thickness

The height of each deposited stairstep is a notable parameter that can be controlled in the extrusion nozzle tip and/or shift in the *Z*-axis between consecutive slices accumulated on the bed. Adjusting the height of each stairstep can improve print quality and reduce the printing time. In general, a smaller stairstep height will produce a higher quality print, but the printing process will take longer [84, 85]. This parameter is the most significant challenge in obtaining a high surface finish in a cost-effective production time. The minimum feature size (smallest linewidth) is determined primarily by the nozzle diameter, which affects layer thickness non-linearly, but geometry and build orientation also play an essential role [86]. Correctly setting up an optimum balance between layer thickness and printing time is highly influential in the pre-processing step. A smaller nozzle tip will generally result in lower layer thickness, better surface quality, and possibly decreased post-processing time. However, it increases the printing cost and time for the as-print parts, leading to more nozzle clocking and quality issues because of the pressure drop [21].
Since the quality of internal surfaces does not engage in the appearance of the part in most cases, consistent layer height has been seen as a waste of time [72]. Thus, it can be varied in different areas of the object according to the expected time-quality factor. For most FFF printers, the domain of layer thickness is variable in a certain range, i.e., there is a maximum and minimum value for changing the nozzle diameter. A few machines are limited to a single value, so it is required to set up other parameters to change the surface quality [21].
In several papers [84, 85], the layer thickness is reported as the most significant process parameter influencing surface roughness. However, this influence also depends on the other process parameters. Anitha et al. [87] established a set of experiments that showed that layer thickness significantly impacts the roughness of the FFF part compared to rod width and speed of deposition. Haque et al. [84] attempted to

minimize the surface roughness of FFF build features using a numerical approach. After investigating various equations to control FFF parameters such as layer thickness, overlap distance, part orientation, and raster width, they reported that layer thickness has more influence on roughness than other parameters. They observed that increasing the overlap distance between two layers and part orientation leads to lower surface roughness. However, higher layer thickness and raster width increased surface roughness.

#### 4.1.4. Infill density and air gap

The infill density defines the level of incorporated material inside the fabricated object. It might be varied from 0 to 100 percent according to the required balance between material consumption and mechanical properties [88]. Generally, a higher infill density leads to a heavier and stronger part, which increases the cost and the amount of material used in the printing process. Infill density and pattern are significant process parameters influencing surface quality [72]. Support structures must also be designed appropriately to support the geometry. Thus, they should be accurately chosen by considering the design and strength requirement, as well as the build time of the printed part. For instance, surface artifacts such as gaps and porosity have been observed even for 100 % infill density under a scanning electron microscope (SEM) [89].

The distances or spaces between two adjacent rasters on the same layer are called the air gap or road gap [90]. Fig. 10 depicts the air gap compared to other adjustable FFF process parameters. The default value taken for the air gap is zero, which means the end of the two nearest beads is in touch. There are two types of positive and negative gaps. The positive gap increases the gap to reduce the density and build time of structures, whereas the negative gap means overlapping two roads resulting in a long printing time and dense objects. While both positive and negative air gaps can enhance the surface finish, zero air-gap minimizes dimensional accuracy and part quality [21].

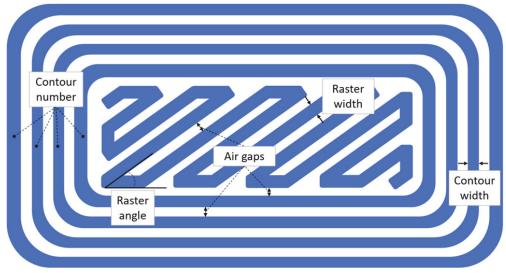


**Fig. 10** Controllable parameters in FFF machine.

#### 4.1.5. Raster width and angle

The raster width, also called road or contour width and (tool) path width, refers to the width of the melted bead path, which is added to fill interior regions of the FFF-printed samples [21]. According to the filament material, it is regularly 1.2 to 1.5 times the nozzle tip size [80]. As seen in Fig. 10, the contour tool path width surrounding the object is defined as the contour width, slightly smaller than the nozzle diameter [21, 86]. The width of the most minor features in the *XY*-plane in FFF is about two times the path, much larger than the thickness of the layer in the *Z*-direction. To reach high mechanical performance, dimensional accuracy, and surface quality, the raster width should be minimized [86, 91]. It has been noticed that a wide contour width enhances geometrical precision and surface quality because heat evolved during extrusion can easily deform thin contours [92].

The raster direction compared to the *X*-axis of the build platform is known as the raster angle (Fig. 10). This parameter significantly affects the internal layer bonding and object appearance. The main approaches to raster angle are criss-cross (−45°/+45°), cross (0°/90°), and 30/°60°. Because of the variation of CAD models and printing parameters, there is a loose correlation among the studied strategies. Sood et al. [91] used a bacterial foraging algorithm to show that the 0° raster angle is the best option for dimensional accuracy, and 45° results in the best surface appearance. Kumar et al. [93] stated -45°/+45 as the best raster angle for the surface characteristics, including roughness.

#### 4.1.6. Build orientation

The orientation (deposition) angle is a notable and highly flexible process parameter involving surface quality. It corresponds to the CAD model and coordinates machine system (Fig. 11). Wang et al. [94] considered the build orientation the most substantial PPP factor regarding dimensional accuracy. As a result of gravity and residual stresses, overhanging surfaces should be supported at less than 45° from the horizontal plane [19]. Several papers have studied the role of positioning the models in various *X*- and *Y*-directions on the surface finish and build times. For instance, Kattethota and Henderson [95] reported that the orientation angle of 0° yielded the best surface finish. Moreover, 0° and 90° were reported as the optimum build angles for balancing the build times, cost, and surface finish. By contrast, orientation angles between 40° and 60° were neither cost-effective nor quality-enhancing due to the maximum support material required for tilting the model [21].

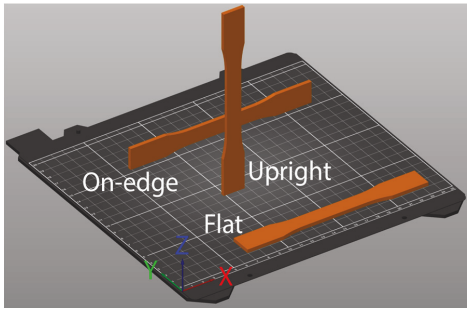


**Fig. 11** Orientations commonly used for FFF parts.

Since different surface angles result in various surface roughness, the test part should comprise features considering different surface angles. In 1997, Reeves and Cobb [96] introduced a benchmark model called twisted pillar. It can consist of 18 or 31 square blocks, depending on the intervals (step), twisted 5° or 3° compared to the previous square (see Fig. 6a). Durgun and Ertan [97] also confirmed the close relationship between build direction and surface roughness.

Among the defects associated with different build orientations are warping, layer delamination, deformed overhangs, and poor surface quality [98, 99]. In terms of surface roughness, Buj-Corral et al. [99] reported both simulated and experimental amplitude roughness values to rise with build orientation angle, due to the stair-stepping effect. As reviewed by Jiang et al. [98], a change in print orientation also affects support generation, which ultimately affects the surface roughness after support removal. The choice of support structures can have a significant impact on the surface roughness of FFF prints, thereby influencing the post-processing process. Furthermore, the orientation of the part impacts the support contact area, the build time, and the cost of the fabricated part.

#### 4.1.7. Adaptive slicing

Adaptive slicing is termed as a protocol to slice various zones of the part into different thicknesses during building [78]. It contains balancing techniques needed to reach the optimum printing time versus surface finish. Generally, the CAD model is divided into polygons or closed curves by either the CAD software or a slicer before transferring the mesh model (STL file) to the printer. This process is called slicing, and the distance between two sequential horizontal planes is known as a slice [100]. The slicing process and the tessellation of the CAD file are expected to be the significant parameters involved in creating rough surfaces in the procedures of layer fabrication. The containment problem causes the original CAD model to deviate from the designed form when slicing a tessellated CAD model. Aside from the containment issue, the layers deposition causes a problem known as staircase effects [101].

Several researchers [17, 102] have studied several types of stepwise refinement, adaptive slicing, and identifying nonuniform fillet radius at different areas of printed objects. These methods consider

automatically slicing algorithms, generating variable tool paths (.gcode), reducing build time, and minimizing surface roughness through varying heights depending on geometry [103]. These specific parameters rely entirely on the shape and dimensions of the designed part [21].

The major categories of slicing methods available for FFF printing are flat-layer, non-planar, and mixed-layer adaptive slicing, respectively. Zhao and Guo [104] listed the most important research studies on non-planar and mixed-layer adaptive slicing. They suggested method planning of mixed-layer adaptive slicing, which discusses the strategy for the process planning of more straightforward adaptive slicing approaches. Table 6 provides an overview of these slicing methods.

**Table 6** Adaptive slicing classification. Extracted from references [103, 104].

| Method | Specification | Advantages | Disadvantages | Application |
|---|---|---|---|---|
| Planar slicing | Uniform layer thickness | Simple, effective, and robust | Lack of strength (poor performance)<br>Stairstep effects (poor surface finish)<br>Large numbers of layers (longer build time) | Widely used in slicing simple designs |
| Non-planar (curved layer) slicing | The nozzle is collinear with the normal direction of the curved surface<br>Longer length filaments in curved inter-layer<br>Fewer layers | Preserve randomly located, minute and critical surface features<br>Reduced stairstep effects, at least in the tangential direction of the deposited filament<br>High strength<br>Enhanced surface quality<br>Fewer build times | Complex method | For some specific shapes like thin, curved shell-type structures (skull bones, turbine blades, etc.) |
| Mixed-layer slicing | Multi-direction and variable layer thickness | Reduced stairstep effects<br>Alleviated support structures<br>Less building times<br>Less anisotropy | No detailed automatic algorithms<br>Complexity in decision-making logic | Complex parts Requiring more capable slicing methods |

### 4.2. Surface roughness studies and discussion

The literature on process parameter optimization is classified according to the resulting properties. It can be based on the surface finish and smoothness, dimensional accuracy, build time, material behavior, dynamic and static (tribo-) mechanical/thermal behaviors, and manufacturing cost. Studies have centered on finding the best combinations of geometry and operation-specific characteristics. For instance, Durgun and Ertan [97] reported that surface roughness significantly impacts the flexural strength of ABS parts manufactured with infill 100% at different orientations and angles. Among the factors responsible for PLA and ABS surface roughness, the researchers identified layer thickness [105-107], build orientation [107], printing speed [105, 106], nozzle diameter [105, 106], and temperature [106] as the most critical parameters. Table 7 summarizes some of the significant literature on the essential parameters in the process optimization of FFF on the roughness range. Optimizing these parameters is one of the highly critical tasks for acquiring the desired surface quality and improving superior mechanical properties and material response.

**Table 7** Overview of studies on surface roughness in FFF (see text* below the table for abbreviations).

| Materials \| Machines | Methodology and studied parameters | Roughness range (µm) | Remarks | Ref. |
|---|---|---|---|---|
| PLA \| 3D Ultimaker 2+ | l.t. (0.06-0.18 mm), r.w. (0.2-0.25 mm), i.d. (20-40 %), p.s. (20-100 mm/s), b.o. (0°-45°), f.r. (99-101%) a.m. (DoE Taguchi L9), s.r.m.m. (contact profilometry) | $R_a$: 0.7-10.5 (T.), 4.7-12.8 (S.) | - l.t. was the most influential parameter on the s.r and d.a.<br>- Shape and p.s. affected the T. $R_a$<br>- S. $R_a$, influenced by l.t., and then by walls p.s. and b.o. | [108] |
| PLA \| Tevo Tarantula Prusa i3 | l.t. (0.10-0.38 mm), p.s. (19.46-76.54 mm/s), p.temp. (171.22-218.78 °C) a.m. (ANN and SOS), s.r.m.m. (contact profilometry) | $R_a$: 1.705-4.373 | - Integrating ANN and SOS had a significant impact on performing the FFF process parameter for minimizing s.r., compared to the RSM method<br>- Decreasing l.t., p.s., p. temp., and outer shell p.s for ANN-SOS resulted in minimum s.r. (2.011 µm), which was 12.36% smaller than the RSM method | [109] |
| PLA \| FLSUN-QQ | l.t. (0.1-0.4 mm), r.w. (0.2-0.4 mm), p.temp. (190-210 °C), p.s. (60 mm/s), plat.temp. (60 °C), a.m. (ANN and SOS), s.r.m.m. (non-contact profilometry) | $R_a$: 5.40-33.65 | - The effect of l.t. and p.temp. was more significant on the 3D s.r. compared to the other parameters<br>- A theoretical model was developed based on the bonding neck-forming process | [110] |
| PLA & PLA-Graphene \| BQ Witbox | i.d. (100%), m.c. (20-80 mm/s), l.t. (0.06-0.24 mm) and b.o. (H., on-edge, and V.) were studied to determine their influence on the geometric characteristics (d.a., f.e., s.t., and s.r.), a.m. (ANOVA, ANN, and RSM), s.r.m.m. (contact profilometry) | $S_a$ H. orientation: 1.1-4.3 (PLA), 1.2-3.4 (PLA-Graphene) | - Compared to PLA filaments, PLA-Graphene improved functional properties with no loss in geometric quality<br>- The best s.f. was obtained in the H. orientation<br>- Variation of b.o. resulted in two different behaviors of s.r.: on-edge and V. orientations s.r. showed a quasi-linear growth with increasing l.t., but with no significant effect of m.c. H. orientation: filament crushing by the extruder in each layer produced lower values of s.r.<br>- When texture was evaluated in the H. orientation, $S_a$ depended on n.d. and l.t.<br>- For the V. and on-edge orientation, $S_a$ was affected only by l.t.<br>- The effect of b.o. on $S_a$ was primarily due to the deposition and cooling of the fused filament | [111] |
| Heat-resistant PEEK \| Indmatec | p.temp nozzle (380-420 °C), p.temp platform (220-300 °C), p.s. (5-25 mm/s), l.t. (0.1-0.3 mm), r.w. (0.4 mm), overlap interval (0 mm), extrusion flow (100%), s.r.m.m. (non-contact profilometry) | $R_z$: 30-75 | - s.r. model, considering diffusion, was introduced based on heat transfer<br>- Diffusion affects surface morphology<br>- The proposed design predicts s.r. by considering the printing parameters (r.w., l.t., p.s, and p.temp.)<br>- The actual s.r. was affected by diffusion and tightening of the nozzle<br>- s.r. decreases with the increase of p.temp. considering that nozzle temperature had a greater influence compared to platform temperature<br>- Lower l.t. decreases the surface quality as the nozzle squeezing deteriorates the surface morphology. l.t. (0.15 mm) and p.s. (20 mm/s) were the optimal values<br>- Application: Thermoplastic heat-resistant resins for aerospace, biomedical, mechanical, and electronic field | [112] |
| PLA \| Tevo Tarantula Prusa i3 | p.temp (185-205 °C), p.s. (36-60 mm/s), o.s.s. (29-40 mm/s), l.t. (0.18-0.30 mm), a.m. (ANOVA, RSM, PSO, and SOS, s.r.m.m. (contact profilometry) | $R_a$: 2.2 (SOS), 2.2 (PSO), 2.4 (RSM) | - All parameters with the order of p.s., l.t., o.s.s., and p.temp. affected s.r.<br>- PSO and SOS improved by 8.5% and 8.8% of s.r., respectively, compared with the conventional RSM method<br>- Lower l.t. and p.s., and higher p.temp. and o.s.s. resulted in a better s.f. | [44] |
| PLA \| BQ Witbox | b.o. (V., on-edge, H.), l.t. (0.06-0.24 mm), p.s. (20-80 mm/s), p.temp. (190-220 °C), n.d. (0.4 mm), i.d. (100%), a.m. (ANOVA, RSM, and ANN), s.r.m.m. (contact profilometry) | $S_a$: 2.5-2.8 (T.), ~25 (H.) | - The effect of b.o. in the object's positioning on the build plate, l.t., and p.s. on the d.a., f.e., s.t., and s.r. were analyzed<br>- s.r. exhibited two different behaviors depending on the build orientation at the optimum p.temp. (205 °C)<br>- The V. and on-edge positions showed a linear increase in $S_a$ and $S_z$ at higher l.t., but p.s. had no significant effect. In the H. orientation, s.r. was conditioned by n.d., leading to a nearly 10 times increase in s.r. | [113] |

| | | | | |
|---|---|---|---|---|
| ABS + TPU \| Creality CR10 | TPU contents (10 to 30 w.t.%) in ABS+TPU blends, p.temp. (230 °C), p.s. (30mm/s, 8mm/s for V.-printed specimens), travel speed (120 mm/s), o.s.s. (15 mm/s), r.a. (0°), i.d (100%), l.t. (0.2 mm), plat.temp. (90 °C), support-less printing, f.r. (100%), a.m. (ANOVA), s.r.m.m. (contact profilometry) | $R_a$: 2-7 (H.), 21-38 (V.); $R_q$: ~150-500 (H.), ~160-210 (V.) | - s.r. raised by increasing TPU content, resulting in higher adhesion of the ABS parts to the build platform<br>- 3D printability without heating the platform by adding TPU to the filament is achieved due to new intermolecular interactions<br>- Application: Large-scale industrial applications as an alternative to pure ABS | [114] |
| PETG \| Tevo Black Widow | l.t. (0.16- 0.24 mm), p.temp. (240-250 °C), p.s. (40- 60 mm/s), p.a. (500-1500 mm/s$^2$), f.r. (90-110%), a.m. (DoE Taguchi L27, ANOVA), s.r.m.m. (contact profilometry) | $R_a$: 0.91-10.64 (H.), 5.41-32.99 (V.) | - Influential parameters were studied to obtain lower values of $R_a$ and $S_a$.<br>- f.r. and p.a. had the greatest influences on the s.r.<br>- Application: Fabrication of traffic signs for the manufacture of LED spotlights | [115] |
| ABS & ABS+GF \| Generous Twin | l.t. (0.4 mm), p.temp. (225-245 °C), p.s. (600 mm/min), i.d. (100% Rectilinear), r.a. (-45°, 0°, 45°, 90°), GF (0-15 wt.%), a.m. (DoE Taguchi L23, ANOVA), s.r.m.m. (contact profilometry) | $R_a$: 6.51-13.47 | - s.r.became worse with increasing GF<br>- p.temp. and coupling agent did not have any significant effects on s.r. | [116] |
| PEEK \| Customized FFF | Printing parameters were set based on the FEA results. n.d. (0.4-0.8 mm), p.temp. (380-440 °C), p.s. (17-26 mm/s), l.t. (0.1-0.45 mm), s.r.m.m. (non-contact profilometry) | 7.8-10.8 (H.), 10.1-19.3 (V.) | - Reduced s.r. for both H. and V. directions due to increased p.s.<br>- Increased s.r. with higher n.d.<br>- Thinner layers in a 0.4 mm nozzle caused sensitive s.r. to p.s.<br>- Thicker l.t. resulted in higher s.r.<br>- Gaps between layers were the leading cause of s.r.<br>- Application: To replace traditional metal or ceramic parts for biomedical and aerospace applications | [117] |

*Abbreviations a.m.: analysis methods, b.o.: build orientation, d.a.: dimensional accuracy, f.e.: flatness error, f.r.: flow rate, i.d.: infill density, l.t.: layer thickness (height), m.c.: material consumption, n.d.: nozzle diameter, o.s.s.: outer shell speed, p.a.: printing acceleration, p.s.: printing speed, p.temp.: printing (nozzle) temperature, plat.temp.: platform temperature, r.a.: raster angle, r.w.: raster width, s.f.: surface finish, s.r.: surface roughness, s.r.m.m.: surface roughness measurement method, s.t.: surface texture, S.: side, T.: top, H.: horizontal (XY), V.: vertical (Z)

Table 7 indicates that layer thickness can be considered the most significant FFF parameter that affects surface roughness and surface finish. Based on the results, surface roughness was reported primarily by $R_a$, $S_a$, $R_z$, and $R_q$. Furthermore, the range of roughness can be significantly different depending on the processing conditions from sub-micrometers to 33.65 µm for $R_a$ in the studied works. Although the reported roughness varies tremendously, it is generally between 0.1 to 1 times the layer thickness, depending on the materials and measurement geometry. Also, build orientation is crucial in determining print quality, as horizontal and vertical surfaces differ. Slicing settings, object orientation, and considerations regarding the design for additive manufacturing (DfAM) guidelines could enhance roughness and resolution while decreasing the number of PPFTs required [118]. These results did not consider more complex features, such as ridges, holes, slots, and posts, coupled with motion and material flow dynamics.

## 5. Selective laser sintering (SLS)

Parts produced by SLS are expected to have a high surface quality because of the precise nature of the laser, resulting in extensive usage in meeting functional needs. On the other hand, SLS-produced components have generally a greater surface roughness than other polymer AM techniques [119]. Several functional properties are affected by surface roughness, including frictional properties, heat transfer, and fatigue resistance in polymers, as well as the possibility of powder becoming loose, e.g., as a medical implant in the human body [120]. During SLS, the build platform is heated uniformly to exactly below the material melting point; this is a highly effective method to boost the build rate. However, it can cause unwanted "caking" of powder on the outer surface of the part. A preheating lamp to maintain the temperature under the melting temperature reduces thermal stresses, leading to part distortion, shrinkage, and lower dimensional accuracy at the surface. Due to entrapped air, many grainy features, voids, and porosities can be formed inside the packed powder (Fig. 12). Therefore, porosity is an inherent defect in SLS objects that can appear on the surface [3, 121].

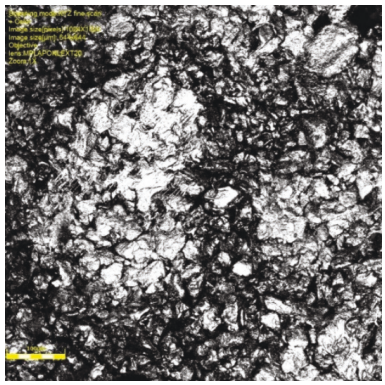

**Fig. 12** 2D laser scanning image of a part made of PA6, showing the typical surface texture of solid part samples printed with an EOS P500 FDR system.

SLS typically prints features as fine as 0.1-0.5 mm, making them an excellent choice for printing intricate latticework with thin walls and beams. While SLS parts do not need support due to a powder bed, temperature gradients during printing may deform the part and create very thin surface issues. In addition, because of thicker layers (90-150 μm) in SLS, the technique is more sensitive to the staircase effect. This effect in an SLS object is most prevalent on semi-horizontal surfaces [3]. In a similar method, SLM, since the melt pool is typically more extensive than the laser spot, the scan contour tracks are naturally shifted inwards to account for this issue and, consequently, rougher surfaces [122]. PPFTs usually improve the quality of large surfaces in these cases, but it would be more demanding for more complex and minor features.

There is a direct correlation between the amount of porosity in a part and material properties, such as the shape and size distribution of the powder and part processing conditions. Compared to semi-crystalline thermoplastics, amorphous thermoplastics produce more porous parts, which can either be an advantage or a disadvantage depending on the desired property of the piece. The fundamental problems with sintering are porosity and shrinkage in the parts. Still, they can be overcome with an optimal packing density (for porosity) and a careful choice of the sintering parameters [123, 124].

Low porosity is required if the appearance and mechanical properties are essential. The size distribution, reduced porosity, and enhanced surface finish affect powder flowability and packing density. Using infrared lamps or ambient heating helps prevent non-uniform shrinkage by keeping the polymer above the glass transition temperature, allowing the shrinkage process to be controlled. This requires slow cooling after the build is complete and must be considered when calculating the processing time for each part. On the other hand, semi-crystalline thermoplastics experience a volume reduction during cooling due to crystallization, making amorphous thermoplastics the better choice [123, 124].

Poor surface quality is a common complaint when working with powdered raw materials. The conventional roughness range (referred to by $R_a$) of PBF is 5-25 µm. As well as the printing parameters, the quality of the surface can also be affected by the 3DP machine itself. Depending on the SLS machine, $R_a$ can range from 10 to 20 µm with a peak-to-valley distance of up to 0.2 mm [3]. Sachdeva et al. reported a range of 8-12 µm for $R_a$ [124]. Mechanical properties, particularly fatigue, can be affected by different surface roughness. The AM powder-based procedure comprises semi-molten grains adhering to the outer surface, with occasional sharp grooves in between, prone to crack initiation [3]. Fig. 13 depicts the three states influencing the surface quality in PBF.

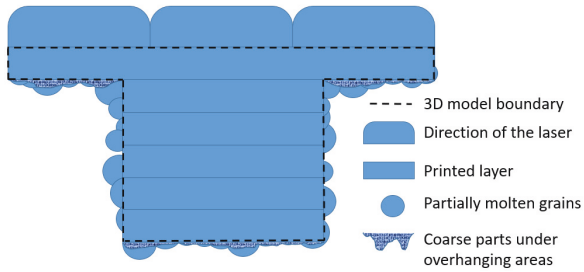


**Fig. 13** Typical PBF surface configurations that impact surface quality.

The incomplete composition of powder materials may cause "orange peel" surfaces (Fig. 14). Incorrect powder reuse or non-homogeneous mixing is the main reason for this surface issue in the SLS technique [125, 126].

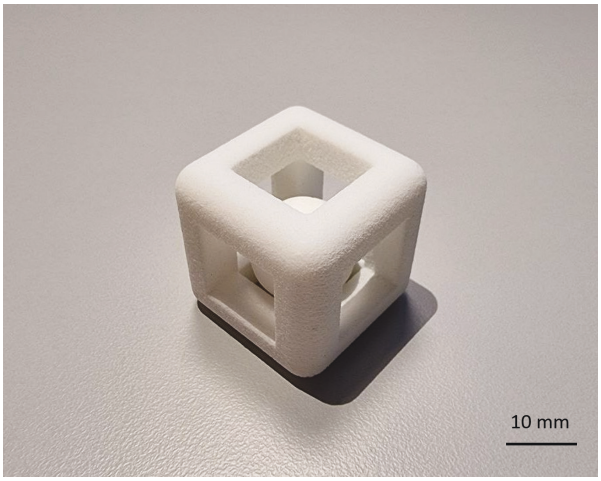


**Fig. 14** Orange peel surface texture on PA12 (2200) SLS part.

### 5.1. Process parameters

Several factors influence the performance of SLS systems. Precision and resolution are limited by the combination of powder particle size, layer thickness, and laser spot diameter. The selective melting of powder is done using two main tracks, including the contour and hatching tracks. In contour tracking, the outer layer of the required profile is melted, while the hatching track is used to melt the internal area bounded by the contour track [122].

The SLS as-printed surface roughness values differ considerably based on the preparation method, the equipment utilized, and the position of the sample surface concerning the layer accumulation [3]. The SLS parameters of the process (see Fig. 15) have been widely investigated in engineering fields [32, 127]. They can be classified into three major categories: laser, material, and chamber. The average powder size, layer thickness, and surface orientation all influence surface roughness. The physics of melting and solidification are also important. It is influenced by scan speed, laser power, hatch spacing (distance) or laser scan spacing, material viscosity, surface tension, and thermal boundary conditions like bed temperature. Research has shown that materials that have been degraded for enough time adversely affect the surface quality and increase the viscosity of melted powder [119]. Several factors determine the accuracy of the part and the minimum feature size, including powder sizes, laser spot sizes, feature orientation, aspect ratio, ability to control the melted region, and the resulting solidified geometry of the scanned areas. A thin layer of unfused powder adheres to the part surface due to heat dispersion into the surrounding powder, which must be eliminated during post-processing to achieve the best surface finish [32]. Overall, the main SLS printing factors influencing surface roughness can be classified as design, laser, material, and build chamber.

Particle size distribution and particle shape can impact the quality and strength of the manufactured objects. These procedures are continued until the component has been produced entirely. SLS processes encounter many difficulties due to the complexity of the thermal interactions involved, which calls for technology-appropriate design and process planning. Relative stresses, microstructural formation, and surface quality are a few difficulties resulting in part deformation or failure [19]. To avoid thermal deformation, the component stays in the powder bed throughout the slow cooling phase [9, 128].

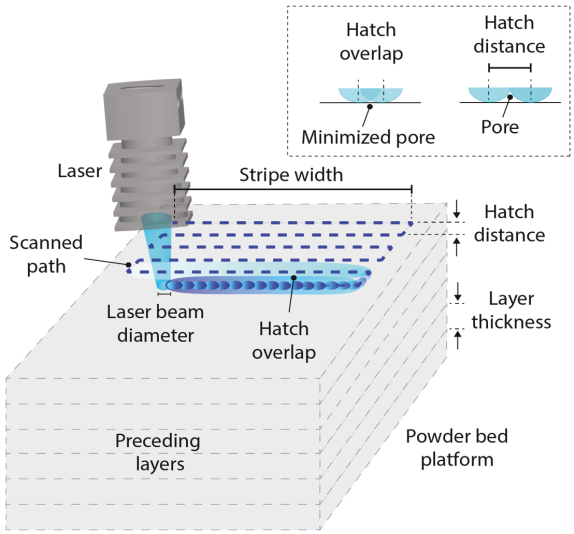


**Fig. 15** A schematic of the SLS 3D printing process.

#### 5.1.1. Design

The position and orientation of the SLS chamber are crucial when using 3D nesting during the design stage. As a result of the lower temperature of the platform, the bottom section of the construction volume is not as warm as the upper area. Due to the high temperature in the top half of the build volume, this area is more likely to experience powder adhesion. Process modeling for powder sintering might aid in predicting essential aspects that must be addressed during the early design phase [16].

The size of geometrical features has been discovered to be a significant determinant for the volume of partly sintered powders adhering to the component surface owing to heat intensities, severely impacting manufacturing precision. SLS design criteria should consider massive hot masses, a well-known phenomenon. For this purpose, Minetola et al. [16] suggested the SLS modulus, a metric developed to detect crucial heat concentrations in the chamber that can affect the dimensional accuracy of the produced part. Generally, an approximate part accuracy of ±200 µm for small dimensions and ±0.1-1% for large dimensions, as well as a minimum feature size of 0.5-1 mm, should be considered in the design of SLS

parts [32, 121]. In Fig. 16, SLS shows sensitivity to feature size where there is a distinct area of separation using a gradient lattice-based design.

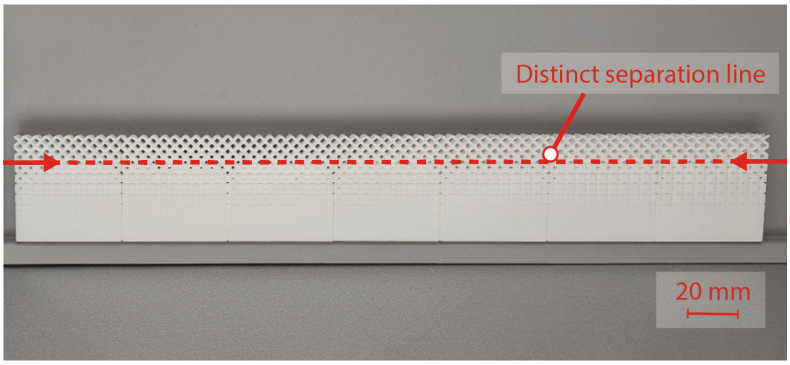


**Fig. 16** Accuracy of gradient lattice-based structures in as-printed SLS samples.

A cross-section of SLS parts shows how local and global features in the design influence part quality. The microscale portion comprises fused polymer powder particles ranging from 10 μm to 100 μm in diameter. The laser heats the particles, fusing them together before solidification. However, incomplete fusion can leave pores within the part, reducing strength, durability, and surface inhomogeneity. SLS parts feature a coarse surface texture at the mesoscale due to particle size polydispersity and unfused powder adhesion based on heat diffusion into the surrounding powder. Non-vertical features are stepped based on layer thickness and orientation [28, 129].

The laser spot size and heat dispersion into the powder limit the minimum feature size in the design step. Freeform geometries, interior cavities (with holes for loose powders), and delicate lattice structures are all possible with SLS. Living hinges, latches, and interlocking parts can also be developed. Then, the interior features must be constructed so that loose powder may evacuate when the component is formed.

Because no support structures are required, and cooling warpage is minimal, unsupported walls and horizontal bridges are more flexible than the MEX system. Nevertheless, design and tolerancing must consider temperature gradients during printing shrinkage. Otherwise, very thin features can deform due to temperature variations in the print environment [130]. SLS cannot attain the same surface quality as other polymer AM, such as photopolymerization (SLA). In general, PBF AM processes, including SLS, slice in the *Z*-direction with constant or adaptive layer thickness, whereas the slicing method in filament-based AM is strictly a limiting factor due to lower dimensional precision because of the staircase effect, the required support structures for overhangs, and poor performance because of the anisotropic design caused by the slicing method [104].

#### 5.1.2. Materials

SLS is versatile as it can process many types of polymers available in powder form, either thermoset or thermoplastic. The powder is vital for the packing density, which is influenced by other parameters, including particle size distribution, particle shape, and spreading system. Bimodal powder distribution can improve the packing density [131, 132], which is given by other parameters, such as particle shape, size width, distribution exponent, and packing mode [133]. Particle shape can affect the powder size distribution as the finer powder can facilitate reaching higher packing densities and improve flow and spreadability. The spreading system is also responsible for optimizing the packing density. A wrong method for the powder on the bed can cause flaws in the packing process and entail artifacts or holes in the part once sintered [134, 135]. The most common materials used in SLS are semi-crystalline polymers of PA12 and PA11 due to their well-defined melting temperature and melt-freeze thermal hysteresis [32]. Compared with amorphous thermoplastics, these polymers result in more favorable processing conditions and improved powder recyclability. Table 8 lists the common polymers used in SLS and their applications.

**Table 8** SLS AM polymer powders classified by structure and performance [32, 129, 136].

| | Structure | | |
|---|---|---|---|
| Application class | Amorphous | Semi-crystalline | Main applications |
| High-performance polymers | - | PEK, PEEK, PEKK | Motorsports, medical engineering, aerospace |
| Engineering polymers | PC* | PA6, PA11, PA12, TPE, POM*, PCL*, UHMWPE*, PLA* | Automotive industry, mechanical components, housings |
| Commodity polymers | PS, SAN*, PMMA* | PP, HDPE | Piping, chemical containers, tooling, medical devices, low-cost prototyping |

* Commercially not available, only studied in the scientific literature

SLS can fabricate complex internal cavities with 3D lattice structures, but features for draining unfused powder must be included. Powder parameters, such as diameter, morphology, size distribution, crystallinity point, flowability, and melting point, also significantly affect the SLS method and the part quality. As a result, there is an increased demand for powders capable of performing SLS [137].

Powders were described as pre-processing parameters but can also be included as printing parameters. Since lasers and powder are connected, it is necessary to study and determine the power based on the powder that will be melted before picking up a laser. Polymers must be considered in terms of their heating properties to be suitable for SLS. Furthermore, the optical characteristics of powders determine the wavelength of light the materials absorb [138]. Semi-crystalline polymers are preferred because of their processability (e.g., PA12). There is a clear temperature range for these polymers, ranging from the glass transition temperature to the melting temperature, with a hysteresis window between melting and re-crystallization. The powder type, including recycled and virgin, can affect the surface quality. In general, recycled powders increase the instability of the feedstock properties, resulting in a higher surface roughness [119]. High flowability is a critical property of materials in the SLS technique. Powders must be highly flowable to minimize highly jagged and microscopic particles with strong inter-particle forces that lead to agglomeration and surface

issues. Goodridge et al. [139] reported 45 and 90 μm as the most favorable range for powder size in SLS 3DP.

In PBF processes, loose powder is typically removed manually. However, it can be more aggressively removed by shockwave cleaning or dry-ice blasting [140], which alters the surface roughness significantly. Low-temperature heat treatment would be beneficial to improve surface quality. It would relieve imposed stress during laser sintering and improve mechanical properties.

Surface modification of powders can increase laser light absorption, flow, and spreadability. Feedstock enhancement could be used to investigate various powder blends with various or multi-modal particle size distributions (PSDs) and create particle-based models for forecasting the deposition parameters (e.g., spreading speed) and the powder beds packing (e.g., inter-particle friction) and [69]. The thermal history of the polymers is also essential as the molecular weight of the polymer can change when it goes through heat cycles, influencing its melting and solidification behavior. The working conditions significantly impact this powder, and the sintered cake cannot be recycled near the component. Fresh powder must be mixed with the remaining powder from the previous 3D-printing procedure to closely match the specifications [3].

This technology works with a higher layer thickness (90-150 μm), making it more susceptible to the staircase effect. Because of the sintered grains on the surface, cleaning is difficult [3]. Powder-bed systems are exposed to a frictional force with the bed and an inter-particle force that restrains their motion. For this reason, chemical additives can be added to the powder to have a higher spreadability [141, 142]. There is a variation in the laser beam over the whole build plate. The angle of incidence can significantly impact the outcome of the part [143]. Therefore, new machines with two laser beams are currently available. However, having two different power sources leads to a slightly different sintering process. Furthermore, portions of the stage where the two lasers work almost simultaneously cause a point or line of poor or no sintering.

#### 5.1.3. Laser

The mechanical strength and density of SLS objects depend heavily on the laser beam energy density. As the laser rasterizes over the powder bed, its movement strategy and direction are essential. Generally, higher laser beam energy density results in higher densities and greater mechanical strength of the final part, up to a certain point. If the powder particles are over-melted beyond this threshold, the properties of the part may begin to deteriorate [144]. The most often used SLS printers use diode lasers. The laser power ($P$), the laser scan speed ($v$), the focus diameter, and the hatch distance (scan line distance) all affect energy density ($ED$) [145]. The hatch distance includes two parameters: layer thickness ($t$) and scan space ($s$). Depending on the laser power ($P$) and beam movement on the materials, the powder bed obtains the proper heat for fusion. Accordingly, ED is the laser beam input energy per unit area ($J/mm^2$), and it can be calculated using Equation 17 [146]:

$$ED = P/(v \times t \times s)$$ Equation 17

In this equation, if the hatch distance (in *mm*) is more than the effective laser diameter (in *mm*), the effective laser spot size would be considered [147].
Sintering requires a certain amount of laser power due to laser-powder interaction, which depends on the material and layer thickness. Because the laser beam diameter and materials formulation affect absorption, they can raise or lower the sintering/melting temperature. It affects the laser wavelength required for sintering. In addition, pulse durations (for pulsed lasers), geometries, and frequencies can impact surface quality. Shorter pulse durations can lead to more precise melting and less heat buildup, resulting in smoother surfaces with less porosity. There is usually an offset between the laser and the design border because of the light spot that must be considered. During the sintering process, a low-power laser is used to smear the particles that can remain attached along the contour [134, 148].

The dimensional accuracy of the printed product causes excellent process accuracy in SLS. Shrinkage is one of the critical factors influencing accuracy, and the quantity of shrinkage seen hugely depends on materials and laser sources. Laser power and scan length have a substantial impact on *X*-direction shrinkage, whereas beam speed and laser power have a significant effect on *Y*-direction shrinkage. In contrast, bed temperature, beam speed, and hatch spacing considerably affect shrinkage in the *Z*-direction [130].

#### 5.1.4. Build Chamber

A typical mainstream SLS system has a medium build size of 340 × 340 × 600 (mm). When a product exceeds the build platform volume, it must be split into multiple pieces, designing separation planes, and considering subsequent assembly procedures affecting the surface quality [149]. The part size is constrained on the upper end, restricted by the build volume of the printer and the ability of the optics system to scan the entire area. This volume typically ranges between 10 and 1000 L (0.01-1 $m^3$). However, it is possible to reach a smaller size in some designs as 0.005 $m^3$. Due to the minimal residual stresses, the entire build volume may be utilized by stacking pieces on top of one another without the requirement for support to connect the parts to the build platform. The size of small parts is constrained by the minimal feature size, the related precision and resolution, and the assembly of the components [149]. The powder particle and laser spot size restrict the precision of less prominent features. All these variables, coupled with the powder material and thermal boundary conditions, affect solidification kinetics and, hence, dimensional accuracy. In terms of depth and length, the larger-the-better rule applies to the part size to obtain the desired object. Whereas roughness and geometric precision are determined by the nominal-the-better rule [127].
Several build chamber parameters, such as layer thickness, roller speed, heating-cooling rates, build size, and powder and feed bed temperatures, impact the SLS process. There are several gradients of temperature

in the build chamber to be considered [150]. Besides the *Z*-axis, where the part suffers a decrease in temperature for the higher layers while the stage moves downward, the platform has some increased temperature along the diagonals, and the center can be caused by the presence of heaters or mechanical components underneath. The blade shape used for powder application also affects the surface quality. Beitz et al. [69] demonstrated a flat bottom form was more advantageous than sharp or slightly rounded edges. Due to the larger horizontal contact zone between the powder bed and blade, the powder material is compressed evenly, resulting in a more dense and consistent powder layer.

### 5.2. Surface roughness studies and discussion

SLS allows the production of components with high levels of complexity, almost no geometrical constraints, and no need for a tool or a mold. The resulting parts have an enhanced surface roughness due to optimizing the processing settings, the build orientation, and the powder characteristics [66]. Although roughness cannot be removed entirely, several researchers have attempted to decrease the deficiency by modifying the printing process parameters and operating at different parameter levels.

In many cases, PPFTs primarily affect the surface roughness obtained through SLS. Nevertheless, several studies have attempted to optimize the parameters of the process. Sachdeva et al. [124] investigated and used response surface methodology (RSM) to optimize the SLS process parameters for roughness ($R_a$, $R_z$, and $R_q$). Beitz et al. [66] reported that the CLSM measurement yielded roughness ranges of $R_a$: ~24-31 µm and $R_z$: ~157-181 µm, while the XMT method produced $R_a$: ~22-27 µm and $R_z$: ~128-148 µm for PA12 powder. Most research has focused on PA12 as the feedstock material to determine optimal parameters for processing based on roughness conditions. However, limited research [151, 152] has been conducted on other materials. As listed in Table 9, different process parameters were considered in the method.

**Table 9** Overview of studies on surface roughness in SLS (see text* below the table for abbreviations).

| Materials \| Machines | Methodology and studied parameters | Roughness range (µm) | Remarks | Ref. |
|---|---|---|---|---|
| PA12 (2221) \| EOS Formiga P110 | p.temp. (167 °C), l.p. (25 W), h.d. (0.25 mm), p.s. (2500 mm/s), l.t. (0.1 mm), p-p. (glass-bead), s.r.m.m. (contact + non-contact profilometry) | Tactile A: $R_z$: 95-120; $R_a$: 13-17<br>Tactile B: $R_z$: 100-124; $R_a$: 13-17<br>FV: $S_z$: 180-240; $S_a$: 14-18<br>FPT: $S_z$: 270-400; $S_a$: 15-22<br>CLSM: $S_z$: 350-450; $S_a$: 23-27 | - Optical and tactile methods showed increased values for $R_z$, which was typical for SLS parts<br>- $R_z$ and $S_z$ were easily influenced by outliers, so they are not ideal for describing s.r.<br>- $R_a$ and $S_a$ allow a narrower distribution, but peaks and valleys can cancel out<br>- The tip in the tactile method changed the surface<br>- The tip pulls loose particles from the surface or cannot detect valleys. The measured values are quickly reproducible, but the actual topography was uncharacterizable<br>- Optical measuring methods allowed 3D visualization of surface topography, but results vary. FV results closely resembled tactile measurements | [66] |
| PA12 \| DTM 2500plus | l.p. (12.5-17.5 W), plat.temp. (128-138 °C), l.t. (0.12-0.18 mm), a.m. (DoE Taguchi L9, ANOVA), s.r.m.m. (contact profilometry) | $R_a$: 1.45-1.79 | - Optimal values of PPP for s.r. were l.p. (15 W), plat.temp. (133 °C), and l.t. (0.15 mm)<br>- The portion of key parameters influencing s.r. were plat.temp. (55.6%), l.t. (23.11%) and l.p. (16.07%) | [127] |
| PA12 \| DTM 2500 & Sinterit Lisa desktop SLS | DTM 2500: l.p. (10 and 13 W), r.s. (7.62 and 12.7 cm/s), h.d. (0.152 and 0.127 mm), plat.temp. (175 °C), l.t. (0.1 mm), e.d. (0.15 J/mm$^2$)<br>Sinterit Lisa: p.r. (0.84 and 1.08), e.d. (400-700 J/mm$^2$), a.m. (ANOVA), s.r.m.m. (non-contact profilometry (FV)) | DTM: $S_a$: 12.431-23.847; a.r.: 1.620-2.454<br>Lisa: $S_a$: 13.757-14.328; a.r.: 1.620-2.454 | - Lower r.s. and recycled powder (compared to virgin) contributed to a higher s.r.<br>- The greatest average s.r. was recorded when l.p. (13 W), r.s. (7.62 cm/s), h.d. (127 µm), and recycled powder was used<br>- The smallest average s.r. was recorded when l.p. (13 W), r.s. (12.7 cm/s), h.d. (127 µm), and virgin powder was used<br>- The same settings were used to maximize and minimize the area ratio, which helped investigate the tribological properties of SLS parts<br>- s.r. was not significantly affected by powder type or p.r.<br>- Based on ANOVA for s.r., the main effects were powder type, h.d., and r.s. | [119] |
| PA12 \| Sintratec Kit | 3 different combinations of blade and roller (counter-rotating roller, forward-rotating roller, and a combination of blade and roller), l.p. (Diode Laser: 2.3 W, 445 nm), plat.temp. (bed: 171 °C, | CLSM: $R_a$: ~24-31; $R_z$: ~157-181<br>XMT: $R_a$: ~22-27; $R_z$: ~128-148 | - Forward-rotating roller caused defects in the powder bed<br>- The lowest $R_a$ was achieved with a flat bottom geometry of the blade | [69] |

| | | | | |
|---|---|---|---|---|
| | chamber: 147 °C), h.d. (550 mm/s), l.t. (0.120 mm), f.d. (0.25 mm), h.d. (0.3 mm), s.r.m.m (non-contact profilometry (CLSM and XMT)) | | - A round or sharp blade reduced the effective V. compression force, leading to increased $R_a$<br>- The obtained s.r. was affected mainly by the measuring method<br>- There was no significant difference between the three fractions of PA12 surface quality, confirmed by s.r. measurements in powder deposition direction and perpendicular to it<br>- A flat bottom shape was found to be more advantageous than sharp or slightly rounded edges for the surface quality of a powder bed, resulting in lower s.r.<br>- There was no significant difference between the direction of application of the powder and that perpendicular to it<br>- As with the arithmetic s.r., powder composition and blade geometry had a similar influence on the average s.r.<br>- The fine and coarse powders and the powder deposition direction had no significant influence on s.r. | |
| PA12 (2200) \| EOS Formiga P110 | The cross-sections were hatched alternately, p.size (d50, 3: 58 µm) l.p. (25 W), p.s. (2500 mm/s), plat.temp. (167 °C), l.t. (0.1 mm), e.d ( 0.4 (J/mm$^2$), b.o. (0°, 45°, 90°), s.r.m.m (non-contact profilometry | $S_a$: ~25 (H.), 30 (45°), ~25 (V.); $S_z$: ~285 (H.), 315 (45°), 235 (V.); $R_z$: 3 (H.), 0.5 (45°), 1.5 (V.) | - Highest s.r. measured at a layer orientation of 45°<br>- Tribological applications: 90° orientation partially led to a longer running-in-phase as higher wear | [153] |
| PS & PS+ CB \| DTM 2000 | $CO_2$ laser at a chamber filled with the nitrogen atmosphere with a maximal 5.5% $O_2$<br>PS at preheating conditions: plat.temp. (90 and 100 °C), l.p. (6-21 W), p.s. (1000 mm/s), h.d. (0.15 mm: about one-third of f.d.), plat.temp. (167 °C), l.t. (0.1 mm), e.d. (0.1-0.12 J/mm$^2$)<br>PS with 0.3 wt-% CB at plat.temp. (100 °C), l.t. (0.1 mm), preheated at 65 °C by infrared radiation heating s.r.m.m (contact profilometry) | PS at plat.temp. (90 °C): $R_a$: ~14-42; $R_z$: ~100-270<br>PS at plat.temp. (100 °C): $R_a$: ~3-13; $R_z$: ~10-100<br>PS + CB at plat.temp. (100 °C): $R_a$: ~18-34; $R_z$: ~125-240 | - Evaluation of the processability of PS and the use of CB as a coloring additive was conducted, focusing on the bed temperatures and laser parameters<br>- s.r. of the monolayer parts indicated the coalescence between the consecutive laser tracks<br>- Higher plat.temp., different laser scan strategies, or more l.p. optimization can improve surface quality<br>- Higher $R_a$ and $R_z$ at plat.temp. (90 °C) when used higher l.p., especially in the transversal direction due to lousy coalescence between consecutive laser scan tracks at this bed temperature<br>- Optimal processing parameters being at plat.temp. (100 °C) and l.p. (18 W)<br>- Application: Investment casting | [151] |
| PA12 (2200) \| EOS P395 | The DeVIDE software was used to predict $R_a$ values for various implants using CT scan data, the material, and the standard build parameters: laser type $CO_2$, l.p. (50 W), p.s. (8000 mm/s), plat.temp. (176 °C), l.t. (0.12 mm) | Predicted $R_a$: 14.4-34.67 | - A simulation-based s.r. evaluation was performed to assess various implant prototypes<br>- Application: Medical purpose, bone implants | [154] |
| PA12 (650) & PCL \| OpenSLS | p.size (55 µm for PA12 and 600 µm for PCL), s.r.m.m (SEM) | Unsmoothed: $R_a$: ~34.0 (PA12), ~115.6 (PCL)<br>Smoothed: $R_a$: ~3.9 | - $R_a$ was proportional to particle size for both nylon and unsmoothed PCL<br>- Large powder grain (~500 µm) led to part surfaces with high s.r.<br>- Unsmoothed PCL had $R_a$ that reflected the visible rough texture of sintered PCL<br>- Smoothed PCL exhibited significantly improved mechanical properties, making it a superior material for bone medical purposes<br>- Application: Tissue engineering | [155] |
| PA11 \| - | b.o. (H. and V.), s.r.m.m (contact profilometry) | As-printed $R_a$: ~25-50 (T.), ~7-35 (B.)<br>After p-p. $R_a$: ~15-25 (T.), ~3-15 (B.) | - An increase in the *XY* and *ZY*-orientations was shown to increase s.r.<br>- p-p. significantly reduced s.r. due to a more consistent density | [156] |
| SLS: PA12 \| EOS Formiga P110<br>MJF: PA12 \| HP MultiJet Fusion 3D 4200 | SLS: l.p. (16 W), plat.temp. (167 °C), l.t. (0.1 mm), p.s. (1500 mm/s), and h.d. (0.25 mm), $CO_2$ laser (λ: 10.6 µm)<br>MJF: l.t. (0.08 mm), p.s. (10 s/layer) s.r.m.m. (contact profilometry) | SLS: $R_a$: ~14.62 (T.), ~14.40 (B.)<br>MJF: $R_a$: ~15.58 (T.), ~6.31 (B.) | - The set of parameters for SLS could be optimized for the best s.f.<br>- T. and B. s.r. of the SLS were very similar<br>- T. s.r. of SLS and MJF were extremely close, but B. s.r. of MJF was significantly better than SLS, likely due to detailing agent application<br>- In SLS, the un-melted core was distinctly smaller than in MJF due to the powerful instant heating capability of the laser | [157] |

| | | | | |
|---|---|---|---|---|
| | | | - A higher crystallinity was observed in SLS parts compared to MJF, which resulted in higher impact properties and better d.a. | |
| SLS: PA12 \| DTM 2500plus<br>MJF: PA12 \| HP MultiJet Fusion 3D 4200 | l.p. (38 W), p.s. (10 mm/s), h.d. (0.25 mm), plat.temp. (175 °C), l.t. (0.1 mm), e.d. (0.15 J/mm$^3$), a.m. (ANOVA), s.r.m.m. (contact profilometry) | SLS: $S_q$: ~17.5 (B.), ~24 (S.), ~19 (T.); $S_{sk}$: ~–0.3 (B.), ~–0.15 (S.), ~–0.1 (T.); $S_{ku}$: ~3.2 (B.), ~3.5 (S.), ~3.3 (T.)<br>MJF: $S_q$: ~16-17.5 (B.), ~17-19 (S.), ~17.5-24 (T.); $S_{sk}$: ~–0.4-0 (B.), ~–0.45-–0.1 (S.), ~0.1-0.5 (T.); $S_{ku}$: ~3.0-4.5 (B.), ~3.2-4.3 (S.), ~3.1-4.2 (T.) | - There was a significant impact of the orientation within the build chamber on the bottom surface of the cubes<br>- The influence of orientation was reflected in a similar value of $S_q$ for all the cubes, but a distinct height distribution was indicated by $S_{sk}$ and $S_{ku}$<br>- Because of thermal bleeding, T. s.r. of SLS varied depending on the selected build region<br>- SLS and MJF exhibited this inhomogeneity issue, and the cube closest to the platform's center (usually the most isothermal region) revealed a skewed and spiked height distribution<br>- Homogeneous surface topography across parts requires thermal bleeding control | [28] |

*Abbreviations a.m.: analysis methods, a.r.: area ratio, b.o.: build orientation, d.a.: dimensional accuracy, e.d.: energy density, f.d.: focus diameter, h.d.: hatch distance, l.t.: layer height, l.p.: laser power, p.r.: power ratio, p.s.: printing speed (laser scanning speed), p.size: powder size, p.temp.: printing temperature, plat.temp.: platform temperature, p-p.: post-processing, r.s.: roller speed, s.f.: surface finish, s.r.: surface roughness, s.r.m.m: surface roughness measurement method, B.: bottom, S.: side, T.: top, H.: horizontal, V.: vertical

In agreement with the reviewed papers in Table 9, the average particle size, layer thickness, and surface orientation can substantially influence surface roughness among a wide range of variables. Material viscosity, surface tension, and thermal boundary conditions such as bed temperature play a role in melting and solidification. Heat dispersion into the surrounding powder generates a thin layer of unfused powder to cling to the component surface to achieve the most delicate surface quality. The powder size and the laser spot restrict the part accuracy of less prominent features. These parameters, coupled with the powder material and temperature boundary conditions in the system, influence solidification dynamics, which can also affect dimensional accuracy. Shrinkage during cooling can cause additional losses in part accuracy for bigger features. Concerning laser power, a low energy density can result in loose powder particles that are unable to melt and fuse together sufficiently, resulting in parts that are weak and porous. In contrast, if the energy density is too high, the powder may melt and fuse excessively, resulting in rough surfaces, distortions, and even cracks in the finished parts [119, 127].

While the SLS parts generally show higher surface roughness (10 µm < $R_a$ < 20 µm) compared to FFF (1 µm < $R_a$ < 10 µm), SLS offers many benefits compared to other polymer-based AM techniques [158]. To begin with, no support structures or foundations are needed during the SLS process, since the unused powders support the components. Therefore, there is no roughness caused by support removal. Even though SLS uses unused powders to support the components being printed, this is usually insufficient to prevent all types of deformations. As a result, post-processing steps such as stress relieving and annealing may be required to reduce residual stresses and deformations [119, 157].

Additives such as initiators, binders, and catalysts are not required, which implies the components are more likely to be utilized in the medical field since additives may cause toxicity. Moreover, although SLS resolution is not as excellent as other AM methods, such as SLA, the mechanical properties of SLS

components are usually superior, making the surface of these components more stable over time. The resolution issue may be addressed by improving the laser system. In theory, SLS technology is not material-restricted, and most powders may be utilized in SLS, provided that the laser wavelength and power meet the sintering material requirements. However, this kind of laser/point-based technology (e.g., SLA or SLS) has a common drawback of low processing speed because of the methodology of "point → line → face (slice) → body" [157].

## 6. Vat photopolymerization (VPP)

Vat photopolymerization produces parts with a resolution close to 100 nm [159], leading to superior surface quality. While the design choice can bring some advantages and some disadvantages in terms of texture, the process selection is still critical. In a top-down VPP setup, the build plate dips in the resin to create a new layer, and generally, a recoating system makes the printed surface smoother. Despite this mechanism and a consequent reduction of the necessary supports, the recoating procedure may cause some convex undulations on the resin surface and on the printed layer afterward. It is due to tensions, especially with highly viscous resins or really thin layers. Thus, surface bubbles can remain trapped inside the part but also can groove the surface [160, 161]. Using scraper blades can attenuate these issues by adjusting the layer thickness of the new resin on top of the part [162].
Alternatively, the bottom-up approach, where the light source is placed below the vat, and the build platform moves stepwise upwards, resulting in accurate details but a more corrugated surface [163]. Moreover, confined layers due to the space in between the transparent window at the bottom of the vat and the build plate allow the system to achieve better Z resolution. However, the layer, once cured, attaches to the glass window, and the detachment step might cause it to lose material and have defects. To reduce detachment forces during this phase, the vat is usually coated with a polydimethylsiloxane (PDMS) layer or an anti-adhesive membrane made of PTFE [161, 164] with an additional protective layer of fluorinated ethylene propylene (FEP) to have good anti-sticking effect and durability [165]. The latter seems more resistant to degradation and all the problems this may cause to the quality of microfeatures [166] but has a more complex tightening method that can lead to deformed features and light refraction when applied incorrectly [161]. These approaches constitute a layer-wise method and generate staircases along vertical surfaces.

VPP defects generally occur due to non-optimized print parameters, insufficient supports, improper model generation, and contamination in the build platform and resin material. For each layer to be cured entirely through its thickness and uniformly recoated, the print parameters, such as scan speed, power source, and recoating process, must be optimized [167]. Another common problem with VPP resins is their tendency to turn yellow quickly. This is mainly because of overexposure to ultraviolet light, which also causes clear prints to appear matte yellow (Fig. 17).

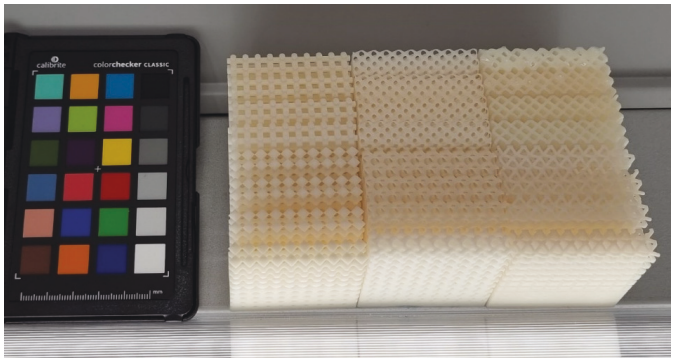


**Fig. 17** Appearance and accuracy of gradient lattice-based structures in as-printed SLA samples using PrimaCreator Value resin. After 12 hours, a yellowish color began to appear.

## 6.1. Process parameters

### 6.1.1. Design

The design role in PPP regards creating the model system on a CAD system and handling the photosensitive resin independently of the technology used. CAD format is tessellated into the STL data, and this is the phase where decisions about surface modeling are made. For instance, essentially flat and/or thick sections are prone to warp because of shrinkage. The STL file approximates three-dimensional surfaces with triangular facets, which may result in errors in dimension, form, and surface [168]. Incorrect conversion of a solid model into an STL file can cause missing or distorted features. In stereolithographic technology, the STL file is sliced into several horizontal layers and then commonly saved in CLI file format [169]. Similar to the FFF method, many parameters such as print direction, layer thickness, the inclination of the part, hatch spacing, fill spacing, hatch over-cure, border over-cure, and fill cure depth are essential to improve surface quality without resorting to a large number of facets and a long build time [168, 170]. Considering the presence of supports is crucial because if the support density is insufficient, the part can also shift or detach entirely from inadequate supports [171]. The supports cause unavoidable staircase effects on bent or sloped surfaces, but they can be reduced by adjusting the printing parameters mentioned above [172]. In this case, the adaptive slicing method, as a typical practice in FFF, is acquiring more attention to improve the surface quality and surface roughness in VPP methods [96, 173].

### 6.1.2. Materials

The most popular materials for VPP are photosensitive resins, usually containing acrylates, methacrylates, vinyl, and epoxies monomers/oligomers. Acrylates and methacrylates monomers/oligomers are a subcategory of the vinyl group and the presence of the carboxylic group (-COOH) in the vinyl position

confers them high photo speed as they react quickly when exposed to UV radiation. Moreover, they behave differently in terms of radical formation. Acrylates tend to form secondary radical ends, whereas methacrylates tend to form tertiary radical ends. This difference in radical end formation makes methacrylates more stable and less reactive than acrylates. However, both of them undergo significant shrinkage with associated stress that might result in warping or curling [174, 175]. Moreover, they suffer from the inhibiting influence of oxygen and this facilitates the formation of a sticky surface appearance due to oligomer formation [176]. They also have low viscosity and critical energy, increased light sensitivity, relatively high dependence on humidity and temperature fluctuations, and controllable mechanical properties [177].

Vinyl monomers appear in both radical and cationic polymerizations and a mix with acrylates or epoxies enhances their respective characteristics. They provide relatively low thermal resistance and low glass transition temperature and they tend to exhibit brittleness, low elongation, toughness, and impact resistance [178]. Epoxy monomers instead have an oxirane functional group, which is a three-member ring formed between oxygen and two carbon atoms and when they react, these rings open, resulting in vacancies for other chemical bonds. This opening is known to have an influence on the volume change because the bonds remain the same and, as a result, epoxy resins typically present much smaller shrinkage and much less tendency to warp and curl. Furthermore, the products have high structural stability, higher mechanical performance, insensitivity to oxygen, and lower shrinkage stresses compared to radical polymerization of (meth)acrylates and vinyl monomers [175, 179]. All these monomers can be also added as additives with the function of chain transfer agents, specifically addition-fragmentation chain transfer (AFCT) agents, in a poly-functional way, with the intent of having, for instance, lower shrinkage stress, higher cross-linking density, or tougher polymers [180, 181]. Besides monomers/oligomers and additives, the photocurable resin generally presents reactive diluents, UV stabilizers/blockers, and photoinitiators.

Also, adding particles as reinforcement in a resin can result in reduced or absent curing or in an accumulation of the particles, leading to a nonuniformity or degradation of the support. Studies about the size of the particles [182] and their interaction [183] were found essential to obtain the best outcome. Therefore in VPP, the cure kinetics of the polymerization process related to the resin viscosity, light intensity, chemical functionality, illumination time, and the additives in the formulations, play a crucial role in determining the final surface finishing and appearance of the prints [179]. In fact, the choice of light absorbers, the photo-initiator, and the monomers and oligomers can reduce the staircase effects, improve the resolution of printed objects and produce optically more transparent layers and surfaces. Kowsari et al. [184] evaluated the influences of polymer formulation on the printing resolution and surface quality. In particular, by trying different formulations of (meth)acrylates-based monomers and oligomers with some of the most common photoinitiators, they found that dimethacrylate-based resins can improve the surface finishing by reducing the staircase effects and removing jagged edges. Moreover, enhancing the expected reflectance at the same wavelength is possible with different photopolymer formulations [177]. The

selection of photocurable resins is usually according to the properties needed, such as quality of finish [185], durability [186], flexibility [187], transparency [188], bio-compatibility [185, 187], and cost [189]. They need to be stored in dark rooms to avoid the photopolymerization process initiates.
Moreover, when the resin is poured into the vat, it may contain air bubbles that reduce the achievable resolution and cause surface artifacts in the final object. Therefore, removing all the impurities and air from the photopolymer is necessary. It is possible to do so by shaking the resin manually or with the help of some machines, such as roller grills or shaking machines [161].
When the resin is not fully polymeric but with a mole percentage of other compounds, another step that is part of the preprocessing is the mixing process, which is requested to be as uniform as possible
Polymers are not the only materials that can be used in photopolymerization processes. Diptanshu et al. [182] assessed how introducing fine ceramic powder can improve the density and reduce the porosity of the prints. The interaction between photopolymer and photons greatly influences the surface quality of the part. As well as laser power and uncontrolled photon flux, a nonuniform surface relief during the material solidification generates features much larger than the voxel size. Ambient factors, such as vibrations and jittering of the laser and its scattering while impinging the surface, may cause voxel displacements and fluctuations of printed voxels, inducing a weaker photon flux and defects in the layer so formed [184, 190]. During the printing process, contaminants, such as partially cured regions or external particles, can cause voids and deficiencies in the build since the resin cannot be recoated evenly. A damaged resin tank or dirty optics may also result in improperly cured regions, resulting in internal voids or inclusions. Last, voids within the resin caused by trapped air or not uniformly recoating the next layer will result in voids in the printed part [177]. Photopolymerization can also be affected by oxygen inhibition due to a different air in the room (with an inert gas), high-intensity irradiance lamps, or physical barriers [191, 192].

#### 6.1.3. Printer setup

The setup of the printer and the influence of polymer mass and viscosity can also affect the surface finish, which is divided into two major categories:

- The bottom-up approach: the material is cured through a window, and a membrane of PTFE is placed in the bottom of the vat with a light source. In this setup, the build-plate is raised every time to let the new resin occupy the volume underneath, and a ‘peel’ step is necessary to detach the cured resin from the bottom of the vat. The ‘peel’ step is time-consuming because the resin needs extra time to recover the initial state before starting the new layer [193].
- The top-down approach: a light source above the vat cures the material, and the build-plate is submerged. Instead of ‘peel’ steps, this setup employs continuous light exposure to cure the resin. It enables the achievement of high resolutions and printing speeds for this approach. The surface is traversed with a scraper to recoat and minimize eventual surface tensions [162] or can provide a

dynamic characterization of the shape of the surface of the resin and adjust the light intensity accordingly [194].

Regarding the exposure strategies, in the bottom-up approach, there are no micro-fluctuations or contamination of the resin during the process since the bottom of the vat flattens each layer but the detaching step might cause a corrugated surface with accurate details in the surface of the products [163]. However, in the top-down approach, there is not as much stress on the printed part during the printing process as in the bottom-up approach since the subsequent layer is not being sheared off after each layer is cured. Nonetheless, the overall distortions of the surface due to the motion of the stage normally require a recoating procedure that still can cause undulations on the printed layer. Moreover, longer printing times and slightly better resolution and quality of the printing drive the choice for the bottom-up approach. Other setups are related to different components that make the technology unique and solve some of the drawbacks. For instance, an oxygen-permeable window in CLIP technology solves the peeling step issue by preventing the resin from attaching to the window. At the same time, it controls the curing of the resin letting it have sufficient time to flow underneath the build plate and completely homogeneously the curing of the subsequent layer. In this way, the platform can move almost continuously upward [191, 192].
DPP technology uses an LCD unit to project the sliced 2D images, which has great potential resolution/cost-wise but has overall limited optical efficiency and lower resolution. In addition, working with an electric field that blocks the passage of light, has a low switching speed (within 20 ms) and this may cause a few liquid crystals to remain trapped, resulting in weak light leakage and lower resolution [169, 179]. Hot lithography has the advantage of having a heating element able to control the viscosity of the resin and the temperature of the process. A higher temperature increases the reactivity of the monomers and the polymerization rate and the efficiency of the process [195].
Two-photon photopolymerization employs a femtosecond compact laser beam as a light source that absorbs two photons simultaneously. The photons are absorbed by the photoinitiators at the same frequency (degenerate process) in the near-infrared range (NIR). To trigger the third-order nonlinear two-photon absorption process, light sources with very high photon density are required. Since the light intensity in the laser beam respects a Gaussian distribution, in TPP the square value is considered and the region where polymerization occurs is lower than in normal conditions. In this way, a pulsed femtosecond laser with an acoustic-optical modulator (AOM) to disperse the beam into zero- and first-order diffractions, or two light beams (stimulated emission depletion or STED) are the most preferred setups, because they can modulate the intensity and better control over the cross-linking process. Therefore, the resolution of the process and the connected feature size of the voxel improve until reaching details of 100 nm [32]. The concept is described in more detail in a study by Malinauskas et al. [258].

#### 6.1.4. Curing system

In most cases of VPP, the substance is sensitive to light (but not necessarily), i.e., it will absorb the energy of the photons [177]. This energy induces either phase transitions (evaporation, melting, plasma) or chemical reaction in the material. As many materials can absorb light energy, VPP is a very versatile method for selection. However, there are significant variations in the specifications of the main VPP branches, such as the light source (UV or laser), feature size (nm to m), applicable materials, sensitivity to processing parameters, and the possibility of multi-material printing and commercialization capability.
In most VPP technologies, the object is created by irradiation of the photosensitive resin with a UV or laser beam source that enables the cross-linking of the polymer chains. It is scattered and absorbed when UV radiation or a laser beam hits the surface. This creates a threshold for the penetration of the light in the resin and, therefore, a cure depth for the photopolymerization process. The cure depth is given by Equation 18 [169]

$$C_d = D_p \ln [E_{max}/E_c] \quad \text{Equation 18}$$

where the maximum exposure energy is represented by $E_{max}$, the critical energy required from the resin to begin the reaction is denoted by $E_c$, and $D_p$ is the depth of penetration defined by

$$D_p = 1/(2.3\ \varepsilon\ [I]) \quad \text{Equation 19}$$

where $[I]$ is the concentration of the photoinitiator and ε is the molar extinction coefficient.
The energy dose considerably affects surface roughness and dimensional accuracy through the curing process [196]. In SLA, the projection system is the key factor that can sensibly modify the appearance of the part. A galvanometer scanning technology provides the steered beam through a movable mirror system to the resin surface and determines the precision grade. The exposure energy at the surface is determined by the steered beam as follows

$$E = \sqrt{2/\pi}(P/W_o V_s) \quad \text{Equation 20}$$

where $P$ denotes the laser power, $W_0$ is the beam radius, and $V_s$ represents the scan speed [169]. In line with the equations above, it is possible to see how much the entire process can undergo the projection system. The power, velocity, and hatching of the laser spot determine the depth and size of the feature.
Independently from the build orientation, there is a low anisotropy set by the cure depth according to the layer thickness. In fact, the layer thickness is lower than the cure depth, which means that an additional beam dose passes through to the previous layer to facilitate the adhesion and the bonds between subsequent layers [161, 197]. Furthermore, the width of cured resin ($L_w$), as determined by the center of the laser beam,

influences the resolution and dimensional accuracy. When the laser beam passes over the same points while hatching the layer, some points might be over-cure or under-cure. For a successful solidification, it is essential to define a hatch-spacing related to the width of the cured resin [169]. Non-uniform laser power density is another important parameter that can be caused by either acceleration or deceleration of the galvanometer at the end of the hatching and along the boundaries. This can be overcome by either modulating the laser power as a function of scanning speed during acceleration or deceleration or keeping the same scanning speed while switching on and off throughout the job [198].

### 6.2. Surface roughness studies and discussion

The parameters affecting the surface quality can be identified by further examination of the most critical technologies in VPP. Nowadays, the research in surface quality for the Vat photopolymerization technique is extensive, mainly because it combines an affordable price with high performance in terms of printing precision and time. There has been considerable research on SLA and DLP, the oldest and most commercialized technologies. Still, new trends are emerging due to their faster print speeds, such as CLIP [32, 191], and higher and higher resolution, like TPP [194]. Instead of surface roughness, recent significant research results are presented, focusing on SLA and DLP in Table 10.

**Table 10** Overview of studies on surface roughness in VPP (SLA and DLP) (see text* below the table for abbreviations).

| Materials \| Machines | Methodology and studied parameters | Roughness range (µm) | Remarks | Ref. |
|---|---|---|---|---|
| Proprietary Resin \| SLA XJRP-SPS600 | f.d. (0.1 mm), l.t. (0.1 mm), p.s. (8 m/s), b.o. ([10º-90º], 10º step), s.r.m.m. (contact profilometry) | $R_a$: ~3-17 | - b.o. 10º and 90º resulted in the highest (17 µm) and lowest (3 µm) s.r.<br>- Increasing b.o. continuously decreased s.r.<br>- The s.r. was remarkably reduced after coating with the polyethylene wax emulsion | [199] |
| UTR9000 resin \| SLA Shanghai Lite-450 | l.t. (0.09, 0.12, 0.15, 0.18 mm), over-cure (0.19, 0.21, 0.23, 0.25 mm), l.p. (270, 290, 310 and 330 mW), h.d. (0.07, 0.08, 0.09 and 0.10 mm), p.t. (5 min), r.h. (34%), a.m. (DoE Taguchi L16), s.r.m.m. (contact profilometry) | $R_a$: ~3.76-3.99 (For different l.t.), ~9.87-20.05 (For different width), ~6-30 (V.), ~1,49-2.6 (H.) | - The process parameters that affect the s.r. in the direction parallel to the scanning direction were based on the following order: l.t. > l.p. > p.t. > h.d.<br>- High random errors in the direction parallel to the scanning direction at various positions for the same part, whereas s.r. differed according to b.o. due to l.p., temperature, and r.h. inside the machine. | [200] |
| PR48 CPS resin \|Ember DLP | l.t. (0.010, 0.025, and 0.050 mm), e.t. (1.2-2 s), s.r.m.m. (non-contact profilometry) | $R_a$: 1.5-6.4 (V.), ~2.2-2.4 (H.); $R_z$: 9.7-21.9 (V.), ~7.1-8.6 (H.); $R_q$: 15.9-49.4 (V.), ~67.5-74 (H.); $R_{sk}$: 0.1-0.4 (V.), 0.1-0.2 (H.) | - The surface profile angle was predicted with a maximum error of 2°, and the average s.r. was predicted with an error of 2.7 µm.<br>- The l.t. was found to influence the light-induced s.r compared to the exposure time | [201] |
| Accura ClearVue \| SLA ProJet 6000 HD | b.o. ([0º-90º], 30º step for each of F., S., and T. direction), a.m. (DoE Taguchi L20, ANOVA), s.r.m.m. (non-contact profilometry) | $R_a$: ~1.2-3.4, 2.102 (F.), 2.181 (S.), 2.177 (T.), 1.733 (H.), 2.686 (30º), 2.546 (60º), 1.649 (V.) | - Very low s.r. values were observed for SLA parts<br>- The surface where layers are parallel to the b.o. showed higher s.r. compared to the surface with perpendicular layers due to the staircase effect | [202] |
| Synthetic Grey Resin V3 \| SLA Formlabs Form 2 | l.t. (0.025, 0.050, and 0.100 mm), b.o. (0º and 15º), Model structure (solid vs. hollow), was printed at different positions and configurations, a.m. (ANOVA, post-hoc tests, and | $R_a$: ~0.025-2.18 (H.), ~0.025-2.86 (15º) | - The model structure did not affect s.r., but b.o. did<br>- Higher printing precision was reached by aligning the models across the front of the build platform, reducing overhangs, using support structures, and selecting a high-printing resolution | [172] |

| | | | | |
|---|---|---|---|---|
| | Student's t-test), s.r.m.m. (contact profilometry) | | - The staircase effect on the bent or sloped surfaces was caused by the support structure and b.o. It can be reduced by adjusting other PPP | |
| Watershed 1120 \| SLA Viper SI2 | b.o. ([0°-180°], 2° step), h.d. (50, 75, 100, 125 µm), l.p. (100 mW for border and 58 mW for h.d.), p.s. (20.5 mW for border and 124.1 mW for h.d.), l.t. (0.1 mm), resolution (7.6 µm (*XY*) and 2.5 µm (Z), continuous-wave laser (Nd:YVO4 solid-state, λ: 354.7 nm) f.d. (250 µm), a.m. (ANOVA), s.r.m.m. (contact + non-contact profilometry) | Contact profilometry: $R_a$: 1.2, $R_q$: 1.6, $R_z$: 6.2<br>Non-contact profilometry: $R_a$: 1.0, $R_q$: 1.3, $R_z$: 6.0 | - Increasing b.o. from 0° to 90° resulted in higher s.r. followed by a slow drop<br>- In the range of 90° to180°, s.r. was increased gradually, followed by a quick drop<br>- Higher h.d. resulted in higher s.r. and less p.s.<br>- The effect of p.t. on s.r. was negligible | [173] |
| - \| SLA apparatus | b.o. (0°-90°), l.t. (0.08, 0.1, and 0.12 mm), a.m. (DoE full factorial design, blocking technique), s.r.m.m. (contact + non-contact profilometry) | $R_a$: ~3.2 | - b.o. and l.t. affected s.r.<br>- Post-curing played a negative role in s.r. | [203] |
| Dental LT Clear Resin \| Customized DLP: projector (OPTOMA EX330e) SLA Formlabs Form 2 | b.o. (0° and 45°), e.t. (18 s), Measurements of s.r. along and perpendicular to the b.o. were carried out, s.r.m.m. (contact profilometry) | DLP $R_a$: 0.57 (H., T.), 1.37 (H., S.), 0.675 (45°, T.), 1.67 (45°, S.)<br>SLA $R_a$: 0.995 (H., T.), 1.225 (H., S.), 1.24 (45°, T.), 1.815 (45°, S.) | - Characterizing the projector light spectrum and using photosensitive resins with detailed curing specifications were significant in terms of material curing to get a higher control on material processing and have lower s.r., good optical properties, and d.a. | [165] |
| NovaFab casting resin \| DLP | a.m. (PSO) | Before optimization $R_a$: 21-38<br>After optimization $R_a$: 13-31 | - p.s. increase by volume decomposition technique and eliminating supports<br>- Segmentation design improves p.s. (by 45.2%), reduces material consumption (by 15.8%), and s.r. (by 19%) through decreasing the support structures and lowering the height of the segment | [204] |
| HDDA, Irgacure 819, SUDAN \| Customized DLP: DMD projection system + UV LED (365 nm) | l.t. (0.050, 0.080 and 0.100 mm), c.t. (2, 3 and 4 s), b.o. (60° to 90°), Gaussian radius (12 µm), Concentrations: Monomer (4460 mol/m$^3$), Photoinitiator (48.27 mol/m$^3$), Stabilizer (4.06 mol/m$^3$), Environmental oxygen (8.69 mol/m$^3$) plat.temp. (300 K), incident light intensity (24.5 mW/cm$^2$), Projection micro-stereolithography (PµSL) for modeling photopolymerization is implemented by Comsol Multiphysics software, a.m. (DoE Taguchi L27, Multi-Objective PSO) | RMSE: 1.45 (V.) 2.13-22.48 (60°) | - All parameters with the order of photoabsorber, c.t., l.t., and oxygen concentrations affected s.r.<br>- Based on PSO, the framework increases p.s. for 50% at the same surface quality for b.o. 90°<br>- Optimized samples showed 18% increases in the surface quality for b.o. 60° at the fastest printing speed<br>- Increasing p.s. resulted in rougher surfaces<br>- V. s.r. (90°) was generally lower than s.r. for tilted surfaces (60°) | [205] |
| 5 different Zortrax resins \| DLP Inkspire 3D | 5 specimens of each resin type were printed with l.t. (0.05 mm), b.o. (0°), i.d. (100%), h.d. (5 mm), and e.t. (10 s).<br>Theoretical s.r. was calculated using analytical pixel analysis measured at 2.4 mm distance, s.r.m.m. (contact profilometry) | $R_a$: 0.410-1.027; $R_z$: 2.370-5.844 | - More rigid materials (Black, Basic grey) showed better flatness because of better bonding during the solidification process<br>- s.r. values were similar for 4 resins. Transparent Yellow resin showed almost 2 times higher s.r. (Maximum $R_a$ and $R_z$) compared other resins<br>- In transparent resins, overcuring might happen as projected UV light while curing the next layer in order might have reached already cured layers. It partially increased e.t in comparison to non-transparent resins. | [206] |

*Abbreviations a.m.: analysis methods, b.o.: build orientation (direction), c.t.: curing time, d.a.: dimensional accuracy, e.t.: (layer) exposure time, f.d.: focus diameter, h.d.: hatch distance, i.d.: infill density, l.p.: laser power, l.t.: layer height (thickness along *Z*-direction), p.s.: printing speed, p.t.: post-cure time, plat.temp.: platform temperature, r.h.: relative humidity, s.f.: surface finish, s.r.: surface roughness, s.r.m.m: surface roughness measurement method, F.: front, S.: side, T.: top, H.: horizontal, V.: vertical

According to Table 10, the quality of VPP printing is primarily determined by the photopolymerization process, exposure strategies, and projection systems. Generally, the projection system plays a prominent role in the resolution and printing quality outcome. The microstructure heavily depends on the technology used, and even if all the parameters are optimized, there will always be an error that is impossible to entirely

remove. For instance, the light permanently distorts how it impinges on the resins. However, the sum of errors can also outperform other optimizations.

In the same VPP technique, the most predominant parameters influencing the roughness are the build orientation and the layer thickness. Indeed, they are directly connected with the staircase effects. In the top-down approach, once immersed in the resin, the part goes down with a depth based on the layer thickness [183]. Reeves and Cobb [207] found a mathematical model for the approximation of the surface roughness considering the layer thickness and the plane orientation (Fig. 18). It consists in

$$R_a = (L_t(\tan\varphi \sin\theta + \cos\theta)/4) + K \qquad \text{Equation 21}$$

where $R_a$ is the roughness average, $L_t$ is the layer thickness, $\varphi$ is the layer profile angle, $\theta$ the surface angle, and $K$ is the composition roughness (up-facing or down-facing roughness).

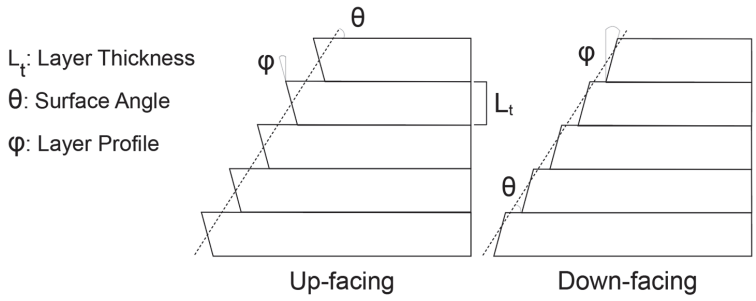


**Fig. 18** Surface roughness for a stepped plane. Adapted from Reeves and Cobb [96].

As discussed above, different systems can offer various methods to get very high resolution, but many other parameters must be considered. Regarding the resin material, the interplay with different photoinitiators, monomers, or oligomers [184], the addition of additives such as stabilizers or light absorbers [32], the addition of ceramic powder [182] and the resulting viscosity [183] in the resin can influence the crosslinking process on the resultant resolution and quality of the features fabricated. On the other side, volumetric shrinkage throughout the curing course is the primary source of errors and the primary parameter of geometrical error [169]. Local temperature variations [208], UV intensity, and exposure time are critical factors that can affect surface roughness and cause under-cured or over-cured parts leading to geometrical errors.

Although various researchers have examined the level of mechanical anisotropy for SLA printed parts [197, 209], Shanmugasundaram et al. [202] and Hague et al. [210] reported SLA printed components can be considered isotropic. The capability to produce isotropic components with SLA is a significant advantage over other AM techniques, such as FFF.

## 7. Material jetting (MJT)

PolyJet technology typically produces high-quality parts with a smooth surface. However, dimensional accuracy for large pieces is usually not similar to other processes, such as VPP, since it uses large droplets, and the accuracy decreases. The accuracy for medium-small size parts is comparable to the other AM technologies [134].

The amount of surface roughness depends on several geometrical and process parameters. MJT produces full-density parts by overlapping adjacent droplets and curing or solidifying them on the spot [8, 211]. A defect can be caused by a clogged nozzle or, in rare instances, by errors in the jetting toolpath. Most AM jetting systems used by professional AM companies are well calibrated and deposit uniform layers without accumulating errors and porosities. However, local variations in topography and layer thickness must be considered when mixing multiple materials and at the interface between the part and the support (Fig. 19). This is caused by the formation of a mini pool and droplets similar to that seen in welding [212, 213].

A variety of methods are available to address and mitigate porosity during the material jetting process, such as using appropriate printing parameters [8, 211], optimizing material properties [214], increasing the number of printed layers to fill in any gaps or voids, as well as modifying the printing pattern [215]. The use of appropriate printing parameters such as droplet size, spacing, and temperature, optimization of material properties such as viscosity, surface tension, and curing time, and modification of the printing pattern such as zigzag instead of straight lines [216], can reduce void formation by ensuring that the material is deposited uniformly and consistently.

While polymer jetting improves the quality and tailor ability of mechanical properties, in general, the properties (particularly toughness and elongation) do not match those of photopolymer parts made by SLA. Jetting compatibility requires resin formulations, compromising the selection of optimal photocuring chemistries [134].

**a)** **b)**

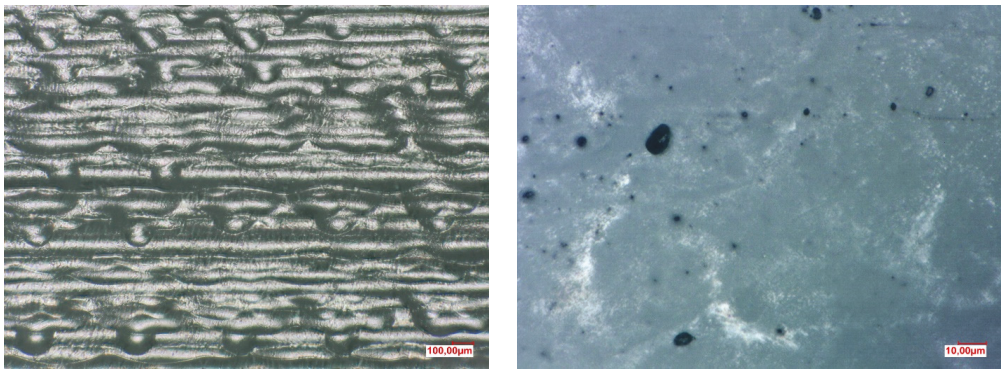


**Fig. 19 a** Deposited droplets in a layer-by-layer structure, and **b** Porosities in the structure of parts printed by Stratasys PolyJet J55 printer.

### 7.1. Process parameters

MJT performance is determined by the fundamentals of the process, such as placement and fusion of consecutive droplets, as well as droplet impact, spreading, and curing. Since the MJT system contains many functions, as described, the printing QAs undergo a higher range of parameters that need to be considered. For instance, part quality in MJT depends on the substrate, material velocity, dynamic viscosity, nozzle distance, total pressure, surface tension, density, the diameter of the nozzle, position accuracy of the *XYZ* motion stages, platform movements, etc. [134]. This section discusses these parameters in four main categories: materials, designs, surface finish settings, and printheads and rollers.

#### 7.1.1. Design

Design plays a crucial role in achieving greater accuracy and preventing printing errors. Due to the layer-by-layer setup of the technology, most of the aspects related to the design of the model described in the section for FFF also have an impact here. However, the layer thickness, orientation, hatch spacing, and speed are more relevant for this technology. Droplet size, spacing, and how they impact the build platform affect the line surface finishing. The less space between droplets results in defects in the reduction of line edges and improvement of the resolution [217]. Accordingly, layer thickness is the most crucial parameter, as seen for most other AM technologies. Generally, a lower layer thickness improves the QAs of the prints. At the same time, a lower space between lines causes a decrease in the eventual ripple along the top and bottom of a layer, resulting in different surface roughness based on the design orientations [24, 70, 217]. Design orientation, including the building location on the build plate, also affects the surface roughness. According to the study by Yang et al. [218], orientation induces different roughness values in the parts. *XZ* build orientation seems to give the highest surface roughness value, while *XY* has the lowest, with the top and the bottom surface reaching high smoothness [218, 219]. Similar to FFF, leveling the build platform prevents distortions and failures and reduces surface defects. An infill density of less than 100% is not regularly achievable for AM parts made from photo resins since support is needed for overhanging features during the printing process to avoid collapse [64]. Fig. 20 illustrates how build orientation (wedge angle) can affect the surface texture of samples printed under similar conditions.

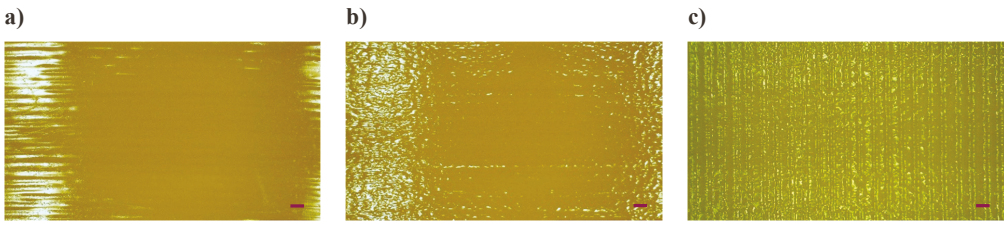


**Fig. 20** MJT-printed samples at different wedge angles: **a** 0°, **b** 45°, and **c** 90° (Scale bar represents 1 mm).

#### 7.1.2. Materials

In most cases, the MJT process uses polymers and plastics, such as Tango and Vero commercial resin. Each of these series has different ingredients. For instance, the FullCure 870 VeroBlack digital material comprises acrylic monomers, epoxy acrylate, urethane acrylate oligomers, and photo-initiators. As an example of support material, FullCure 705 contains acrylic monomers, polyethylene glycol, propane, glycerol, and a photo-initiator [24]. Due to the small and expensive range of materials that can be printed, MJT is limited in its material availability. In particular, waxes and photopolymers are the only commercially available polymers.

MJT "inks" are photo resistors mixed (blended) with waxes and some photopolymers. In modern systems, six liquids (CMYK-W + Support) can be handled simultaneously in separate containers. The printhead can combine multiple materials in a single part and blend pairs and trios of selected base resins to create hybrid properties and colors. They are also called digital materials, defined as composite materials developed for AM (mainly PolyJet 3D printing) with predetermined mechanical and visual properties [220]. Additionally, jetting of multiple materials facilitates support removal and allows high-detail visual representations and functional prototypes to be generated in full-color.

Materials are divided into two main categories of base resins and support materials. The term “resin” refers to solids and highly viscous materials, but more commonly to liquids that harden in response to an agent (e.g., heat, setting agents, or light). Base resins carry the main functional characteristics and colors, each with unique characteristics. Thus, a machine can use them as a palette to receive hybrid materials. They are the basis for inks and can be used without mixing or combined to reveal new properties. Resins are a wide variety of different natural and synthetic materials. They consist of long monomer chains, forming cross-link bonds during the curing process. According to their chemical compounds, resins can be silicones, epoxies, acrylics, alkyds, etc. They can be divided into several categories: strong engineering, rigid general-purpose material, biocompatible, transparent rigid, castable, strong and tough, flexible, simulated (digital) polypropylene, simulated (digital) ABS, and composite resins [221, 222].

Material jetting requires supporting structures, and some resins are optimized for easy removal. They come in various types with different solubility parameters, which affect the range of the chemicals needed to fully dissolve them. Besides, support materials used on the surface will determine whether the surface is glossy or matte, which affects the surface roughness. The supporting resins can become soft during the printing process, which allows them to be removed manually, and the final touches are applied using a water jet. Wax-like support material is generally more rigid than gel-like material and, therefore, cannot be easily removed, resulting in a reduction in surface quality [223].

One of the most challenging aspects of this type of technology is the ejecting of the photocurable resin. For this reason, the materials in play assume a crucial role in the process.

In order to be jetted, resins need to have the correct viscosity according to their composition. For instance, Cheng et al. [224] heated the resin to 70 ºC, while Jabari et al. [225] mixed and sonicated the resin with a

graphene dispersion to obtain an appropriate flowability. There are many methods to gain the correct viscosity for various resins. Still, a resin generally needs to be as liquid as possible to avoid suspending particles that might cause artifacts or reduced accuracy [134]. Particles in the resin lead to imbalances during the drop creation, with sizes that may differ from each other. In fact, this occurs because there are disturbances during the ejection that may change the extrusion setup with an earlier breakup of the drop. Moreover, the droplet spreading and roller performance at each layer deposition can assume different physiognomy [226].

As with binder jetting, another critical parameter to consider is the impact of the droplet on the surface. According to Zhou et al. [227], three forces describe the droplet impact dynamics: inertia, surface tension, and viscous force. At the build plate level, the inertia force is converted into surface energy, and it needs to overcome the surface tension to obtain a flat shape. It means that the inertial force needs to be greater than the surface tension, which is helped by the viscous force. Moreover, the potential difference imparted by the piezoelectric system strengthens the surface tension and increases the impact angle or the height of the ejection [227, 228]. On the other hand, if the height is excessive, head and rear vortexes on the droplet can be formed because the ejection and the drop may impact the surface with different angles and energies [228].

#### 7.1.3. Printhead and roller

Material jetting can print very tiny liquid droplets that reach resolutions around 1600 dpi and 16 μm [229]. The resolution depends on the ejection system but is also related to the droplet size. However, decreasing the specimen thickness increases the magnitude of distortions in the photopolymerization process [219]. Two printing modes are available in PolyJet technology: high speed and high quality with a low layer thickness. If the ejected droplet size is not big enough to cover the spacing between two subsequent ones, the printhead must pass over the same point one more time. According to the offset to fulfill, up to four rounds of jetting may be needed [230]. It is common for MJT printers to jet photocurable resin from different nozzles simultaneously, however, the build platform function may differ (Fig. 21). A roller module leveling mechanism is required to remove the excess resin and flatten the surface to reach the desired layer thickness. After this step, the droplet is immediately cured [223].

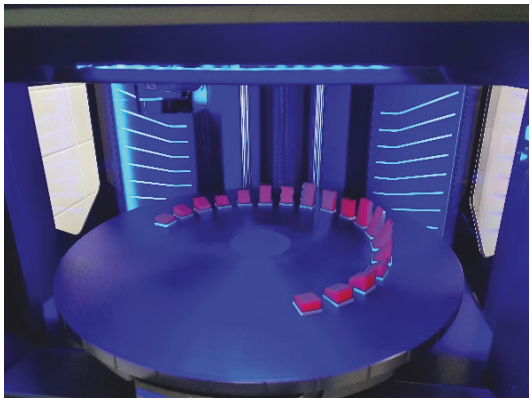

**Fig. 21** An illustrative photo of the rotary build tray of the PolyJet J55 printer.

The hatch spacing in MJT, like other AM techniques such as SLS and BJT, contributes to the texture and morphology of the surface [134, 231]. It comprehends the pulse width and the frequency with which droplets are ejected, and the ejection system series of rounds passes over the same point to create an entire surface. Printing speed is connected with the hatch spacing because it is also based on the sweep speed at which the hatch arises [134].

The quality of the droplet is another aspect to consider. Bussmann et al. [232] showed that impact velocity and angle are essential in terms of quality printing and surface roughness. The effect of rough cured drops may avoid the impact of fingering (perturbed leading edges) and splash (refer to Fig. 20).

Droplet impact, spreading, and curing limit the accuracy of parts and the motion system, which is often a gantry operated by a motor. Droplet spreading and curing restrict the wall thickness, also known as the minimum in-plane feature size (*X*, *Y*). As a result of droplet spreading, the wall thickness is much thicker than the layer thickness (Z) [233]. The minimum feature size increases with the aspect ratio because of the precision of layer-layer registration. Regarding the maximum feature size, it is generally constrained by the build volume of the printer. The foundations of MJT do not restrict feature width, however, few printhead components contain blocking features.

Droplets size and printing speed are the key points for a correct saturation rate and quality printing. Droplets of smaller size can give a better resolution of the printing, but if they are too small, they do not spread effectively. High printing speed can cause a loss of accuracy and resolution because the droplet does not have time to spread effectively [217]. Therefore, adjusting the printing speed makes it possible to favor better material spreading. Accordingly, every droplet indeed has a spreading radius time-dependent, *r(t)*, given by

$$r(t) = (a + bt)^n \qquad \text{Equation 22}$$

where *t* is time, and *a*, *b*, and *n* are constants that determine the growth rate, initial size, and shape of the droplet. These constants can also be related to other factors, such as the viscosity of the liquid, the surface tension between the liquid and the surface, and the contact angle between the liquid and the surface as in other hydrodynamics theories [234].

Imperfections in finishing are a common problem on the surface of MJT parts, which frequently have a rough or ribbed surface finish caused by overlapping material layers [235]. Miyanaji et al. [236] reported that the three most common jetting techniques for polymeric droplets are single, overlapping, and overlaying droplets. Overlapping droplets give better control for fine sizes.

#### 7.1.4. Surface finish setting

Surface roughness values vary depending on the surface finish settings, and a correlation between surface roughness and finish settings can be complicated to establish [8]. In the case of a glossy finish, surfaces will not be covered by support materials except overhanging structures and the bottom of the part. Support materials will be covered when a matte finish is selected [223]. A glossy surface finish produces a lower surface roughness level, resulting in longer fatigue life. Generally, printing parts with a glossy finish setting is recommended to achieve higher surface quality [237].

Many current studies are trying to reach full-color printing by improving resolution and surface finish related to multi-color materials. Some studies have been carried out by Udroiu et al. [24] on matte and glossy surfaces by setting different process parameters. In particular, they found a correlation with the surface roughness $R_a$ given by

$$R_a = t/4\ (|\cot\varphi \sin\theta + \cos\theta| \cdot K_1), \quad K_1 < 1 \qquad \text{Equation 23}$$

where *t* is the layer thickness, $\varphi$ is the droplet contact angle, $\theta$ is the plan orientation and $K_1$ is the correction coefficient based on the PPFTs used. Some other studies instead have been focused on trying to improve the tuning of colors without jagged shifts between adjacent layers [238]

### 7.2. Surface roughness studies and discussion

Compared to other AM techniques, research concerning the surface roughness of MJT technology has been very limited. This contrasts with the fact that MJT appears more relevant to aesthetic applications and artistic purposes. Most of the research in MJT has focused on the relationship between a few pre-processing parameters and the surface finish. However, several publications [70, 239] have used mathematical models to estimate the roughness characteristics of parts printed with PolyJet technologies. Table 11 summarizes significant research related to surface roughness in MJT.

**Table 11** Overview of studies on surface roughness in MJT (see text* below the table for abbreviations).

| Materials \| Machines | Methodology and studied parameters | Roughness range (μm) | Remarks | Ref. |
|---|---|---|---|---|
| RGD720 (SUP706B) \| PolyJet Objet Connex1 | b.o. (H. and V.), s.f. (matte or glossy), high-quality printing mode, l.t. (0.016 mm), s.r.m.m (contact profilometry) | $R_a$: 0.03-13.59 | - Geometries printed along *X*-direction (H.) had lower s.r. than *Y*-direction (V.)<br>- s.r. caused by printing strategies considerably affected the aerodynamic performance of the fixed-wing UAVs<br>- The lift coefficient was more sensitive to s.r. than the drag coefficient<br>- To reduce distortion and improve surface quality, airfoil geometries should be printed horizontally<br>- g.f. produces better surface quality than matte, but it depends on the tray location<br>- Application: UAVs | [237] |
| FullCure830 \| PolyJet Objet 350 | Focused on the relationship between the b.o. (0º, 45º, and 90º), the geometry and s.f. based on the draft angle, roundness, waviness, and s.r.. l.t. (0.016 mm), s.r.m.m. (non-contact profilometry) | $S_q$:1.16-2.86<br>$S_a$: 0.95-2.33<br>$S_{sk}$: -0.12-0.22<br>$S_{ku}$: 2.55-4.7 | - The geometry and surface quality of castings were greatly affected by the d.a. and s.f. of foundry patterns<br>- The lowest values for $S_q$ and the highest surface quality were reported for V. samples (90°), due to the lack of support material<br>- Application: Foundry industry | [240] |
| RGD836 & Agilus 30 FLX 935 (SUP706) \| PolyJet J750 | T. s.r. was examined, s.f. (matte or glossy), s.h. (30, 50, 85, and 100), l.t. (27 μm, 900 dpi), *XY* resolution (0.042 mm, 600 dpi), n.d. (10 μm), 96 nozzles for each head and 4 heads in total, a.m. (ANOVA), s.r.m.m. (contact profilometry) | g.f.: $R_a$: 1.641 (V.), 1.381 (H.)<br>m.f.: $R_a$: 2.606 (V.), 2.280 (H.) | - g.f. showed lower s.r. than matte samples<br>- s.r. was lower with a higher Shore hardness<br>- There was no interaction between these two factors, and the lowest s.r. achieved by combining a g.f. with a Shore hardness rating of 100 | [223] |
| Fullcure 720 (Fullcure 705) \| PolyJet Objet 350V | l.t. (0.016 and 0.030 mm), s.f. (matte v glossy), b.o. ([0°-90°], 30° step), a.m. (ANOVA), s.r.m.m. (contact profilometry) | $R_a$: 2.77-17.63 | - The s.r. prediction model was proposed based on the droplet contact angle<br>- s.f. and b.o. were the significant factors affecting s.r.<br>- Detailed theoretical and experimental analyses of droplet impact and capillary spread were presented to determine droplet contact angles<br>- s.r. increased at higher b.o. up to 90º, then decreased until 180º for m.f.<br>- Higher l.t. caused a marginal increase in s.r.<br>- The proposed model accounted for the surface profile created by samples and support droplet geometry and was thus relevant only for m.f. or downward-facing g.f. | [70] |
| FullCure 720, VeroBlue 840 FullCure 870 (FullCure 705) \| PolyJet Objet 350V | l.t. (0.016 mm), s.f. (matte or glossy), b.o. ([0°-90°], 15° step), p.temp (72 ºC), pre.temp (68 ºC), printhead vacuum (6.2 atm.), r.h. (30%), a.m. (ANOVA and GLM), s.r.m.m. (contact profilometry) | $R_a$: ~0.5-15 | - b.o. an s.f., and their interaction significantly affected $R_a$<br>- Min $R_a$ resulted for g.f., oriented perpendicular to the scanning direction<br>- Maximum $R_a$ resulted for b.o. 75-85°<br>- There were some issues with g.f., including step marks between 75° and 85° and a boundary transition between matte and glossy areas<br>- g.f. had a similar s.r. regardless of b.o. compared to m.f. | [24] |
| Fullcure 720 (Fullcure 705) | l.t. (0.016 and 0.030 mm), s.f. (matte or glossy), s.c. (50 and 90 %), a.m. (DoE Taguchi L4, ANOVA, and | $R_a$: 0.8-12<br>$R_q$:1.01-16<br>$R_z$:4.95-80 | - s.f. significantly affected s.r. compared to l.t. and s.c. | [241] |

| | | | | |
|---|---|---|---|---|
| \| PolyJet Objet 250 | ANOM), s.r.m.m. (contact profilometry) | | - The optimized process parameter values were the same, and the best results were achieved using the 16 μm layer thickness and glossy style. While the scale factor could not be considered a dominant factor | |
| FullCure 720 (Fullcure 705) \| PolyJet Objet 330 | b.o. (6 axis: *XY*, *XZ*, *YZ*, *YX*, *ZX*, and *ZY*), l.t. (0.016 mm), XY resolution (42 and 84 μm) s.f. (matte or glossy), p.p. (water pressure or caustic soda), a.m. (DoE full factorial design, ANOVA), s.r.m.m. (contact profilometry) | $R_a$: 0.78-5.08 (X), 1.04-15.01 (Y), 1.19-21.41 (Z) | - b.o. and s.f. significantly affected s.r.<br>- g.f. resulted in the best s.r. results in all three axes, but it led to geometry limitations (thin walls)<br>- The critical surfaces should be placed close to the *XY*-plane for the best s.r. | [242] |
| FullCure 720 (Fullcure 705) \| PolyJet Objet 330 | H. s.r. and texture were investigated. l.t. (0.016 mm), s.f. (matte or glossy), s.r.m.m. (contact profilometry) | g.f.: $R_a$: 0.84, $R_z$: 3.8<br>m.f.: $R_a$: 1.04, $R_z$: 5.6 | - s.r. of g.f. was lower than that of m.f. but with significant variations in the results | [243] |
| FullCure 720 (Fullcure 705) \| PolyJet Objet 260 | l.t. (0.016 mm), *XY* resolution (42 μm, 600 dpi), s.r.m.m. (contact profilometry) | $R_a$: 0.40 (H.), 4.55 (V.)<br>$R_z$: 4.02 (H.), 30.28 (V.) | - s.r. was heavily influenced by its position relative to the printing axis, affecting mechanical and geometric properties<br>- s.r. (2-8 μm), like osteoblast size, increases cell growth and attachment to scaffolds, promoting proliferation<br>- $R_a$ (4.55 μm) in surfaces parallel to the printing axis (*Z*) was like the s.r. of scaffold surfaces with other polymers, which could facilitate cell adhesion and differentiation into osteoblasts<br>- Application: Porous structures and scaffold design for bone tissue engineering | [244] |
| Fullcure 720 (Fullcure 705) \| PolyJet Objet 260 | l.t. (0.016 mm), s.f (glossy), b.o. ([0°-90°], 5° step), a.m. (regression analysis), s.r.m.m. (contact profilometry) | $R_a$: 0.818-4.024 | - The existing s.r. prediction models were only applicable for m.f. parts, showed high error, while it was checked for the estimation of s.r. of the parts printed with g.f. | [239] |
| VisiJet M2R-WT (VisiJet M2-SUP) \| Project MJP2500 modeled | *XYZ* resolution (800×900×790 dpi) l.t. (0.032 mm), s.r.m.m. (contact profilometry) | $R_a$: 0.338-8.532 | - MJT parts should be placed along the maximum area in contact with the base plate due to better heat dissipation from the hot layers to the base plate, leading to a uniform fusion between the layers and causing less dimensional deviation and better surface properties | [245] |

*Abbreviations a.m.: analysis methods, b.o.: build orientation (direction), d.a.: dimensional accuracy, g.f.: glossy finish, l.t.: layer height (thickness along *Z*-direction), m.f.: matte finish, n.d.: nozzle diameter, p.temp.: printing temperature, pre.temp.: preheating temperature, r.h.: relative humidity, s.f..: surface finish, s.c.: scale of the model, s.r.: surface roughness, s.r.m.m: surface roughness measurement method, H.: horizontal, V.: vertical

In agreement with Table 11, positioning the part along the build tray substantially impacts the surface roughness in MJT parts. There was generally less roughness on horizontal surfaces than on vertical planes. On horizontal surfaces, roughness is determined by the droplet spreading and interaction of successive droplets for line and plane formation. In contrast, on vertical surfaces, it is controlled by the interaction of consecutive layers, resulting in stair-stepping equal to the layer thickness of the printed part. The spreading of droplets leads to extremely thin layers, resulting in smooth horizontal and vertical surfaces at the mesoscale [233]. As Udroiu et al. [243] demonstrated, the build type (matte or glossy) substantially affected surface roughness. Although MJT with $R_a$ generally less than 10 μm, can be considered to be between FFF (~1 μm < $R_a$ < ~ 35 μm) and VPP ($R_a$ < ~ 5 μm) in terms of surface roughness, the machines show much less variability compared to FFF and more variation compared to VPP methods. Again, and similar to FFF, SLS, and VPP methods, $R_a$ and $S_a$ were the most commonly reported roughness parameters.

## 8. Comparative studies and discussion

Table 12 summarizes recent comparative studies on the significant polymer additive manufacturing processes.

**Table 12** Overview of comparative studies on surface roughness in FFF, SLS, VPP (SLA and DLP), and MJT (see text* below the table for abbreviations).

| Materials \| Machines | Methodology and studied parameters | Roughness range (μm) | Remarks | Ref. |
|---|---|---|---|---|
| FFF: PPSF \| Titan Stratasys<br>SLS: PA12 (2210) FR \| EOS P390 | FFF: r.w. (0.5080 mm); l.t. (0.254 mm), solid-normal filling strategy<br>SLS: the sorted strategy (contour, filling, contour), l.t. (0.15 mm), l.p. (30 W), p.s. (1000 mm/s), h.d. (0.3 mm), s.r.m.m (contact profilometer) | FFF: $R_a$: 0.40-28.11; $R_z$: 1.44-126.06; $R_t$: 3.35-144.64<br>SLS: $R_a$: 11.84-29.27; $R_z$: 82.99-187.93; $R_t$: 90.46-227.17 | - SLS/PA produced a much smoother surface, but FFF/PPSF presented slightly better d.a.<br>- FFF produced parts with periodic surface profiles, whereas SLS produced those with irregular surfaces<br>- Application: Flame-retardant plastics were used in critical applications, such as aircraft interior parts | [152] |
| SLS: PA12 \| EOS P390 & P1000 Prodways MJT: VeroBlack resin \| Connex 500 Stratasys | SLS P390: p.size (45-70 μm) and l.t. (120 μm)<br>SLS P1000: p.size (45-60 μm) and l.t. (100 μm)<br>MJT: l.t. (16 and 32 μm), b.o. (0°, 45°, 90°)<br>s.r.m.m (contact profilometer) | SLS P390: $R_a$: 16 (H.), 23 (V.), 22 (45°); $R_z$: 108 (H.), 148 (V.), 149 (45°)<br>SLS P1000: $R_a$: 16.5 (V.); $R_z$: 118 (V.)<br>MJT (16 μm): $R_a$: 12 (V.); $R_z$: 79 (V.)<br>MJT (32 μm): $R_a$: 20 (V.); $R_z$: 125 (V.) | - Higher l.t. resulted in higher p.s., and had a greater influence on s.r. than partly molten grains adhering to the surface<br>- The 45° surfaces were rough and had a stair-like appearance, which was exacerbated by the heaviest layers. This kind of s.r. was difficult to evaluate.<br>- s.r. of the 1-year-old SLS P1000 was better than that of the 10-year-old SLS P390<br>- Surfaces for SLS parts tend to trap impurities more than MJ's smooth and shiny surface | [3] |
| SLS: PA12 (2200) \| EOS P396<br>MJF: PA12 \| HP MultiJet Fusion 3D 4200<br>HL: Cubicure Resin \| Hot Lithography Caligma 200 | Standard parameter setting "Balance" was used for MJF (20% new + 80% aged powder) and SLS<br>s.r.m.m. (contact profilometry) | MJF: $R_a$: 11.9<br>SLS: $R_a$: 13.4<br>HL: $R_a$: 6.1 | - Semicrystalline MJF-PA and LS-PA possessed similar $R_a$<br>- If parts contain pressurized fluid without any further s.f., HL-MA has the potential for rapid crack propagation due to its surface texture<br>- Application: Automotive industry, motorcycle design, and low-pressure parts such as fuel tanks and lightweight fairings or high-pressure parts such as valves | [246] |
| FFF: PLA \| Ultimaker 3 Extended<br>SLA: Proprietary Resin \| Nobel 1.0 A<br>MJT: RGD840 (SUP705) \| PolyJet Objet 260 VisiJet M3-X (VisiJet S300) \| ProJet MJP 3600 | FFF: l.t. (200 μm), *XY* resolution (12.5, 12.5 μm)<br>SLA: l.t. (25 μm), *XY* resolution (130, 130 μm)<br>MJT: PolyJet: l.t. (12 μm), *XY* resolution (42, 42 μm, 600 dpi)<br>ProJet: l.t. (32 μm), *XY* resolution (375, 450 dpi)<br>a.m. (ANOVA), s.r.m.m. (contact profilometry) | FFF: $R_a$: 4.93<br>SLA: $R_a$: 0.34<br>MJT: $R_a$: 2.12 (PolyJet), 3.84 (ProJet) | - PolyJet produced acceptable s.r. and round edges but a superior s.f. when the model was printed in the glossy mode<br>- s.r. and e.d. of ProJet printers were significant weaknesses on a microscopic level<br>- Despite acceptable d.a., FFF printed rough surfaces with poor e.d. on the as-printed raw object. The final product of FFF prints needed to be post-processed<br>- SLA printer produced a significantly smooth surface, but the distortion of thin features (<1mm)<br>- $R_q$ and $R_z$ for all samples followed the same pattern as $R_a$ with similar significance<br>- Application: Prototyping, physical visualization, and end-product manufacturing | [118] |
| SLS: PA 3200 GF \| -<br>MJT: Digital ABS \| - | SLS and MJT were used to manufacture molding for conventionally fabricated aluminum milled tools<br>a.m. (ANOVA), s.r.m.m. (non-contact profilometry) | MJT: $R_a$: 0.77; $R_q$: 1.35; $R_z$: 8.90<br>SLS: $R_a$: 11.59; $R_q$: 14.71; $R_z$: 64.01 | - SLS molds had significantly rougher surfaces than MJT molds, causing more notch effect<br>- The tool surface of the polymer mold inserts should be treated to improve the design modifications of the mold inserts<br>- Application: Rapid tooling, injection molding | [14] |
| FFF: PLA & ABS \| Makerbot replicator & Makerbot replicator 2X | FFF: l.t. (100 μm), i.d. (15% for PLA and 10% for ABS)<br>SLA: l.t. (50 μm), i.d. (100%)<br>MJT: l.t. (16 μm for DM and 32 μm for Vero), i.d. (100%) | FFF: $R_a$: ~8 (PLA), ~9 (ABS); $R_z$: ~33 (PLA); ~37 (ABS); $R_{ku}$: ~2.3 | - Focused on three critical aspects of personal 3D printing processes, including manufacturing cost, sustainability, and visuotactile perception of s.r.<br>- MJT samples had the best subjective quality (all hedonic, tactile, and visual assessments), but the highest costs and environmental impact | [64] |

| | | | | |
|---|---|---|---|---|
| SLA: Proprietary Resin \| Formlabs Form 1+<br>MJT: VeroClear & DM Gray 60 \| PolyJet Objet 260 | a.m. (Kendall's coefficient of concordance, sensorial analysis), s.r.m.m. (contact profilometry) | (PLA) and ~2.5 (ABS)<br>SLA: $R_a$: ~20; $R_z$: ~19; $R_{ku}$: ~2.8<br>MJT: $R_a$: ~4 (Vero), ~3 (DM); $R_z$: ~18 (Vero), ~16 (DM); $R_{ku}$: ~2.7 (Vero), ~2.6 (DM) | - The SLA sample scored middle in tactile and visual assessments, but its hedonic sensation score was significantly higher than the FFF sample<br>- $R_z$ was superior to $R_a$ and $R_q$ in sensory judgments of s.f.<br>- Besides $R_z$, surface texture and color affected sensory judgments<br>- A significant correlation was found between $R_z$ and the tactile and visual assessment<br>- $R_{ku}$ correlated best with the hedonic rank<br>- Application: Prototyping and personal 3D printers | |
| FFF: PLA+ \| Pratham desktop<br>SLS: PA12 (2200) \| EOS P396<br>DLP: ABS TRU Resin \| EKA DLP<br>MJT: VisiJet M2R-WT (VisiJet M2-SUP) \| Projet MJP 2500 | d.a, s.r., and p.s. were considered in the decision criteria. a.m. (Hybrid MCDM and sensitivity analysis), s.r.m.m. (contact profilometry) | FFF: $R_a$: 6.11<br>SLS: $R_a$: 11.79<br>DLP: $R_a$: 3.06<br>MJT: $R_a$: 19.96 | - The ranking obtained to achieve the desired d.a., and surface quality is MJT > SLS > FFF >DLP<br>- MJT provided the highest d.a. and lower s.r. | [247] |
| FFF: PLA \| BQ Witbox II<br>SLS: PA12 \| EOS P760<br>SLA: Digital Wax \| DWS 020X Systems<br>MJT: - \| Polyjet Objet30 Pro | SLA, FFF, SLS, Polyjet are compared in terms of d.a., s.r.,<br>FFF: l.t. (300 µm)<br>MJT: l.t. (16 µm)<br>s.r.m.m. (contact profilometry) | FFF: $R_a$: 39.3; $R_z$: 238.1<br>SLS: $R_a$: 15.4; $R_z$: 133.8<br>SLA: $R_a$: 0.2; $R_z$: 2.8<br>Polyjet: $R_a$: 2.5; $R_z$: 22.3 | - The following ranking in terms of s.r. values were reported FFF > SLS > MJT >SLA<br>- Application: RF/Microwave Components | [248] |
| FFF: ABS \| Fortus 450mc<br>SLA: Gray Pro resin \| Formlabs<br>MJF: PA12 \| HP MultiJet Fusion 3D 4200 | FFF: l.t. (254 µm), i.d. (100 %), r.a. (45°)<br>SLA: l.t. (100 µm)<br>MJF: ratio of pristine to recycled powder (30:70), l.t. (80 µm)<br>T. s.r. was measured at 3 separate locations, s.r.m.m. (non-contact profilometry) | FFF: $S_a$: 5.277-7.111; $S_q$: 6.845-8.782<br>SLA: $S_a$: 1.830-2.137; $S_q$: 2.452-2.856<br>MJF: $S_a$: 8.740-11.980; $S_q$:10.054-16.293 | - SLA resulted in the lowest deviation and values of s.r.<br>- T. $S_a$ and $S_q$ of MJF sample were lower than FFF<br>- Filling patterns in FFF as a trajectory process resulted in rougher H. surfaces compared to nontrajectory MJF<br>- Application: Permeability test rig | [249] |
| SLA: Gray RS-F2-GPGR-04 \| Form 2 SLA<br>DLP: Freeprint model 385 grau (DETAX) \| SolflexW170<br>MJT: VisiJet Wax VisiJet M3 Hi-Cast (VisiJet S300) \| ProJet MJP 3600 | b.o. (45º)<br>SLA: l.t. (25 µm)<br>DLP: l.t. (25 µm)<br>MJT: l.t. (16 µm)<br>a.m. (Shapiro-Wilk test, Tukey post hoc test, and the Kruskal-Wallis test), s.r.m.m. (non-contact profilometry) | $R_z$: 0.012-0.032 (SLA), 0.015-0.043 (DLP), 0.010-0.018 (MJT) | - Skin structure replication was more dependent on the AM method chosen than on other stages of production<br>- MJT showed superior accuracy compared with SLA or DLP<br>- Application: Facial prosthesis fabrication | [250] |
| FFF: PLA, ABS, PVA, PEVA and HIPS \| Wanhao duplicator 6<br>DLP: 405nm Resin \| Wanhao D7 DLP LCD | FFF: l.t. (200 µm), r.a. (Crossed 45°/135°), b.o. (0°, 45°, 90°)<br>DLP: l.t. (100 µm)<br>s.r.m.m. (contact profilometry) | DLP: $R_a$: ~4 (H., S.), ~4.4 (H., T.), ~13.2 (45° S.), ~12.2 (45° T.), ~10.4 (V., S.), ~0.8 (V., T.)<br>FFF: $R_a$: ~1.6 (H., S.), ~10.8 (H., T.), ~10.2 (45° S.), ~17.0 (45° T.), ~9.6 (V., S.), ~3.6 (V., T.) | - Choosing the 3DP method and changing b.o. can significantly affect s.r. and tribological performance<br>- Parts made with DLP are prone to stick-slip phenomena, particularly at b.o. (45° and 90°)<br>- Application: Tribological purposes | [251] |

*Abbreviations a.m.: analysis methods, b.o.: build orientation (direction), d.a.: dimensional accuracy, e.d.: energy density, h.d.: hatch distance, i.d.: infill density, l.t.: layer height, l.p.: laser power, p.s.: printing speed (laser scanning speed), p.size: powder size, r.a.: raster angle, r.w.: raster width, s.f.: surface finish, s.r.: surface roughness, s.r.m.m: surface roughness measurement method, S.: side, T.: top, H.: horizontal, V.: vertical

Most benchmarks developed for AM were intended to measure the implementation of a single technology and a limited number of parameters, as discussed in the previous section. The comparison of various AM methods has been the focus of several studies. For instance, Mou and Koc [118] compared three AM technologies, FFF, SLA, and MJT, on four machines in terms of their surface roughness, edge sharpness, and dimensional accuracy. According to their results, FFF produced a rough surface and irregular dimensional accuracy, SLA manufactured smoother surfaces but resulted in the distortion of thin features (<1 mm), and MJT fabricates surfaces with comparable surface roughness and dimensional accuracy. Sillani et al. [28] reported the trend of surface roughness on the bottom and top surfaces of MJT and SLS seems to be about identical. Minetola et al. [16] evaluated three polymer-based 3DP machines by analyzing their dimensional accuracy using ISO IT grades. They reported a thinner layer gives a greater definition of the features geometry and higher dimensional accuracy. Li et al. [64] compared FFF, SLA, and MJT based on cost, sustainability, and surface roughness quality factors. They reported MJT and SLA as the best and moderate AM methods in tactile and visual assessments, respectively. However, unique SLA materials were considerably more valued in the hedonic sensation category. Results indicated the lowest overall ranking for FFF but with the capability of manufacturing with the lowest environmental problems and costs, confirming its sustainability.

In terms of dimensional accuracy, for instance, Minetola et al. [16] reported despite the increased layer thickness (0.21 mm against 0.10 mm), the Arburg Freeformer machine outperformed the Prusa i3 for more comprehensive ISO ranges of the primary size. However, layer thickness was the most essential element for improved dimensional accuracy for smaller feature sizes. Roach et al. [2] used inkjet printing for PEGDA/PI material over the PEI substrate manufactured by the FFF method. They reported direct-ink-writing (DIW) surface modification process for FFF substrate reduces the surface roughness, resulting in improved conductivity for electronics and radio frequency (RF) applications. Nazir and Jeng [252] introduced high-speed additive manufacturing by merging PBF, MJT, and sintering technology without coupling 3DP with subtractive methods. They showed that while the MJF process was substantially quicker than the SLS method, the SLS PA12 parts showed 15% lower $R_a$ when compared to the high-speed MJF.

## 9. Summary

The 3D-layered nature of AM processes and partially melted particles influence the definition of the component surface. Accordingly, controlling PPPs can dramatically affect the 3D features on a rough surface for AM components. The deliberate surface modification based on surface texture metrics in 3DP products is more demanding than ever with 3D measurement and characterization development, which can comprehensively reflect the surface topography.

Fabricating a part using layer-by-layer deposition in which the produced part exhibits a staircase effect causes the surface to become rougher. It is possible to reduce this problem by being aware of the regular surface roughness of the parts in advance or predicting the roughness values during pre-processing. Accordingly, the PPPs based on process parameter optimization have been discussed to list the parameters that have the most critical influence on the roughness of as-printed polymers. This comparative review emphasized the growing interest in understanding AM system restrictions and discrepancies so that a better selection of 3DP technology can be made based on project constraints. This study summarized the significant advances in additive manufacturing, including the incorporation of AM design decisions to assist in identifying candidate solutions, as well as information regarding roughness considerations for the selected processes.

As mentioned in the previous section, the best possible surface and optimum roughness according to an application can be obtained by adjusting the fabrication parameter. The other choice is to investigate the optimum mix of PPFTs that can be applied to any AM objects. However, it increases the cost, time, and complexity of the process. Production settings may be tweaked to favor speed above surface quality if this combination proves effective.

A variety of strategies have been employed by various groups to achieve this objective. Most studies have focused on the top surface of the parts because many factors contribute to the surface roughness distribution of a 3DP object, such as layer height. It is revealed from the literature review that the workflow of surface modification in the pre-processing step heavily depends on the complexity of the design and the desired quality-time-cost balance. Surface modification techniques are currently not standardized and depend on factors such as geometry and intended application. As a result, the following AM workflow in Fig. 22 can lead to optimum surface modification by altering roughness before and during processing.

Along with the literature review, the Taguchi method, full factorial method, response surface method (RSM), and analysis of variance (ANOVA) were the most used methods for optimizing the surface roughness of 3D printers. In the case of RSM, it is generally a time-consuming method depending on the orthogonal matrix used [44]. Thus, it has been less widely used than the Taguchi method to date. The combination of specific optimization parameters may result in parts with no known surface roughness, which would have to undergo fundamental design changes. Current capabilities are limited without developing a new surface modification workflow that considers the PPFTs requirements during the pre-processing phase. Frequently, DfAM necessitates the redesign of parts initially planned for conventional

methods such as machining. Post-processing must be integrated into the design process at an earlier stage, and the role of each component must be considered. Specifically, post-processing using ultraprecision technology is gaining increasing attention as it provides high-quality parts with improved surface finish and dimensional accuracy [253]. The importance of having precise geometries and smooth surfaces is particularly important for polymer optics and devices, where optimal performance depends on precise geometries and smooth surfaces.

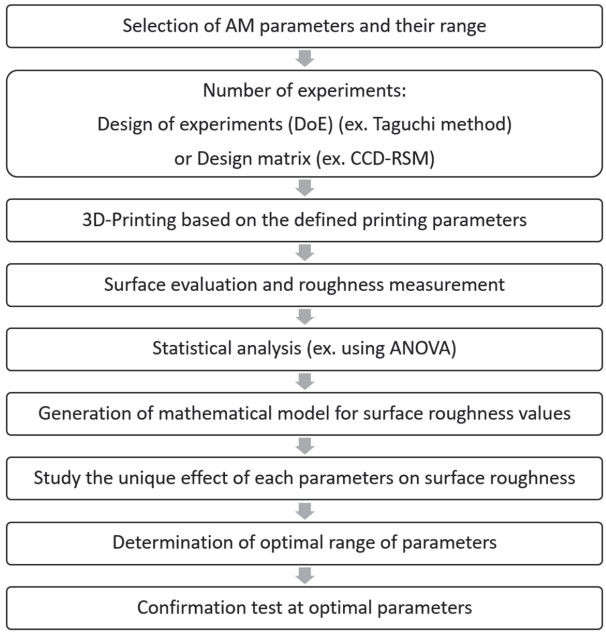


**Fig. 22** Suggested 3DP workflow to enhance as-printed surfaces.

According to the studied literature, the appropriate AM technique selection determines manufacturing efficiency, accuracy, and model size. Thus, it determines whether the actual and nominal roughness is conforming and will allow AM to be better integrated with roughness requirements. For instance, while FFF technology has the advantage of being efficient and cost-effective for small-scale production, accuracy may be limited when the production of large and complex parts is required. The recorded $R_a$ results were generally less than 5 and 10 µm for the studied VPP and MJT methods, respectively, 10 to 20 µm for SLS, and between 1 µm to over 30 µm for FFF. Accordingly, SLA and DLP technologies, offer high accuracy and resolution for larger and more complex parts with more stable roughness results at various printing processes, considering SLS is at the opposite end of the roughness spectrum. While MJT can fabricate ultimately smooth parts in the sub-micrometer ranges similar to VPP, their 3D-printed surface can be as rough as FFF, depending on the selected processing method. However, both VPP and MJT AM categories

can be time-consuming and expensive, limiting their suitability for competing with mass production in the present form.

Selection of the proper AM technique will also require an in-depth examination of the surface measurement techniques. The measuring method results in significant uncertainty in roughness evaluation due to PPP. It is reported that the stylus in contact-based profile measurement scratches and physically smooths the surface, leading to slight compliance with the actual topography. However, it is time efficient, more reproducible, and provides comparable results even when the tip radius varies [3]. Accordingly, tactile roughness measurement and $R_a$ were frequently reported as the main method and roughness metrics in the reviewed articles. However, $R_z$ performed better than $R_a$ since it accurately represents both tactile and visual roughness. Nevertheless, observers are influenced by appearance attributes such as color, texture, glossiness, and translucency when evaluating roughness and surface finish [254]. In particular, polymeric parts represent most of these appearance attributes.

Considering the results, mainstream 3DP technologies differ significantly in terms of surface roughness. The FFF method makes extending applications across various applications challenging due to its poor surface quality. However, FFF objects seem more appropriate for analyzing application-based purposes. SLA is considered a low-cost desktop device that directly competes with FFF because of its higher print resolution and reduced surface roughness. The SLS technique is still being developed for this purpose, and MJF is emerging as a promising technique. In general, the surface roughness of the SLA and MJT was reported to be better than the SLS components. Compared to other polymer AM techniques, their inherent smooth surface finish and great dimensional accuracy imply that painting and coating are rarely required. Combining these data confirms that the reviewed 3DP methods cannot produce ready-to-use end products and that PPFT is necessary. As a significant finding, it is revealed that there is a demand for further investigation on the appearance of 3D-printed structures, dealing explicitly with their QAs issues. Optimization of AM should not be conducted to achieve complete control over roughness. It is primarily due to the lack of reproducibility in AM technology and the role mainly played by post-processing. Further research is required to establish the links between different PPPs and the quality of the surfaces of AM-made components, as discussed in the next section.

## 10. Future trends and capabilities

The importance of surface roughness in the final product is recognized by both conventional and advanced manufacturing methods, especially for critical and small products. To increase the applicability of AM processes, it is necessary to assess the surface finish of as-printed polymers and to provide guidance on AM process windows and limitations [8]. 3D and 2.5D printing with multi-materials and multi-colors will be key to the future development of AM technology [255]. The techniques mentioned in this study can also provide insight into other advanced materials, such as nanoparticle and their suspensions with functional properties [256-258], surface treatment [259, 260], and liquid metals to use in AM technology. Furthermore, fiber reinforcement and composition can be incorporated into almost all AM methods [261]. The development of eco-friendly materials, the use of polymers, durability, and sustainability are also major concerns [262]. As an emerging trend in advanced manufacturing, the combination of several AM technologies presents new challenges in terms of surface finish.

There is a growing interest in 4D additive manufacturing, which is a relatively new research area. Smart materials can be developed more quickly by developing multi-material 4D printing [263, 264]. A 4D-printed part can thus be carefully controlled in terms of surface texture and topography as a microstructure to achieve more complex geometrical transformations. Therefore, monitoring the surface roughness of smart materials is an essential step. As with 3D multi-material printing, it can present similar challenges, such as limited material choice, printing resolution, slow mechanical performance, and dimensional accuracy [263]. It will be necessary to implement multi-material additive manufacturing in a variety of applications as part of multidisciplinary research and development [262].

The lack of aesthetically appropriate materials for AM necessitates further investigation. An understanding of the induced anisotropic arrangements and their impact on the build platform (chamber) and product properties may be improved by using sophisticated algorithms and numerical techniques [211]. The fundamental material application procedure, as well as the actual applied stresses, heat, and weathering agents, requires further investigation. Aside from the roughness value, the roughness distribution is also of critical importance to the use of AM components in the future. Therefore, there are various capabilities available to examine how printing factors impact other mechanical performance factors, such as compressive strength, tensile strength, etc. As a result of these findings, AM products are likely to be applied to parts for automotive, aerospace, and jewelry applications that require high dimensional accuracy and proper surface characteristics.

**Author contribution** Ali Payami Golhin: Conceptualization, Methodology, Investigation, Data curation, Formal analysis, Visualization, Writing – original draft, Writing – review & editing. Riccardo Tonello: Conceptualization, Writing – original draft, Writing – review & editing. Jeppe Revall Frisvad: Writing – review & editing, Supervision. Sotirios Grammatikos: Writing – review & editing, Supervision. Are Strandlie: Writing – review & editing, Supervision, Project administration, Funding acquisition.

**Funding** The authors acknowledge the funding received on this project from the ApPEARS-ITN project funded by the European Union's H2020 research and innovation program under the Marie Skłodowska-Curie grant agreement No. 814158.

**Availability of data and materials** The data supporting the findings of this study are available within the manuscript.

**Code availability** Not applicable.

## Declarations

**Ethics approval** Not applicable.

**Consent to participate** Not applicable.

**Consent for publication** Consent to publication has been received from all co-authors before the work is submitted.

**Conflict of interest** The authors declare no competing interests.

**References**


1. Li S, Li JY, Jiang ZW, et al. (2022) Controlling the columnar-to-equiaxed transition during Directed Energy Deposition of Inconel 625. 57:102958. https://doi.org/https://doi.org/10.1016/j.addma.2022.102958
2. Roach DJ, Roberts C, Wong J, et al. (2020) Surface modification of fused filament fabrication (FFF) 3D printed substrates by inkjet printing polyimide for printed electronics. 36:https://doi.org/10.1016/j.addma.2020.101544
3. Magnien J, Cosemans P, Nutal N, et al. (2020) Current surface issues in additive manufacturing. Wiley Online Library. https://doi.org/10.1002/ppap.201900154
4. Stiles A, Kobler W, Yeole P, et al. (2022) Photopolymer formulation towards large scale additive manufacturing of autoclave capable tooling. 50:https://doi.org/10.1016/j.addma.2021.102571
5. Bertacchini F, Bilotta E, Demarco F, et al. (2021) Multi-objective optimization and rapid prototyping for jewelry industry: methodologies and case studies. 112:2943-2959. https://doi.org/10.1007/s00170-020-06469-2
6. Poyanco J-M, Pizarro F, Rajo-Iglesias E (2022) Cost-effective wideband dielectric planar lens antenna for millimeter wave applications. Sci. Rep. 12:1-10. https://doi.org/10.1038/s41598-022-07911-z
7. Quinlan HE, Hasan T, Jaddou J, et al. (2017) Industrial and consumer uses of additive manufacturing: A discussion of capabilities, trajectories, and challenges. J. Ind. Ecol. 21:S15-S20. https://doi.org/10.1111/jiec.12609
8. Payami Golhin A, Sole AS, Strandlie A (2023) Color appearance in rotational material jetting. Int. J. Adv. Manuf. Technol. 124:1183–1198. https://doi.org/10.1007/s00170-022-10536-1
9. Nath SD, Nilufar S (2020) An overview of additive manufacturing of polymers and associated composites. 12:2719. https://doi.org/10.3390/polym12112719
10. Wohlers T (2021) Technical, market, and strategic advice on additive manufacturing, 3D printing, and rapid product development, in Wohlers Report 2021. Wohlers Associates.
11. Carlota V (2020) Polymer 3D printing market to generate $11.7 billion in 2020. 2020 March 4, 2020. Accessed 10 January; Available from: https://www.3dnatives.com/en/polymer-3d-printing-market-2020-040320204.
12. Panin SV, Buslovich DG, Kornienko LA, et al. (2019) Structure, as well as the tribological and mechanical properties, of extrudable polymer-polymeric UHMWPE composites for 3D printing. J. Frict. Wear 40:107-115. https://doi.org/10.3103/S1068366619020090
13. Goldin N, Dodiuk H, Lewitus D (2017) Enhanced thermal conductivity of photopolymerizable composites using surface modified hexagonal boron nitride fillers. Compos. Sci. Technol. 152:36-45. https://doi.org/10.1016/j.compscitech.2017.09.001
14. Kampker A, Triebs J, Kawollek S, et al. (2019) Direct polymer additive tooling – effect of additive manufactured polymer tools on part material properties for injection moulding. Rapid Prototyping J. 25:1575-1584. https://doi.org/10.1108/RPJ-07-2018-0161
15. Aslani KE, Vakouftsi F, Kechagias JD, et al. (2019) Surface Roughness Optimization of Poly-Jet 3D Printing Using Grey Taguchi Method. in Proceedings - 2019 3rd International Conference on Control, Artificial Intelligence, Robotics and Optimization, ICCAIRO 2019. https://doi.org/10.1109/ICCAIRO47923.2019.00041
16. Minetola P, Calignano F, Galati M (2020) Comparing geometric tolerance capabilities of additive manufacturing systems for polymers. Addit. Manuf. 32:https://doi.org/10.1016/j.addma.2020.101103
17. Vyavahare S, Teraiya S, Panghal D, et al. (2020) Fused deposition modelling: A review. Rapid Prototyping J. 26:176-201. https://doi.org/10.1108/RPJ-04-2019-0106

18. Turner BN, Gold SA (2015) A review of melt extrusion additive manufacturing processes: II. Materials, dimensional accuracy, and surface roughness. Rapid Prototyping J. 21:250-261. https://doi.org/10.1108/RPJ-01-2013-0012
19. Gordon ER, Shokrani A, Flynn JM, et al. (2016) A surface modification decision tree to influence design in additive manufacturing, R. Setchi, et al., Editors., Springer Science and Business Media Deutschland GmbH. p. 423-434. https://doi.org/10.1007/978-3-319-32098-4_36
20. Parandoush P, Lin D (2017) A review on additive manufacturing of polymer-fiber composites. Compos. Struct. 182:36-53. https://doi.org/10.1016/j.compstruct.2017.08.088
21. Chohan JS, Singh R (2017) Pre and post processing techniques to improve surface characteristics of FDM parts: A state of art review and future applications. Rapid Prototyping J. 23:495-513. https://doi.org/10.1108/RPJ-05-2015-0059
22. Panda B, Noor Mohamed NA, Tay YWD, et al. (2018) Effects of slag addition on bond strength of 3D printed geopolymer mortar: An experimental investigation. in Proceedings of the International Conference on Progress in Additive Manufacturing. https://doi.org/10.25341/D4QG6D
23. Piedra-Cascón W, Krishnamurthy VR, Att W, et al. (2021) 3D printing parameters, supporting structures, slicing, and post-processing procedures of vat-polymerization additive manufacturing technologies: A narrative review. https://doi.org/10.1016/j.jdent.2021.103630
24. Udroiu R, Braga IC, Nedelcu A (2019) Evaluating the quality surface performance of additive manufacturing systems: Methodology and a material jetting case study. Mater. 12:https://doi.org/10.3390/ma12060995
25. Gülcan O, Günaydın K, Tamer A (2021) The state of the art of material jetting—a critical review. 13:https://doi.org/10.3390/polym13162829
26. Sinha A, Swain B, Behera A, et al. (2022) A Review on the Processing of Aero-Turbine Blade Using 3D Print Techniques. 6:https://doi.org/10.3390/jmmp6010016
27. Marques A, Miranda G, Silva F, et al. (2021) Review on current limits and potentialities of technologies for biomedical ceramic scaffolds production. 109:377-393. https://doi.org/10.1002/jbm.b.34706
28. Sillani F, Kleijnen RG, Vetterli M, et al. (2019) Selective laser sintering and multi jet fusion: Process-induced modification of the raw materials and analyses of parts performance. Addit. Manuf. 27:32-41. https://doi.org/10.1016/j.addma.2019.02.004
29. (2021) Additive manufacturing - General principles - Fundamentals and vocabulary, in ISO/ASTM 52900:2021. International Organization for Standardization: Geneva, Switzerland. p. 1-36.
30. Jonušauskas L, Juodkazis S, Malinauskas M (2018) Optical 3D printing: Bridging the gaps in the mesoscale. J. Opt. 20:https://doi.org/10.1088/2040-8986/aab3fe
31. Elkholy A, Kempers R (2020) Enhancement of pool boiling heat transfer using 3D-printed polymer fixtures. Exp. Therm. Fluid Sci. 114:https://doi.org/10.1016/j.expthermflusci.2020.110056
32. Ligon SC, Liska R, Stampfl J, et al. (2017) Polymers for 3D Printing and Customized Additive Manufacturing. Chem. Rev. 117:10212-10290. https://doi.org/10.1021/acs.chemrev.7b00074
33. Alex Xu BL, Martin Erharter, Vatche Kourkejian (2021) Polymer additive manufacturing market today and in the future. 2021. Accessed 1 July; Available from: https://www.rolandberger.com/en/Insights/Publications/Polymer-additive-manufacturing-Market-today-and-in-the-future.html.

34. Gorjan L, Tonello R, Sebastian T, et al. (2019) Fused deposition modeling of mullite structures from a preceramic polymer and γ-alumina. J. Eur. Ceram. Soc. 39:2463-2471. https://doi.org/10.1016/j.jeurceramsoc.2019.02.032
35. Ojansivu M, Johansson L, Vanhatupa S, et al. (2018) Knitted 3D scaffolds of polybutylene succinate support human mesenchymal stem cell growth and osteogenesis. Stem cells international 2018:https://doi.org/10.1155/2018/5928935
36. Ou-Yang Q, Guo B, Xu J (2018) Preparation and characterization of poly(butylene succinate)/polylactide blends for fused deposition modeling 3D printing. 3:14309-14317. https://doi.org/10.1021/acsomega.8b02549
37. Zhakeyev A, Wang P, Zhang L, et al. (2017) Additive manufacturing: Unlocking the evolution of energy materials. Adv. Sci. 4:https://doi.org/10.1002/advs.201700187
38. De Matos Costa AR, Crocitti A, Hecker De Carvalho LHD, et al. (2020) Properties of biodegradable films based on poly (butylene succinate)(PBS) and Poly (butylene adipate-co-terephthalate)(PBAT) blends. 12:2317. https://doi.org/10.3390/polym12102317
39. Williams JM, Adewunmi A, Schek RM, et al. (2005) Bone tissue engineering using polycaprolactone scaffolds fabricated via selective laser sintering. 26:4817-4827. https://doi.org/10.1016/j.biomaterials.2004.11.057
40. Eshraghi S, Das S (2010) Mechanical and microstructural properties of polycaprolactone scaffolds with 1-D, 2-D, and 3-D orthogonally oriented porous architectures produced by selective laser sintering. Acta Biomater. 6:2467. https://doi.org/10.1016/j.actbio.2010.02.002
41. Salmoria GV, Fancello EA, Roesler CR, et al. (2013) Functional graded scaffold of HDPE/HA prepared by selective laser sintering: microstructure and mechanical properties. J. Adv. Manuf. Technol. 65:1529-1534. https://doi.org/10.1007/s00170-012-4277-y
42. Han X, Yang D, Yang C, et al. (2019) Carbon fiber reinforced PEEK composites based on 3D-printing technology for orthopedic and dental applications. 8:https://doi.org/10.3390/jcm8020240
43. Wu H, Fahy WP, Kim S, et al. (2020) Recent developments in polymers/polymer nanocomposites for additive manufacturing. Prog Mater Sci 111:https://doi.org/10.1016/j.pmatsci.2020.100638
44. Saad MS, Nor AM, Baharudin ME, et al. (2019) Optimization of surface roughness in FDM 3D printer using response surface methodology, particle swarm optimization, and symbiotic organism search algorithms. Int J Adv Manuf Technol 105:5121-5137. https://doi.org/10.1007/s00170-019-04568-3
45. Mikhalchan A, Tay TE, Banas AM, et al. (2020) Development of continuous CNT fibre-reinforced PMMA filaments for additive manufacturing: A case study by AFM-IR nanoscale imaging. Mater. Lett. 262:127182. https://doi.org/10.1016/j.matlet.2019.127182
46. Stewart ML (2020) 3D-printed polypropylene transtibial sockets: Mechanical behavior. Proc. Inst. Mech. Eng. https://doi.org/10.1177/0954406220943922
47. Mckeen LW (2018) The effect of sterilization on plastics and elastomers. William Andrew Publishing.
48. Chen N, Wan C, Zhang Y, et al. (2004) Effect of nano-CaCO3 on mechanical properties of PVC and PVC/Blendex blend. Polym. Test. 23:169-174. https://doi.org/10.1016/S0142-9418(03)00076-X
49. Rostam S, Ali AK, Abdalmuhammad FH (2016) Experimental investigation of mechanical properties of PVC polymer under different heating and cooling conditions. J. Eng. 2016:https://doi.org/10.1155/2016/3791417
50. Sobha A, Sreekala P, Narayanankutty SK (2017) Electrical, thermal, mechanical and electromagnetic interference shielding properties of PANI/FMWCNT/TPU composites. Prog. Org. Coat. 113:168-174. https://doi.org/10.1016/j.porgcoat.2017.09.001

51. Eom R-I, Lee H, Lee Y (2019) Evaluation of thermal properties of 3D spacer technical materials in cold environments using 3D printing technology. 11:1438.
52. Tricco AC, Lillie E, Zarin W, et al. (2018) PRISMA extension for scoping reviews (PRISMA-ScR): checklist and explanation. Ann. Intern. Med. 169:467-473. https://doi.org/10.7326/M18-0850
53. Burck C (2005) Comparing qualitative research methodologies for systemic research: The use of grounded theory, discourse analysis and narrative analysis. 27:237-262. https://doi.org/10.1111/j.1467-6427.2005.00314.x
54. Wohlers T (2020) 3D printing and additive manufacturing: Global state of the industry, in Wohlers Report 2020. Wohlers Associates.
55. Du S, Liu C, Huang D (2015) A shearlet-based separation method of 3D engineering surface using high definition metrology. Precis. Eng. 40:55-73. https://doi.org/10.1016/j.precisioneng.2014.10.004
56. Geng H, Li J, Xiong J, et al. (2018) Formation and improvement of surface waviness for additive manufacturing 5A06 aluminium alloy component with GTAW system. Rapid Prototyping J. 24:342-350. https://doi.org/10.1108/RPJ-04-2016-0064
57. Scheers J, Vermeulen M, De Maré C, et al. (1998) Assessment of steel surface roughness and waviness in relation with paint appearance. Int. J. Mach. Tools Manuf. 38:647-656. https://doi.org/10.1016/S0890-6955(97)00113-2
58. Wi K, Suresh V, Wang K, et al. (2020) Quantifying quality of 3D printed clay objects using a 3D structured light scanning system. Addit. Manuf. 32:https://doi.org/10.1016/j.addma.2019.100987
59. Triantaphyllou A, Giusca CL, Macaulay GD, et al. (2015) Surface texture measurement for additive manufacturing. Surf. Topogr.-Metrol. Prop. 3:8. https://doi.org/10.1088/2051-672x/3/2/024002
60. Iso (2021) Geometrical product specifications (GPS) — Surface texture: Profile — Part 2: Terms, definitions and surface texture parameters, in ISO 21920-2:2021. International Organization for Standardization: Geneva, Switzerland. p. 1-86.
61. Iso (2021) Geometrical product specifications (GPS) — Surface texture: Areal — Part 2: Terms, definitions and surface texture parameters, in ISO 25178-2:2021. International Organization for Standardization: Geneva, Switzerland. p. 1-64.
62. Gadelmawla ES, Koura MM, Maksoud TMA, et al. (2002) Roughness parameters. 123:133-145. https://doi.org/10.1016/S0924-0136(02)00060-2
63. Bruce RW (2012) Handbook of lubrication and tribology, volume II: Theory and design. Vol. 2. CRC press.
64. Li Y, Linke BS, Voet H, et al. (2017) Cost, sustainability and surface roughness quality – A comprehensive analysis of products made with personal 3D printers. CIRP J. Manuf. Sci. Technol. 16:1-11. https://doi.org/10.1016/j.cirpj.2016.10.001
65. Townsend A, Senin N, Blunt L, et al. (2016) Surface texture metrology for metal additive manufacturing: a review. Precis Eng 46:34-47. https://doi.org/10.1016/j.precisioneng.2016.06.001
66. Launhardt M, Worz A, Loderer A, et al. (2016) Detecting surface roughness on SLS parts with various measuring techniques. Polym. Test 53:217-226. https://doi.org/10.1016/j.polymertesting.2016.05.022
67. Krolczyk G, Raos P, Legutko S (2014) Experimental analysis of surface roughness and surface texture of machined and fused deposition modelled parts. 21:217-221.
68. Leach R (2011) Optical measurement of surface topography. Vol. 8. Springer.
69. Beitz S, Uerlich R, Bokelmann T, et al. (2019) Influence of powder deposition on powder bed and specimen properties. Mater. 12:https://doi.org/10.3390/ma12020297

70. Kumar K, Kumar GS (2015) An experimental and theoretical investigation of surface roughness of poly-jet printed parts: This paper explains how local surface orientation affects surface roughness in a poly-jet process. Virtual Phys. Prototyping 10:23-34. https://doi.org/10.1080/17452759.2014.999218
71. Kim GD, Oh YT (2008) A benchmark study on rapid prototyping processes and machines: Quantitative comparisons of mechanical properties, accuracy, roughness, speed, and material cost. 222:201-215. https://doi.org/10.1243/09544054jem724
72. Payami Golhin A, Strandlie A, John Green P (2021) The influence of wedge angle, feedstock color, and infill density on the color difference of FDM objects. J. Imaging Sci. Technol. 65:1-15. https://doi.org/10.2352/J.ImagingSci.Technol.2021.65.5.050408
73. Grimm T, Wiora G, Witt G (2015) Characterization of typical surface effects in additive manufacturing with confocal microscopy. 3:014001.
74. Sood AK, Ohdar RK, Mahapatra SS (2009) Improving dimensional accuracy of fused deposition modelling processed part using grey Taguchi method. Mater. Des. 30:4243-4252. https://doi.org/10.1016/j.matdes.2009.04.030
75. Livesu M, Ellero S, Martínez J, et al. (2017) From 3D models to 3D prints: an overview of the processing pipeline. in Computer Graphics Forum. Wiley Online Library.2. https://doi.org/10.1111/cgf.13147
76. Taufik M, Jain PK (2020) Part surface quality improvement studies in fused deposition modelling process: a review. Aust. J. Mech. Eng. https://doi.org/10.1080/14484846.2020.1723342
77. Turner BN, Strong R, Gold SA (2014) A review of melt extrusion additive manufacturing processes: I. Process design and modeling. Rapid Prototyp. J. 20:192-204. https://doi.org/10.1108/RPJ-01-2013-0012
78. Singh D, Singh R, Boparai KS (2018) Development and surface improvement of FDM pattern based investment casting of biomedical implants: A state of art review. J. Manuf. Process. 31:80-95. https://doi.org/10.1016/j.jmapro.2017.10.026
79. Popescu D, Zapciu A, Amza C, et al. (2018) FDM process parameters influence over the mechanical properties of polymer specimens: A review. Polym. Test. 69:157-166. https://doi.org/10.1016/j.polymertesting.2018.05.020
80. Agarwala MK, Jamalabad VR, Langrana NA, et al. (1996) Structural quality of parts processed by fused deposition. Rapid Prototyp. J. https://doi.org/10.1108/13552549610732034
81. Abdulhadi HS, Mian A (2019) Effect of strut length and orientation on elastic mechanical response of modified body-centered cubic lattice structures. Proc. Inst. Mech. Eng. Part L J. Mat. Des. Appl. 233:2219-2233. https://doi.org/10.1177/1464420719841084
82. Hafsa MN, Kassim N, Ismail S, et al. (2018) Study on surface roughness quality of FDM and MJM additive manufacturing model for implementation as investment casting sacrificial pattern. J. Mech. Eng. 5:25-34.
83. Guessasma S, Belhabib S, Nouri H (2019) Microstructure, Thermal and Mechanical Behavior of 3D Printed Acrylonitrile Styrene Acrylate. Macromol. Mater. Eng. 304:https://doi.org/10.1002/mame.201800793
84. Haque ME, Banerjee D, Mishra SB, et al. (2019) A numerical approach to measure the surface roughness of FDM build part. Elsevier Ltdhttps://doi.org/10.1016/j.matpr.2019.07.659
85. Reddy V, Flys O, Chaparala A, et al. (2018) Study on surface texture of Fused Deposition Modeling. Elsevier B.V.https://doi.org/10.1016/j.promfg.2018.06.108
86. Czyżewski P, Marciniak D, Nowinka B, et al. (2022) Influence of extruder's nozzle diameter on the improvement of functional properties of 3D-printed PLA products. 14:https://doi.org/10.3390/polym14020356

87. Anitha R, Arunachalam S, Radhakrishnan P (2001) Critical parameters influencing the quality of prototypes in fused deposition modelling. J. Mater. Process. Technol. 118:385-388. https://doi.org/10.1016/S0924-0136(01)00980-3
88. Srinivasan R, Ruban W, Deepanraj A, et al. (2020) Effect on infill density on mechanical properties of PETG part fabricated by fused deposition modelling. Materials Today: Proceedings https://doi.org/10.1016/j.matpr.2020.03.797
89. Xia H, Lu J, Dabiri S, et al. (2018) Fully resolved numerical simulations of fused deposition modeling. Part I: fluid flow. Rapid Prototyp. J. https://doi.org/10.1108/RPJ-12-2016-0217
90. Gebisa AW, Lemu HG (2018) Investigating effects of Fused-deposition modeling (FDM) processing parameters on flexural properties of ULTEM 9085 using designed experiment. Mater. 11:https://doi.org/10.3390/ma11040500
91. Sood AK, Mahapatra S, Ohdar R (2011) Weighted principal component approach for improving surface finish of ABS plastic parts built through fused deposition modelling process. Int. J. Rapid Manuf. 2:4-27. https://doi.org/10.1504/IJRapidM.2011.040687
92. Peng AH (2012) Methods of improving part accuracy during rapid prototyping. Adv. Mater. Res. 430:760-763. https://doi.org/10.4028/www.scientific.net/AMR.430-432.760
93. Sugavaneswaran M, Nayak U, Saha S, et al. (2018) Additive manufacturing of fractal antenna for electronics applications. Pro-AMhttps://doi.org/10.25341/D49W29
94. Wang T-M, Xi J-T, Jin Y (2007) A model research for prototype warp deformation in the FDM process. Int. J. Adv. Manuf. Technol. 33:1087-1096. https://doi.org/10.1007/s00170-006-0556-9
95. Kattethota G, Henderson M (1998) A visual tool to improve layered manufacturing part quality. in 1998 International Solid Freeform Fabrication Symposium. https://doi.org/10.26153/tsw/616
96. Reeves PE, Cobb RC (1997) Reducing the surface deviation of stereolithography using in-process techniques. Rapid Prototyp. J. https://doi.org/10.1108/13552549710169255
97. Durgun I, Ertan R (2014) Experimental investigation of FDM process for improvement of mechanical properties and production cost. Rapid Prototyp. J. https://doi.org/10.1108/RPJ-10-2012-0091
98. Jiang J, Xu X, Stringer J (2018) Support Structures for Additive Manufacturing: A Review. J. manuf. mater. process. 2:64. https://doi.org/10.3390/jmmp2040064
99. Buj-Corral I, Domínguez-Fernández A, Durán-Llucià R (2019) Influence of print orientation on surface roughness in fused deposition modeling (FDM) processes. 12:3834. https://doi.org/10.3390/ma12233834
100. Pandey PM, Reddy NV, Dhande SG (2003) Slicing procedures in layered manufacturing: a review. Rapid Prototyp. J. https://doi.org/10.1108/13552540310502185
101. Rahmati S, Vahabli E (2015) Evaluation of analytical modeling for improvement of surface roughness of FDM test part using measurement results. Int J Adv Manuf Technol 79:823-829. https://doi.org/10.1007/s00170-015-6879-7
102. Böning G, Jahnke P, Feldhaus F, et al. (2020) Stepwise analysis of potential accuracy-influencing factors of iodine quantification on a fast kVp-switching second-generation dual-energy CT: from 3D-printed phantom to a simple solution in clinical routine use. Acta Radiol. 61:424-431. https://doi.org/10.1177/0284185119861312
103. Pandey PM, Reddy NV, Dhande SG (2003) Real time adaptive slicing for fused deposition modelling. 43:61-71. https://doi.org/10.1016/S0890-6955(02)00164-5
104. Zhao D, Guo W (2020) Mixed-layer adaptive slicing for robotic additive manufacturing (AM) based on decomposing and regrouping. 31:985-1002. https://doi.org/10.1007/s10845-019-01490-z

105. Yang L, Li S, Li Y, et al. (2019) Experimental investigations for optimizing the extrusion parameters on FDM PLA printed parts. J Mater Eng Perform 28:169-182. https://doi.org/10.1007/s11665-018-3784-x
106. Shirmohammadi M, Goushchi SJ, Keshtiban PM (2021) Optimization of 3D printing process parameters to minimize surface roughness with hybrid artificial neural network model and particle swarm algorithm. 6:199-215.
107. Hooshmand MJ, Mansour S, Dehghanian A (2021) Optimization of build orientation in FFF using response surface methodology and posterior-based method. 27:967-994. https://doi.org/10.1108/RPJ-07-2020-0162
108. Mendricky R, Fris D (2020) Analysis of the accuracy and the surface roughness of FDM/FFF technology and optimisation of process parameters. 27:1166-1173. https://doi.org/10.17559/TV-20190320142210
109. Saad MS, Mohd Nor A, Abd Rahim I, et al. (2022) Optimization of FDM process parameters to minimize surface roughness with integrated artificial neural network model and symbiotic organism search. https://doi.org/10.1007/s00521-022-07370-7
110. Jiang S, Hu K, Zhan Y, et al. (2022) Theoretical and experimental investigation on the 3D surface roughness of material extrusion additive manufacturing products. 14:https://doi.org/10.3390/polym14020293
111. García E, Núñez PJ, Chacón JM, et al. (2020) Comparative study of geometric properties of unreinforced PLA and PLA-Graphene composite materials applied to additive manufacturing using FFF technology. Polym. Test. 91:https://doi.org/10.1016/j.polymertesting.2020.106860
112. Wang P, Zou B, Ding S (2019) Modeling of surface roughness based on heat transfer considering diffusion among deposition filaments for FDM 3D printing heat-resistant resin. Appl. Therm. Eng. 161:https://doi.org/10.1016/j.applthermaleng.2019.114064
113. García Plaza E, Núñez López PJ, Caminero Torija MÁ, et al. (2019) Analysis of PLA geometric properties processed by FFF additive manufacturing: Effects of process parameters and plate-extruder precision motion. Polym. 11:https://doi.org/10.3390/polym11101581
114. De Leon AS, Dominguez-Calvo A, Molina SI (2019) Materials with enhanced adhesive properties based on acrylonitrile-butadiene-styrene (ABS)/thermoplastic polyurethane (TPU) blends for fused filament fabrication (FFF). Mater. Des. 182:11. https://doi.org/10.1016/j.matdes.2019.108044
115. Barrios JM, Romero PE (2019) Improvement of surface roughness and hydrophobicity in PETG parts manufactured via fused deposition modeling (FDM): An application in 3D printed self-cleaning parts. 12:https://doi.org/10.3390/ma12152499
116. Amiri A, Zolfaghari A, Shakeri M (2022) 3D printing of glass fiber reinforced acrylonitrile butadiene styrene and investigation of tensile, flexural, warpage and roughness properties. Polym. Compos. https://doi.org/10.1002/pc.26937
117. Wang P, Zou B, Xiao H, et al. (2019) Effects of printing parameters of fused deposition modeling on mechanical properties, surface quality, and microstructure of PEEK. J Mater Process Technol 271:62-74. https://doi.org/10.1016/j.jmatprotec.2019.03.016
118. Mou YA, Koc M (2019) Dimensional capability of selected 3DP technologies. Rapid Prototyp. J. 25:915-924. https://doi.org/10.1108/RPJ-03-2019-0061
119. Petzold S, Klett J, Schauer A, et al. (2019) Surface roughness of polyamide 12 parts manufactured using selective laser sintering. Polym Test 80:https://doi.org/10.1016/j.polymertesting.2019.106094
120. Kim TB, Yue S, Zhang Z, et al. (2014) Additive manufactured porous titanium structures: Through-process quantification of pore and strut networks. J Mater Process Technol 214:2706-2715. https://doi.org/10.1016/j.jmatprotec.2014.05.006

121. Kruth J-P, Levy G, Klocke F, et al. (2007) Consolidation phenomena in laser and powder-bed based layered manufacturing. CIRP Ann. 56:730-759. https://doi.org/10.1016/j.cirp.2007.10.004
122. Van Bael S, Kerckhofs G, Moesen M, et al. (2011) Micro-CT-based improvement of geometrical and mechanical controllability of selective laser melted Ti6Al4V porous structures. Mater. Sci. Eng. A 528:7423-7431. https://doi.org/10.1016/j.msea.2011.06.045
123. Allison J, Sharpe C, Seepersad CC (2017) A test part for evaluating the accuracy and resolution of a polymer powder bed fusion process. J Mech Des, Trans ASME 139:https://doi.org/10.1115/1.4037303
124. Sachdeva A, Singh S, Sharma VS (2013) Investigating surface roughness of parts produced by SLS process. Int. J. Adv. Manuf. Technol. 64:1505-1516. https://doi.org/10.1007/s00170-012-4118-z
125. Yang F, Schnuerch A, Chen X (2021) Quantitative influences of successive reuse on thermal decomposition, molecular evolution, and elemental composition of polyamide 12 residues in selective laser sintering. 115:3121-3138. https://doi.org/10.1007/s00170-021-07368-w
126. Uddin M, Williams D, Blencowe A (2021) Recycling of selective laser sintering waste Nylon powders into fused filament fabrication parts reinforced with Mg particles. 13:https://doi.org/10.3390/polym13132046
127. Akilesh M, Elango PR, Devanand AA, et al. (2018) Optimization of selective laser sintering process parameters on surface quality. in 3D Printing and Additive Manufacturing Technologies. p. 141-157.
128. Wang X, Jiang M, Zhou Z, et al. (2017) 3D printing of polymer matrix composites: A review and prospective. 110:442-458. https://doi.org/10.1016/j.compositesb.2016.11.034
129. Yuan S, Shen F, Chua CK, et al. (2019) Polymeric composites for powder-based additive manufacturing: Materials and applications. Prog. Polym. Sci. 91:141-168. https://doi.org/10.1016/j.progpolymsci.2018.11.001
130. Raghunath N, Pandey PM (2007) Improving accuracy through shrinkage modelling by using Taguchi method in selective laser sintering. Int. J. Mach. Tools Manuf. 47:985-995. https://doi.org/10.1016/j.ijmachtools.2006.07.001
131. Xiong Y, Pei H, Lv Q, et al. (2022) A facile fabrication of PA12/CNTs nanocomposites with enhanced three-dimensional segregated conductive networks and electromagnetic interference shielding property through selective laser sintering. 7:4293-4304. https://doi.org/10.1021/acsomega.1c06021
132. Sofia D, Chirone R, Lettieri P, et al. (2018) Selective laser sintering of ceramic powders with bimodal particle size distribution. Chem. Eng. Res. Des. 136:536-547. https://doi.org/10.1016/j.cherd.2018.06.008
133. Brouwers H (2006) Particle-size distribution and packing fraction of geometric random packings. Phys. Rev. E 74:031309. https://doi.org/10.1103/PhysRevE.74.031309
134. Gibson I, Rosen D, Stucker B, et al. (2014) Additive manufacturing technologies. Vol. 17. Springer.
135. Chatham CA, Long TE, Williams CB (2019) A review of the process physics and material screening methods for polymer powder bed fusion additive manufacturing. Prog. Polym. Sci. 93:68-95. https://doi.org/10.1016/j.progpolymsci.2019.03.003
136. Xia M, Nematollahi B, Sanjayan J (2019) Printability, accuracy and strength of geopolymer made using powder-based 3D printing for construction applications. 101:179-189. https://doi.org/10.1016/j.autcon.2019.01.013
137. Zhu X, Yang Q (2020) Sintering the feasibility improvement and mechanical property of UHMWPE via selective laser sintering. Plast. Rubber Compos. https://doi.org/10.1080/14658011.2020.1718321

138. Charoo NA, Barakh Ali SF, Mohamed EM, et al. (2020) Selective laser sintering 3D printing–an overview of the technology and pharmaceutical applications. 46:869-877. https://doi.org/10.1080/03639045.2020.1764027
139. Goodridge RD, Dalgarno KW, Wood DJ (2006) Indirect selective laser sintering of an apatite-mullite glass-ceramic for potential use in bone replacement applications. 220:57-68. https://doi.org/10.1243/095441105X69051
140. Uhlmann E, Rethmeier M, Graf B, et al. (2015) Flexible manufacturing with an additive process chain design, production and surface finish. in ASPE Spring topical meeting - Achieving precision tolerances in additive manufacturing (Proceedings). Raleigh, NC, USA
141. Gao X, Abreu Faria G, Zhang W, et al. (2020) Numerical analysis of non-spherical particle effect on molten pool dynamics in laser-powder bed fusion additive manufacturing. Comput Mater Sci 179:https://doi.org/10.1016/j.commatsci.2020.109648
142. Puttonen T, Salmi M, Partanen J (2021) Mechanical properties and fracture characterization of additive manufacturing polyamide 12 after accelerated weathering. Polym. Test. 104:https://doi.org/10.1016/j.polymertesting.2021.107376
143. Bibas C (2022) Lens-free optical scanners for metal additive manufacturing. 74:1176-1187. https://doi.org/10.1007/s11837-021-05044-8
144. Zhan S, Guo AXY, Cao SC, et al. (2022) 3D printing soft matters and applications: A review. Int. J. Mol. Sci. 23:https://doi.org/10.3390/ijms23073790
145. Caulfield B, Mchugh PE, Lohfeld S (2007) Dependence of mechanical properties of polyamide components on build parameters in the SLS process. J. Mater. Process. Technol. 182:477-488. https://doi.org/10.1016/j.jmatprotec.2006.09.007
146. Gibson I, Shi D (1997) Material properties and fabrication parameters in selective laser sintering process. Rapid prototyping journal https://doi.org/10.1108/13552549710191836
147. Zhang H, Leblanc S (2018) Processing parameters for selective laser sintering or melting of oxide ceramics. in Additive Manufacturing of High-performance Metals and Alloys-Modeling and Optimization, I. Shishkovsky, Editor., IntechOpen. p. 1-44.
148. Lupone F, Padovano E, Casamento F, et al. (2022) Process phenomena and material properties in selective laser sintering of polymers: A review. 15:https://doi.org/10.3390/ma15010183
149. Liu W, Zhu ZC, Ye SH, et al. (2019) Investigation of professional design practice: a framework for designing plastic consumer products for additive manufacturing. Int. J. Mater. Prod. Technol. 58:104-128. https://doi.org/10.1504/ijmpt.2019.097663
150. Yaagoubi H, Abouchadi H, Taha Janan M (2021) Numerical simulation of heat transfer in the selective laser sintering process of Polyamide12. 7:189-199. https://doi.org/10.1016/j.egyr.2021.08.089
151. Strobbe D, Dadbakhsh S, Verbelen L, et al. (2018) Selective laser sintering of polystyrene: a single-layer approach. Plast. Rubber Compos. 47:2-8. https://doi.org/10.1080/14658011.2017.1399532
152. Borille AV, De Oliveira Gomes J, Lopes D (2017) Geometrical analysis and tensile behaviour of parts manufactured with flame retardant polymers by additive manufacturing. Rapid Prototyping J. 23:169-180. https://doi.org/10.1108/RPJ-09-2015-0130
153. Wörz A, Drummer D (2018) Tribological anisotropy of selective laser sintered PA12 parts. Polym Test 70:117-126. https://doi.org/10.1016/j.polymertesting.2018.06.028
154. Modi YK, Sanadhya S (2018) Design and additive manufacturing of patient-specific cranial and pelvic bone implants from computed tomography data. J. Braz. Soc. Mech. Sci. Eng. 40:https://doi.org/10.1007/s40430-018-1425-9

155. Kinstlinger IS, Bastian A, Paulsen SJ, et al. (2016) Open-Source Selective Laser Sintering (OpenSLS) of nylon and biocompatible polycaprolactone. PLoS ONE 11:https://doi.org/10.1371/journal.pone.0147399
156. Ellis A, Brown R, Hopkinson N (2015) The effect of build orientation and surface modification on mechanical properties of high speed sintered parts. Surf. Topogr. Metrol. Prop. 3:https://doi.org/10.1088/2051-672X/3/3/034005
157. Xu Z, Wang Y, Wu D, et al. (2019) The process and performance comparison of polyamide 12 manufactured by multi jet fusion and selective laser sintering. J. Manuf. Processes 47:419-426. https://doi.org/10.1016/j.jmapro.2019.07.014
158. Goodridge RD, Tuck CJ, Hague RJM (2012) Laser sintering of polyamides and other polymers. Prog Mater Sci 57:229-267. https://doi.org/10.1016/j.pmatsci.2011.04.001
159. Glückstad J, Palima D (2017) Light robotics: Structure-mediated nanobiophotonics. Elsevier.
160. Bártolo PJ (2011) Stereolithography: materials, processes and applications. Springer Science & Business Media.
161. Ribo MM (2020) Vat photopolymerization process chain. Technical University of Denmark: Kgs. Lyngby.
162. Renap K, Kruth J-P (1995) Recoating issues in stereolithography. Rapid Prototyp. J. https://doi.org/10.1108/13552549510094223
163. Santoliquido O, Colombo P, Ortona A (2019) Additive manufacturing of ceramic components by digital light processing: A comparison between the “bottom-up” and the “top-down” approaches. J. Eur. Ceram. Soc. 39:2140-2148. https://doi.org/10.1016/j.jeurceramsoc.2019.01.044
164. Pedersen DB, Zhang Y, Nielsen JS, et al. (2016) A self-peeling vat for improved release capabilities during DLP materials processing. in 2nd International Conference on Progress in Additive Manufacturing. Research Publishing Services
165. Barone S, Neri P, Paoli A, et al. (2019) Development of a DLP 3D printer for orthodontic applications. in Procedia Manufacturing. https://doi.org/10.1016/j.promfg.2020.01.187
166. Ribó MM, Islam A (2017) 3D Printing of Bio-inspired surfaces. in Wilhelm und Else Heraeus Seminar: Bio-inspired, Nano-and Microstructured Surfaces: New Functionality by Material and Structure.
167. Thompson MK, Mischkot M (2015) Design of test parts to characterize micro additive manufacturing processes. Elsevierhttps://doi.org/10.1016/j.procir.2015.07.065
168. Zhou JG, Herscovici D, Chen CC (2000) Parametric process optimization to improve the accuracy of rapid prototyped stereolithography parts. Int. J. Mach. Tools Manuf. 40:363-379. https://doi.org/10.1016/S0890-6955(99)00068-1
169. Salonitis K (2014) Stereolithography. in Comprehensive materials processing, S. Hashmi, Editor., Elsevier Ltd. p. 19-67.
170. Khorasani ER, Baseri H (2013) Determination of optimum SLA process parameters of H-shaped parts. J. Mech. Sci. Technol. 27:857-863. https://doi.org/10.1007/s12206-013-0111-1
171. Pagac M, Hajnys J, Ma Q-P, et al. (2021) A review of vat photopolymerization technology: Materials, applications, challenges, and future trends of 3D printing. 13:598. https://doi.org/10.3390/polym13040598
172. Arnold C, Monsees D, Hey J, et al. (2019) Surface quality of 3D-printed models as a function of various printing parameters. 12:https://doi.org/10.3390/ma12121970
173. Khodaii J, Rahimi A (2020) Improving the surface roughness in stereolithography by controlling surface angle, hatch spaces, and postcuring time. 2:e12193. https://doi.org/10.1002/eng2.12193

174. Bagheri A, Jin J (2019) Photopolymerization in 3D Printing. ACS Appl. Polym. Mater. 1:593-611. https://doi.org/10.1021/acsapm.8b00165
175. Rosen DW (2008) Stereolithography and rapid prototyping. in BioNanoFluidic MEMS. p. 175-196.
176. Hanemann T, Honnef K (2018) Optical and Thermomechanical Properties of Doped Polyfunctional Acrylate Copolymers. 10:337. https://doi.org/10.3390/polym10030337
177. Corbel S, Dufaud O, Roques-Carmes T (2011) Materials for stereolithography. in Stereolithography: Materials, Processes and Applications, P.J. Bártolo, Editor., Springer US: Boston, MA. p. 141-159.
178. Crivello JV, Reichmanis E (2014) Photopolymer Materials and Processes for Advanced Technologies. Chemistry of Materials 26:533-548. https://doi.org/10.1021/cm402262g
179. Shaukat U, Rossegger E, Schlögl S (2022) A Review of Multi-Material 3D Printing of Functional Materials via Vat Photopolymerization. 14:2449. https://doi.org/10.3390/polym14122449
180. Manapat JZ, Chen Q, Ye P, et al. (2017) 3D Printing of Polymer Nanocomposites via Stereolithography. Macromol. Mater. Eng. 302:https://doi.org/10.1002/mame.201600553
181. Peer G, Eibel A, Gorsche C, et al. (2019) Ester-Activated Vinyl Ethers as Chain Transfer Agents in Radical Photopolymerization of Methacrylates. 52:2691-2700. https://doi.org/10.1021/acs.macromol.9b00085
182. Diptanshu, Miao G, Ma C (2019) Vat photopolymerization 3D printing of ceramics: Effects of fine powder. Manuf. Let. 21:20-23. https://doi.org/10.1016/j.mfglet.2019.07.001
183. Medellin A, Du W, Miao G, et al. (2019) Vat photopolymerization 3D printing of nanocomposites: A literature review. J. Micro Nano-Manuf. 7:https://doi.org/10.1115/1.4044288
184. Kowsari K, Zhang B, Panjwani S, et al. (2018) Photopolymer formulation to minimize feature size, surface roughness, and stair-stepping in digital light processing-based three-dimensional printing. 24:627-638. https://doi.org/10.1016/j.addma.2018.10.037
185. Srinivasan M, Kalberer N, Kamnoedboon P, et al. (2021) CAD-CAM complete denture resins: an evaluation of biocompatibility, mechanical properties, and surface characteristics. J. Dent. 114:103785. https://doi.org/10.1016/j.jdent.2021.103785
186. Miedzińska D, Gieleta R, Popławski A (2020) Experimental study on influence of curing time on strength behavior of sla-printed samples loaded with different strain rates. 13:5825. https://doi.org/10.3390/ma13245825
187. Zips S, Hiendlmeier L, Weiß LJK, et al. (2020) Biocompatible, flexible, and oxygen-permeable silicone-hydrogel material for stereolithographic printing of microfluidic lab-on-a-chip and cell-culture devices. ACS Appl. Polym. Mater. 3:243-258. https://doi.org/10.1021/acsapm.0c01071
188. Park HK, Shin M, Kim B, et al. (2018) A visible light-curable yet visible wavelength-transparent resin for stereolithography 3D printing. NPG Asia Mater. 10:82-89. https://doi.org/10.1038/s41427-018-0021-x
189. Zuchowicz NC, Belgodere JA, Liu Y, et al. (2022) Low-cost resin 3-D printing for rapid prototyping of microdevices: Opportunities for supporting aquatic germplasm repositories. 7:49. https://doi.org/10.3390/fishes7010049
190. Takada K, Sun H-B, Kawata S (2005) Improved spatial resolution and surface roughness in photopolymerization-based laser nanowriting. Appl. Phys. Lett. 86:071122. https://doi.org/10.1063/1.1864249
191. Janusziewicz R, Tumbleston JR, Quintanilla AL, et al. (2016) Layerless fabrication with continuous liquid interface production. Proc. Natl. Acad. Sci. U. S. A. 113:11703-11708. https://doi.org/10.1073/pnas.1605271113

192. Tumbleston JR, Shirvanyants D, Ermoshkin N, et al. (2015) Continuous liquid interface production of 3D objects. Science 347:1349-1352. https://doi.org/10.1126/science.aaa2397
193. Yao H, Wang J, Mi S (2017) Photo processing for biomedical hydrogels design and functionality: A review. 10:11. https://doi.org/10.3390/polym10010011
194. Eiríksson ER (2018) Computer vision for additive manufacturing, in DTU Compute. Technical University of Denmark: Kgs. Lyngby.
195. Steyrer B, Busetti B, Harakály G, et al. (2018) Hot Lithography vs. room temperature DLP 3D-printing of a dimethacrylate. Additive Manufacturing 21:209-214. https://doi.org/10.1016/j.addma.2018.03.013
196. Kim I, Kim S, Andreu A, et al. (2022) Influence of dispersant concentration toward enhancing printing precision and surface quality of vat photopolymerization 3D printed ceramics. 52:https://doi.org/10.1016/j.addma.2022.102659
197. Dulieu-Barton J, Fulton M (2000) Mechanical properties of a typical stereolithography resin. 36:81-87. https://doi.org/10.1111/j.1475-1305.2000.tb01177.x
198. Luo X, Li J, Lucas M (2017) Galvanometer scanning technology for laser additive manufacturing. SPIEhttps://doi.org/10.1117/12.2252973
199. Yang Q, Lu Z, Zhou J, et al. (2017) A novel method for improving surface finish of stereolithography apparatus. Int J Adv Manuf Technol 93:1537-1544. https://doi.org/10.1007/s00170-017-0529-1
200. Hui J, Yan Z, Lv J, et al. (2022) An investigation on energy consumption and part quality of stereolithography apparatus manufactured parts. 28:52-67. https://doi.org/10.1108/RPJ-06-2020-0143
201. Mostafa KG, Nobes DS, Qureshi AJ (2020) Investigation of light-induced surface roughness in projection micro-stereolithography additive manufacturing (PμSLA). in Procedia CIRP. https://doi.org/10.1016/j.procir.2020.05.177
202. Shanmugasundaram SA, Razmi J, Mian MJ, et al. (2020) Mechanical anisotropy and surface roughness in additively manufactured parts fabricated by stereolithography (SLA) using statistical analysis. 13:https://doi.org/10.3390/ma13112496
203. Zhao J, Yang Y, Li L (2020) A comprehensive evaluation for different post-curing methods used in stereolithography additive manufacturing. 56:867-877. https://doi.org/10.1016/j.jmapro.2020.04.077
204. Kazemi M, Rahimi A (2019) Improving the efficiency of fabrication of AM parts by segmentation design in DLP process. Rapid Prototyping J. 25:1155-1168. https://doi.org/10.1108/RPJ-09-2018-0253
205. Kim N, Bhalerao I, Han D, et al. (2019) Improving surface roughness of additively manufactured parts using a photopolymerization model and multi-objective particle swarm optimization. Appl. Sci. 9:https://doi.org/10.3390/app9010151
206. Milde J, Peterka J, Jurina F, et al. (2021) Influence of selected photopolymers on the resulting accuracy and surface roughness of the component in digital light processing technology. in Annals of DAAAM and Proceedings of the International DAAAM Symposium. https://doi.org/10.2507/32nd.daaam.proceedings.034
207. Reeves P, Cobb R (1997) Surface roughness investigation of Stereolithography ACES components. in Proceedings of the Second National Conference on Rapid Prototyping and Tooling Research.
208. Andrzejewska E, Andrzejewski M (1998) Polymerization kinetics of photocurable acrylic resins. J. Polym. Sci. A. Polym. Chem. 36:665-673. https://doi.org/10.1002/(SICI)1099-0518(199803)36:4<665::AID-POLA15>3.0.CO;2-K
209. Puebla K, Arcaute K, Quintana R, et al. (2012) Effects of environmental conditions, aging, and build orientations on the mechanical properties of ASTM type i specimens

manufactured via stereolithography. Rapid Prototyping J. 18:374-388. https://doi.org/10.1108/13552541211250373
210. Hague R, Mansour S, Saleh N, et al. (2004) Materials analysis of stereolithography resins for use in Rapid Manufacturing. 39:2457-2464. https://doi.org/10.1023/B:JMSC.0000020010.73768.4a
211. Payami Golhin A, Srivastava C, Strandlie A, et al. (2023) Effects of accelerated aging on the appearance and mechanical performance of materials jetting products. Materials & Design 228:111863. https://doi.org/10.1016/j.matdes.2023.111863
212. Baharnezhad S, Golhin A (2017) In-situ measurement and finite element simulation of thermo-mechanical properties of AA 6063 aluminum alloy for MIG weldment. 32:https://doi.org/10.18720/MPM.3222017_15
213. Payami Golhin A, Strandlie A (2023) Appearance evaluation of digital materials in material jetting. Opt. Lasers Eng.
214. Liravi F, Salarian M, Dal Castel C, et al. (2019) High-speed material jetting additive manufacturing of silicone structures: mechanical characterization. Prog. Addit. Manuf. 4:479-495. https://doi.org/10.1007/s40964-019-00097-3
215. Suresh Babu A, Binish KM, Jaivignesh M, et al. (2018) Modelling of Functional Gradient Porous Structure and its Fabrication using Additive Manufacturing Process. Elsevier Ltdhttps://doi.org/10.1016/j.matpr.2018.10.253
216. Tan WS, Suwarno SR, An J, et al. (2017) Comparison of solid, liquid and powder forms of 3D printing techniques in membrane spacer fabrication. J. Membr. Sci. 537:283-296. https://doi.org/10.1016/j.memsci.2017.05.037
217. Holman RK, Cima MJ, Uhland SA, et al. (2002) Spreading and infiltration of inkjet-printed polymer solution droplets on a porous substrate. J. Colloid Interface Sci. 249:432-440. https://doi.org/10.1006/jcis.2002.8225
218. Yang H, Lim JC, Liu Y, et al. (2017) Performance evaluation of ProJet multi-material jetting 3D printer. 12:95-103. https://doi.org/10.1080/17452759.2016.1242915
219. Khoshkhoo A, Carrano AL, Blersch DM (2018) Effect of build orientation and part thickness on dimensional distortion in material jetting processes. Rapid Prototyping J. 24:1563-1571. https://doi.org/10.1108/RPJ-10-2017-0210
220. Singh Tomar RP, Ulu FI, Kelkar A, et al. (2019) Investigation of process induced variations in polyjet printing with digital polypropylene via homogeneous 3D tensile test coupon. American Society of Mechanical Engineers (ASME)https://doi.org/10.1115/IMECE2019-11639
221. Liravi F, Toyserkani E (2018) Additive manufacturing of silicone structures: A review and prospective. Addit. Manuf. 24:232-242. https://doi.org/10.1016/j.addma.2018.10.002
222. Giorleo L, Stampone B, Trotta G (2022) Micro injection moulding process with high-temperature resistance resin insert produced with material jetting technology: Effect of part orientation. 56:https://doi.org/10.1016/j.addma.2022.102947
223. Wei X, Bhardwaj A, Zeng L, et al. (2019) Experimental investigation of stratasys J750 polyjet printer: Effects of finish type and shore hardness on surface roughness. in ASME 2019 14th International Manufacturing Science and Engineering Conference, MSEC 2019. https://doi.org/10.1115/MSEC2019-2998
224. Cheng YL, Huang KC (2020) Preparation and characterization of color photocurable resins for full-color material jetting additive manufacturing. Polymers (Basel) 12:650. https://doi.org/10.3390/polym12030650
225. Jabari E, Liravi F, Davoodi E, et al. (2020) High speed 3D material-jetting additive manufacturing of viscous graphene-based ink with high electrical conductivity. Addit. Manuf. 35:101330. https://doi.org/10.1016/j.addma.2020.101330

226. Furbank RJ, Morris JF (2004) An experimental study of particle effects on drop formation. Phys Fluids 16:1777-1790. https://doi.org/10.1063/1.1691034
227. Zhou W, Loney D, Degertekin FL, et al. (2013) What controls dynamics of droplet shape evolution upon impingement on a solid surface? 59:3071-3082. https://doi.org/10.1002/aic.14050
228. Raman KA, Birgersson E, Sui Y, et al. (2020) Electrically induced droplet ejection dynamics under shear flow. Phys. Fluids. 32:032103. https://doi.org/10.1063/1.5143757
229. Yap YL, Wang C, Sing SL, et al. (2017) Material jetting additive manufacturing: An experimental study using designed metrological benchmarks. Precis Eng 50:275-285. https://doi.org/10.1016/j.precisioneng.2017.05.015
230. Cheng YL, Chang CH, Kuo C (2020) Experimental study on leveling mechanism for material-jetting-type color 3D printing. 26:11-20. https://doi.org/10.1108/RPJ-09-2018-0227
231. Payami Golhin A (2021) Generation of micro-and nano-textured surfaces. European Commission: Brussels. p. 1-6. https://doi.org/10.5281/zenodo.7293168
232. Bussmann M, Chandra S, Mostaghimi J (2000) Modeling the splash of a droplet impacting a solid surface. Phys. Fluids. 12:3121-3132. https://doi.org/10.1063/1.1321258
233. Howland CJ, Antkowiak A, Castrejón-Pita JR, et al. (2016) It's harder to splash on soft solids. Phys. Rev. Lett. 117:184502. https://doi.org/10.1103/PhysRevLett.117.184502
234. Mohammad Karim A, Suszynski WJ (2022) Physics of Dynamic Contact Line: Hydrodynamics Theory versus Molecular Kinetic Theory. 7:318. https://doi.org/10.3390/fluids7100318
235. Tofan-Negru A, Barbu C, Stefan A, et al. (2021) Analysis and characterization of additive manufacturing processes. 13:167-180. https://doi.org/10.13111/2066-8201.2021.13.4.14
236. Miyanaji H, Momenzadeh N, Yang L (2019) Effect of powder characteristics on parts fabricated via binder jetting process. Rapid Prototyping J. 25:332-342. https://doi.org/10.1108/RPJ-03-2018-0069
237. Gülcan O, Günaydın K, Çelik A (2022) Investigation on surface roughness of polyjet-printed airfoil geometries for small UAV applications. 9:https://doi.org/10.3390/aerospace9020082
238. Yuan J, Chen C, Yao D, et al. (2020) 3D printing of oil paintings based on material jetting and its reduction of staircase effect. 12:1-12. https://doi.org/10.3390/polym12112536
239. Pandey P, Nayak A, Taufik M (2022) Evaluation of mathematical models for surface roughness prediction of PolyJet 3D printed parts. https://doi.org/10.1080/2374068X.2022.2097416
240. Zmarzły P, Kozior T, Gogolewski D (2019) Dimensional and shape accuracy of foundry patterns fabricated through photo-curing. Teh. Vjesn. 26:1576-1584. https://doi.org/10.17559/TV-20181109115954
241. Kechagias J, Iakovakis V, Giorgo E, et al. (2014) Surface roughness optimization of prototypes produced by polyjet direct 3D printing technology. in OPT-i 2014 - 1st International Conference on Engineering and Applied Sciences Optimization, Proceedings.
242. Cazón A, Morer P, Matey L (2014) PolyJet technology for product prototyping: Tensile strength and surface roughness properties. 228:1664-1675. https://doi.org/10.1177/0954405413518515
243. Udroiu R, Mihail L (2009) Experimental determination of surface roughness of parts obtained by rapid prototyping. 9:283-286.
244. Velasco MA, Lancheros Y, Garzón-Alvarado DA (2016) Geometric and mechanical properties evaluation of scaffolds for bone tissue applications designing by a reaction-diffusion models and manufactured with a material jetting system. J. Comput. Des. Eng. 3:385-397. https://doi.org/10.1016/j.jcde.2016.06.006

245. Chand R, Sharma VS, Trehan R, et al. (2022) Investigating the dimensional accuracy and surface roughness for 3D printed parts using a multi-jet printer. https://doi.org/10.1007/s11665-022-07153-0
246. Tasch D, Schagerl M, Wazel B, et al. (2019) Impact behavior and fractography of additively manufactured polymers: Laser sintering, multijet fusion, and hot lithography. Addit. Manuf. 29:https://doi.org/10.1016/j.addma.2019.100816
247. Raigar J, Sharma VS, Srivastava S, et al. (2020) A decision support system for the selection of an additive manufacturing process using a new hybrid MCDM technique. 45:https://doi.org/10.1007/s12046-020-01338-w
248. Gomez-Torrent A, Teberio F, Martinez A, et al. (2017) A study of the additive manufacturing technology for RF/microwave components. Institute of Electrical and Electronics Engineers Inc.https://doi.org/10.23919/EuCAP.2017.7928732
249. Bodaghi M, Mobin M, Ban D, et al. (2022) Surface quality of printed porous materials for permeability rig calibration. 37:548-558. https://doi.org/10.1080/10426914.2021.1960994
250. Unkovskiy A, Spintzyk S, Kiemle T, et al. (2022) Trueness and precision of skin surface reproduction in digital workflows for facial prosthesis fabrication. https://doi.org/10.1016/j.prosdent.2021.06.050
251. Hanon MM, Zsidai L (2020) Sliding surface structure comparison of 3D printed polymers using FDM and DLP technologies. in IOP Conference Series: Materials Science and Engineering. https://doi.org/10.1088/1757-899X/749/1/012015
252. Nazir A, Jeng JY (2019) A high-speed additive manufacturing approach for achieving high printing speed and accuracy. Proc. Inst. Mech. Eng. Part C J. Mech. Eng. Sci. https://doi.org/10.1177/0954406219861664
253. Jiao F, Cheng K (2014) An experimental investigation on micro-milling of polymethyl methacrylate components with nanometric surface roughness. 228:790-796. https://doi.org/10.1177/0954405413507251
254. Whitaker TA, Simões-Franklin C, Newell FN (2008) Vision and touch: Independent or integrated systems for the perception of texture? Brain Res. 1242:59-72. https://doi.org/10.1016/j.brainres.2008.05.037
255. Parraman C, Segovia MVO (2018) 2.5 D Printing: Bridging the gap between 2D and 3D applications. John Wiley & Sons.
256. Ansari N, Payami Z, Feghhi F (2020) Synthesis of iron/graphene composites with controlled magnetization by electrochemical exfoliation/deposition using sodium dodecyl sulfate as surfactant. J. Magn. Magn. Mater. 500:166398. https://doi.org/10.1016/j.jmmm.2020.166398
257. Ansari N, Payami Z (2020) Synthesis of magnetic graphene-Fe3O4 nanocomposites by electrochemical exfoliation method. J. Nanostructures. 10:39-43. https://doi.org/10.22052/JNS.2020.01.005
258. Rafiee F, Khavari P, Payami Z, et al. (2019) Palladium nanoparticles immobilized on the magnetic few layer graphene support as a highly efficient catalyst for ligand free Suzuki cross coupling and homo coupling reactions. J. Organomet. Chem. 883:78-85. https://doi.org/10.1016/j.jorganchem.2019.01.014
259. Golhin AP, Kamrani S, Fleck C, et al. (2022) Corrosion protection of Mg-SiC nanocomposite through plasma electrolytic oxidation coating process.
260. Payami-Golhin A, Amrooni Hossaini M, Eslami-Farsani R, et al. (2014) Phosphate-free protective nanoceramic coatings for galvanized steel sheet with H2O2 additive. in Advanced Materials Research. Trans Tech Publhttps://doi.org/10.4028/www.scientific.net/AMR.829.436

261. Zindani D, Kumar K (2019) An insight into additive manufacturing of fiber reinforced polymer composite. Int. j. lightweight mater. manuf. 2:267-278. https://doi.org/10.1016/j.ijlmm.2019.08.004
262. Payami Golhin A, Srivastava C, Tingstad JF, et al. (2022) Additive manufacturing of multilayered polymer composites: Durability assessment. in Proceedings of the 20th European Conference on Composite Materials-Composites Meet Sustainability (Vol 1-6). Lausanne, Switzerland: EPFL Lausanne, Composite Construction Laboratory Switzerlandhttps://doi.org/10.5075/epfl-298799_978-2-9701614-0-0
263. Rafiee M, Farahani RD, Therriault D (2020) Multi-material 3D and 4D printing: a survey. Adv. Sci. 7:1902307. https://doi.org/10.1002/advs.201902307
264. González-Henríquez CM, Sarabia-Vallejos MA, Rodriguez-Hernandez J (2019) Polymers for additive manufacturing and 4D-printing: Materials, methodologies, and biomedical applications. Prog. Polym. Sci. 94:57-116. https://doi.org/10.1016/j.progpolymsci.2019.03.001

## Paper IV:

A. P. Golhin, C. Srivastava, A. Strandlie, A. S. Sole, S. Grammatikos, Effects of accelerated aging on the appearance and mechanical performance of materials jetting products. Materials and Design, 228, 111863 (2023). https://doi.org/10.1016/j.matdes.2023.111863

Materials & Design 228 (2023) 111863

Contents lists available at ScienceDirect

Materials & Design

journal homepage: www.elsevier.com/locate/matdes

# Effects of accelerated aging on the appearance and mechanical performance of materials jetting products

Ali Payami Golhin [a,*], Chaman Srivastava [a], Are Strandlie [a], Aditya Suneel Sole [b], Sotirios Grammatikos [a]

[a] ASEMlab – Laboratory of Advanced and Sustainable Engineering Materials, Department of Manufacturing and Civil Engineering, NTNU – Norwegian University of Science and Technology, 2815 Gjøvik, Norway
[b] Department of Computer Science, Norwegian University of Science and Technology, 2815 Gjøvik, Norway

## HIGHLIGHTS

- The long-term performance of 3D-printed bilayer polymer structures shows dynamic appearance variation because of the aging effect.
- The changing trend among glass transition temperatures over time is similar and regardless of surface finish.
- Up to 49% more elastic modulus and 4 to 15% higher glass transition temperature due to aging are recorded.
- The maximum variation in mechanical and physicochemical properties is observed following 58 days of accelerated aging.
- Magenta and black photopolymers exhibit the lowest and highest performance during accelerated aging, respectively.

## GRAPHICAL ABSTRACT

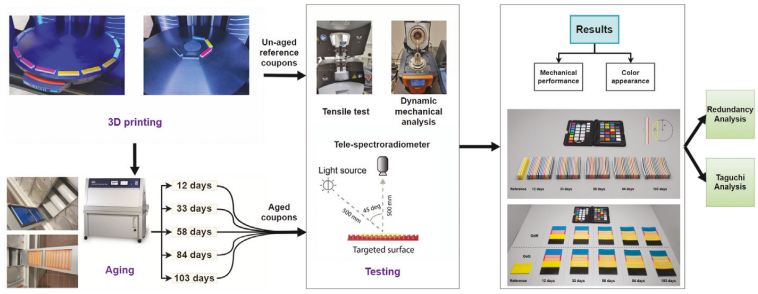


## ARTICLE INFO

*Article history:*
Received 29 January 2023
Revised 14 March 2023
Accepted 22 March 2023
Available online 27 March 2023

*Keywords:*
Material jetting
Accelerated aging
Dynamic mechanical analysis
Tensile properties

## ABSTRACT

As a result of the associated costs and environmental impacts, Material Jetting (MJT) plays a limited role in Additive Manufacturing (AM). Research on the durability and long-term performance of MJT objects by evaluating their appearance is lacking. The objective of this study is to investigate the effect of aging on the color and the physico-mechanical performance of MJT parts. This work examines the influence of production settings on objects subjected to a total of 103days of accelerated aging. The studied Printing Primary Parameters (PPPs) were resin color, build platform position (swath), and finishing configurations. The results indicated the response of the studied PPP according to the aging time was non-linear due to the dynamic appearance response to aging time. VeroBlackPlus and VeroCyan photo resins demonstrated superior color fidelity through aging by a color difference of less than 10. Based on Taguchi and Redundancy Analysis (RDA), mechanical and physicochemical properties varied the most after 58 days

*Abbreviations:* AM, Additive manufacturing; CCA, Correspondence canonical analysis; CMYK, Cyan, Magenta, Yellow, and Black colors; DCA, Detrended correspondence analysis; DMA, Dynamic mechanical analysis; DoE, Design of Experiments; E, E-modulus (stiffness); E′, Storage modulus; FDM, Fused deposition modeling; GoG, Glossy-on-Glossy finish; GoM, Glossy-on-Matte finish; LOM, Laminated object manufactured; MCDM, Mean color difference from the mean; MJT, Material jetting; PC, Principal component; PCA, Principal component analysis; PPP, Printing primary parameter; RDA, Redundancy analysis; RMSE, Root-mean-square error; rs, Spearman rho; S/N, Signal-to-Noise ratio; SD, Standard deviation; Tan δ peak, Damping; $T_g$, Glass transition temperature; TSR, Tele-spectroradiometer; $\sigma_s$, Tensile strength.

* Corresponding author.
*E-mail address:* ali.p.golhin@ntnu.no (A.P. Golhin).

https://doi.org/10.1016/j.matdes.2023.111863

Color appearance
Long-term performance

of accelerated aging, with elastic modulus retention up to 149.21% and Glass Transition temperature ($T_g$) up to 116.6%. This study demonstrates the importance of considering long-term performance during the design process of AM products, depending on the intended application and service conditions.



## 1. Introduction

Additive Manufacturing (AM) includes methods of creating an object by adding material according to a defined design, layer by layer. AM parts were restricted to the color of the raw material until full-color 3D printing became accessible using polymers. Material Jetting (MJT) technology, including PolyJet® technology, is an AM technique that has revolutionized multi-material 3D printing, employing UV-curable polymer inks. In terms of color reproduction, MJT is one of the main AM categories [1].

The increasing application of polymers in various AM techniques necessitates a thorough understanding of their on-demand long-term performance according to their application. Assessing the long-term performance of parts can be complex and time-consuming. Still, it is common for consumers to associate inferior quality with the visual differences they notice between related items. Color accuracy is critical when printing 3D objects, and the hue of the 3D-printed part should match that of the intended color in the genuine design [2]. Furthermore, the 3D-printed part is expected to be durable and meet quality standards. Developing mass production of 3D-printed items requires accurate reproduction and maintenance of color when using 3D printing for product prototyping. For instance, models used in medical education and surgical planning [3] may benefit from more accurate color representations immediately after printing and over an extended period.

The innovative r-theta rotating build platform concept with a fixed print head is an alternative to conventional XYZ build platforms for 3D printers [4]. The disc-shaped build platform was chosen for numerous reasons, including improved consistency, simplicity in maintenance, and less environmental impact. Although the layering technique and pattern differ from those of other additive manufacturing machines, this necessitates additional thought when assessing design, appearance, and long-term performance. A detailed examination, in particular, exposes some damaged and glued parts in the various assembled models printed on rotational construction platforms. Moreover, the commercial printer creates brittle, stiff components [5].

Although MJT-printed products present an attractive appearance, their long-term performance is crucial because of the high cost and negative environmental effects. Different process Printing Primary Parameters (PPPs) can affect the surface quality of MJT-printed objects, such as varied materials, part design, size, build orientation, surface finish, layer thickness, and environmental factors during use /service [6,7]. Our previous work [4] highlighted the significance of modifying both the placement on the build platform and the model thickness. There is a tradeoff between cheaper and faster 3D printing and accurate color reproduction in the inner area of a rotary build platform. The 3D printing process PPP can also affect the functionality and mechanical performance of both un-aged and aged MJT products. Bass et al. [8] reported the ultimate tensile stress and the elongation of VeroWhitePlus parts increased over time while lighting conditions did not affect material properties significantly. Vu et al. [9] characterized the influence of print build orientations on the fracture strength energy of trilayer systems comprising an elastomeric material, bridging two glassy-acrylic sections for multi-MJT AM processes. As suggested by Siegfarth et al. [10], MJT can manufacture durable hydraulic actuators for medical robots.

Accelerated aging (weathering test) has been widely employed to study the long-term performance of polymers in laboratory settings. Weathering protocols involve intense aging of specimens for a short duration to replicate long-term natural degradation. The effect on different aging mechanisms should be studied to assess and predict expected long-term performance. Therefore, research based on altering accelerated aging variables over longer exposure time could provide an understanding of degradation in real life [11,12].

Taguchi method of designing experiments can reduce the number of runs and adjust the mean values to a target value [13]. As a result of this approach, it is possible to conduct long-term and costly experiments. Based on the identification of aging degradation mechanisms, the Taguchi method can identify the optimal combination of input variables that will cause the best quality product [14]. Accordingly, the main effects of means and signal-to-noise ratios explain the quality of the manufacturing phase intended for applications, such as surgical planning, tooling, and testing [15].

Understanding the intrinsic correlation between the static and dynamic mechanical response is crucial for comparing mechanical properties, such as stress relaxation, tensile, loss modulus, and creep of materials [16–18]. Due to different layering systems, there is a significant difference between the mechanical performance and appearance of MJT objects and other AM techniques for polymers, such as Fused Deposition Modeling (FDM) [19,20], Laminated Object Manufacturing (LOM) [21], Vat photopolymerization [22] and Selective Laser Sintering (SLS) [23].

Long-term mechanical performance is vital in engineering applications. However, appearance is crucial for several polymer-based products [24], where enhanced aesthetic properties facilitate marketing [1]. Furthermore, performance assessment by mechanical properties is not possible during the service /use /operation of a structure or product [25]. As such, a direct link between appearance and mechanical performance would be ideal for engineering applications. Chen et al. [26] studied the laws of appearance and mechanical behavior in additive manufacturing. However, the concept of appearance in their work was restricted to the morphology and microstructure of AM components, rather than color, gloss, and translucency.

In this study, the mechanical and optical properties of 3D-printed bilayer polymers were examined to assess the performance of the rotary PolyJet method. To the best of our knowledge, this is the first study that relates appearance to durability in materials jetting. The coupons were manufactured by varying three PPPs, namely color, swath selection (position on the build platform), and finishing between the white background and colored layers (finish). The samples were then aged in laboratory conditions following an accelerated aging protocol. The coupons were removed periodically at 12, 33, 58, 84, and 103 days and evaluated in terms of color appearance, as well as physicochemical and mechanical properties. A multivariate analysis using Redundancy Analysis (RDA) was conducted to determine the effects of accelerated aging on appearance and physico-mechanical performance and their interrelationships. The main effect plot studies a link between

color change and mechanical properties. The results investigated the correlation between appearance measurements and mechanical testing to assess the long-term performance of coupons via studying changes in color attributes.

## 2. Materials and methods

### 2.1. Materials and manufacturing

The polymeric coupons were manufactured by Stratasys J55 PolyJet 3D printer (Stratasys Ltd., Israel) using VeroCyan (RGD843), VeroBlackPlus (RGD875), VeroYellow (RGD836), VeroMagenta (RGD851), VeroPureWhite (RGD837), and support material (sup710) photo-resins. To designate colors of coupons, "cyan", "magenta", "yellow", and "black" terms have been used throughout this paper as a term for referring to the corresponding primary photo resin materials. The Vero materials from Stratasys include low-viscosity acrylic oligomer, (octahydro-4,7methano-1 H-indenediyl) bis(methylene) diacrylate, 4-(1-oxo-propenyl)-morpholine, and *exo*-1,7,7-trimethylbicyclo hept-2-yl acrylate [27]. The materials datasheet for the Vero photo-resins family shares similar mechanical, thermal, and electrical attributes [28].

The design method follows Pantone-validated color matching procedures and Stratasys best practices for PolyJet, which recommends that printed components have a minimum wall thickness of 1 ± 0.02 mm, creating a white background to ensure optimum color representation [29]. An orthogonal L8 array from Taguchi analysis for three PPPs - color, swath selection, and surface finishing between layers were chosen to examine the influence of 3D printing PPP on the color appearance and mechanical performance as output variables. For this purpose, two configurations of surface finish, including a Glossy colored layer on Glossy (GoG) and Matte (GoM) white substrate, were chosen. The width of the swaths, defined by the area covered by the print heads concerning the radius of the build platform, determines the design positioning (Fig. 1). At least three repetitions in a randomized order were performed for each experimental trial indicated by the orthogonal array. The desirability technique defined a set of three factors that allowed for the simultaneous optimization of all input variables (printing parameters).

To assess the physico-mechanical performance, Dynamic Mechanical Analysis (DMA) and tensile testing were employed on coupons accelerated aged for five aging durations and a total of 103 days of aging (12, 33, 58, 84, and 103 days). For reference, the mechanical property changes of aged coupons were compared to the mechanical properties of un-aged coupons. In this study, color appearance changes were studied using the DMA coupons. In total, 323 polymeric coupons were 3D-printed using eight runs for the five different aging durations, including un-aged reference coupons (0 days). The coupons used for DMA testing were prepared to have a white background of 2 ± 0.02 mm with a colored top layer of 1 ± 0.02 mm. This is due to match the thickness of the colored layer as the tensile testing and having constancy in the colored layer as a PPP. The criteria for each parameter were designed to decrease the constraints imposed by the processing software and 3D printer and the impact of post-processing. Due to the configuration of the build platform, i.e., the rotary disc, the minimum size possible for coupons is considered to reduce the impact of the radial effects on the coupons. Table 1 summarizes the PPP and the Design of Experiments (DoE) levels used for testing.

Table 2 summarizes the types of specimens that were examined according to eight runs of the DoE.

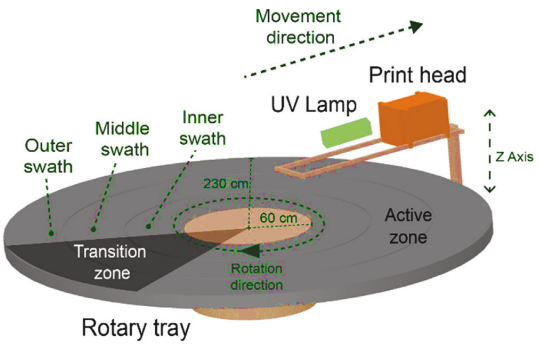


**Fig. 1.** Illustration of principal components of the build platform in a J55 PolyJet 3D printer.

### 2.2. Accelerated aging process

To study aging, the manufactured coupons (DMA and tension) were aged in a QUV accelerated aging tester (Q-Lab Corporation, USA) for a total of 103 days. Five different aging intervals were selected to determine the effect of aging over time on appearance and mechanical performance. ASTM G154 standard [30] was used to establish the aging regime resembling accelerated natural weathering. In each weathering cycle, the colored surface of the coupon was exposed to UVA radiation at 340 nm with an intensity of 0.8 W/m$^2$nm for 6 h at 60 °C (Fig. 2). The irradiation was followed by condensation at 40 °C in the dark for 4 h and deionized water spray at 24 °C for 2 h. The coupons were cycled weekly, and two cycles were repeated daily.

### 2.3. Appearance measurement protocol

Spectral radiance was measured between 380 and 780 nm and under D50 illuminant. Using a CS-2000 (Konica Minolta, Japan) Tele-Spectroradiometer (TSR), the optical resolution was 1 nm, and the physical sample interval was set to 10 nm. The TSR was placed at 50 cm from the target, normal to the surface (Fig. 3 (a)). The measurement field of view was set to 0.2° to prevent inaccuracies caused by targeting areas with dust or stains. A 45°:0° viewing geometry was used for the surface analysis of the 3D-printed specimen following CIE Publication 15.2 [31]. The device was calibrated using the standard Spectralon before each series of measurements. Each measurement was based on average radiance in six locations chosen and evenly distributed around the surface of the DMA coupons immediately after being removed from the aging chamber (Fig. 3 (b)), after wiping the coupons dry with

**Table 1**
DoE levels and factors.

| Run | DoE factor (3D printing parameter) | | |
|---|---|---|---|
| | Color [a] | Swath [b] | Finish [c] |
| 1 | C | I | GoG |
| 2 | C | O | GoM |
| 3 | M | I | GoG |
| 4 | M | O | GoM |
| 5 | Y | I | GoM |
| 6 | Y | O | GoG |
| 7 | K | I | GoM |
| 8 | K | O | GoG |

[a] C: Cyan, M: Magenta, Y: Yellow, and K: Black photo resins.
[b] GoG: Glossy-on-Glossy finish, and GoM: Glossy-on-Matte finish.
[c] I: Inner (r-tray less than 105 mm), and O: Outer (169 mm < r-tray < 229 mm) swath.

a paper towel. Errors were reduced by avoiding sites with unusual colors, external particles, and support materials. Measurements of appearance were performed before and after weathering exposure for each sample.

Calculations of colorimetric values were performed in MATLAB R2022a using the computational color science toolbox [32]. A color-matching function, according to ASTM E308-01 [33] was used to calculate CIEXYZ. Thus, tristimulus values were calculated using the CIE 2° color-matching functions under the D50 illuminant. The coordinates for CIEL*a*b* were then determined using CIE1976 and CIEXYZ tristimulus values using Eqs. (1) to (3)

$$L^* = 116(Y/Y_n)^{1/3} - 16 \tag{1}$$

$$a^* = 500\left[(X/X_n)^{1/3} - (Y/Y_n)^{1/3}\right] \tag{2}$$

$$b^* = 200\left[(Y/Y_n)^{1/3} - (Z/Z_n)^{1/3}\right] \tag{3}$$

**Table 2**
Specimen studied for each of the 8 DoE runs.

| | Experiment for each DoE run (Replica × Measurement) | | | |
|---|---|---|---|---|
| Aging time (days) | Color appearance | Sagitta | Tensile | DMA |
| 0 – Reference | 2 × 3 | 2 × 1 | 5 × 1 | 2 × 1 |
| 12 | 2 × 3 | 2 × 1 | 5 × 1 | 2 × 1 |
| 33 | 2 × 3 | 2 × 1 | 5 × 1 | 2 × 1 |
| 58 | 2 × 3 | 2 × 1 | 5 × 1 | 2 × 1 |
| 84 | 2 × 3 | 2 × 1 | 5 × 1 | 2 × 1 |
| 103 | 2 × 3 | 2 × 1 | 5 × 1 | 2 × 1 |

where $X_n$, $Y_n$, and $Z_n$ stand for the tristimulus values of Spectralon. Using Eqs. (4) and (5), CIEL*C*h* values were determined to calculate the color difference according to CIEDE2000

$$C^* = \sqrt{a^{*2} + b^{*2}} \tag{4}$$

$$h^* = \arctan(b^*/a^*) \tag{5}$$

CIEDE2000 colorimetric difference was calculated between control samples (un-aged) and the same sample after weathering, according to Eq. (6)

$$CIEDE2000 = \sqrt{\left(\frac{\Delta L^*}{k_L S_L}\right)^2 + \left(\frac{\Delta C^*}{k_C S_C}\right)^2 + \left(\frac{\Delta h^*}{k_h S_h}\right)^2 + R_T f(\Delta C^* \Delta h^*)} \tag{6}$$

where the constant values of $k_L$ (lightness), $k_C$ (chroma), and $k_h$ (hue) were considered unity. Further variables involve the hue rotation term ($R_T$), and the compensation for lightness ($S_L$), chroma ($S_C$), and hue ($S_h$) [34].

The statistical analysis was performed in line with ISO/TS 23031:2020 (E) [35]. The Mean Color Difference from the Mean (MCDM) is calculated to evaluate the color difference between test and reference spectra. To conduct spectrum analysis and compare the spectra of the target surfaces, the Root-Mean-Square Error (RMSE) for each quantitative variable is calculated as below

$$RMSE = \sqrt{\frac{1}{N}\sum_{i=1}^{N}(r_{r,i} - r_{t,i})^2} \tag{7}$$

$$MCDM = \frac{1}{N}\sum_{i=1}^{N}\Delta E(C_i, C_m) \tag{8}$$

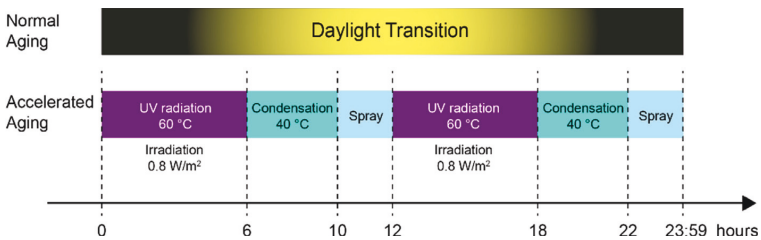


**Fig. 2.** Aging cycle using a QUV weathering chamber as per ASTM G154.

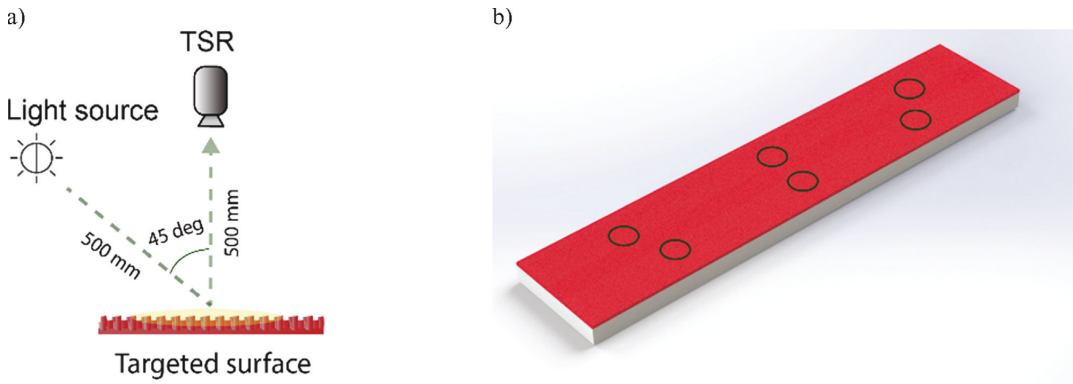


**Fig. 3.** a) A schematic view of the measurement setup for color appearance, and b) Illustration of appearance measurement locations across each DMA specimen.

where $N$ is the number of reflectance readings, $r_t$ and $r_r$ are the tests and references spectrum, $C_i$ and $C_m$ indicate the colors coordinate of the $i^{th}$ measurements, and the reflectance average, respectively.

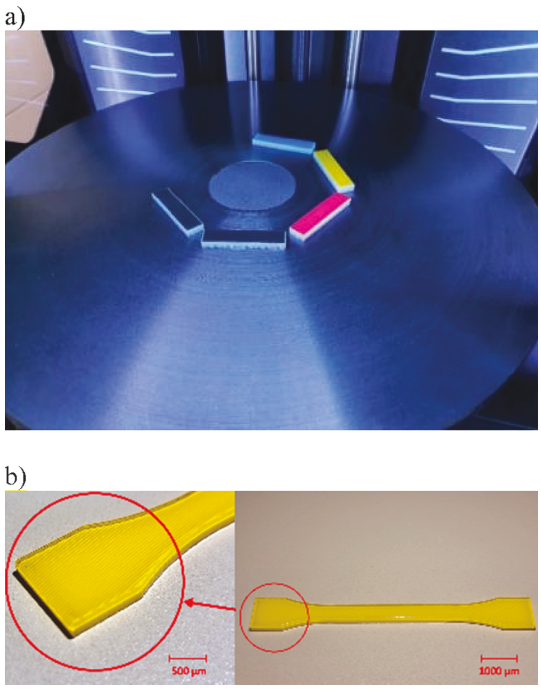


**Fig. 4.** a) DMA coupons printed in the inner swath, and b) view of un-aged tensile coupons at different scales.

### 2.4. Physico-mechanical performance characterization

To characterize the extent of degradation in the polymeric 3D-printed coupons after each aging interval, physico-mechanical properties were measured by employing viscoelastic (Dynamic Mechanical Analysis - DMA) and tensile property changes. DMA analysis of polymeric coupons allows for determining the Glass Transition temperature ($T_g$) and any $T_g$ shift resulting from aging [36]. ASTM D4065 [37] was employed to test the coupons under 3-point bending mode on a Discovery DMA 850 (TA Instruments, USA), with coupon dimensions of 60 × 13 × 3 (mm) (Fig. 4 (a)). Tests were performed at 1 Hz with an amplitude of 20 µm. Temperature ramp tests were conducted at lower degradation temperatures of the material, ranging from 20 °C to 95 °C, at a rate of 2 °C per minute. Two coupons were tested for each batch, and the average $T_g$ was reported. The $T_g$ values were calculated using TRIOS 5 software based on the corresponding temperature of the maximum peak value of the tan δ curve.

The strength value and tensile modulus of the polymer material were determined based on the ISO 527–02 standard [38] as a function of aging duration. Uniaxial tensile testing was performed on dogbone-shaped coupons of 75 × 10 × 2 (mm) (Fig. 4 (b)), using an Instron 5966 (Instron, USA) universal testing machine at a 2 mm/min loading rate. An AVE2 video-extensometer was used to measure mechanical strain.

The tensile chord modulus of bilayer material was determined by force–displacement curves, and ultimate tensile stress was used to report polymer strength. The material response is characterized based on material stiffness (E-Modulus, $E$) and strength ($\sigma_s$) changes. The slope of the stress–strain curve is used to calculate the chord modulus, and the stress–strain curve maximum is represented as the ultimate strength. The retention curves for stiffness and strength are then calculated as follows

$$E\ \ retention = \left(\frac{E_c}{E_r}\right) \tag{9}$$

$$\sigma_s\ \ retention = \left(\frac{\sigma_{sc}}{\sigma_{sr}}\right) \tag{10}$$

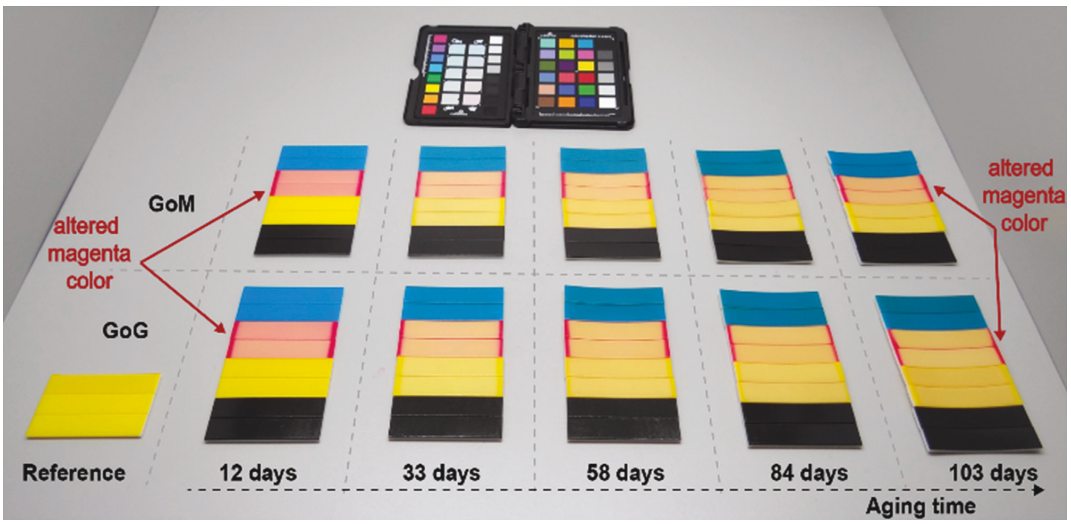


**Fig. 5.** DMA coupons before and after weathering exposure for different periods, as observed under D50 daylight illumination. Dark-red areas on the margins of magenta represent the original color covered by sample holders. (For interpretation of the references to color in this figure legend, the reader is referred to the web version of this article.)

where $E_c$ and $\sigma_{sc}$ denote the mean values of $E$ and $\sigma_s$ for aged coupons, and $E_r$ and $\sigma_{sr}$ are the mean values for un-aged (as-printed) references. Furthermore, property-retention values have been used to compare elastic modulus and glass transition temperature variation due to accelerated aging. The curvature in the bent coupons, i.e., the distance from the center of the arc and its base (sagitta), was measured using a digital caliper.

### 2.5. Multivariate analysis

The initial statistical analysis and classification were performed using Detrended Correspondence Analysis (DCA) to select the classification model based on gradient length. The Redundancy Analysis (RDA) is a valid model if the gradient length in the DCA analysis is short (less than3); otherwise, Correspondence Canonical Analysis (CCA) would be more appropriate [39]. Accordingly, because of the short gradient length (less than 0.1), multivariate analysis of the response variables based on the studied parameters was performed using RDA and Spearman rank correlations.

RDA is a multivariate extension of linear regression to matrices containing dependent and independent variables. RDA can also be described as Principal Component Analysis (PCA) with instrumental variables. The model assumes that two datasets have distinct functions [40]. This study included color attributes (dL, dC, and dh) in the matrix of appearance variables. Statistical and Taguchi analyses were performed using Origin 2022 (OriginLab, Northampton, MA, USA), R statistical software 4.2.1 (The R Foundation for Statistical Computing, Vienna, Austria), and Minitab 21 (State College, PA, USA), respectively.

## 3. Results and discussions

### 3.1. Color appearance evaluation

Fig. 5 illustrates DMA coupons after aging for the selected periods of time. MCDM results for CIEDE2000 in Fig. 6 (a) present a significant color difference for aged magenta samples compared to their as-printed color. While black parts reflect comparably low

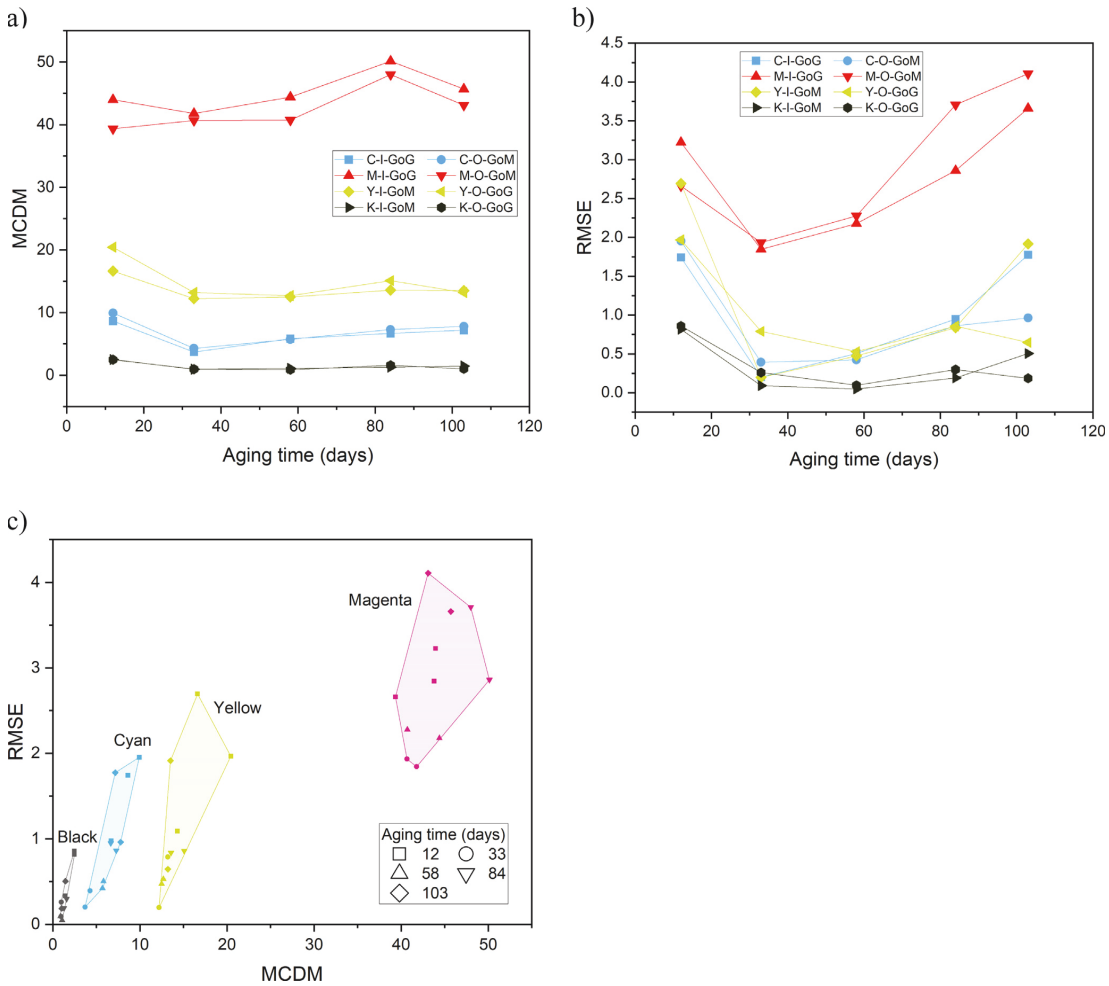


**Fig. 6.** a) MCDM for CIEDE2000 color difference, b) associated RMSE after the aging process, and c) MCDM vs. RMSE based on a convex hull containing results.

MCDM for different aging periods, cyan and yellow coupons exhibited more noticeable color differences. RMSE follows a similar trend (Fig. 6 (b)), with a strong Spearman rho (rs) correlation observed between MCDM and RMSE with rs = 0.86 and P-value = 1.5E-12. According to the convex hull containing results for each color in Fig. 6 (c), magenta-colored layers exhibited a more significant variation in color appearance because of aging compared to other investigated photo resins, particularly VeroBlackPlus, regardless of the swath and finish used. Nevertheless, a higher color difference was also observed in the GoG coupons compared to their GoM pair.

In general, MCDM and RMSE values were significantly higher at the beginning of aging (after 12 days) compared to 33 days, reached minimum values between 33 and 58 days, and increased again after 84 days (Fig. 6 (a) and (b)). Over time, the variation in lightness, chroma, and hue provides more insight into the alteration of color attributes (Fig. 7 (a)). The hue of cyan and yellow photo resins increased with aging, while it dramatically decreased for magenta samples, with a more dominant effect for GoG finishes. Over more extended periods, however, variations in hue reached a plateau, especially after 84 days. In Fig. 7 (b), magenta samples displayed a significant variation in hue, showing comparable hues as yellow samples at longer aging times. Black samples, however, displayed closer values of u′ and v′, indicating a more negligible hue difference. In supplementary materials available in Appendix A, Figs. A1 and A2 represent the mean values for spectral measurements and detailed CIE1976 u′, v′ chromaticity diagrams for all the studied photo resins.

### 3.2. Physico-mechanical performance

Fig. 8 illustrates tensile stress–strain curves after testing polymeric MJT coupons from different finishes and aging durations. During the initial days of aging, the tensile response of the material exhibits an increase in the stiffness, strength, and strain-to-failure of the polymeric materials compared to the reference un-aged coupons. A reduction in the mechanical parameters is observed after long-term aging. It can also be observed that the two finishes also indicate remarkably similar behavior in terms of mechanical response.

Fig. 9 (a)-(c) illustrates property-retention plots, for the elastic modulus, strength, and strain-to-failure of polymeric coupons as a function of aging duration for two different finishes. It can be observed that throughout accelerated aging, the elastic modulus retention for both the finishes (Fig. 9 (a)) follows a monotonic increase till 58 days, where the retention values increase above 100%, signifying an improvement in the mechanical properties. During this short-term aging, it can be hypothesized that the combination of temperature and UV exposure can lead to a further post-curing which can be initiated due to photo- and thermal effect [41] inside the polymeric material leading to a higher degree of polymerization, re-arrangement and residual crosslinking of the polymeric chains. This chemical transformation can hence lead to increased resistance towards a uniaxial deformation, which can be manifested as an increase in the stiffness of the material. In the case of the materials strength and strain-to-failure, the speculated post-curing effect was limited to 33 days and 12 days, respectively, whilst the onset of degradation starts at an earlier stage.

The behavioral changes in the material due to aging were observed in the long-term as changes in the mechanical properties by the property-retention plots. An interplay of the crosslinking, thermo photooxidation, chain scission, and crazing of the polymeric chain leads to changes in the structural performance that gradually result in degradation over long-term exposure [42]. In our case, strength, and strain-to-failure reduction due to degradation are observed, whilst stiffness remains practically unaffected at the end of the aging duration, compared to the original state (day 0). It can be hypothesized that the combined effect of temperature, water, and UV may lead to increased surface roughness and cause micro-crack formation. As such, despite the initial post-curing sites

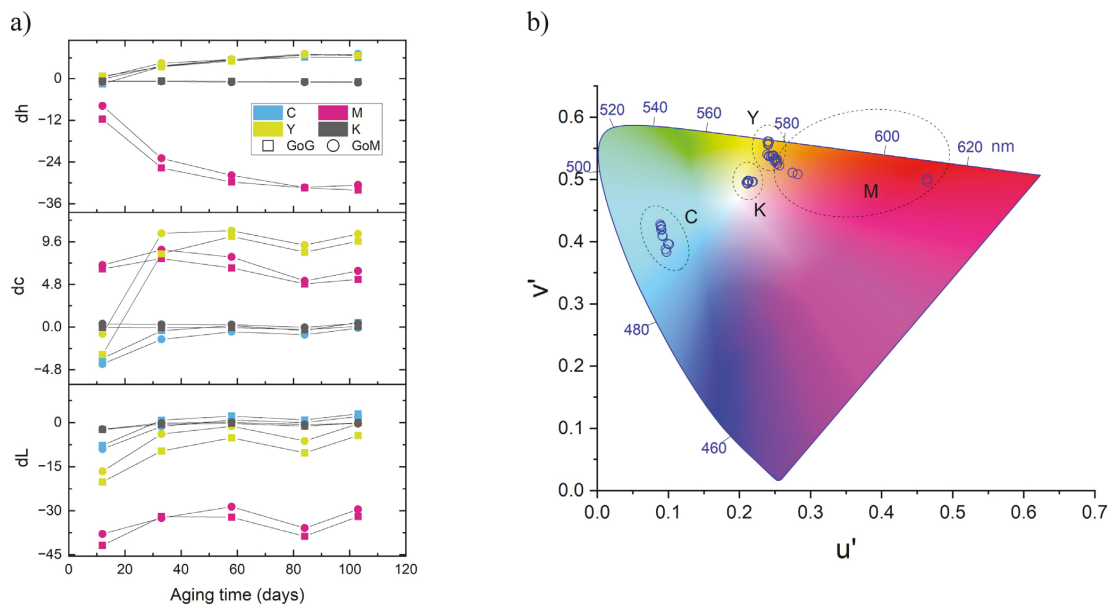


**Fig. 7.** a) Distribution of variation in the mean value of lightness (l), chroma (c), and hue (h) over aging time, and b) the distribution of the mean hue stimuli in the CIE1976 u′, v′ chromaticity diagram for aged coupons. The blue line indicates the corresponding wavelengths between 420 and 680 nm for each color. (For interpretation of the references to color in this figure legend, the reader is referred to the web version of this article.)

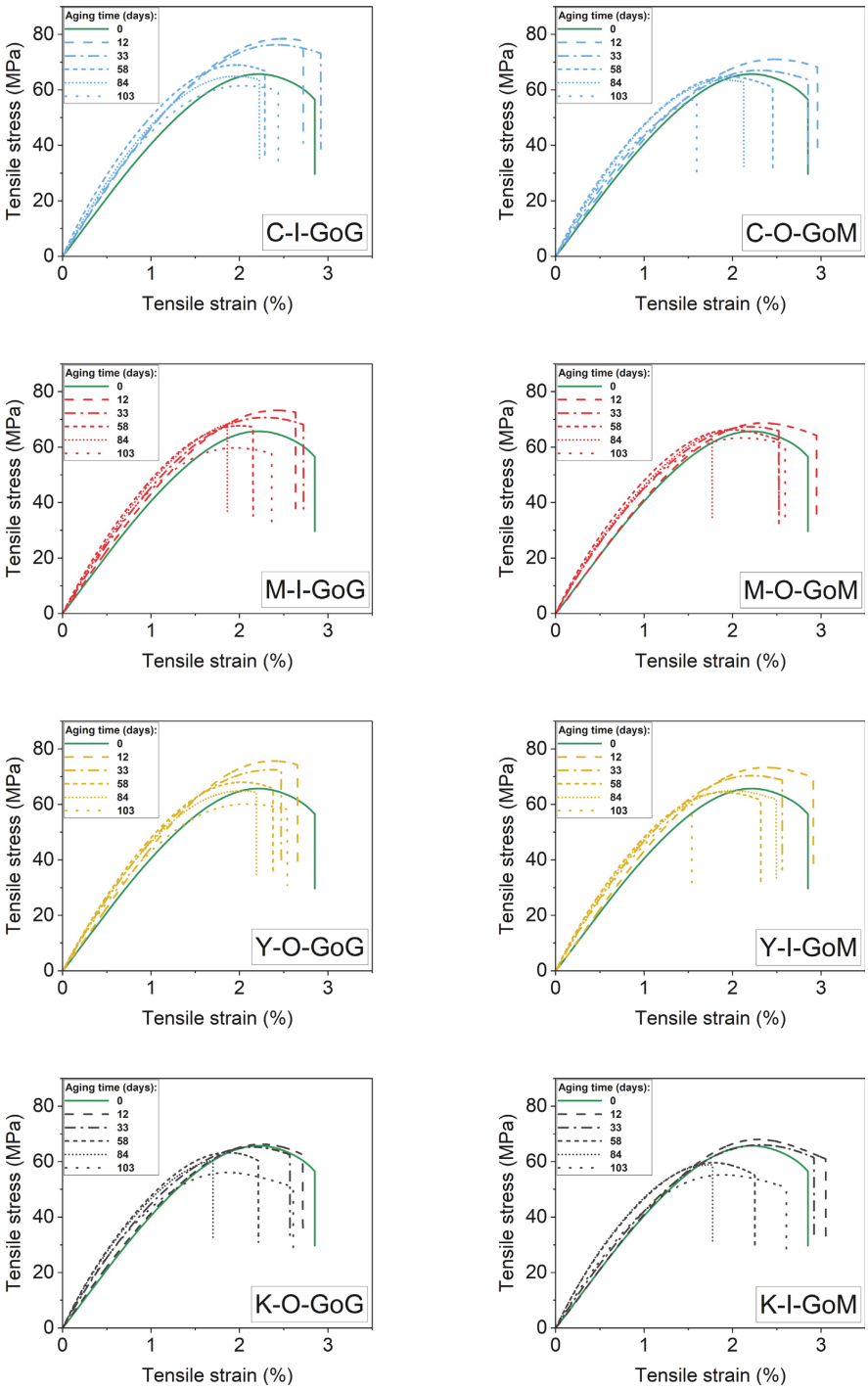


**Fig. 8.** Stress–strain curves for aged coupons compared to the un-aged reference.

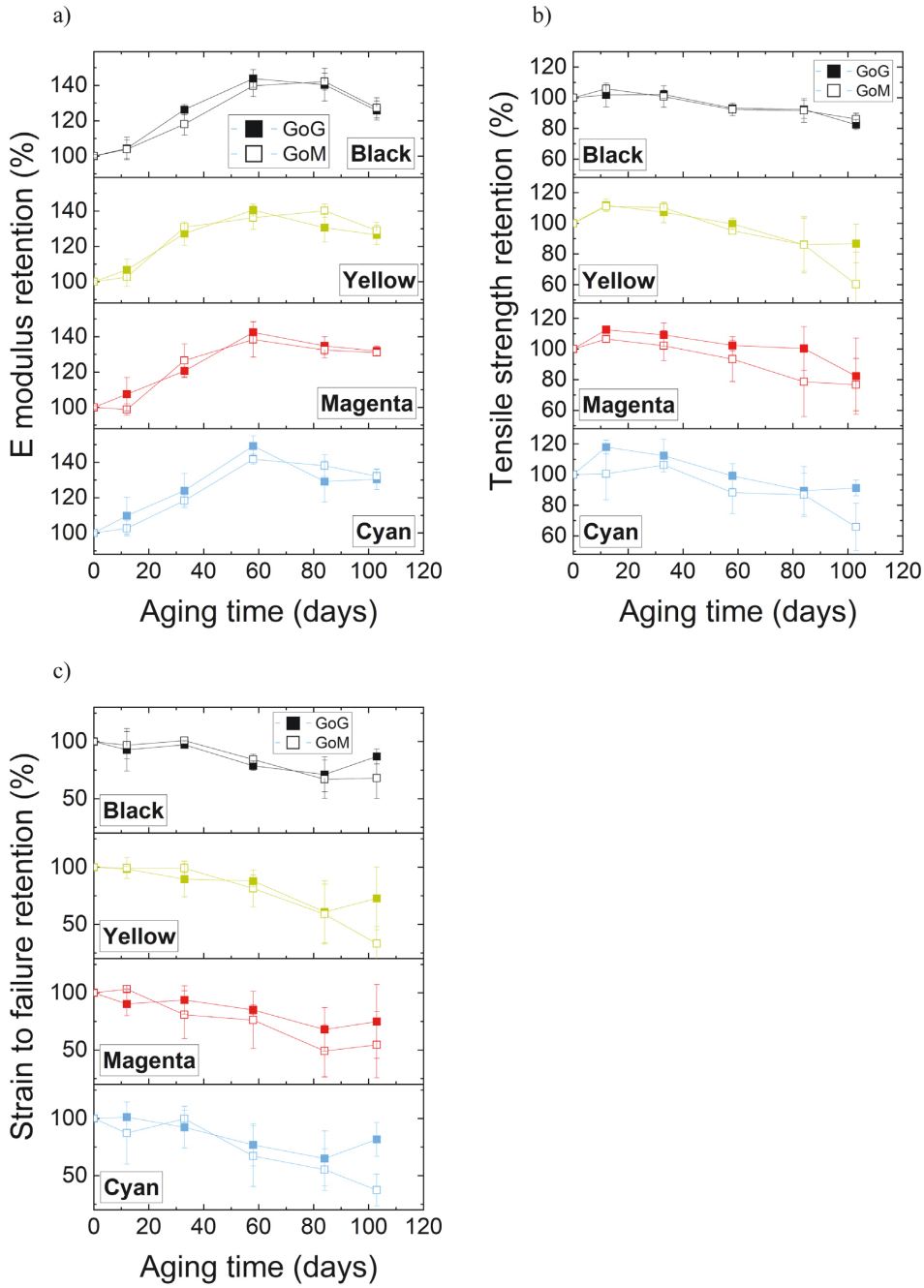


**Fig. 9.** a) E modulus (stiffness), b) strength, and c) strain-to-failure retention vs. aging time for studied photo resins. Error bars represent Standard Deviation (SD).

for crack initiation may at the same time be generated, thus leading to a reduction in both the strength and strain-to-failure. The post-curing effect leads to brittleness, which causes an increase in stiffness, until day 58. After that, aging degradation is more prominent than post-curing, causing a reduction in stiffness. Although at the end of the aging period, stiffness remains at higher levels than in the original state, it is evident that if aging continues further than 103 days, stiffness will eventually degrade. It is also

**Table 3**
Stiffness retention for different samples and finishes.

| Aging time (Days) | C-I-GoG | C-O-GoM | M-I-GoG | M-O-GoM | Y-I-GoM | Y-O-GoG | K-I-GoM | K-O-GoG |
|---|---|---|---|---|---|---|---|---|
| 12 | 109.78 | 102.65 | 107.47 | 98.87 | 102.71 | 106.75 | 103.92 | 104.32 |
| 33 | 123.95 | 118.34 | 120.64 | 126.54 | 130.82 | 127.24 | 118.04 | 126.30 |
| 58 | 149.21 | 141.76 | 142.45 | 138.34 | 136.22 | 140.53 | 139.77 | 143.84 |
| 84 | 129.14 | 138.09 | 134.82 | 132.49 | 140.18 | 130.53 | 142.10 | 140.35 |
| 103 | 130.37 | 132.19 | 131.93 | 130.94 | 129.00 | 126.51 | 127.29 | 125.77 |

**Table 4**
Strength retention for different samples and finishes.

| Aging time (Days) | C-I-GoG | C-O-GoM | M-I-GoG | M-O-GoM | Y-I-GoM | Y-O-GoG | K-I-GoM | K-O-GoG |
|---|---|---|---|---|---|---|---|---|
| 12 | 117.99 | 100.55 | 112.58 | 106.53 | 111.07 | 111.83 | 105.82 | 101.78 |
| 33 | 112.39 | 106.27 | 109.24 | 102.15 | 110.27 | 107.22 | 100.71 | 102.18 |
| 58 | 99.13 | 88.24 | 102.34 | 93.41 | 95.23 | 99.70 | 92.28 | 93.14 |
| 84 | 89.56 | 86.83 | 100.32 | 78.60 | 85.98 | 86.11 | 91.65 | 92.39 |
| 103 | 91.23 | 65.82 | 82.27 | 76.68 | 60.15 | 86.78 | 86.10 | 82.38 |

**Table 5**
Strain-to-failure retention values for different samples and finishes.

| Aging time (Days) | C-I-GoG | C-O-GoM | M-I-GoG | M-O-GoM | Y-I-GoM | Y-O-GoG | K-I-GoM | K-O-GoG |
|---|---|---|---|---|---|---|---|---|
| 12 | 101.28 | 87.22 | 90.27 | 103.22 | 99.35 | 98.46 | 96.89 | 92.73 |
| 33 | 92.35 | 99.80 | 93.77 | 80.82 | 99.20 | 89.60 | 100.99 | 97.27 |
| 58 | 76.95 | 67.20 | 85.13 | 76.20 | 81.49 | 87.96 | 84.39 | 78.88 |
| 84 | 65.04 | 55.22 | 67.94 | 49.19 | 58.94 | 60.87 | 66.98 | 71.22 |
| 103 | 81.71 | 37.36 | 74.94 | 54.55 | 33.09 | 72.71 | 68.02 | 86.92 |

seen from Fig. 9 that GoG coupons generally maintained higher stiffness, strength, and strain-to-failure than GoM coupons after 103 days of aging.

During the aging, a ductile to brittle behavior transition was observed. The extent of the plastic deformation and softening in the tensile stress–strain curve were reduced in samples aged for a longer duration. It was contrary to un-aged, and samples aged for a shorter duration. Interestingly, the polymeric coupons also showed a gain in the strain to failure and tensile strength at the end of the aging duration (103 days), especially in the GoG finish. This could be attributed to recombination and residual crosslinking activated due to long UV exposure, which could help gain both the tensile strength and correspondingly the strain to failure. Similar observations have been also reported by Woo et al. [43].

Tables 3-5 present the property-retention percentage results for all three mechanical parameters.

To investigate the changes observed in tensile testing further, DMA was used to substantiate the findings viscoelastically. Fig. 10 presents storage modulus (E′) which is a measure of stiffness as a function of temperature (of testing). Compared to the un-aged reference, aged samples exhibited lower stiffness, which does not coincide with the tensile testing results shown in Fig. 8 and Fig. 9 due to a weak baseline for measurement of the stiffness transition. Fig. 11 shows the tan d curves for un-aged and aged DMA coupons. A decrease in the peak value of the tan δ curve indicates a worsening of damping behavior. In contrast, shifts in the peak value indicate intrinsic changes because of aging that may correspond to degradation or improvement in the viscoelastic performance.

Fig. 12 depicts the changes in the absolute value of $T_g$ (°C), calculated from the tan d curve obtained from DMA. The variation in the glass transition temperature exhibited a similar trend when compared with the stiffness retention values. The mean $T_g$ values of the aged polymeric coupons increased significantly until day 58, compared with the reference mean value of 73.3 °C resulting from the as-printed coupons. There was a noticeable increase in the $T_g$ of the studied materials (CMYK) within the first 12 days. $T_g$ values continued to increase to a peak of 83.9 °C at 58 days (114% retention) and then decreased to 79.6 °C at the end of aging (103 days). Both the GoG and GoM finishes, as well as the cyan and magenta colors, followed the same trend. However, the black and yellow coupons reached their maximum peak value after 84 days of aging.

Residual post-curing was noticeable as a potential reason behind the increase in the $T_g$ values due to the combined effect of UV, temperature, and moisture. Post-curing typically causes re-arrangement of the polymeric chains and leads to strengthening [44,45]. The polymeric chain re-arrangement leads to a denser polymeric chain network, creating more deformation resistance [46]. Hence, the stiffness and $T_g$ of the polymeric coupons were significantly increased for 58 days of aging. Fig. 13 concludes the variation in $T_g$ and E from Fig. 9 (a) and Fig. 12. It illustrates $T_g$ and E, occurring after 58 days of aging, a period that post-curing becomes less pronounced than degradation. Supplementary data for mechanical and physical evaluation is available in Appendix B.

Fig. 14 shows coupon deformations over aging regimes, presented as a slight bend. According to the formula for the sagitta of a circular arc, the curvature of the aged coupons $d$ is related to their length $l$ and radius of curvature $R_1$

$$d = R_1 - \sqrt{R_1^2 - \frac{l^2}{4}} \tag{11}$$

where $d$ is the sagitta, $l$ is the length of the as-printed specimen, and $R_1$ is the radius of the arc.

As shown in Fig. 15, the curvature of MJT coupons increased over time regardless of their manufacturing condition, reaching a maximum between 84 and 103 days of aging. GoM samples generally showed more curvature for the same color than GoG pairs after aging for extended periods. During printing and post-processing, the only difference between GoG and GoM finishes is retaining a thin layer of support material. As with the color appearance results, black coupons exhibited the lowest sagitta values compared to the Vero photo-resins studied.

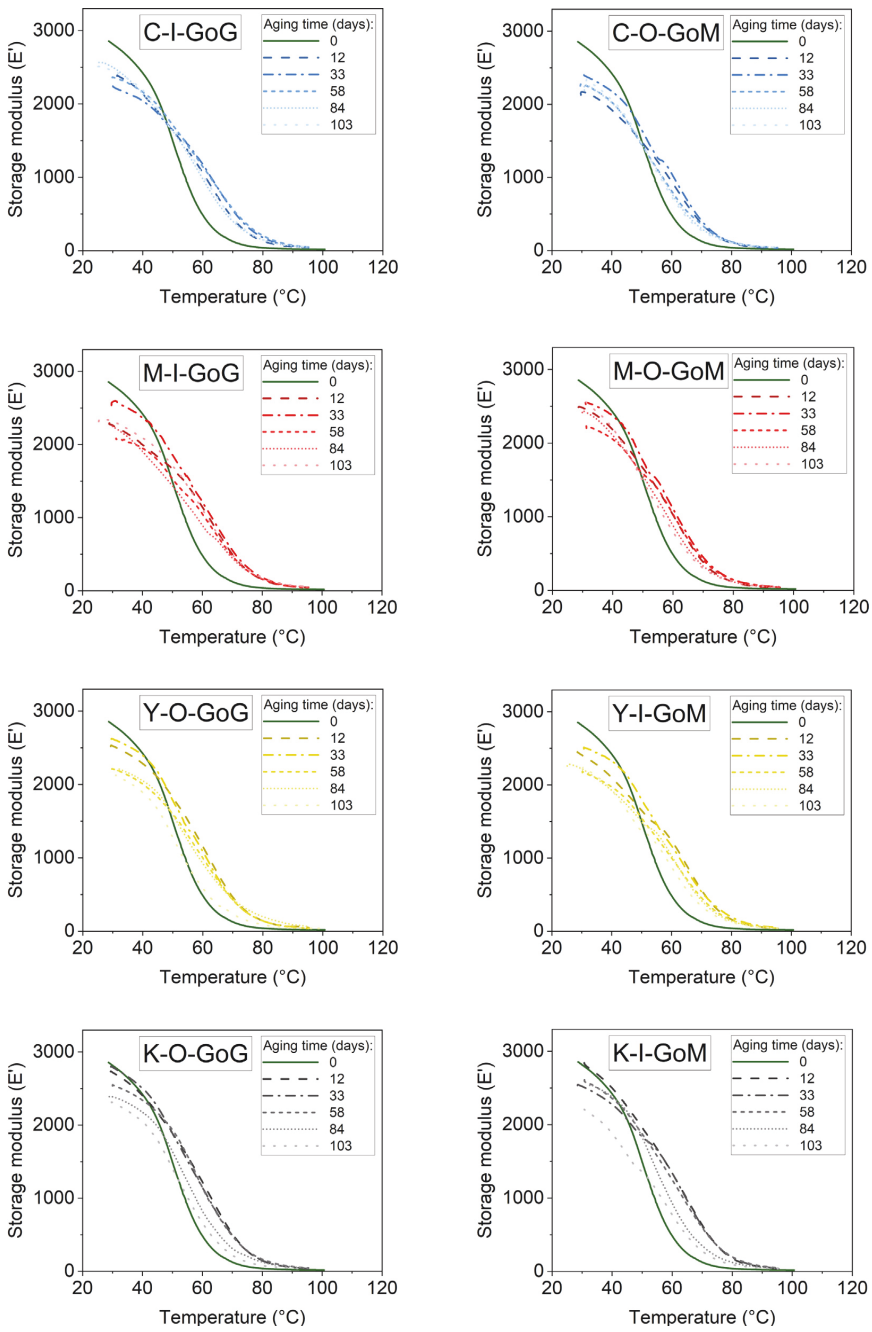


**Fig. 10.** Storage modulus (E') vs. temperature graphs for aged coupons compared to the un-aged reference (green curves). (For interpretation of the references to color in this figure legend, the reader is referred to the web version of this article.)

3D printing using the J55 printer imposes a semicircular-layered structure due to the centrifugal force generated by rotating the build platform. Further UV absorbance during the aging process may have altered the internal structure of polymeric chains in the layer-by-layer structure, resulting in curvature along the length of DMA coupons. In other words, covalent bonds link mass units, such as monomers to polymer chains, the formation of polymer networks via crosslink polymer chains, and connect polymer

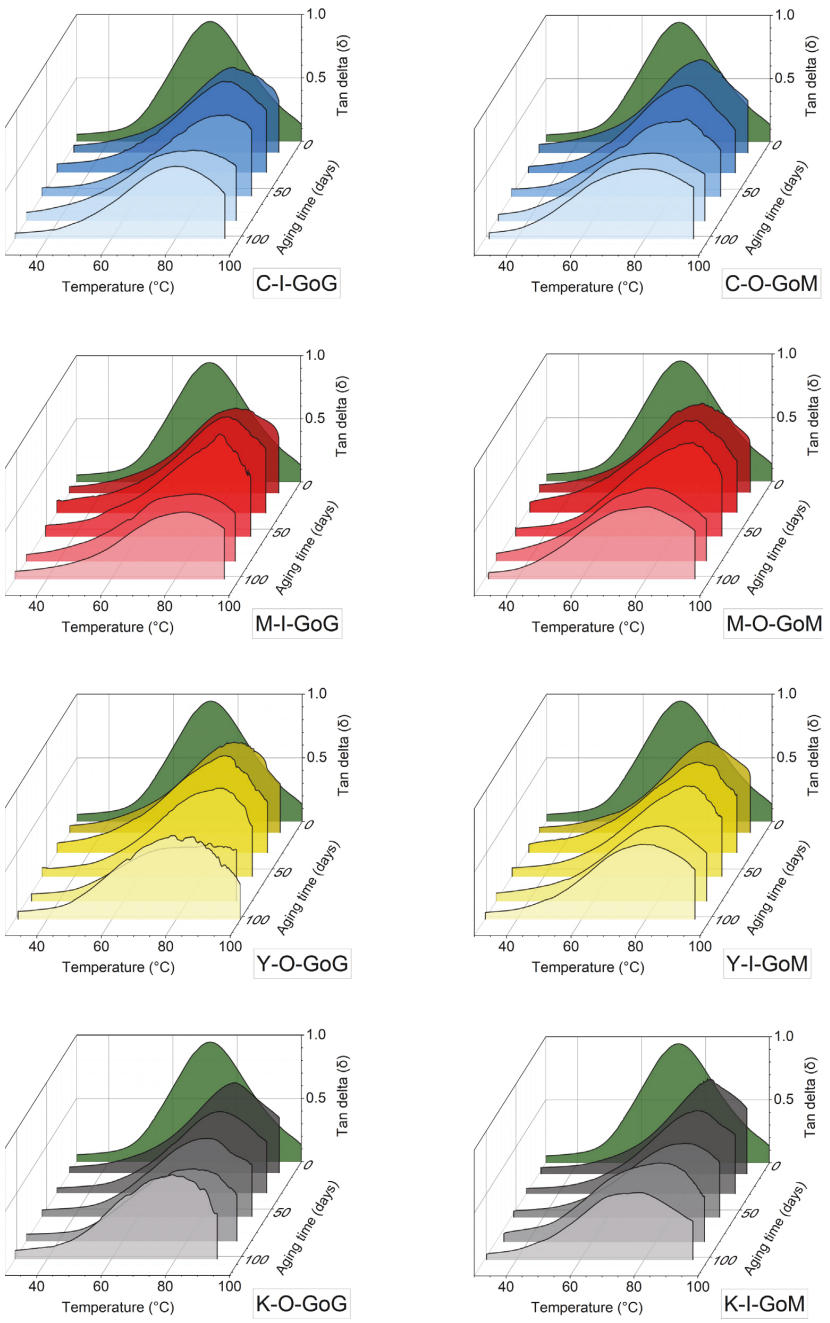


**Fig. 11.** Damping (Tan δ peak) vs. temperature graphs for aged coupons compared to the un-aged reference (0 days).

networks from distinct layers asymmetrically. This statement is supported by the resulting lower UV absorbance of the dark colors (lower lightness) and GoG finishes compared to GoM due to the retention of a thin layer of support material between white and colored layers.

### 3.3. Statistical analysis

RDA results are presented in Fig. 16 as ranking diagrams using figurative symbols. The short gradient length in the DCA with axis lengths less than 0.14 for all DCAs confirmed the suitability of RDA

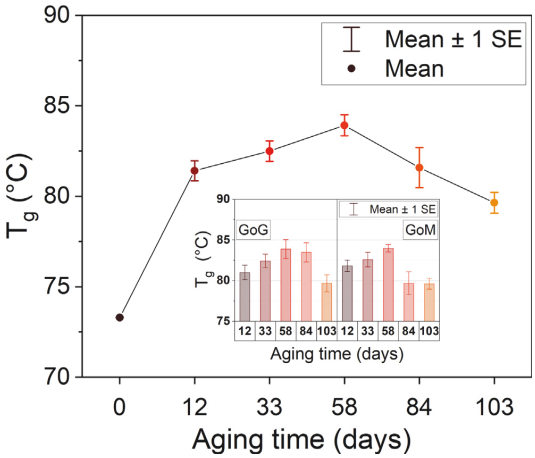


**Fig. 12.** Arithmetic mean values for $T_g$ and Standard Error (SE) over the aging process.

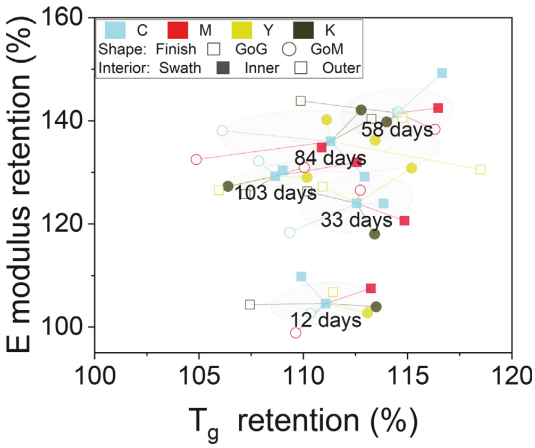


**Fig. 13.** Variation in elastic modulus vs. glass transition temperature of aged MJT coupons. Each aging period represented 95% confidence centroid ellipses in the gray zone.

results to discuss the link between color attributes and physico-mechanical responses. In Table 6, the first two Principal Components (PCs) account for 95.20% of the variance in the response variables, i.e., strength retention, stiffness retention, and $T_g$. Therefore, two PCs are appropriate enough to clarify the possible correlation among the data.

The first and second principal components (PC1 and PC2) are indicated by horizontal and vertical axes for related vector colors. Angles between vectors represent corresponding correlations of variables, with a smaller angle indicating a more significant correlation. Positively correlated variables are represented by vectors pointing in the same direction and vice versa. With 58 days of aging, $T_g$ and stiffness retentions were primarily increased, with the highest contribution from PC2 aligned with the increase in dh. Whereas strength was primarily affected by PC1, which tends to sharply increase generally within the first 12 to 33 days of aging due to the increased lightness variation in the color appearance (dL). These results are in agreement with the observation in Fig. 7 (a), Fig. 9, and Fig. 12. However, the variation in chroma (dC) was significantly higher at the end of the aging experiment (103 days) for most of the materials. The opposite direction of vectors for dC and stiffness demonstrated a correlation of rs = -0.45. Nevertheless, the correlation between color difference (MCDM) and mechanical performance during the aging process was weak for all materials except magenta photo resins, as indicated by the different angles between the color attribute vectors.

### 3.4. Taguchi analysis

In Fig. 17, the main effect plots for data mean at different aging times illustrate that color solely had the most considerable effect on color difference and RMSE, with the highest significant effect in magenta samples, followed by yellow and cyan. Compared to other photo resins, black samples showed a negligible response. While the swath and finish input variables did not significantly affect MCDM output, the GoM finish contributed to a slightly higher RMSE. The selection of swaths in the inner region did not reduce RMSE at the beginning and end of the aging period. It did not significantly affect the color appearance over time.

In terms of the physico-mechanical response to the variables studied (Fig. 18), the trend was not as straightforward as color appearance. In contrast to yellow samples, which showed the highest E modulus after 33 days of aging, black and cyan samples demonstrated the highest E modulus after 58 days of aging. Generally, the highest $T_g$ values were observed for magenta and yellow hues among the studied photo resins, with similar trends observed

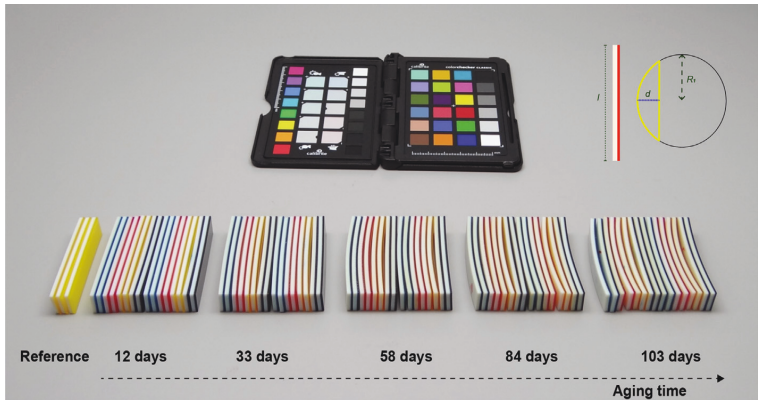


**Fig. 14.** Side view of DMA samples representing the bending in pieces over 103 days of aging time as observed under D50 daylight illumination.

in color appearance analyses. However, a direct link between mechanical response and color was not observed. This is because colors on the MJT objects changed over time, and the response to environmental aging was altered as a result. A greater UV absorbance of magenta materials compared to cyan specimens during the aging test may clarify the post-curing effect, leading to more rigid polymers with altered colors and mechanical properties.

Based on the finishing options, matte finishes between layers during the first 58 days led to lower E modulus and higher $T_g$. After 84 days, however, the response changed. In terms of swath selection on the build tray, 3D printing in the inner area of the rotary disc resulted in higher values of E and $T_g$. The results suggest that swath selection impacted mechanical performance despite its negligible importance in terms of color appearance. The signal-to-noise ratio plots in Appendix C confirm the same trends.

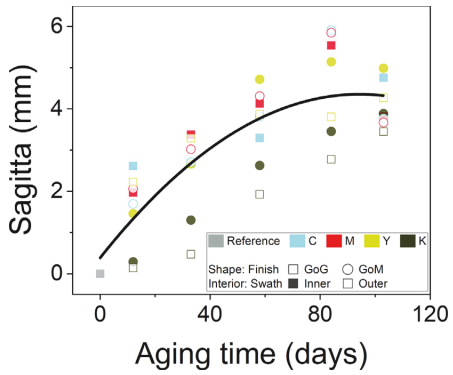


**Fig. 15.** Results of fitting the mean values for sagitta concerning the curvature appearing over the aging process ($R^2$: 0.63).

## 4. Conclusions

In this work, a PolyJet 3D printer has been employed to manufacture bilayer polymer structures on a rotary build platform based on Material Jetting technology. Our study focused on the appearance and physico-mechanical properties of acrylic-simulated parts over 103 days of accelerated aging. Taguchi analysis was used to determine the impact of processing characteristics, such as color, position on the build platform (swath), and finishing options between layers on the response variables. A desirability analysis was set to minimize the color and corresponding RMSE values and maximize the elastic modulus and glass transition temperature. This study led to the following conclusions:

1. Studied polymer coupons exhibited an increase in tensile and viscoelastic performance. The stiffness and strength of the materials increased after 12 days of aging, with stiffness values continuing to increase until 58 days and strength values diminishing monotonically until the end of the aging duration. On the other hand, strain-to-failure values generally diminished during the aging period.

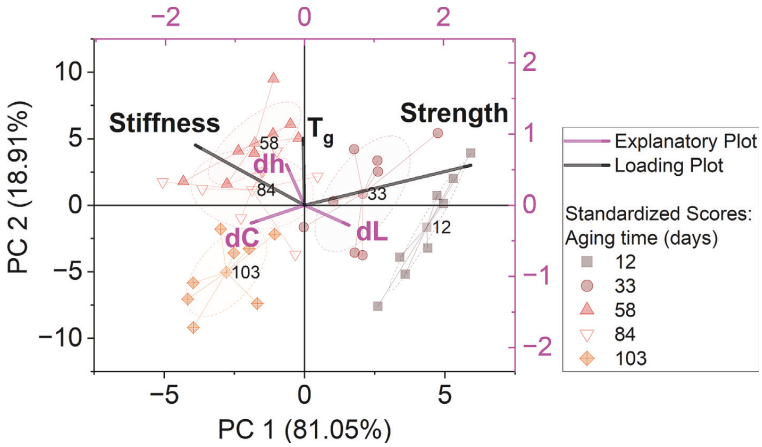


**Fig. 16.** RDA ordination diagram (triplot) showing aged coupons by denoted points for different aging days, explanatory variables (color attributes; purple vectors), and response variables (mechanical performance - retention; black vectors). Each aging period represented 95% confidence centroid ellipses in the gray zone. (For interpretation of the references to color in this figure legend, the reader is referred to the web version of this article.)

**Table 6**
Principal components ranking according to their cumulative roles in PCA.

| | Eigenvalues for constrained axe: Explanatory variables | | | Eigenvalues for unconstrained axe: Principal components | | |
|---|---|---|---|---|---|---|
| Ranking | Eigenvalue | Percentage of Inertia (%) | Cumulative Inertia (%) | Eigenvalue | Percentage of Inertia (%) | Cumulative Inertia (%) |
| 1 | 14.72 | 11.65 | 11.65 | 63.92 | 50.56 | 64.93 |
| 2 | 3.43 | 2.72 | 14.36 | 38.26 | 30.27 | 95.20 |
| 3 | 0.01 | 0.01 | 14.37 | 6.06 | 4.80 | 100.00 |

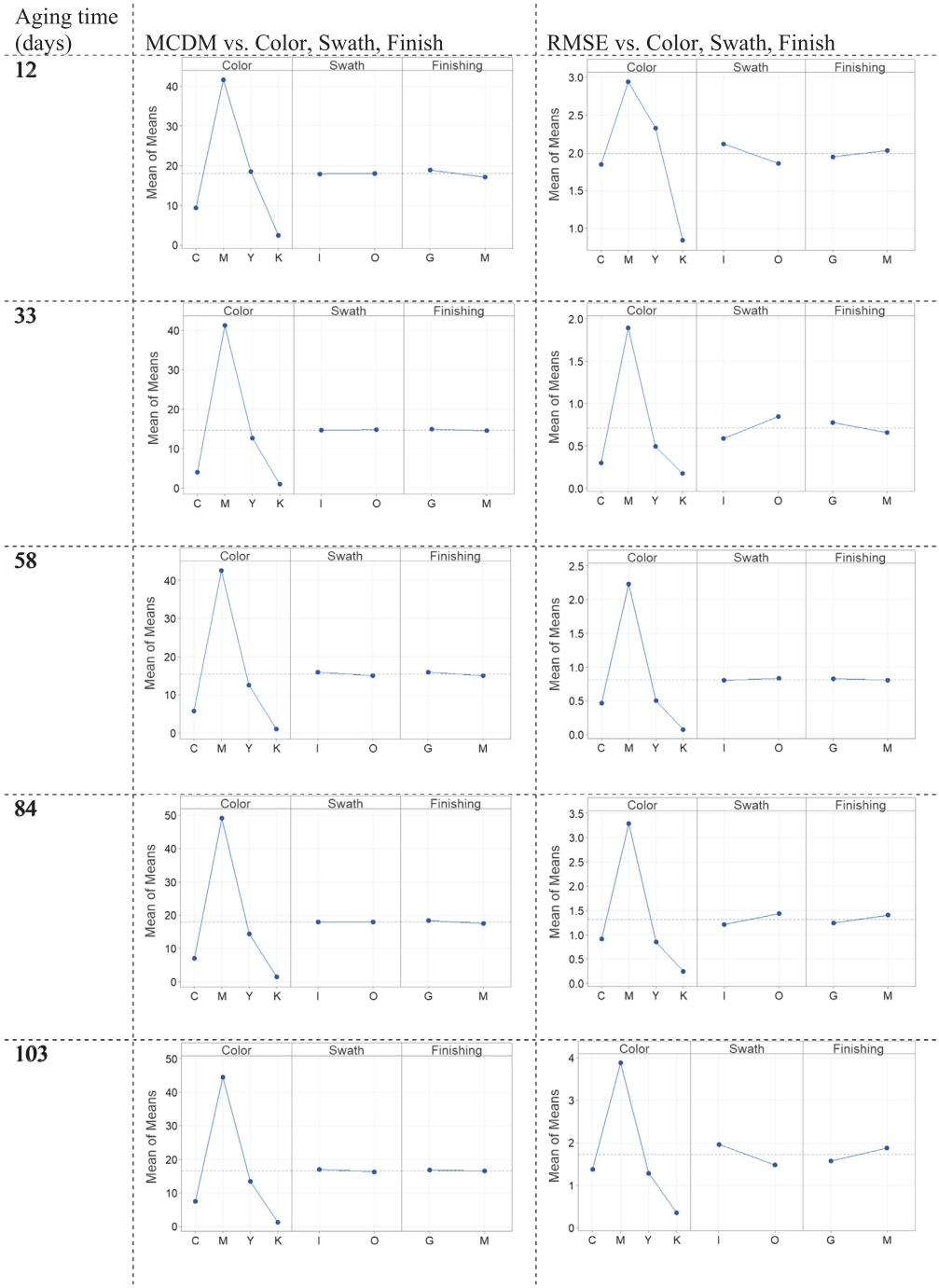


**Fig. 17.** Main effects plots for data means according to Taguchi analysis for the color appearance factors at the different aging times.

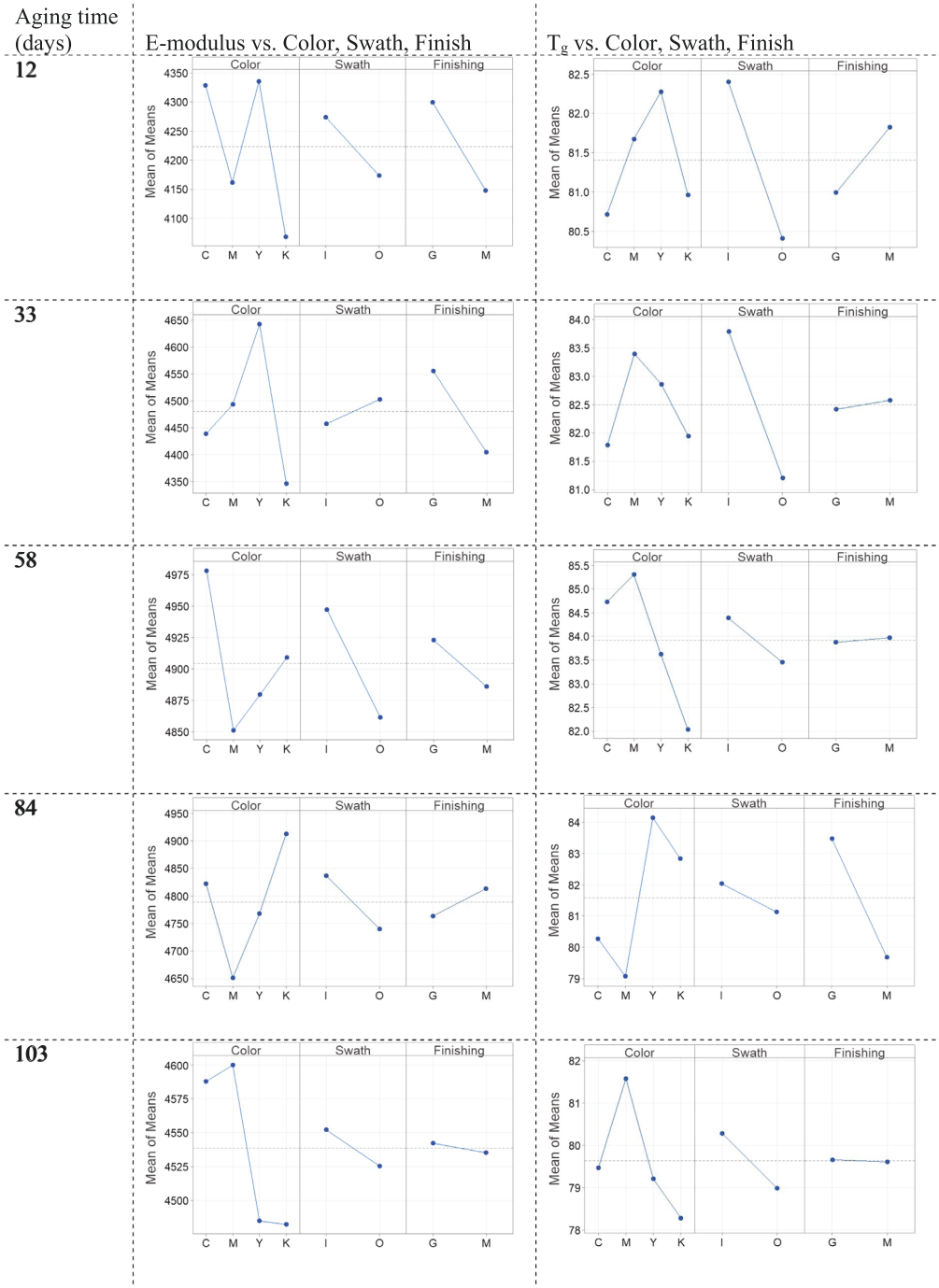


**Fig. 18.** Main effects plots for data means according to Taguchi analysis for the mechanical performance factors at the different aging times.

2. Based on mechanical performance, cyan photo resin had a higher level of tensile test results over an extended time, and the performance of the Glossy-on-Glossy finish was higher than that of Glossy-on-Matte specimens.
3. As a result of the dynamic response of the photo resins to weathering, distinct colors, and physico-mechanical performance was observed over time. The maximum variation in stiffness and $T_g$ was observed following 58 days of accelerated aging in the QUV chamber. As MJT coupons aged, their curvature, hue variation, and measurement errors for color and stiffness increased, regardless of their manufacturing PPP, reaching a maximum between 84 and 103 days, respectively.
4. Color appearance is solely affected by the photo resin color factor compared to other PPPs studied, while E and $T_g$ were influenced by all the studied PPPs, including color, swath, and finishing. Magenta specimens resulted in a hue distribution remarkably close to yellow materials in the CIE1976 u′, v′ chromaticity diagram after 12 days of aging. For both the color difference and its RMSE, most of the minimum values were reached between 33 and 58 days of the experiment. Black and cyan showed significantly less color difference and higher reliability than magenta and yellow photo resins over different aging periods.
5. Post-curing and the circular layer-by-layer structure observed in MJT coupons were the leading causes for the curvature along the length of DMA coupons. Due to the radial form of layers in 3D-printed coupons, the curvature is propagated into colored layers by forming new covalent bonds in polymer chains.
6. Multivariate RDA analysis revealed within the first 12 to 33 days of aging, lightness variations in the color appearance (dL) were involved as the first principal components (PC1). After 58 days of aging, $T_g$ and stiffness retentions were primarily increased, with the highest contribution coming from PC2, which aligned with the increase in dh. At the end of the aging experiment (103 days), most materials showed a significantly higher variation in chroma (dC). Furthermore, a strong negative correlation was observed between dC and stiffness. It is proposed that the correlation is a consequence of the different responses of coupons with various appearances to UV absorbance, which significantly impacts the material properties.
7. According to the Taguchi analysis, color appearance is solely affected by the photo resin color factor compared to other PPPs studied. However, E and $T_g$ were influenced by all the studied PPPs, including color, swath, and finishing. As a result of printing on the outer swath or selecting a Glossy-on-Matte finish, the MJT coupons appear to have less variation in elastic modulus and glass transition temperature. In terms of color, fidelity based on mean CIEDE2000 color differences, black and cyan showed significantly less color difference and higher reliability than magenta and yellow photo resins over different aging periods.

In summary, this study demonstrated the importance of understanding the mechanisms that affect the appearance and performance of multi-layered 3D-printed objects from the long-term perspective. Future research will have the opportunity to examine how different aging conditions, processing parameters, and materials and compositions affect the long-term properties of printed materials, intending to improve the durability and longevity of 3D-printed objects. It opens new avenues for improving 3D printing algorithms and multi-layer compatibility in additive manufacturing.

## Data availability

The main part of the raw/processed data required to reproduce these findings is available at https://doi.org/10.5281/zenodo.7314465.

The rest cannot be shared at this time as the data also forms part of an ongoing study.

## CRediT authorship contribution statement

**Ali Payami Golhin:** Conceptualization, Methodology, Investigation, Data curation, Formal analysis, Visualization, Writing – original draft, Writing – review & editing. **Chaman Srivastava:** Conceptualization, Methodology, Data curation, Writing – review & editing. **Are Strandlie:** Writing – review & editing, Supervision, Project administration, Funding acquisition. **Aditya Suneel Sole:** Writing – review & editing, Supervision. **Sotirios Grammatikos:** Writing – review & editing, Conceptualization, Supervision, Funding acquisition.

## Data availability

https://doi.org/10.5281/zenodo.7314465

## Declaration of Competing Interest

The authors declare the following financial interests/personal relationships which may be considered as potential competing interests: Ali Payami Golhin reports financial support, and article publishing charges were provided by Horizon 2020 (EU) ApPEARS-ITN project [grant No. 814158]. Ali Payami Golhin reports financial support, and travel was provided by the Research Council of Norway - LIFETIME project [Ref: 309943].

## Acknowledgments

This work was supported by the ApPEARS-ITN project funded by the European Union's H2020 research and innovation program under the Marie Skłodowska-Curie grant agreement No. 814158 and from the LIFETIME project, Ref: 309943, funded by the Research Council of Norway.

## Appendix A. Supplementary data

Supplementary data to this article can be found online at https://doi.org/10.1016/j.matdes.2023.111863.

## References

[1] J. Yuan, G. Chen, H. Li, H. Prautzsch, K. Xiao, Accurate and Computational: A review of color reproduction in Full-color 3D printing, Mater. Des. 209 (2021) 1–17, https://doi.org/10.1016/j.matdes.2021.109943.
[2] A. Payami Golhin, A. Strandlie, P. John Green, The influence of wedge angle, feedstock color, and infill density on the color difference of FDM objects, J. Imaging Sci. Technol. 65 (5) (2021) 1–15, https://doi.org/10.2352/J.ImagingSci.Technol.2021.65.5.050408.
[3] X. Wei, N. Zou, L. Zeng, Z. Pei, PolyJet 3D Printing: Predicting Color by Multilayer Perceptron Neural Network, Annals of 3D, Printed Medicine 5 (2022) 1–7, https://doi.org/10.1016/j.stlm.2022.100049.
[4] A.P. Golhin, A.S. Sole, A. Strandlie, Color appearance in rotational material jetting, Int. J. Adv. Manuf. Technol. 124 (3) (2023) 1183–1198, https://doi.org/10.1007/s00170-022-10536-1.
[5] G. Elber, M.-S. Kim, Synthesis of 3D jigsaw puzzles over freeform 2-manifolds, Comput Graphics (Pergamon) 102 (2022) 339–348.
[6] R. Chand, V.S. Sharma, R. Trehan, M.K. Gupta, M. Sarikaya, Investigating the dimensional accuracy and surface roughness for 3D printed parts using a multi-jet printer, J. Mater. Eng. Perform. 32 (3) (2023) 1145–1159.
[7] A. Payami Golhin, Generation of micro-and nano-textured surfaces, European Commission, Brussels, 2021, pp. 1-6. https://doi.org/10.5281/zenodo.7293168.
[8] L. Bass, N.A. Meisel, C.B. Williams, Exploring variability of orientation and aging effects in material properties of multi-material jetting parts, Rapid Prototyping J. 22 (5) (2016) 826–834, https://doi.org/10.1108/RPJ-11-2015-0169.
[9] I.Q. Vu, L.B. Bass, C.B. Williams, D.A. Dillard, Characterizing the effect of print orientation on interface integrity of multi-material jetting additive manufacturing, Addit. Manuf. 22 (2018) 447–461, https://doi.org/10.1016/j.addma.2018.05.036.

[10] M. Siegfarth, T.P. Pusch, A. Pfeil, P. Renaud, J. Stallkamp, Multi-material 3D printed hydraulic actuator for medical robots, Rapid Prototyping J. 26 (6) (2020) 1019–1026.
[11] T. Puttonen, M. Salmi, J. Partanen, Mechanical properties and fracture characterization of additive manufacturing polyamide 12 after accelerated weathering, Polym. Test 104 (2021) 107376.
[12] S.A. Grammatikos, M. Evernden, J. Mitchels, B. Zafari, J.T. Mottram, G.C. Papanicolaou, On the response to hygrothermal aging of pultruded FRPs used in the civil engineering sector, Mater. Des. 96 (2016) 283–295, https://doi.org/10.1016/j.matdes.2016.02.026.
[13] S. Kumar, I. Singh, D. Kumar, M.Y. Yahya, S.S. Rahimian Koloor, Mechanical and Morphological Characterizations of Laminated Object Manufactured 3D Printed Biodegradable Poly (lactic) acid with Various Physical Configurations, J. Marine Sci. Eng. 10 (12) (2022) 1954, https://doi.org/10.3390/jmse10121954.
[14] A. Payami Golhin, C. Srivastava, J.F. Tingstad, A.S. Sole, A. Strandlie, S. Grammatikos, Additive manufacturing of multilayered polymer composites: Durability assessment, Proceedings of the 20th European Conference on Composite Materials-Composites Meet Sustainability (Vol 1-6), EPFL Lausanne, Composite Construction Laboratory Switzerland, 2022. https://doi.org/10.5075/epfl-298799_978-2-9701614-0-0.
[15] C. Camposeco-Negrete, Optimization of FDM parameters for improving part quality, productivity and sustainability of the process using Taguchi methodology and desirability approach, Prog. Addit. Manuf. 5 (1) (2020) 59–65.
[16] Y. Duan, L. Zhang, J. Qiao, Y.-J. Wang, Y. Yang, T. Wada, H. Kato, J. Pelletier, E. Pineda, D. Crespo, Intrinsic Correlation between the Fraction of Liquidlike Zones and the β Relaxation in High-Entropy Metallic Glasses, Phys Rev Lett 129 (17) (2022), https://doi.org/10.1103/PhysRevLett.129.175501 175501.
[17] A. Foerster, V. Annarasa, A. Terry, R. Wildman, R. Hague, D. Irvine, D.S.A. De Focatiis, C. Tuck, UV-curable silicone materials with tuneable mechanical properties for 3D printing, Mater. Des. 205 (2021) 109681.
[18] S. Baharnezhad, A. Golhin, In-situ measurement and finite element simulation of thermo-mechanical properties of AA 6063 aluminum alloy for MIG weldment, Mater. Phys. Mech. 32 (2) (2017), https://doi.org/10.18720/MPM.3222017_15.
[19] S. Kumar, I. Singh, S.R. Koloor, D. Kumar, M. Yahya, On Laminated Object Manufactured FDM-Printed ABS/TPU Multimaterial Specimens: An Insight into Mechanical and Morphological Characteristics, Polymers 14 (19) (2022) 4066.
[20] S. Garzon-Hernandez, D. Garcia-Gonzalez, A. Jérusalem, A. Arias, Design of FDM 3D printed polymers: An experimental-modelling methodology for the prediction of mechanical properties, Mater. Des. 188 (2020) 108414.
[21] I. Singh, S. Kumar, S.R. Koloor, D. Kumar, M. Yahya, J. Mago, On Comparison of Heat Treated and Non-Heat-Treated LOM Manufactured Sample for Poly (lactic) acid: Mechanical and Morphological View Point, Polymers 14 (23) (2022) 5098.
[22] N. Vidakis, M. Petousis, N. Michailidis, J.D. Kechagias, N. Mountakis, A. Argyros, O. Boura, S. Grammatikos, High-performance medical-grade resin radically reinforced with cellulose nanofibers for 3D printing, J. Mech. Behav. Biomed. Mater. 134 (2022), https://doi.org/10.1016/j.jmbbm.2022.105408 105408.
[23] Z. Meng, J. He, Z. Cai, F. Wang, J. Zhang, L. Wang, R. Ling, D. Li, Design and additive manufacturing of flexible polycaprolactone scaffolds with highly-tunable mechanical properties for soft tissue engineering, Mater. Des. 189 (2020) 108508.
[24] R.D. Goodridge, R.J.M. Hague, C.J. Tuck, Effect of long-term ageing on the tensile properties of a polyamide 12 laser sintering material, Polym. Test 29 (4) (2010) 483–493, https://doi.org/10.1016/j.polymertesting.2010.02.009.
[25] R. Sepe, S. Franchitti, R. Borrelli, F. Di Caprio, E. Armentani, F. Caputo, Correlation between real geometry and tensile mechanical behaviour for Ti6Al4V electron beam melted thin specimens, Theor. Appl. Fract. Mech. 107 (2020) 102519.
[26] C. Chen, F. Chen, Y. Yang, H. Zhang, Study on appearance and mechanical behavior of additively manufacturing of Ti–6Al–4V alloy by using cold metal transfer, CIRP J. Manuf. Sci. Technol. 35 (2021) 250–258, https://doi.org/10.1016/j.cirpj.2021.06.017.
[27] Y.L. Tee, C. Peng, P. Pille, M. Leary, P. Tran, PolyJet 3D printing of composite materials: experimental and modelling approach, JOM 72 (3) (2020) 1105–1117, https://doi.org/10.1007/s11837-020-04014-w.
[28] Stratasys, Vero: Realistic, Multi-Color Prototypes in Less Time, Stratasys Datasheet, 2022, pp. 1-4.
[29] Stratasys, 3D Printing with Pantone Colors, Stratasys Ltd., 2021, pp. 1-6.
[30] ASTM, Standard practice for operating fluorescent ultraviolet (UV) lamp apparatus for exposure of nonmetallic materials, ASTM G154 (2016) 1-12.
[31] C.I.d. l'Éclairage, Colorimetry CIE 015:2004, Commission Internationale de l'Éclairage, 2004, pp. 1-82.
[32] S. Westland, C. Ripamonti, V. Cheung (Eds.), Computational Colour Science using MATLAB®, Wiley, 2012.
[33] A. International, Standard Practice for Computing the Colors of Objects by Using the CIE System, 2018, p. 45.
[34] G. Sharma, W. Wu, E.N. Dalal, The CIEDE2000 color-difference formula: Implementation notes, supplementary test data, and mathematical observations, Color Res. Appl. 30 (1) (2005) 21–30, https://doi.org/10.1002/col.20070.
[35] Assessment and validation of the performance of spectrocolorimeters and spectrodensitometers, ISO/TS 23031:2020; Graphic technology, International Organization for Standardization: Geneva, Switzerland, 2020.
[36] S.C. Das, D. Paul, S.A. Grammatikos, M.A.B. Siddiquee, S. Papatzani, P. Koralli, J. M.M. Islam, M.A. Khan, S.M. Shauddin, R.A. Khan, N. Vidakis, M. Petousis, Effect of stacking sequence on the performance of hybrid natural/synthetic fiber reinforced polymer composite laminates, Compos. Struct. 276 (2021) 114525.
[37] A.S. D–01, Standard practice for plastics: dynamic mechanical properties: determination and report of procedures, ASTM International West Conshohocken, PA, 2000.
[38] Plastics - Determination of Tensile Properties: Test Conditions for Moulding and Extrusion Plastics, ISO 527-2:2012; ISO/TC 61/SC 2 Mechanical behavior, International Organization for Standardization: Geneva, Switzerland, 2012.
[39] J. Lepš, P. Šmilauer (Eds.), Multivariate Analysis of Ecological Data using CANOCO, Cambridge University Press, 2003.
[40] C.R. Rao, The use and interpretation of principal component analysis in applied research, Sankhyā: Indian J. Statist. Ser. A (1964) 329–358.
[41] F. Segovia, C. Ferrer, M.D. Salvador, V. Amigo, Influence of processing variables on mechanical characteristics of sunlight aged polyester–glass fibre composites, Polym Degradation Stab 71 (1) (2000) 179–184, https://doi.org/10.1016/S0141-3910(00)00168-3.
[42] E. Boinard, R.A. Pethrick, J. Dalzel-Job, C.J. Macfarlane, Influence of resin chemistry on water uptake and environmental ageing in glass fibre reinforced composites-polyester and vinyl ester laminates, J Mater Sci 35 (8) (2000) 1931–1937, https://doi.org/10.1023/A:1004766418966.
[43] R.S.C. Woo, H. Zhu, C.K.Y. Leung, J.-K. Kim, Environmental degradation of epoxy-organoclay nanocomposites due to UV exposure: Part II residual mechanical properties, Compos. Sci. Technol. 68 (9) (2008) 2149–2155, https://doi.org/10.1016/j.compscitech.2008.03.020.
[44] S. Mora, N.M. Pugno, D. Misseroni, 3D printed architected lattice structures by material jetting, Mater. Today 59 (2022) 107–132.
[45] K. Kardel, A. Khoshkhoo, A.L. Carrano, Design guidelines to mitigate distortion in material jetting specimens, Rapid Prototyping J. 27 (6) (2021) 1148–1160, https://doi.org/10.1108/RPJ-08-2020-0192.
[46] Z. Tang, J. Gong, P. Cao, L. Tao, X. Pei, T. Wang, Y. Zhang, Q. Wang, J. Zhang, 3D printing of a versatile applicability shape memory polymer with high strength and high transition temperature, Chem. Eng. J. 431 (2022) 134211.

## Paper V:

A. P. Golhin, A. Strandlie, Appearance evaluation of digital materials in material jetting, Optics and Lasers in Engineering, 168, (2023) 107632.
https://doi.org/10.1016/j.optlaseng.2023.107632

Optics and Lasers in Engineering 168 (2023) 107632

Contents lists available at ScienceDirect

Optics and Lasers in Engineering

journal homepage: www.elsevier.com/locate/optlaseng

# Appearance evaluation of digital materials in material jetting

Ali Payami Golhin*, Are Strandlie

*Department of Manufacturing and Civil Engineering, NTNU - Norwegian University of Science and Technology, Gjøvik, 2815 Norway*

ARTICLE INFO

*Keywords:*
Material jetting
Optical properties
Appearance measurement
Additive manufacturing
Structured surfaces

ABSTRACT

Material jetting (MJT) products have a high subjective appearance quality in additive manufacturing (AM). MJT objects are typically manufactured from multiple layers of semi-transparent photo resins to achieve the desired appearance. This study explores the optical properties of photopolymer plates in monolayer and bilayer combinations. The role of the white substrate as the background plate in bilayer configurations is discussed concerning appearance reproduction in MJT parts. For this purpose, spectral reflectance, transmittance, absorbance, color difference, and texture were investigated for MJT objects with different plate combinations. The primary digital materials in MJT were further investigated for haze, gloss, scattering variations, and their corresponding bidirectional reflectance distribution functions (BRDFs). The optical properties of the studied surfaces were then applied to three-dimensional (3D) models to illustrate the variation in visual appearance and texture. According to the results, it was inevitable to use a white background plate for color reproduction. Therefore, increasing the layer thickness did not improve color fidelity. Due to the role of microfacet normals in the surface texture, gloss, haze, and scattering, results followed the same analysis pattern but depended on the measurement direction.

## 1. Introduction

MJT[1], including the PolyJet®, is an AM[2] technique that promotes multi-material 3D printing, utilizing UV[3]-curable polymer inks. In terms of full-appearance reproduction, MJT is one of the main AM categories. 3D printers with PolyJet technology are ideal for depositing tiny droplets of material with different appearances into voxels following the design. MJT machines can print fine details and achieve a consistent surface finish using a PolyJet 3DP process with little to no visible layering [1]. Unlike conventional printers, MJT models can represent relatively smooth, glossy surfaces with consistent colors since the materials are mixed in the same layer but with different color cartridges.

The MJT printers are able to mix and match colors since each droplet of material contains its own mini pool of ink. The flow of fluid in pools can affect the appearance and shape of structured layers, as seen previously in high-temperature process methods, such as the welding process [2–4]. This allows designers to have a great deal of flexibility regarding the appearance of their products. Thus, the MJT is ideally suited to applications in which appearance is essential for consumer goods, such as medical models [5] or jewelry [6]. However, the movement of the printhead, i.e., nozzles, and build platform, affects the shape and combination of the voxels, resulting in variations in the appearance [7,8]. The design of a 3D object, along with multiple printer parameters, must be carefully controlled to achieve high-fidelity reproductions of both the shape and appearance of the 3D object [8,9]. Aside from this, optical metrology systems are closely related to similarity evaluations of topography measurements in additive manufacturing [10], which depend on the design of the parts.

Since the optical properties of an object determine its visual quality, industries are concerned about the appearance of their products. Furthermore, customers expect uniformity when dealing with groups of the same product. As a result of observing the differences between similar products, consumers commonly attribute the inferior quality [11]. As Yuan [8] described, color reproduction can be divided into four categories: colorimetric difference assessment, computer-aided colorization, optical parametric modeling, and droplet jetting. Based on Pointer [12], total appearance can be described as size, shape, gloss, texture, and other visual characteristics.

In order to reach the high appearance fidelity of the 3D-printed part with the designed model, several characteristics that contribute to the optical properties of objects should be studied, including color, gloss, texture, translucency, haze, and subsurface scattering [13,14]. Texture mapping is essential to the reproduction of an appearance using AM. This process involves applying an image texture to a 3D surface to create the appearance of a real surface [15,16]. For this purpose, a list of vertex-to-UV coordinate mappings is included in the 3D model when a 3D object with texture mapping is imported [17]. Texture mapping provides several advantages for measurement, including accurate representation, increased detail, and rapid and non-destructive measurement [18]. It can be used in a wide range of measurement applications, ranging from engineering and manufacturing [19] to preserving cultural

* Corresponding author.
*E-mail address:* ali.p.golhin@ntnu.no (A.P. Golhin).

[1] Material jetting
[2] Additive manufacturing
[3] Ultraviolet

https://doi.org/10.1016/j.optlaseng.2023.107632
Received 30 January 2023; Received in revised form 19 April 2023; Accepted 25 April 2023

heritage and restoring art [20]. Although limited research has been conducted on the appearance of MJT parts [8,21-24], the study of these various attributes simultaneously is lacking in the literature.

As we discussed in our previous works [8,25,26], the MJT object should be manufactured in a bilayer structure (overlay of two plates) to achieve optimal color reproduction. The influence of bilayer structure on MJT 3D printing, however, was not studied. Bilayer structures have been used in advanced manufacturing in a variety of aspects, including functional and optical properties. A review by Hong et al. [27] examined structural color materials and their applications in optical encryption and anticounterfeiting, in particular bilayer structures. Nam et al. [28] addressed full-color woodpile photonic crystals via interference from a conformal multilevel phase mask based on bilayer structures. Using different polymer and composite abutments, Hsu et al. [29] evaluated the color accuracy of multilayer pre-colored zirconia polycrystal dental prostheses. Egorov et al. [30] compared 3D printing with simple bilayer objects using fused deposition modeling (FDM) and stereolithography (SLA) methods for electrochemical energy storage. However, these works were limited to the functional and only color-appearance attributes of the bilayer structures. Accordingly, no studies discussed the significance of the white plate of the bilayer objects in appearance, particularly for non-color attributes and in rotational MJT.

This study provides insight into the appearance and texture mapping of structured surfaces manufactured using PolyJet technology. The role of bilayer structure using a white background in MJT technology is examined for the first time concerning appearance reproduction using various optical attributes. For this purpose, this work includes studies on color, gloss, translucency, texture, haze, scattering, and BRDFs[4] for printed plates with different thicknesses and color combinations. It is described how the appearance of 3D printing, as a unique approach to additive manufacturing, interacts with the hard proofing and quality improvement of AM surfaces.

## 2. Materials and methods

### 2.1. Material jetting

A Stratasys J55 PolyJet material jetting machine was used to 3D print the polymeric coupons, which were made of VeroCyan (RGD843), VeroBlackPlus (RGD875), VeroYellow (RGD836), VeroMagenta (RGD851), and VeroPureWhite (RGD837) photo-resins. The standard tray material was applied to the 3D models imported to the Stratasys GrabCAD Print software. In this paper, the terms "cyan", "magenta", "yellow", "black", and "white" have been used to designate the colors of coupons. Vero materials offer low viscosity acrylic oligomers mixed with exo-1,7,7-trimethylbicyclo[2,2,1]hept-2-yl acrylate, (octahydro-4,7methano-1H-indenediyl) bis(methylene) diacrylate, and 4-(1-oxo-propenyl)-morpholine [31]. Vero photo-resins share similar material properties, including mechanical, thermal, and electrical characteristics [32].

As shown in Fig. 1, the role of the white color background was studied using three sets of specimens. The monolayer (plate) of cyan, magenta, yellow, black, and white (CMYKW) photo resins were manufactured at various thicknesses (1.00 ± 0.02 mm and 2.00 ± 0.02 mm), hereafter referred to as 1 mm and 2 mm samples. Bilayer structures were built using 1 mm plates of each CMYKW color separately with a white background of 1 mm thickness. The size of the specimens was 35.50 ± 0.50 mm (width) × 40.00 ± 0.50 mm (length), fabricated on the middle swath of a rotary disc as the build platform with a glossy-on-glossy surface finish. The process was followed by support removal using a waterjet system. Five measurements from two sets of specimens were collected for each for reproducibility in measuring appearance.

[4] Bidirectional reflectance distribution functions

### 2.2. Appearance study

Spectrophotometry was conducted using a UV/Vis/NIR Spectrometer (PerkinElmer Lambda 1050+) equipped with the 3-detector module in an integrating sphere configuration (150 mm) with a wavelength accuracy of 1 nm. The reflectance, specular transmission, and absorbance spectra of photopolymer plates in the wavelength range 200-2000 nm and sampling interval of 5 nm were recorded with the specimens aligned regarding the detector window. Spectral reflectance results were collected in the visible range of 380 to 780 nm for color evaluation. To minimize the effect of layer-by-layer inhomogeneity and the edge effect resulting from light scattering, the largest possible area in the middle of the specimens was exposed to a light beam. Thus, the measurement area was limited to the size of the transmittance (25 mm × 16 mm) and reflectance (24 mm in diameter) ports (Fig. 2).

The computational color science toolbox in MATLAB R2022a [33] was used to calculate colorimetric values. A color-matching function derived from ASTM E308-01 [24] and designed by the International Commission on Illumination (CIE[5]) was used to calculate CIEXYZ tristimulus values. The CIE 2° color matching functions and the D50 illuminant were used to determine tristimulus values. As a result, CIEL*a*b* coordinates were further determined according to CIE1976. CIEL*a*b* and CIEL*C*h* color spaces define colors based on three coordinates for each, where L* is the lightness, a* and b* stand for the red-green and blue-yellow axes, C* corresponds to chroma, and h* relates to hue angle. Colorimetric differences of 1 mm and 2 mm sample types were compared with bilayer samples using CIEDE2000 color difference according to the following equation

$$CIEDE2000 = \sqrt{\left(\frac{\Delta L^*}{k_L S_L}\right)^2 + \left(\frac{\Delta C^*}{k_c S_C}\right)^2 + \left(\frac{\Delta h^*}{k_h S_h}\right)^2 + R_T f(\Delta C^* \Delta h^*)} \quad (1)$$

where $\Delta L^*$ (lightness), $\Delta C^*$ (chroma) and $\Delta h^*$(hue) represent their variant due to the color change, and the $R_T$ variable consists of the hue rotation term. $S_L$, $S_C$, and $S_h$ correspond to CIEL*C*h* lightness compensation, and $k_L$, $k_C$, and $k_h$ constants were set to the unit value. The color space is designed to be perceptually uniform, meaning that the same amount of distance between two points corresponds to roughly the same amount of perceived color difference. As a result, they can be used for comparing color differences and specifying colors across different media and devices.

To assess the color difference among CMYKW plates with different thicknesses and their corresponding bilayer reference spectra, the MCDM[6] and the RMSE[7] were determined as

$$MCDM = \frac{1}{N}\sum_{i=1}^{N} \Delta E(C_i, C_m) \quad (2)$$

$$RMSE = \sqrt{\frac{1}{N}\sum_{i=1}^{N} (r_{r,i} - r_{t,i})^2} \quad (3)$$

where $N$ is the number of results, $r_t$ and $r_r$ relate to the spectral results of tests and references, $C_i$ implies the color coordinate of the i$^{th}$ measurements, and $C_m$ is the reflectance average.

To assess the texture, the xTex scanner by Vizoo was used, and the 3D texture models were rendered using Blender 2.79 engine. For this purpose, collected surface maps, including alpha, base, displacement, material, surface normal, and roughness, were imported as texture data. Using a light-controlled Lightbox, multiple photos were taken of a sample under varying lighting conditions to minimize the errors due to stray lights or lighting variation at different observation angles. Optical microscopy was performed by the Keyence VH-ZST microscope (20X to

[5] Commission Internationale de l'éclairage
[6] Mean color difference from the mean
[7] Root-mean-square error

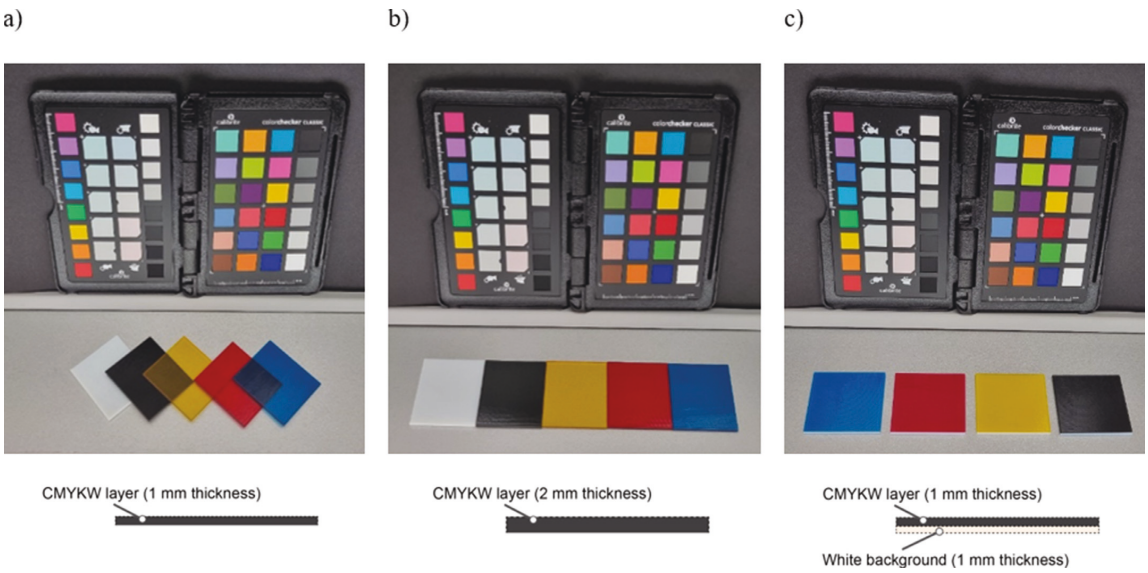


**Fig. 1.** CMYKW monolayers (plates) with a thickness of a) 1 mm, b) 2 mm, and c) bilayers of CMYK plate on white background, as observed under D50 daylight illumination.

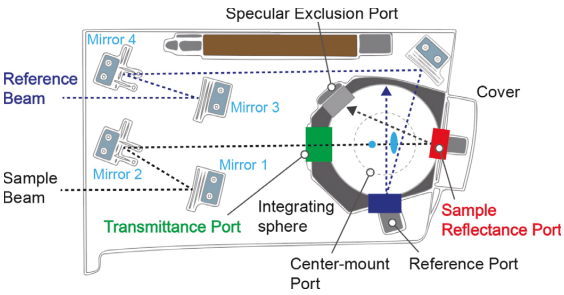


**Fig. 2.** A top-down schematic representation of the UV/VIS/NIR spectrometer and the measurement geometry.

2000X). An RA-532H surface reflectance analyzer was used to analyze haze and gloss per ASTM D523 – 14. Further, it provided Canon scattering indices C20 and C60 for lighting angles of 20° (ASTM D5767) and 60° (JIS K7374), respectively. The C20 index addresses the DOI[8], and the C60 index refers to IC[9]. Reduction measurement errors were considered by avoiding sites with unusual colors, external particles, stains or dust, and support materials. Data analysis was performed using Origin 2022 (OriginLab) and R statistical software 4.2.1.

## 3. Results and discussions

### 3.1. Visual observations

Fig. 3 illustrates how typical PolyJet parts were semi-translucent, hazy, and complex in appearance due to the addition of layering photo resins and the agitation in the manufacturing process. There was a distinction between the appearance of MJT objects under different illumi-

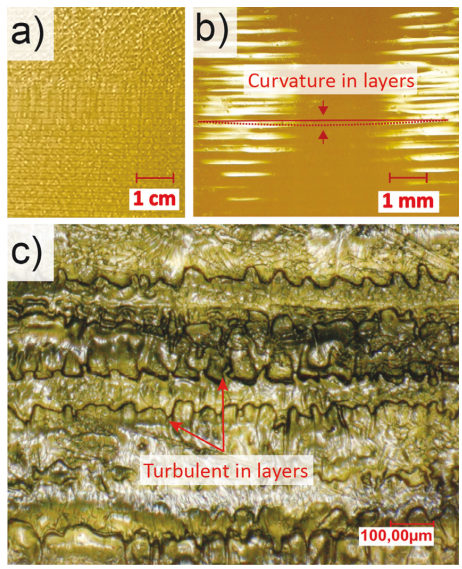


**Fig. 3.** The polymeric surface of the 3D-printed yellow photo resin as seen through an optical microscope at a) macroscopic 1X, b) macroscopic 10X, and c) microscopic scales.

nations and microscopes. As a result of the disc-shaped build platform (rotary disc), parallel layers (swaths) were not perfectly horizontal, resulting in a slight curvature observable on the surface (Fig. 3b). The added layers were oriented in the same direction as the rotation of the rotary disc. The curvature in layers was primarily determined by the printing speed, as well as the design, which are connected to the UV curing time (the print head) and the rotational speed of the disc. As a

[8] Distinctness of the image
[9] Image clarity

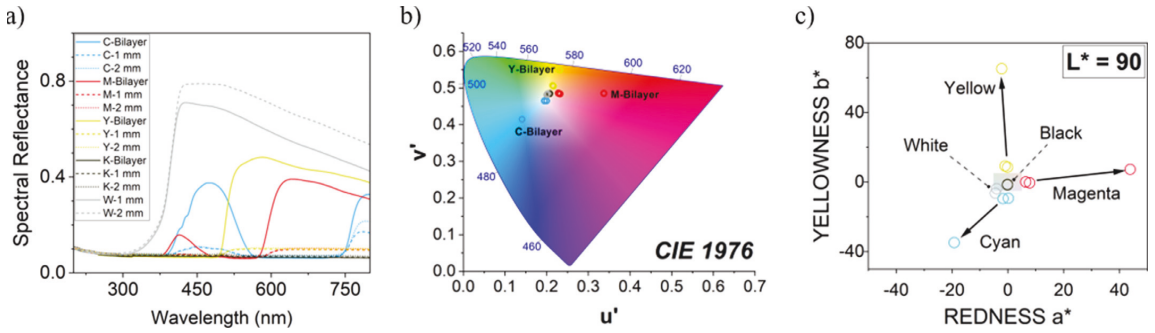


**Fig. 4.** a) Reflectance, b) the mean hue stimuli in the CIE1976 u', v' chromaticity diagram, and c) redness and yellowness at constant lightness in CIEL*a*b* color space.

**Table 1**
The color difference results compared with the corresponding bilayer configuration.

| Photo resin | Thickness: 1 mm | | | | | Thickness: 2 mm | | | | |
|---|---|---|---|---|---|---|---|---|---|---|
| | MCDM | RMSE | dL | dC | dh | MCDM | RMSE | dL | dC | dh |
| Cyan | 18.83 | 0.20 | 9.30 | 14.71 | -4.60 | 21.12 | 0.08 | 8.96 | 14.98 | -7.68 |
| Magenta | 19.83 | 0.12 | 8.62 | 17.67 | 2.56 | 20.43 | 0.05 | 7.96 | 18.75 | 1.55 |
| Yellow | 38.56 | 0.09 | 32.39 | 20.88 | -1.38 | 38.03 | 0.08 | 31.52 | 21.29 | 0.32 |
| Black | 0.50 | 0.01 | -0.48 | -0.14 | -0.02 | 1.52 | 0.01 | -1.51 | -0.20 | -0.04 |
| White | 4.19 | 0.01 | 3.63 | -1.58 | -1.37 | - | - | - | - | - |

result of typical build vibration during the manufacturing process, the swaths were subject to subsurface turbulence in layers and microscopic inhomogeneity (Fig. 3c).

### 3.2. Spectrophotometry

Spectrophotometry results, including reflectance, transmittance, and absorbance, indicate that the white background plate for CMYKW plates plays a vital role in visual appearance. As seen in Fig. 4, only using colored plates with 1 mm or 2 mm thickness could not provide the intended color. The spectral reflectance results indicate significantly lower lightness (albedo) due to lower reflectance values (Fig. 4a). Besides, hue stimuli were closely distributed in the middle of the CIE1976 u', v' chromaticity diagram (Fig. 4b). Using white background was crucial to alter the colors to their intended u', v' in GrabCAD, and a* and b* values. It is particularly highlighted for CMY colors as represented by vectors in Fig. 4c.

Table 1 lists the mean color difference of monolayer specimens according to their corresponding bilayer type. According to the results, color reproduction in yellow photo resins was more dependent on the presence of a white background with the highest MCDM of 38.56 for 1 mm thickness and 38.03 for 2 mm thickness. Results were followed by cyan and magenta photo resins, which were mainly affected by color changes associated with chroma (dC) and lightness (dL). The black and white photo resins exhibited the smallest color difference. Furthermore, it was evident that increasing the thickness did not compensate for the color difference.

Table 2 lists the measured CIEL*a*b* values along with their representative color HEX compared to the closest Pantone color codes extracted from GrabCAD. Color variation was inevitable during the reproduction of colors using the J55 3D printer, where the same Pantone code was referred to for the monolayers of cyan and yellow. In the manufacturing design, even 1 mm monolayers and bilayers of black photo resin follow the same Pantone code. A darker specimen with less lightness, particularly for monolayer specimens, suggests that studying color appearance alone is insufficient for the optical assessment of MJT products. Translucency, gloss, and scattering are essential factors to accurately reproduce an appearance to fulfill hard proofing in the appearance of 3D printing.

Fig. 5 shows that using a white background significantly decreases transmission and increases the absorbance of light through the specimens. Yellow, cyan, and magenta photo resins showed a similar trend in reflectance compared to black and white resins, which appeared opaquer. While the 1 mm thickness exhibited considerably greater transparency than the 2 mm, the role of the white background was the dominant factor in translucency and appearance reproduction.

### 3.3. Gloss appearance

To characterize gloss nuances, distinct aspects of gloss appearance have been compared in Fig. 6. This includes specular gloss, haze, and scattering results of C20 and C60 derived from BRDF. Compared to monolayer specimens, adding a white background plate results in generally increased gloss and haze, but had no significant influence on the sublayer scattering. Haze in reflection indicates a cloudy or milky appearance caused by light scattering [34]. As part of surface quality assessment, haze is considered an appearance attribute that reduces the quality of the appearance because of imperfections, including surface texture. High haze occurs around reflections of light sources on high-gloss and high-scattering (C20 and C60) surfaces due to image diffusion.

The results show the gloss results of the same samples measured vertically (Fig. 6a) were generally higher than that measured horizontally (Fig. 6b). In addition, results were more correlated depending on the photo resin used, as indicated by the stronger fitting of the mean (red lines in Fig. 6a and b) for vertical gloss ($R^2$ = 0.46) and associated haze ($R^2$ = 0.50) measurements. According to Spearman's rank correlation coefficient ($\rho$) in Fig. 6c, robust correlations were observed between measurement direction and studied variables, including gloss ($\rho$ = 0.59), and the haze and scattering results ($\rho$ = 0.87). Therefore, surface reflectance analysis was significantly affected by the measurement direction. Furthermore, gloss showed a correlation of $\rho$ = 0.50 with the sample type.

In the vertical direction, higher $R^2$ values indicate a strong correlation in the data, suggesting that the type of photo resins plays a less

**Table 2**
Measured color compared to the corresponding Pantone color at the design level.

| Digital material | Type | Color measurement | | | | | Pantone Solid Coated | | | | | |
|---|---|---|---|---|---|---|---|---|---|---|---|---|
| | | $L^*$ | $a^*$ | $b^*$ | HEX | | Code | $L^*$ | $a^*$ | $b^*$ | HEX | |
| Cyan | Bilayer | 43.67 | -19.23 | -34.73 | 0073A0 | | 641 C | 41.18 | -30.48 | -38.07 | 00719F | |
| | 1 mm | 32.84 | -1.76 | -9.45 | 424F5C | | 7540 C | 33.71 | -1.57 | -3.98 | 495055 | |
| | 2 mm | 33.27 | 0.13 | -9.26 | 464F5D | | 7540 C | 33.71 | -1.57 | -3.98 | 495055 | |
| Magenta | Bilayer | 42.23 | 43.81 | 7.34 | A64159 | | 7419 C | 44.77 | 42.90 | 6.77 | AC4960 | |
| | 1 mm | 32.04 | 7.80 | -0.38 | 57474C | | 438 C | 30.87 | 11.34 | -0.28 | 5A4249 | |
| | 2 mm | 32.86 | 6.40 | 0.16 | 584A4D | | 2335 C | 34.08 | 5.60 | 4.57 | 5C4D49 | |
| Yellow | Bilayer | 70.72 | -2.23 | 65.20 | C9AB2A | | 7752 C | 70.86 | 3.66 | 66.63 | D2A827 | |
| | 1 mm | 37.08 | -1.02 | 9.27 | 5C5748 | | 411 C | 35.93 | 4.72 | 2.72 | 5E5250 | |
| | 2 mm | 37.81 | -0.14 | 8.59 | 5E594B | | 411 C | 35.93 | 4.72 | 2.72 | 5E5250 | |
| Black | Bilayer | 30.92 | -0.16 | -1.32 | 48494B | | 2336 C | 31.98 | 0.66 | 1.41 | 4D4B49 | |
| | 1 mm | 31.53 | -0.16 | -1.47 | 494A4C | | 2336 C | 31.98 | 0.66 | 1.41 | 4D4B49 | |
| | 2 mm | 32.83 | -0.16 | -1.53 | 4C4D50 | | 7540 C | 33.71 | -1.57 | -3.98 | 495055 | |
| White | Bilayer | 83.24 | -4.50 | -6.31 | C0D2DB | | 5455 C | 82.44 | -3.63 | -9.38 | BCD0DE | |
| | 1 mm | 88.82 | -4.02 | -3.72 | D3E2E6 | | 621 C | 88.31 | -5.84 | 0.03 | D2E1DD | |

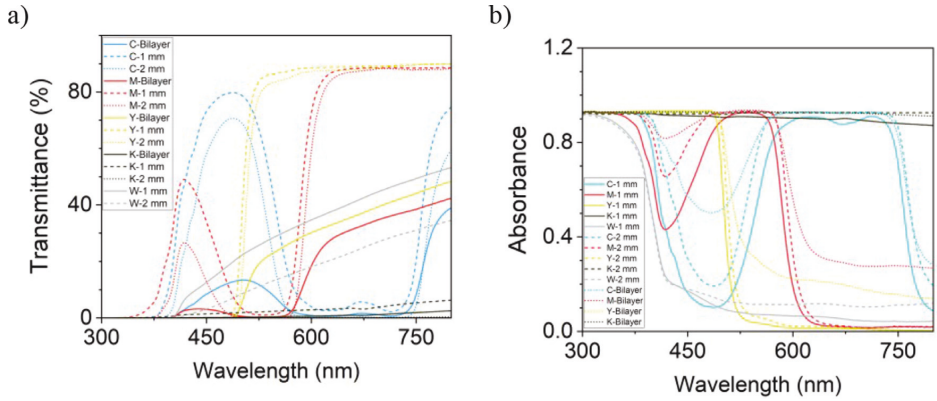


**Fig. 5.** a) Transmittance and b) absorbance in the visible spectrum.

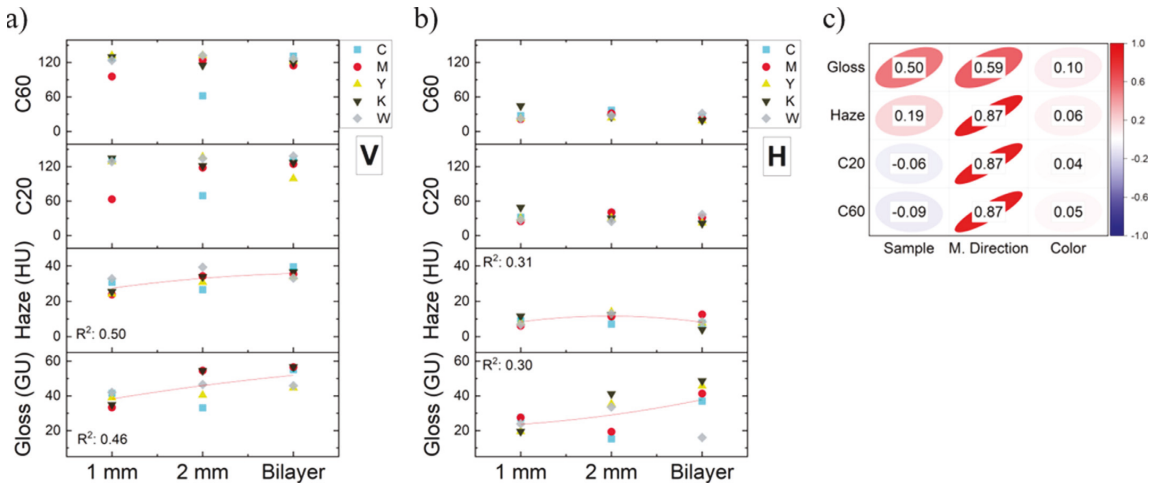


**Fig. 6.** Gloss nuances in a) vertical and b) horizontal measurement directions, and c) Spearman rank correlation coefficients.

significant role in surface reflectance variations. This can be explained by considering the more significant effect of $\vec{m}$, microfacets normals (Fig. 7), facing toward the measurement direction in the vertical mode. According to Fresnel's equation [35], the $f_{r,m}$ term explains the reflectance from a smooth microfacet in translucent objects in the BSDF[10]:

$$f_{r,m}(x_m, \vec{\omega}_i, \vec{\omega}_o) = F\left(\vec{m}, \vec{\omega}_i, \frac{n_t}{n_i}\right) \frac{\delta(\vec{\omega}_o - \vec{\omega}_s)}{\cos\theta_i} \tag{4}$$

where $x_m$ is the microfacet surface point, $\vec{\omega}_i$, $\vec{\omega}_s$ and $\vec{\omega}_o$ are the unit vectors for illumination, scattering, and observation of light. F is the expansion of Maxwell's equations along the surface using Fourier transformation. $n_t$ and $n_i$ are the transmission and illumination normals. $\delta$ is the Dirac delta function and $\theta_i$ is the illumination angle relative to the surface normal ($\vec{n}$).

The macroscopic BSDF is a function that includes both reflectance (BRDF) and transmittance (BTDF[11]). In this case, the light is incident on and emerges from the same macroscopic surface [36]. Accordingly, smoother BRDFs were captured for vertical measurement compared to

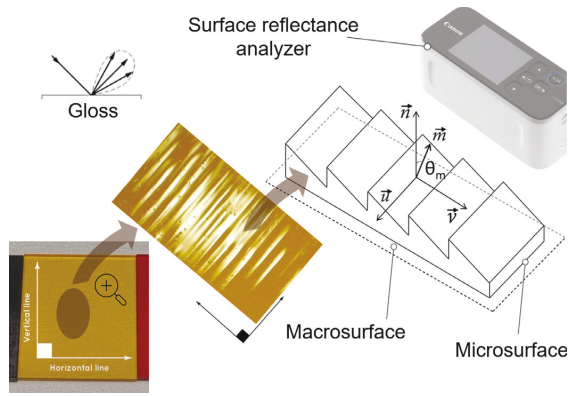


**Fig. 7.** Gloss measurement for structured surfaces in additive manufacturing.

[10] Bidirectional scattering distribution function
[11] Bidirectional transmittance distribution function

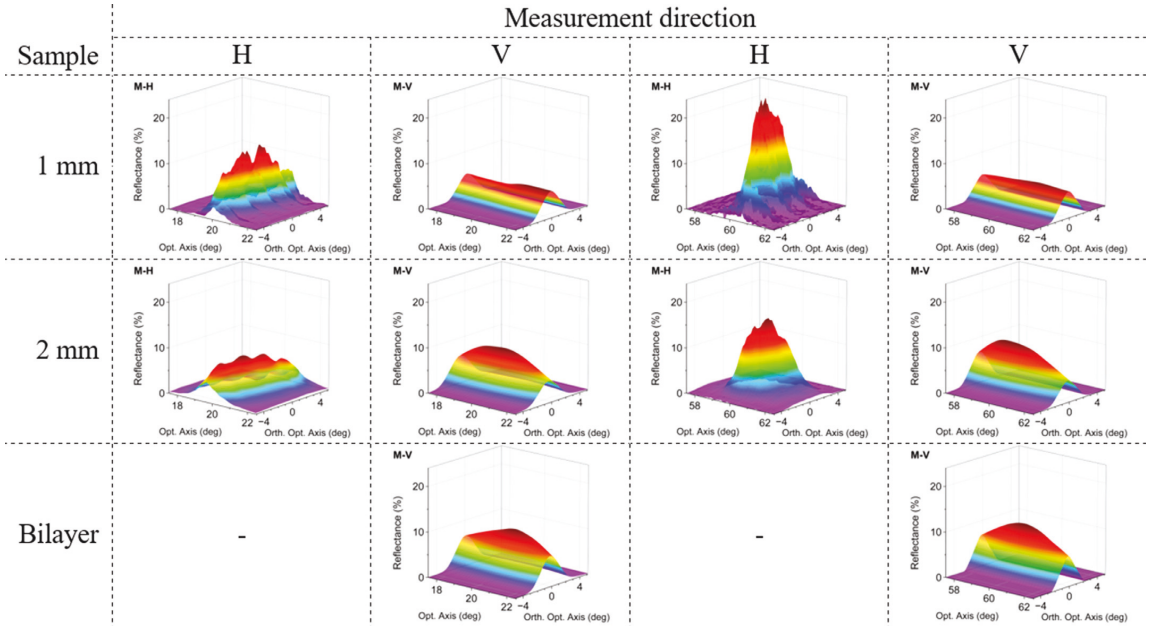


**Fig. 8.** BRDF representations for magenta resin at specular angles of 20° and 60°.

the horizontal direction (Fig. 8). The mixture of curvature on the surface shown in Fig. 3b which can affect the direction of microfacet normals provides an insight into the reason behind these perturbed BRDF graphs. Supplementary BRDF data for specular gloss measurements are available in Appendix A.

### 3.4. Visual texture mapping

Illustrations of texture mapping on spherical 3D models using surface textural maps are shown in Fig. 9. Photo resins of cyan and magenta exhibited notable parallel horizontal swathes fabricated in the manufacturing process. The swath patterns were also apparent for yellow bilayer samples. However, black photo resins did not show the same texture characteristics. The bilayer specimens for the CMY photo resins exhibited significantly different appearances with more specular reflection, particularly for the color attribute. However, in black materials, the role of the white background film was less apparent. Table 2 confirms this behavior for monolayers of black resins of 1 mm and bilayers of black resins of 2 mm with more diffuse reflection. Results for CMY photo resins also suggest a higher glossiness and less transparency than monolayers, which is consistent with the results of the spectrophotometry and gloss measurements. Because of the high exposure surface of the white photo resins, it was impossible to generate rendered spheres properly for this material. Although yellow specimens experienced the same problem at lower significance, particularly monolayer samples, they rendered the results. Supplementary results for texture mapping, including surface displacement and normal maps, are available in Appendix B.

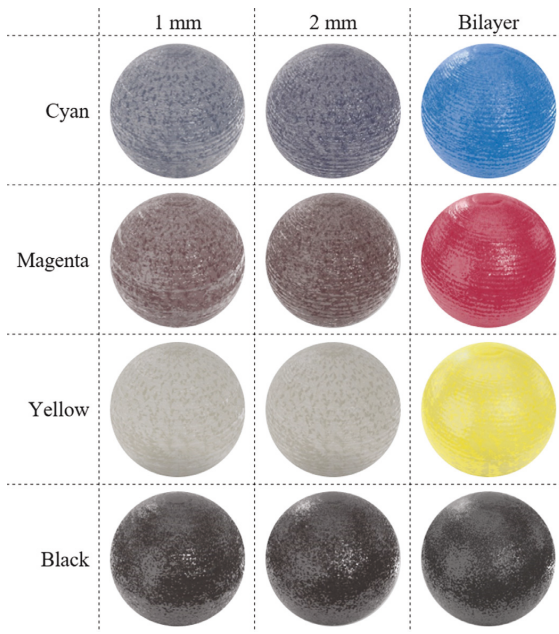


**Fig. 9.** A series of spheres rendered in different texture levels.

## 4. Conclusions

This study aimed to provide insight into the role of bilayer structure in material jetting appearance reproduction. A PolyJet printer was used to deposit photo resins in CMYKW colors in monolayers varying in thickness, as well as bilayers using a white background plate. According to the findings of this study:

- Microscopical observations revealed a distinction between the appearance of MJT objects and their visual complexity under different illuminations and microscopic scales. As a result of layer-by-layer rotational printing, vibrations of the rotary disc as the build plat-

form, and translucency of photo resins, the texture, and appearance showed more subsurface turbulence in layers and microscopic inhomogeneities.
- Spectrophotometry revealed that the lack of a white background plate led to an increase in transparency and a decrease in albedo and color fidelity.
- Using only monolayer CMYKW resins resulted in significant deviations in CIEL*a*b* and CIE1976 u', v' from the Pantone color matching scheme, with more significant deviations in chroma and lightness.
- The increase in absorbance due to doubling the thickness of monolayer samples did not compensate for losing albedo and higher reflectance because of the lack of white background plates in the monolayer samples.
- The gloss perception was characterized by a monolayer/bilayer structure similar to that seen in transmittance conditions. Color and texture of the reflective surface changed according to the embedding illumination. Higher gloss and haze were recorded for bilayer specimens compared to monolayers.
- The white background had a greater impact on color, translucency, and scattering than gloss and haze. Vertical measurements resulted in higher values of gloss, haze, and scattering compared to the horizontal measurements.
- In monolayer structures, cyan, magenta, and yellow photo resins had significantly different appearances, as shown in rendered spherical 3D models. MJT photo resins exhibited high transparency, specular reflections, and non-uniform albedo due to textured surfaces.

In summary, assessing the appearance attributes of detailed properties on MJT surfaces using only color and gloss in a fixed measurement direction is challenging due to the full-color capability of this AM method. Future research needs to focus on detailed BRDF and BTDF analysis using gonio-spectrophotometers to reproduce accurate appearances.

## Declaration of Competing Interest

The authors declare the following financial interests/personal relationships which may be considered as potential competing interests:

Ali Payami Golhin reports financial support, and article publishing charges were provided by Horizon 2020 (EU) ApPEARS-ITN project [grant No. 814158].

## CRediT authorship contribution statement

**Ali Payami Golhin:** Conceptualization, Methodology, Investigation, Data curation, Formal analysis, Visualization, Writing – original draft, Writing – review & editing. **Are Strandlie:** Writing – review & editing, Supervision, Project administration, Funding acquisition.

## Data availability

The main part of the raw/processed data required to reproduce these findings is available at https://doi.org/10.5281/zenodo.7580082.

## Acknowledgments

This work was supported by the European Union's H2020 research and innovation program under the Marie Skłodowska-Curie grant agreement No. 814158 "ApPEARS - Appearance Printing - European Advanced Research School". The authors would like to thank Dr. Aditya Suneel Sole (NTNU, Norway) for his support. The authors appreciate the support provided by Dr. Andreas Kraushaar (Fogra, Germany) and Donatela Saric (NTNU & Fogra) for the gloss measurement.

## Supplementary materials

Supplementary material associated with this article can be found, in the online version, at doi:10.1016/j.optlaseng.2023.107632.

## References

[1] Msallem B, Sharma N, Cao S, et al. Evaluation of the dimensional accuracy of 3D-printed anatomical mandibular models using FFF, SLA, SLS, MJ, and BJ printing technology. 2020;9:https://doi.org/10.3390/jcm9030817
[2] Baharnezhad S, Golhin A. In-situ measurement and finite element simulation of thermo-mechanical properties of AA 6063 aluminum alloy for MIG weldment. 2017;32:https://doi.org/10.18720/MPM.3222017_15
[3] Ai Y, Liu X, Huang Y, et al. Numerical analysis of the influence of molten pool instability on the weld formation during the high speed fiber laser welding. 2020;160:120103. https://doi.org/10.1016/j.ijheatmasstransfer.2020.120103
[4] Ai Y, Yu L, Huang Y, et al. The investigation of molten pool dynamic behaviors during the "∞" shaped oscillating laser welding of aluminum alloy. 2022;173:107350. https://doi.org/10.1016/j.ijthermalsci.2021.107350
[5] Dorweiler B, Baqué PE, Chaban R, et al. Quality control in 3D printing: accuracy analysis of 3D-printed models of patient-specific anatomy. 2021;14:1-13. https://doi.org/10.3390/ma14041021
[6] Di Nicolantonio M, Rossi E, Stella P. Generative design for printable mass customization jewelry products, E. Rossi, T. Alexander, and M. Di Nicolantonio, Editors., Springer Verlag 2020; p. 143-152. https://doi.org/10.1007/978-3-030-20216-3_14
[7] Ulu FI, Mohan RV. Voxel and stereolithographic digital design framework in additive manufacturing: effects in a PolyJet printing process and relevant digital solutions. Prog. Addit. Manuf. 2021;6:653–62. doi:10.1007/s40964-021-00186-2.
[8] Golhin AP, Sole AS, Strandlie A. Color appearance in rotational material jetting. Int. J. Adv. Manuf. Technol. 2023;124:1183–98. doi:10.1007/s00170-022-10536-1.
[9] Payami Golhin A, Strandlie A, John Green P. The influence of wedge angle, feedstock color, and infill density on the color difference of FDM objects. J. Imag. Sci. Technol. 2021;65:1–15. doi:10.2352/J.ImagingSci.Technol.2021.65.5.050408.
[10] Zheng Y, Zhang X, Wang SD, et al. Similarity evaluation of topography measurement results by different optical metrology technologies for additive manufactured parts. Opt. Lasers Eng. 2020;126:7. doi:10.1016/j.optlaseng.2019.105920.
[11] Choudhury AKR. Principles of colour and appearance measurement: Object appearance, colour perception and instrumental measurement. Elsevier; 2014.
[12] Pointer MR. Measuring visual appearance-a framework of the future. Project 2.3 measurement of appearance. 2003;
[13] Hunt RWG, Pointer MR. Measuring colour. John Wiley & Sons; 2011.
[14] Payami Golhin A. Generation of micro-and nano-textured surfaces. Eur. Commission: Brussels 2021:1–6. doi:10.5281/zenodo.7293168.
[15] Yuan J, Chen G, Li H, et al. Accurate and computational: a review of color reproduction in full-color 3D printing. Mater. Des. 2021;209:1–17. doi:10.1016/j.matdes.2021.109943.
[16] Wei X, Bhardwaj A, Zeng L, et al. Prediction and compensation of color deviation by response surface methodology for polyjet 3d printing. J. Manuf. Mater. Process. 2021;5. doi:10.3390/jmmp5040131.
[17] Zeng J, Deng H, Zhu Y, et al. Lenticular objects: 3D printed objects with lenticular lens surfaces that can change their appearance depending on the viewpoint. In: UIST 2021 - Proceedings of the 34th Annual ACM Symposium on User Interface Software and Technology; 2021.
[18] Sohaib A, Amano K, Xiao KD, et al. Colour quality of facial prostheses in additive manufacturing. Int. J. Adv. Manuf. Technol. 2018;96:881–94. doi:10.1007/s00170-017-1480-x.
[19] Urban P. Graphical 3D printing: challenges, solutions and applications. London Imaging Meeting. Society for Imaging Science and Technology, 1; 2020. doi:102352/issn2694-118X2020LIM-35.
[20] Elkhuizen W, Essers T, Song Y, et al. Gloss, color, and topography scanning for reproducing a Painting's appearance using 3D printing. 2019;12:https://doi.org/10.1145/3317949
[21] Zheng L, Li C, Yang S. Analysis of color gamut in color 3D printing. 2020;600:148-155. https://doi.org/10.1007/978-981-15-1864-5_21
[22] Cheng YL, Huang KC. Preparation and characterization of color photocurable resins for full-color material jetting additive manufacturing. Polymers (Basel) 2020;12:650. doi:10.3390/polym12030650.
[23] Wei X, Zeng L, Pei Z. Experimental investigation of polyjet 3D printing process: effects of finish type and material color on color appearance. In: ASME International Mechanical Engineering Congress and Exposition, Proceedings (IMECE); 2019.
[24] Acosta-Vélez GF, Zhu TZ, Linsley CS, et al. Photocurable poly(ethylene glycol) as a bioink for the inkjet 3D pharming of hydrophobic drugs. Int. J. Pharm. 2018;546:145–53. doi:10.1016/j.ijpharm.2018.04.056.
[25] Payami Golhin A, Srivastava C, Tingstad JF, et al. Additive manufacturing of multilayered polymer composites: durability assessment. In: Proceedings of the 20th European Conference on Composite Materials-Composites Meet Sustainability, 1-6. EPFL Lausanne, Composite Construction Laboratory Switzerland; 2022.
[26] Payami Golhin A, Srivastava C, Strandlie A, et al. Effects of accelerated aging on the appearance and mechanical performance of materials jetting products. Materials & Design 2023;228:111863. doi:10.1016/j.matdes.2023.111863.
[27] Hong W, Yuan Z, Chen X. Structural color materials for optical anticounterfeiting. 2020;16:https://doi.org/10.1002/smll.201907626
[28] Nam SH, Park J, Jeon S. Rapid and large-scale fabrication of full color woodpile photonic crystals via interference from a conformal multilevel phase mask. Adv. Funct. Mater. 2019;29:10. doi:10.1002/adfm.201904971.

[29] Hsu WC, Peng TY, Kang CM, et al. Evaluating the effect of different polymer and composite abutments on the color accuracy of multilayer Pre-colored Zirconia Polycrystal dental prosthesis. 2022;14:doi:10.3390/polym14122325.
[30] Egorov V, Gulzar U, Zhang Y, et al. Evolution of 3D printing methods and materials for electrochemical energy storage. 2020;32:doi:10.1002/adma.202000556.
[31] Tee YL, Peng C, Pille P, et al. PolyJet 3D printing of composite materials: experimental and modelling approach. JOM 2020;72:1105–17. doi:10.1007/s11837-020-04014-w.
[32] Stratasys. Vero: realistic, multi-color prototypes in less time, in Stratasys Datasheet. 2022; p. 1-4.
[33] Westland S, Ripamonti C, Cheung V. Computational colour science using MATLAB. John Wiley & Sons; 2012.
[34] Astm. Standard terminology of appearance, A. E284-17, Editor., ASTM International West Conshohocken, PA 2017; p. 1-25. doi:10.1520/E0284-17.
[35] Bell EE. Optical Constants and their Measurement. In: Genzel L, editor. Light and Matter Ia /Licht und Materie Ia. Berlin, Heidelberg: Springer Berlin Heidelberg; 1967. p. 1–58. Editor.
[36] Frisvad JR, Jensen SA, Madsen JS, et al. Survey of models for acquiring the optical properties of translucent materials. Computer graphics forum, 2. Wiley Online Library; 2020. doi:10.1111/cgf.14023.

**Ali Payami Golhin** is a Ph.D. candidate at NTNU - Norwegian University of Science and Technology. He has research experience in the optical properties of structured surfaces as an APPEARS fellow, which is funded by the Marie Sklodowska-Curie Actions under the Horizon Europe program. He has research experience in additive manufacturing, optical measurement, tribology, and surface science.

**Are Strandlie** is a Professor of Physics at NTNU - Norwegian University of Science and Technology. His main research interests are data analysis methods for high-energy physics experiments and numerical methods for material physics. Recently, an increasing interest has emerged within cross-disciplinary topics, such as the link between appearance and material properties.

## Paper VI:

A. P. Golhin, A. Strandlie, Optical properties of tilted surfaces in material jetting, Optics and Laser Technology, (2023), Submitted

# Optical properties of tilted surfaces in material jetting

Ali Payami Golhin [a,*], Are Strandlie [a]

[a] Department of Manufacturing and Civil Engineering, NTNU - Norwegian University of Science and Technology, Gjøvik, 2815, Norway

[*] Corresponding author – payami.ag@gmail.com; ali.p.golhin@ntnu.no

**Abstract:**

Material jetting (MJT) is one of the promising additive manufacturing (AM) techniques that offers high-quality appearance reproduction. Due to the limited selection of aesthetic materials available for use with MJT technology, a thorough optical analysis is required to determine their optimal application. This study focuses on the prominent appearance attributes in MJT and the role of texture variation due to different build orientations (BOs). For this purpose, tilted surfaces were manufactured in a direction ranging from 0° to 90° degrees at 15° intervals. The spectral reflectance, absorbance, transmittance, color difference, gloss, haze, scattering, and texture of MJT objects with varying BOs were investigated. To illustrate the variation in visual appearance and texture of the studied surfaces, the optical properties were rendered to three-dimensional (3D) spherical models. Further, the interaction of the appearance of 3D printing interacts with the quality improvement of AM surfaces is discussed. The results indicated that BO significantly affected the surface texture and layers orientation, leading to variation in surface quality by impacting all studied appearance attributes. Furthermore, tilted MJT surfaces exhibited more variation in reflectance than transmittance. As a result of the Kendall rank correlation coefficient and principal component analysis (PCA), light transmittance through parts manufactured at BO 75° showed the largest variation compared to 0°. Regarding light reflectance, 60° showed more variation among studied angles. The results of gloss, haze, and scattering studies revealed the significance of the measurement direction due to the role of microsurface normals in the surface texture.

**Keywords:** Material jetting, Digital materials, Spectral analysis, Appearance measurement, Principal component analysis

## 1. Introduction

Rapid prototyping converts digital models to physical inventory. Prototyping allows for identifying new opportunities for continued exploration of an unexplored space of designs [1]. High-detail prototyping has been the primary goal of AM technologies for many years, and it still drives the sales of most 3D printers [2]. Prototyping efficiency can be enhanced by improving the surface quality of as-printed objects, both for short-term [3] and long-term [4] applications. As a result of full-color 3D printing (3DP) equipment, including material jetting (MJT) systems, the expectation for photorealistic and complex prototypes is increasing [5].

MJT, as reported in the ISO/ASTM 52900:2021, is an AM category for which droplets of 3DP material are selectively deposited [6]. This technology is a full-color 3DP process, which directly deposes resins in CMYK-W (cyan, magenta, yellow, black, and white) when required. Furthermore, MJT technology reproduces color gradients and variations unavailable with other 3DP technologies. Therefore, MJT plays a vital role in full-appearance reproduction.

Both conventional and advanced manufacturing technologies recognize the importance of surface quality in final products, mainly for critical and small products. Thus, it is essential to assess the surface finish of as-printed polymers and provide guidance on AM process windows and limitations to increase their applicability. To enhance the appearance of materials, 3DP systems must capture the optical properties of materials, communicate the attributes related to appearance, scan, model, and control 3D printing systems. Surface issues hinder the development of the workflows for the full appearance of materials during the design and manufacturing phases [7].

Appearance assessment is qualitative, subjective, and controversial [8]. An instrumental appearance measurement is an indirect technique for evaluating the quality and processing performance of a manufactured product based on its surface. Quality control has evolved into an industry concept through controlling color, gloss, haze, scattering, transparency, and texture, describing the “total appearance” [8]. Among these appearance attributes, the level of transparency, i.e., translucency, plays a defining role in the optical properties of MJT parts, affecting other characteristics as it describes how light travels through a medium.

Even though the surface finish of MJT parts was assumed to be consistent and detailed with minimal layering [9], the conditions of drop-on-demand high-speed manufacturing of translucent materials significantly affect their appearance. In the rotary-based MJT technique using PolyJet® machines, the objects are created by jetting materials onto a rotary tray as the build plate. Since each droplet of material contains its own mini pool of ink, the shape of the voxels and layers can be affected by printing parameters [10]. Therefore, MJT products can be designed in various approaches, bringing flexibility and manufacturing challenges. In aesthetic applications, such as jewelry [11] and medical models [12], the shape and combination of voxels are essential factors. Consequently, the dimensional accuracy and appearance of a 3D object must be accurately reproduced using multiple printer parameters to achieve high-fidelity reproductions [5].

Limited research [13, 14] has been conducted on the influence of build orientation (BO), also known as wedge/slope angle, on the surface quality of additively manufactured parts. In MJT, BO can affect the mechanical performance of manufactured parts. [15] showed prints along the Z-direction had the greatest influence of orientation on loading response, especially at larger strains and slower strain rates. Khoshkhoo et al. [16] studied the influence of BO on dimensional accuracy in MJT.

The bi-directional reflectance distribution function (BRDF) was originally introduced as a fundamental radiometric concept. BRDF captures all the details of how light interacts with surfaces [17, 18]. The alteration of the appearance of MJT parts due to printing parameters has been studied in limited research [5, 19, 20]. However, it is yet to be shown whether these various attributes can be studied simultaneously in rotational MJT. Besides, no studies have addressed the significance of BO for 3DP tilted surfaces on a rotary disc. Accordingly, this study examines the influence of BO on various appearance attributes of MJT surfaces. For this purpose, the color, gloss, haze, scattering, transparency, and texture of the PolyJet parts were characterized as part of the quality improvement approach of AM surfaces. Based on the Kendall rank correlation coefficient and principal component analysis (PCA), the results were ranked, and possible correlations were discussed.

## 2. Materials and methods

### 2.1. Manufacturing process

The polymeric tilted surfaces were manufactured using a Stratasys J55 PolyJet 3D printer. 3D models were imported into the GrabCAD Print software and 3D printed using the standard tray material. Photo-resins VeroCyan, VeroBlackPlus, VeroYellow, VeroMagenta, and VeroPureWhite were used as feedstocks, hereafter referred to as their corresponding colors of "cyan", "magenta", "yellow", and "black". In the Vero family of materials, acrylic oligomers are mixed with proprietary components to provide low-viscosity materials. Photo-resins from Vero share similar mechanical, thermal, and electrical properties [21]. According to the best practices of Stratasys for PolyJet and Pantone's guidelines for color matching [22], bilayer structures were constructed using 1 mm thick plates of each CMYK color on a 1 mm thick white background to achieve optimal color reproduction. Each CMYK photo resin (digital material) specimen was printed with seven different build orientations ranging from 0° (reference) to 90° at intervals of 15°. Each sample was 35.50 ± 0.50 mm wide, 40.00 ± 0.50 mm long, and fabricated on the middle swath of a rotary disc as the build platform with a glossy-on-glossy finish (Fig. 1). A waterjet system was then used to remove the support waxes. The appearance of each specimen was measured five times using two sets of models for reproducibility purposes.

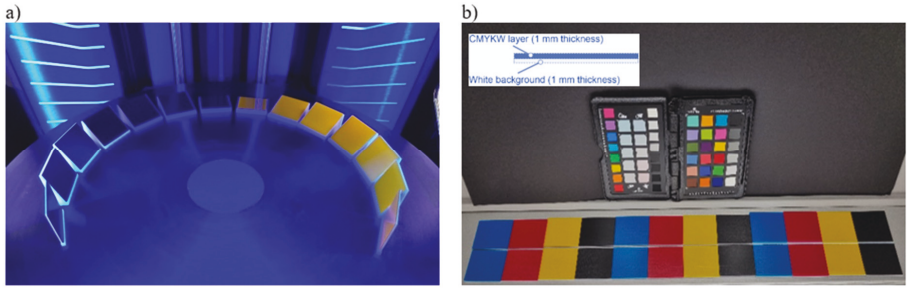


**Fig. 1.** a) As-printed YK specimens manufactured on white background as seen on the build platform - BO ([0°-90°], 15° step), and b) CMYK specimens observed under D50 daylight standard illumination.

### 2.2. Appearance measurement

A Keyence VH-ZST microscope was used for optical microscopy (20X to 2000X). The RA-532H surface reflectance analyzer was used to analyze gloss according to ASTM D523, haze, and scattering. The scattering results were discussed in terms of the C20 and C60 Canon scattering indices for illumination angles of 20° according to ASTM D5767 and 60° as per JIS K7374, respectively. In computer graphics, the C20 index measures the distinctness of the image (DOI), while the C60 index measures the clarity of the image (IC).

The spectroscopy was conducted using a spectrometer (PerkinElmer Lambda 1050+) equipped with the 3-detector module in an integrating sphere configuration (150 mm). Spectra of reflectance, transmission, and absorbance were measured from photopolymer plates aligned in the detector window. The wavelength length was limited to 380 to 780 nm, and sampling intervals of 5 nm. The largest area possible in the middle of the specimens was exposed to a light beam to minimize the effects of layer-by-layer inhomogeneity and edge effects caused by light scattering. The measurement area was therefore limited to the size of the reflectance (24 mm in diameter) and the transmittance (25 mm × 16 mm) ports (Fig. 2). Transmittance data were recorded from the front (F) and back (B) of the specimens. The measurement error was reduced by avoiding sites with support materials, unusual colors, stains, and external particles.

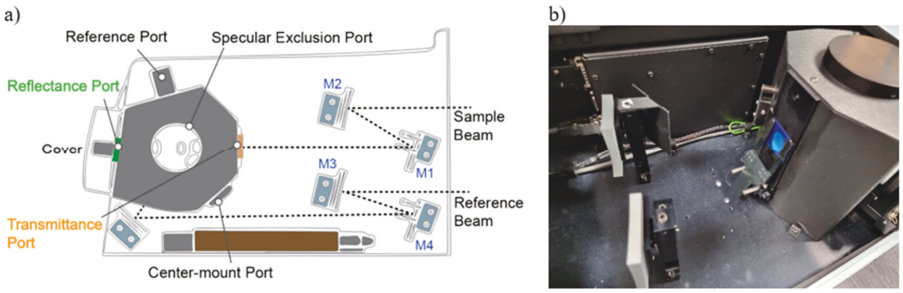


**Fig. 2.** a) Schematic of the UV/VIS/NIR spectrometer in top view, and b) the measurement geometry of the sample (cyan color) located on the transmittance port.

To calculate tristimulus values, CIEXYZ, a color-matching function derived from ASTM E308-01 [23], was applied using CIE 2° and the D50 standard daylight illuminant. CIEL$^*$a$^*$b$^*$ coordinates were further determined using CIE1976. The CIEDE2000 color differences for each BO compared to the 0° orientation were calculated using the computational color science toolbox in MATLAB R2022a [24] as follows

$$CIEDE2000 = \sqrt{(\frac{\Delta L^*}{k_L S_L})^2 + (\frac{\Delta C^*}{k_c S_C})^2 + (\frac{\Delta h^*}{k_h S_h})^2 + R_T f(\Delta C^* \Delta h^*)} \quad (1)$$

where color attributes variation due to the color change expressed by $\Delta L^*$ (lightness), $\Delta C^*$ (chroma) and $\Delta h^*$(hue), $R_T$ corresponds to the hue rotation, $S_L$, $S_C$, and $S_h$ communicate CIEL*C*h* lightness compensation, and constants of $k_L$, $k_C$, and $k_h$ were defined as unity.

A Vizoo xTex scanner was used to collect texture data, including displacement, material, alpha, base, surface roughness, and surface normals. With the Blender 2.79 render engine, the 2D surface texture maps were further applied onto 3D spherical models.

### 2.3. Statistical analysis

The mean color difference from the mean (MCDM) and the corresponding root-mean-square error (RMSE) variables were used to discuss the color difference according to CIEDE2000 using the following equations

$$MCDM = \frac{1}{N}\sum_{i=1}^{N} \Delta E(C_i, C_m) \quad (2)$$

$$RMSE = \sqrt{\frac{1}{N}\sum_{i=1}^{N}(\mathrm{r}_{r,i} - \mathrm{r}_{t,i})^2} \quad (3)$$

where $r_t$ and $r_r$ are the tests and references spectral results for $N$ samples. $C_i$ and $C_m$ indicate the color coordinate of the i$^{th}$ measurements and the reflectance average, respectively.

To assess spectral deviations among transmittance and reflectance results in different BOs compared to horizontal samples (0°), Kendall's tau (τ) rank correlation coefficients were employed. Statistical significance is well-defined when the p-value is less than 0.05 [25]. It is an appropriate measure of the strength of association between continuous-ordinal variables or two ordinal variables. Kendall's τ helps identify monotonic relationships due to its resistance to outlier effects [26].

Principal component analysis (PCA) was applied to examine the spectral data and response variables. For matrices that contain dependent and independent variables, PCA extends linear regression to a multivariate setting [25]. Considering the first batch (build orientation) as an independent variable, and the second batch (spectral data) as a dependent variable, it is possible to view the two sets of variables as asymmetrical. This study used two types of PCA to evaluate the data: ordinary PCA to assess the BO effect and spectroscopy PCA to consider the material impact on the spectral variables. The raw sensor data was converted using linear transformation into principal components (PCs) space. R statistical software 4.2.1 and Origin 2022 (OriginLab) were used to analyze the data.

## 3. Results and discussions

### 3.1. Optical microscopy

In Fig. 3, a micro digital camera was used to illustrate the variation in the surface texture of MJT objects manufactured at various BO ([0°-90°], 15° step) as seen in the manufacturing workspace. The direction in which the printing was carried out significantly impacted the surface texture, resulting in a variation in the distribution of high-exposure light reflections on the surface. In particular, a difference can be seen for 0° compared to 45° to 90°, which is discussed in further detail for gloss results.

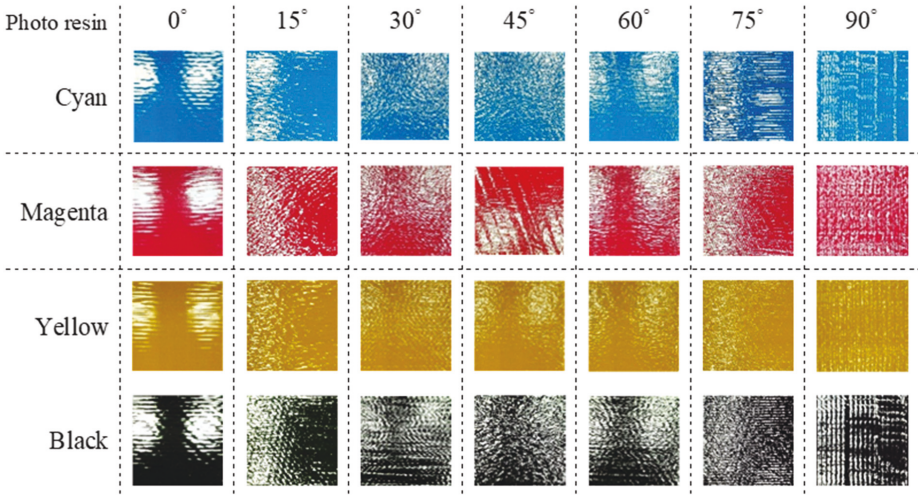


**Fig. 3.** Variation in the surface texture of material jetting products with the build orientation.

Fig. 4 provides a closer look at the full focal images of MJT surfaces without being affected by specular reflections. The surface printed at the horizontal reference orientation (0°) can be described by parallel microscopic layers with porous surfaces due to incubated gas release on the surface (Fig. 4a). Furthermore, focal images revealed subsurface turbulence in layers in the 1 mm thick translucent-colored layer (Fig. 4b). Light transmission affected by microscopic inhomogeneities within the subsurface layers was discussed within the transmittance results. Fig. 4c illustrates how tilting the surface at 15° significantly altered the order of microscopic layers due to the separation of microscopic droplets. Several factors can explain the reason behind the appearance of these droplets at BO 15°. It includes centrifugal force and gravity, which were connected to the rotation of the disc-shape build platform, the viscosity of the resin, and the UV curing process affected by manufacturing speed.

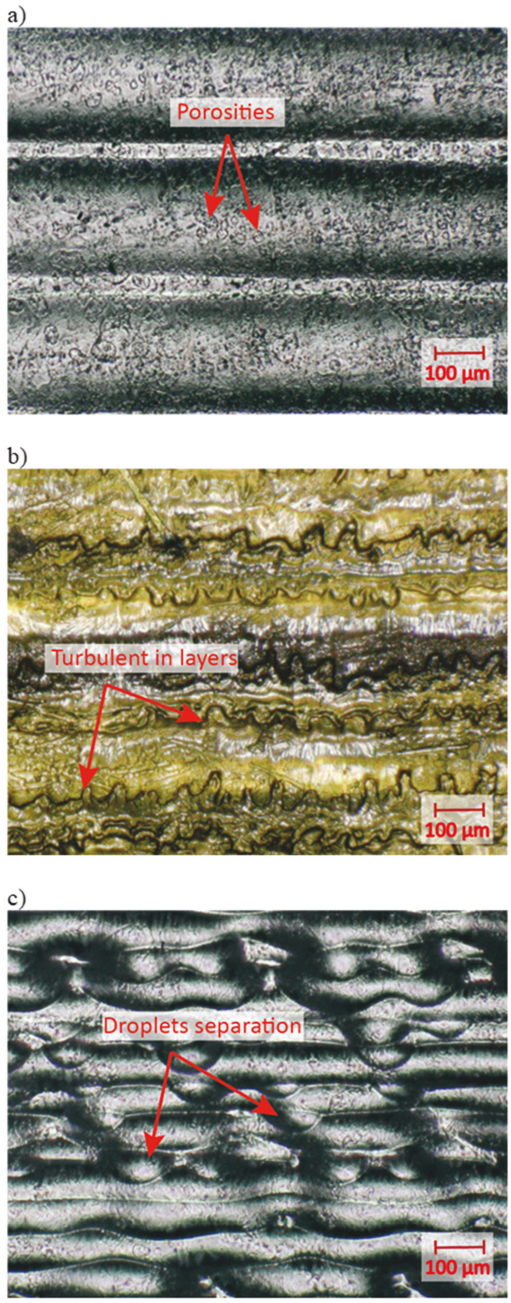


**Fig. 4.** Focal microscopic images of a) bilayer - BO 0°, b) monolayer of the colored plate - BO 0°, and c) bilayer - BO 15°.

### 3.2. Spectral analysis

Fig. 5 illustrates spectral data, including reflectance, absorbance, and transmittance. According to the spectrophotometry results, there was a spectral shift for different BOs in CMY resins. However, the black color did not significantly change the spectral characteristics at various BOs. According to Fig. 5a, reflectance values increased with increasing BO, indicating higher lightness (albedo) at higher wedge angles. In the case of absorbance (Fig. 5b) and transmittance (Fig. 5c and d), this shifting behavior was dependent on the digital material. For cyan, higher transmittance and lower absorbance were observed, while yellow and magenta resins generally showed lower transmittance and absorbance. The transmittance spectra resulting from spectrometry in the broader wavelength range, including near-infrared (NIR), are presented in supplementary data in Appendix A.

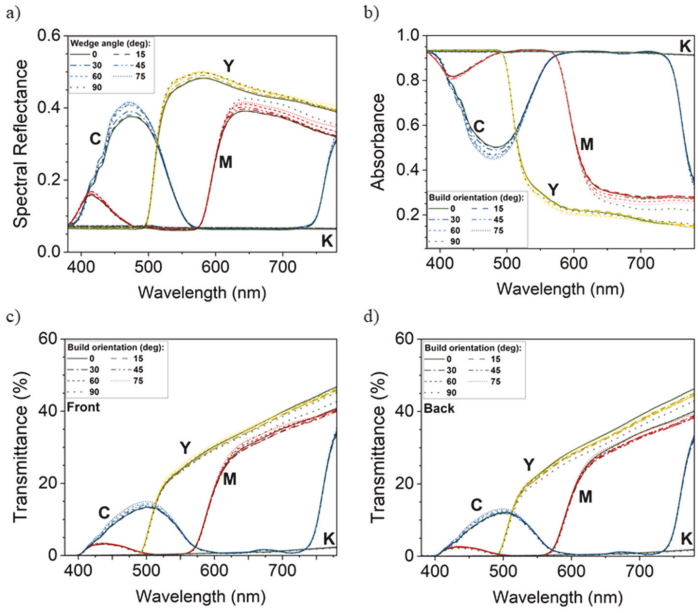


**Fig. 5.** a) Spectral reflectance, b) absorbance, and transmittance from c) front and d) back of MJT specimens with tilted surfaces.

The PCA results in Fig. 6 suggest two principal components of PC1 and PC2 with a cumulative percentage variance (CPV) of greater than 90.71% adequately explaining the observed behavior in spectral data. The CMYK materials were used as the observation group, and the spectral results addressed the studied variables. Results revealed the same pattern in the PCA results for both reflectance and transmittance. The spectral shifts in the spectrophotometry results can be explained by considering their PCA score distribution. According to the results, PC1 affected magenta and yellow positively while negatively

impacting black and cyan. By contrast, PC2 had a negative impact on cyan and yellow, and it had a positive influence on magenta and black.

Furthermore, the score distribution, i.e., the 95% confidence ellipses for the studied BO angles, indicated a higher impact on yellow from both PC1 and PC2 than particularly on black. Furthermore, magenta scores were affected more by PC1, while cyan scores were altered more according to the PC2 axis, indicating opposite responses due to manufacturing different wedge angles. The similar behavior of front and back transmittance measurements showed that reflectance and absorbance had a negligible effect on light transmission through CMYK layers combined with a white background.

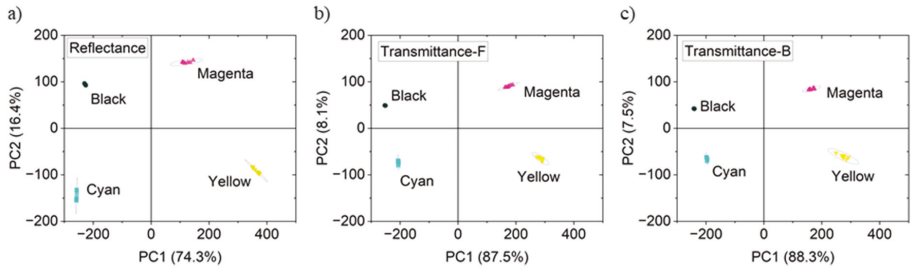


**Fig. 6.** PCA results for a) spectral reflectance (CPV: 90.71%), and transmittance from b) front (CPV: 95.59%) and c) back (CPV: 95.78%) of MJT specimens. The ellipses represent 95% confidence of PCA score data (BOs).

Fig. 7 demonstrates how different BOs affect the optical properties of the manufactured surface in the spectrophotometry measurement compared to horizontal 3D-printed surfaces, regardless of the applied material. While BO 75° resulted in more deviation in transmittance measurements ($\tau_F$=0.989 and $\tau_B$=0.988), BO 60° ($\tau$=0.949) and then 90° (vertical orientation, $\tau$=0.950) led to more significant spectral shifts in reflectance measurements. Kendall's $\tau$ rank correlation results revealed a more substantial influence of variation in the texture and manufactured layers due to different BOs on the reflectance results compared to transmittance. The RMSE was also higher for the reflectance spectra, where it is maximized at a critical BO 60° (RMSE=0.028) for the reflectance spectra and 75° (RMSE=0.007) for the transmittance spectra. Strong correlations with $\tau$>0.949 and p-value<0.050 were observed for all studied materials. Appendix B provides supplementary data on statistical analysis for PCA and $\tau$ rank correlation results for each pair of build orientation.

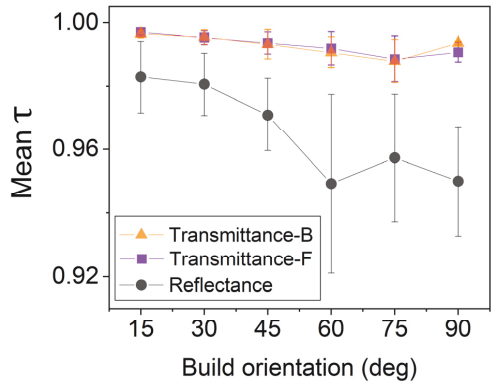


**Fig. 7.** Kendall's τ rank correlation coefficient in the spectrophotometry measurements of tilted surfaces according to the horizontal reference surface (Error bars: RMSE).

The color measurement results are displayed in Fig. 8 to evaluate the effects of spectral reflectance on the visual appearance. As shown in Fig. 8a, MCDM generally increased and peaked at a BO angle of 75° before decreasing for cyan, yellow, and black materials. For magenta resins, however, the increase in color difference due to a rise in BO angle was constant and even sharper for 90°. As shown in Fig. 8b and c, a weak alteration in color has been observed due to BO, which was more pronounced for cyan, magenta, and then yellow when compared to black resins. For all studied materials, the MCDCM was less than 2, and the RMSE was negligible, indicating high color fidelity and barely noticeable color differences due to tilting the surface.

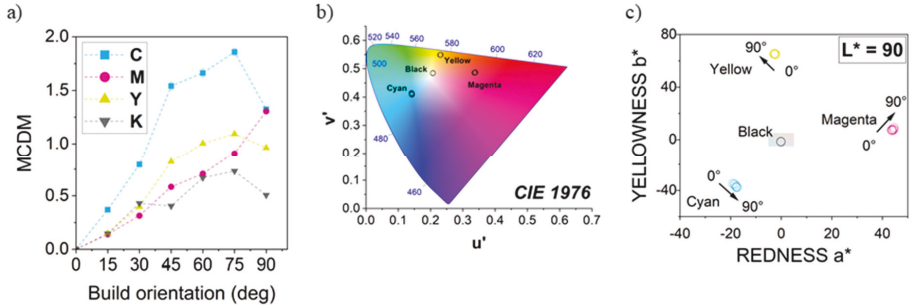


**Fig. 8.** a) MCDM of color difference, b) the mean hue u', v' stimuli according to CIE1976 chromaticity diagram, and c) color change in CIEL*a*b* color space. Vectors represent color change as a result of using different BO.

Fig. 9 shows that all color attributes (LCh) varied to negative values, where similar trends were observed for all materials based on their MCDM. Magenta showed high dL at 90°, whereas cyan, yellow, and black had a robust negative shift in lightness at 75°. Hue and chroma also demonstrated the same trend. The variations in lightness were, however,

generally more substantial than hue and chroma. This indicates lightness change has a significant role in reflectance due to the alteration in surface texture caused by build orientation.

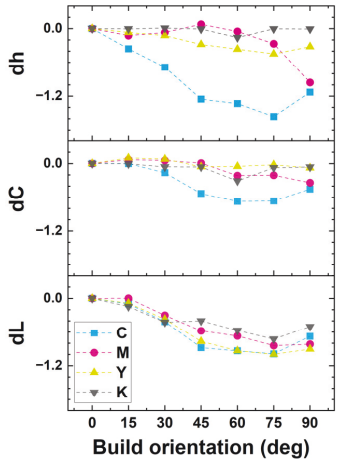


**Fig. 9.** Variations in color attributes due to changing the build orientation.

### 3.3. Gloss measurement

Fig. 10 compares several aspects of gloss appearance, including specular gloss, haze, and scattering indices of C20 and C60 derived from BRDF. As can be seen from the fitting lines in the vertical (V) and horizontal (H) directions according to layer-by-layer structures, the measurement direction affected the gloss measurements. The specular gloss and haze decreased more linearly with increasing BO angles in the V direction. Conversely, the H direction resulted in nonlinear behavior, with gloss and haze maximized at 45° to 60° degrees of BO. The BO 90° displayed a distinct low-gloss and low-haze characteristic, as well as high scattering, in both measurement directions. Nevertheless, results indicated that an increase in BO led to an increase in the C20 and C60 indices representing scattering. High $R^2$ suggested a stronger correlation between BO and haze and specular gloss as opposed to sublayer scattering, which was in agreement with the spectral results observed for reflectance compared to transmittance.

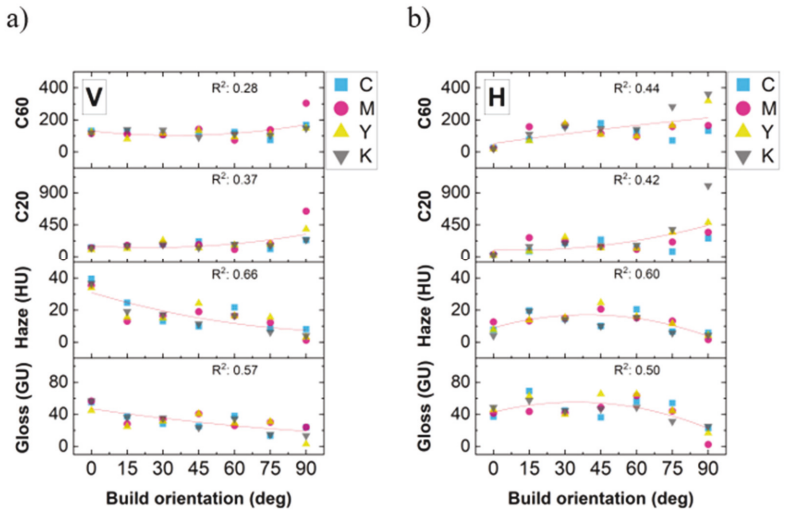


**Fig. 10.** Fitting results of the mean for gloss nuances in a) vertical and b) horizontal measurement directions according to the directions of the layers.

According to the V measurement direction (Fig. 10a), gloss and its surrounding haze display higher specular reflections for lower BO angles. Reflected haze is characterized by a milky or cloudy appearance due to light scattering [27]. Haze is generally considered an appearance attribute that refers to lower surface quality due to defects, including surface texture or porous surface (see Fig.4), as part of the assessment of surface quality.

Fig. 11 illustrates the importance of the direction and size of microsurfaces in textured surfaces influenced by building orientation. Bidirectional reflectance distribution function (BRDF) graphs decreased in size at higher BO, indicating a decline in reflectance, resulting in lower gloss and haze. The supplementary data in Appendix C contains more BRDF graphs for gloss measurements.

Higher gloss and haze for lower BOs can be attributed to larger microsurfaces and lower $\theta_m$. This resulted in stronger microsurface normals that were closer to the surface normals determined by $\cos\theta_m$. As a result, gloss and haze are significantly higher at BO 0° where microfacet's normal ($\vec{m}$) is acting similarly to the surface normal ($\vec{n}$), which was normal to the surface reflectance analyzer. However, in the horizontal direction, a slight curvature in the layers, as seen in our previous study [5], and subsurface turbulence in layers played a more important role compared to microsurface variations due to BO. It resulted in a more nonlinear behavior in gloss nuances for horizontal glass measurement (Fig. 10b).

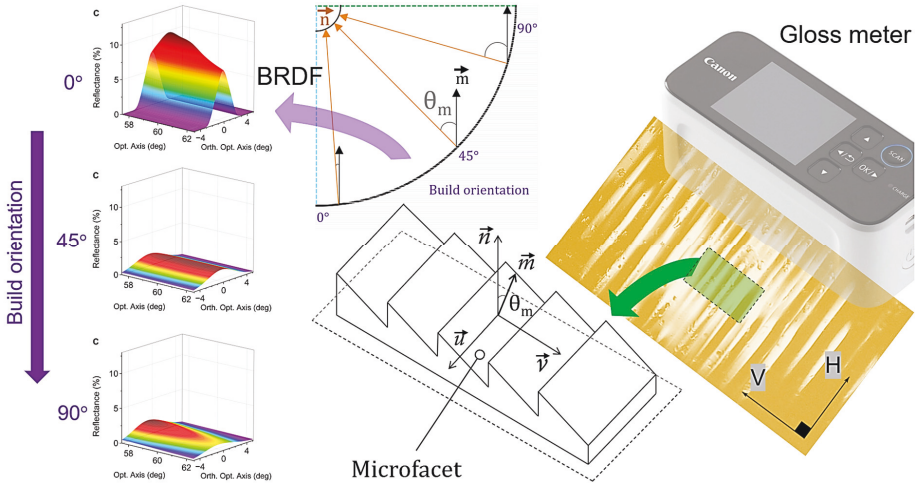


**Fig. 11.** Gloss measurement of textured AM surfaces. BRDF graphs represent light distribution around vertical measurements around the angle of 60° for BO 0°, 45° and 90° for the cyan specimen.

Microfacets' role in translucent textured surfaces can be explained by Fresnel's equation [28], using bidirectional scattering distribution functions (BSDF):

$$f_{r,m}(x_m, \vec{\omega}_i, \vec{\omega}_o) = F\left(\vec{m}, \vec{\omega}_i, \frac{n_t}{n_i}\right)\frac{\delta(\vec{\omega}_o - \vec{\omega}_s)}{\cos\theta_i} \tag{4}$$

where the $f_{r,m}$ term denotes the reflectance from a smooth microsurface in a semi-transparent part for a specific surface point ($x_m$), considering the unit light vectors for illumination ($\vec{\omega}_i$), scattering ($\vec{\omega}_s$), and observation ($\vec{\omega}_o$). The expansion of Maxwell's equations using the Fourier transform is referred to as F for the unit of the surface, where $n_t$ and $n_i$ represent the transmission and illumination normals. The Dirac δ function is applied to observation and scattering unit vectors of lights. The illumination angle relative to the surface normal ($\vec{n}$) is shown by $\theta_i$.

BSDF comprises both reflectance and transmittance terms for the same macroscopic surface point from which light is incident and emerges [29]. It can be regarded as the sum of BRDF and BTDF (bidirectional transmittance distribution function), shown in Fig. 12.

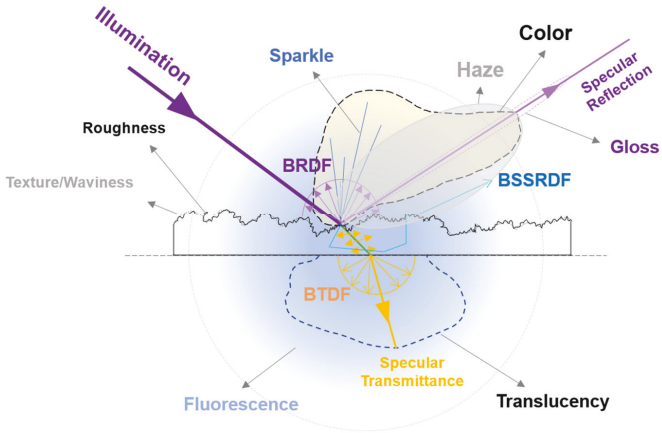


**Fig. 12.** Light-matter interactions and optical properties of textured surfaces. BSSRDF: Bidirectional scattering-surface reflectance distribution function.

### 3.4. Surface texture mapping

Fig. 13 illustrates the use of optical surface maps to create textured spheres. In contrast to the black and yellow resins, cyan and magenta clearly displayed layers orientation fabricated in the manufacturing process. The parallel layers were particularly evident in BO 0°, 45°, and 90°. The low absorption of yellow materials made optical texture mapping more challenging to render than other digital materials.

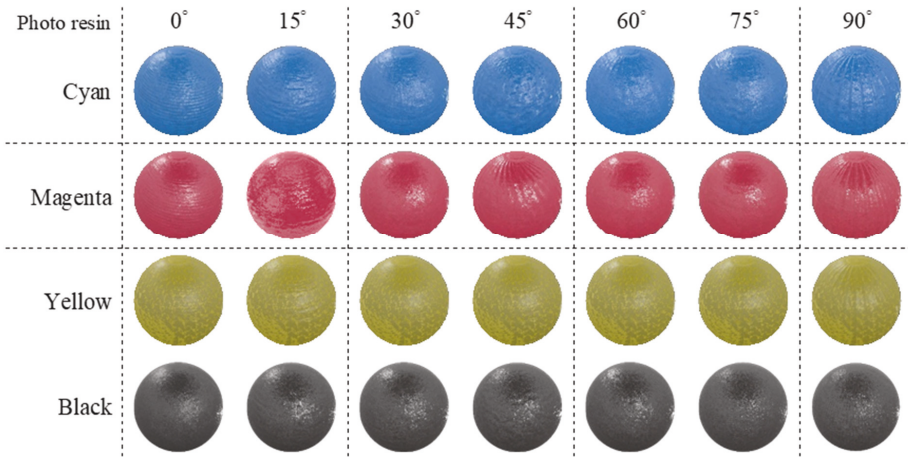


**Fig. 13.** 3D-rendered sphere models from optical texture mapping of 3D-printed CMYK digital materials with different build orientations.

## 4. Conclusions

This study discussed how build orientation affects the optical properties of 3D-printed objects in material jetting, which is a necessary step toward reproducing full-color appearances. CMYK colors were applied using the primary digital materials in PolyJet 3D printers. As part of the appearance reproduction approach in MJT, the color, gloss, haze, scattering, and transparency of the objects were characterized.

A microscopical examination revealed that MJT objects produced at various BOs displayed different textures and surface characteristics, including layer configurations, gas porosities, droplet separation, and subsurface turbulence in layers. Tilting the manufactured surface resulted in microscopic inhomogeneities that affected the optical properties of translucent MJT materials. Accordingly, the effect of applied forces during processing, such as gravity and centrifugal force, on texture variation was discussed.

As shown by spectrophotometric analysis, BO influenced the reflectance, transmittance, and absorbance of CMY colors more than black photo resin. The spectral shifts in spectrophotometry were explained by PCA score distribution. Although each photo resin responded differently to the principal components, the same pattern of variation for the materials studied was observed for both reflectance and transmittance. The Kendall rank correlation coefficient for transmittance measurements indicated that BO 75° resulted in a more significant deviation. In terms of reflectance, BOs 60° and then 90° resulted in the largest spectral shifts. Kendall's $\tau$ also showed that texture and manufactured layer variation caused by various BOs impacted the reflectance more than the transmittance results.

There was a substantial effect of measurement direction on gloss, haze, and scattering results, indicating the importance of microsurface normal direction on the gloss measurements. A slight increase in color difference by less than 2 according to CIEDE2000 was recorded. Gloss and haze in vertical measurement directions decreased significantly when the surfaces were tilted from 0° to 90°. The subsurface scattering results, however, increased with the increase in BO, regardless of the direction of measurement.

Overall, the results indicated that BO significantly affected the surface texture and layer orientation, leading to a variation in surface quality due to its impact on all studied attributes. Results also suggest that the measurement direction of the gloss meter can significantly affect the gloss measurements in additive manufacturing. The findings of this study indicated that gloss and scattering were more critical than color appearance in the optical assessment of MJT products in response to different BO.

For future studies, it is expected that full-color 3D printing, particularly MJT technology, gain significant attention. Computational fluid dynamics and numerical techniques for the simulation of manufacturing processes can enhance knowledge of induced anisotropic arrangements and their impact on manufacturing and product properties. Furthermore, it is necessary to conduct further research on the materials application procedure and the actual stress, heat, and aging that will affect the texture and appearance of objects in material jetting.

Data availability

The main part of the raw/processed data required to reproduce these findings is available at https://doi.org/10.5281/zenodo.7579455

The rest cannot be shared at this time as the data also forms part of an ongoing study.

Acknowledgments

This work is funded by the European Union's H2020 research and innovation program under the Marie Skłodowska-Curie grant agreement No. 814158 "ApPEARS - Appearance Printing - European Advanced Research School". The authors appreciate the support provided by Dr. Andreas Kraushaar (Fogra, Germany) and Donatela Saric (NTNU & Fogra) for the gloss measurement. The authors would like to thank Dr. Aditya Suneel Sole (NTNU, Norway) for his support and contributions to this work.

## 5. Appendix A. Supplementary data for spectrometry in VIS-NIR wavelength range

Fig. A1 illustrates transmittance spectra in the visible (VIS) and near-infrared (NIR) wavelength ranges. While the transmittance was similar for both the front and back sides of CMYK specimens, the distribution was opposite in the NIR range. Furthermore, the spectral shifts were more significant in the NIR than in the VIS range. One explanation for this behavior can be the presence of impurities such as water molecules due to porous structure at the microscopic level.

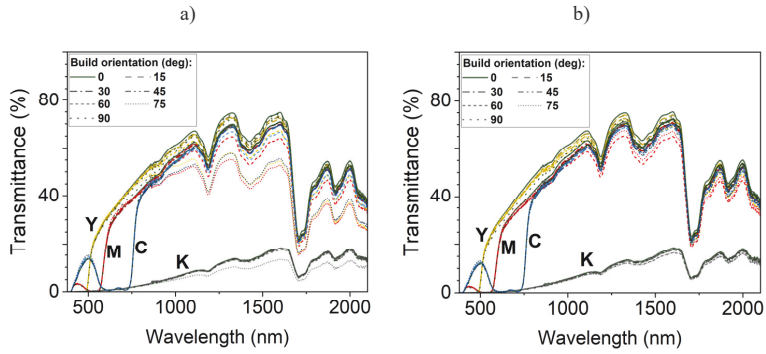


**Fig. A1.** VIS-NIR transmittance measurements at a) front and b) back of MJT parts manufactured at different build orientations.

## 6. Appendix B. Supplementary data for statistical analysis

Fig. B1 illustrates PCA results using relevant spectra as the input variable and the build orientation angles as the observation group. As can be seen, PC1 had a determining role in BO's influence on the reflectance and transmittance spectra, except for the reflectance results for black resins. Additionally, the PCA analysis showed 75°, 60°, 0°, and 90° as the indicative build orientation angles, which were explained in Kendall's rank correlation coefficient.

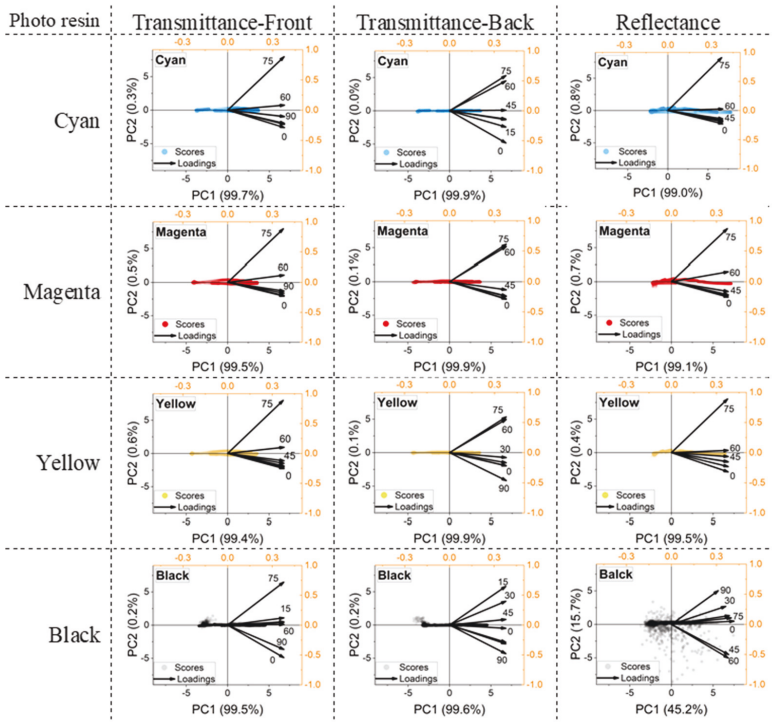


**Fig. B1.** PCA results for spectral measurements of MJT specimens. The numeric labels on the loading vectors signify the related BO angles. In addition, score dots correspond to the spectral results.

Tables B1 to B12 list Kendall correlations for pairs of build orientation angles using a 2-tailed test of significance.

**Table B1.** Kendall correlations for build orientation angles ([0°-90°], 15° step) for the reflectance of cyan.

| **BO (deg)** | | 0 | **15** | **30** | **45** | **60** | **75** | **90** |
|---|---|---|---|---|---|---|---|---|
| 0 | Kendall Corr. | 1 | 0.98081 | 0.97862 | 0.96202 | 0.95527 | 0.94647 | 0.93007 |
| | p-value | -- | 0 | 0 | 0 | 0 | 0 | 0 |
| **15** | Kendall Corr. | 0.98081 | 1 | 0.98205 | 0.97155 | 0.96539 | 0.95597 | 0.94278 |
| | p-value | 0 | -- | 0 | 0 | 0 | 0 | 0 |
| **30** | Kendall Corr. | 0.97862 | 0.98205 | 1 | 0.97464 | 0.97124 | 0.95972 | 0.94339 |
| | p-value | 0 | 0 | -- | 0 | 0 | 0 | 0 |
| **45** | Kendall Corr. | 0.96202 | 0.97155 | 0.97464 | 1 | 0.98243 | 0.97382 | 0.95387 |
| | p-value | 0 | 0 | 0 | -- | 0 | 0 | 0 |
| **60** | Kendall Corr. | 0.95527 | 0.96539 | 0.97124 | 0.98243 | 1 | 0.97601 | 0.95815 |
| | p-value | 0 | 0 | 0 | 0 | -- | 0 | 0 |
| **75** | Kendall Corr. | 0.94647 | 0.95597 | 0.95972 | 0.97382 | 0.97601 | 1 | 0.97069 |
| | p-value | 0 | 0 | 0 | 0 | 0 | -- | 0 |
| **90** | Kendall Corr. | 0.93007 | 0.94278 | 0.94339 | 0.95387 | 0.95815 | 0.97069 | 1 |
| | p-value | 0 | 0 | 0 | 0 | 0 | 0 | -- |

**Table B2.** Kendall correlations for build orientation angles ([0°-90°], 15° step) for the reflectance of magenta.

| **BO (deg)** | | 0 | **15** | **30** | **45** | **60** | **75** | **90** |
|---|---|---|---|---|---|---|---|---|
| 0 | Kendall Corr. | 1 | 0.99643 | 0.99456 | 0.98897 | 0.99095 | 0.98975 | 0.97677 |
| | p-value | -- | 0 | 0 | 0 | 0 | 0 | 0 |
| **15** | Kendall Corr. | 0.99643 | 1 | 0.99527 | 0.99061 | 0.99225 | 0.99116 | 0.97623 |
| | p-value | 0 | -- | 0 | 0 | 0 | 0 | 0 |
| **30** | Kendall Corr. | 0.99456 | 0.99527 | 1 | 0.99309 | 0.99407 | 0.99039 | 0.97461 |
| | p-value | 0 | 0 | -- | 0 | 0 | 0 | 0 |
| **45** | Kendall Corr. | 0.98897 | 0.99061 | 0.99309 | 1 | 0.99429 | 0.98816 | 0.97081 |
| | p-value | 0 | 0 | 0 | -- | 0 | 0 | 0 |
| **60** | Kendall Corr. | 0.99095 | 0.99225 | 0.99407 | 0.99429 | 1 | 0.99202 | 0.97557 |
| | p-value | 0 | 0 | 0 | 0 | -- | 0 | 0 |
| **75** | Kendall Corr. | 0.98975 | 0.99116 | 0.99039 | 0.98816 | 0.99202 | 1 | 0.98227 |
| | p-value | 0 | 0 | 0 | 0 | 0 | -- | 0 |
| **90** | Kendall Corr. | 0.97677 | 0.97623 | 0.97461 | 0.97081 | 0.97557 | 0.98227 | 1 |
| | p-value | 0 | 0 | 0 | 0 | 0 | 0 | -- |

**Table B3.** Kendall correlations for build orientation angles ([0°-90°], 15° step) for the reflectance of yellow.

| **BO (deg)** | | 0 | **15** | **30** | **45** | **60** | **75** | **90** |
|---|---|---|---|---|---|---|---|---|
| 0 | Kendall Corr. | 1 | 0.98856 | 0.9824 | 0.97307 | 0.93677 | 0.93586 | 0.9412 |
| | p-value | -- | 0 | 0 | 0 | 0 | 0 | 0 |
| **15** | Kendall Corr. | 0.98856 | 1 | 0.98986 | 0.98141 | 0.94668 | 0.94569 | 0.95088 |
| | p-value | 0 | -- | 0 | 0 | 0 | 0 | 0 |
| **30** | Kendall Corr. | 0.9824 | 0.98986 | 1 | 0.98657 | 0.9533 | 0.95132 | 0.95714 |
| | p-value | 0 | 0 | -- | 0 | 0 | 0 | 0 |
| **45** | Kendall Corr. | 0.97307 | 0.98141 | 0.98657 | 1 | 0.96358 | 0.96061 | 0.96648 |
| | p-value | 0 | 0 | 0 | -- | 0 | 0 | 0 |
| **60** | Kendall Corr. | 0.93677 | 0.94668 | 0.9533 | 0.96358 | 1 | 0.98893 | 0.98695 |
| | p-value | 0 | 0 | 0 | 0 | -- | 0 | 0 |
| **75** | Kendall Corr. | 0.93586 | 0.94569 | 0.95132 | 0.96061 | 0.98893 | 1 | 0.98516 |
| | p-value | 0 | 0 | 0 | 0 | 0 | -- | 0 |
| **90** | Kendall Corr. | 0.9412 | 0.95088 | 0.95714 | 0.96648 | 0.98695 | 0.98516 | 1 |
| | p-value | 0 | 0 | 0 | 0 | 0 | 0 | -- |

**Table B4.** Kendall correlations for build orientation angles ([0°-90°], 15° step) for the reflectance of black.

| **BO (deg)** | | 0 | **15** | **30** | **45** | **60** | **75** | **90** |
|---|---|---|---|---|---|---|---|---|
| **0** | Kendall Corr. | 1 | 0.96592 | 0.96712 | 0.96014 | 0.914 | 0.95722 | 0.95205 |
| | p-value | -- | 0 | 0 | 0 | 0 | 0 | 0 |
| **15** | Kendall Corr. | 0.96592 | 1 | 0.9655 | 0.96527 | 0.91216 | 0.96434 | 0.95416 |
| | p-value | 0 | -- | 0 | 0 | 0 | 0 | 0 |
| **30** | Kendall Corr. | 0.96712 | 0.9655 | 1 | 0.9632 | 0.91362 | 0.96352 | 0.95243 |
| | p-value | 0 | 0 | -- | 0 | 0 | 0 | 0 |
| **45** | Kendall Corr. | 0.96014 | 0.96527 | 0.9632 | 1 | 0.91563 | 0.95965 | 0.95349 |
| | p-value | 0 | 0 | 0 | -- | 0 | 0 | 0 |
| **60** | Kendall Corr. | 0.914 | 0.91216 | 0.91362 | 0.91563 | 1 | 0.91487 | 0.9158 |
| | p-value | 0 | 0 | 0 | 0 | -- | 0 | 0 |
| **75** | Kendall Corr. | 0.95722 | 0.96434 | 0.96352 | 0.95965 | 0.91487 | 1 | 0.96169 |
| | p-value | 0 | 0 | 0 | 0 | 0 | -- | 0 |
| **90** | Kendall Corr. | 0.95205 | 0.95416 | 0.95243 | 0.95349 | 0.9158 | 0.96169 | 1 |
| | p-value | 0 | 0 | 0 | 0 | 0 | 0 | -- |

**Table B5.** Kendall correlations for build orientation angles ([0°-90°], 15° step) for T% front of cyan.

| **BO (deg)** | | 0 | **15** | **30** | **45** | **60** | **75** | **90** |
|---|---|---|---|---|---|---|---|---|
| 0 | Kendall Corr. | 1 | 0.99632 | 0.99321 | 0.98873 | 0.98382 | 0.97697 | 0.98873 |
| | p-value | -- | 0 | 0 | 0 | 0 | 0 | 0 |
| **15** | Kendall Corr. | 0.99632 | 1 | 0.99599 | 0.99154 | 0.98696 | 0.98042 | 0.99138 |
| | p-value | 0 | -- | 0 | 0 | 0 | 0 | 0 |
| **30** | Kendall Corr. | 0.99321 | 0.99599 | 1 | 0.9949 | 0.99032 | 0.9825 | 0.9945 |
| | p-value | 0 | 0 | -- | 0 | 0 | 0 | 0 |
| **45** | Kendall Corr. | 0.98873 | 0.99154 | 0.9949 | 1 | 0.9946 | 0.98582 | 0.99532 |
| | p-value | 0 | 0 | 0 | -- | 0 | 0 | 0 |
| **60** | Kendall Corr. | 0.98382 | 0.98696 | 0.99032 | 0.9946 | 1 | 0.99133 | 0.99205 |
| | p-value | 0 | 0 | 0 | 0 | -- | 0 | 0 |
| **75** | Kendall Corr. | 0.97697 | 0.98042 | 0.9825 | 0.98582 | 0.99133 | 1 | 0.98347 |
| | p-value | 0 | 0 | 0 | 0 | 0 | -- | 0 |
| **90** | Kendall Corr. | 0.98873 | 0.99138 | 0.9945 | 0.99532 | 0.99205 | 0.98347 | 1 |
| | p-value | 0 | 0 | 0 | 0 | 0 | 0 | -- |

**Table B6.** Kendall correlations for build orientation angles ([0°-90°], 15° step) for T% front of magenta.

| **BO (deg)** | | **0** | **15** | **30** | **45** | **60** | **75** | **90** |
|---|---|---|---|---|---|---|---|---|
| 0 | Kendall Corr. | 1 | 0.99819 | 0.99741 | 0.99545 | 0.99311 | 0.98916 | 0.98859 |
| | p-value | -- | 0 | 0 | 0 | 0 | 0 | 0 |
| **15** | Kendall Corr. | 0.99819 | 1 | 0.99814 | 0.99687 | 0.99452 | 0.99093 | 0.99027 |
| | p-value | 0 | -- | 0 | 0 | 0 | 0 | 0 |
| **30** | Kendall Corr. | 0.99741 | 0.99814 | 1 | 0.99687 | 0.99486 | 0.99085 | 0.99014 |
| | p-value | 0 | 0 | -- | 0 | 0 | 0 | 0 |
| **45** | Kendall Corr. | 0.99545 | 0.99687 | 0.99687 | 1 | 0.9974 | 0.99325 | 0.99271 |
| | p-value | 0 | 0 | 0 | -- | 0 | 0 | 0 |
| **60** | Kendall Corr. | 0.99311 | 0.99452 | 0.99486 | 0.9974 | 1 | 0.9954 | 0.99504 |
| | p-value | 0 | 0 | 0 | 0 | -- | 0 | 0 |
| **75** | Kendall Corr. | 0.98916 | 0.99093 | 0.99085 | 0.99325 | 0.9954 | 1 | 0.99841 |
| | p-value | 0 | 0 | 0 | 0 | 0 | -- | 0 |
| **90** | Kendall Corr. | 0.98859 | 0.99027 | 0.99014 | 0.99271 | 0.99504 | 0.99841 | 1 |
| | p-value | 0 | 0 | 0 | 0 | 0 | 0 | -- |

**Table B7.** Kendall correlations for build orientation angles ([0°-90°], 15° step) for T% front of yellow.

| **BO (deg)** | | 0 | **15** | **30** | **45** | **60** | **75** | **90** |
|---|---|---|---|---|---|---|---|---|
| 0 | Kendall Corr. | 1 | 0.99612 | 0.99326 | 0.99266 | 0.99316 | 0.99248 | 0.9899 |
| | p-value | -- | 0 | 0 | 0 | 0 | 0 | 0 |
| **15** | Kendall Corr. | 0.99612 | 1 | 0.99097 | 0.99071 | 0.9912 | 0.9927 | 0.98957 |
| | p-value | 0 | -- | 0 | 0 | 0 | 0 | 0 |
| **30** | Kendall Corr. | 0.99326 | 0.99097 | 1 | 0.99194 | 0.99375 | 0.99191 | 0.99151 |
| | p-value | 0 | 0 | -- | 0 | 0 | 0 | 0 |
| **45** | Kendall Corr. | 0.99266 | 0.99071 | 0.99194 | 1 | 0.99562 | 0.99506 | 0.99367 |
| | p-value | 0 | 0 | 0 | -- | 0 | 0 | 0 |
| **60** | Kendall Corr. | 0.99316 | 0.9912 | 0.99375 | 0.99562 | 1 | 0.99563 | 0.99317 |
| | p-value | 0 | 0 | 0 | 0 | -- | 0 | 0 |
| **75** | Kendall Corr. | 0.99248 | 0.9927 | 0.99191 | 0.99506 | 0.99563 | 1 | 0.99261 |
| | p-value | 0 | 0 | 0 | 0 | 0 | -- | 0 |
| **90** | Kendall Corr. | 0.9899 | 0.98957 | 0.99151 | 0.99367 | 0.99317 | 0.99261 | 1 |
| | p-value | 0 | 0 | 0 | 0 | 0 | 0 | -- |

**Table B8.** Kendall correlations for build orientation angles ([0°-90°], 15° step) for T% front of black.

| **BO (deg)** | | 0 | **15** | **30** | **45** | **60** | **75** | **90** |
|---|---|---|---|---|---|---|---|---|
| 0 | Kendall Corr. | 1 | 0.99746 | 0.99758 | 0.99791 | 0.99803 | 0.99614 | 0.99599 |
| | p-value | -- | 0 | 0 | 0 | 0 | 0 | 0 |
| **15** | Kendall Corr. | 0.99746 | 1 | 0.99744 | 0.99769 | 0.9975 | 0.99655 | 0.99634 |
| | p-value | 0 | -- | 0 | 0 | 0 | 0 | 0 |
| **30** | Kendall Corr. | 0.99758 | 0.99744 | 1 | 0.99827 | 0.99768 | 0.99648 | 0.99619 |
| | p-value | 0 | 0 | -- | 0 | 0 | 0 | 0 |
| **45** | Kendall Corr. | 0.99791 | 0.99769 | 0.99827 | 1 | 0.99804 | 0.99651 | 0.99642 |
| | p-value | 0 | 0 | 0 | -- | 0 | 0 | 0 |
| **60** | Kendall Corr. | 0.99803 | 0.9975 | 0.99768 | 0.99804 | 1 | 0.99733 | 0.99669 |
| | p-value | 0 | 0 | 0 | 0 | -- | 0 | 0 |
| **75** | Kendall Corr. | 0.99614 | 0.99655 | 0.99648 | 0.99651 | 0.99733 | 1 | 0.99714 |
| | p-value | 0 | 0 | 0 | 0 | 0 | -- | 0 |
| **90** | Kendall Corr. | 0.99599 | 0.99634 | 0.99619 | 0.99642 | 0.99669 | 0.99714 | 1 |
| | p-value | 0 | 0 | 0 | 0 | 0 | 0 | -- |

**Table B9.** Kendall correlations for build orientation angles ([0°-90°], 15° step) for T% back of cyan.

| **BO (deg)** | | 0 | **15** | **30** | **45** | **60** | **75** | **90** |
|---|---|---|---|---|---|---|---|---|
| 0 | Kendall Corr. | 1 | 0.99632 | 0.99185 | 0.98552 | 0.98277 | 0.97707 | 0.99384 |
| | p-value | -- | 0 | 0 | 0 | 0 | 0 | 0 |
| **15** | Kendall Corr. | 0.99632 | 1 | 0.9947 | 0.98805 | 0.98568 | 0.9802 | 0.99556 |
| | p-value | 0 | -- | 0 | 0 | 0 | 0 | 0 |
| **30** | Kendall Corr. | 0.99185 | 0.9947 | 1 | 0.99242 | 0.98941 | 0.98351 | 0.99596 |
| | p-value | 0 | 0 | -- | 0 | 0 | 0 | 0 |
| **45** | Kendall Corr. | 0.98552 | 0.98805 | 0.99242 | 1 | 0.99546 | 0.98828 | 0.98987 |
| | p-value | 0 | 0 | 0 | -- | 0 | 0 | 0 |
| **60** | Kendall Corr. | 0.98277 | 0.98568 | 0.98941 | 0.99546 | 1 | 0.99211 | 0.98686 |
| | p-value | 0 | 0 | 0 | 0 | -- | 0 | 0 |
| **75** | Kendall Corr. | 0.97707 | 0.9802 | 0.98351 | 0.98828 | 0.99211 | 1 | 0.98024 |
| | p-value | 0 | 0 | 0 | 0 | 0 | -- | 0 |
| **90** | Kendall Corr. | 0.99384 | 0.99556 | 0.99596 | 0.98987 | 0.98686 | 0.98024 | 1 |
| | p-value | 0 | 0 | 0 | 0 | 0 | 0 | -- |

**Table B10.** Kendall correlations for build orientation angles ([0°-90°], 15° step) for T% back of magenta.

| **BO (deg)** | | 0 | **15** | **30** | **45** | **60** | **75** | **90** |
|---|---|---|---|---|---|---|---|---|
| 0 | Kendall Corr. | 1 | 0.99846 | 0.99753 | 0.99472 | 0.99183 | 0.98899 | 0.99279 |
| | p-value | -- | 0 | 0 | 0 | 0 | 0 | 0 |
| **15** | Kendall Corr. | 0.99846 | 1 | 0.99839 | 0.99603 | 0.99343 | 0.99041 | 0.99438 |
| | p-value | 0 | -- | 0 | 0 | 0 | 0 | 0 |
| **30** | Kendall Corr. | 0.99753 | 0.99839 | 1 | 0.99657 | 0.99325 | 0.99056 | 0.99492 |
| | p-value | 0 | 0 | -- | 0 | 0 | 0 | 0 |
| **45** | Kendall Corr. | 0.99472 | 0.99603 | 0.99657 | 1 | 0.99612 | 0.99324 | 0.99696 |
| | p-value | 0 | 0 | 0 | -- | 0 | 0 | 0 |
| **60** | Kendall Corr. | 0.99183 | 0.99343 | 0.99325 | 0.99612 | 1 | 0.99658 | 0.99768 |
| | p-value | 0 | 0 | 0 | 0 | -- | 0 | 0 |
| **75** | Kendall Corr. | 0.98899 | 0.99041 | 0.99056 | 0.99324 | 0.99658 | 1 | 0.99516 |
| | p-value | 0 | 0 | 0 | 0 | 0 | -- | 0 |
| **90** | Kendall Corr. | 0.99279 | 0.99438 | 0.99492 | 0.99696 | 0.99768 | 0.99516 | 1 |
| | p-value | 0 | 0 | 0 | 0 | 0 | 0 | -- |

**Table B11.** Kendall correlations for build orientation angles ([0°-90°], 15° step) for T% back of yellow.

| **BO (deg)** | | 0 | **15** | **30** | **45** | **60** | **75** | **90** |
|---|---|---|---|---|---|---|---|---|
| 0 | Kendall Corr. | 1 | 0.9953 | 0.99702 | 0.9963 | 0.99201 | 0.99024 | 0.99388 |
| | p-value | -- | 0 | 0 | 0 | 0 | 0 | 0 |
| **15** | Kendall Corr. | 0.9953 | 1 | 0.99612 | 0.99582 | 0.99093 | 0.98943 | 0.9918 |
| | p-value | 0 | -- | 0 | 0 | 0 | 0 | 0 |
| **30** | Kendall Corr. | 0.99702 | 0.99612 | 1 | 0.99679 | 0.99346 | 0.99124 | 0.99311 |
| | p-value | 0 | 0 | -- | 0 | 0 | 0 | 0 |
| **45** | Kendall Corr. | 0.9963 | 0.99582 | 0.99679 | 1 | 0.99225 | 0.99052 | 0.99321 |
| | p-value | 0 | 0 | 0 | -- | 0 | 0 | 0 |
| **60** | Kendall Corr. | 0.99201 | 0.99093 | 0.99346 | 0.99225 | 1 | 0.99554 | 0.99048 |
| | p-value | 0 | 0 | 0 | 0 | -- | 0 | 0 |
| **75** | Kendall Corr. | 0.99024 | 0.98943 | 0.99124 | 0.99052 | 0.99554 | 1 | 0.9904 |
| | p-value | 0 | 0 | 0 | 0 | 0 | -- | 0 |
| **90** | Kendall Corr. | 0.99388 | 0.9918 | 0.99311 | 0.99321 | 0.99048 | 0.9904 | 1 |
| | p-value | 0 | 0 | 0 | 0 | 0 | 0 | -- |

**Table B12.** Kendall correlations for build orientation angles ([0°-90°], 15° step) for T% back of black.

| **BO (deg)** | | 0 | **15** | **30** | **45** | **60** | **75** | **90** |
|---|---|---|---|---|---|---|---|---|
| 0 | Kendall Corr. | 1 | 0.9959 | 0.99568 | 0.99665 | 0.99629 | 0.99571 | 0.99423 |
| | p-value | -- | 0 | 0 | 0 | 0 | 0 | 0 |
| **15** | Kendall Corr. | 0.9959 | 1 | 0.99637 | 0.99676 | 0.99616 | 0.99539 | 0.99437 |
| | p-value | 0 | -- | 0 | 0 | 0 | 0 | 0 |
| **30** | Kendall Corr. | 0.99568 | 0.99637 | 1 | 0.99615 | 0.9955 | 0.99628 | 0.99463 |
| | p-value | 0 | 0 | -- | 0 | 0 | 0 | 0 |
| **45** | Kendall Corr. | 0.99665 | 0.99676 | 0.99615 | 1 | 0.99742 | 0.99564 | 0.99434 |
| | p-value | 0 | 0 | 0 | -- | 0 | 0 | 0 |
| **60** | Kendall Corr. | 0.99629 | 0.99616 | 0.9955 | 0.99742 | 1 | 0.99637 | 0.99515 |
| | p-value | 0 | 0 | 0 | 0 | -- | 0 | 0 |
| **75** | Kendall Corr. | 0.99571 | 0.99539 | 0.99628 | 0.99564 | 0.99637 | 1 | 0.99546 |
| | p-value | 0 | 0 | 0 | 0 | 0 | -- | 0 |
| **90** | Kendall Corr. | 0.99423 | 0.99437 | 0.99463 | 0.99434 | 0.99515 | 0.99546 | 1 |
| | p-value | 0 | 0 | 0 | 0 | 0 | 0 | -- |

## 7. Appendix C. Supplementary BRDF data for gloss measurements

BRDF data are displayed in Fig. C1 and C2 to spatially illustrate the measurement of reflected light in each direction. A BRDF can distinguish surface texture and irregularities, such as orange-peel defects, which are usually not visible or perceived by the human eye. As shown in the following figures, the decrease in BRDF corresponding to an increase in BO indicates a decline in specularly reflected light. In other words, it corresponds to gloss and haze. Further, the uneven multipeak shape of BRDF graphs suggests a textured surface in MJT products.

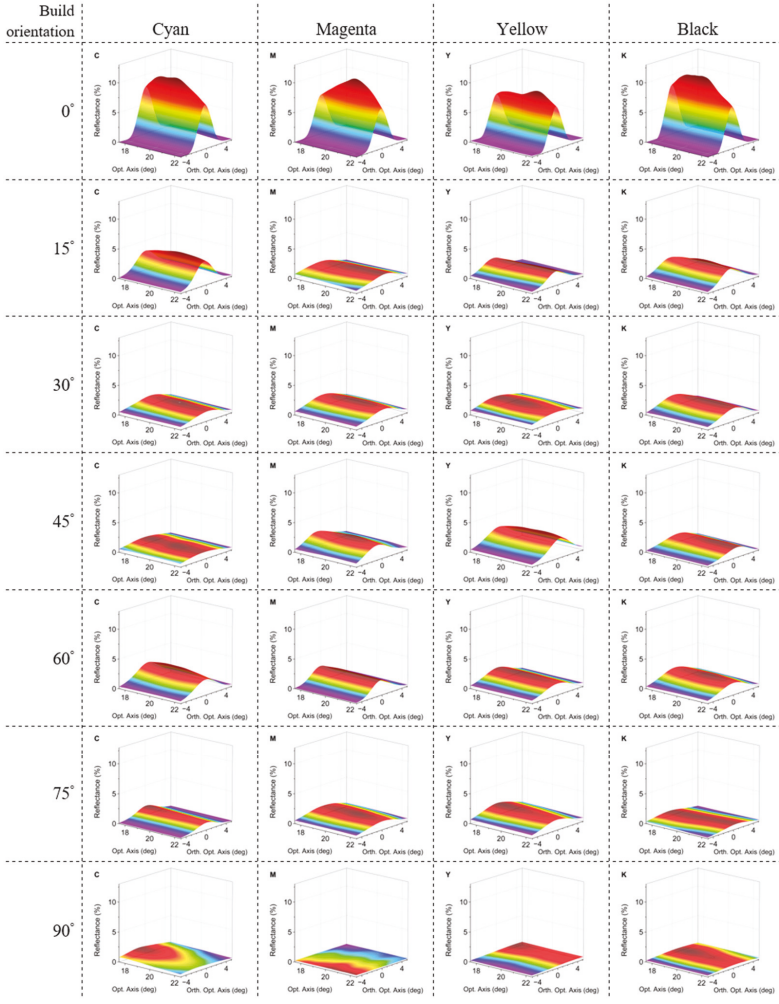


**Fig. C1.** Vertical measurement of BRDFs at a specular angle of 20° for various build orientations of CMYK resins.

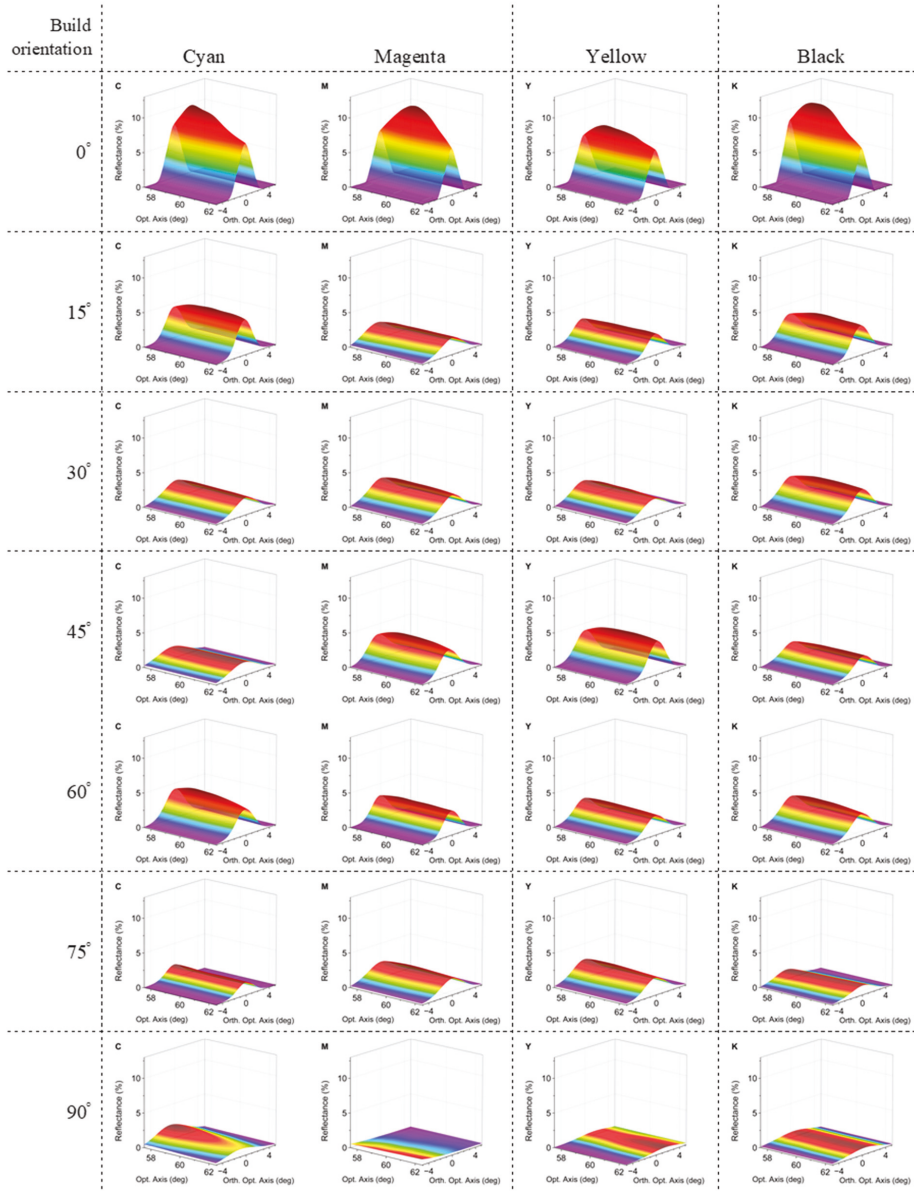


**Fig. C2.** Vertical measurement of BRDFs at a specular angle of 60° for various build orientations of CMYK resins.

## 8. References


[1] H.E. Quinlan, T. Hasan, J. Jaddou, A.J. Hart, Industrial and consumer uses of additive manufacturing: A discussion of capabilities, trajectories, and challenges, J. Ind. Ecol., 21 (2017) S15-S20. https://doi.org/10.1111/jiec.12609

[2] S. Rouf, A. Raina, M. Irfan Ul Haq, N. Naveed, S. Jeganmohan, A. Farzana Kichloo, 3D printed parts and mechanical properties: Influencing parameters, sustainability aspects, global market scenario, challenges and applications, Advanced Industrial and Engineering Polymer Research, (2022). https://doi.org/10.1016/j.aiepr.2022.02.001

[3] A. Payami Golhin, C. Srivastava, J.F. Tingstad, A.S. Sole, A. Strandlie, S. Grammatikos, Additive manufacturing of multilayered polymer composites: Durability assessment, in: Proceedings of the 20th European Conference on Composite Materials-Composites Meet Sustainability (Vol 1-6), EPFL Lausanne, Composite Construction Laboratory Switzerland, Lausanne, Switzerland, 2022, pp. 298-305. https://doi.org/10.5075/epfl-298799_978-2-9701614-0-0

[4] A. Payami Golhin, C. Srivastava, A. Strandlie, A. Suneel Sole, S. Grammatikos, Effects of accelerated aging on the appearance and mechanical performance of materials jetting products, Mater. Des., 228 (2023) 111863. https://doi.org/10.1016/j.matdes.2023.111863

[5] A. Payami Golhin, A.S. Sole, A. Strandlie, Color appearance in rotational material jetting, The International Journal of Advanced Manufacturing Technology, 124 (2023) 1183–1198. https://doi.org/10.1007/s00170-022-10536-1

[6] R. Magisetty, N.S. Cheekuramelli, Additive manufacturing technology empowered complex electromechanical energy conversion devices and transformers, Appl. Mater. Today, 14 (2019) 35-50. https://doi.org/10.1016/j.apmt.2018.11.004

[7] A. Payami Golhin, A. Strandlie, P. John Green, The influence of wedge angle, feedstock color, and infill density on the color difference of FDM objects, J. Imaging Sci. Technol., 65 (2021) 1-15. https://doi.org/10.2352/J.ImagingSci.Technol.2021.65.5.050408

[8] M.R. Pointer, Measuring visual appearance-a framework of the future. Project 2.3 measurement of appearance, (2003).

[9] B. Msallem, N. Sharma, S. Cao, F.S. Halbeisen, H.F. Zeilhofer, F.M. Thieringer, Evaluation of the dimensional accuracy of 3D-printed anatomical mandibular models using FFF, SLA, SLS, MJ, and BJ printing technology, Journal of Clinical Medicine, 9 (2020). https://doi.org/10.3390/jcm9030817

[10] Y. Feng, J. Liu, H. Li, X. Ma, P. Du, K. Li, Y. Liu, Deposition behavior optimization of on-demand tin droplet with gravity based on piezoelectric micro-jet, Int. J. Heat Mass Transf., 192 (2022). https://doi.org/10.1016/j.ijheatmasstransfer.2022.122902

[11] M. Di Nicolantonio, E. Rossi, P. Stella, Generative design for printable mass customization jewelry products, in: E. Rossi, T. Alexander, M. Di Nicolantonio (Eds.), Springer Verlag, 2020, pp. 143-152. https://doi.org/10.1007/978-3-030-20216-3_14

[12] B. Dorweiler, P.E. Baqué, R. Chaban, A. Ghazy, O. Salem, Quality control in 3D printing: Accuracy analysis of 3D-printed models of patient-specific anatomy, Materials, 14 (2021) 1-13. https://doi.org/10.3390/ma14041021

[13] J.A. Gonzalez, J. Mireles, S.W. Stafford, M.A. Perez, C.A. Terrazas, R.B. Wicker, Characterization of Inconel 625 fabricated using powder-bed-based additive manufacturing technologies, J. Mater. Process. Technol., 264 (2019) 200-210. https://doi.org/10.1016/j.jmatprotec.2018.08.031

[14] N. Mohammadian, S. Turenne, V. Brailovski, Surface finish control of additively-manufactured Inconel 625 components using combined chemical-abrasive flow polishing, J. Mater. Process. Technol., 252 (2018) 728-738. https://doi.org/10.1016/j.jmatprotec.2017.10.020

[15] F.F. Abayazid, M. Ghajari, Material characterisation of additively manufactured elastomers at different strain rates and build orientations, Addit. Manuf., 33 (2020). https://doi.org/10.1016/j.addma.2020.101160

[16] A. Khoshkhoo, A.L. Carrano, D.M. Blersch, Effect of build orientation and part thickness on dimensional distortion in material jetting processes, Rapid Prototyping J., 24 (2018) 1563-1571. https://doi.org/10.1108/RPJ-10-2017-0210

[17] H. Shi, Y. Liu, C. He, C. Wang, Y. Li, Y. Zhang, Analysis of infrared polarization properties of targets with rough surfaces, Opt. Laser Technol., 151 (2022). https://doi.org/10.1016/j.optlastec.2022.108069

[18] Y. Han, H. Sun, H. Guo, Analysis of influential factors on a space target's laser radar cross-section, Opt. Laser Technol., 56 (2014) 151-157. https://doi.org/10.1016/j.optlastec.2013.08.007

[19] L. Zheng, C. Li, S. Yang, Analysis of color gamut in color 3D printing, Lecture Notes in Electrical Engineering, 600 (2020) 148-155. https://doi.org/10.1007/978-981-15-1864-5_21

[20] Y.L. Cheng, K.C. Huang, Preparation and characterization of color photocurable resins for full-color material jetting additive manufacturing, Polymers (Basel), 12 (2020) 650. https://doi.org/10.3390/polym12030650

[21] Stratasys, Vero: Realistic, Multi-Color Prototypes in Less Time, in: Stratasys Datasheet, 2022, pp. 1-4.

[22] Stratasys, 3D Printing with Pantone Colors, in, Stratasys Ltd., 2021, pp. 1-6.

[23] ASTM, Standard practice for computing the colors of objects by using the CIE system, in, 2018, pp. 1-45.

[24] S. Westland, C. Ripamonti, V. Cheung, Computational colour science using MATLAB, John Wiley & Sons, 2012.

[25] Y. Xia, Chapter Eleven - Correlation and association analyses in microbiome study integrating multiomics in health and disease, in: J. Sun (Ed.) Progress in Molecular Biology and Translational Science, Academic Press, 2020, pp. 309-491. https://doi.org/10.1016/bs.pmbts.2020.04.003

[26] C.A. Gotway, Statistical Methods in Water Resources, Technometrics, 36 (1994) 323-324. https://doi.org/10.1080/00401706.1994.10485818

[27] ASTM, Standard Terminology of Appearance, in: A. E284-17 (Ed.), ASTM International West Conshohocken, PA, 2017, pp. 1-25. https://doi.org/10.1520/E0284-17

[28] E.E. Bell, Optical Constants and their Measurement, in: L. Genzel (Ed.) Light and Matter Ia / Licht und Materie Ia, Springer Berlin Heidelberg, Berlin, Heidelberg, 1967, pp. 1-58. https://doi.org/10.1007/978-3-642-46074-6_1

[29] J.R. Frisvad, S.A. Jensen, J.S. Madsen, A. Correia, L. Yang, S.K.S. Gregersen, Y. Meuret, P.E. Hansen, Survey of models for acquiring the optical properties of translucent materials, in: Comput. Graph. Forum, Wiley Online Library, 2020, pp. 729-755. https://doi.org/10.1111/cgf.14023

## Paper VII:

A. P. Golhin, A. S. Sole, A. Strandlie, BRDF representation in response to the build orientation in 3D-printed digital materials, Journal of Manufacturing Processes, (2023), Submitted

# BRDF representation in response to the build orientation in 3D-printed digital materials

Ali Payami Golhin [a,*], Aditya Suneel Sole [b], Are Strandlie [a]

[a] Department of Manufacturing and Civil Engineering, NTNU - Norwegian University of Science and Technology, 2815 Gjøvik, Norway

[b] Department of Computer Science, Norwegian University of Science and Technology, 2815 Gjøvik, Norway

## Abstract

Additively manufactured (AM) parts still lack a thorough understanding of their optical properties, particularly in terms of surface texture and reflectance characteristics at different viewing angles. This study examines the reflectance properties of material jetting (MJT) parts using bidirectional reflectance distribution functions (BRDFs). The visual appearance of the MJT parts was analyzed using a gonio-spectrophotometer at 328 unique incidence and viewing geometries for seven different wedge angles for build orientation (BO) from 0° to 90° at 15° intervals. The redundancy analysis (RDA) and principal component analysis (PCA) were used to study BO and to determine the prominent measurement geometries. The results indicate higher BOs resulted in more color and texture variation and rougher surfaces, with $S_q$ 4.21 µm vertical compared to 1.42 µm for horizontal BOs. Furthermore, it affected the visual representation and parametric estimation of BRDF, where significantly lower luminance, more diffuse reflection, and less hue distribution were observed for all CMYK resins printed at higher BOs. Accordingly, vertically printed surfaces showed a wider near-to-specular luminance area than other BOs. An analysis of the bidirectional reflectance property suggests that a gonio-spectrophotometer can be embedded in the printing process and quality assurance in AM as a computationally efficient model.

**Keywords:** Bidirectional reflectance distribution function, Spectral analysis, Digital materials, Appearance, 3D printing

## List of Abbreviations

| | |
|---|---|
| AM | Additive manufacturing |
| BO | Build orientation |
| BRDF | Bidirectional reflectance distribution function |
| BSSRDF | Bidirectional scattering-surface reflectance distribution function |
| BTDF | Bidirectional transmittance distribution function |
| CMYK | Cyan, Magenta, Yellow, and Black colors |
| FDM | Fused deposition modeling |
| GoG | Glossy-on-Glossy finish |
| MJT | Material jetting |
| PC | Principal component |
| PCA | Principal component analysis |
| RDA | Redundancy analysis |
| $S_a$ | Height deviations from the mean reference plane of the measurement area |
| SD | Standard deviation |
| $S_{ku}$ | Kurtosis |
| $S_q$ | Root mean square of surface heights |
| $S_{sk}$ | Skewness |
| svBRDF | spatially varying BRDF |
| $\theta_i$ | Incident angle |
| $\theta_r$ | Viewing angle |
| $\theta_{r\text{-}S}$ | Specular reflection angle |

## 1. Introduction

A key advantage of additive manufacturing (AM) is the ability to create complex geometries and customized designs. However, the poor surface finish of 3D-printed models has limited the widespread adoption of this technology and requires additional post-processing for most applications. Material jetting (MJT) techniques, such as PolyJet, have become popular to produce functional polymers, scaffolds for tissue engineering, multi-material structures, and memory shape polymers for 4D printing [1, 2]. It is primarily due to their general homogeneity, accuracy, and low surface roughness compared to the other AM processes [3].

The quality of a printed part can be affected by a number of parameters throughout the printing process [4]. To discuss how primary processing parameters can be optimized to improve surface quality for appearance, it is necessary to investigate the role of measurement in appearance assessment. The color of a material is determined by wavelength-specific light phenomena, while the gloss, translucency, and similar properties are determined by geometric or directional selectivity [5]. Numerical expressions of appearance attributes are essential for simplifying quantification and advancing the science and technology of the material appearance field [6]. However, the measurement geometry and direction play a significant role in the evaluation of the material appearance [5, 7].

Physical-based reflectance models can be used to accurately model light interactions with materials by incorporating the surface properties of the material, such as the bidirectional reflectance distribution [8]. Measurement of light reflected bidirectionally from the material surface is widely used for understanding material appearance by modeling a reflectance model like the bidirectional reflectance distribution function (BRDF) [7], spatially varying BRDF (svBRDF) [9], or the bidirectional scattering-surface reflectance distribution function (BSSRDF) [10] depending on the optical properties [11]. BRDF modeling can be computationally efficient [10] and a reliable appearance assessment method for homogenous and opaque surfaces. BSSRDF and svBRDF are considered to be more reliable methods for non-opaque and non-homogenous materials [12]. However, for applications such as online quality assurance for 3D-printed products, the BRDF model is significantly faster and simpler to implement than the svBRDF and BSSRDF models given its reduced dimensionality [13]. MJT surfaces are typically printed smooth and can be glossy [14]. As a result, the BRDF model can be suitable for simulating surface reflectance for MJT surfaces with specular reflections.

Several measurement techniques, such as a gonio-reflectometer [15], a dome-shaped system [16], robotic arms integrated with cameras, or an image-based system [17], have been used in the past to measure surface reflectance bidirectionally. However, the process of bidirectional reflectance measurement can also be time-consuming and tedious [18], which requires workflow improvement. Color science and colorimetry widely use the CIEXYZ tristimulus values [19] that are calculated using the surface reflectance, the CIE color matching function, and spectral power distribution of the light source. The CIEXYZ – Y component represents luminance, which is an important aspect of color reproduction and color matching of surfaces in AM. The chromaticity coordinates are represented by the CIEXYZ – X and CIEXYZ – Z components [4]. BRDF modeling is heavily influenced by the luminance of the color [7, 15]. Although the L* component in the CIELAB and CIELCH color models reflects the lightness of the color [4], this component is based on a nonlinear transformation using the CIEXYZ – Y and therefore is used to model surface reflectance in most of the cases [19, 20].

It is common for MJT objects to be complicated in appearance, and to represent a mixture of textures created by the application of layers of ink [18]. As a result, it is crucial to study the detailed texture properties of the 3D-printed surfaces when evaluating BRDF models [21]. MJT printing technology has been widely used to produce complex and visually appealing 3D objects due to its stability to

produce homogeneous surfaces compared to other AM techniques [22], particularly using recently developed machines, such as Stratasys J55 [14]. By reducing the influence of errors in the measurement process and following a reproducible procedure, satisfactory results can be achieved [23].

Typical MJT machines such as PolyJet J750 follow a three-dimensional Cartesian coordinate system equipped with a multi-nozzle printhead [24]. We discussed in our earlier work [14] how high-resolution and rotary tray printers enable the printing of materials with vastly unique properties. Consequently, components with even more complex shapes and appearances can be produced.

The build orientation (BO) and the wedge angle for tilted surfaces are considerably flexible, but specific orientations may be required depending on the design and to control the surface texture [25, 26]. Furthermore, a wrong orientation and high speeds can also impair accuracy and functionality [27-29]. In terms of how BO influences the functionality and quality of MJT parts, there is limited research available [22, 30-32] that focused on the typical MJT machines with Cartesian systems. Nevertheless, the role of rotary discs in studying BRDFs has not yet been addressed.

In this paper, we discuss the role of measurement in appearance assessment using BRDF and color variation models. A detailed analysis of the influence of the build orientation on the MJT surface reflectance is also provided. As part of explaining the role of BO in the surface reflectance model, the variation in the surface texture and roughness in the manufactured parts produced with CMYK resins is discussed as well. The findings are summarized by providing multivariate statistical score results for the most important measurement geometries.

## 2. Methodology

### 2.1. Test samples and bidirectional surface reflectance measurement

A J55 PolyJet 3D printer (Stratasys, Israel) was employed to generate test samples using VeroCyan, VeroMagenta, VeroYellow, and VeroBlackPlus, as corresponding CMYK colors. Vero materials are composed of acrylic oligomers combined with proprietary components, providing low-viscosity materials with similar mechanical, thermal, and electrical properties [33]. Bilayer structures of 35.50 × 40.00 (mm) were constructed using 1 mm thick CMYK plates on a 1 mm thick white background following the best practices of Stratasys for PolyJet and Pantone's guidelines for color matching [34]. An array of seven different build orientations was printed at intervals of 15° from 0° (reference) to 90° on the middle swath of a rotary disc using a glossy-on-glossy (GoG) finish. To collect data, experiments were designed with a full factorial approach. Fig. 1a represents specimens manufactured at BO 0°,15°, 75°, and 90° as viewed at 45° and under standard daylight illumination.

Bidirectional reflectance was measured spectrally using the GON 360 gonio-meter (Instrument Systems, Germany) equipped with a CAS 140CT array spectrophotometer (Instrument Systems, Germany). Fig. 1b and c depict the geometry of measurements and the main components of the measurement equipment. Bidirectional spectral reflectance was captured in the range of 380 nm to 780 nm at 5 nm intervals and at 328 unique pairs of the incident ($\theta_i$) and viewing ($\theta_r$) directions, as measurement geometries. Incidence angles were set between -60° and 0°, and the bidirectional reflectance at viewing angles between -30° and 65° was measured at intervals of 1° for specular and near-to-specular angles, and 5° for the rest.

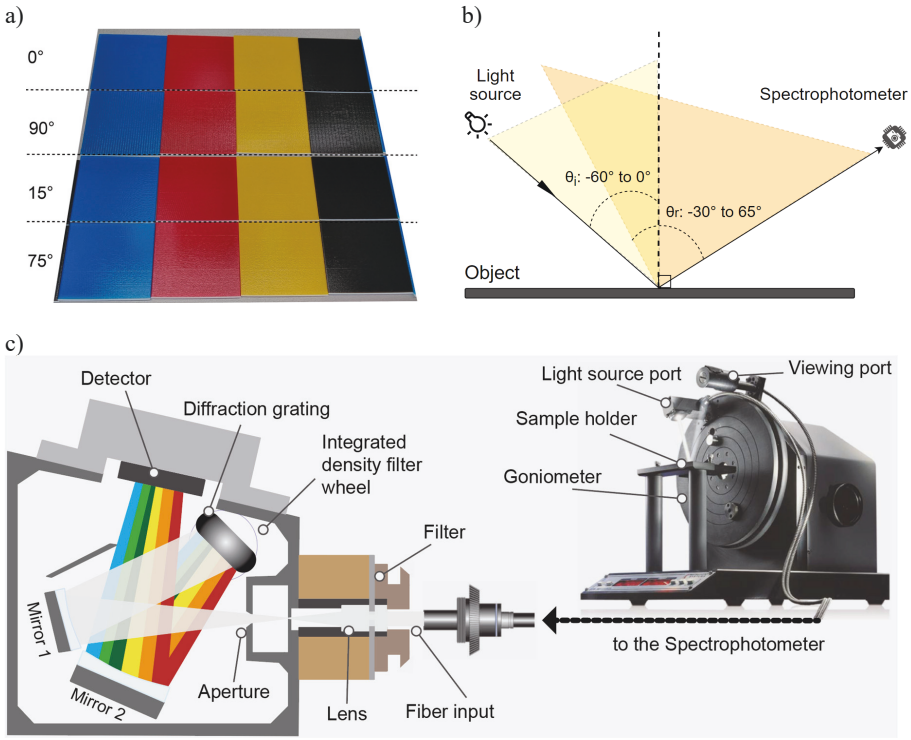


**Fig. 1.** a) CMYK specimens manufactured at BO 0°,15°, 75°, and 90°, as observed under D50 daylight standard illumination, b) measurement geometries, and c) gonio-spectrophotometer components.

CIEXYZ tristimulus values were further calculated based on the spectral reflectance of the sample surface $S(\lambda)$, D50 illuminant $I(\lambda)$, and CIE standard observer (2°) $\overline{x}$, $\overline{y}$, and $\overline{z}$ color matching functions according to CIE15.2 [5].

Keyence VH-ZST microscope (Keyence International, Belgium) was used to evaluate the surface morphology and roughness measurements of the 3D-printed objects.

### 2.2. Redundancy and principal component analysis

Redundancy analysis (RDA) was set to use $\theta_i$ and $\theta_r$ as observed variables, as well as BOs associated with build orientation as explanatory labels. To validate luminance evaluation by reflectance data and determine the prominent measurement angles, principal component analysis (PCA) was used to analyze multivariate spectral data. PCAs were performed for all 328-reflectance data of each printed resin at different build orientations, considering the correlation matrix. The periodic peaks of pulse integration results for PCA scores were used to identify the most important spectral bands or wavelengths that contribute to the observed changes in the Y value as a function of build orientation. Identifying significant wavelengths and frequencies in the spectra resulted in detecting critical BRDF

measurement angles. Data analysis was conducted using R statistical software 4.2.1 and Origin 2022 (OriginLab).

## 3. Results and discussions

CIE1976 u',v' chromaticity diagrams in Fig. 2 show the distribution of 328 points corresponding to the measurement geometries for each of the CMYK colors at various build orientations according to their corresponding BOs in the specimens. Results indicate that when the specimens were manufactured at the horizontal direction (BO 0°), there was generally a higher distribution of points for each of the CMYK colors than for higher angles, particularly 90°. Furthermore, the distribution was more pronounced for cyan and magenta colors as compared to black, where yellow resin showed a mediate distribution.

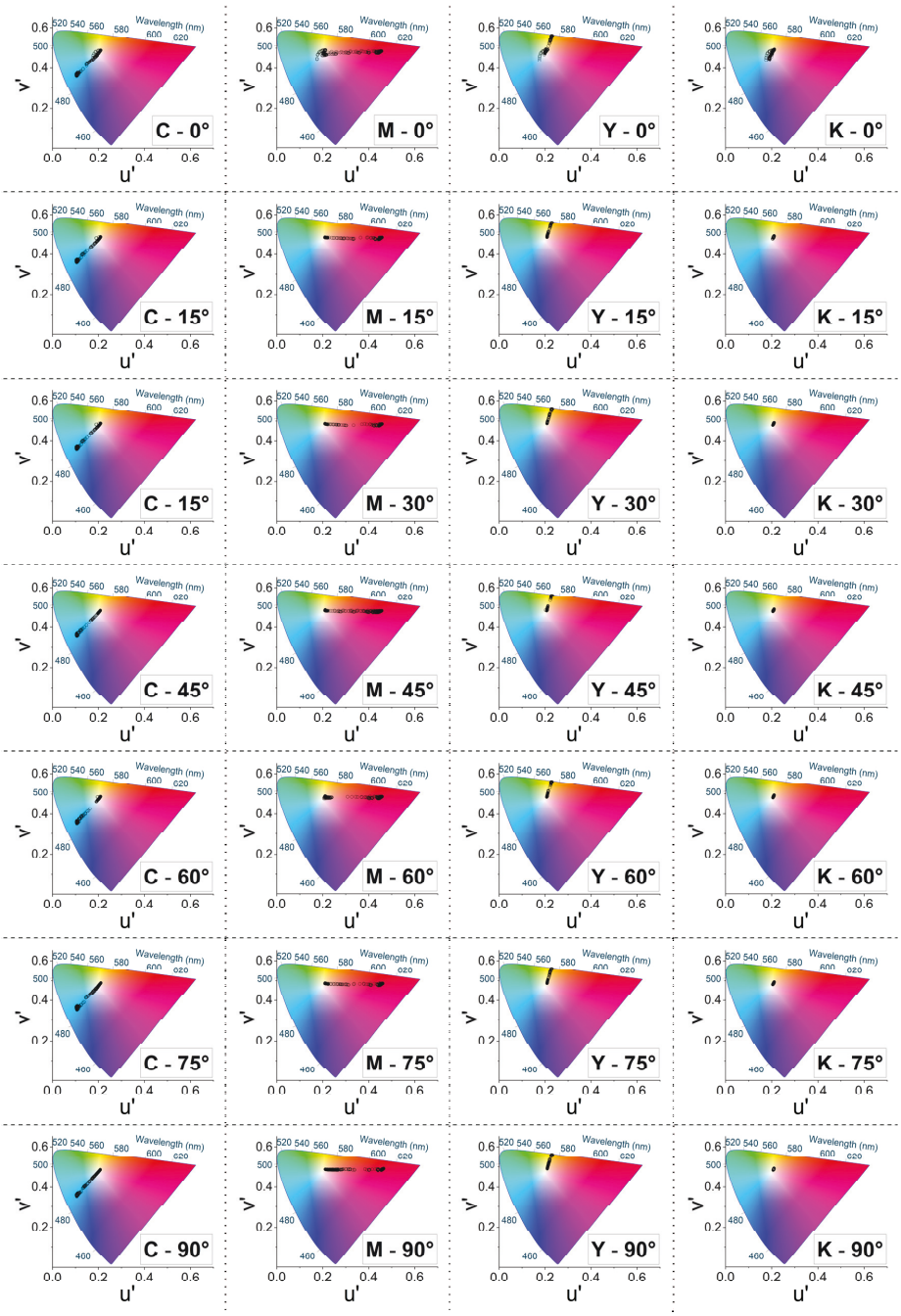


**Fig. 2.** Hue u', v' stimuli distribution according to CIE1976 chromaticity diagram. C: Cyan, M: Magenta, Y: Yellow, and K: Black.

As CMYK colors interact with light at different angles, the distribution of points on the CIE1976 u', v' chromaticity diagram varied. The microsurfaces of 3D-printed objects with zero BOs reflect light directly (Fig. 3a), which may interact for a longer period and more directly. It led to more scattering of light thus resulting in a high variation of u' and v' values in the CIE1976 u', v' chromaticity diagram for each of the CMYK colors and texture variation as can be seen in Fig. 3b. With the increasing BO, the microsurfaces of the 3D-printed object were oriented away from the direction of the light source. As a result, light scattering was reduced, resulting in a small variation of u' and v' values in the CIE1976 u', v' chromaticity diagram. The scattering of the reflected light was higher for cyan, and magenta compared to the black material. Therefore, adjusting the object orientation or modifying the resin properties might need to be considered to achieve a more consistent color distribution in MJT.

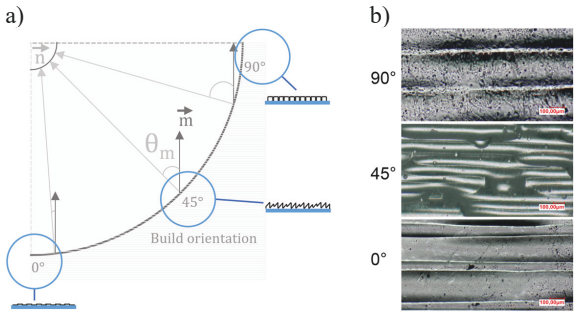


**Fig. 3.** a) Variation in the surface texture with the build orientation and b) focal microscopic images of BO 0°,45°, and 90°.

As listed in Table 1, MJT produced exceptionally smooth surfaces, although it was affected by the build orientation. The smoothest surface was obtained with a flat orientation ($S_a$=1.02 µm), followed by a BO 45° angle ($S_a$=2.09 µm) and a vertical angle ($S_a$=3.83 µm). All specimens had slightly positive skewness values ($S_{sk}$), resulting in more peaks and asperities than valleys, according to ISO 25178-2 [35]. These profile peaks were slightly sharp as indicated by high kurtosis ($S_{ku}$) values.

**Table 1** Results of mean surface roughness.

| | Area roughness parameter* | | | |
|---|---|---|---|---|
| Build orientation (°) | $S_a$ (µm) | $S_q$ (µm) | $S_{sk}$ | $S_{ku}$ |
| 0 | 1.02 | 1.42 | 0.03 | 2.20 |
| 45 | 2.09 | 2.65 | 0.05 | 3.13 |
| 90 | 3.83 | 4.21 | 0.06 | 2.95 |

* $S_a$: Height deviations from the mean reference plane of the measurement area (A); $S_q$: Root mean square of surface heights.

As a result of multilayering semi-transparent digital materials to achieve desired aesthetics, MJT objects tend to appear glossy and hazy [36], which can be explained by studying the specular and near-to-specular measurement angles, i.e., at most 10° away from specular reflection ($\theta_{r\text{-}S}$) [15]. A specular reflection occurs when light reflects off a surface at an angle equal to its angle of incidence, resulting in a bright, mirror-like reflection [8]. Y values differ between specular and near-to-specular angles due to differences in reflectance properties. A near-to-specular reflection occurs when light is

reflected off a surface at an angle slightly different from the angle of incidence, which results in a diffuse reflection [11]. As evident from the test results in Fig. 4, certain angles showed higher luminances, suggesting that the optical properties at these angles were more efficient at reflecting light and were specular. It provides information about the surface gloss and reflectance of the printed material, which can be correlated with its underlying physical properties, e.g., texture.

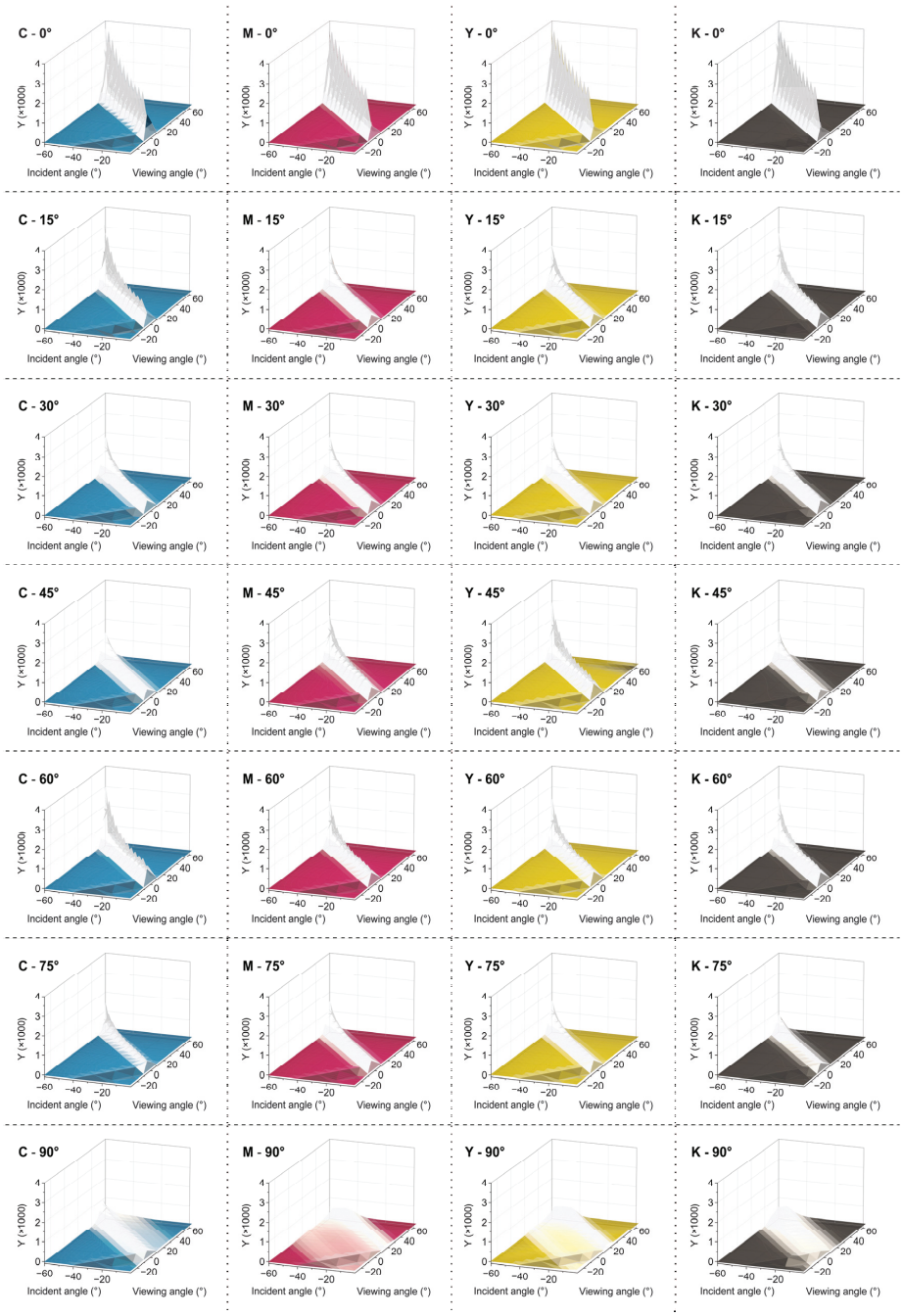


**Fig. 4.** Luminance Y plot of the CMYK resins test sample manufactured at different build orientations. Colors represent the corresponding sRGB hues.

Fig. 5 illustrates that the Y component of the tristimulus color value for 3D-printed objects was the maximum for specular angles and decreased as the build orientation increased. In particular, the Y values for specular angles were consistently higher and narrower than those for near-to-specular angles, with maximum values observed at BO 0°. The Y values for both specular and near-to-specular angles decreased with increasing BOs, with a greater decrease for specular angles. Moreover, BO 90° demonstrated significantly more hazy luminance compared to other specimens for all resins, leading to a complex visual appearance. It was attributed to the change in surface texture and reflectance properties of the printed objects (Fig. 3b). As the wedge angle for BO increased, the surface texture became rougher (Table 1), leading to an increase in diffuse reflection, a decrease in specular reflection, and reducing the Y values.

Parts printed in a horizontal orientation resulted in smooth surfaces because layers of material were deposited on top of each other. Conversely, when pieces were printed in a non-horizontal orientation, i.e., tilted surfaces, the materials were deposited at an angle. It caused stair-stepping effects and a rougher surface finish, resulting in a diffuse appearance [37]. There were, however, several other factors that could affect the surface finish of parts produced by MJT, such as the size of the droplets and the duration of the curing process. For instance, reducing the droplet size could improve the surface finish of parts produced in a vertical orientation, as seen previously for fused deposition modeling (FDM) [3].

Table 2 lists the mean CIEXYZ – Y (luminance) at specular ($\theta_{r\text{-}S}$) and near-to-specular ($\theta_{r\text{-}S} \pm 4°$) angles from 18 geometries for each, associated with Fig. 5. The maximum $\bar{Y}$ at specular angles could be found for BO 0° by 1600.43 ± 924.31, 1410.02 ± 843.26, 1399.56 ± 807.55, and 1376.93 ± 793.8 for CMYK colors, respectively. On the other hand, vertical printing (BO 90°) resulted in the lowest luminances at specular angles by 273.56 ± 166.87, 78.65 ± 42.92, 136.67 ± 55.97, and 174.36 ± 111.41 for CMYK, respectively. The standard deviation followed the same trend. Although increasing BO in most cases resulted in lower luminances, BO 45°, and 60° exhibit different behavior depending on the color. In the case of BO 60°, for instance, the luminance for the cyan color was considerably high (1011.95 ± 683.7) compared to BO 45°. As well, near-to-spectral angles for BO 90° displayed greater luminance than specular angles, while in all other BOs, specular angles constantly showed maximum $\bar{Y}$.

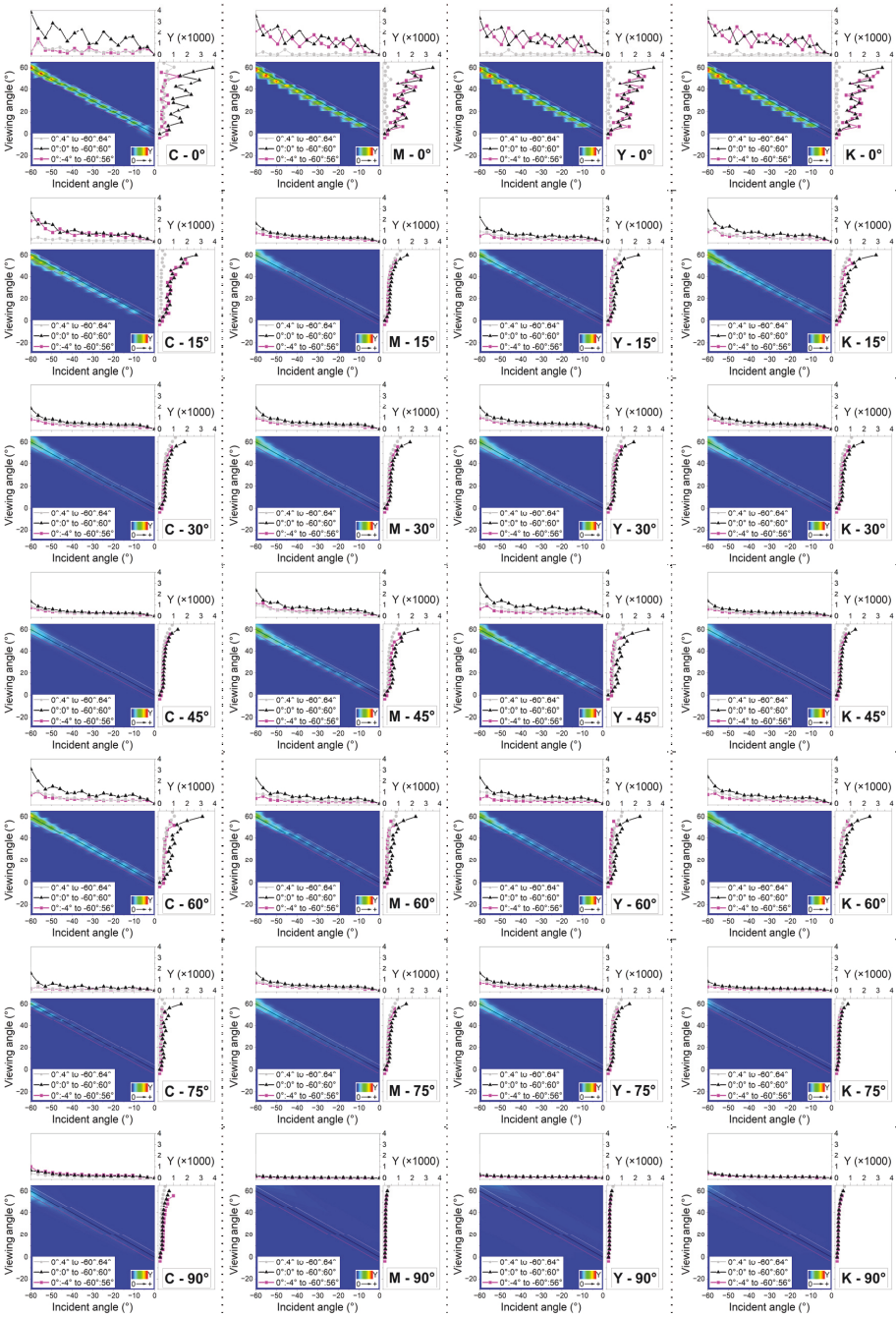
C - 0°
M - 0°
Y - 0°
K - 0°
C - 15°
M - 15°
Y - 15°
K - 15°
C - 30°
M - 30°
Y - 30°
K - 30°
C - 45°
M - 45°
Y - 45°
K - 45°
C - 60°
M - 60°
Y - 60°
K - 60°
C - 75°
M - 75°
Y - 75°
K - 75°
C - 90°
M - 90°
Y - 90°
K - 90°
Y (×1000)
Viewing angle (°)
Incident angle (°)
0°:4° to -60°:64°
0°:0° to -60°:60°
0°:-4° to -60°:56°

**Fig. 5.** Luminance Y distribution contour plots and their respective incident angle projection (top graph) and viewing angle projection (right graph). The black line represents the specular ($\theta_{r\text{-}S}$) angles, and the purple and gray lines are corresponding to the near-to-specular ($\theta_{r\text{-}S} \pm 4°$) angles.

**Table 2** The mean luminance at specular ($\theta_{r\text{-}S}$) and near-to-specular ($\theta_{r\text{-}S} \pm 4°$) angles.

| | | Photo resin | | | |
|---|---|---|---|---|---|
| Build orientation (°) | Measurement geometry | Cyan (Ȳ±SD*) | Magenta (Ȳ±SD) | Yellow (Ȳ±SD) | Black (Ȳ±SD) |
| 0 | $\theta_{r\text{-}S}$ | 1600.43 ± 924.31 | 1410.02 ± 843.26 | 1399.56 ± 807.55 | 1376.93 ± 793.8 |
| | $\theta_{r\text{-}S}$+4° | 389.09 ± 231.37 | 99.48 ± 110.4 | 103.44 ± 100.1 | 68.41 ± 100.11 |
| | $\theta_{r\text{-}S}$-4° | 359.77 ± 314.11 | 1156.69 ± 733.18 | 1228.17 ± 782.74 | 1340.52 ± 869.43 |
| 15 | $\theta_{r\text{-}S}$ | 906.39 ± 617.64 | 539.32 ± 370.55 | 661.17 ± 478.09 | 867.62 ± 633.52 |
| | $\theta_{r\text{-}S}$+4° | 152.7 ± 88.3 | 413.54 ± 277.46 | 377.33 ± 224.51 | 436.76 ± 278.26 |
| | $\theta_{r\text{-}S}$-4° | 768.06 ± 519.23 | 309.36 ± 185.91 | 287.62 ± 164.2 | 417.41 ± 266.05 |
| 30 | $\theta_{r\text{-}S}$ | 592.98 ± 403.33 | 614.59 ± 411.9 | 652.19 ± 415.42 | 621.43 ± 424.08 |
| | $\theta_{r\text{-}S}$+4° | 422.93 ± 276.51 | 421.07 ± 277.61 | 450.8 ± 273.96 | 402.29 ± 266.71 |
| | $\theta_{r\text{-}S}$-4° | 346.65 ± 204.08 | 379.47 ± 226.22 | 419.34 ± 232.3 | 365.35 ± 221.36 |
| 45 | $\theta_{r\text{-}S}$ | 432.74 ± 298.01 | 781.14 ± 530.7 | 935.59 ± 633.23 | 438.87 ± 306.58 |
| | $\theta_{r\text{-}S}$+4° | 321.04 ± 220.39 | 394.1 ± 244.82 | 511.39 ± 284.67 | 297.59 ± 200.58 |
| | $\theta_{r\text{-}S}$-4° | 291.66 ± 179.51 | 470.51 ± 291.23 | 362.26 ± 193.01 | 252.7 ± 157.46 |
| 60 | $\theta_{r\text{-}S}$ | 1011.95 ± 683.7 | 668.91 ± 496.39 | 715.43 ± 503.93 | 768.9 ± 533.4 |
| | $\theta_{r\text{-}S}$+4° | 467.23 ± 268.64 | 358.39 ± 230.6 | 447.33 ± 261.38 | 489.79 ± 321.3 |
| | $\theta_{r\text{-}S}$-4° | 406.7 ± 223.21 | 238.97 ± 139.12 | 257.03 ± 128.74 | 364.53 ± 213.48 |
| 75 | $\theta_{r\text{-}S}$ | 392.08 ± 336.27 | 518.78 ± 346.86 | 532.54 ± 342.15 | 264.94 ± 185.86 |
| | $\theta_{r\text{-}S}$+4° | 120.32 ± 77.08 | 344.21 ± 222.38 | 374.59 ± 226.03 | 197.73 ± 140.99 |
| | $\theta_{r\text{-}S}$-4° | 118.45 ± 69.99 | 300.28 ± 174.64 | 300.96 ± 158.37 | 142.42 ± 86.87 |
| 90 | $\theta_{r\text{-}S}$ | 273.56 ± 166.87 | 78.65 ± 42.92 | 136.67 ± 55.97 | 174.36 ± 111.41 |
| | $\theta_{r\text{-}S}$+4° | 155.63 ± 92.75 | 105.21 ± 64.43 | 162.25 ± 78.31 | 195.43 ± 135.63 |
| | $\theta_{r\text{-}S}$-4° | 335.49 ± 226.29 | 61.06 ± 30.89 | 116.7 ± 43.86 | 154.89 ± 92.81 |

* Ȳ±SD: The mean CIEXYZ – Y (luminance) ± one standard deviation

RDA can provide valuable insights into the relative importance of studied factors, and how they interact with each other to influence the appearance characteristics of 3D-printed objects [38]. An RDA plot for Y results is shown in Fig. 6a, which includes vectors representing $\theta_i$ and $\theta_r$ (observed variables), as well as associated BOs (explanatory labels in Fig. 6b). Since principal component 1 (PC1) represents 99.24% of the cumulative eigenvalue, a linear correlation between the variables, including measurement geometry and build orientation, could be signified.

The variation in BOs was positively correlated with $\theta_r$, whereas $\theta_i$ variation showed a weaker and negative correlation. It can be explained by the alignment of all build orientation vectors toward $\theta_r$, and the opposite direction of $\theta_i$ with a shorter vector. Moreover, the vector associated with a BO 90° was assigned to positive PC2, while the remaining vectors were assigned to negative PC2. In other

words, printing vertically appeared differently from printing tilted surfaces. This suggests that the build orientation BOs play a critical role in determining the characteristics of the 3D-printed objects in this study. Furthermore, this indicates that the effect of additional factors other than BO variations, including resin colors, was negligible. Appendix A provides complementary data on the RDA results.

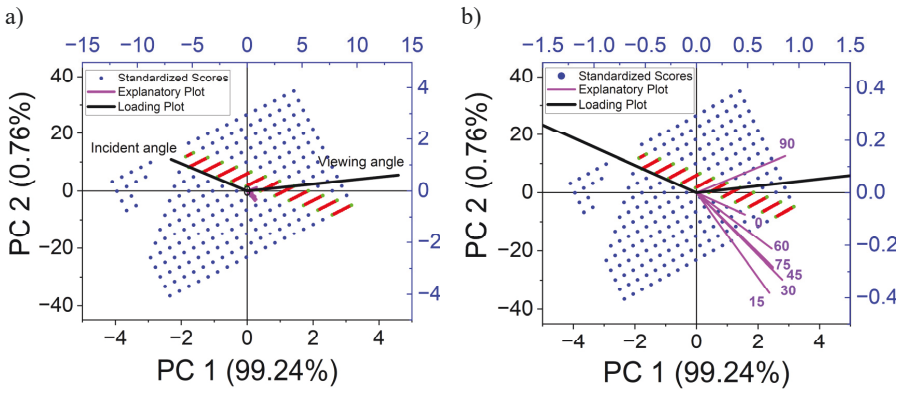


**Fig. 6.** a) RDA ordination diagram (triplot) of CMYK specimens and b) its corresponding enlarged (10X) triplot considering the explanatory vectors related to the build orientations. The red points represent specular and near-to-specular scores for luminance Y, and the blue points represent the remaining scores.

PCA scores are presented in Fig. 7, which illustrates the relationship between the $\theta_i$ and $\theta_r$ and the corresponding PCA scores. The sizes of the points on the graph indicate their corresponding PCA scores, with larger points indicating higher scores distributed mainly around -60°:60°. Similar to the observed trends in Fig. 4 and Fig. 5, PCA and CIEXYZ – Y demonstrated ties in terms of surface appearance and texture. However, BO 90° represented shifted results to higher viewing angles, due to different textures. Contrary to specular reflection for other BOs, vertical BO demonstrated diffuse reflectance and a wider near-to-specular reflectance zone. PCA for spectral data indicated a cumulative percentage of eigenvalues between 97.2% to 100% for PC1. It suggests that all the variability in the spectral data could be explained by PC1 and the spectral data for each BRDF measurements batch were linearly correlated.

There were a few measurement geometries, mainly within the specular region could contribute the most to BRDF estimation using the measured bidirectional reflectance. The number of crucial geometries ranged from 12 to 14 pairs of the $\theta_i$ and $\theta_r$ angles out of the 328 measurement pairs. The bidirectional reflectance measurement process may therefore be optimized for these measurement geometries compared to measuring all the possible directions. This would result in a quicker and cost-effective method for measuring the bidirectional reflectance of these materials that can be used for reflectance modeling. Complementary data on the pulse integration results and PCA are listed in Appendix B.

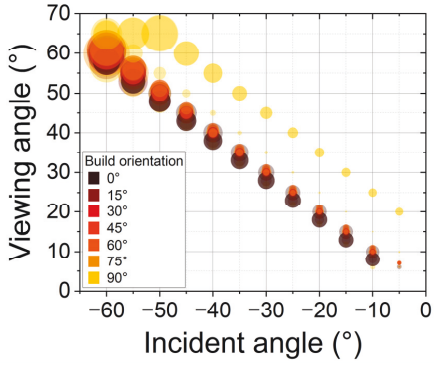


**Fig. 7.** PCA-based representation of the most prominent measurement angles. Point sizes correspond to standardized PC1 scores.

## 4. Conclusions

Bidirectional reflectance measurements are crucial for understanding the 3D-printed surface texture and appearance. This study evaluated the light reflection on the MJT surfaces using the bidirectional reflectance measured using a gonio-spectrophotometer. The surface texture and roughness of parts produced using the material jetting 3D printing process can significantly be affected by build orientation. According to the results, the combination of a wrong orientation can result in poor accuracy. The texture and surface roughness study revealed a higher build orientation resulted in higher surface roughness, particularly for vertical 3D-printed surfaces. When parts were printed horizontally, the layers of material were deposited on top of one another, resulting in a more uniform surface texture. Alternatively, printed in a vertical orientation, the layers were deposited at an angle, which resulted in an irregular surface texture, especially for BOs of 90 degrees.

In addition, the results indicated that the orientation of the object results in hue and chroma variation, particularly for cyan and magenta resins compared to yellow and black. The orientation of the build during printing also affects the quality of the 3D-printed part. As a result of the high-speed technology of MJT, large volumes of material can be jetted simultaneously, but a wrong orientation can lead to a decrease in print accuracy. RDA and PCA techniques allowed for the identification of significant spectral bands or wavelengths that contributed more to the change in reflectance, as well as the relationship between different variables, such as build orientation and surface reflectance. PCA results suggested that a few illumination and viewing directions were critical for the accurate BRDF estimation. Incorporating luminance distribution (CIEXYZ – Y) and PCA scores of reflectances provided a better understanding of 3D-printed surface appearance attributes like texture, and roughness and can lead to better 3D print process optimization. As opposed to specular reflection for other BOs, vertical BOs demonstrated diffuse reflectance and a wider near-to-specular reflectance zone.

The choice of model for modeling the interaction of light with materials in AM depends on the properties of the material and the application requirements. It may be more accurate to model translucent or transparent materials or materials that scatter light in all directions with a spatially varying BRDF and/or a BSSRDF model. The BRDF model, however, remains the most popular

model to model surface reflectance due to its computational efficiency and suitability for modeling surfaces with specular reflection.

The combination of materials improvement with targeted appearance attributes of 3D structures opens unprecedented opportunities for further application of AM in the industry. The PolyJet technique represented an exciting and versatile MJT printing technology that confirmed significant potential to produce complex and visually appealing 3D objects. For future studies, optimizing primary processing parameters and accurate measurement of appearance attributes are critical to improving surface quality in MJT technology. It would be crucial to evaluate and compare the use of more complex reflectance models like the svBRDF, BSSRDF, and bidirectional transmittance distribution function (BTDF). It would also be important to consider other factors that may affect the appearance of AM products, including but not limited to material properties and printing parameters.

**Acknowledgments**

This work was supported by the ApPEARS-ITN project funded by the European Union's H2020 research and innovation program under the Marie Skłodowska-Curie grant agreement No. 814158. The authors appreciate the support provided by Dr. Andreas Kraushaar (Fogra, Germany) and Donatela Saric (NTNU & Fogra) for the BRDF and roughness measurement.

**Data availability**

The main part of the raw/processed data required to reproduce these findings is available at https://doi.org/10.5281/zenodo.7716929

The rest cannot be shared at this time as the data also forms part of an ongoing study.

## Appendix A. Supplementary data for RDA

The material jetting (MJT) process entails precisely dispensing digital materials through tiny nozzles to achieve the desired shape and dimensions of the part. To achieve desired aesthetics, MJT objects are typically constructed using multiple layers of semi-transparent digital materials. Typical PolyJet parts exhibit semi-translucency, haziness, and complexity due to the layering and agitation of photo resins during manufacture, which should be considered in the appearance assessment of MJT parts. However, using dimension reduction techniques is recommended to determine the main influencing factors due to the complexity of the appearance of MJT parts. Multivariate statistical analysis techniques, such as principal component analysis (PCA) and redundancy analysis (RDA) can provide deeper insights into the surface appearance and texture of 3D-printed objects. Table A.1. to A.4. list further information on the RDA method used in this work.

**Table A.1.** Eigenvalues for the constrained axe.

| | Eigenvalue | Percentage of Inertia | Cumulative Inertia |
|---|---|---|---|
| RDA1 | 208.21 | 20.64% | 20.64% |
| RDA2 | 1.60 | 0.16% | 20.80% |

**Table A.2.** Eigenvalues for the unconstrained axe.

| | Eigenvalue | Percentage of Inertia | Cumulative Inertia |
|---|---|---|---|
| PC1 | 516.85 | 51.24% | 72.04% |
| PC2 | 282.10 | 27.96% | 100.00% |

**Table A.3.** Response variables.

| | Coefficients of RDA1 | Coefficients of RDA2 |
|---|---|---|
| Incident angle | -6.92 | 1.21 |
| Viewing angle | 13.76 | 0.61 |

**Table A.4.** Explanatory variables.

| | Coefficients of RDA1 | Coefficients of RDA2 |
|---|---|---|
| 0 | 0.47 | -0.08 |
| 15 | 0.71 | -0.38 |
| 30 | 0.84 | -0.33 |
| 45 | 0.75 | -0.28807 |
| 60 | 0.74 | -0.21 |
| 75 | 0.75 | -0.28 |
| 90 | 0.87 | 0.14 |

## Appendix B. Supplementary data for PCA

Measurements of BRDF deliver information about how light interacts with printed materials, including $\theta_i$ and $\theta_r$ angles. Using these measurements, printing processes can be optimized for different applications. As discussed in this study, the build orientation affected the surface appearance and texture of 3D-printed objects. It influenced the reflectance properties of the printed material, leading to changes in the surface properties, such as texture and roughness, gloss, and color appearance. To determine the main measurement geometries, significant PCA scores were determined using pulse integration results shown in Fig. B1 and their PC shares listed in Table B.1. PC1 solely was responsible for the correlation observed between the spectral data and build orientation, however, a few geometries ($\theta_i|\theta_r$) had a more significant effect on the PC1 by higher scores. These scores were read from the peak shown in the following graphs.

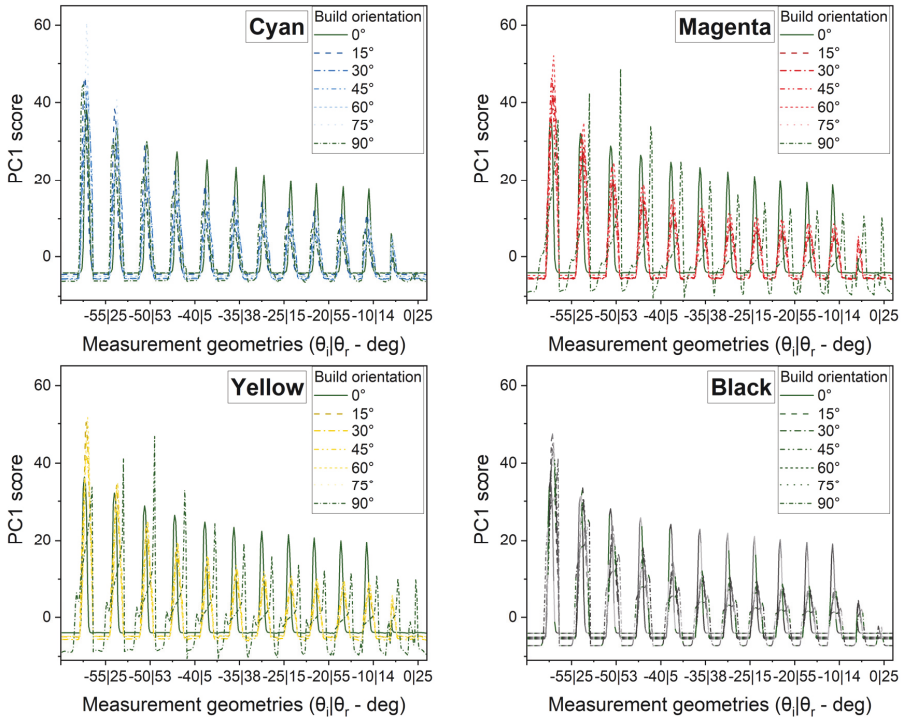


**Fig. B1.** Pulse integration results. Measurement geometries represent a few of 328 geometries.

**Table B.1.** Cumulative eigenvalues of PC1 and PC2 for the appearance measurement for studied build orientations.

| Resin | Build orientation (°) | PC1 % | PC2 % |
|---|---|---|---|
| Cyan | 0 | 98 | 1.9 |
| Cyan | 15 | 99.6 | 0.4 |
| Cyan | 30 | 100 | 0 |
| Cyan | 45 | 100 | 0 |
| Cyan | 60 | 99.8 | 0.2 |
| Cyan | 75 | 99.8 | 0.1 |
| Cyan | 90 | 100 | 0 |
| Magenta | 0 | 97.4 | 2.4 |
| Magenta | 15 | 100 | 0 |
| Magenta | 30 | 100 | 0 |
| Magenta | 45 | 100 | 0 |
| Magenta | 60 | 99.9 | 0.1 |
| Magenta | 75 | 100 | 0 |
| Magenta | 90 | 99.8 | 0.2 |
| Yellow | 0 | 97.2 | 2.6 |
| Yellow | 15 | 100 | 0 |
| Yellow | 30 | 100 | 0 |
| Yellow | 45 | 99.9 | 0.1 |
| Yellow | 60 | 99.9 | 0 |
| Yellow | 75 | 100 | 0 |
| Yellow | 90 | 99.8 | 0.2 |
| Black | 0 | 97.4 | 2.4 |
| Black | 15 | 100 | 0 |
| Black | 30 | 100 | 0 |
| Black | 45 | 100 | 0 |
| Black | 60 | 100 | 0 |
| Black | 75 | 100 | 0 |
| Black | 90 | 100 | 0 |

## References


1. Sugavaneswaran M, Arumaikkannu G. Analytical and experimental investigation on elastic modulus of reinforced additive manufactured structure. Mater. Des. 2015;66:29-36. https://doi.org/10.1016/j.matdes.2014.10.029
2. Eren O, Sezer HK, Yalçın N. Effect of lattice design on mechanical response of PolyJet additively manufactured cellular structures. J. Manuf. Process. 2022;75:1175-1188. https://doi.org/10.1016/j.jmapro.2022.01.063
3. Khoo ZX, Teoh JEM, Liu Y, et al. 3D printing of smart materials: A review on recent progresses in 4D printing. Virtual Phys. Prototyping 2015;10:103-122. https://doi.org/10.1080/17452759.2015.1097054
4. Payami Golhin A, Strandlie A, John Green P. The influence of wedge angle, feedstock color, and infill density on the color difference of FDM objects. J. Imaging Sci. Technol. 2021;65:1-15. https://doi.org/10.2352/J.ImagingSci.Technol.2021.65.5.050408
5. L'éclairage CID. Colorimetry in CIE 015:2004. Commission Internationale de l'Éclairage 2004; p. 1-82.
6. Sole A, Guarnera GC, Farup I, et al. Measurement and rendering of complex non-diffuse and goniochromatic packaging materials. Vis. Comput. 2021;37:2207-2220. https://doi.org/10.1007/s00371-020-01980-9
7. Sole A, Farup I, Nussbaum P. Evaluating an image based multi-angle measurement setup using different reflection models. in IS and T International Symposium on Electronic Imaging Science and Technology. 2017;https://doi.org/10.2352/ISSN.2470-1173.2017.8.MAAP-280
8. Nicodemus FE, Richmond JC, Hsia JJ, et al. Geometrical considerations and nomenclature for reflectance. 1977;
9. Rouiller O, Bickel B, Kautz J, et al. 3D-printing spatially varying BRDFs. IEEE Comput. Graph. Appl. 2013;33:48-57. https://doi.org/10.1109/MCG.2013.82
10. D'eon E, Irving G. A quantized-diffusion model for rendering translucent materials. ACM Trans. Graph. 2011;30:1-14. https://doi.org/10.1145/2010324.1964951
11. Guarnera D, Guarnera GC, Ghosh A, et al. BRDF representation and acquisition. in Computer Graphics Forum. Wiley Online Library 2016;2. https://doi.org/10.1111/cgf.12867
12. Haindl M, Filip J. Representation. in Visual Texture. Springer 2013; p. 9-22.
13. Hullin MB, Ihrke I, Heidrich W, et al. State of the art in computational fabrication and display of material appearance. in Eurographics Annual Conference (STAR). 2013;
14. Golhin AP, Sole AS, Strandlie A. Color appearance in rotational material jetting. Int. J. Adv. Manuf. Technol. 2023;124:1183–1198. https://doi.org/10.1007/s00170-022-10536-1
15. Habib ST, Green PJ, Nussbaum P. Estimation of BRDF Measurements for Printed Colour Samples, in 29th Color and Imaging Conference Final Program and Proceedings. Society for Imaging Science and Technology 2021; p. 123-128. https://doi.org/10.2352/issn.2169-2629.2021.29.123
16. Elkhuizen WS, Lenseigne BaJ, Baar T, et al. Reproducing oil paint gloss in print for the purpose of creating reproductions of old masters. in Proceedings of SPIE - The International Society for Optical Engineering. 2015;https://doi.org/10.1117/12.2082918
17. Arteaga Y, Marchioni D, Courtier S, et al. Appearance-based evaluation of varnish removal methods in gilded surfaces. Herit. Sci. 2023;11:31. https://doi.org/10.1186/s40494-023-00868-w
18. Yuan J, Chen G, Li H, et al. Accurate and Computational: A review of color reproduction in Full-color 3D printing. Mater. Des. 2021;209:1-17. https://doi.org/10.1016/j.matdes.2021.109943
19. Hunt RWG, Pointer MR. Measuring colour. 2011: John Wiley & Sons.
20. Sole A, Farup I, Nussbaum P, et al. Bidirectional reflectance measurement and reflection model fitting of complex materials using an image-based measurement setup. J. Imaging 2018;4:1-16. https://doi.org/10.3390/jimaging4110136

21. Kumar H, Ramkumar J, Venkatesh K. Surface texture evaluation using 3D reconstruction from images by parametric anisotropic BRDF. Measurement 2018;125:612-633. https://doi.org/10.1016/j.measurement.2018.04.090
22. Khoshkhoo A, Carrano AL, Blersch DM. Effect of build orientation and part thickness on dimensional distortion in material jetting processes. Rapid Prototyping J. 2018;24:1563-1571. https://doi.org/10.1108/RPJ-10-2017-0210
23. Goh GD, Sing SL, Lim YF, et al. Machine learning for 3D printed multi-materials tissue-mimicking anatomical models. Mater. Des. 2021;211:1-11. https://doi.org/10.1016/j.matdes.2021.110125
24. Ulu FI, Mohan RV. Voxel and stereolithographic digital design framework in additive manufacturing: effects in a PolyJet printing process and relevant digital solutions. Prog. Addit. Manuf. 2021;6:653-662. https://doi.org/10.1007/s40964-021-00186-2
25. Calignano F, Giuffrida F, Galati M. Effect of the build orientation on the mechanical performance of polymeric parts produced by multi jet fusion and selective laser sintering. J. Manuf. Process. 2021;65:271-282. https://doi.org/10.1016/j.jmapro.2021.03.018
26. Taufik M, Jain PK. Laser assisted finishing process for improved surface finish of fused deposition modelled parts. J. Manuf. Processes 2017;30:161-177. https://doi.org/10.1016/j.jmapro.2017.09.020
27. Hanon MM, Ghaly A, Zsidai L, et al. Tribological characteristics of digital light processing (DLP) 3D printed graphene/resin composite: Influence of graphene presence and process settings. Mater. Des. 2022;218:1-17. https://doi.org/10.1016/j.matdes.2022.110718
28. Zhu Z, Majewski C. Understanding pore formation and the effect on mechanical properties of High Speed Sintered polyamide-12 parts: A focus on energy input. Mater. Des. 2020;194:1-16. https://doi.org/10.1016/j.matdes.2020.108937
29. Payami Golhin A, Srivastava C, Tingstad JF, et al. Additive manufacturing of multilayered polymer composites: Durability assessment. in Proceedings of the 20th European Conference on Composite Materials-Composites Meet Sustainability (Vol 1-6). Lausanne, Switzerland: EPFL Lausanne, Composite Construction Laboratory Switzerland 2022;https://doi.org/10.5075/epfl-298799_978-2-9701614-0-0
30. Gao H, Yang Z, Lin WS, et al. The Effect of Build Orientation on the Dimensional Accuracy of 3D-Printed Mandibular Complete Dentures Manufactured with a Multijet 3D Printer. J. Prosthodont. 2021;30:684-689. https://doi.org/10.1111/jopr.13330
31. Das SC, Ranganathan R, Murugan N. Effect of build orientation on the strength and cost of PolyJet 3D printed parts. Rapid Prototyping J. 2018;24:832-839. https://doi.org/10.1108/RPJ-08-2016-0137
32. Zelený P, Šafka J, Elkina I. The mechanical characteristics of 3D printed parts according to the build orientation, in Applied Mechanics and Materials. 2014; p. 381-386. https://doi.org/10.4028/www.scientific.net/AMM.474.381
33. Stratasys. Vero: Realistic, Multi-Color Prototypes in Less Time, in Stratasys Datasheet. 2022; p. 1-4.
34. Stratasys. 3D Printing with Pantone Colors. Stratasys Ltd. 2021; p. 1-6.
35. Iso. Geometrical product specifications (GPS) — Surface texture: Areal — Part 2: Terms, definitions and surface texture parameters, in ISO 25178-2:2021. International Organization for Standardization: Geneva, Switzerland 2021; p. 1-64.
36. Park JM, Jeon J, Koak JY, et al. Dimensional accuracy and surface characteristics of 3D-printed dental casts. J. Prosthet. Dent. 2021;126:427-437. https://doi.org/10.1016/j.prosdent.2020.07.008
37. Témun A, Mattsson L, Heikkilä I. Localizing micro-defects on rough metal surfaces. in 4M 2006 - Second International Conference on Multi-Material Micro Manufacture, W. Menz, S. Dimov, and B. Fillon, Editors., Elsevier: Oxford 2006; p. 169-172.
38. Lepš J, Šmilauer P. Multivariate analysis of ecological data using CANOCO. 2003: Cambridge university press.

**Biographies**

**Ali Payami Golhin** is a Ph.D. candidate at NTNU - Norwegian University of Science and Technology. He has research experience in the optical properties of structured surfaces as an ApPEARS fellow, which is funded by the Marie Sklodowska-Curie Actions under the Horizon Europe program. He has research experience in additive manufacturing, optical measurement, tribology, and surface science.

**Aditya Sole** received his doctoral degree from the Department of Computer Science at the Norwegian University of Science and Technology, Gjøvik, Norway in 2019 and currently is working as an Associate Professor at the computer science department at NTNU Gjøvik campus mainly focusing his research in the field of measuring, understanding, and reproduction of visual appearance and 3D printing. He is also involved in MSCA-ITN-ETN funded ApPEARS project as a deputy scientific co-ordinator and RCN-INTPART funded MANER project as a project manager.

**Are Strandlie** is a Professor of Physics at NTNU - Norwegian University of Science and Technology. His main research interests are data analysis methods for high-energy physics experiments and numerical methods for material physics. Recently, an increasing interest has emerged within cross-disciplinary topics, such as the link between appearance and material properties.

## Paper VIII:

A. P. Golhin, C. Srivastava, J. F. Tingstad, A. S. Sole, A. Strandlie, S. Grammatikos, Additive manufacturing of multilayered polymer composites: Durability assessment, the 20th European Conference on Composite Materials (ECCM20), École Polytechnique Fédérale de Lausanne (EFPL), Switzerland, 26-30 June 2022. https://doi.org/10.5075/epfl-298799_978-2-9701614-0-0

ECCM 20

26-30 JUNE 2022

LAUSANNE SWITZERLAND

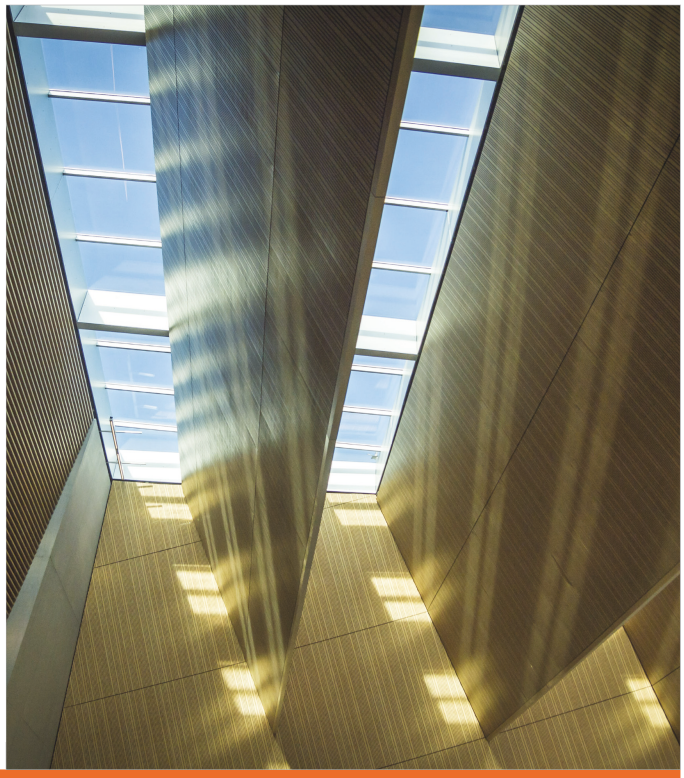

# Proceedings of the 20th European Conference on Composite Materials

## COMPOSITES MEET SUSTAINABILITY

## Vol 6 – Life Cycle Assessment

**Editors : Anastasios P. Vassilopoulos, Véronique Michaud**

Organized by : EPFL

Under the patronage of : CCLAB Composite Construction Laboratory; LPAC Laboratory for Processing of Advanced Composites; ESCM European Society for Composite Materials

ISBN: 978-2-9701614-0-0

DOI: 10.5075/epfl-298799_978-2-9701614-0-0

# ADDITIVE MANUFACTURING OF MULTILAYERED POLYMER COMPOSITES: DURABILITY ASSESSMENT

*Ali, Payami Golhin [a], Chaman, Srivastava [a], Jens Fossan, Tingstad [b], Aditya Suneel, Sole [b], Are, Strandlie [a], Sotirios, Grammatikos [a]*

a: Laboratory for Advanced and Sustainable Engineering Materials (ASEMlab), Department of Manufacturing and Civil Engineering, Norwegian University of Science and Technology, 2815 Gjøvik, Norway – ali.p.golhin@ntnu.no
b: Department of Computer Science, Norwegian University of Science and Technology, 2815 Gjøvik, Norway

**Abstract:** *This study examines the impact of additive manufacturing (AM) settings on the durability of 3D-printed polymer composite objects in terms of object color appearance and corresponding mechanical properties when subjected to simulated environmental conditions using accelerated aging. For this purpose, the AM pre-processing factors that influence the performance of the composite material, such as build platform position, color, and finishing configurations, are discussed. The experimental campaign was designed according to the Taguchi method to minimize the color difference and maximize the mechanical parameters. The results indicate that the best factor parameters for each performance characteristic differ following the design goal. Accordingly, black-on-white with a glossy-on-matte finish manufactured on the outer swath demonstrated the best color and mechanical performance fidelity, where the studied properties were not altered significantly due to aging.*

**Keywords:** PolyJet 3D printing, Accelerated aging, Structural degradation, Object appearance, Color change

## 1. Introduction

The new r-theta rotating build platform approach with a fixed print head was recently introduced as an alternative to traditional XYZ build platform 3D printers. The stated reasons for the disc-shaped build platform include increased reliability, easier maintenance, and a smaller footprint. However, the distinct layering mechanism and pattern compared to other AM machines necessitates new considerations in the design, appearance, and durability evaluation. In particular, a close inspection of the various assembled models printed on a rotary build platform reveals a few broken and glued small parts, indicating that the commercial PolyJet printer currently in use produces rigid and brittle parts with microscopic textures [1, 2]. In addition, while Material jetting (MJT)-printed products represent a desirable appearance, their durability is vital due to their prohibitive costs and environmental impact, especially for engineering applications [3].

The surface quality of 3D-printed objects can be affected by various process parameters. According to the Taguchi approach in the design of experiments, the process variables can be reduced, and the mean values must be adjusted to a target value. Orthogonal arrays are used to execute the tests and measure process quality. Thus, the signal-to-noise (S/N) ratios can

  doi:10.5075/epfl-298799_978-2-9701614-0-0 

assess the quality of the production process designed for regular application in testing, surgical planning, and tooling [4].

In this work, we present the results of an investigation into the optical and mechanical properties of 3D-printed bi-layer polymer specimens manufactured under various parametric conditions. The effect of three 3D printing parameters, including color, the position of the piece on the build platform (swath selection), and finishing on the mechanical and appearance variables, was investigated using the Taguchi methodology. The novelty of the work presented herein lies in the unique linkage between appearance and long-term mechanical properties, providing new insight into assessing the durability of AM products.

## 2. Materials and methods

A Stratasys J55 PolyJet 3D printer has been used to manufacture samples under different conditions. The characteristics of the VeroPureWhite (RGD837), VeroBlackPlus (RGD875), VeroCyan (RGD843), VeroYellow (RGD836), and VeroMagenta (RGD851) photo-resins (Stratasys Ltd., USA) are investigated in this study. These rigid polymers mainly consist low-viscosity acrylic oligomer, exo-1,7,7-trimethylbicyclo [2,2,1] hept-2-yl acrylate, (octahydro-4,7methano-1H-indenediyl) bis(methylene) diacrylate, and 4-(1-oxo-propenyl)-morpholine [5].

Parts were designed with a minimum thickness of 2 mm when a 1 mm white background was covered by 1 mm of colored material. The reference materials for color studies were the same as-printed samples before aging. For mechanical testings, the specimens were selected from the magenta samples printed on the middle swath and glossy on the glossy (GoG) finish. According to the datasheet for used photo-resins [6], the Vero materials family shares similar mechanical, thermal, and electrical properties.

To investigate the impact of 3D printing parameters on the variables, an L8(4^1 2^2) orthogonal array was chosen for three parameters of color, swath, and finishing process. As a result, 63 specimens were manufactured for 8 runs and as references. The process parameters and their levels are summarized in Table 1.

*Table 1: Taguchi factors and their levels.*

| | Factor | | |
|---|---|---|---|
| Run | Color | Swath | Finish |
| 1 | Cyan | Inner | Glossy on Glossy |
| 2 | Cyan | Outer | Glossy on Matte |
| 3 | Magenta | Inner | Glossy on Glossy |
| 4 | Magenta | Outer | Glossy on Matte |
| 5 | Yellow | Inner | Glossy on Matte |
| 6 | Yellow | Outer | Glossy on Glossy |
| 7 | Black | Inner | Glossy on Matte |
| 8 | Black | Outer | Glossy on Glossy |

  doi:10.5075/epfl-298799_978-2-9701614-0-0 

For the assessment of mechanical performance, tensile and viscoelastic testing were considered (Figure 1).

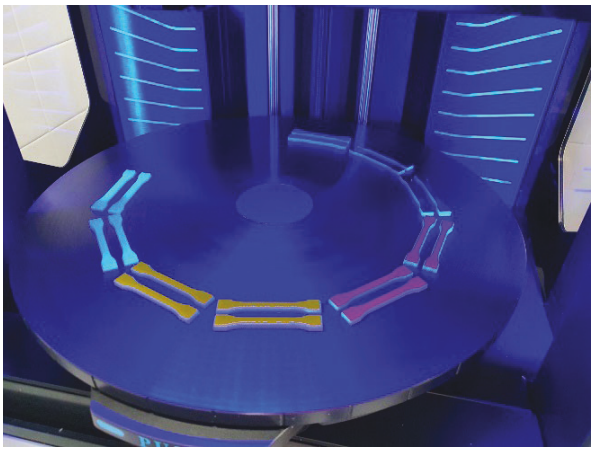

*Figure 1. Reference tensile specimen in the middle swath of the rotary build platform.*

To determine the durability of the polymeric specimens, the specimens were aged in a QUV chamber from QLab for a maximum duration of 2 weeks. The aging regime representing natural weathering was selected according to the ASTM G154 standard. The weathering cycle had a UV exposure at 0.8 W/m$^2$ for 6 hours at 60 °C, followed by condensation at 40 °C and spray at 24 °C, where the humidity is set at 60% and 100%, respectively.

A Konica Minolta CS-2000 tele-spectroradiometer (TSR) was used to measure appearance by recording radiance at the specimen surface within the 380-780 nm spectral range. The optical resolution and physical sampling intervals were 1 and 10 nm, respectively. The device was placed 50 cm in front of the target object, normal to the surface (Figure 2). The measurement field of view was set to 0.2 degrees to avoid error due to targeting areas covered by stains or dust. The surface of the 3D-printed specimen was studied using a 45°:0° viewing geometry according to CIE Publication 15.2 [7]. The spectral results of targets were calibrated using the standard spectralon white ceramic patch. The colorimetric values were calculated using the computational color science toolbox in MATLAB R2021a [8].

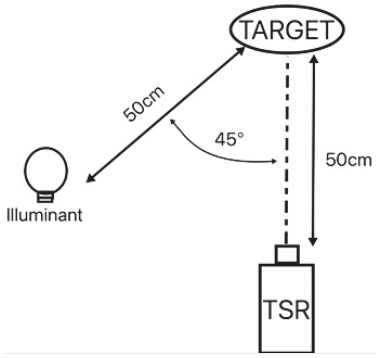


*Figure 2. Schematic view of the color appearance measurement setup.*

  doi:10.5075/epfl-298799_978-2-9701614-0-0 

Dynamic Mechanical Analysis (DMA) of the polymer coupons is carried out to determine the glass transition temperature ($T_g$) and the relative shift in the $T_g$ as a function of the aging time and temperature [9]. The test was performed on Discovery DMA 850 from TA instruments, as per the ASTM D4065 standard. The specimen dimensions were 60 × 13 × 3 $mm^3$. A temperature ramp test was performed at a heating rate of 2 °C. The test temperature range was set from 20°C to 95°C, which was below the degradation temperature of the material. The amplitude of the test was set to 20 µm with a frequency of 1 Hz. The maxima of the tan δ curve and its corresponding temperature are referred to as the $T_g$ reported in the paper.

To determine the tensile modulus and the strength of the polymer material as a function of aging duration, ISO 527-02 was used [10]. The dimensions of the dog bone specimens were 75 × 10 × 2 $mm^3$. Uniaxial tensile testing was performed on Instron 5966 universal testing machine, and the strain was measured using an AVE2 virtual extensometer. The loading rate was set to 2 mm/min. The force-displacement curves were used to determine the tensile chord modulus, and the ultimate tensile stress was chosen as the tensile strength of the bi-layer material.

## 3. Results and discussions

Figure 3 depicts the color difference for DMA coupons after two weeks of accelerated weathering. According to CIEDE2000 colorimetric difference [7], in Figure 3a, magenta samples are notably altered in color compared to reference samples. On the other hand, cyan and yellow samples represent noticeable color differences compared to the control parts and at a lower level. Similar advantages for cyan color over red feedstock were described before for fused deposition modeling (FDM) [11]. In magenta and yellow samples, significantly higher color differences were observed for the GoG samples.

On the other hand, cyan and black objects respond in reverse as their average CIEDE2000 has slightly decreased. The redness (a*) and yellowness (b*) shifts in the CIE L*a*b* values at a constant lightness of 90 suggest yellower yellow samples, less red magenta samples, and bluer/greener cyan samples after two weeks of aging (Figure 3b). The color of the black objects did not change enough to be recognized without measurement.

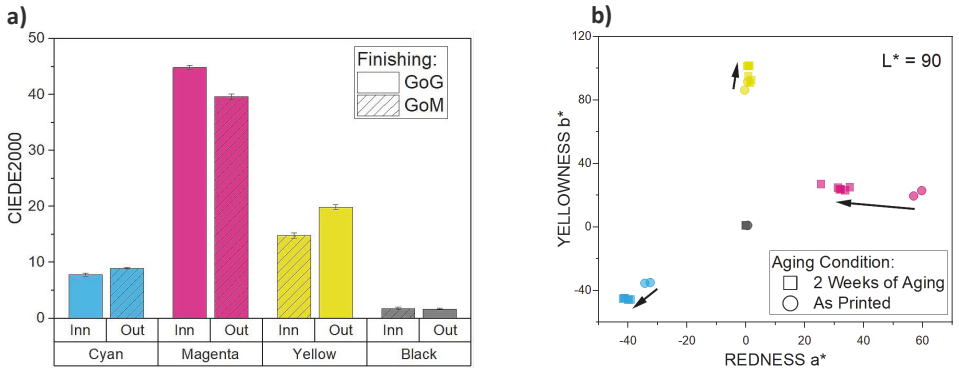


*Figure 3. a) CIEDE2000 color difference and associated root mean square error (RMSE) bars, and b) shift in the a*b* values after the aging process.*

  doi:10.5075/epfl-298799_978-2-9701614-0-0 published under CC BY-NC 4.0 license

The DMA coupons after two weeks of weathering are depicted in Figure 4. In magenta samples, the marginal dark-red area represents the original color obscured by the sample holders. As seen from the edges, the color differences for magenta samples were significant, while the color differences for cyan and yellow pieces were barely noticeable after aging.

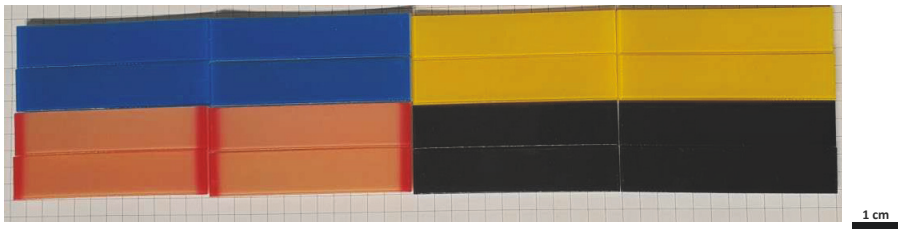


*Figure 4. DMA specimens after two weeks of weathering exposure.*

Figure 5a depicts representative stress-strain curves for each type of specimen aged and tested. The results are compared with the reference specimens before aging. It is observed that the tensile modulus of the polymer specimen increases during the 2 weeks aging regime, which complements the findings from the DMA analysis and in conjunction with the stiffness increase. The table shown in Figure 5b populates the results for glass transition temperature measurements from the tan $\delta$ curve from the DMA analysis. It is observed that the glass transition temperature of the polymeric material has increased significantly to a range of 80-84°C for each specimen, where the reference value of 53°C is taken from the reference manual for the feedstock material. The sharp increase in the change in the $T_g$ of the material is very anomalous. This can be attributed to the material being cured during 3D printing, pre-aging due to storage, and weathering process, where the $T_g$ increased slowly.

**a)**

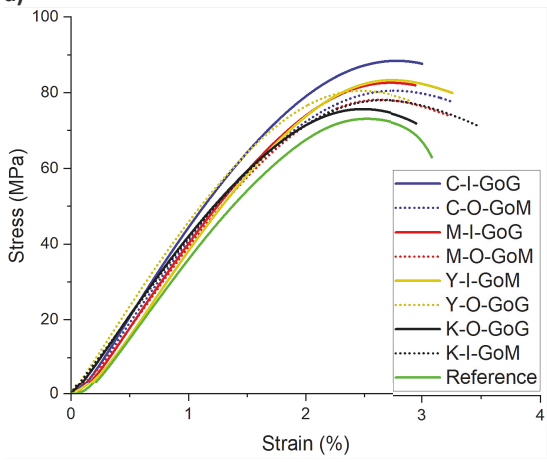


**b)**

| Sample | Elastic Modulus [GPa] | $T_g$ [°C] |
|---|---|---|
| Reference | 3.99 ± 0.03 | 73.29 |
| C-I-GoG | 4.51 ± 0.12 | 83.18 |
| C-O-GoM | 4.15 ± 0.20 | 83.00 |
| M-I-GoG | 4.23 ± 0.13 | 82.88 |
| M-O-GoM | 4.09 ± 0.08 | 80.55 |
| Y-I-GoM | 4.29 ± 0.11 | 80.88 |
| Y-O-GoG | 4.37 ± 0.07 | 81.30 |
| K-I-GoM | 4.00 ± 0.08 | 80.36 |
| K-O-GoG | 4.07 ± 0.14 | 81.67 |

*Figure 5. a) Stress-strain curves for tensile specimens, and b) E modulus and $T_g$ results; C: Cyan, M: Magenta, Y: Yellow, K: Black, I: Inner Swath, O: Outer Swath, GoG: Glossy on Glossy finish, GoM: Glossy on Matte finish.*

  doi:10.5075/epfl-298799_978-2-9701614-0-0 

According to the S/N ratio plots in Figure 6a, color, as expected, had the most significant influence on the color difference. In contrast, swath and finishing had no considerable impact on this variable. However, after two weeks of weathering, the choice of outer swath and GoG finish resulted in more stable color difference calculations (Figure 6 b)). In terms of color, black and then cyan samples demonstrated significantly more reliable color fidelity than magenta and yellow samples after aging.

On the other hand, S/N ratio plots for mechanical properties (Figures 6c and d) revealed, in addition to color, that the swath and finishing significantly influenced the elastic modulus and $T_g$ of the studied samples. Accordingly, the inner swath and GoG finish resulted in higher elastic modulus and $T_g$. Cyan provided higher E and $T_g$ than black, while magenta and yellow samples demonstrated unstable behavior in mechanical testing. The ultraviolet (UV) absorbance of samples during the weathering test can explain the possible effect of post-curing behind these mechanical behaviors of the studied specimens, resulting in more rigid materials with altered mechanical properties and color appearances.

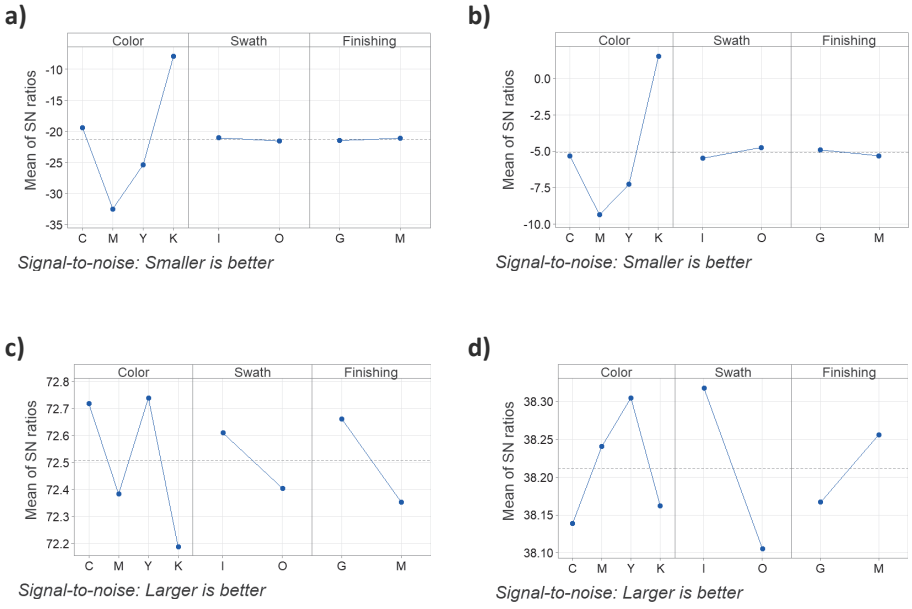


*Figure 6. Main effects S/N plots for a) CIEDE2000, b) RMSE for CIEDE2000, c) Elastic modulus, and d) $T_g$.*

  doi:10.5075/epfl-298799_978-2-9701614-0-0 

4. Camposeco-Negrete C. Optimization of FDM parameters for improving part quality, productivity and sustainability of the process using Taguchi methodology and desirability approach. Prog Addit Manuf. 2020.
5. Tee YL, Peng C, Pille P, Leary M, Tran P. PolyJet 3D printing of composite materials: experimental and modelling approach. Jom. 2020;72(3):1105-17.
6. Vero: Realistic, Multi-Color Prototypes in Less Time. 2022.
7. l'Éclairage CId. Colorimetry CIE 015:2004: Commission Internationale de l'Éclairage; 2004. p. 1-82.
8. Westland S, Ripamonti C, Cheung V. Computational colour science using MATLAB: John Wiley & Sons; 2012.
9. Das SC, Paul D, Grammatikos SA, Siddiquee MAB, Papatzani S, Koralli P, et al. Effect of stacking sequence on the performance of hybrid natural/synthetic fiber reinforced polymer composite laminates. Compos Struct. 2021;276.
10. Plastics - Determination of tensile properties. Part 2: Test conditions for moulding and extrusion plastics: International Organization for Standardization ISO/TC 61/SC 2 Mechanical behavior; 2012.
11. Payami Golhin A, Strandlie A, John Green P. The Influence of Wedge Angle, Feedstock Color, and Infill Density on the Color Difference of FDM Objects. J Imaging Sci Technol. 2021;65(5):050408-1–-15.

  doi:10.5075/epfl-298799_978-2-9701614-0-0 

## Paper IX:

A. P. Golhin, A. Strandlie, A. S. Sole, Evaluation of surface texture in material jetting, euspen's 23rd International Conference & Exhibition (ICE 2023), Technical University of Denmark (DTU), Copenhagen, Denmark, 12-16 June 2023, Accepted

euspen's 23rd International Conference & Exhibition, Copenhagen, DK, June 2023
www.euspen.eu

# Evaluation of surface roughness and periodical layers in material jetting

Ali Payami Golhin[1,*], Aditya Suneel Sole[2], Are Strandlie[1]

[1] *Department of Manufacturing and Civil Engineering, Norwegian University of Science and Technology, 2815 Gjøvik, Norway*
[2] *Department of Computer Science, Norwegian University of Science and Technology, 2815 Gjøvik, Norway*

**ali.p.golhin@ntnu.no*

**Abstract**

Studying surface texture and morphology is essential to developing Additive Manufacturing (AM). Assessing the quality of part layer compounds in the process will assist with adjusting process parameters for optimal part quality in the manufacturing process. For this purpose, Material Jetting (MJT) system has been used to manufacture objects at various platform locations (swathes) to examine the surface morphology, including surface roughness and texture. Due to the rotating disc used as the build platform, the studied parts showed a different surface morphology from parts printed using other material jetting machines. To study the surface texture, we generated high-resolution surface mesh grids after scanning the surface using a coordinate measuring machine (CMM) and a 3D scanner. The surface topography was decomposed into scan lines using a fast Fourier transform (FFT). The power spectral density (PSD) of a surface was calculated and compared to roughness to discuss the surface topography. Signal processing demonstrated that different textures can be fabricated by tuning the printing position conditions. As a result of determining the surface texture and roughness characteristics in conjunction with 3D printing parameters in the design process, it was possible to categorize the build platform regions based on their surface textures.

**Keywords:** Additive manufacturing, Material Jetting, Texture, Object appearance

## 1. Introduction

Material Jetting (MJT), as reported in the ISO/ASTM 52900:2015, fabricates objects by jetting materials onto a build platform in either a Drop on Demand (DOD) or continuous manner. The jetting process is similar to that of a standard inkjet printer. PolyJet, Multi Jet Printing (MJP), Objet, and XJet's NanoParticle Jetting (NPJ) are the fundamental processes in MJT. Thanks to high-resolution MJT 3D printers, manufactured objects show detailed appearance attributes, such as texture, color, gloss, and gonio-chromatic effects [1, 2].

MJT-based products not only depose resins in CMYKW (cyan, magenta, yellow, black, and white) but can also print different materials. It is now possible to 3D print MJT materials with vastly different properties, such as a rigid, glassy polymer and a soft, rubbery material with elastic moduli that differ by nearly three orders of magnitude at room temperature [1]. Therefore, MJT has been adopted to produce a wide range of prototypes with complex shapes and appearances, as well as functional polymers such as scaffolds for tissue engineering, multi-material structures, and memory shape polymers for 4D printing [3]. MJT objects are semi-translucent, complicated in appearance, and represent a mixture of textures by applying ink in layers [2]. Thus, the detailed properties are difficult to capture by conventional methods. Still, it is possible to achieve satisfying results by decreasing the influence of errors in the measurement process and following a reproducible workfellow.

Some of the MJT printers, such as the Stratasys J55, use a rotary disc as the build platform for 3D printing. The rotating tray decreases the size of the MJT 3D printer, which allows it to be used at home or in an office due to the reduced dimensions. However, it impacts surface morphology and appearance. The spatial frequency components of additively manufactured surfaces include texture profile, form, waviness, and roughness [4]. Each of these components has a unique origin and influences the appearance and functionality of the product distinctly. The waviness may indicate machine vibration. The form is typically the result of poor manufacturing system performance, and the profile can be identified by layer-by-layer manufacturing. In contrast, surface irregularities caused by printing and material removal errors generate roughness [5]. Considering surface morphology is essential in creating functional surfaces such as super-hydrophobic and super-hydrophilic surfaces, surfaces with structural colors, and bio-inspired/bio-mimetic surfaces [6]. Accordingly, the role of surface textures in 3D-printed polymers has been studied and addressed for tribological behavior [7] and biomechanical [8].

Although the appearance of 3D-printed parts is qualitative, subjective, and controversial [9, 10], instrumental texture measurements can be used to indirectly evaluate the performance of AM methods based on their topography as a quality control concept [11].

The coordinate-measuring machine (CMM) is a valuable tool used to measure the geometrical characteristics of physical objects [12]. Holmberg et al. [13] investigated the changes in surface morphologies during machining using optical microscopy and full width at half maximum (FWHM) assessment. Texture evaluation enables the reconstruction of AM profile and the execution of appearance evaluation and data registration. Fast Fourier Transform (FFT) analysis filters out high-frequency waves to uncover the underlying signal. Calta et al. [14] employed the 1D FFT of the line profile of track height to measure the periodicity of surface characteristics, ignoring the start and end of the scanning track to eliminate inaccuracies produced by boundary effects.

In this context, the structure of the study aims to present a novel approach to studying surface morphology by investigating texture profiles and surface roughness on MJT surfaces. The procedure described in the next section as the experimental procedure, involves 3D scanning, optical profilometry, and CMM testing. A rotary MJT system has been used to manufacture objects at different platform locations (swathes). The outcome of the experiments has been presented in the results and discussion section. It opens opportunities for high-quality structures through high-fidelity printing and reduces the post-processing requirement, as discussed in the conclusion section.

## 2. Experimental procedure

Specimens were created using acrylate-based materials and photoinitiators in a Stratasys J55 3D printer. A J55 placement zone comprises three equal-width areas: inner, middle, and outer (see Figure 1A). For optimal placement and faster construction, the innermost side of the rotary disc should be used first. The influence of printing location (swath) on the texture formation is investigated using a full factorial experimental design. For this purpose, nine specimens, including three parts for each swath, were manufactured in sizes of 60 × 13 × 3.5 mm for texture evaluation and 3D scanning, as well as 40 × 30 × 3.5 mm for roughness measurements. White as-printed parts with a glossy on matte (GoM) finish between the colored and white layer were selected for 3D scanning (Figure 1B).

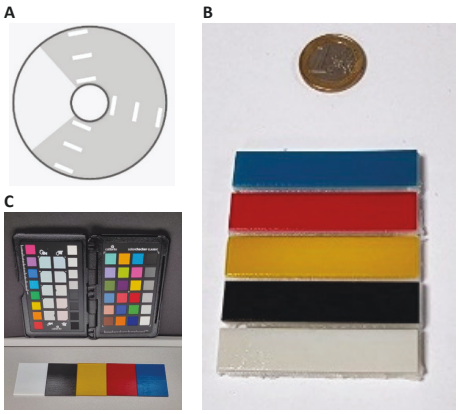


**Figure 1A.** Rotary build platform and parts positions on three different swaths, **B.** as-printed specimens for texture evaluation, and **C.** trial specimens for 3D scanning (scale bar 10 mm).

Specimens have been scanned in width (Z-axis) and length (X-axis) directions (Figure 2B) using a ZEISS DuraMax CMM machine equipped with ZEISS VAST XXT tactile scanning probe and ZEISS CALYPSO 2021 software. The measurement was conducted with a step width of 20 µm, a probe radius of 1.5 mm, and 2.4 µm accuracy in the measuring length of 30 mm in XYZ directions. A desktop 3D scanner (AutoScan Inspec, Shining 3D) was used in a dimmed condition. The samples were mounted on a turntable and rotated eight times, once every 45°, to provide a 360° panorama. Using a projector that produced structured light patterns allowed a scanning accuracy of 10 µm. Two 5.0-megapixel CCD cameras are installed in the scanner and used to measure distorted sizes. Multiple scans from different angles are used to compile the registered point cloud. After combining the scans in UltraScan 2022, the model was exported in OBJ format to SolidWorks Visualize (v2021). A Keyence VH-ZST microscope (20X to 2000X) is used to measure the surface roughness and display surface morphology.

Results from the CMM were compared with the object's 3D coordinates in the computer-aided design (CAD) part. Once the CMM data was gained, it was processed in Gwyddion (v2.59) to calculate the layer heights, thicknesses, and topography. To investigate the height distribution, we employed FWHM, the width measured at the half level between the peak of the line and the continuum, using the Gauss function to fit the height distribution curve. OriginPro v9.5 was employed for data analysis.

ISO 11562 [15] specifies the use of a 1D Gaussian filter to extract surface contour reference lines by a weight function, *s(x)*, defined as follows

$$s(\mathrm{x}) = \frac{1}{\alpha\lambda_c}\exp\left(-\pi\left(\frac{x}{\alpha\lambda_c}\right)^2\right) \qquad (1)$$

where *x* is a spatial domain variable as the distance from the maximum of *s(x)*, $\lambda_c$ is the cutoff wavelength, and the constant value of $\alpha$ delivers 50 % transmission characteristic at $\lambda_c$. The equations below show that the power output is normalized as the space-integral squared amplitude (TISA), where time represents space in standard annotations.

$$P_{xx}\left(e^{j\omega}\right) = \sum_{m=-\infty}^{\infty} r_{xx}(m)e^{-j\omega m} \qquad (2)$$

$$TISA\ (Power) = \frac{\Delta t\left(R_e{}^2 + I_m{}^2\right)}{n} \qquad (3)$$

where $P_{xx}\left(e^{j\omega}\right)$ is the spectrum or power density (PSD), $r_{xx}(m)$ acts as the auto-correlation function for the response signal, $\Delta t$ is the sampling interval, $R_e$ and $I_m$ are the real and imaginary elements of the transform data, and *n* is considered as the length of the response sequence. The following function is used to mitigate leakage.

$$N/\sum_{n=0}^{N-1} w(n)^2 \qquad (4)$$

where $w(n) = 1$ for $0 \le n \le N-1$, and 0 for the other range.

## 3. Results and Discussion

J55 printers produce rigid, brittle 3D-manufactured components that are slightly bent over a short period [2]. As shown in our previous study [16], a closer examination of the several built models reveals some minor damage and glue to the pieces. As shown in Figure 2A, the semicircle pattern is visible in the surface texture images associated with the 3D-printed layers. Therefore, the scanning strategy is crucial for establishing the appropriate traceability of measurements on CMMs (Figure 2B).

Figure 2C depicts the 3D view of the printed surface after rasterization. Analysis of the XYZ coordination indicates that the distribution of Z heights of the surface asperities is less than 17 µm. As a result of the slight bending of the parts that typically occurs a few days after printing, which was observed in our previous work [9, 16], there is a concentration of missed scanned meshes in the middle of the models. This can be attributed to possible post-curing exposure to natural light.

High-resolution optical images of the specimens can be seen in Figure 3. The glossy and translucent appearance of MJT products, along with the curvature resulting from UV absorbance during storage, make it difficult to study them using

an optical profilometer (see Figure 3A). The mean parameters of the area roughness in Table 1 were calculated based on the surface topography analysis on a region of 2.5 × 2.5 (mm), as shown in Figure 3B.

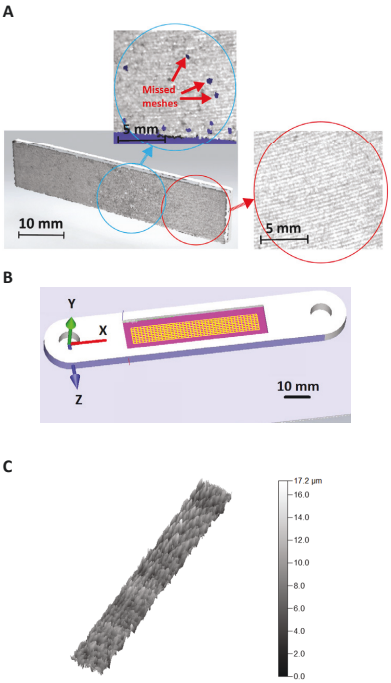


**Figure 2A.** 3D-scanned model of the printed parts, **B.** CMM setup for the contact scanning strategy (yellow grid) on the scanned area (purple area). A specific sample holder (the piece in white) is 3D-printed to decrease the bending effect through the length of the specimens. **C.** 3D model of the surface morphology through the CMM-scanned area, with the exaggerated scale bars showing the height distributions over height direction.

According to Table 1, MJT can produce an exceptionally smooth surface. The surface roughness was influenced by the location of printing on the build platform. The smoothest surface was obtained in the middle swath ($S_a$=1.02 µm), followed by the outer ($S_a$=1.16 µm) and the inner ($S_a$=1.65 µm) swaths. Due to the slightly positive skewness ($S_{sk}$) values of all specimens, there were more peaks and asperities than valleys on the surfaces. As a result of high kurtosis ($S_{ku}$), these profile peaks were slightly sharp.

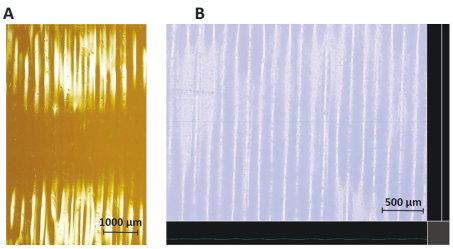


**Figure 3A.** Periodical layers as seen under the optical microscope, and **B.** selected surface area for roughness measurement.

**Table 1** Mean surface roughness results

| | Area roughness parameter* | | | |
|---|---|---|---|---|
| **Swath** | **$S_a$ (µm)** | **$S_q$ (µm)** | **$S_{sk}$** | **$S_{ku}$** |
| **Inner** | 1.65 | 2.21 | 0.15 | 3.2 |
| **Middle** | 1.02 | 1.42 | 0.03 | 2.2 |
| **Outer** | 1.16 | 1.90 | 0.08 | 2.9 |

* $S_a$: Height deviations from the Mean Reference Plane of the measurement area (A); $S_q$: Root mean square of surface heights; $S_{sk}$: the skewness and $S_{ku}$: the kurtosis of the surface

Figure 4A depicts the FFT analysis applied to height grids and a deeper look at additively built layers generated using CMM data (Z height). It indicates FWHM and the mean layer height of different swaths display a meaningful correlation, in which FWHM (3.8 µm) and the minimum arithmetic means of layer height (5.7 µm) were within the middle swath. Figure 4B shows clear peaks for the averaged data, validating the periodicity of the layers and their related surface texture in the investigated parts. Averaging the distances between the PSD peaks gives an arithmetic mean of the periodic gap between layers. According to Figure 4C, as the radius of the build location increases, thinner layers result from 305 µm to 303 µm. An increased centrifugal force on the outer region of the disc allows the printhead to build closer layers as it moves from the inner to the outer edge of the tray. However, CMM results for mean layer height and FWHM in Figure 4C followed the same trend as the roughness measurement results in Table 1.

## 4. Conclusions

This morphology study was conducted on the surface roughness and texture of polymer parts manufactured by material jetting technology. It provided a method for determining the surface morphology and appearance of components printed on various areas of a rotary disc tray as a build platform. CMM results indicated the minimum arithmetic mean (5.7 µm) and maximum FWHM (3.8 µm) of Z height values were within the middle swath, indicating a meaningful trend in the swath selection. The optical profilometry surface roughness results followed the same trend, with the lowest roughness observed in the middle swath and the roughest in the inner swath. The PSD results confirmed the periodicity of the layers and determined their widths. As the print head moved from the inner to the outer area, the thickness of the layer decreased from 305 µm to 303 µm, and closer layers were printed. This can be due to increased centrifugal forces along the radius of the disc. Accordingly, the middle swath on the build platform produced smoother surfaces. However, it required more time to print in this area than in the inner swath. Implementing 3D printing technology under optimized conditions resulted in parts with enhanced surface quality in the middle swath. Since the MJT technology with a rotary tray now makes it possible to create prototypes for home and office use, these findings can lead to a better knowledge of the surface texture in these printers and fewer post-processing operations.


## Acknowledgments

The authors appreciate the support provided by Dr. Andreas Kraushaar (Fogra Forschungsinstitut für Medientechnologien e.V.) and Donatela Saric (NTNU & Fogra) for the roughness measurement. This work is funded by the European Union's H2020 research and innovation program under the Marie Skłodowska-Curie grant agreement No. 814158 "ApPEARS - Appearance Printing - European Advanced Research School".

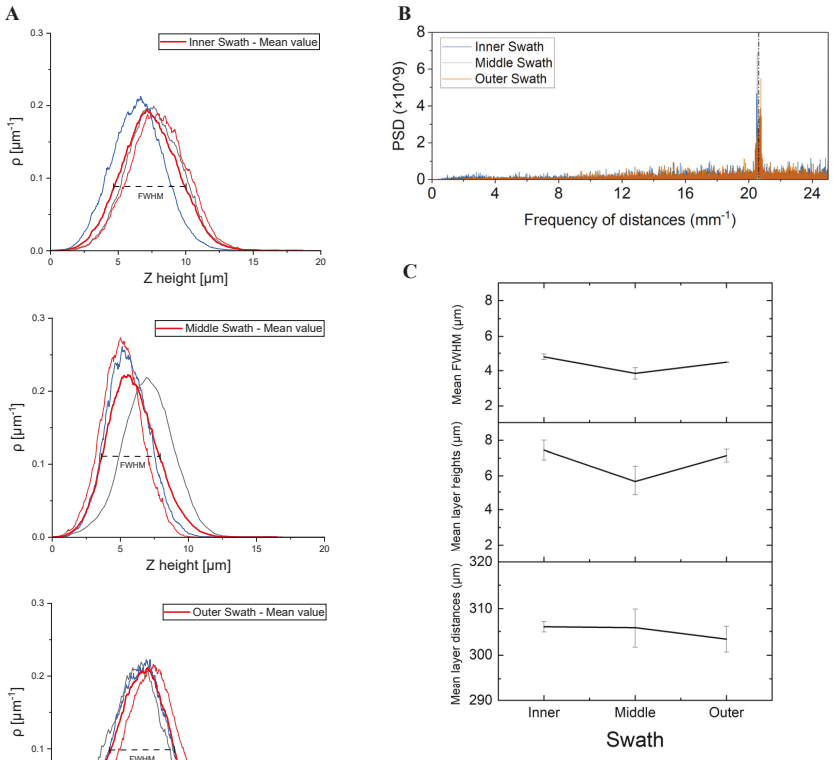


**Figure 4A.** Z height distribution profile for parts manufactured at different swaths, **B.** PSD results over the scanned profile, and **C.** periodic texture characteristics.

## References


[1] De Noni L, Zorzetto L, Briatico-Vangosa F, et al. 2022 Modelling the interphase of 3D printed photo-cured polymers *Compos. B. Eng.* **234** 109737

[2] Golhin AP, Sole AS, Strandlie A 2023 Color appearance in rotational material jetting *Int. J. Adv. Manuf. Technol.* **124** 1183

[3] Khoo ZX, Teoh JEM, Liu Y, et al. 2015 3D printing of smart materials: A review on recent progresses in 4D printing *Virtual Phys. Prototyping* **10** 103

[4] Payami Golhin A 2021 Generation of micro-and nano-textured surfaces *European Commission: Brussels*. 1

[5] Du S, Liu C, Huang D 2015 A shearlet-based separation method of 3D engineering surface using high definition metrology *Precis. Eng.* **40** 55

[6] Afshar-Mohajer M, Zou M 2020 Multi-Scale In Situ Tribological Studies of Surfaces with 3D Textures Fabricated via Two-Photon Lithography and Replica Molding *Adv. Mater. Interfaces* **7** 2000299

[7] Luo M, Huang S, Man Z, et al. 2022 Tribological behaviour of fused deposition modelling printed short carbon fibre reinforced nylon composites with surface textures under dry and water lubricated conditions *Friction* **10** 2045

[8] Lindsay C, Ruppert D, Abumoussa S, et al. 2020 Benefits of additive manufacturing and micro and nano surface texture modifications on mechanical strength and infection resistance of skin–implant interfaces in rats. *J. Biomater. Appl* **0** 1

[9] Payami Golhin A, Srivastava C, Tingstad JF, et al. 2022 Additive manufacturing of multilayered polymer composites: Durability assessment *Proceedings of the 20th European Conference on Composite Materials-Composites Meet Sustainability* EPFL Lausanne, Switzerland **6**

[10] Yuan J, Chen G, Li H, et al. 2021 Accurate and Computational: A review of color reproduction in Full-color 3D printing *Mater. Des.* **209** 1

[11] Payami Golhin A, Strandlie A, John Green P 2021 The influence of wedge angle, feedstock color, and infill density on the color difference of FDM objects. *J. Imaging Sci. Technol.* **65** 1

[12] Anadioti E, Kane B, Zhang Y, et al. 2022 Accuracy of Dental and Industrial 3D Printers *J. Prosthodont.* **31** 30

[13] Holmberg J, Berglund J, Wretland A, et al. 2019 Evaluation of surface integrity after high energy machining with EDM, laser beam machining and abrasive water jet machining of alloy 718 *Int. J. Adv. Manuf. Technol.* **100** 1575

[14] Calta NP, Martin AA, Hammons JA, et al. 2020 Pressure dependence of the laser-metal interaction under laser powder bed fusion conditions probed by in situ X-ray imaging *Addit. Manuf.* **32** 101084

[15] Geometrical product specifications (GPS) — Surface texture: Areal — Part 2: Terms, definitions and surface texture parameters 2012 *ISO* **25178-2** 1

[16] Payami Golhin A, Srivastava C, Strandlie A, et al. 2023 Effects of accelerated aging on the appearance and mechanical performance of materials jetting products *Mater. Des.* In Press 111863

ISBN 978-82-326-7060-4 (printed ver.)
ISBN 978-82-326-7059-8 (electronic ver.)
ISSN 1503-8181 (printed ver.)
ISSN 2703-8084 (online ver.)





NTNU

Norwegian University of
Science and Technology